3D FE SIMULATION OF THE WELDING PROCESS TO OPTIMISE RESIDUAL STRESS PROFILES IN COMPLEX GEOMETRIES

WEI JIANG BSc., MSc.

A thesis submitted in partial fulfilment of the
requirements of the University of Wolverhampton
for the degree of Doctor of Philosophy

April 2006

Signature....Jiang.....

Date..12/04/2006.....

ACKNOWLEDGEMENTS

I would like to express my sincere gratitude to Dr. K. Yahiaoui for his careful supervision and continuous support and advice throughout the project. I am very grateful to have had the opportunity to learn the advanced finite element technique to reshape my future research direction.

I would like to give my thanks to co-supervisors Dr. T. Laoui and Professor F.R. Hall for their help and encouragement.

I would like to thank all the colleagues for their friendship, collaboration and support over the past three years. Further thanks should go to Mr. S. J. Boyle for his technical assistance. Thanks are also addressed to the staff of the Research Institute for Advanced Technology and the School of Engineering and the Built Environment for their friendliness and support. Thanks are also due to IT services for the pleasant work environment.

The author gratefully acknowledges the financial support from the School of Engineering and the Built Environment, University of Wolverhampton.

Finally, I would like to express my appreciation and love to my family. Without their patience and encouragement, I would not have been able to successfully complete this dissertation. Any credit given to me for the success of this work equally belongs to them.

ABSTRACT

Welded, thick-walled, tee branch junctions are complex piping components commonly used in the nuclear power and petrochemical industries. Owing to the relatively large wall thickness, weldments are often constructed in several passes. Each successive pass alters the stresses caused by previous passes. Consequently, complex residual stresses of significant levels can develop at the welding stage. Tensile welding residual stresses can, in combination with operating stresses, lead structures to be prone to catastrophic premature failure. It is most desirable that residual stresses be predicted and optimized well in advance of welding execution.

This dissertation documents the development of a full 3D FE model for multipass welding simulation. A generalized plane strain model was first developed. Modelling techniques, including standard versus contact boundary conditions, sequentially versus fully coupled models, were investigated. A 3D sequentially coupled model with standard constraint was then proposed and applied to multipass butt-welded plates and pipes for validation. Good agreements between the predictions and independent experimental measurements have been obtained.

To extend the work to thick and intricate welded structures, a newly developed all-hexahedral meshing technique was employed to mesh the complex intersection area in a tee branch junction. The moving heat source and filler material deposition were simulated by assigning reactivated elements with a volumetric heat flux progressing along the weld path. Temperature dependent material properties, latent heat and large deformation were considered. Detailed temperature and residual stress distributions have been reported.

The correlations between welding parameters and residual stresses have been established and issues concerning residual stress profile optimization have been addressed via extensive parametric studies. The parameters investigated included the number of passes, welding sequence, heat input, preheat and interpass temperature and cooling rate. Cooling rate and interpass temperature were found to be the most important parameters affecting residual stresses. The model can be applicable to other multipass welded complex geometries for residual stress prediction and optimization.

TABLE OF CONTENTS

LIST OF FIGURES

LIST OF TABLES

NOMENCLATURE

Symbols	Definition	Units
c	Specific heat	kJ/kg°C
k_x, k_y, k_z,	Thermal conductivities in the coordinate directions	W/m°C
k	Thermal conductivity	W/m°C
h	Convective heat transfer coefficient	W/m^2°C
I	Welding current	A
n_x, n_y, n_z	Direction cosines of the outward drawn normal to the boundary	
Q	Net heat generation rate per unit volume	$J/s \cdot m^3$
T	Current temperature	°C
T_a	Ambient temperature	°C
T_m	Melting temperature	°C
t	Time	s
U	Welding voltage	V
v	Travel speed of the heat source	mm/s
α	Linear coefficient of thermal expansion	1/°C
ε	True total strain	
ε_{nom}	Nominal strain	
ε^{el}	True elastic strain	
ε^{pl}	True plastic strain	
$d\varepsilon^{total}$	Total strain increment	
$d\varepsilon^{elastic}$	Elastic strain increment	
$d\varepsilon^{plastic}$	Plastic strain increment	
$d\varepsilon^{thermal}$	Thermal strain increment	
$d\varepsilon^{creep}$	Strain increment associated with creep	
η	Arc efficiency	
$\kappa=k/c\rho$	Thermal diffusivity	m^2/s
ν	Poisson's ratio	
ρ	Density	kg/m^3
σ	True stress	MPa
σ_{nom}	Nominal stress	MPa
σ_y	Room temperature yield stress	MPa

ABBREVIATIONS

Abbreviations	Descriptions
DOF	Degrees of Freedom
FE	Finite element
GMAW	Gas metal arc welding
GTAW	Gas tungsten arc welding
HAZ	Heat affected zone
MIG	Metal inert gas
MMA	Manual metal arc
SAW	Submerged arc welding
SMAW	Shielded metal arc welding
TIG	Tungsten inert gas
1D	One dimensional
2D	Two dimensional
3D	Three dimensional

Chapter 1 Introduction

Welded, thick walled, tee branch junctions (or cylinder-cylinder intersections) are complex piping components commonly used in the nuclear power and in oil or gas transport systems, amongst others. Owing to their relatively large wall thickness, weldments are often constructed in several passes (Chuse 1977). Each successive pass alters the temperatures, stresses and distortions caused by previous passes. Consequently, complex residual stresses of significant levels can develop at the welding stage (Gunnert 1955). Tensile welding residual stresses can, in combination with operating stresses, lead structures to be prone to catastrophic premature failure by fatigue and/or fracture. The structural integrity and safety of such welded structures depends largely on the performance of the welded joints. It is thus most desirable that residual stresses be predicted and optimized well in advance of welding execution.

Previously, welding residual stresses were only assessed by experimental methods (Masubuchi 1980). However, experimental residual stress measurements have practical limitations. First, they are expensive and require special equipments. Methods, such as hole-drilling are also destructive. Second, even when non-destructive, e.g. X-ray diffraction and ultrasonic techniques, residual stresses are measured only at discrete locations near the weld surface. Such data not only tend to show significant scatter but also spatial variations. Consequently, it is impossible for any experimental technique to give a complete mapping of 3D residual stress distributions. Moreover, the results obtained from one particular weldment may not be directly applicable to other weldments.

With modern computing facilities, the finite element (FE) technique has become an effective tool for predicting and assessing welding residual stresses. The FE approach not only provides complete 3D residual stress profiles which are difficult to obtain by measurement, but also allows parametric studies for residual stress optimization. For large, heavy welded structures, where post weld heat treatment procedures to relieve residual stresses are not possible, there is no alternative but to opt for such numerical analyses and optimization procedures. Moreover, residual stress predictions using

well-established and proven commercial codes can be readily transferred to industrial applications. As a matter of fact, it is expected that, in future, FE simulations will play a more pivotal role in process analysis, prediction, control and optimization.

Welding process simulation requires a high degree of expertise in interdisciplinary applied sciences, including heat transfer, material science, welding process physics, computational mechanics and geometrical modelling. To successfully undertake welding simulation, several major aspects of the problem need to be carefully addressed, i.e. geometric modelling and multipass weld preparations, correct description of material properties involved in the process, and accurate coding of the thermomechanical phenomena associated with welding.

In order to develop a realistic and accurate full 3D continuum model to predict residual stress distributions in complex multipass welded geometries, the development of a computational model was undertaken into three stages, using recent advanced features of ABAQUS (Hibbitt, Karlsson & Sorensen 2002) code. Firstly, a generalized plane strain model was developed and applied to multipass butt-welded thick plates. Various factors, including standard versus contact boundary conditions, sequentially versus fully coupled modelling, have been investigated and evaluated. Based on the comparison of simulation results and computational costs, the sequentially coupled model with standard constraint was selected for further investigation. Secondly, full 3D sequentially coupled thermomechanical models were developed and applied to butt-welded mild carbon steel plates and stainless steel pipes for validation. The simulation parameters were identical to those used in the experiments reported in the literature. The simulation results of temperatures and residual stresses were compared with independently obtained experimental measurements and predicted data from generalized plane strain and axisymmetric models. Good agreements between experimental data and predictions from the current model have been obtained. Finally, the model was extended to a large, multipass, circumferentially fillet-welded, stainless steel tee branch junction. The latter is a much more involved geometry for residual stress prediction.

A newly developed all-hexahedral meshing technique was employed to mesh the complex 'saddle like' geometry with a graded mesh suitable for multipass welding

simulation. The element removal/reactivation technique was used to simulate material deposition. Temperature dependent material properties, latent heat and large deformation were taken into account. The temperature history, thermal stress evolution and residual stress distribution at the branch and run cross section, as well as along the weldline circumferentially around the run and branch pipe were investigated.

The model will eventually not only predict residual stress distribution at the preliminary design stage but also help improve welding procedures by optimizing residual stress profiles through parametric studies. The parameters investigated included number of passes, welding sequence, heat input, preheat temperature, interpass temperature and cooling rate. It was found that the interpass temperature and cooling rate are the most sensitive parameters affecting the magnitude and distribution of residual stresses. A recommendation has been proposed to optimise residual stress profiles.

This dissertation is structured as follows: Chapter 1 gives an overview of the project and highlights research problems to do with modelling realistic multipass welding of complex geometries. A comprehensive literature review of the state-of-the-art modelling techniques of various aspects of welding simulation is provided in Chapter 2, followed by an introduction of theoretical backgrounds and modelling techniques employed in the current research in Chapter 3. Temperature dependent material properties necessary for the thermomechanical analysis are presented in Chapter 4. Chapter 5 details the development of the computational model, from a simple 2D geometry to a complex 3D geometry. An innovative all-hexahedral element meshing technique is also described in this chapter. In Chapter 6, different modelling techniques were first evaluated using generalized plane strain models and the most suitable model was chosen for the 3D model development. The latter model was then validated by comparing the predicted results from 3D butt-welded plates and pipes with published experimental data. Finally, the 3D validated model was extended to a tee branch junction and detailed simulation results of thermal history, thermal stress evolution and residual stress distributions are presented. An extensive investigation of the effects of welding parameters on the magnitudes and distributions of residual stresses are reported in Chapter 7. Overall conclusions and suggestions for future work are summarised in Chapter 8.

The method employed here can be an adequate tool for predicting and optimizing residual stresses in multipass welded complex structures. It has proved to be effective in modelling residual stress in various geometries considered in this project. Combined with all-hexahedral meshing technique, it has the potential to be applied to other kinds of welding process or large complex geometries to simulate realistic multipass welding process and optimize it more efficiently than would be possible through expensive experimental trials.

Chapter 2 Literature Review

A welding process simulation can be understood differently by workers in different fields. A metallurgist may take it to mean a thermo-dynamical simulation to address the molten zone and microstructural evolution (Grong 1994). The engineer, on the other hand, would be interested in temperature and residual stress distributions. The current research will concentrate on the thermomechanical simulation of general fusion welding processes and will not enter into much detail about welding metallurgical simulation.

Beginning in the 1930's, researchers had tried to give a mathematical representation of the welding process and to establish methods for understanding material behaviour during welding. Usually the welding process was analysed in two steps: a heat transfer analysis for temperature distributions, followed by a mechanical analysis for residual stress and distortion distributions.

Analytical models for predicting temperature distributions were usually developed by a line or a moving point heat source assumption. Rosenthal (1941, 1946) proposed an analytical quasi-steady state temperature solution using a point/line heat source in a semi-infinite body. Goldak, Chakravarti and Bibby (1984) proposed a more accurate double ellipsoid heat source model and later extended it to arbitrary distribution functions (Goldak *et al.* 1986a, 1986b). Leung, Pick and Mok (1990) employed the double ellipsoidal to model the heat input. The model assumed a Gaussian heat flux distribution in the weld pool and was simulated by two ellipsoids. It required an estimation of the heat input and distribution of this heat into each of the ellipsoids to properly simulate the heat flow in the longitudinal direction. In this way, 3D heat flow effects could be simulated in a 2D cross sectional analysis. Recently, Nguyen *et al.* (1999) developed a 3D transient solution using a 3D double ellipsoidal moving heat source for straight line and single pass welds. However, the use of analytical solution inevitably involved the spatial and time simplification about heat sources. Constant properties usually had to be used and heat convection and radiation were often neglected. In contrast, complex geometries, temperature dependent material properties and nonlinear boundary conditions may be taken into account without any restriction in

FE solutions. Therefore, there is no longer any reason to use the analytical solution as the numerical simulation of the thermal field is much more straightforward.

Analytical models for calculating stresses had also been developed based on the line/point heat source assumptions. The mechanical analysis used temperature fields from the thermal analysis as thermal load input. Temperature dependent elasto-plastic material model could also be incorporated. It generally showed good residual stress agreement between predictions and experimental data but were often limited to single pass weld and simple geometries (Masubuchi 1980). The complexities inherent in performing analytical studies of welding stresses for various weld configurations, in particular, irregular geometries and inelastic material response, suggested the need of using numerical method.

Numerical methods, such as the FE analysis, were first used for welding simulation at the end of the 1970's and attracted a lot of interest since then (Gordon 1996, Mackerle 1996, 1999, 2001, 2002, 2005). However, until quite recently, the numerical studies of welding residual stresses have only concentrated on simple geometries where modelling approximations can be justified. Hence large amount of publications covered plate and pipe welding where 2D generalized plane strain conditions or axisymmetry can be invoked. When dealing with real complex geometries used in industry, these simplifications may not be universally considered acceptable. The distinct nonlinearity characteristic, such as temperature dependent material properties, latent heat, convection, radiation and moving heat source boundary conditions, large deformations and also the lack of expertise in modelling and simulation are the major obstacles for 3D residual stress analysis of multipass welded complex geometries. The problems involved in welding residual stress simulation led Marcal (1974) to state that "welding is perhaps the most nonlinear problem encountered in structural mechanics."(Lindgren 2001a)

Welding simulation can be conducted either by specially designed software or by use of existing commercial FE code. Several specific welding simulation software, such as SYSWELD (Roelens 1995a, 1995b) and WELDSIM (Zhu and Chao 2002), had been developed. However, the dominant trend in welding residual stress simulation is still by using general purpose commercial FE codes. This is mainly because residual stress analysis procedures based on commercial FE codes can be readily transferred to

industrial applications (Dong 2001). The solution procedures and built-in algorithms of commercial codes have also been validated and benchmarked.

This Chapter firstly gives a detailed review of the state-of-the-art modelling techniques which cover various aspects of welding simulation, including geometric modelling of structures, complete description of material properties, correct modelling of the moving heat source, accurate coding of the coupling phenomena and multipass welding process. Then a review of parametric studies will be provided.

2.1 Geometrical modelling

2.1.1 One dimensional analysis

Tall (1964) developed the first 1D mechanical model to predict residual stress, although the analytical solution for temperature was 2D. Thus, the longitudinal residual stresses were predicted as if by collection of many, parallel uniaxial specimens. Goff (1979) suggested a procedure to estimate residual stresses in welded thin steel plates, assuming temperature independent material properties and taking a simplified linear temperature distribution in the transversal direction to the weld. Masubuchi (1980), Agapakis and Masubuchi (1984) developed a method, based on pioneering work by Tall (1964), which used the analytical thermal solution of Rosenthal's. The complete load history was followed by means of small increments of temperature and plastic deformations that arose during welding. Although the versatility and rapidity of the use of a 1D model made it suitable for stress relieving procedure selection, too many simplifications usually result in inaccuracies in the residual stress prediction.

2.1.2 Two dimensional analysis

The typical 2D FE models for welding simulation are plane stress, plane strain/generalized plane strain and axisymmetric.

In a plane stress model, it is assumed that temperature and stress are constant through the thickness. 2D plane stress models are usually used to simulate the welding of thin plates (Andersson and Karlsson 1981, Jonsson, Karlsson and Lindgren 1985,

Cañas 1996). The stress in the thickness direction is negligible and the deformation was assumed to be in the plane of the plate. These models follow the heat source that moves in the plane of the mesh, which required a large number of elements for a long weld.

The plane perpendicular to the direction of the weld is normally analysed as a plane strain condition and applies to the welding simulation of the thick plates. The plane strain condition means that the weld is divided into thin slices perpendicular to the motion of the heat source and these slices are assumed not to interact with each other. Longitudinal heat flow and displacements are assumed to be zero. It is as if the whole plate is rigidly fixed in the longitudinal direction. Free and Goff (1989) used 2D plane strain elements for residual stress simulation in welded plates. However, the use of these elements resulted in higher stress predictions, as these elements could not accommodate any thermal expansion in the longitudinal direction. This too high longitudinal restraint due to the plane strain assumption can be alleviated by assuming a generalized plane strain condition.

The generalized plane strain theory assumes that the model between two initially parallel planes in the thickness direction may move as rigid bodies with respect to each other, so strains vary linearly throughout the cross-section. Shim *et al.* (1992), Leung and Pick (1990) and Lindgren, Runnemalm and Nasstrom (1999) favoured the use of generalized plane strain elements to account for straining in the welding direction, which dramatically improved the predicted results.

Another kind of 2D model, i.e. axisymmetric, was used to simulate residual stress distribution in multipass girth butt-welded pipes by Rybicki *et al.* (1978,1979), Brust and Kanninen (1981), Josefson (1982), Chandra (1985) and Teng and Chang (1997). By using an axisymmetric model, it is assumed that the filler material is deposited simultaneously all around the circumference of the joint. Rybicki *et al.* (1978) developed an axisymmetric FE model by using the analytical solution presented by Rosenthal (1941) as a thermal load to predict residual stresses in a two pass girth butt-welded pipe. The model was based on an FE representation recognizing individual passes, temperature dependent elastic–plastic constitutive behaviour, elastic unloading for material in the nonlinear stress–strain range, and changes in geometry due to the deformation of each weld pass. Load incrementation and incremental stress–strain

relations were also used. The limitations of the model were in the use of approximate analytical solutions for the thermal history and the neglect of the effects of the latent heat of fusion. Good agreement between numerical and experimental results was obtained for the axial residual stress at the inner surface. For the axial residual stress at the outer surface and the hoop residual stress at both the inner and outer surfaces, the agreement was not so good.

Michaleris (1996) implemented a residual stress simulation in multipass-welded girth welds of both thin- and thick-walled pipes with various radius-to-thickness ratios and validated their results by experiment. The heat generated by the welding process was modelled with a 'double ellipsoid' heat source model. Multipoint constraints were employed in a consistent element activation approach in the axisymmetric model. An elasto-plastic material response was assumed with kinematic work hardening. The computed and measured axial and hoop residual stresses at the inner surface agreed rather well considering the limitations of the blind hole drilling technique used in the experiments. The results on the outer surface were not reported.

2.1.3 Three dimensional analysis

By modelling a typical cross section, whether assuming generalized plane strain or axisymmetric conditions, it is assumed that welds are formed instantaneously, which seldom occur in practice as far as the welding process are concerned. As such, the results obtained tend to reflect average values of residual stress distribution (Brown and Song 1992a,b). Besides, as demonstrated in Dong and Brust's (2000) investigation, both the travelling arc and start/stop effects tended to violate the axisymmetric assumptions by introducing circumferential variations of residual stresses. Such effects could be further enhanced in multipass welds if travel directions or start/stop positions are changed from pass to pass, which often occurs in practice. Although axisymmetric models yield useful information, the thermal and stress–strain responses of all weldments under a moving heat source are transient and 3D in nature. 3D modelling is of great importance in reflecting the reality of residual stress distribution.

Tekriwal and Mazumder (1988,1991) performed a 3D uncoupled thermal and

stress analysis of a single pass butt weld of two 5.8mm thick plates. The model employed the gradual element addition technique to simulate realistically the metal transfer in a gas metal arc welding process. The model incorporated all the thermo-physical and mechanical properties of material as functions of temperature.

Hansen, Hattel and Lorentzen (2001) investigated a sequential thermal and mechanical analysis of submerged metal arc welding of single pass, butt-welded, 10mm plates. The research focused on modelling the moving heat source and filler metal as well as its effect on the subsequent mechanical analysis. The heat source was modelled by filler material being added continuously in connection with a body flux. In order to obtain realistic weld pool geometry, a surface flux, Gaussian distributed transversely to the weld, had been included. Although the mechanical analysis was based on small strain assumption, good agreement was obtained near the weldline.

Karlsson and Josefson (1990) analysed a single pass weld of an 8mm thick pipe with an outer diameter of 114.3mm. In the uncoupled thermomechanical analyses, the whole pipe in the hoop direction and the complete welding sequence of one revolution and subsequent cooling were covered. Although a thermo-elasto-plastic material formulation and temperature dependent material properties were used, the small strain and displacement assumption resulted in deviations of residual stresses in the weld region between the predictions and experimental data.

Full 3D models are based on solid models where all strain and stress components are included. However, shell elements can also be considered as 3D models because they are described with three coordinates although the thickness must be thin. Shell models assume that stress to be zero in the thickness direction. The same pipe was modelled as a solid model (Karlsson and Josefson 1990), a shell model (Lindgren and Karlsson 1988), and an axisymmetric model (Karlsson 1989). The results from these different models were consistent. They agreed well with measurements except for the residual hoop stress at the surface of the weld. Dong *et al.* (1997) used shell elements to investigate the effect of wall thickness and welding speed on residual stresses of a pipe. They also implemented a layer removal/reactivation scheme in a composite shell element for simulating multipass welding. Dong, Zhang and Li (1998) developed a composite shell element model for modelling multipass girth welds. The

thermo-plasticity constitutive law was incorporated in the model. A combined analysis procedure, using both 3D shell and local 2D/Axisymmetric models, was also introduced for an improved prediction of the local residual stress distributions as well as the 3D global residual stress. The availability of such facilities made it possible to analyze detailed residual stress evolutions in 3D structures that had been treated as 2D or axisymmetric problems in the past (Rybicki *et al.* 1978; Brust and Rybicki 1981; Leung and Pick 1990; Hong, Tsai and Dong 1998).

Differences between 2D and 3D predictions have also been investigated. Michaleris, Feng and Campbell (1997) evaluated both 2D and 3D models in determining the effects of restraint in the formation of welding distortion. The 2D model simulated all the six passes of an aluminium joint, while the 3D model considered the first pass only. It was found that the 3D model could respond to the constraint while the 2D model was inadequate in doing so. Sarkani, Tritchkov and Michaelov (2000) compared the predicted residual stress in a welded T-joint by both 2D and 3D models. The residual stresses predicted by the 2D model agreed fairly well with the 3D predictions in the plane of the 2D model. More substantial differences were observed in the out-of-plane stresses, which were attributed primarily to the different boundary conditions in the out-of-plane direction of the 2D and 3D models.

Although it has gradually become feasible to conduct a full 3D FE simulation for transient temperature and residual stress distributions, previous 3D investigations were limited to relatively coarse meshes, rather small dimensions, and single pass welding of simple geometries. As a result, most models are not representative enough of the type of structures or the length of the weld under investigation. Hence, this research is to develop a full size 3D model with all-hexahedral graded meshes to assess residual stresses in a multipass welded large piping branch junction.

2.2 Material modelling

Material modelling is another key problem in welding simulation. A correct description of material behaviour and pertinent data for material properties within the welding temperature range is essential for an accurate model. Recently, Lindgren

(2001b) gave a detailed review on this topic, which included the development of material constitutive relationships and material properties as functions of temperature.

During the welding process, the temperature field changes with time as the heat source moves and the material properties change with temperature. When the temperature increases towards the melting point, the material properties change from elastic to plastic. This requires a nonlinear transient thermo-elasto-plastic analysis.

Hibbitt and Marcal (1973), Friedman (1975), Andersson (1978) and Murthy, Rao and Iyer (1996) studied thermo-elasto-plastic constitutive models, while Argyris, Szimmat and Willam (1982) studied thermo-elasto-visco-plastic constitutive models for obtaining stress distributions during the welding process. Ronda and Oliver (1998) compared the various thermo-visco-plastic constitutive models in welding simulation. These studies indicated that time independent thermo-elasto-plastic formulations were sufficient for analysing mechanical behaviour during welding.

Dong, Zhang and Li (1998) and Dong (2000) developed an integrated framework for modelling the welding process. As the centrepiece of the integrated framework, a unified constitutive model including the elastic, plastic, thermal, annealing and phase transformation strains was proposed. A combined isotropic/kinematic hardening law was used to properly characterize the material stress-strain relationship at high temperatures. It was found that creep strain was overall insignificant when compared with plastic strain and its effects on residual stress were minimal. The predictions which incorporated annealing strain effects predicted better results than those without consideration of the annealing strain. Phase transformation plasticity only affected local residual stress details. Dong (2000) suggested that it should be adequate to perform residual stress analysis without considering a phase transformation effect, since such effects often involved significantly increased complexity in numerical procedures and input data interpretation.

Temperature dependent material properties are important in a welding simulation. In the thermal modelling, the dependency on temperature was completely ignored by those using Rosenthal's or other analytical solutions. Free and Goff (1989) and Dong *et al.* (1997) assumed constant thermal properties despite the use of the FE method. Their

statement that variations in thermal properties resulted in very small changes of the transient temperatures was inconsistent with the findings of McDill *et al.* (1990). Currently most publications to do with welding simulation consider temperature dependent material properties and no effects of phase transformations except for the associated latent heats.

In the mechanical modelling, the material properties required are the elastic modulus, Poisson's ratio, yield stress and coefficient of thermal expansion. Although it is relatively easier to obtain thermal properties of materials, it is quite difficult to obtain mechanical properties, especially at high temperatures. To circumvent this problem, assumptions and simplifications, such as using extrapolated material properties at high temperature or using cut-off temperatures (above which no changes in the mechanical properties are accounted for) are often proposed for welding simulation. Chen *et al.* (1999) numerically studied the effect of material properties on the welding simulation using extrapolated material properties at high temperature and concluded that the unavailable material property data at high temperature had almost no effects on the residual stresses and distortion. Tekriwal and Mazumder (1991) showed that the use of a cut-off temperature lower than melting point resulted in up to 15% overestimation of the transverse residual stress in the melt-pool zone.

Zhu and Chao (2002) systematically investigated the errors associated with the material model assumptions by performing detailed 3D nonlinear analyses on an aluminum plate. Three sets of material models, namely, properties that were functions of temperature, room temperature values, and average values over the entire temperature history in welding, were considered. The effects of each temperature dependent material property on transient temperature, residual stress and distortion were investigated. It was found that thermal conductivity had certain effects on the distribution of transient temperature field, while material density and specific heat had negligible effects. It was also found that the yield stress was the key mechanical property in welding simulation and temperature dependency of the yield stress must be considered in the simulation in order to obtain correct results. The Young's modulus and thermal expansion coefficient had a small effect on the residual stress and distortion. Based on these conclusions, a simplified material model constituting of a piece-wise linear function with temperature for yield stress and constant room-temperature values of all other properties was

proposed.

The modelling of material behaviour at higher temperatures is perhaps one of the most crucial ingredients in successful welding simulations and is still on going. The improvement in material modelling and increasing availability of material parameters will, in combination with the computational development, greatly increase the application of and improve the results of welding simulations.

2.3 Heat source modelling

Two different coordinate systems can usually be used when modelling a moving heat source in a welding simulation: a steady-state temperature profile within a moving coordinate system or a moving heat source within a fixed coordinate system.

In a moving coordinate system, the heat source stays stationary, while the plate to be welded moves under the heat source. The temperature profile does not change after the initial period of welding. Rosenthal (1941, 1946) first used a moving coordinate system to get an analytical quasi-steady state temperature solution for weld-oriented heat transfer problem with a moving point heat source travelling at a constant speed along a line on an infinitely thick plate. Goldak and Gu (1995) compared the analysis using a moving heat source within a fixed coordinate system with the analysis using a steady state temperature profile within a moving coordinate system and found that with the latter system, the calculation efficiency dramatically increased and the results accuracy greatly improved.

By comparison with moving coordinate system problems, fixed coordinate system problems do have some disadvantages. For example, fixed coordinate system problem requires very dense meshes around the heat source along the complete weld path; it needs transient analysis; and most of all, it requires the heat source to move in jumps as a function of time along the weldline. In order to be close to the real continuous moving process, fine time steps are required. This increases the computational time and data storage. However, because of its direct relationship to reality and the limited number of codes capable of implementing moving coordinate problems, most FE software, such as

ABAQUS, are still based on fixed coordinate system.

FE solutions for temperature field prediction are often included in the majority of publications relating to FE analysis of welding residual stresses. When dealing with heat sources in these models, they were usually modelled as heat flux distributed uniformly over an area (in 2D), or a volume (in 3D), of elements that represent the weld.

Shim *et al.* (1992) applied heat flux to 2D elements by using a ramp heat input model. The ramp heat input model was developed to avoid numerical convergence problems due to the instantaneous increase in temperature near the fusion zone and to include the effect of a moving heat source in the 2D plane. It was found that a ramp time consisting of 20% of the total heat input time gave the best correlation with experiments. Wen and Farrugia (2001) conducted an uncoupled analysis. In the transient nonlinear heat transfer analysis, the heat input was simulated by definition of a moving heat source with a uniform body heat flux and recommended the incorporation of a distributed heat flux input.

Jiang *et al.* (2004) and Jiang, Yahiaoui and Hall (2005) modelled the heat input as a column of activated elements with specified body heat flux progressing along the weld path corresponding to the welding speed. This heat input was imposed onto the specified newly activated elements representing a deposited pass at a given time. Body heat flux was uniformly distributed over the volume of each weld droplet. The heat content of filler metal droplets was assumed to be deposited at melting temperature. The predicted temperatures were compared with experimental data and quite satisfactory results were obtained.

An FE thermal model has the ability to model complex welding configurations with respect to intricate geometries, welding procedures and material properties with minimum assumptions. With the knowledge of welding parameters and the joint geometry, the heat source model can be conveniently built in the thermal analysis.

2.4 Coupling phenomena modelling

Welding involves the interaction of thermal, metallurgical and mechanical phenomena. Roelens (1995a,b) and Inoue (1998) investigated the coupling among these phenomena during multipass welding. The thermo-metallurgical analysis was performed first followed by thermomechanical calculation on the basis of the results obtained.

However, the current research will focus on the thermomechanical simulation only and will not include metallurgical consideration. The coupling between the thermal and mechanical fields are usually analysed by two kinds of method: sequentially and fully coupled models. Most welding simulations are performed by sequentially/uncoupled model. That is, a pure heat transfer problem is performed first, followed by a stress analysis that used the temperature solution as thermal input, as performed by Free and Goff (1989), Leung and Pick (1990), Lindgren, Runnemalm and Nasstrom (1999), amongst other researchers. Michaleris, Tortorelli and Vidal (1995) predicted residual stress which evolved during the welding process by solving a nonlinear thermo-elasto-plastic problem for a weakly coupled thermo-elasto-plastic system. The plane stress, rate-independent, elastic-plastic material response with isotropic hardening was assumed.

Welding often leads to deformation that may be visible, and thus a large deformation analysis is appropriate. In order to update the deformation, the thermal and mechanical analyses can then be performed in a so-called staggered approach when the mechanical effects on the thermal field are accounted for. Argyris, Szimmat and Willam (1982) conducted such staggered solution strategy for the weak thermomechanical coupling by solving the temperatures, T_{n+1}, for time t_{n+1} by using the geometry x_n at the start of each time step. The geometry was updated in the subsequent mechanical analysis for each time step. Teng, Chang and Ko (2000) employed a similar analysis to evaluate the distribution of residual stresses in circular patch welds. During each weld pass, the thermal stresses were calculated from the temperature distributions obtained from the thermal model. The residual stresses from each temperature increment were added to the nodal point location to determine the updated behaviour of the model before the next temperature increment.

A fully coupled model is not as widely used as a sequentially coupled model in welding simulation. It is a commonly held view that the heat generated by the straining is quite small compared with the large heat input. Boley and Weiner (1960) stated that it was possible to neglect it for a wide class of thermo-elastic problems including welding. Jiang *et al.* (2005a) developed both a sequentially and a fully coupled generalized plane strain thermomechanical model to investigate the coupling between the thermal and mechanical fields. It was found that both models gave similar results but the fully coupled model was computationally more expensive. The investigation confirmed that the coupling between thermal and mechanical field was very weak and a sequentially coupled model was recommended.

2.5 Multipass welding modelling

The accurate prediction of residual stresses and distortions induced by multipass welding is extremely difficult. This is so not only because of the thermal and mechanical behaviours which include highly localized temperatures, temperature dependent material properties, large deformation and a moving heat source, but also because each successive weld pass alters the temperatures, stresses and distortions caused by previous passes. Nevertheless, despite these complications, multipass welding simulation has still received considerable attention in recent years and significant progress has been made.

Computational models for predicting residual stress distributions due to one or two pass welds have been successfully developed, and good correlations between predicted and measured residual stress have been obtained by Ueda and Yamakawa (1971). Theoretically, the extension of these techniques to multipass welds should be straightforward. However, analysing multipass welds with these straightforward techniques in large weldments quickly becomes economically demanding. Two challenges exist when dealing with multipass welding simulation. These are the computational costs and the modelling of filler metal deposition.

2.5.1 Lumping technique

Lumping successive passes together is one way to reduce the computational cost. The sequence of lumped passes follows the deposition sequence of the weld passes.

Several lumping schemes exist. Ueda *et al.* (1976) studied the multipass welding of plates with thickness of 100mm, 200mm, and 300mm, respectively. Welds in the lower groove were assumed to be laid simultaneously with corresponding welds in the upper groove. The cases had 7, 43, and 83 welds in each groove. These were lumped in the models in 5, 10, and 17 layers where the heat conduction analysis was performed for all passes, but the stress analysis was only carried out for the last pass in each layer of welds. Good agreement with experiments was obtained.

Leung and Pick (1990) investigated a method of grouping the build-up of many weld passes into fewer layers with an envelope of combined temperature histories in the stress analysis. It was found that the method of grouping passes in a layer into two analyses (one involving all passes in the layer except the last one and the other involving the last pass only) gave results that were identical to a complete simulation.

Shim *et al.* (1992) developed an uncoupled lumped pass model to reduce the computational time and cost when predicting through-thickness residual stress distribution during multipass welding of thick plates. In the thermal model, each layer of the weld bead was assumed as one lumped pass. The heat input for each pass in that layer was added and applied on the top surface of the layer. To model the heat input to the cross section, a ramp heat input was used to avoid numerical instability and to include the effect of a moving heat source. The generalized plane strain assumption was used in the stress analysis. The results by the lumped model showed good agreement with experimental data, however, the selection of the ramp time was quite arbitrary, i.e. based on trial and error.

Smith, Bouchard and George (2000) employed an uncoupled model to predict the distribution of residual stresses in a cylinder-to-nozzle junction weld. The weld bead lumping approach was employed. The entire weld was represented by 11 layers of filler metal, sequentially added to the model, one half layer at a time. The half-layer

"lumped" beads were each divided into two elements in the thickness direction. The final "lumped" beads represented the weld cap region. The model used hybrid 8-noded axisymmetric reduced integration quadrilaterals, with a smaller number of six-noded axisymmetric triangles employed where necessary for mesh refinement. Temperature dependent thermo-physical properties were considered in the analysis while latent heat was ignored. The residual stress predictions agreed well with the deep-hole drilling measurements.

These previous researches appear to give an overwhelming support to the grouping and enveloping technique for reducing computational costs. However, all lumping and enveloping techniques change the temperature history and will affect the transient and residual strains near the weld. Lumping by merging several weld passes that conserve the total heat input is preferred. Thus, the simulation will correspond to a multipass weld but with fewer weld passes than the original.

2.5.2 Filler material deposition modelling

The process of sequential filler material deposition can be modelled using an element removal/reactivation scheme. Two basic approaches are possible:

The first approach is to generate all elements making up the weld at the initial mesh creation stage, that is, welds that have not been laid yet are presented in the model. The elements, corresponding to nonlaid welds, are given normal material properties at the start of the weld pass. It is important to remove all strains and stresses that have possibly accumulated in these elements. This approach has two advantages: it is easy to implement in most FE codes and the whole model can be defined initially.

Jonsson, Karlsson and Lindgren (1985) employed this technique for plane stress models and Karlsson and Josefson (1990), Tekriwal and Mazumder (1991) for 3D models where filler material was added in each time step as the arc travelled along the weld path. Zhang *et al.* (2000) characterized the detailed evolution of residual stresses in multipass girth weld of 304 stainless steel cylinders by axisymmetric model. The weld temperature history generated by the thermal analysis was read into the special

user subroutine as a field variable for stress analysis. The effect of sequential metal deposition associated with multipass welding was simulated by assigning a negligible material stiffness (a stiffness comparable to the one at melting temperature) to the filler elements that were not yet deposited. This was to ensure that these filler elements did not affect any deformation mechanism even though they were present. Once a filler element was deposited, its stiffness was restored.

The second approach requires adjusting the topology of the weld elements to accommodate previous deformation, i.e. a restructuring of data each time the model is extended. The elements and nodes that correspond to nonlaid welds are not included in the FE model until the weld is laid. This is a more correct approach but requires a FE code with appropriate facilities and may require time-consuming user interaction at each new weld pass.

Lindgren and Hedblom (2001) compared the two approaches when modelling multipass welding of two 200mm thick plates and found that both techniques gave the same results and the predictions agreed well with the experimentally obtained transient temperature and residual stresses. Strains accumulated during the initial phase between the time at which the element was added and the time at which it reached the expected temperature would not affect the results if its plastic strains were completely removed when this expected temperature was reached. It did not matter if interface elements were used when connecting molten elements corresponding to the filler to the rest of the model or if some kind of preheating of the surface was performed before the weld was laid in order to raise the temperature of the structure to the temperature of the laid weld. The only difference between these two methods was that there was soft, molten material pressing on the surface during the initial temperature increase of material connected to the weld in the first case. The removal of plastic strains would erase any possible differences between these two methods. Therefore, the choice of method was more a matter of what was more practical for the particular finite element code in use.

Multipass welding modelling is an extremely time-consuming task, especially when a thick component is involved. Although analysing multipass welds as a series of single pass welds reflects welding reality, proper lumping can provide advantages in terms of both acceptable results and reasonable computational time. The ABAQUS

element removal/reactivation facility provides an excellent tool for the simulation of filler material deposition.

2.6 Parametric studies

Welding is a highly nonlinear and multivariable process. Each variable affect the residual stress in different ways. Parametric studies and optimization are an effective method in obtaining a high level of weld quality. Previous researches on parametric studies are reviewed in the following sections.

2.6.1 Welding pass sequence

The selection of welding pass sequences has two meanings depending on the thickness of the welded component. For a single pass welded thin component, it means welding sequence along the welding path. Teng, Chang and Tseng (2003) investigated various types of welding sequence in a single pass and a multipass butt-welded plate as well as in a circular patch weld. The effects of welding sequences, i.e. progressive, backstep and symmetric welding, on residual stresses for a thin-wall butt-weld were firstly studied. It was found that the longitudinal residual stress of symmetric welding in the weld path direction were smaller than those of the other welding sequences. In the butt-welded thick plate, it was found that the longitudinal residual stresses between various weld sequences did not differ significantly, while transverse residual stress of symmetric welding sequence in the thickness direction was smaller than other weld sequences. In the investigation of the effect of progressive, backstep and jump welding sequence on residual stresses for the circular patch weld, it was found that the circumferential residual stresses between various weld sequences did not appear to significantly differ. However, the radial residual stress of the backstep welding was smaller than the other welding sequences. This is because the post-weld heat treatment and preheating effect in backstep welding were better than other welding sequences.

Kadivar, Jafarpur and Baradaran (2000) linked a genetic algorithm with a thermomechanical model to determine the optimum welding sequence in a circular patch welded thin plate. It was found that the optimum welding sequence was not

unique and depended on the type of restraint. The authors also concluded that the welding sequence had little effect on the maximum residual stresses and it affected mainly the distortion of the weldment.

For a multipass welded thick component, welding pass sequence is referred to as a welding sequence arrangement in the thickness direction. Radaj (1992) found that symmetric pass sequences for a doubled-V groove thick plate have proven satisfactory in practice. Mochizuki, Hayashi and Hattori (2000) studied the effects of pass sequences on residual stresses during multipass welding of a large diameter butt-welded thick-walled pipe joint with an X-shaped groove. According to the criteria of minimum axial through-thickness stress near the inner surface, the optimum welding sequence was proposed, i.e. half the outside groove, half the inside groove, the remaining outside groove, then the remaining inside groove.

Ji *et al.* (2005) investigated welding sequence on the weld induced residual stress in a thick plate. The authors started with a three-pass welded single groove. Several schemes of welding directions were proposed. It was found that converse welding direction between adjacent layers in a multi-layer weld produced less longitudinal and transverse residual stress. As for the double-groove welding, it was found that symmetrically filling each side of the V-groove gave less residual stresses. It was also found that converse welding would reduce longitudinal and transverse residual stresses in the double V-groove thick plate as well.

2.6.2 Constraint

Fanous, Younan and Wifi (2003) studied the effect of boundary conditions on residual stress by performing 3D single pass FE analysis. It was found that welding a free plate caused a much lower residual stresses than welding a plate that was part of a larger structure.

Abid and Siddique (2005) investigated the effect of mechanical constraints on welding distortions and residual stresses in a pipe-flange joint by 3D sequentially coupled single pass thermomechanical FE analysis. Four different constraint conditions

representing welding of (a) unassembled joints, (b) assembled joints, (c) assembled joints with reflective symmetry and (d) perfectly constrained joints were analysed. Minimum axial distortion on the flange face was found for rigidly clamped flanges. However, residual stresses had a weak dependence on the constraint set.

2.6.3 Heat input/Preheat/Interpass temperature

Lin and Lee (1997a), Lin and Perng (1997) investigated experimentally the effect of welding parameters on residual stress in 7mm and 30mm thick plates, respectively. It was found that preheat process did not have much effect on the welding residual stress, only about 28MPa difference in maximum principal residual stresses for the variation of preheating temperature within a range of 200°C. The experimental results showed that residual stresses increased with increasing heat input during welding. However, according to the study of Fanous, Younan and Wifi (2003), the change in the amount of heat input had very slight effect on the residual stresses in the 5mm thick plates. Smith, Bouchard and George (2000) also found that the predicted residual stress field for the cylinder-to-nozzle weld was fairly insensitive to the heat input used.

Brickstad and Josefson (1998) conducted a parametric study on residual stresses in muiltpass butt-welded stainless pipes using nonlinear thermomechanical axisymmetric FE model. In particular, the through-thickness variation at the weld and heat affected zone (HAZ) of the axial and hoop stresses and their sensitivity to variation in weld parameters were studied. It was found that with increasing pass numbers, i.e. pipe thickness, the effect of heat input on the axial and hoop stress decreased.

2.6.4 Cooling rate

Rybicki and McGuire (1982) investigated the effects of induction heating condition on controlling residual stresses in butt-welded 304 stainless steel pipes. The process involved inductively heating the outside of a welded pipe while cooling the inner surface with flowing water. Several induction heating treatments subsequent to welding were then examined computationally to determine the effect of induction coil length and maximum outer surface temperature on the final residual stress state. It was found that

all induction heating treatments gave reduced tensile stresses on the inner surface of the girth welded pipes. Longer coil and higher outer surface temperature led to inner surface stresses that were more compressive. However, this process was very expensive and restricted by field conditions.

Nayama *et al.* (1997) studied the effects of a double sided heating method and its controlling parameters on reducing tensile residual stress on the inner and outer surfaces of butt-welded pipe. In the double sided heating method, an annular region on both sides of the weld line was heated from the outside at the same time to generate a temperature differential between the weld line and the region being heated. The effects of the controlling parameters of the method, such as the heating width, position and conditions (intensity and time), on the residual stress were investigated. It was found that the generated temperature differential and residual stress reduction effect increased with an increasing heating density and time. The tensile residual stress on the inner surface near the welded joint decreased and could be altered to compression after treatment by this method. Lin and Lee (1997b) investigated the effects of parallel heat welding on the reduction of residual stresses on a butt-welded plate. A pair of parallel heating torches was attached to both sides of the welding torch. It was found that the residual stress increased with the increase of heating temperature and width of the heating torches.

2.7 Conclusions

In this chapter, state-of-the-art weld modelling techniques which cover various aspects of welding simulation, including geometric modelling of structures, proper description of material properties involved in the process, correct modelling of the moving heat source, accurate coding of the coupling phenomena and multipass welding process, as well as parametric studies, have been reviewed.

As noted in the literature review above, the thermal and stress-strain responses of a weldment under a moving heat source are transient and 3D in nature. Consequently, a full size 3D model with all-hexahedral graded meshes in a multipass welded piping branch junction will be developed. Thermo-elasto-plastic formulation as well as temperature dependent material properties will be incorporated in the model. With the

knowledge of welding parameters and the joint geometry, the heat source can be conveniently modelled as a column of activated elements with specified body heat flux progressing along the weld path corresponding to the welding speed. Sequentially coupled model, lumping technique and the ABAQUS element removal/reactivation methods will be employed in the 3D multipass welding simulation.

Welding simulation is of great importance for better understanding the complex nature and evolution of welding residual stress. It also provides an opportunity for parametric studies to provide recommendations regarding welding procedures to meet specific residual stress distribution requirements. These techniques will hopefully reduce the time and expense associated with developing new welding procedures for complex structural components or components where specific weld properties are required.

Chapter 3 Finite Element Analysis of Multipass Welding

This chapter provides a general theoretical background to the modelling techniques employed in the current research. Starting with an introduction to the welding residual stresses generation in Section 3.1, the coupling phenomena between the thermal and mechanical fields and the two modelling procedures, i.e. sequentially and fully coupled modelling, are then described in Section 3.2. Several important issues arising from the FE welding simulation, i.e. the method of multipass welding and material deposition modelling, the generation of all-hexahedral meshes in a complex geometry, the techniques of efficient solving highly nonlinear FE problems, are discussed in Section 3.3. These techniques were applied to the model development and are discussed in further detail later in Chapter 5.

3.1 Weld-induced residual stresses

Residual stresses are self-equilibrating internal stresses existing in a free body which has no external forces or constraints on its boundaries. Figure 3.1 shows schematically the changes of temperature and resulting stresses that occur during a simple welding procedure. Figure 3.1(a) shows a heat source, initially located at the origin *O*, moving along the *X*-axis at a speed v.

Figure 3.1(b) shows the temperature distribution along several cross sections. Along Section *A-A*, which is remotely ahead of the heat source, no temperature change occur. Along Section *B-B*, which crosses the heat source, the temperature distribution is very uneven and high temperature gradient is observed. Along Section *C-C*, which is some distance behind the heat source, the distribution of temperature tends to be even. Along Section *D-D*, which is far behind the heat source, the temperature change due to welding again vanishes as the result of cooling.

Figure 3.1(c) shows the longitudinal stress distribution along these sections. Along Section *A-A*, the thermal stresses due to welding are zero. Figure 3.1(c)-2 shows the

stress distribution along Section *B-B*. Since molten metal will not support a load, stress underneath the heat source is close to zero. Stresses in regions at a short distance either side of the heat source are compressive. This is because the expansion of these areas is restrained by the surrounding metal where the temperatures are lower. Since the temperature of these areas is high and the yield strength of the material is low, stresses in these regions are as high as the yield strength of the material at corresponding temperatures. Stresses further away from the weld are tensile and balance with the compressive stresses in areas near the weld. Stress distribution along Section *C-C* is shown in Figure 3.1(c)-3. Since the region near the weld has cooled, tensile stresses will generate due to contraction. Figure 3.1(c)-4 shows the stress distribution along Section *D-D*. High tensile stresses are produced in regions near the weld, while compressive stresses are produced in regions either side away from the weld. This is the typical distribution of longitudinal residual stresses after welding (Masubuchi, 1980).

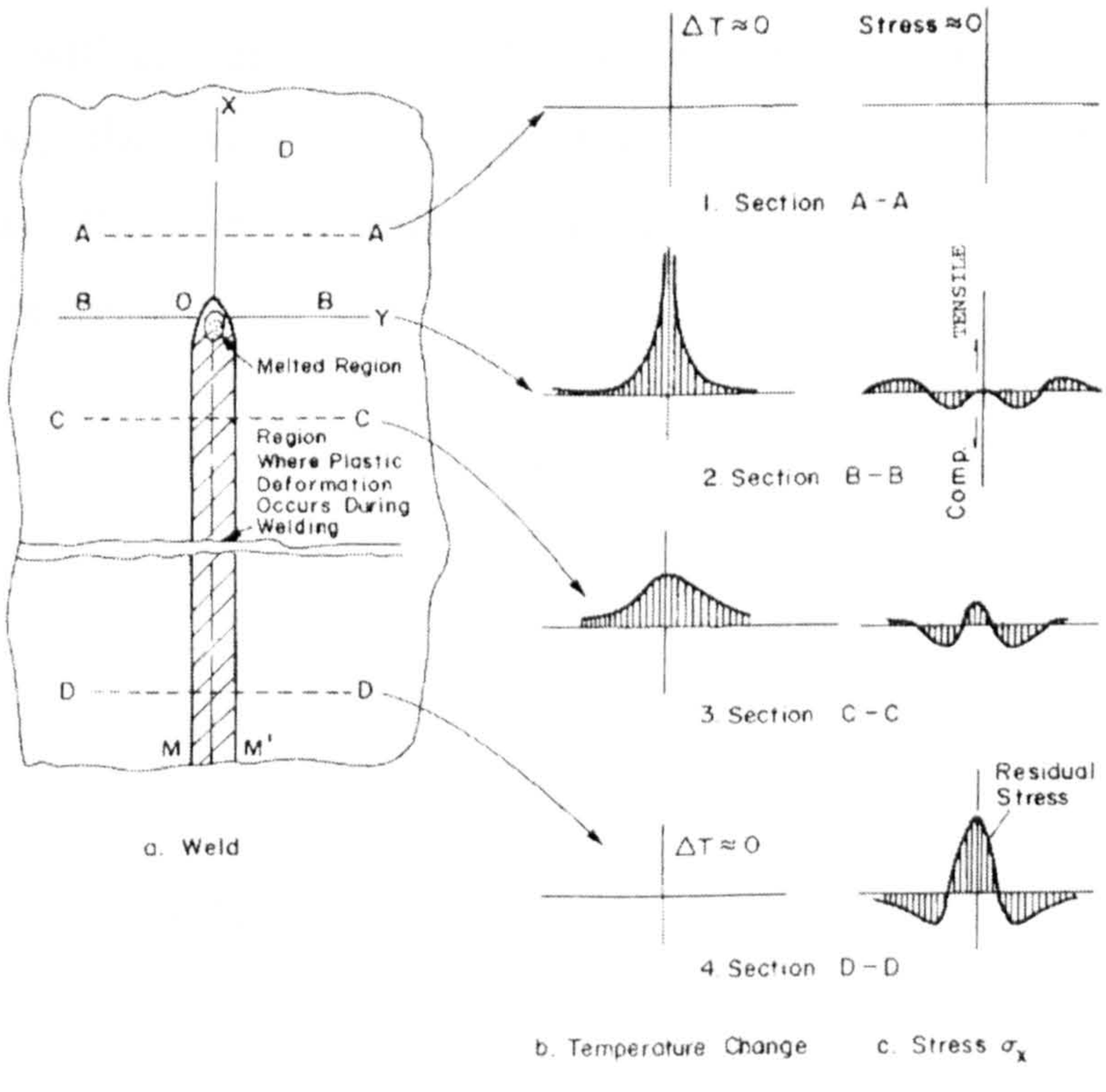

Figure 3.1 Schematic representation of changes of temperature and stresses during welding (Masubuchi, 1980)

In summary, the materials in the weld undergo severe thermal cycles: with rapid heating to melting temperature followed by gradually cooling to room temperature. Accordingly, the materials in the weld region change their properties from elastic to elasto-plastic and plastic, and then recover to elasto-plastic and finally back to elastic.

The maximum tensile stress can reach as high as the material's yield stress or more than the yield strength of the material if strain hardening is taken into account.

The thermal expansion during heating and subsequent contraction on cooling causes inhomogeneous plastic deformation and hence residual stresses in the weldment. The presence of residual stresses, especially when tensile, is generally detrimental, increasing the susceptibility of a weld to fatigue damage, stress corrosion cracking and fracture.

3.2 Thermomechanical analysis

Welding is a complex multiphysics problem that involves coupling between thermal, metallurgical and mechanical phenomena, as shown in Figure 3.2. As the current research will concentrate on the thermomechanical simulation of multipass welding processes, the analysis will only deal with coupling between thermal and mechanical fields. The coupling phenomena related to microstructure is beyond the scope of current research.

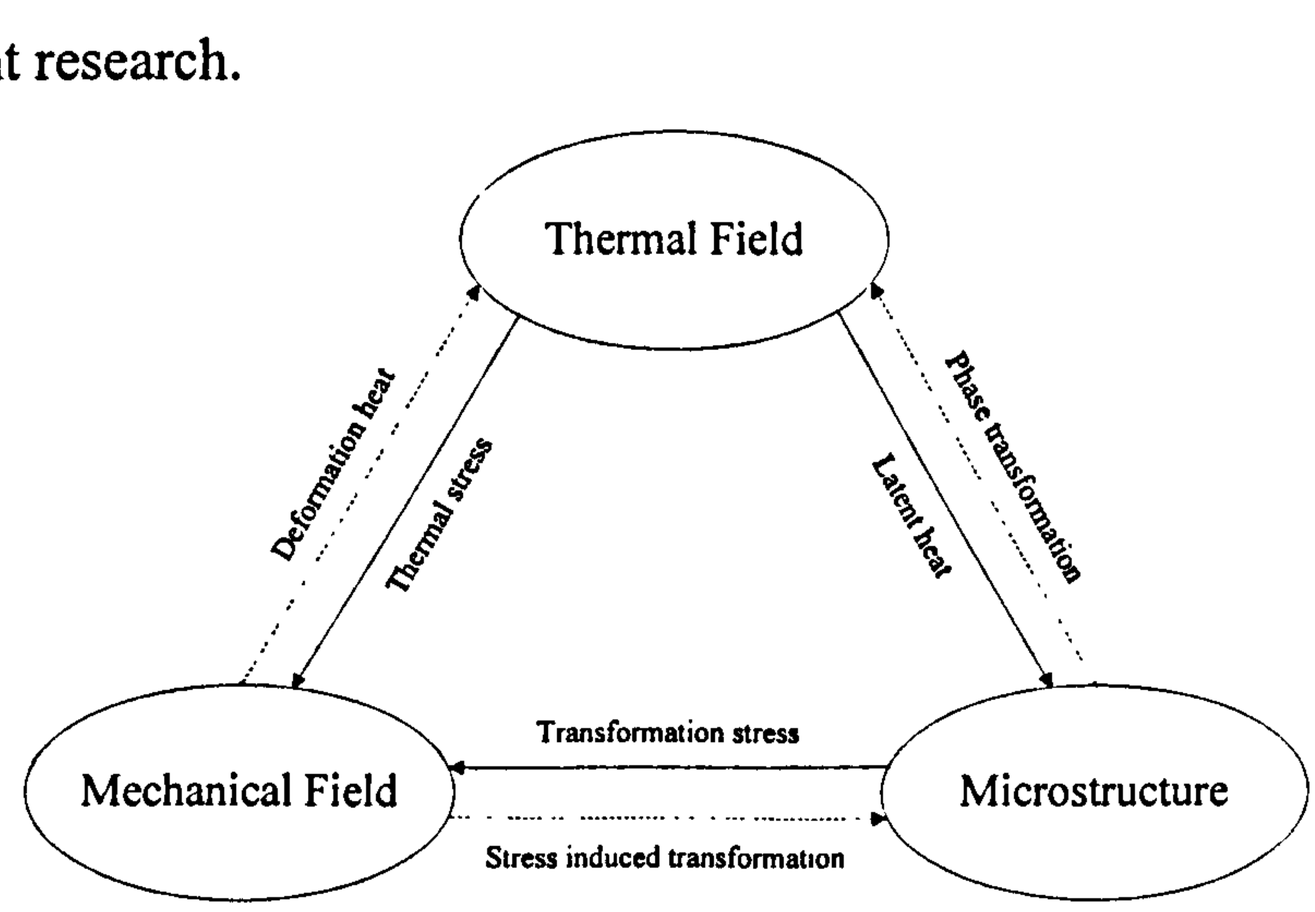

Figure 3.2 Coupling between thermal, mechanical field and microstructure

The coupling between thermal and mechanical fields is realized firstly by temperature dependent material properties, latent heat and thermal expansion related to temperature differences at given time intervals and secondly by the heat generated by plastic deformation. The thermal expansion, along with the sharp decrease in mechanical properties during heating, induces plasticity and yields non-homogeneous permanent strains and residual stresses after welding.

3.2.1 FE analysis procedures

In order to ultimately determine the residual stresses in the weldment, this thermomechanical problem requires solutions for both thermal and mechanical problems. Two kinds of FE models can be used to predict welding residual stress distribution: sequentially or fully coupled thermomechanical models. Finite element procedures for both sequentially and fully coupled model are shown in Figures 3.3 to 3.4, respectively.

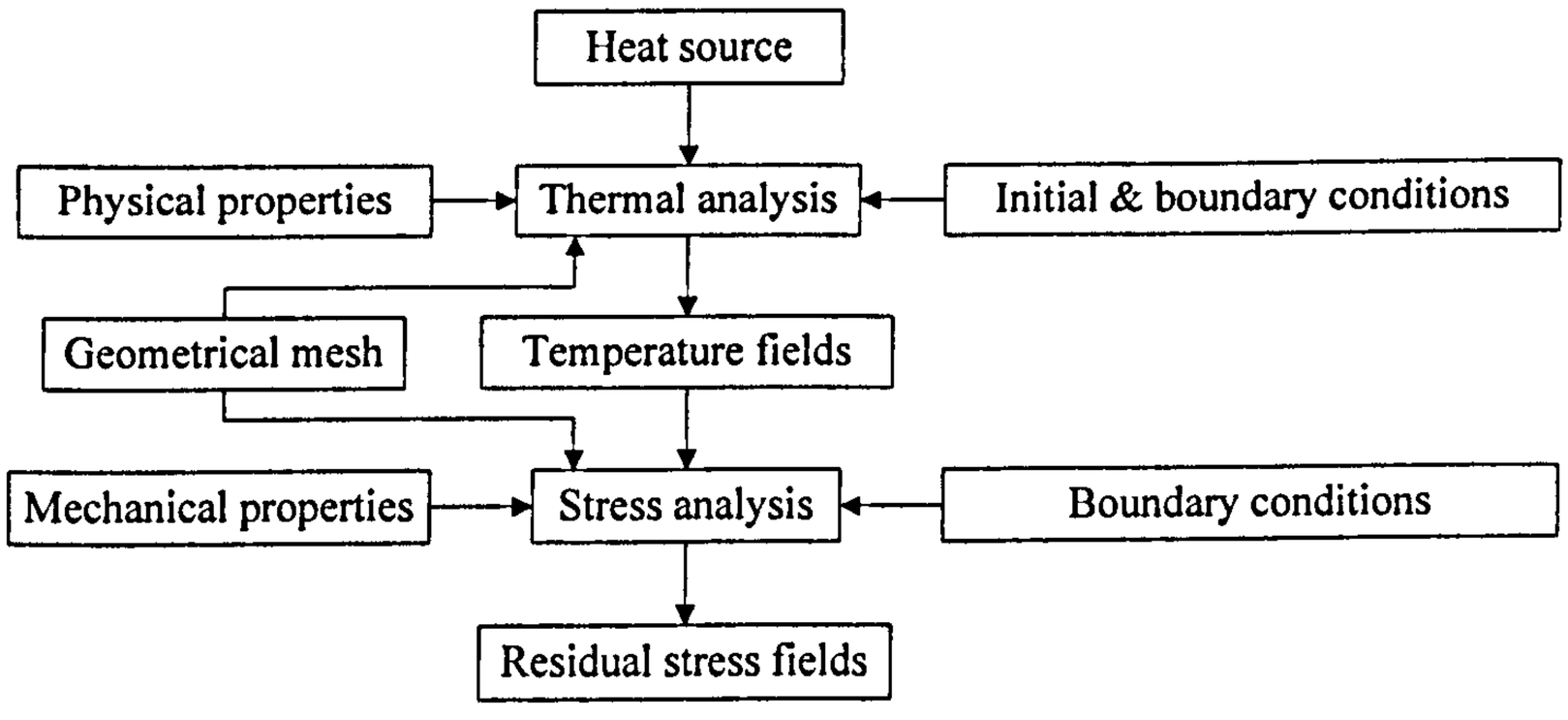

Figure 3.3 Welding simulation procedure for a sequentially coupled model

A sequentially coupled thermomechanical analysis is conducted when the stress solution is dependent on a temperature field but there is no inverse dependency. It is performed by first solving a pure heat transfer problem, then reading the temperature solution into a subsequent stress analysis as a predefined field. This can be conveniently carried out by using the same FE mesh in both analyses.

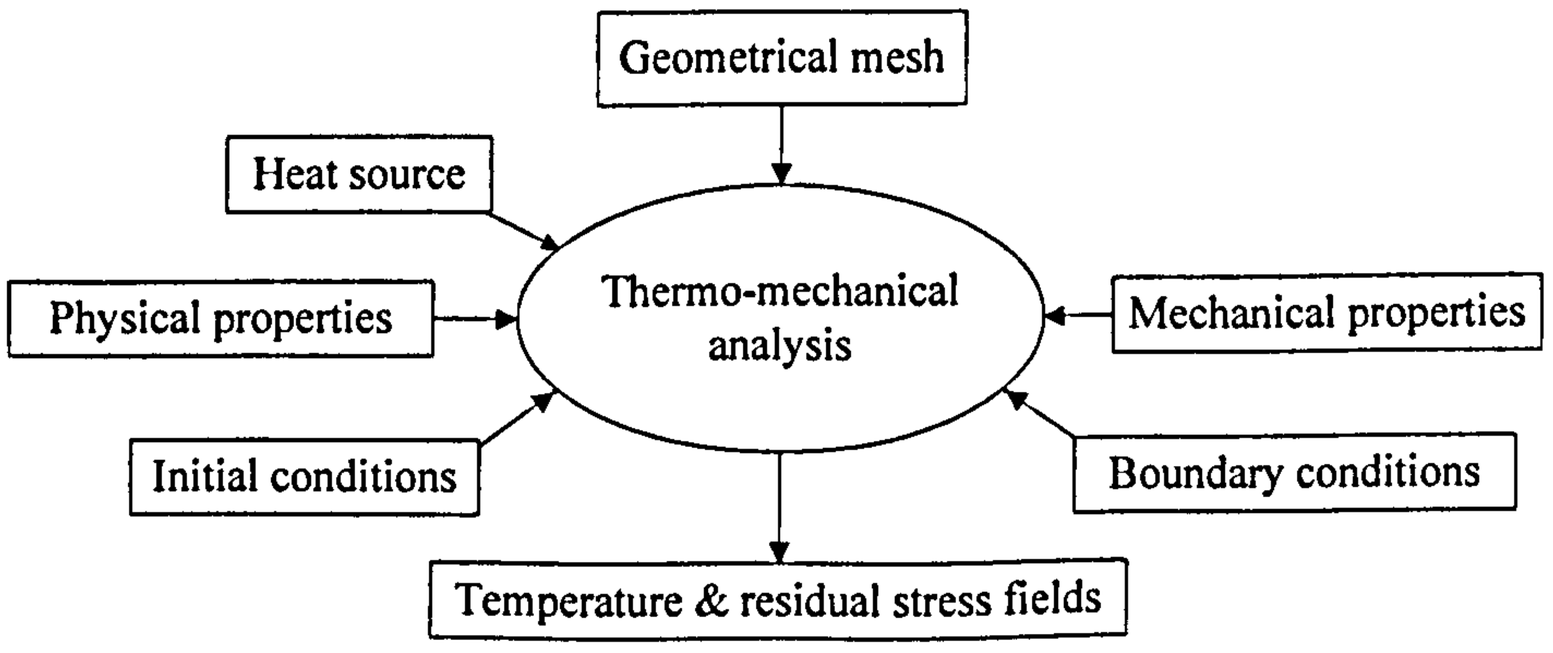

Figure 3.4 Welding simulation procedure for a fully coupled model

A fully coupled thermomechanical procedure is used to solve temperature, stress and displacement fields simultaneously. It is used when the thermal and mechanical solutions strongly affect each other. However, it should be noticed that there is a limitation for the fully coupled thermomechanical analysis to be applied to curved element edges as temperature is always interpolated linearly (Hibbitt, Karlsson & Sorensen 2002). This limitation implies that fully coupled models may not be applicable to a multipass welded tee branch junction, which has highly curved surfaces and is of our main interest. Detailed descriptions of the development of both models will be provided in Chapter 5.

3.2.2 Thermal analysis

The objective of thermal analysis is to determine the transient temperature field. As stated before, welding is a process that creates a nonuniform temperature distribution and complex thermal cycles in the material. The most significant heat transfer mechanisms in welding are the heat input from a heat source and the heat losses due to conduction, convection and radiation from the weldment surfaces. The governing equation for the transient thermal analysis is given as (Carslaw and Jaeger 1947):

$$\frac{\partial}{\partial x}(k_x \frac{\partial T}{\partial x})+\frac{\partial}{\partial y}(k_y \frac{\partial T}{\partial y})+\frac{\partial}{\partial z}(k_z \frac{\partial T}{\partial z})+Q=\rho c \frac{\partial T}{\partial t} \qquad \text{Equation 3.1}$$

Equation 3.1 is an energy balance equation which states that the rate of heat conduction plus the rate of energy input by the welding heat source is equal to the rate of energy storage in the weldment.

To solve the above partial differential equation, initial conditions as well as boundary conditions are necessary to completely define the thermal transient problem. The initial condition is that

$$T = T(x, y, z, t_0) = T_a \qquad \text{Equation 3.2}$$

The general boundary conditions due to convection from the surfaces are governed by,

$$k_x \frac{\partial T}{\partial x} n_x + k_y \frac{\partial T}{\partial y} n_y + k_z \frac{\partial T}{\partial z} n_z = -h(T - T_a) \qquad \text{Equation 3.3}$$

Equation 3.3 is the Newton's cooling law. Heat losses through radiation were neglected. For the present study, it is assumed that the thermal conductivity is the same in all directions and can be denoted simply by *k*.

Equation 3.1 is highly nonlinear since thermal conductivity, specific heat and density are strongly dependent on temperature. This equation can be discretized for the FE solution of the transient temperature field conveniently (Lewis *et al.*1996).

When analysing nonuniform transient temperature fields, it is extremely important to simulate welding heat input accurately. In order to do that, three factors need to be considered (Radaj 1992), i.e. mobility (stationary or moving), dimension (plane or volume heat distribution) and duration (instantaneous or continuous).

In the current research, different heat source models were used for the 2D and 3D analyses. A stationary and continuous plane heat source was selected for the 2D model, while a moving and instantaneous volume heat source was considered for the 3D model. They were simulated as heat flux imposed onto newly activated area or volume elements that represent deposited material. The specific surfaces and boundary conditions for heat input and heat losses are incorporated in the FE input files, as will be described in detail in Chapter 5.

3.2.3 Mechanical analysis

The determination of stress and strain consists of combining the equation of equilibrium and compatibility with the constitutive (stress-strain) relations, and solving the resulting differential equations (Stouffer and Dame 1996). Equilibrium and compatibility equations are the same for both elastic and inelastic problems, but the stress-strain relations are different.

In the area around the weld, the thermal stress is high and the yield strength of material is very low; as a result, plastic deformation occurs in this region. Plasticity

theories model the material's mechanical response by "incremental" theories in which the total strain increment is decomposed into elastic, thermal and inelastic parts (Boley and Weiner 1960). The inelastic strain can be further decomposed into plastic strain and strain associated with creep, which gives:

$$d\varepsilon^{total} = d\varepsilon^{elastic} + d\varepsilon^{plastic} + d\varepsilon^{thermal} + d\varepsilon^{creep} \qquad \text{Equation 3.4}$$

It is well known that viscous effects become important only during prolonged exposure to high temperature (Hibbit and Marcal 1973). During welding, the time during which the material stays at a high temperature is rather short. Thus, creep effects are unlikely to have any significant influence on the final residual stress distribution and are neglected in the current research. Therefore, Equation 3.4 can be simplified to:

$$d\varepsilon^{total} = d\varepsilon^{elastic} + d\varepsilon^{plastic} + d\varepsilon^{thermal} \qquad \text{Equation 3.5}$$

Thus the thermo-elasto-plastic formulation, together with the von Mises yield criterion and associated flow rule with isotropic hardening were assumed to simulate the material behaviour during welding.

The same material properties were assumed for both the base and weld metal in the current research. Different weld metal material properties would be expected to change the magnitude of the resulting residual stresses, but not the overall residual stress distribution characteristics. Temperature dependent mechanical properties were taken into account. All of these introduced material nonlinearities in the thermomechanical analysis.

3.3 Implementation

3.3.1 Multipass welding

Multipass welding is the most frequently used method in joining thick section components, during which the grooves are filled by sequentially deposited weld beads layer by layer. As the thickness of components increases, the number of weld passes required for a complete joint penetration also increases.

During multipass welding, each successive weld alters the temperatures, stresses and distortions caused by previous passes. Consequently, both base and weld metals are subjected to complex thermal cycles and inelastic strain patterns. The effects, while cumulative, are not precisely additive. Analysing multipass welds as a series of single pass welds is certainly the most rigorous, albeit a costly process. Lumping successive passes together is one way to reduce the computational cost.

The lumping technique can be realized in several ways. Successive passes can be grouped together by taking one thermal history to represent all the passes and then performing a single mechanical analysis. This single thermal history might be the history from one pass or the history obtained by superimposing several thermal histories and taking the current temperature of any point from the maximum temperature found at that location, for that point in time, from any of the histories. Another method is to perform a complete thermal analysis, accounting for each weld pass and post processing these temperature histories to form some kind of a temperature envelope in order to simplify the mechanical analysis. A third approach is to merge several passes into one larger weld, i.e. to reduce the number of weld passes. All welds in one layer can then be merged into a single weld pass. However, all these lumping techniques involve some loss in accuracy because they limit the way in which the stress field from one pass may contribute to the stress history of subsequent passes.

Since the analysis of temperature distribution and residual stress build-up after each pass will provide the most accurate information for understanding the evolution of thermal stresses and the final profiles of residual stresses, analysing multipass welds as a series of single pass welds will be mainly employed in the current study. However, the lumping technique will also be investigated in Chapter 7 in order to find out the most cost-effective method for predicting residual stresses in thick-walled tee branch junction.

3.3.2 Element removal/reactivation technique

The ABAQUS element removal/reactivation technique is a proven method of simulating sequential deposition of filler material in both thermal and mechanical

analysis. This technique 'can be used to simulate removal of part of the model, either temporarily or for the remainder of the analysis'. It 'allows reactivation of elements strain-free or with strain' (Hibbitt, Karlsson & Sorensen 2002).

In this technique, the fusion zone is partitioned comprehensively and meshed with the rest of the model initially. Elements representing each weld pass are then grouped in sets and disactivated at the start of the analysis. As the analysis progresses, element sets representing consecutive passes are reactivated strain-free to simulate material deposition.

Just prior to the removal step, ABAQUS stores the forces/fluxes that the region to be removed is exerting on the remaining part of the model at the nodes on the boundaries between them. The forces are ramped down gradually to ensure that element removal has a smooth effect on the model. If the fluxes are high and the step is long in transient heat transfer or fully coupled temperature-displacement analysis, this ramping down may have the effect of cooling down or heating up the rest of the body. This problem can be avoided by removing the elements in a very short transient step prior to the rest of the analysis (Hibbitt, Karlsson & Sorensen 2002). A step time of 0.0001s was assumed in the current research.

No further calculations are performed for the elements being removed. The removed elements remain inactive in subsequent steps unless they are reactivated with the *MODEL CHANGE, ADD option.

The element reactivate technique might introduce serious problems into the thermal stress analysis. These problems are caused by large displacements induced by the heating process. However, ABAQUS provides a method by using the ADD=STRAIN FREE parameter on the *MODEL CHANGE option to reactivate stress/displacement elements in a strain-free state. These newly reactivated strain-free elements in large-displacement analysis 'fit into whatever configuration is given by its nodes at the moment of reactivation' (Hibbitt, Karlsson & Sorensen 2002). However, this configuration must be meaningful in such that it should not be severely distorted. Strain-free reactivation is usually used to model the creation of an undeformed and unstrained region of the model that is sharing a boundary with another, possibly stressed

or deformed region.

After reactivation, the strains and the deformation gradients are based on the displacements subsequent to the moment of reactivation, rather than on their total displacements. Thus, the current configuration at the start of the reactivation step is the new initial configuration for the element.

3.3.3 Element formulation

The accuracy of the simulation results depend on element type, element shape, interpolation scheme, integration scheme and element size. Choosing the correct element for a particular analysis is thus very important. The element selection process is summarized in Figure 3.5. By considering each of these aspects carefully, the best element for a given analysis can be selected.

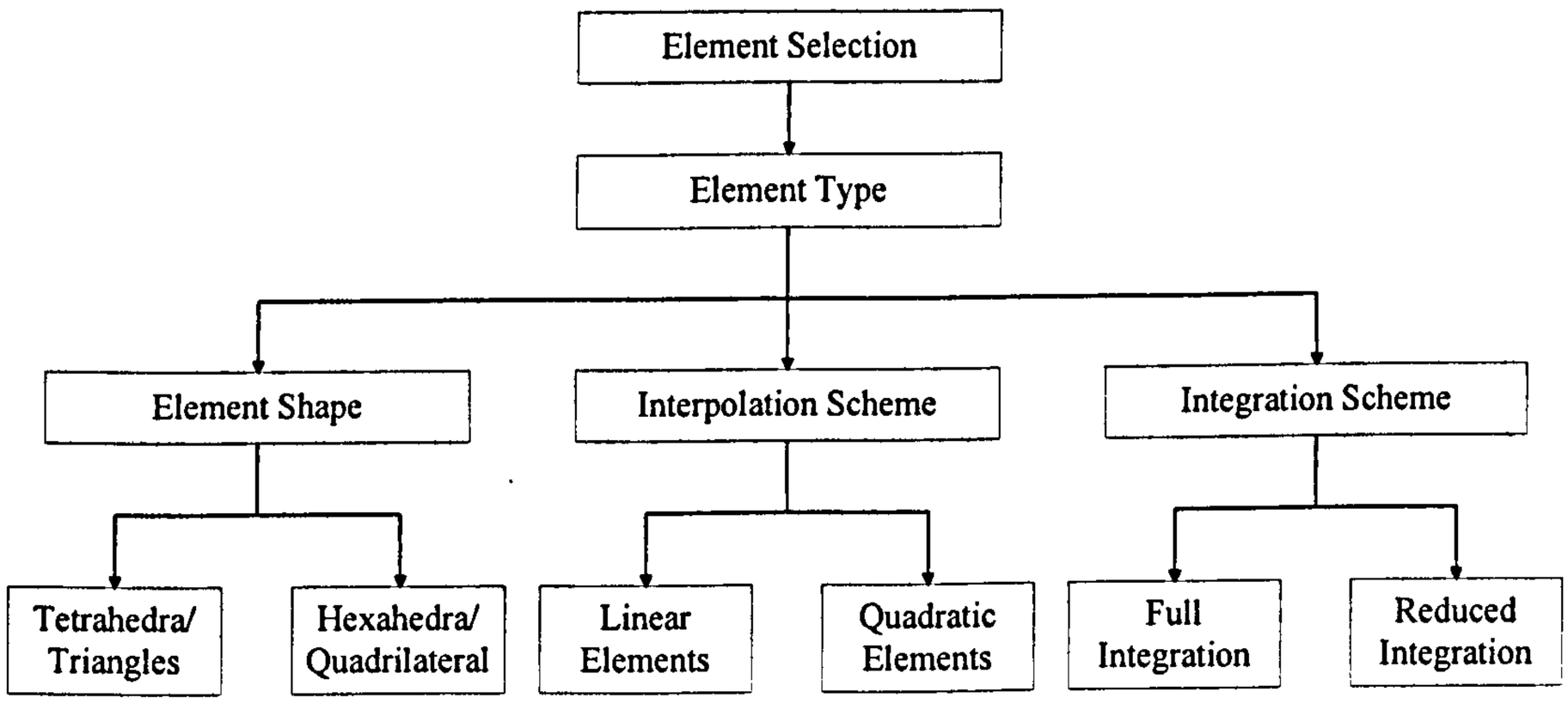

Figure 3.5 Element selection process

3.3.3.1 Element type

Three types of elements, i.e. heat transfer element, stress/displacement element and coupled temperature-displacement element, were employed in the present research.

The heat transfer elements are commonly used for thermal analysis, which provide temperature output as an input for the equivalent stress elements. When used for thermal analysis, these elements only have temperature as a degree of freedom.

Stress/displacement elements are used for the modelling of linear or complex nonlinear mechanical analyses that involve plasticity and/or large deformations. They can also be used for thermal-stress analysis, where the temperature history can be obtained from a heat transfer analysis. Solid stress/displacement elements have only displacement degrees of freedom.

Coupled temperature-displacement elements are used in problems for which stress analysis depends on the temperature solution and the thermal analysis depends on the displacement solution. Coupled temperature-displacement elements have both displacement and temperature degrees of freedom.

Coupled temperature-displacement elements use either linear or parabolic interpolation for the geometry and displacements. The temperature is always interpolated linearly. Curved element edges should be avoided, as exact linear spatial temperature variations cannot be obtained with curved edges (Hibbitt, Karlsson & Sorensen 2002). For output purposes the temperature at the midside nodes of second-order elements is determined by linear interpolation from the corner nodes. This requirement limits the use of coupled temperature-displacement elements in the multipass simulation of the highly curved structures of 3D pipes and/or tee branch junctions.

3.3.3.2 Element shape

The two main classes of elements used in 3D FE analysis are tetrahedral and hexahedral elements. Tetrahedral elements are geometrically versatile and are more easily generated for almost all models with complex shapes as compared with hexahedral meshes.

Because it uses higher order interpolation functions, the hexahedral mesh, on the other hand, contribute to more computational efficiency and to highly accurate solutions, especially in the nonlinear analysis regime, in comparison with the tetrahedral mesh. Whenever a simulation of elastic-plastic material behaviour in a 3D analysis is made, it

is necessary to use at least quadratic tetrahedral elements or preferably linear hexahedral elements (Benzley *et al.* 1995). This is because the use of quadratic elements will increase the number of degrees of freedom, which makes the analysis very expensive. Also, linear tetrahedral elements should be avoided as much as possible in stress analysis; these elements are usually overly stiff, exhibit slow convergence, and extremely fine meshes are required to obtain results of sufficient accuracy. Finally, a tetrahedral mesh usually increases the number of elements from four to tenfold over a hexahedral mesh.

3.3.3.3 Interpolation scheme

Displacements are calculated at the nodes of the element. At any other point in the element, the displacements are obtained by interpolating from the nodal displacements. Usually the interpolation order is determined by the number of nodes used in the element.

Elements that have nodes only at their corners use linear interpolation in each direction and are often called linear or first-order elements. This assumes a linear variation in properties (temperature/displacement) across the element, and that the sides of the element remain straight during deformation for isoparametric formulation.

Elements with midside nodes use quadratic interpolation and are often called quadratic or second-order elements. This allows the properties to vary in a quadratic manner across the element. This greater flexibility makes quadratic elements more accurate than the linear elements. The quadratic elements capture stress concentrations more effectively and are better for modelling a curved surface with fewer elements. However, their greater complexity also makes them significantly slow. They are not recommended for coupled temperature-displacement problems.

3.3.3.4 Integration scheme

A reduced integration element calculates the material behaviour at a lower number of integration points than would a fully integrated element. Reducing the number of

integration points reduces the number of computations per element and hence increases the speed of the analysis.

ABAQUS uses numerical techniques to integrate various quantities over the volume of each element. In full integration, the shape function for the particular problem is solved for all the higher order terms of the equation, whereas in reduced integration, the higher order terms are neglected.

Reduced integration is available for hexahedral elements. It uses a lower-order integration to form the element stiffness matrix. The mass matrix and distributed loadings use full integration. Reduced integration reduces its running time, especially in three dimensions. For example, element type C3D20 has 27 integration points, while C3D20R only has 8; therefore, element assembly is roughly 3.5 times more costly for C3D20 than for C3D20R (Hibbitt, Karlsson & Sorensen 2002).

3.3.4 Meshing methods

An appropriate mesh is of critical importance in welding simulation. The elements must be sufficiently small to capture the steep thermal and mechanical gradients close to the weld. However, the use of small elements will increase the total number of elements in the model, and consequently result in prohibitive computational times.

Remeshing is one option to solve this problem (Lindgren *et al.* 1997, Runnemalm and Hyun 2000, Shi *et al.* 2002). Instead of remeshing along the entire welding path, the mesh can be refined only in the area adjacent to the heat source. As welding progresses, the previously defined coarse mesh is substituted in order to maintain a suitable degree of refinement. Remeshing decreases the number of elements required, thus reducing the computational expense. However interpolating variables from one mesh to another is computationally expensive and may also introduce further errors. Although many commercial FE packages offer a remeshing facility, ABAQUS unfortunately does not. Consequently, a well-graded all-hexahedral mesh is required for effective multipass welding simulation in the current study.

When meshing complex geometries with all-hexahedral elements, apart from subjective variables such as user expertise and software maturity, the topological and geometric aspects of a solid and element size, are the important variables that affect meshing complexity. The following section only introduces general rules and issues concerning hexahedral meshing method. The particular meshing procedures for the tee branch junction will be described in more detail in Chapter 5.

3.3.4.1 Hexahedral meshing constraints

As stated before, hexahedral elements are preferred to tetrahedral elements in 3D FE analysis. However, unlike tetrahedral meshes, hexahedral meshes are much more constrained and, therefore, much more difficult to generate. These constraints are tied to the element shape itself as well as the connectivity requirements of the resulting mesh, which pose significant technical challenges in all-hexahedral meshing.

The first constraint is that a hexahedral element is a volume composed of three sets of opposing quadrilateral faces; this implies that equal numbers of elements should be on the opposite sides in 3D meshing. However, this can often be impossible for an arbitrary geometric configuration or can involve considerable user interaction to decompose geometry into structured meshable regions and assign boundary intervals.

Another important constraint is the well-known even boundary interval constraint, where the number of mesh edges bounding a surface must be even for a quadrilateral mesh to exist for that surface (a similar constraint exists on the number of quadrilaterals bounding a volume to be meshed with hexahedra).

Finally, since geometric curves can be shared by two or more geometric surfaces, the number of intervals on a given curve must satisfy constraints on all surfaces to which it is connected. These constraints propagate across the volume because of the shared surfaces. In order to ensure that all constraints are met, the interval assignment problem must be solved globally.

3.3.4.2 Hexahedral mesh generation algorithms

Most of the hexahedral meshing algorithms currently in use are limited to certain classes of geometry. While it is always worth considering general algorithms viable for a more general geometry, a combination of the well-established algorithms is ready to take on complicated geometry. In practice, when hexahedral meshing is required, decomposition of the entire volume to conform to the requirements of the available hexahedral meshing tools remains a fundamental step in the meshing process (Tautges 2001). By partitioning the volume into multiple recognizable primitive shapes (i.e. a brick) or swept volumes, the complexity of the geometry and topology of the original model is reduced, thus the model becomes meshable with well established approaches. Besides improving the meshability, the quality of the mesh can be enhanced and the meshing time can be reduced.

However, the partitioning process is very user-intensive and time-consuming, especially for complex and large scale 3D models, as it uses human reasoning to decide both where to perform decomposition and when to stop decomposing a given part.

3.3.5 Model sources of nonlinearity

In order to reflect the real nature of thermal and mechanical phenomena during multipass welding process, three sources of nonlinearity, i.e. material, geometric and boundary nonlinearities, were incorporated in the model.

As stated in Section 3.2, temperature dependent thermal and mechanical properties, latent heat and plastic behaviour of the base and weld materials introduce material nonlinearity into both the thermal and stress analyses.

Large deformation is an important phenomenon during multipass welding and this geometric nonlinearity was included in the model by specifying NLGEOM in the *STEP option of ABAQUS. Accordingly, most elements are formulated at their current configuration using current nodal positions.

A moving heat source is a predominant source of boundary nonlinearity which

introduces nonlinear thermal loading cycles. This thermally induced loading produces nonlinear thermal strains that result in residual stresses after welding.

In stress analysis, contact problems are another common source of boundary nonlinearity. Contact conditions are a special class of discontinuous constraint, allowing forces to be transmitted from one part of the model to another. The constraint is discontinuous because it is applied only when the two surfaces are in contact. When the two surfaces separate, no constraint is applied. Contact boundary conditions have been considered in the 2D sequentially coupled model for comparison purposes.

3.3.6 Analysis solution and control

3.3.6.1 Solving nonlinear problems

As stated before, welding residual stress simulation is a highly nonlinear analysis which includes geometry, material and boundary nonlinearities. The objective in solving nonlinear problems is to obtain a converged solution accurately and economically.

Usually, the analysis is divided into several steps according to practical welding procedures. Each step defines an analysis type, e.g. heat transfer analysis, static stress analysis, etc., as well as different loads, boundary conditions, to be performed during the step. The analysis procedure can be changed from step to step in any meaningful way. Since the state of the model (stress, strain, temperature, etc.) is updated throughout the whole analysis steps, the effects of previous history are always included in the response in each new step.

ABAQUS combines incremental and iterative procedures when solving nonlinear problems. In nonlinear analyses, each step is broken into increments so that the nonlinear solution path can be followed. A reasonable initial increment size in each step of the simulation must be provided so that ABAQUS automatically chooses the size of the subsequent increments to solve nonlinear problems efficiently.

In each increment, several iterations are performed. The number of iterations needed to find a converged solution for a time increment varies depending on the degree

of nonlinearity in the system. If the model is not in equilibrium at the end of the iteration, ABAQUS tries another iteration. Within each iteration, the solution that ABAQUS obtains should be closer to equilibrium. However, the iteration process itself may sometimes diverge and subsequent iterations may move away from the equilibrium state. In that case, ABAQUS may terminate the iteration process and attempt to find a solution with a smaller increment size.

Time increment control is an important issue in FE modelling. Analyses are generally divided into a number of time increments. The smaller the time increment is, the greater the number of increments will be required to complete a given analysis. Small elements in the mesh can also unduly control the size of time increment. However, if the increments are too large, the analysis may lose accuracy or fail to converge. The calculation time required for each increment depends on the number of degrees of freedom in the model.

ABAQUS usually uses automatic time increment schemes for the solution of transient problems that have a physical time scale. This scheme was employed in both the thermal and mechanical analysis in the current research. ABAQUS provides tolerance parameters to indicate the level of accuracy required in the approximate time integration of transient effects. In transient heat transfer analysis, the temperature increment tolerance, DELTMX, is used for automatically controlling time increment sizes. For the history dependent stress analysis, the equilibrium equation is solved in a series of small increments. ABAQUS will automatically select a time increment required for the solution to converge.

3.3.6.2 Analysis convergence controls

Solving nonlinear problems in ABAQUS involves the use of the Newton method for solving nonlinear equations, determining convergence and choosing suitable time increments automatically. There are numerous control parameters associated with the convergence and integration accuracy algorithms in ABAQUS. These parameters are assigned default values that are chosen to optimize the accuracy and efficiency of the solution for a wide spectrum of nonlinear problems. However, in certain cases, the

nonlinear equation solution accuracy, efficiency and time increment can be improved by adjusting some of the most important solution control parameters in the *CONTROLS option. Values given by the *CONTROLS option remain in effect for the remainder of the analysis or until they are reset by another use of this option.

Most nonlinear engineering calculations will be sufficiently accurate if the error in the residuals is less than the default value of 0.5%. This value is rather strict by engineering standards but, in all but exceptional cases will, guarantee an accurate solution to complex nonlinear problems. The value for this ratio can be increased to a larger number if some accuracy can be sacrificed for computational speed.

In addition to sufficiently small residuals, ABAQUS requires that the largest correction to the solution provided by the current Newton iteration is also small compared to the largest corresponding incremental solution. The default value is 1% (Hibbitt, Karlsson & Sorensen 2002).

Both of the above convergence checks must be satisfied before a solution is said to have converged for that time increment. Some analyses may not require such accuracy, or require fast convergence, thus permitting these ratios to be increased, as described in Section 5.4.3.

3.4 Conclusions

Finite element analysis of multipass welding process can be very challenging and time consuming. It is not only because of the tedious task of generating a graded all-hexahedral mesh when creating FE models involving filler material deposition, but also because of the high computational cost, especially when solving the highly nonlinear problem in the multipass welded large, heavy and complex component.

This chapter described the FE procedures employed in the current research. The ABAQUS commercial software was selected for the simulation of residual stresses induced by multipass welding process. Sequentially and fully coupled simulation procedures can be used to account for the coupling between the thermal and mechanical

field. Lumping schemes and the element removal/reactivation technique are effective tools in simulating filler metal transfer during multipass welding process. All-hexahedral elements are preferred in the 3D analysis and their meshing technique was discussed in detail. Nonlinearities involved in the weld simulation and the techniques of efficient solving highly nonlinear FE problems were also discussed.

These modelling techniques were implemented into a working code in ABAQUS. They included a complete description and definitions of the meshes, heat input, filler metal deposition, appropriate boundary conditions, material physical and mechanical properties, proper selection of the steps of calculations and appropriate analysis control. The detailed development of the computational model will be presented in more detail in Chapter 5.

Chapter 4 Material Properties

4.1 Introduction

Welding can join a wide range of materials. Amongst the many structural materials used in industry, carbon steel and stainless steel are probably the most commonly used materials because of their desirable properties. These are the materials that were chosen for both modelling and experimental validation in the current study. Unless specifically mentioned, it is assumed that the weld and base metals are the same.

A correct description of material behaviour and proper use of pertinent material data within a welding temperature range are essential for establishing an accurate model for welding simulation. It is extremely important that the analysis includes temperature dependent material properties. This chapter provides relevant data collected from published sources in the open literature. The chemical compositions of the two materials considered in this work are given in Tables 4.1- 4.2. Material properties necessary for the simulation are presented in Sections 4.2 and 4.3, respectively. Most data for the ASTM specifications A36 mild carbon steel are from Shim *et al.* (1992) and ASM International Handbook Committee (1990). Data for the AISI type 304 and 316L stainless steel are from Rybicki *et al.* (1978, 1982), Dong (2001) and ASM International Handbook Committee (1990). These data can be applied to a quite wide range of steels in each of the carbon and stainless steel categories respectively, because minor variations in alloy content have negligible influence on these properties (ASM International Handbook Committee 1990).

Table 4.1 Chemical composition of ASTM A36
(Chang *et al.* 2004)

C	Mn	P	S	Si	Ni	Cr	Mo	Cu	Fe
0.16	0.69	0.033	0.039	0.21	<0.1	<0.08	<0.1	<0.1	Bal.

Table 4.2 Chemical composition of AISI 304 stainless steel
(Peckner and Bernstein 1977)

C	Mn	P	S	Si	Ni	Cr	Mo	Fe
0.03	2	0.045	0.03	1	12	17	2.5	Bal.

4.2 Thermo-physical properties

Temperature dependent thermo-physical properties, i.e. thermal conductivity, specific heat and density, were used in the transient thermal analysis. Above the melting temperature, the properties were held constant, except for the thermal conductivity. The latter was doubled to compensate for the effect of heat transfer due to convection stirring in the molten weld pool material, as was proposed in Dong (2001). Both temperature dependent thermal properties and latent heat introduce nonlinearities in the heat transfer analysis, although the former has a lesser effect than the latter.

4.2.1 Thermal conductivity

The thermal conductivity is a material property that describes the rate at which heat is transferred through a material. The temperature dependent isotropic thermal conductivities for the mild carbon steel ASTM A36 and stainless steels 304 used in the present work are shown in Figure 4.1.

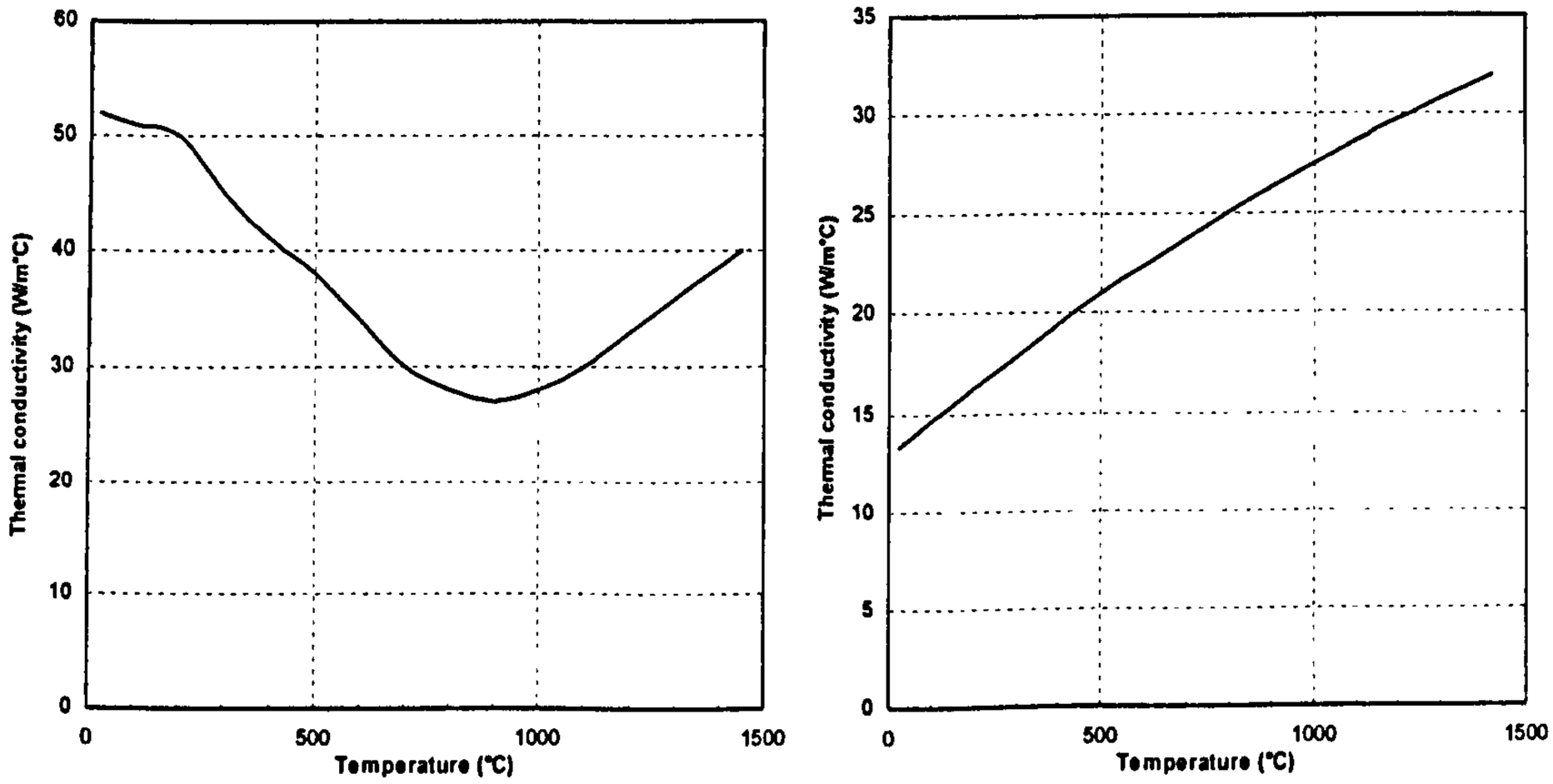

(a) ASTM A36 (b) 304 stainless steel

Figure 4.1 Temperature dependent thermal conductivity

4.2.2 Specific heat capacity

The specific heat is the amount of heat per unit mass required to raise the temperature by one degree Celsius. The temperature dependent specific heat for mild

carbon steel and stainless steel used in the present work are shown in Figure 4.2.

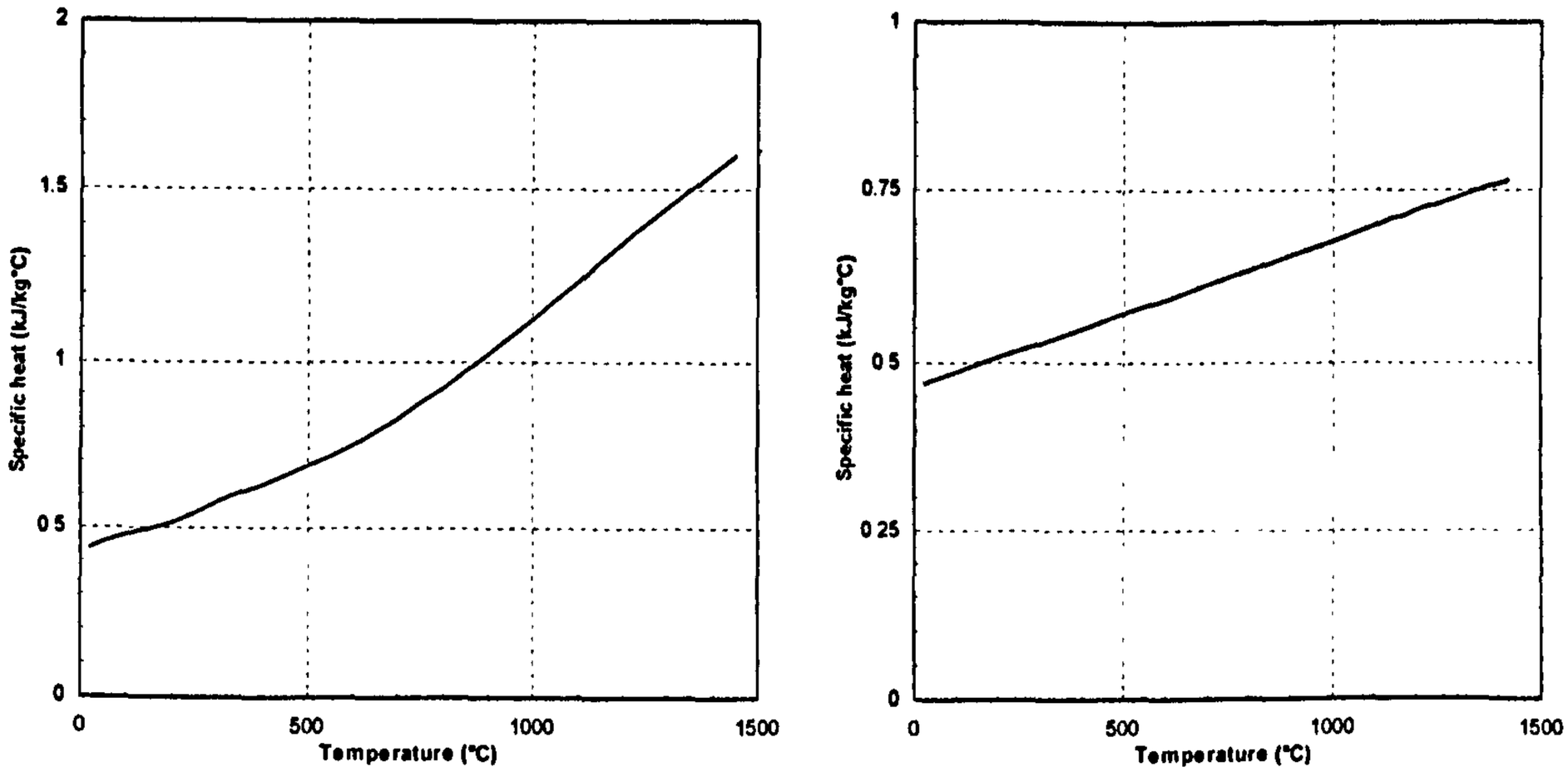

(a) ASTM A36 (b) 304 stainless steel

Figure 4.2 Temperature dependent specific heat

4.2.3 Thermal expansion coefficient

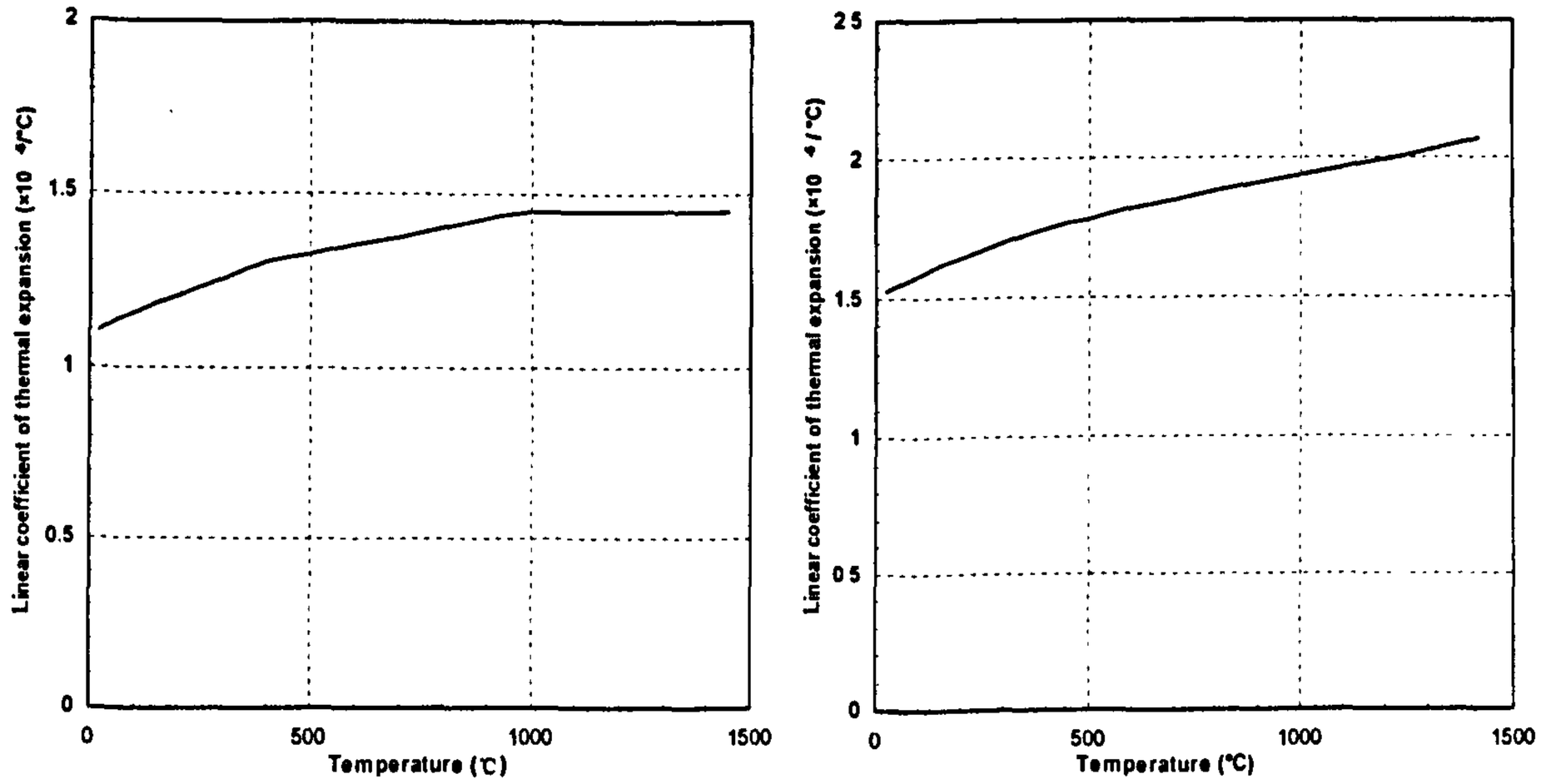

(a) ASTM A36 (b) 304 stainless steel

Figure 4.3 Temperature dependent coefficient of thermal expansion

In addition to the changes of properties with increasing temperature, most materials expand with increasing temperature. The temperature dependent coefficients of thermal expansion for the materials used in this study are presented in Figure 4.3.

4.2.4 Latent heat and melting point

When a material undergoes a phase transformation, thermal energy in the form of latent heat is either absorbed or released. This latent heat is the total energy change due to phase change and is assumed to be in addition to the specific heat. When the material is cooled slowly by a constant rate of heat extraction, the latent heat released during the transformation, at least, retards the rate at which temperature drops. This will appear as a discontinuity in the cooling curve, and the converse is also true.

Latent heat effects were assigned a value of 247 kJ/kg between the solidus temperature of 1465°C and liquidus temperature of 1544°C for the ASTM A36 mild carbon steel and 300 kJ/kg between the solidus temperature of 1420°C and liquidus temperature of 1465°C for 304 stainless steel, respectively.

The approximate melting points for ASTM A36 mild carbon steel and 304 stainless steel are 1510°C and 1460°C, respectively.

4.2.5 Density

Since metal usually expands at higher temperature, it results in a lower density. The temperature dependent density for mild carbon steel and stainless steel used in the present work are shown in Figure 4.4.

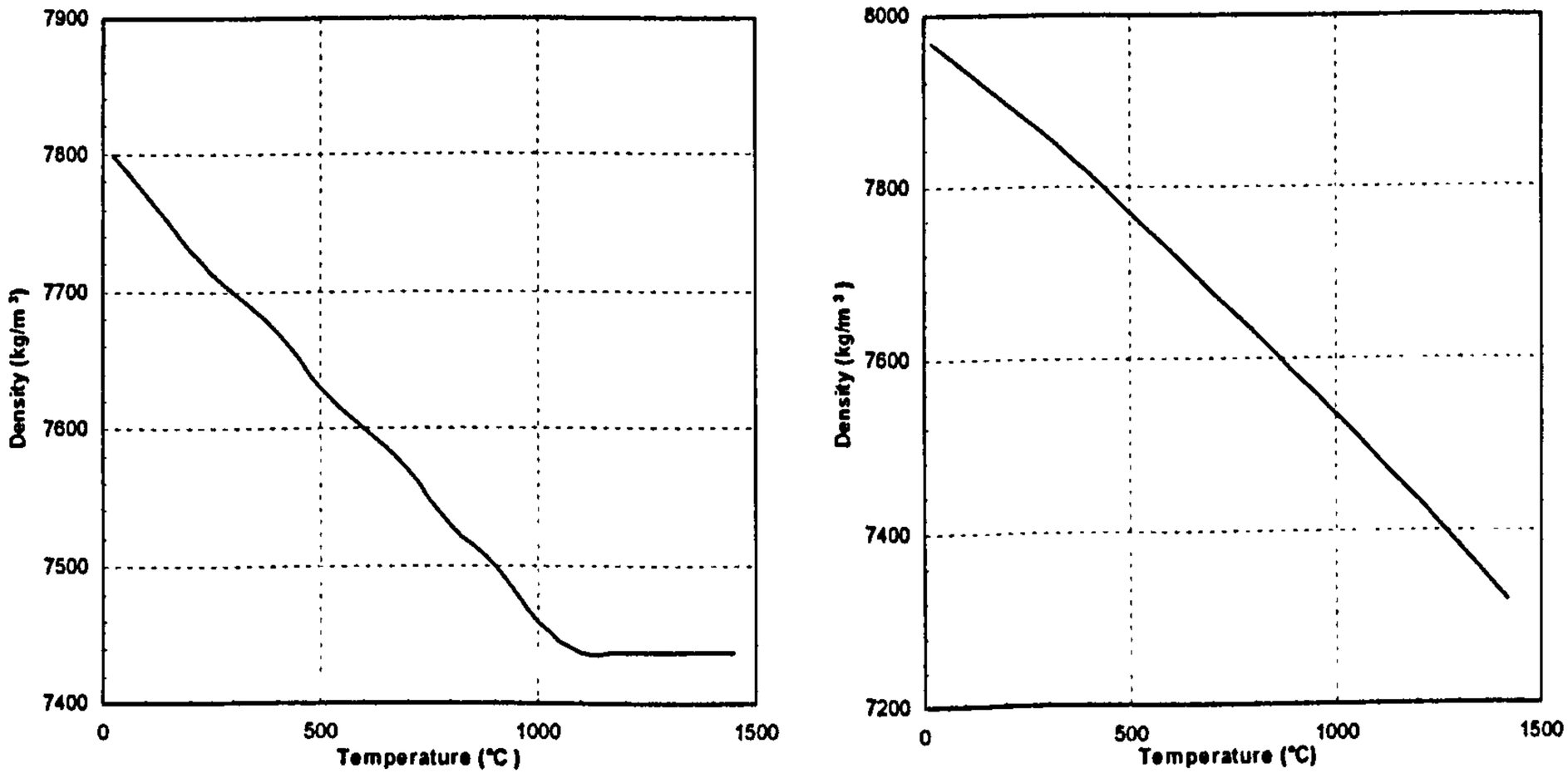

(a) ASTM A36 (b) 304 stainless steel

Figure 4.4 Temperature dependent density

4.3 Mechanical Properties

Apart from the coefficient of thermal expansion, accurate stress analysis to determine residual stresses after cooling requires the temperature dependent elastic modulus, Poisson's ratio and yield stress. These also introduce important material nonlinearities in the stress analysis.

4.3.1 Elastic modulus

The elastic modulus of a material represents its relative stiffness in the elastic range and can be determined from an experimentally obtained stress-strain curve.

As temperature increases, the modulus of elasticity of most metals generally decreases. Most of the stiffness of the metal is lost at about 700°C. As can be noticed from Figure 4.5(a), the elastic modulus of mild carbon steel is reduced to approximately half the value at ambient temperature when the temperature is about 550°C. The variations of the modulus of elasticity with temperature for the ASTM A36 and 304 stainless steel are presented in Figure 4.5.

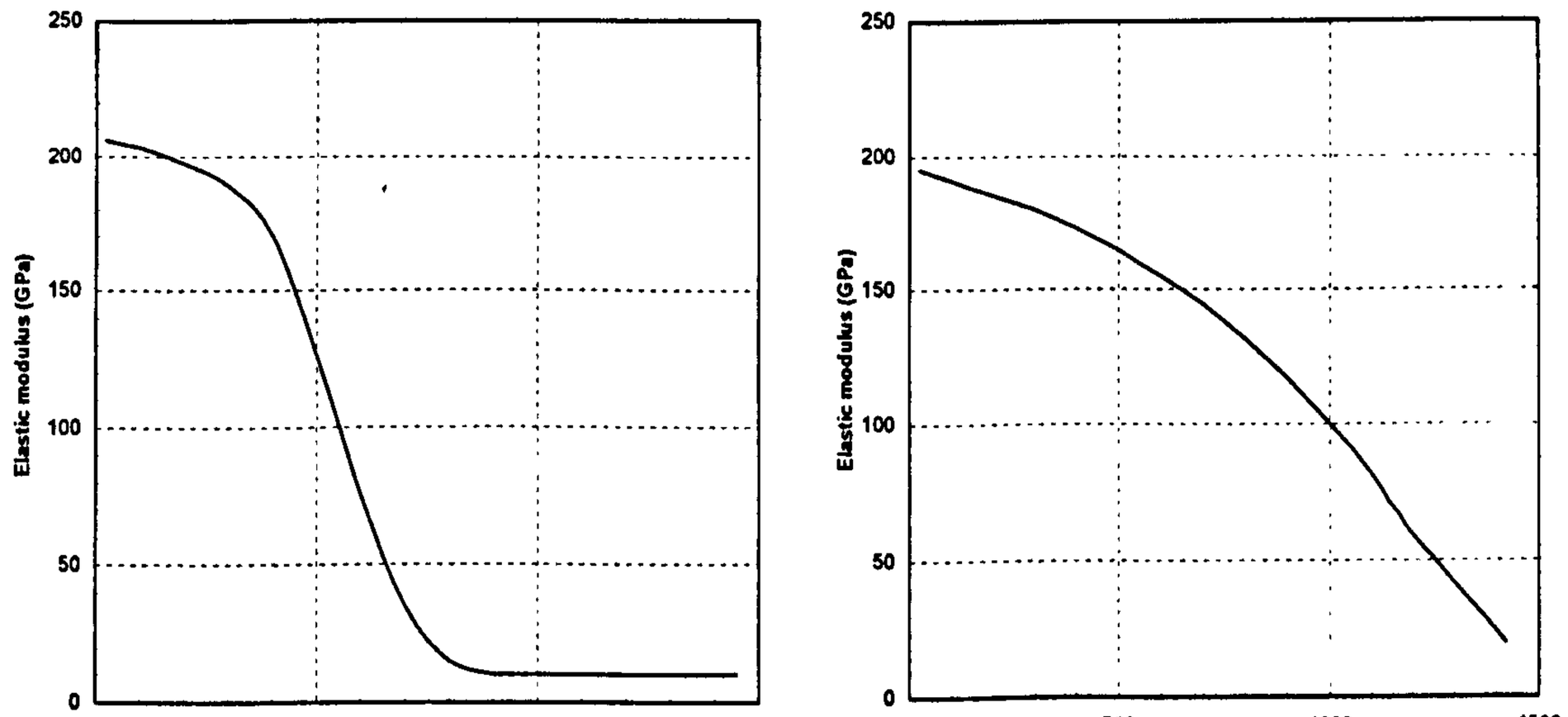

(a) ASTM A36 (b) 304 stainless steel

Figure 4.5 Temperature dependent elastic modulus

4.3.2 Poisson's ratio

This quantity determines the absolute value of the ratio between the transverse strain and the corresponding axial strain in the elastic range. The temperature dependent Poisson's ratios for the materials used in this study are presented in Figure 4.6.

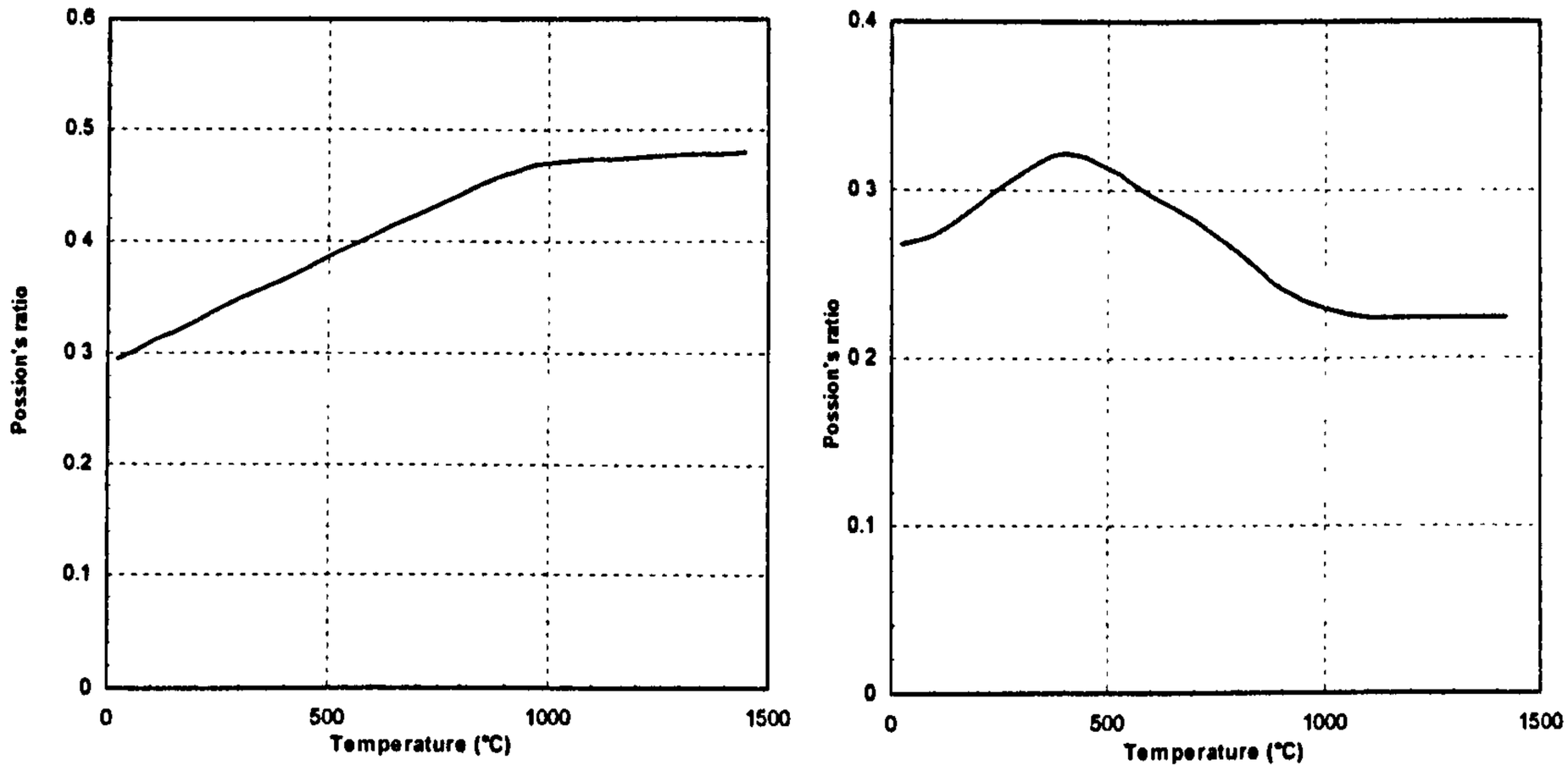

(a) ASTM A36 (b) 304 stainless steel

Figure 4.6 Temperature dependent Possion's ratio

4.3.3 Yield stress and stress-strain curves

Yield stress (0.2% Proof stress) is defined as the stress at which the residual strain after unloading is not greater than 0.2%. Yield stress of metals generally decreases as temperature increases. In fact, at the liquidus temperature, a metal will loose their strength completely. To avoid computational errors due to division by zero in ABAQUS, a small non-zero value is assumed for the yield stress at the liquidus temperature.

The thermo-elasto-plastic formulation, together with the von Mises yield criterion and associated flow rule with isotropic hardening were assumed to simulate the material behaviour during welding. If isotropic hardening is defined, the yield stress must be entered as a function of a uniaxial equivalent plastic strain and temperature on the data lines of the ABAQUS *PLASTIC option. These data are obtained from stress-strain curves at a range of temperatures. The yield stress at a given state is interpolated linearly between the data provided, and it remains constant for plastic strains exceeding the last value given as tabular data.

It should be mentioned that stress-strain curves are often supplied using values of nominal stress and strain (Boyer 1987). However, the true stress and strain, which are based on the instantaneous cross sectional area, must be used when defining plasticity in ABAQUS. Thus the nominal stress/strain values should be converted to the true stress/strain values by using the expressions below:

$$\varepsilon = \ln(1+\varepsilon_{nom}) \qquad \text{Equation 4.1}$$

$$\sigma = \sigma_{nom}(1+\varepsilon_{nom}) \qquad \text{Equation 4.2}$$

The data on the *PLASTIC option define the true yield stress of the material as a function of true plastic strain. The first piece of data given defines the initial yield stress of the material and, therefore, should have a plastic strain value of zero. The strains provided in the material test data used to define the plastic behaviour are not likely to be the plastic strains in the material. Instead, they will probably be total strains, which include elastic and plastic strain in the material. The plastic strain is then obtained by

$$\varepsilon^{pl} = \varepsilon - \varepsilon^{el} = \varepsilon - \sigma / E \qquad \text{Equation 4.3}$$

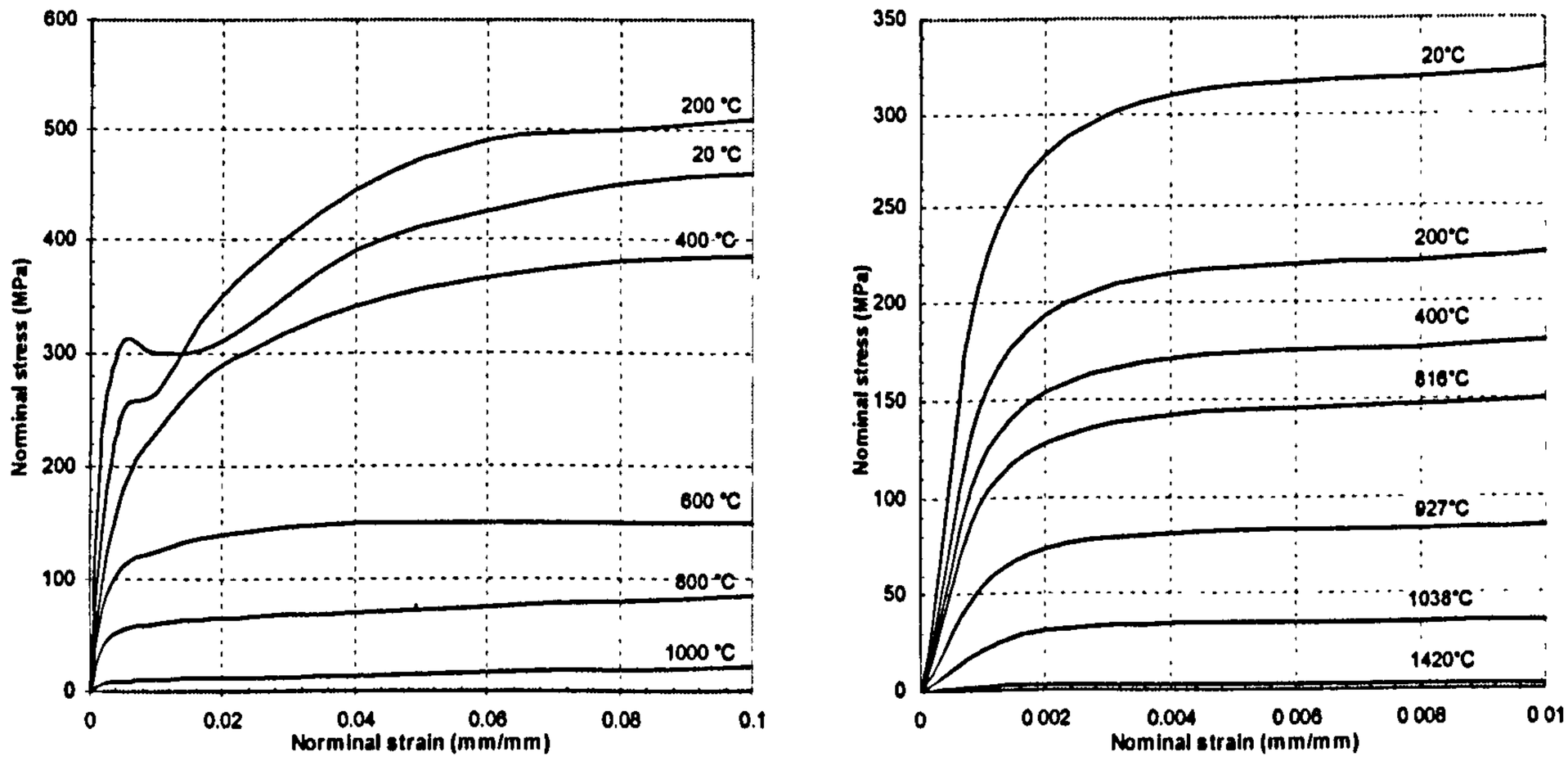

(a) ASTM A36 (b) 304 stainless steel

Figure 4.7 Stress-strain curves at a range of temperatures

The nominal stress-strain curves as a function of temperature for ASTM A36 mild

carbon steel and 304 stainless steel are shown in Figure 4.7.

4.4 Conclusions

In the current research, it is assumed that the filler and base metal are of the same homogeneous material. The thermo-elasto-plastic formulation, together with the von Mises yield criterion and associated flow rule with isotropic hardening will be employed in the stress analysis.

Temperature dependent thermal and mechanical properties were used in both the thermal and stress analyses. Detailed material data from open literature at elevated temperature has been provided in this chapter and will be incorporated in the models in the following chapters.

Chapter 5 Model Development

This chapter presents the detailed model development for predicting residual stress built-up during multipass welding process. In order to develop the expertise and compare existing modelling techniques, sequentially and fully coupled generalized plane strain models were firstly developed and evaluated in Section 5.1. Following this, 3D sequentially coupled thermomechanical models were then developed for simple geometries such as butt-welded plates and pipes, as described in Sections 5.2 and 5.3. Finally, the model was extended to a complex geometry, i.e. a multipass, circumferentially fillet-welded, stainless steel tee branch junction for residual stress prediction and optimization in Section 5.4.

All runs were performed on a platform that used a Pentium III 600 MHz with 512MB RAM. The pre/post processing was performed using ABAQUS/CAE (Hibbitt, Karlsson & Sorensen 2003) and the analyses were performed using ABAQUS/Standard, Versions 6.3 (Hibbitt, Karlsson & Sorensen 2002) in a Windows 2000 environment.

5.1 2D model of butt-welded plates

5.1.1 Sequentially coupled model

During welding, the heat source transfers a certain amount of energy to the top surface of the plates. When the welding speed is sufficiently high, it is generally assumed that heat conduction in the welding direction is negligible compared with that in the direction perpendicular to the weld centreline. This can be used as a justification for reducing the 3D problem to an ideal 2D case, where heat flow is limited to a cross section perpendicular to the welding direction. However, in the stress analysis, plane strain elements could not accommodate any thermal expansion in the longitudinal direction, consequently a generalized plane strain condition had to be assumed to account for the out-of-plane expansion in the model.

For proper comparison with existing experimental data, the geometry, dimensions

and welding parameters used in the sequentially and fully coupled models were identical to those reported by Shim *et al.* (1992). An ASTM A36, 25.4mm thick, butt-welded plate was chosen for model evaluation. A lumping scheme similar to that used by Shim *et al.*, i.e. a total of 11 passes were lumped into 6 passes in a double V-groove thick plate, was adopted to reduce the computational costs. Heat flux for each pass in the same layer was added and distributed over the whole area of that layer. The same material properties were used for base metal, weld metal and heat affected zone. Temperature dependent thermal and mechanical properties were defined in the thermal and mechanical models respectively in the sequentially coupled model.

5.1.1.1 Geometry and mesh

A cross section in the middle of the plate was considered to represent the 2D model. Since the butt-welded plate was symmetrical about the plane passing through the weld centreline, only half of the plate was considered. Small size elements were chosen for the region with high temperature and stress gradients. Away from the weld centreline, element sizes were increased to reduce the total number of elements in the model. The same meshes have been used for the heat transfer and stress analysis in the sequentially coupled generalized plane strain model, as shown in Figure 5.1. The numbers in the figure indicate the welding pass sequences.

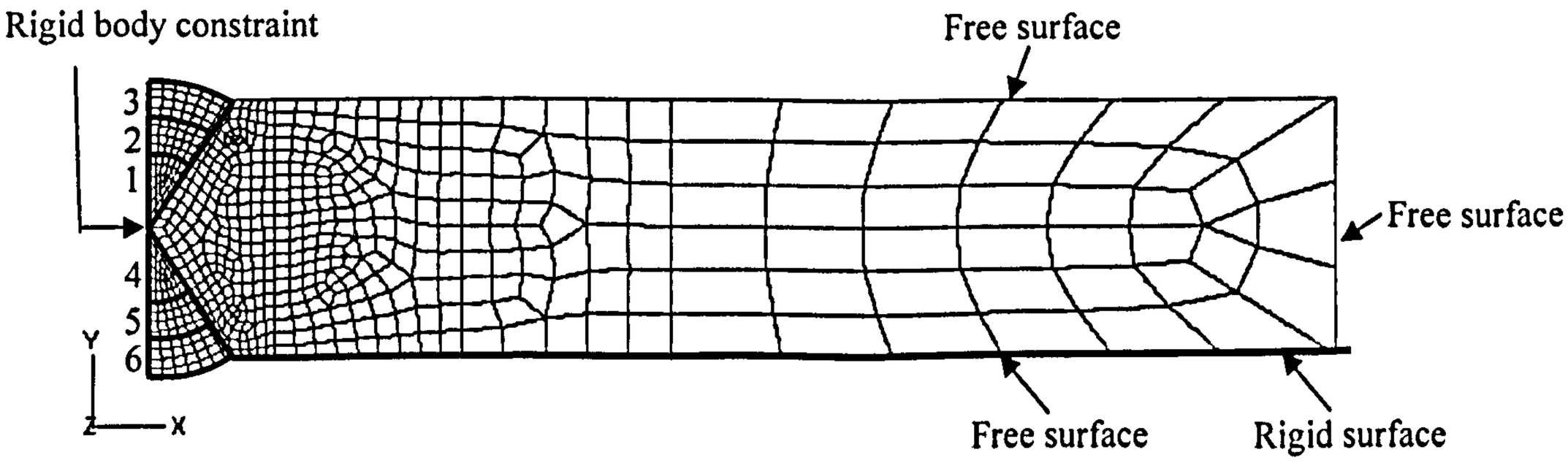

Figure 5.1 2D plate finite element mesh

In the thermal model, 591 four-noded linear quadrilateral heat transfer elements (DC2D4) and a three-noded linear triangle heat transfer element (DC2D3) from the ABAQUS library were used. In the mechanical model, the plane perpendicular to the direction of the weld was analysed as a generalized plane strain condition. The model consisted of 591 four-noded bilinear quadrilateral generalized plane strain elements

(CPEG4) and a three-noded linear triangle generalized plane strain element (CPEG3).

5.1.1.2 Initial and boundary conditions

The butt-welded plate investigated was symmetrical about the plane passing through the weld centreline perpendicular to the plate surfaces. It was assumed that this symmetry plane was impermeable to heat. The plate cross section used in the 2D analysis was insulated on both sides in the *Z*-direction.

The heat loss by free convection was modelled by Newton's cooling law. Boundary conditions were applied to all free surfaces of the component except for the successive boundaries created after each new weld pass. The surfaces exposed to the environment were subjected to the same convective boundary conditions, using a convective heat transfer coefficient of $h=30W/m^2°C$ to ambient air. The ambient temperature for both base and weld metal was set at 25°C.

In the mechanical model, symmetric boundary conditions were imposed along the weld centreline since only half of the component was analysed. To simulate the free boundary condition used in the experiment, only one node under the root of the first pass was constrained in the *Y*-direction to prevent rigid body motion. Gravitational forces were deemed not to have much influence on residual stresses and were ignored.

In ABAQUS, there are two additional degrees of freedom associated with generalized plane strain elements. The first defines the rotation of an imaginary *XY* plane that is offset in the *Z*-direction. This was restrained at a reference node. The second refers to the displacement of this plane in the *Z*-direction. For generalized plane strain, this freedom remained in effect.

The contact boundary condition was also investigated to simulate the interaction between the plate and "ground" in order to reconstruct the real welding process into the mechanical model. The "ground" was modelled as an analytical rigid surface (See Figure 5.1). The use of a rigid surface is cost-effective since the only variables associated with a rigid surface are the translation and rotation on a single node, known

as a rigid body reference node. In addition, ABAQUS does not need to calculate the stiffness or stresses within the rigid body. The applied gravitational forces were included in the contact constraint model.

5.1.1.3 Analysis procedure

Two types of heat input were considered in the thermal model, i.e. heat flux and heat content of filler metal droplets. The heat flux was imposed onto the specified newly activated elements representing a deposited pass at any given time and was uniformly distributed over the area of each weld droplet. The heat content of filler metal droplets was assumed to be deposited at melting temperature and separate solution steps were needed in the thermal analysis to account for this. After the final pass was analysed, the model was allowed to cool down for 1800 seconds.

In the sequentially coupled analysis, a transient thermal analysis was performed first, during which, the time-dependent temperature distribution was determined for the successive build-up of welding passes. Nodal temperatures were stored in the heat transfer results file (.fil) by using the *NODE FILE option. The temperature field at each time step was then read as predefined fields at the nodes by the *TEMPERATURE option in a subsequent thermal stress analysis. This data transfer interface required that the node numbers were the same in both the stress and heat transfer analyses.

In the mechanical model, the fusion zone elements were incrementally activated in strain-free states to model the continuous deposition of filler material by removal/reactivation technique. The mechanical response during welding was calculated by solving a generalized plane strain problem. During the welding process, the temperature field changes with time as the heat source moves and the material properties change with temperature. When the temperature rises towards melting point, the yield strength decreases significantly, i.e. the elastic range is drastically reduced and plasticity initiates sooner. This requires a transient thermo-elasto-plastic analysis.

The combined nonlinearities due to large displacement effects, temperature dependent material properties and boundary nonlinearities were considered in the

sequentially coupled model. Since the problem involves history-dependent response, the solution was obtained as a series of increments, with iterations to obtain equilibrium within each increment. The initial time increments were suggested as 0.0001s in each step in both the heat transfer and stress analysis. Time incrementations in the heat transfer analyses were controlled automatically by a maximum allowable nodal temperature change of 100°C, specified by the DELTMX parameter. ABAQUS would restrict the time increment to ensure that this value was not exceeded at any node (except at nodes with boundary conditions) during any increment of the analysis. Default convergence criteria in ABAQUS, i.e. residual control of 0.005 and solution correction control of 0.01, were used in both heat transfer and stress analyses.

5.1.2 Fully coupled model

Theoretically, during a welding process, the temperature field is thermodynamically coupled with the mechanical field because of the possible heat generation due to inelastic deformation. Although it is generally agreed that the heat caused by plastic straining of the material in the case of welding is very small compared to the heat input from the welding source, it is still deemed worth investigating how this coupling phenomena will affect residual stresses. It is also hoped to provide a suggestion for a 3D analysis through the assessment of the sequentially and fully coupled modelling techniques.

In order to assess the sequentially and fully coupled thermomechanical FE models in predicting residual stress built-up during multipass welding, the same modelling technique and nonlinearity factors were taken into account. The simulation parameters were also identical to those in the sequentially coupled model and were obtained from the paper of Shim *et al.* (1992). Contrary to the sequentially coupled model, both thermal and mechanical properties were defined in the fully coupled model. Exactly the same material properties were used in both models. The accuracy and efficiency of these two models were evaluated on the basis of comparisons of residual stress predictions, computational time and disk storage requirement. This will be reported in Chapter 6.

5.1.2.1 Geometry and mesh

In the fully coupled model, the plane perpendicular to the welding direction was also analysed as a generalized plane strain condition. Exactly the same meshes as the sequentially coupled model were used in the fully coupled model, as shown in Figure 5.1.

Simultaneous temperature/displacement solutions required the use of elements that have both displacements and temperatures as nodal variables. The model consisted of 641 nodes and 591 2D coupled temperature-displacement generalized plane strain bilinear quadrilateral elements (CPEG4T) and a three-noded coupled temperature-displacement generalized plane strain linear triangle element (CPEG3T) with full integration from ABAQUS library.

5.1.2.2 Initial and boundary conditions

Exactly the same thermal and mechanical boundary conditions as those in the sequentially coupled model were applied to the fully coupled model, as described in Section 5.1.1.2. The *BOUNDARY option was used to prescribe both melting temperatures for the deposited filler material and the constraints at nodes in the fully coupled thermomechanical analysis.

5.1.2.3 Analysis procedure

In the fully coupled thermomechanical analysis, the thermal and stress solutions were obtained simultaneously rather than sequentially. This was realized by the *COUPLED TEMPERATURE-DISPLACEMENT option.

In using the element removal/reactivation technique in a fully coupled analysis, continuum elements can attain their full mechanical stiffness immediately upon strain-free reactivation. However, to ensure smoothness of the solution, thermal conductivity was ramped up from zero over the step.

The same convergence criteria as those used in the sequentially coupled model were used in the fully coupled model. As the thermal and mechanical equations were solved simultaneously, each equation had to reach equilibrium within any iteration. This resulted in slower convergence rates and consequently longer computational time than solving them separately, as in the case of the sequentially coupled model.

5.2 3D model of butt-welded plates

As the 2D analysis neglected the effect of heat propagation in the direction perpendicular to the considered plane, it introduced higher predicted temperatures than the analogous 3D scheme. In order to obtain more accurate results, a full 3D FE model has been developed to simulate the step-by-step multipass welding process.

A pilot temperature simulation to reproduce the experimental results reported by Murugan *et al.* (1998) was first performed. After the thermal model had been validated, a mechanical model was then developed and applied to multipass butt-welded mild carbon steel plates for validation. For proper comparison, the dimensional details and welding parameters used in the simulations were identical to those reported by Murugan *et al.* (1998) and Shim *et al.* (1992), respectively.

5.2.1 Geometry and mesh

The validation of the thermal model was based on the experiments of Murugan *et al.* (1998). In order to obtain temperatures at locations exactly corresponding to those in Murugan's experiment and also to represent the large temperature gradients near the weld centreline, the model was partitioned at distances of 11.5, 16.5, 21.5 and 26.5mm, respectively, from the weld centreline, as shown in Figure 5.2(a). Twelve elements were used in the Z direction, each with a length of 12.5mm. The smallest elements were located in the region that represented the deposition of filler material and HAZ.

Figure 5.2(a) shows the FE model used for the thermal model validation. It consisted of 960 eight-noded 3D heat transfer hexahedral elements of the ABAQUS type DC3D8 and 1365 nodes. Figure 5.2(b) shows the details of the mesh near the weld

centreline and HAZ. The numbers indicate the elements representing the individual pass required to fill the groove.

During the welding process, each pass was distributed among elements arranged in the *Y*-shaped groove between the plates. The welding speeds were 1.68, 2.88 and 2.08mm/s for the first, second and third passes, respectively. In order to correspond to these speeds, the heat source shifted its position every 7.44s, 4.34s and 6.00s by one element in the *Z*-direction for the first, second and third passes, respectively.

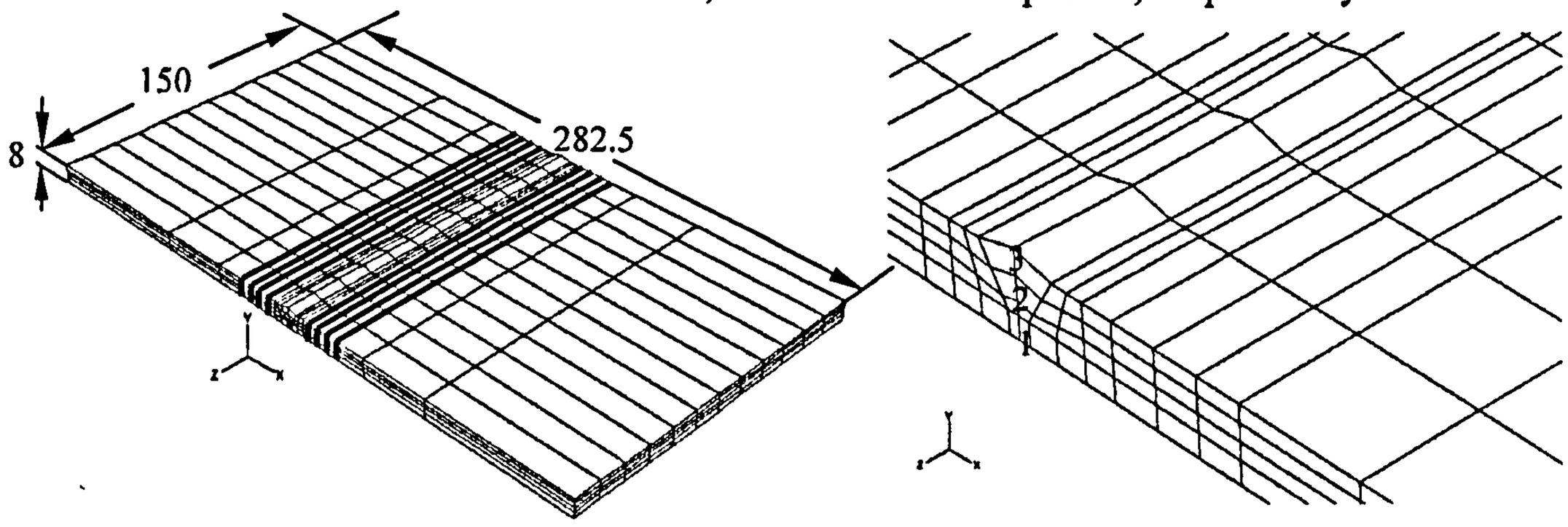

(a) FE mesh

(b) Detailed mesh near the weld area

Figure 5.2 3D plate finite element mesh for thermal model validation

The validation of the mechanical model was based on the experimental work by Shim *et al.* (1992). Only half of the butt-welded plate was modelled due to the geometrical symmetry. The fusion zone was partitioned comprehensively and meshed with the rest of the model initially. Elements representing each weld pass were then grouped in sets and disactivated at the start of the analysis. As the analysis progressed, element sets representing consecutive passes were reactivated strain-free to simulate material deposition. A similar lumping scheme to that used by Shim *et al.* (1992) was employed.

Figure 5.3 shows the 3D FE mesh for the welded joint, along with the refined meshes at the weld toe. Based on a preliminary mesh sensitivity study, the detailed element design with mesh refinement near and within the weld area proved to be adequate for such analysis. The symmetrical plate model had 10240 linear hexahedral elements and 12195 nodes. Eight-noded 3D hexahedral elements of the ABAQUS type DC3D8 were used in the heat transfer analysis, while continuum elements with reduced

integration, C3D8R, were used in the stress analysis.

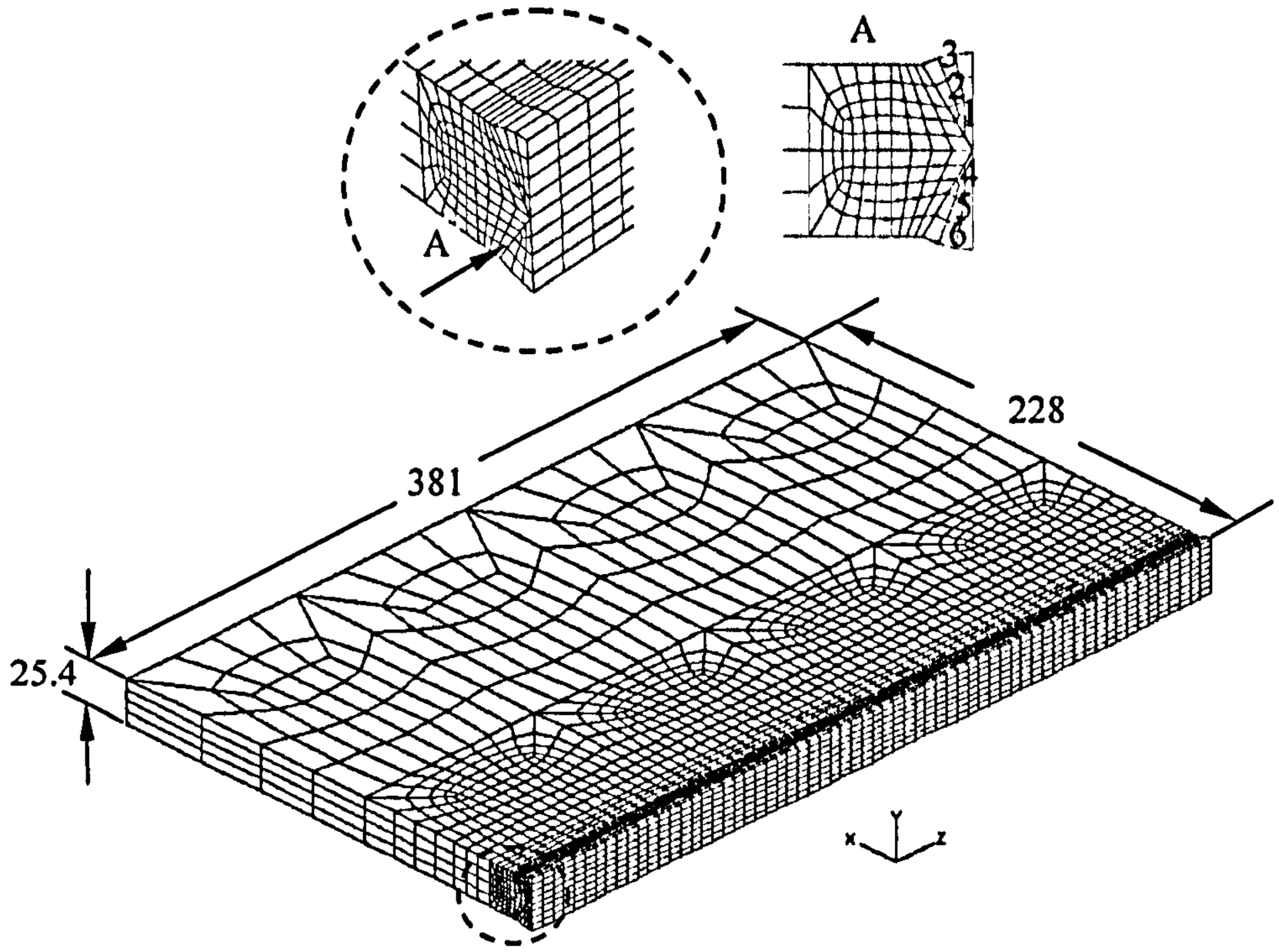

Figure 5.3 3D plate finite element mesh for mechanical model validation

5.2.2 Initial and boundary conditions

Similar thermal initial and boundary conditions to the 2D model, as described in the previous section, were applied to the current 3D model.

The applied loading was assumed to be purely thermal. Mechanical boundary conditions were applied only to prevent rigid body motion of the plate. The nodes under the root pass were constrained in the *Y*-direction. One node at the bottom of one corner of the plate was constrained in the *Y*- and *Z*-directions and the corresponding node at the other corner of the plate was constrained in the *Y*-direction only. Reaction forces were output to assess whether they represented unrealistic constraints as compared with what would be expected in a typical welding execution. Symmetrical boundary conditions were imposed along the weld centreline.

5.2.3 Analysis procedure

Similarly to the 2D model, the heat input in the 3D model can be viewed as

including volumetric heat flux and heat content of filler metal droplets. The volumetric heat flux was modelled as a column of elements with specified body heat flux progressing along the weld path corresponding to the welding speed. This heat input was imposed onto the specified newly activated elements representing a deposited pass at a given time. Body heat flux was uniformly distributed over the volume of each weld droplet by *DFLUX in ABAQUS. The deposited weld was also assumed to be at a melting temperature of 1510°C upon reactivation. After the final pass had been analysed, the model was allowed to cool down to ambient temperature.

The same mesh and step time were used for both heat transfer and stress analysis. Geometric nonlinearity caused by large deformations and thermo-elasto-plastic constitutive formulation with temperature dependent material properties were considered. The essential factors when calculating residual stresses introduced by thermal strains in welds were the effects of temperature and the thermal history on the mechanical properties. These temperature histories were obtained from the thermal analysis and were used as thermal loading onto the structural model by using the ABAQUS *TEMPERATURE option to calculate thermal strains and stresses for each time increment in the stress analysis. Any difference between the applied and initial temperatures would cause thermal strain. The thermal stresses were then accumulated to produce the final state of residual stresses.

5.3 3D model of butt-welded pipes

In order to develop a robust and flexible model, the full 3D model was also applied to another commonly used welded geometry, i.e. multipass girth butt-welded pipes, for further validation.

5.3.1 Geometry and mesh

The circumferentially butt-welded pipe from the paper of Rybicki *et al.* (1978) was chosen for the validation of the current 3D model. In Rybicki's paper, two 228.7mm pieces (323.85mm O.D. by 4.572mm wall-thickness), 304 stainless steel pipes were girth butt-welded. Since the butt-welded pipe was symmetrical about the weld centreline,

only half of the component was modelled. The geometrical models were partitioned into various regions in order to produce well-graded FE meshes. Each region consisted of meshes of different density. The symmetrical pipe model had 7776 eight-node 3D hexahedral elements (ABAQUS type DC3D8) and 12123 nodes in the heat transfer analysis, as shown in Figure 5.4. The same mesh was used for both thermal and stress analyses. Eight-node linear hexahedral continuum elements with reduced integration, C3D8R, were used in the mechanical model.

An indication of the elements representing the individual passes required to fill the groove is shown in Figure 5.4. As no filler metal was added to the root pass in Rybicki's experiment, element removal/reactivate technique was applied only to the second pass to simulate the filler metal deposition.

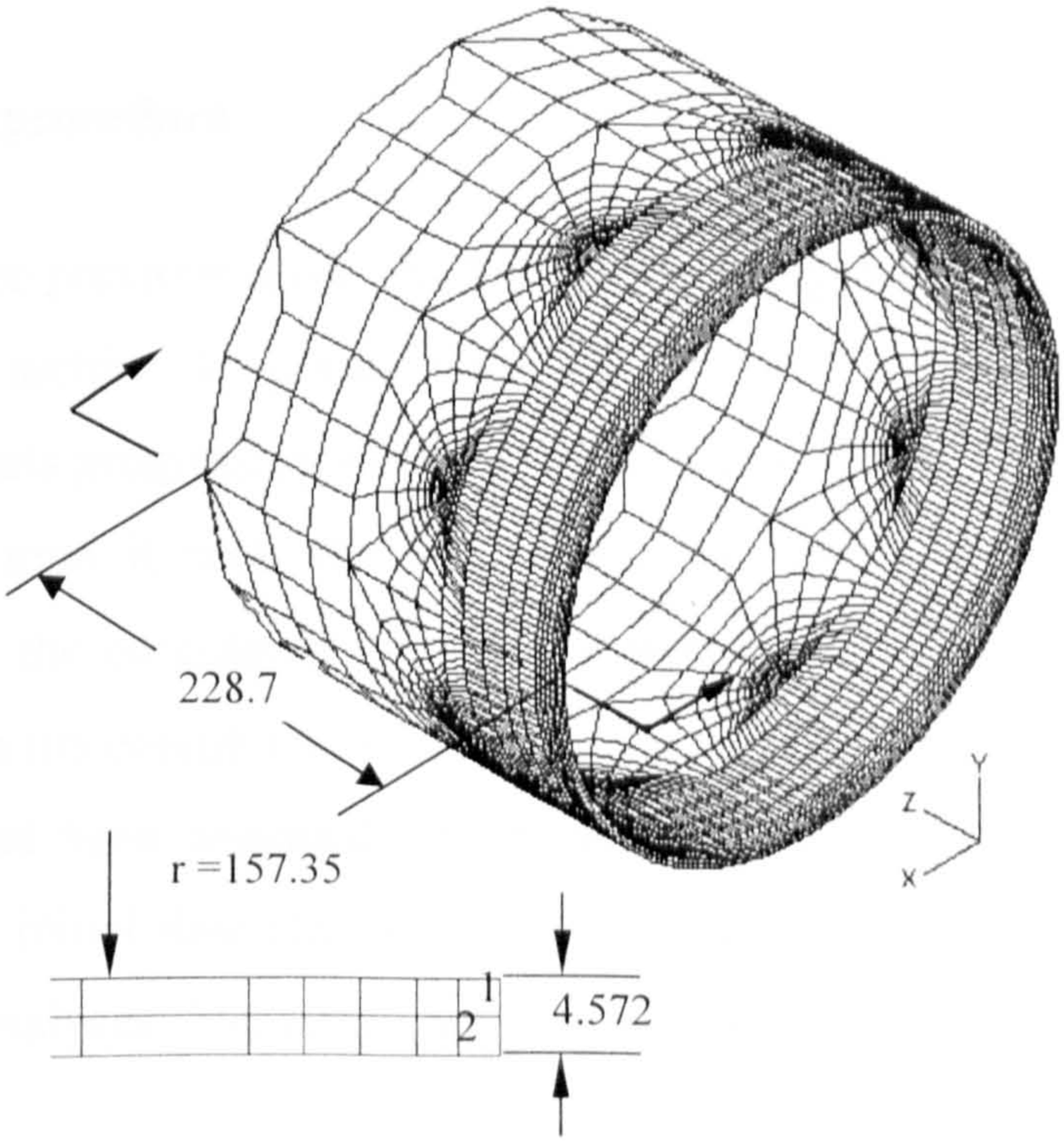

Figure 5.4 3D pipe finite element mesh

In the 3D pipe model, quadratic elements may be more suitable for the curved surfaces of the butt-welded pipes. However, based on comparisons using these two types of element, it was found that linear elements gave almost the same results as quadratic elements; however, the running time was much shorter. Therefore linear elements were preferred as long as meshes were fine enough in the high gradient area.

5.3.2 Initial and boundary conditions

Similar initial and boundary thermal conditions to the previous plate model were applied to the current pipe model.

In Rybicki's experiments, an insert ring was tack welded to one of the pipe. The two pieces of pipe were then mounted on a spider frame to maintain joint alignment. To simulate this constraint in the model, symmetrical boundary conditions were imposed along the weld centreline. Another two symmetric nodes at the end of the welded pipe were restrained in both the radial and tangential directions. This leaves the pipe free to expand in the axial direction. Reaction forces were assessed to determine whether they represented unrealistic constraints.

5.3.3 Analysis procedure

Similar to the previous cases, the heat input was applied by assigning each element in the weld the melting temperature of 1460 °C, and applying body heat flux to a column of elements progressing along the circumferential weld path. The time duration was set to the time it took the heat source to move around a part of the path corresponding to the considered weld pass volume. An elapsed time of 1835 seconds occurred between the completion of the root pass and the start of the second pass. After the final pass had been analysed, the model was allowed to cool down to ambient temperature. The initial time step as well as time incrementation control were the same as the previous analyses. The stress analysis similarly modelled the sequential build-up of the weld bead.

5.4 3D model of a fillet-welded tee branch junction

A piping branch lateral connection is the joining of two pieces of pipe at some predetermined angle to split the flow of fluid, gas or particulate flowing in the piping system. In this research, a welded 90° intersection, or a tee branch junction, which is commonly used in power and chemical industries, was selected for investigation. It is a significantly complicated 3D geometry where no modelling simplifications can be

justified for welding simulation. As far as the author is aware, there is no suggested procedure to model the continuous weld profile in tee branch junctions.

Having been validated by the butt-welded plates and girth butt-welded pipes, the model was fine-tuned and extended to a multipass welded tee branch junction. In order to model realistic welding practice, the simulation was performed on a sector-by-sector welding basis. A total of 16 sectors are along the circumferential weldline in each pass. Each welding sector was activated only when it was deposited. Pass deposition followed the actual welding sequences.

5.4.1 Geometry and mesh

In order to clarify the basic terms used in this dissertation, Figure 5.5 gives the relevant nomenclature for the tee branch junction.

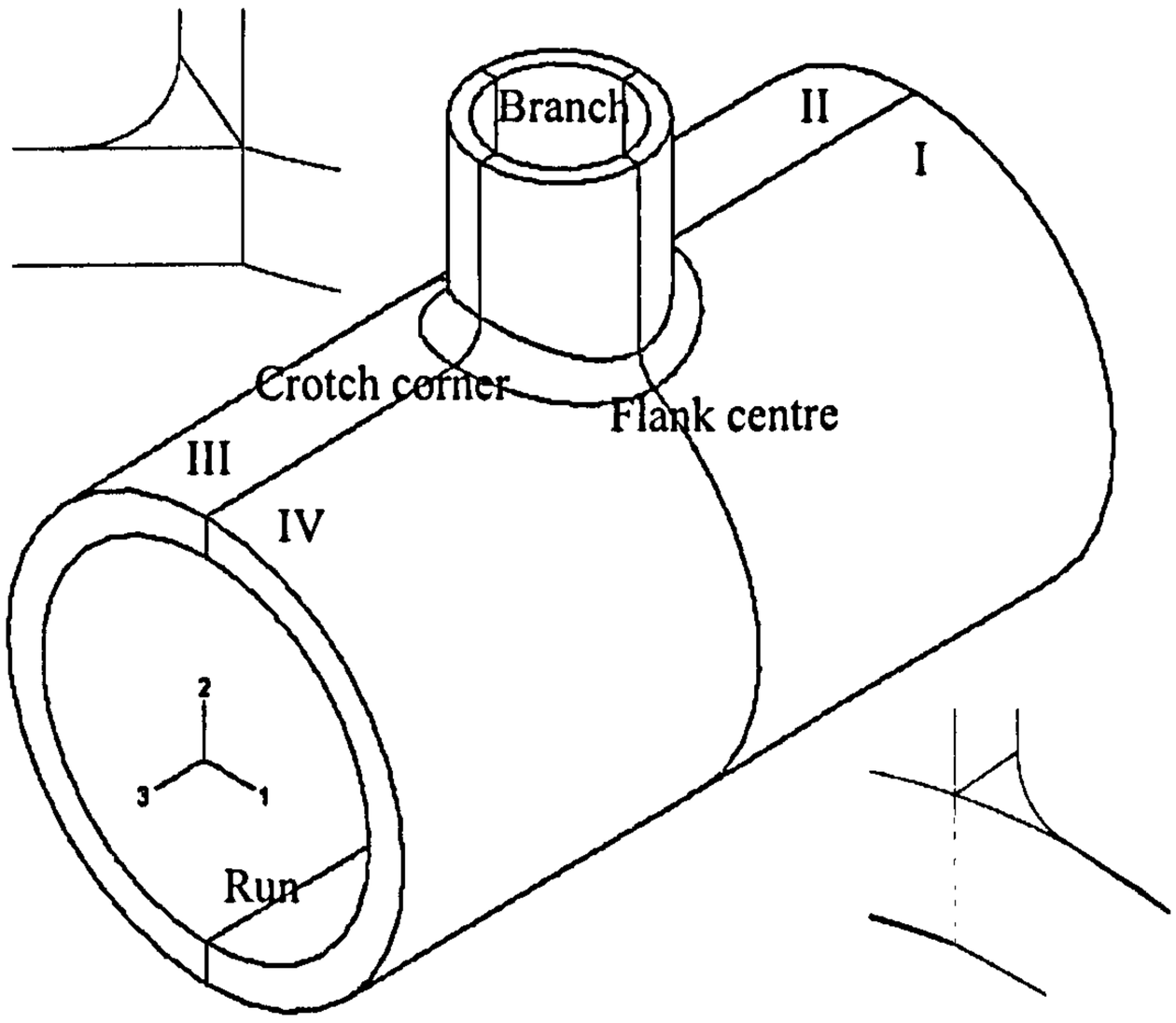

Figure 5.5 Tee branch junction nomenclature

Table 5.1 Geometric dimension of the tee branch junction

Run pipe			Branch pipe		
OD (mm)	Thickness (mm)	Length (mm)	OD (mm)	Thickness (mm)	Length (mm)
891	77	1600	356	36	800

The outside diameter of the run pipe is 891mm with a thickness of 77mm. The

outside diameter of the branch pipe is 356mm with a thickness of 36mm, as summarised in Table 5.1. This configuration gives branch-to-run outside diameter and thickness ratios of 0.40 and 0.468, respectively. The direct branch on pipe requires welding along the "saddle-like" intersection between the run and branch pipe fittings and modelling a full circumferential multipass weld sector by sector. The complexity of the tee branch junction, especially the intricate "saddle like" intersection area, coupled with the inclusion of multipass welding effects, made the all-hexahedral mesh generation the most challenging and tedious task in the FE analysis.

In the current study, the all-hexahedral meshing approach were divided into three phases, i.e. cutting surface generation, volume partitioning and meshing algorithm assignment, as shown in Figure 5.6.

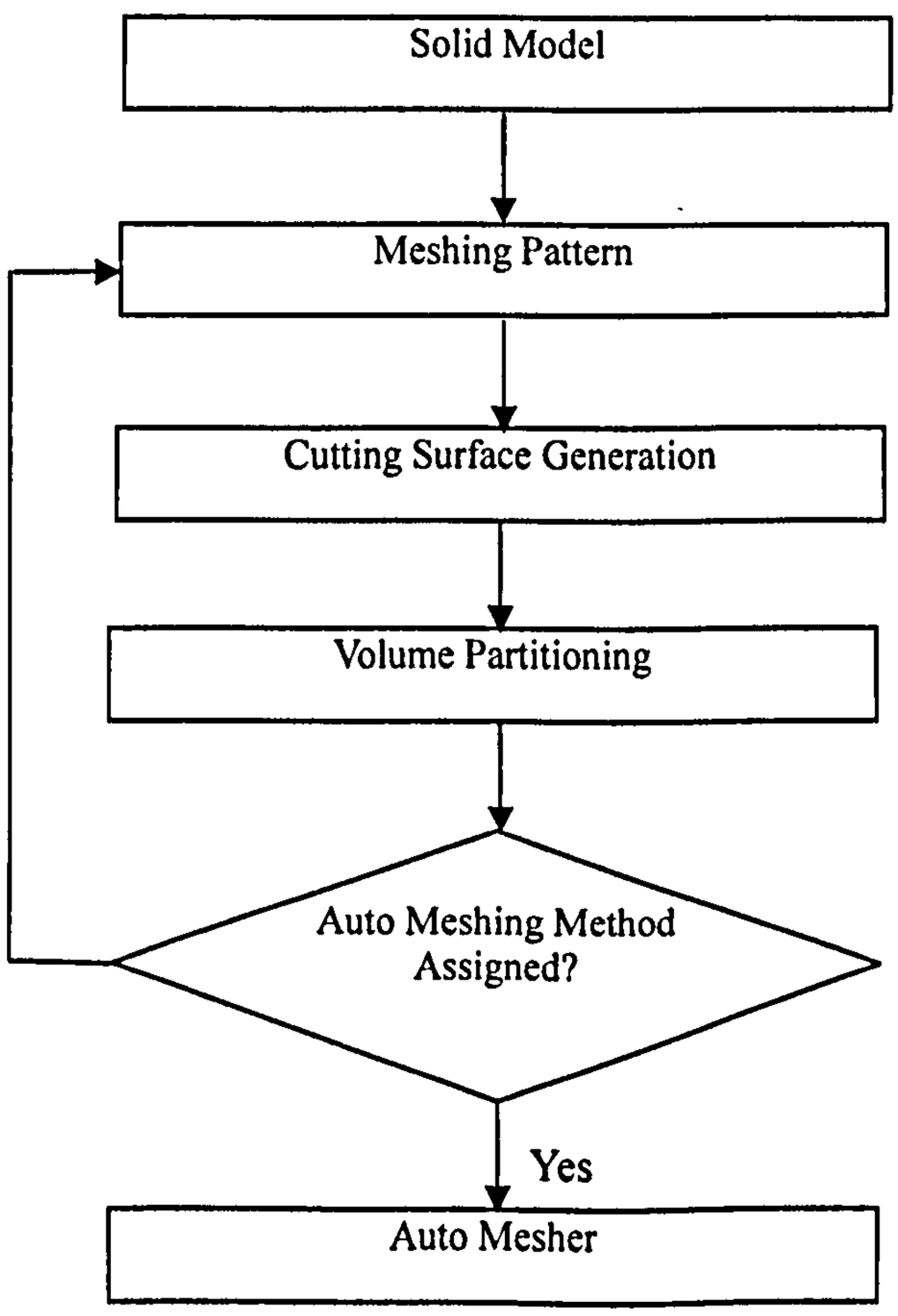

Figure 5.6 Meshing process

The tee branch junction was first partitioned into three parts, i.e. run pipe, branch pipe and weld seam; each could be meshed by a structured meshing technique. The cutting surfaces for generating them were formed in a rather straightforward way and based on bounding separators, as shown in Figure 5.7.

Since the sector-by-sector multipass welding simulation needed to be performed,

the weld seam was then partitioned into 16 sub-volumes along the circumference, four sub-volumes in each quadrant. Each of such sub-volumes was then needed to be further partitioned into eight (or six) sectors to represent corresponding deposited material during each welding pass. Each sector is determined by an index of $P_i\_Q_j\_S_k$, where P_i represents pass number (i=1,6), Q_j represents quadrant number (j=1,4) and S_k stands for sector number (k=1,4).

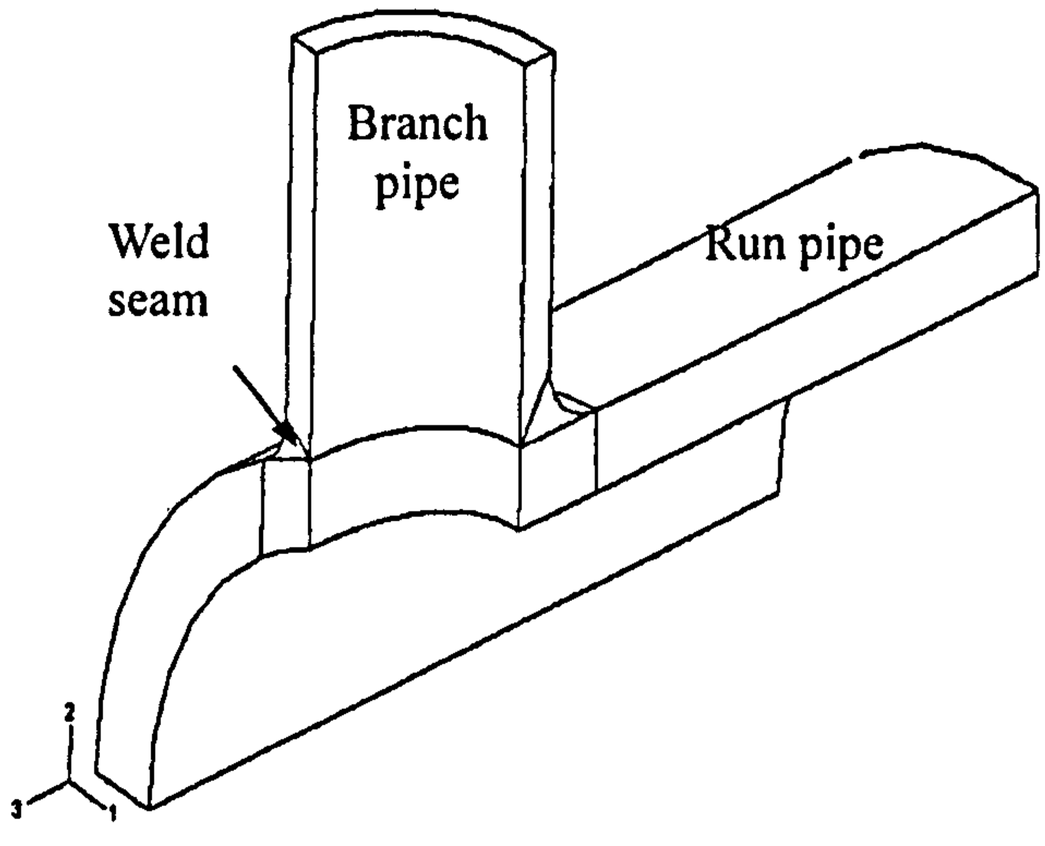

Figure 5.7 Separation of run pipe, branch pipe and weld seam

Usually the geometry information of adjacent or distant surfaces in the neighbourhood of the edges was used in the procedure of constructing cutting surfaces. However, when such information was not available, such as the above sub-volumes of the weld seam, the edges of the two straight lines were firstly partitioned according to the thickness of each deposited pass. Then the connecting faces were partitioned again by proper schemes.

Two partitioning schemes on the connecting faces were initially suggested, as shown in Figure 5.8(a)-(b). Although theoretically, a more realistic cutting scheme that simulated the geometry of each deposited pass was preferred, as shown in Figure 5.8(a), this partitioning scheme was computationally expensive and caused severe skew and resulted in poor mesh quality. This is probably due to the high curvature face involved. After several trials, the best solution had been found to manipulate the geometry, as shown in Figure 5.8(b). This cutting scheme further evolved into Figure 5.8(c). The purpose of this evolution was twofold: Firstly, it helped alleviate severe distortion and propagation of the distortion through the mesh due to sliver faces with sharp angles at

the last pass in Figure 5.8(b). Secondly, it reduced the numbers of passes from eight to six hence reducing the computational cost. The numbers in the figures indicate the individual pass sequences following which the filler material would be added.

Finally, the cutting surfaces were constructed for partitioning the weld seam sub-volumes into several sectors. Each sector should be amenable to meshing by an available auto-meshing tool. Different face cutting scheme brought significantly different geometry and had a huge impact on mesh quality, as shown in Figure 5.8. This meshing procedure required considerable knowledge of meshing algorithms and partitioning tools.

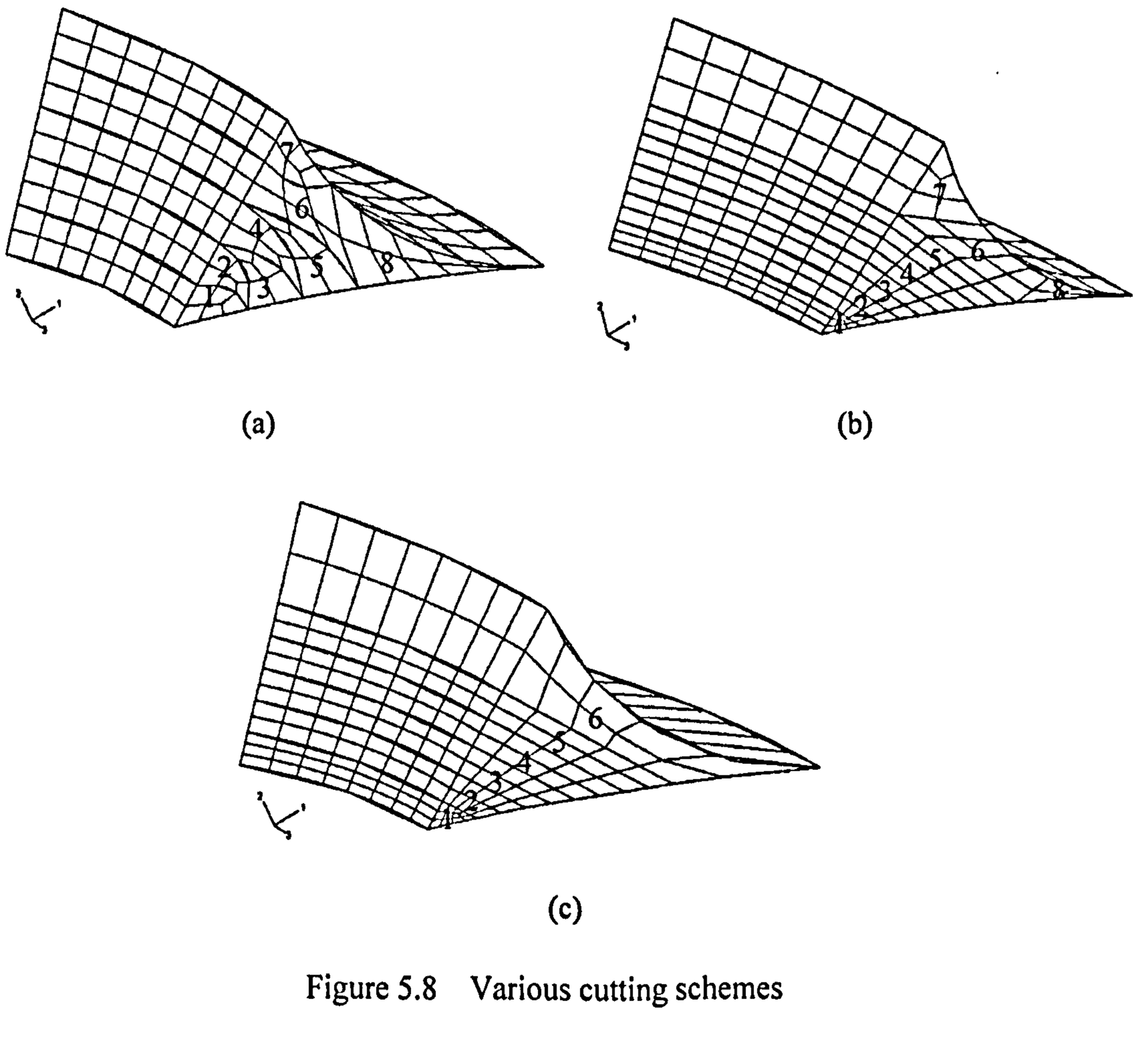

Figure 5.8 Various cutting schemes

The process of meshing multi-region models is significantly difficult and time consuming because of the coupling introduced by mesh matching on the interfaces. When the weld seam was partitioned to accommodate multipass welding simulation, the originally structured meshable branch pipe and other connected volumes became unmeshable, these parts had to be partitioned again to suit the changes made on the weld seam. Partitioning continued until all pieces could be meshed by hexahedral elements.

During the mesh generation procedure, the mesh generator referred to the geometrical model defined in the previous sections and discretized the tee branch junction with multipass welding details into a structured mesh using hexahedral elements. The mesh of each region was generated individually and later they were merged together to form the complete mesh. It was found that it was much more flexible and convenient to generate the mesh individually in different region. The mesh generation was tightly controlled by indicating the number of nodes placed on each solid edge. By this method, the total numbers of elements created were reduced and the quality of the elements was improved.

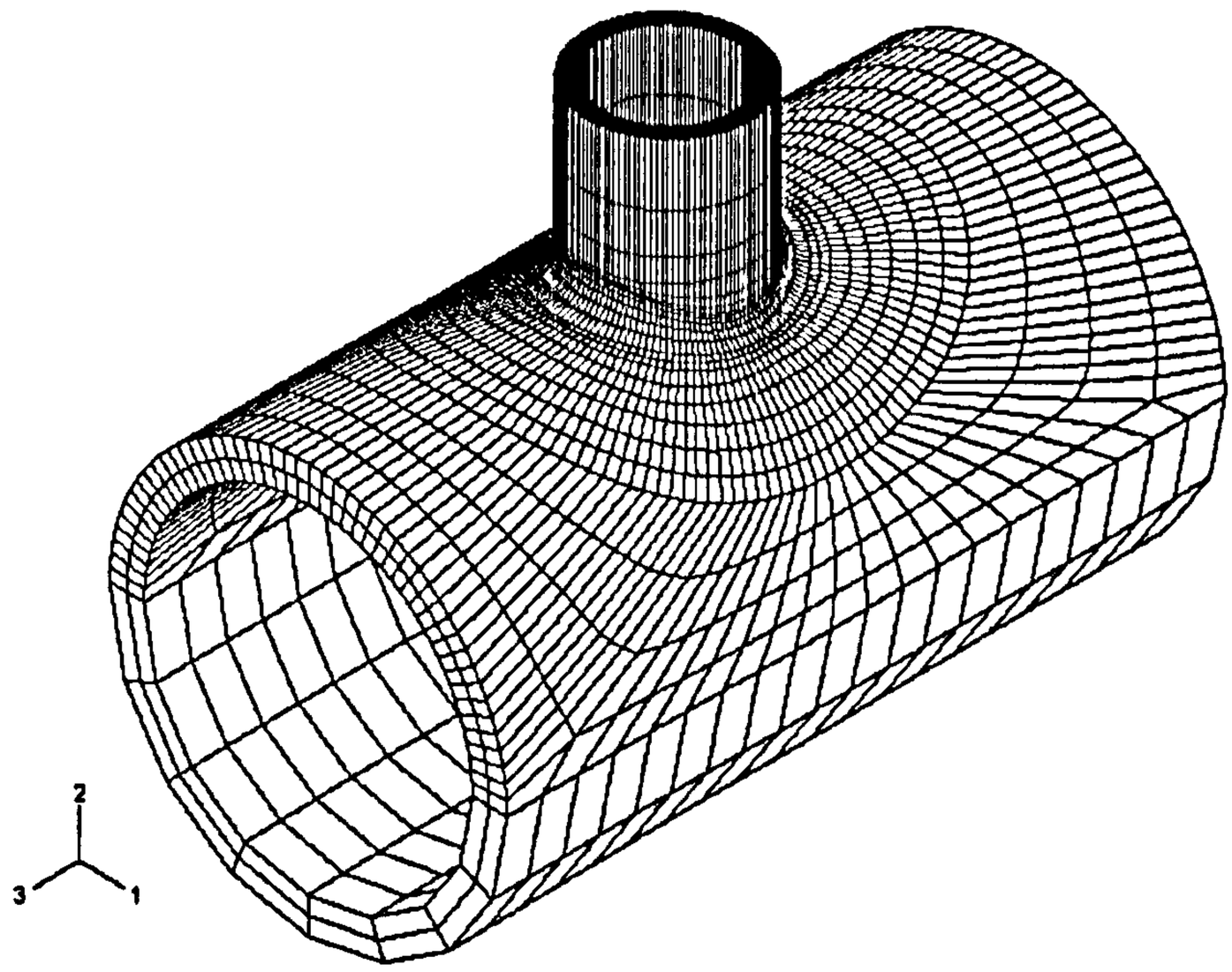

Figure 5.9 FE mesh of a tee branch junction

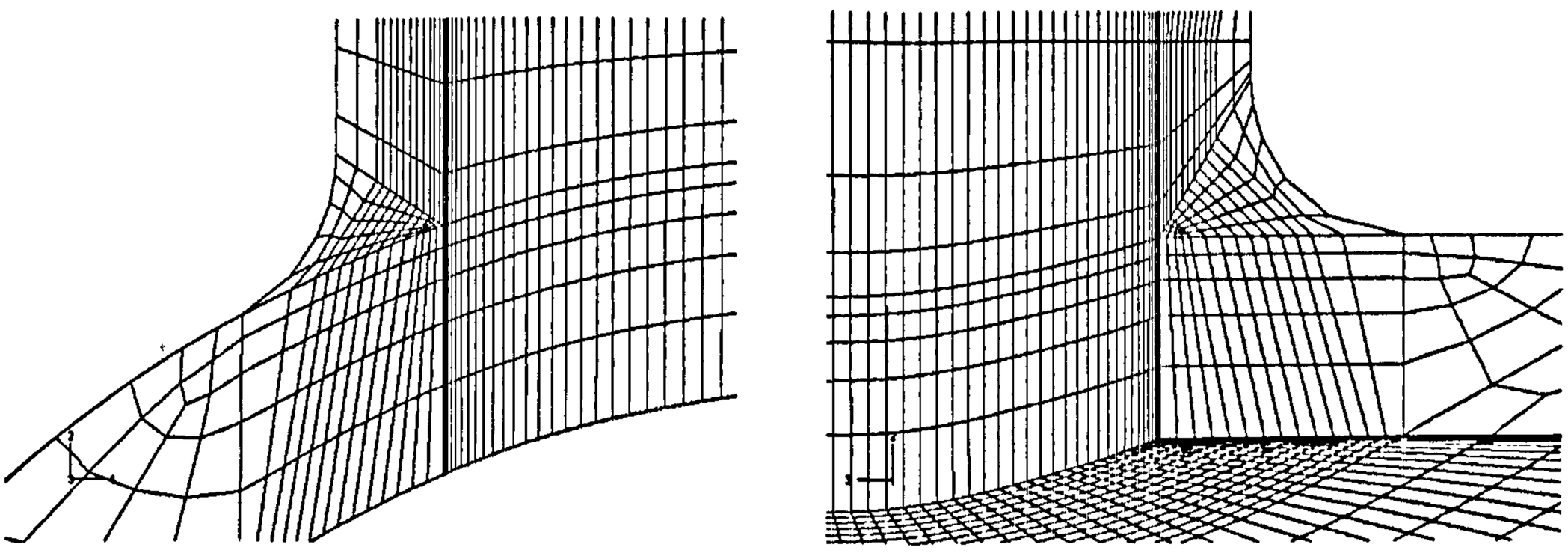

(a) Flank area mesh detail

(b) Crotch corner mesh detail

Figure 5.10 Detailed FE mesh near weld metal region

Since the size of the FE mesh has a great effect on the accuracy of the simulation results and computational cost, mesh refinement studies were performed to determine a mesh size accurate enough to resolve the temperature distribution as well as the residual stress field. From the trial runs of the models, it was found that the element size used for the weld area and HAZ should be around 2-8mm in all three directions. It was also found that with increasing mesh density, the number of elements doubled. At the same time, the calculation time did not double, but approximately tripled. This happened because not only the number of elements had increased, but also the fine mesh required smaller time steps during the calculations. Consequently, in the case of finer meshes, the number of time increments increased.

Theoretically, quadratic elements may be more suitable for curved surfaces of 3D tee branch junction. However, using quadratic elements would result in several times more degrees of freedom than using linear elements. Since welding simulation required quite refined meshes near the weld, using quadratic elements in the already dense mesh make it impossible to run the analysis. Considering the previous study about linear and quadratic element in the 3D pipe model in Section 5.3.1, linear hexahedral elements were selected in the thermomechanical analysis.

Figure 5.9 shows the tee branch junction mesh generated by the above technique. The FE model consists of 36817 nodes and 31816 hexahedral elements. Eight-noded 3D linear hexahedral elements of the ABAQUS type DC3D8 were used in the heat transfer analysis, while the continuum elements with reduced integration, C3D8R, were used in the stress analysis. Figures 5.10(a)-(b) show details of the mesh at the flank and crotch corner locations, respectively. To reduce the number of elements in the model without reducing the accuracy, the model was partitioned into several regions. Each region consisted of meshes of different element density. In the critical fusion region near the joint intersection area, where temperature gradients were expected to be the most severe, fine meshes were generated. On the other hand, in the regions remote from the joint, the mesh was rather coarse. Between the refined regions and the remote regions, transitions regions in the run pipe were used to reduce the number of layers of elements in the thickness direction from five to two. Element seeding was slightly biased towards the outer surface in the run pipe and towards the weld seam in the branch pipe. With these

arrangements, the resulting FE model was found to be able to capture the temperature and stress gradients near the HAZ.

5.4.2 Initial and boundary conditions

Similar thermal initial and boundary conditions to the previous models were applied to the tee branch junction model. The ambient temperature was set at 20°C. The regions near the weld bead along both the run and branch pipe were assumed to be preheated to 65°C before weld execution.

Mechanical boundary conditions were applied only to prevent rigid body movement. Two symmetric nodes at one end of the run pipe were restrained in the radial, tangential and axial directions. The corresponding nodes at the other end of the run pipe were restrained in the radial and tangential directions only. Thus the run pipe could expand freely in the axial direction.

5.4.3 Analysis procedure

The thermal and stress analysis in the tee branch junction were somewhat similar to the previous analyses except for the thermal boundary conditions. Apart from being preheated to 65°C before weld execution, the regions near the weld bead were also reset to an assumed interpass temperature of 120°C using a steady state step before applying each of the subsequent passes. After the final pass had been analysed, the model was allowed to cool down for 6000s to ambient temperature.

When performing nonlinear analysis, an appropriate time increment scheme is required to achieve fast convergence of the solution and reasonable accuracy. The time steps must be fine enough to accurately predict the peak temperatures during the thermal solution and to prevent divergence or an excessive number of iterations in the plasticity analysis. Automatic time stepping was used to solve the nonlinear thermal and mechanical problems. Time incrementation during the thermal analysis was controlled automatically by keeping the largest temperature change DTMAX in every integration point less than 150°C. The DTMAX should not be too big; otherwise, too much

temperature differences could cause convergence difficulty. The time step should be kept small at the initial stage, and allowed to get larger at the cooling stage to reduce computational time.

In a preliminary analysis of the relationship between convergence criteria and simulation accuracy, two models with different convergence criteria were performed. The first model used default criteria, i.e. residual control of 0.005 and solution correction control of 0.01, while the second model used an increased value of 0.05 and 0.1 for the above criteria respectively. It was found that the convergence criteria affected the total number of iterations for convergence. With the relaxed convergence criteria, the computational time was reduced by about 16%, the disk space was reduced by 23%, and the simulation result difference was only 0.37%.

Based on this investigation, the convergence criteria of the residual control and the solution correction control were increased to 0.05 and 0.1 respectively by *CONTROL option in both the thermal and mechanical models to speed up the computation.

5.5 Conclusions

This chapter presents the detailed model development for predicting residual stress built-up during multipass welding process. Starting from the 2D sequentially and fully coupled models, the model was then extended to a 3D sequentially coupled model and validated by experimental data from multipass butt-welded plates and pipes.

A newly developed partitioning technique had been employed to generate well-shaped, graded, all-hexahedral elements in the complex tee branch junction. With proper partitioning schemes, the mesh density and quality could be easily controlled.

Combined with the all-hexahedral meshing technique, the novel full 3D sequentially coupled thermomechanical FE model, which simulated filler material being added continuously along the circumferential path with a moving heat source in the tee branch junction, has been developed. The model incorporates various phenomena and nonlinearities associated with multipass welding, such as moving heat source, filler

material deposition, material, geometric and boundary nonlinearities. All these factors are identified as essential factors for the accurate prediction of residual stress field.

Chapter 6 Model Validation and Simulation Results

The simulation results based on the models developed in Chapter 5 are presented in this Chapter. After comparison of several modelling techniques, including standard versus contact boundary conditions, sequentially versus fully coupled modelling, suitable techniques were suggested for the 3D simulation.

The full 3D model was then applied to both mulitpass butt-welded plates and pipes. For proper validation, the dimensional details, material properties and welding parameters, used in the simulations, were identical to those used in the experiments, which were obtained from published data. The validation results are reported in Sections 6.1 and 6.2, respectively.

Finally, the full 3D model was fine-tuned and extended to a thick-walled tee branch junction. Detailed transient temperature and thermal stresses, as well as residual stress distributions at several critical regions are presented in Section 6.3.

6.1 Butt-welded plates

6.1.1 Specimens and welding parameters

Due to the limited information provided in the general literature, only two separate specimens were selected for the validation of the current model and are described as Cases 1 and 2, respectively.

Case 1: Murugan's specimen

An 8mm thick, ASTM A36 mild carbon steel specimen produced by a three-pass manual metal arc (MMA) welding technique was selected from the experiments of Murugan *et al.* (1998) for the validation of the 3D thermal model.

Before commencing welding, the two plates were tack-welded together by MMA welding at both ends, with a uniform gap of 2.5mm between them. Three passes were

deposited in the 8mm mild carbon steel welds. Weld beads were laid parallel to the weld pad centreline, using the stringer bead technique. The weld passes were started at one end and finished at the other. Thermocouples were mounted around the middle of the transverse cross section of the specimens to measure the transient temperatures during welding. The temperature variations during the experiments were recorded using multipen X-Y recorders.

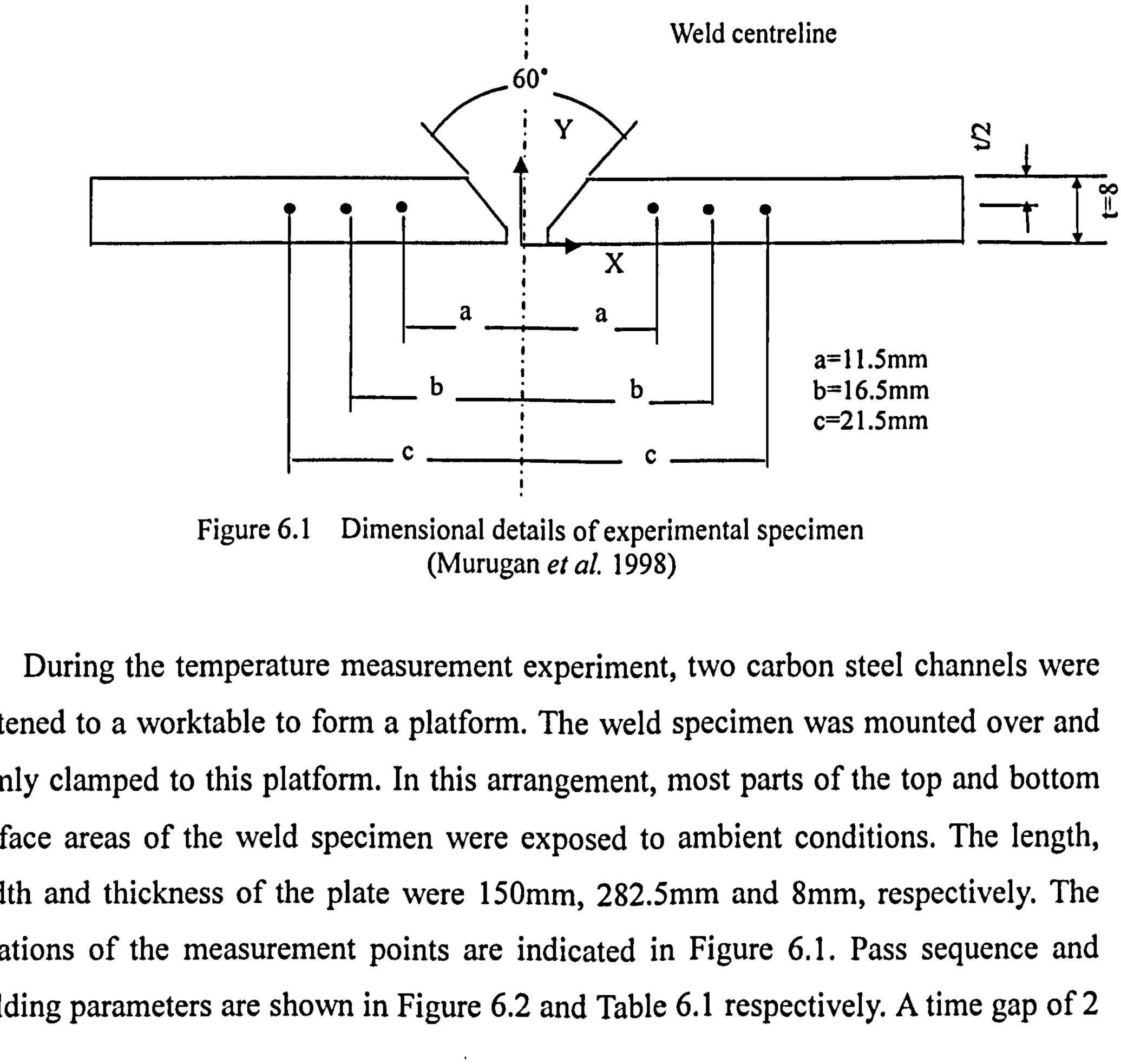

Figure 6.1 Dimensional details of experimental specimen (Murugan *et al.* 1998)

During the temperature measurement experiment, two carbon steel channels were fastened to a worktable to form a platform. The weld specimen was mounted over and firmly clamped to this platform. In this arrangement, most parts of the top and bottom surface areas of the weld specimen were exposed to ambient conditions. The length, width and thickness of the plate were 150mm, 282.5mm and 8mm, respectively. The locations of the measurement points are indicated in Figure 6.1. Pass sequence and welding parameters are shown in Figure 6.2 and Table 6.1 respectively. A time gap of 2

minutes was allowed between successive passes. The heat input per mm length of weld was calculated by assuming an arc efficiency of 0.75.

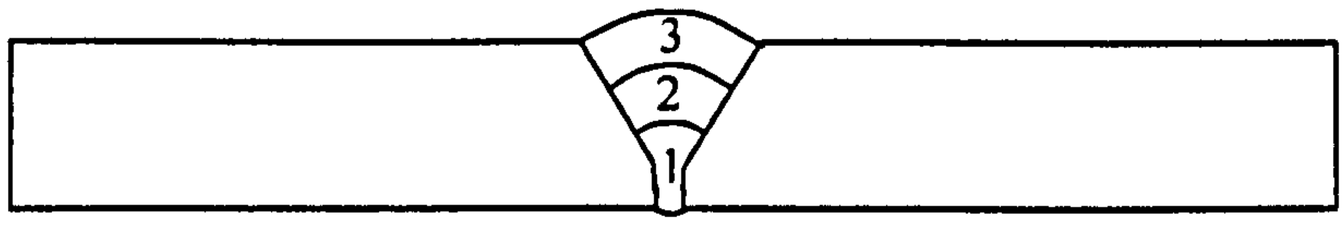

Figure 6.2 Pass sequences of Murugan's specimen

Table 6.1 Welding parameters: 8mm thick plate (Murugan *et al.* 1998)

Pass number	Voltage (V)	Current (A)	Speed (mm/s)	Heat input (kJ/mm)
1	21	65-75	1.68	0.656
2	24	170-180	2.88	1.094
3	22	175-185	2.08	1.427

Case2: Shim's specimen

A butt-welded plate from the paper by Shim *et al.* (1992) was chosen for the validation of the 3D plate model. The 2D model was also based on this experiment. This was the only model for which full information was available in that paper. The specimen consisted of two ASTM A36 mild steel plates of thickness 25.4mm with a double V groove, which were welded by gas metal arc welding (GMAW). The component was fabricated by 11 passes. Pass sequences and weld parameters are shown in Figure 6.3 and Table 6.2 respectively. An arc efficiency of 0.85 was chosen, as was reported in the paper by Shim *et al.* (1992). The blind hole-drilling method was used to determine experimentally the surface residual stresses at locations around the middle transverse cross section of the specimen.

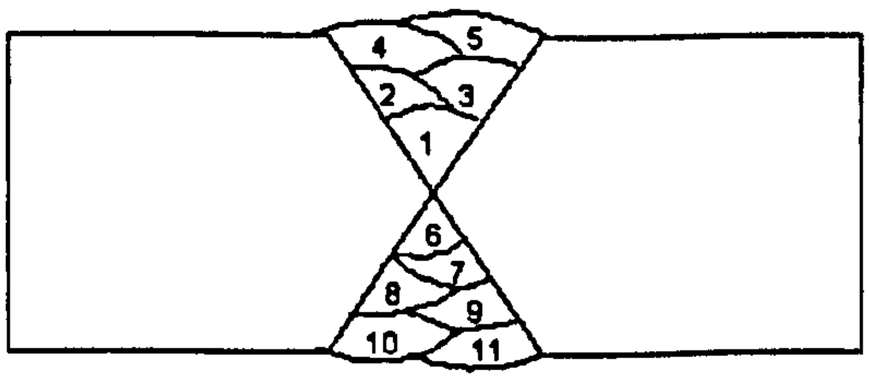

Figure 6.3 Pass sequences of Shim's specimen

Table 6.2 Welding parameters: 25.4mm thick plate (Shim *et al.* 1992)

Pass number	Voltage (V)	Current (A)	Speed (mm/s)	Heat input (kJ/mm)
1	25	190	3.34	1.21
2-5	26	215	4.7	1.01
6	25	190	3.34	1.21
7-9	26	220	4.7	1.03
10-11	27	250	4.7	1.22

6.1.2 Simulation results of 2D models

6.1.2.1 Standard versus contact boundary conditions

6.1.2.1.1 Thermal/Residual stress distributions

In order to simulate free welding condition, a model with a contact analysis was developed. Simulation results were compared with those obtained from another one that used a standard constraint condition. In the standard constraint case, clamping applied only sufficient restraint to prevent rigid body motion of the plates. While in the more realistic contact boundary condition, clamping used a rigid surface beneath the weld.

The stress parallel to the direction of the weldline is called longitudinal stress, while the stress normal to the direction of the weldline is known as transverse stress. The comparisons of the simulation results with experimental measurements are shown in Figure 6.4. It is clearly noticed that the predicted longitudinal residual stresses from both the standard and contact constraint models agree well with the experimental measurements. Figure 6.5 shows the longitudinal thermal stress distribution predicted by the two models at times after deposition of the first, third and sixth passes and the final residual stress distribution. It was observed that both models gave almost identical longitudinal stress distributions.

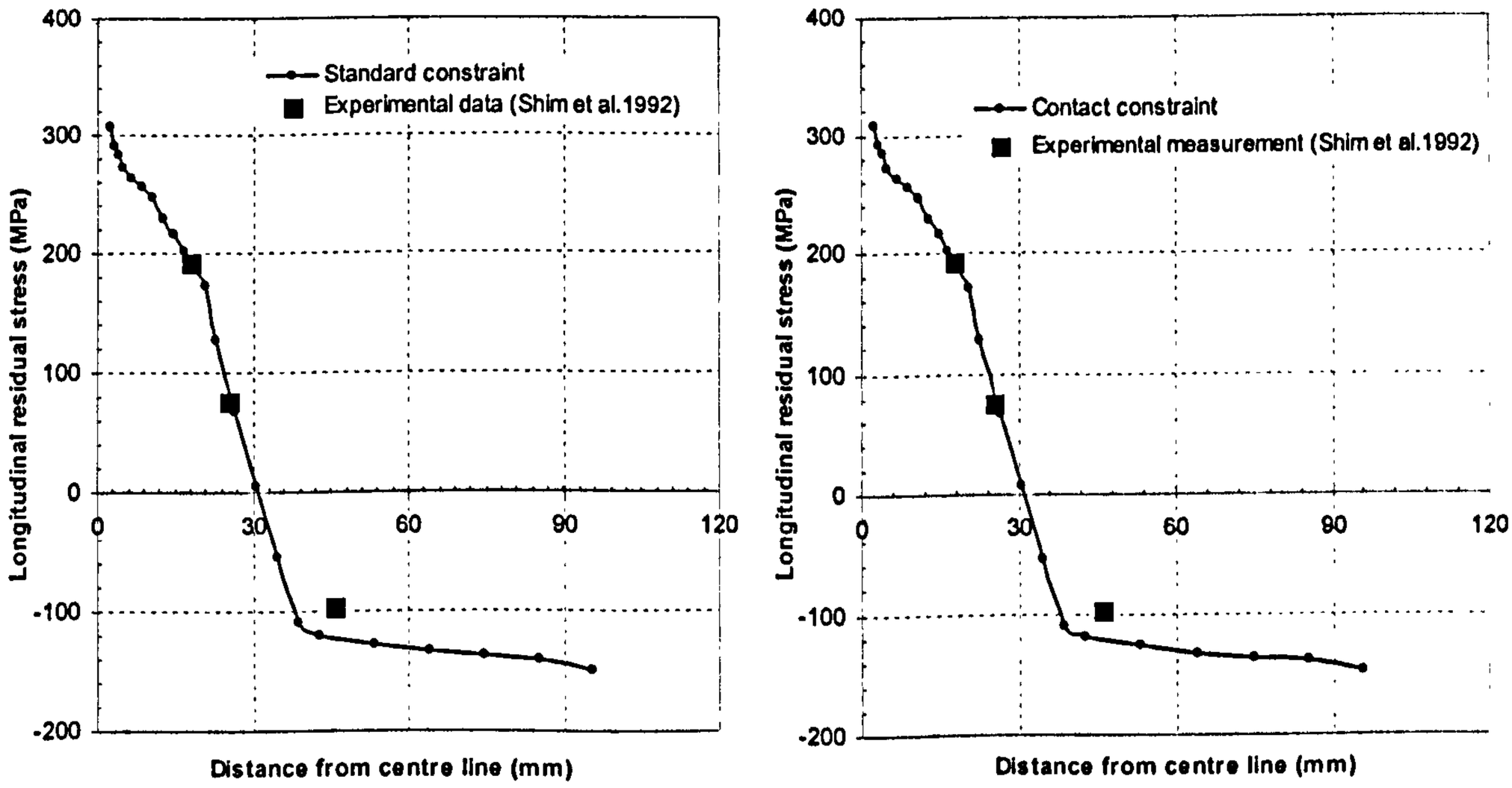

(a) Standard constraint (b) Contact constraint

Figure 6.4 Longitudinal residual stress predictions vs experimental data

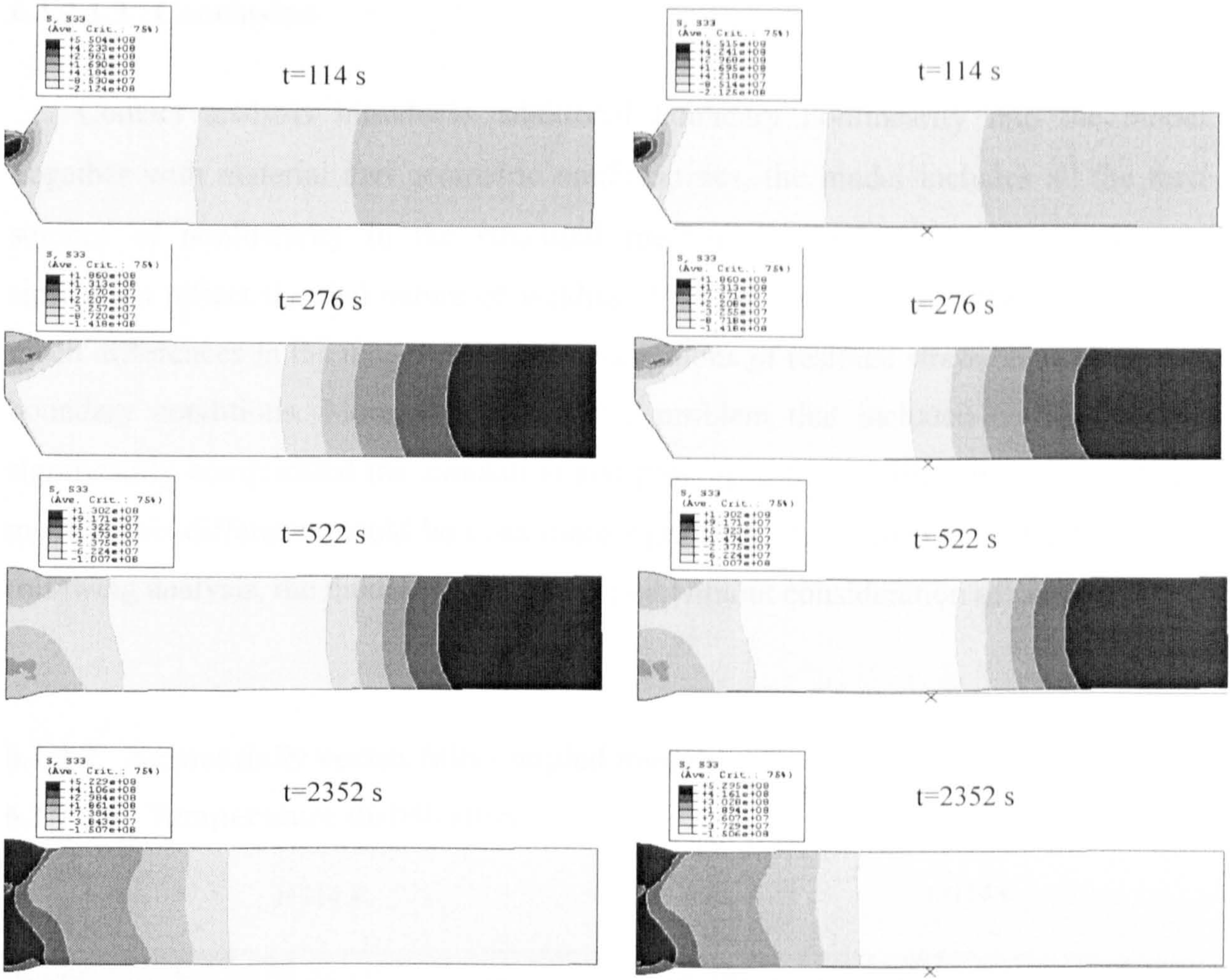

(a) Standard constraint

(b) Contact constraint

Figure 6.5 Longitudinal stresses predicted by standard and contact constraint models

(Note: Due to lumping, there are only six passes in total in the models)

6.1.2.1.2 Computational cost comparison

Table 6.3 Computational cost comparison for the standard and contact constraint models

	Number of model DOFs	Output file size (*ODB) (Mb)	Total CPU time (s)	Wallclock time (s)
Standard constraint	1283	63.0	151.1	485
Contact constraint	1328	62.8	188.6	983

The computational cost parameters are listed in Table 6.3. From the latter, it can be noticed that although both models have similar number of DOFs and required almost the same disk space, the wallclock time for the contact boundary condition is 983 seconds, approximately doubling the computational time for the similar problem without contact analysis (485 seconds).

6.1.2.1.3 Conclusion

Contact analysis introduces additional boundary nonlinearity into the model. Together with material and geometric nonlinearities, the model includes all the three sources of nonlinearity in the structural mechanics simulation, which makes the simulation reflect the real nature of welding. However, it is noticed that there are not much differences in the magnitudes and distributions of residual stress between the two boundary conditions. Moreover, solving the problem that included contact analysis significantly complicated the simulation and prolonged the calculation time. For larger models, this difference could be even more significant. It is thus concluded that in the following analysis, the model will be developed without consideration of contact.

6.1.2.2 Sequentially versus fully coupled models

6.1.2.2.1 Temperature distribution

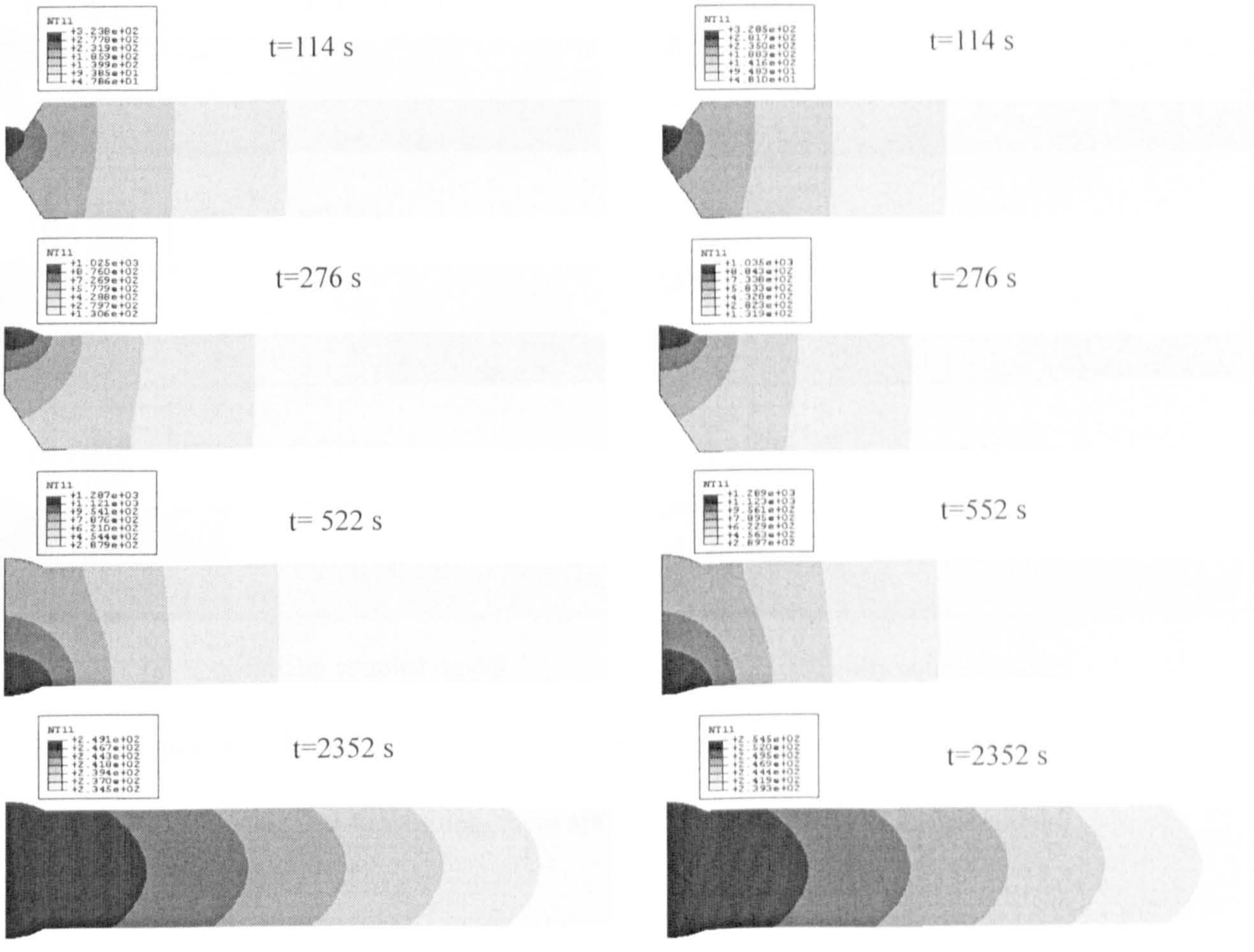

(a) Sequentially coupled model (b) Fully coupled model

Figure 6.6 Temperature history predicted by sequentially and fully coupled models

(Note: Due to lumping, there are only six passes in total in the models)

Figure 6.6 shows the temperature distribution contour plots predicted by the two models at times after deposition of the first, third and sixth passes, as well as after cooling for 1800s. Both models exhibit similar temperature distribution patterns, with the fully coupled model predictions being about 1-2% higher than those predicted by the sequentially coupled model. These slight differences indicate that the fully coupled model has taken into account the heat generated by plastic straining and at the same time show that the coupling is rather weak.

6.1.2.2.2 Thermal /Residual stress distributions

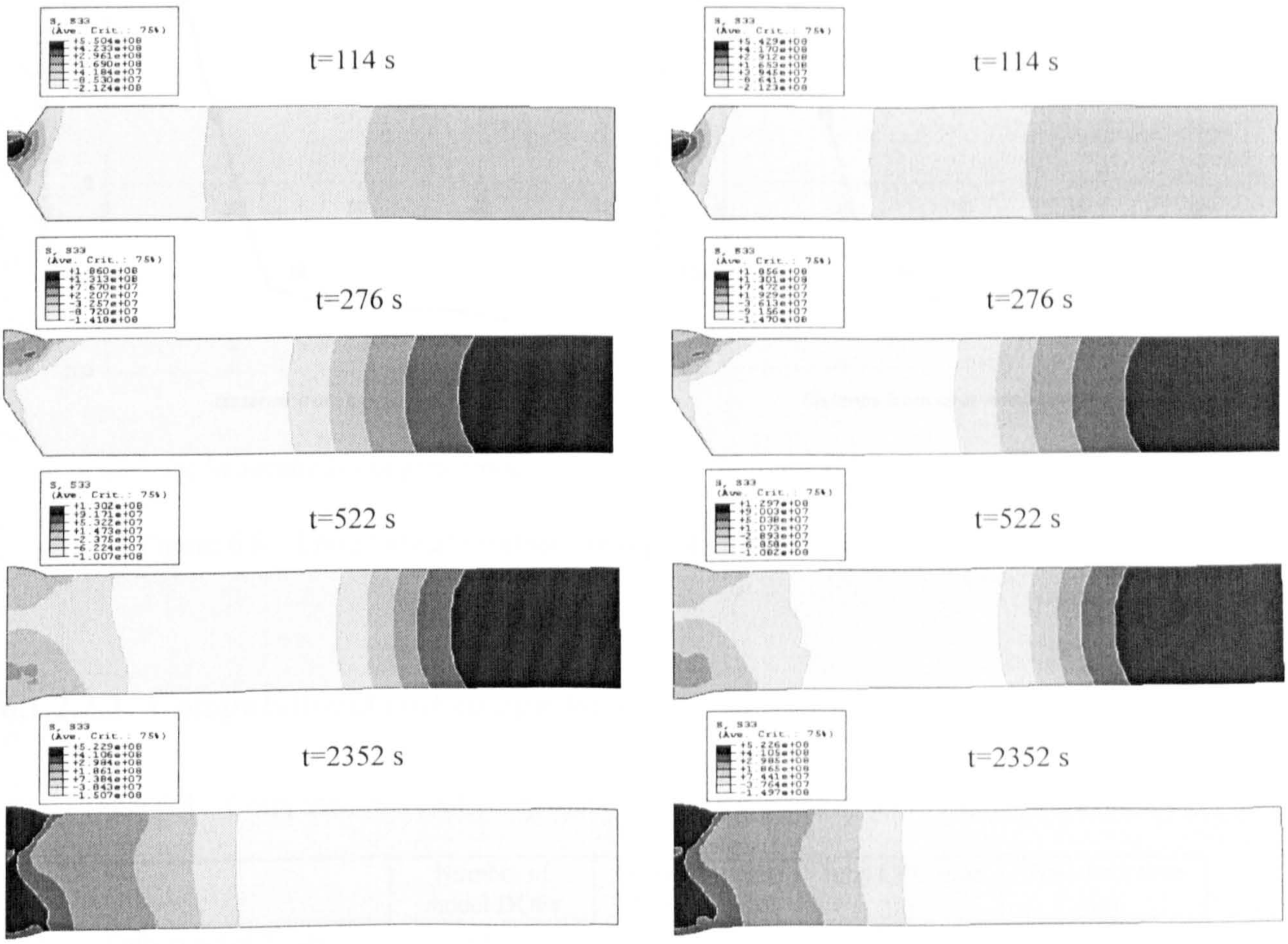

(a) Sequentially coupled model (b) Fully coupled model

Figure 6.7 Longitudinal stress predicted by sequentially and fully coupled models

(Note: Due to lumping, there are only six passes in total in the models)

Figure 6.7 shows the longitudinal stress distributions predicted by the two models at times after deposition of the first, third and sixth passes and the final residual stress distribution. It is noticed that both models predicted similar thermal and residual stress distributions at various welding stages.

Figure 6.8 depicts the longitudinal residual stresses predicted by two models at the top surface of the mid section of the plate. The experimental measurements by Shim *et al.* (1992) are also included for comparison. The agreement with experimental data is rather good for both models. These results demonstrate again that the coupling between the thermal and mechanical stress field is rather weak.

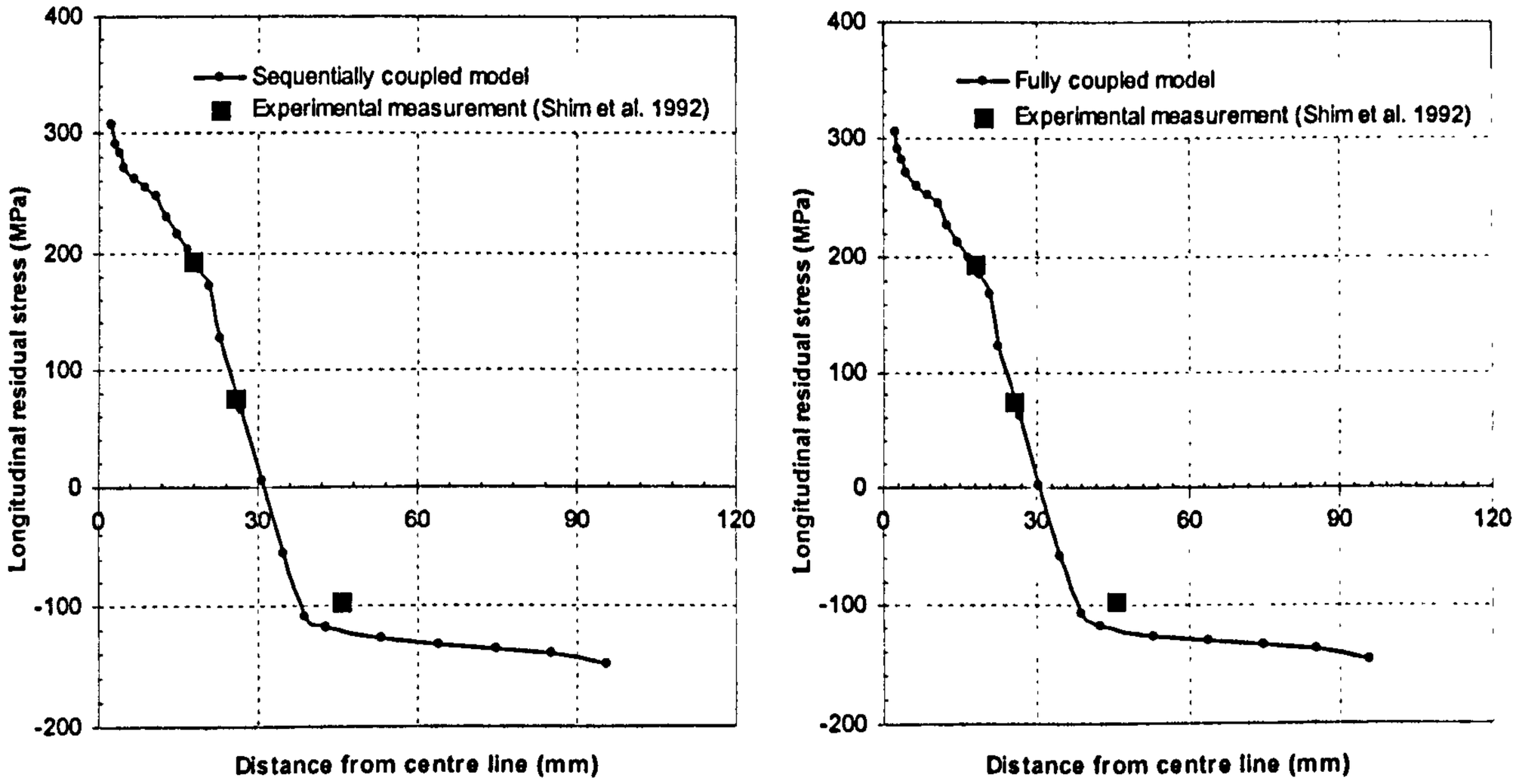

(a) Sequentially coupled model (b) Fully coupled model

Figure 6.8 Longitudinal residual stress predictions vs experimental measurements

6.1.2.2.3 Computational cost comparison

Table 6.4 Computational cost comparison for the sequentially and fully coupled models

		Number of model DOFs	Output file size (*ODB) (Mb)	Total CPU time (s)	Wallclock time (s)
Fully coupled model		1923	96.7	378.6	1029
Sequentially coupled model	Thermal model	640	22.8	66.4	285
	Mechanical model	1283	64.1	147.1	469
	Total	1923	86.9	213.5	754

From Table 6.4, it is noticed that although both models have the same total numbers of variables, the computational cost are significantly different. The output file size for the sequentially coupled model is 86.9Mb, compared to 96.7Mb for the fully coupled model. This means that, for the fully coupled model, the disk space required for the output data is about 11% more than that of the sequentially coupled model.

The total CPU time and wallclock time for the sequentially coupled analysis are 214 seconds and 754 seconds, respectively compared to 379 seconds and 1029 seconds for the fully coupled analysis. This shows that reductions of 44% and 27% in total CPU time and wallclock time, respectively, for the sequentially coupled model than those for the fully coupled model.

6.1.2.2.4 Summary

In comparing results, it is observed that the thermal and stress history and the residual stress distributions predicted by both techniques do not differ much and the residual stresses obtained by both models compare well with experimental data. However, in terms of computer resources, the sequentially coupled model required less computational time and disk space than the fully coupled model.

These results indicate that the coupling between the thermal and mechanical fields in welding is rather weak. Consequently the simpler and cheaper method, which involves sequential coupling, is recommended for the further model development.

6.1.3 Simulation results of 3D models

6.1.3.1 Temperature fields

The validation of the 3D thermal model was based on the comparison of the predicted temperature with experimental data obtained from Murugan's (1998) paper.

The predicted and measured temperature history at distances of a=11.5mm, b=16.5mm and c=21.5mm on the right side of the weld centreline (see Figure 6.1) are shown in Figures 6.9(a)-(c), respectively. As the figures indicate, the temperature distributions predicted by the 3D thermal model closely match those data obtained experimentally, both at the heating and cooling stages.

The good agreement of temperature profiles between the simulation and experimental data at several locations gives great confidence in the further 3D residual

stress analysis during multipass welding, which uses the temperature results of each pass as thermal loading.

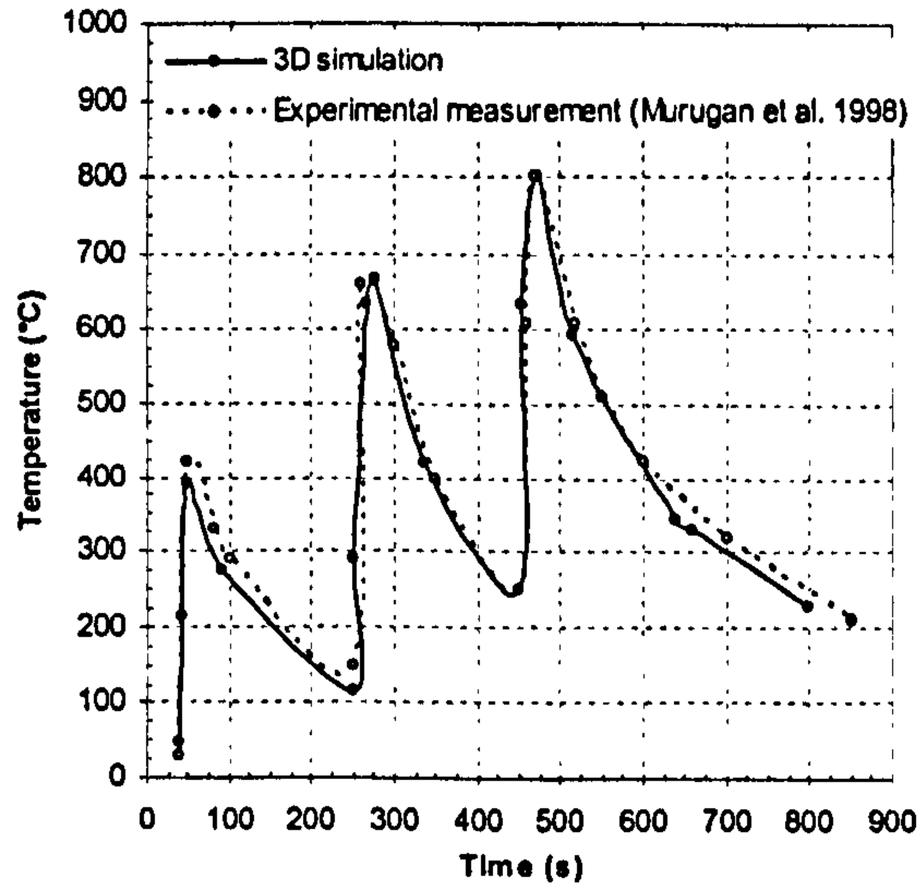

(a) Predicted vs measured temperature distributions at location *a* (11.5mm from weld centre line)

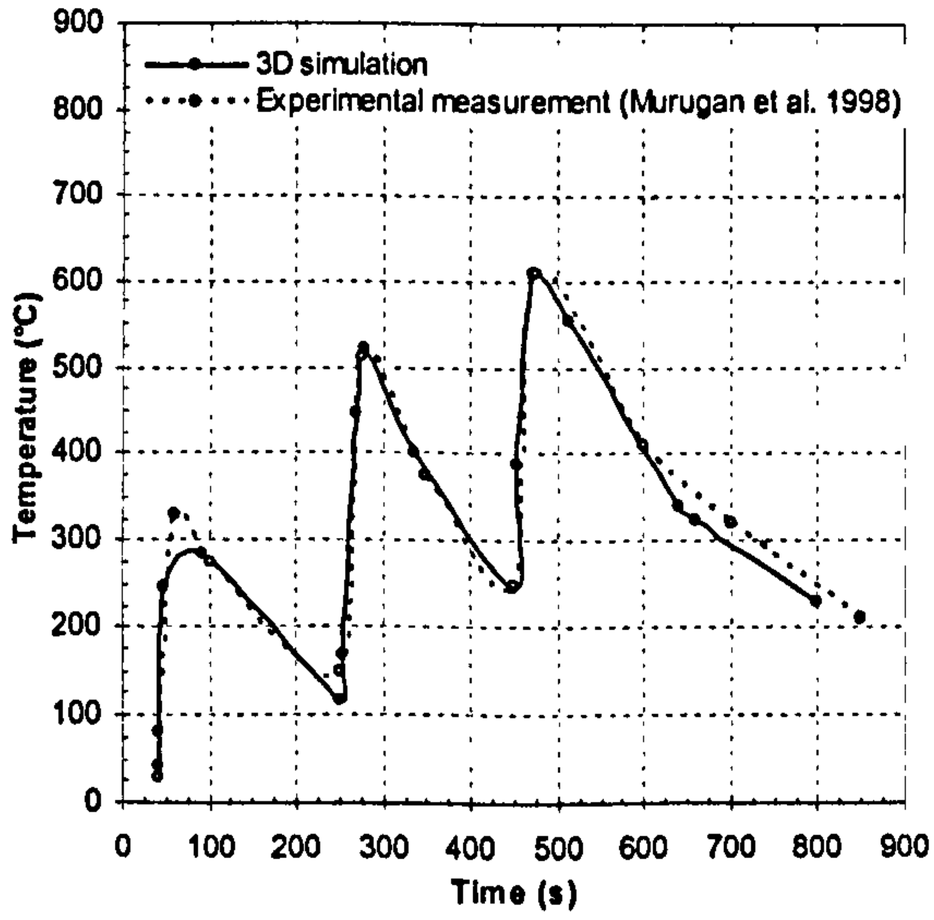

(b) Predicted vs measured temperature distributions at location *b* (16.5mm from weld centre line)

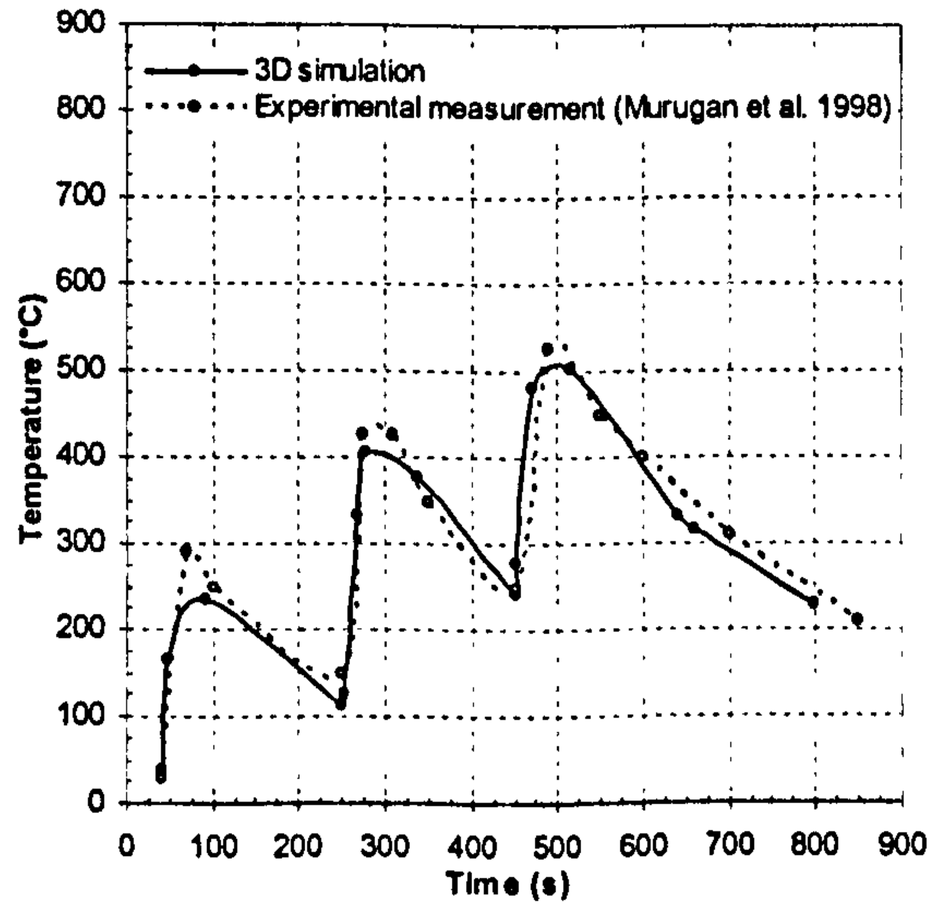

(c) Predicted vs measured temperature distributions at location *c* (21.5mm from weld centre line)

Figure 6.9 Comparison of predicted and experimental temperature results

6.1.3.2 Residual stress fields

Figure 6.10 shows the longitudinal and transverse residual stress distributions on the top surface of the mid-section of the plate. The experimental measurements and simulation results from Shim's 2D model are also plotted.

From Figure 6.10(a), it is observed that a similar peak tensile longitudinal residual stress is noted around the weld centreline. Within a distance of 30mm from the weld centreline, the predicted results from the 3D model agree extremely well with both the experimental data and the 2D predictions. Besides, the 3D model gives the same tensile zone as that of the 2D model. In the compressive zone, the 3D model agrees with experimental results better than the 2D model. The 3D model shows slightly higher peak longitudinal compressive stress than that of the 2D model.

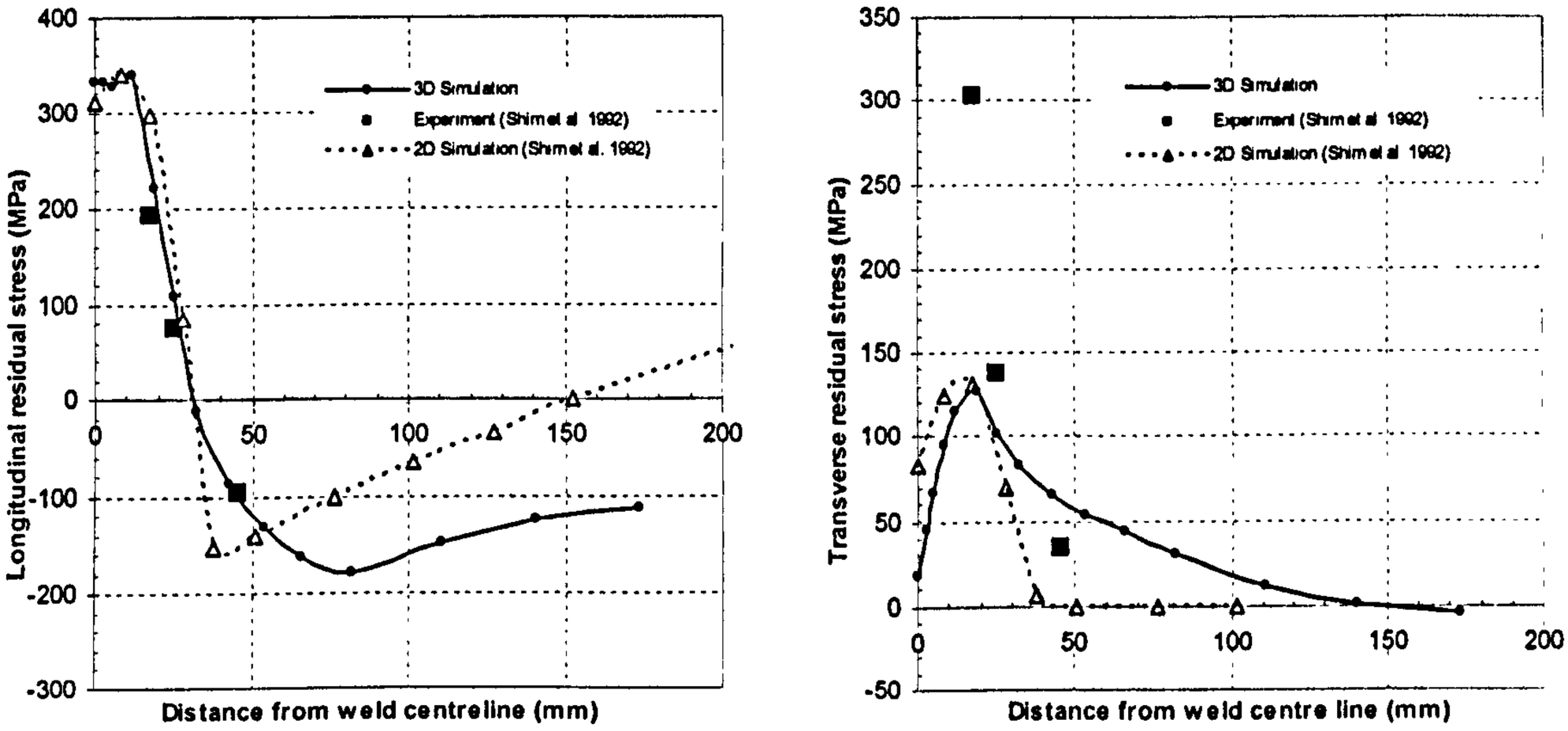

(a) Longitudinal residual stresses (b) Transverse residual stresses

Figure 6.10 Comparison of predicted and experimental residual stresses

The transverse residual stress distributions from both models shows similar patterns and peak tensile transverse residual stress are almost the same, as shown in Figure 6.10(b). The 3D model results in a wider tensile transverse stress zone than the 2D model. As regards the lone experimental data point at a stress level of 300MPa, although it appears at this stage like a 'rogue' point, this may not be truly the case. There is a possibility that, since both FE simulations used the lumped pass method, they could be under-predicting the stress level at this location and such an experimental data point can prove invaluable if there is a need for the lumping technique to be improved.

In the region remote from the weld seam, both predicted results and measurements show that the transverse residual stress tends to be zero.

In summary, both the 2D and 3D models give not only nearly the same peak value but also similar distributions for both longitudinal and transverse residual stresses. However, the predicted results from the 3D model show better agreement with the experimental data than the 2D model. Ignoring the above statement about the lumping technique, it is also noted that the transverse stresses may be more sensitive than the longitudinal stress to the lumping technique.

6.2 Butt-welded pipes

6.2.1 Specimen and welding parameters

The circumferentially butt-welded pipe from the paper by Rybicki *et al.* (1978) was chosen for the validation of the current 3D pipe model. It was a 304 stainless steel pipe, 457.4mm in length, 323.85mm outer diameter by 4.572mm wall thickness, which was cut in half before the cut edges were weld prepared. The weld required two passes. Both passes started at the same point and proceeded in the same direction. The root pass was made by gas tungsten arc welding (GTAW) and the second pass by gas metal arc welding (GMAW). The arc efficiencies were 0.687 for the GTAW of the first pass, and 0.81 for the GMAW of the second pass, respectively. No filler metal was added to the root pass. An elapsed time of 1835 seconds occurred between the completion of the root pass and the start of the second pass. The welding parameters are listed in Table 6.5.

Table 6.5 Welding parameters for the two-pass girth butt-welded pipe (Rybicki *et al.* 1978)

Pass number	Welding method	Voltage (V)	Current (A)	Speed (mm/s)	Heat input (kJ/mm)
1	GTAW	9	115	1.27	0.559
2	GMAW	22	220	8.47	0.462

6.2.2 Simulation results

6.2.2.1 Temperature fields

Figure 6.11 shows the temperature distributions obtained from the current 3D

model. The results from the axisymmetric model and thermocouple measurements are also provided. The reference time in the figures corresponds to the time at which the thermocouple nearest the weld centreline reached its maximum temperature. It can be seen that the agreement between predictions from both models and the experimental values are quite good.

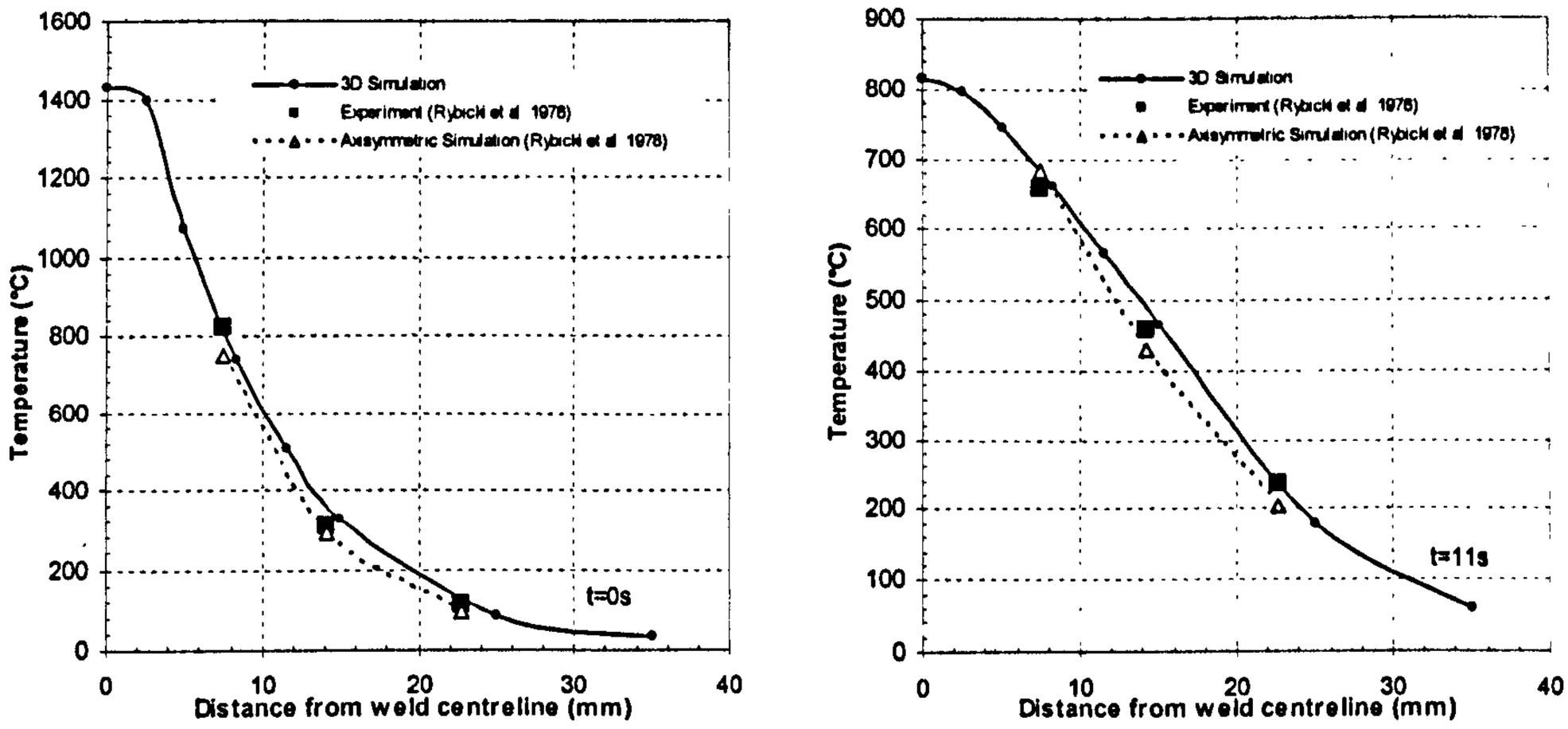

(a) t=0s (b) t=11s

Figure 6.11 Predicted vs. experimental temperatures for the root pass

6.2.2.2 Residual stress fields

Figure 6.12 gives the 3D prediction of axial and hoop residual stresses on the inner surface of the pipe. The results obtained from the experiment and the axisymmetric model of Rybicki *et al.* (1978) are also plotted for comparison. As can be noted from the figures, the latter results are rather limited. They only cover a distance of about 20mm from the weld centreline.

It is noticed from Figure 6.12(a) that the predicted hoop residual stress from the 3D model shows a similar pattern to that from the axisymmetric model within a distance of about 20mm from the weld centreline except at the centreline itself. Both have almost the same peak compressive stress value, which does not occur at exactly the same distance from the weld centreline for the two models. The 3D prediction of the hoop stresses also fall between the axisymmetric predictions and the experimental measurements at a distance from the weld centreline between 8 and 20mm. For the weld

centreline location, it is surprising to note that both the axisymmetric model and experimental results show a 'trough' in the hoop stress distribution, which is not depicted by the 3D model.

The 3D prediction of axial residual stresses shows a similar trend to those obtained by the axisymmetric model, as can be noticed in Figure 6.12(b), except again at the weld centreline. Both give almost the same tensile zone. However, the 3D model predicts higher peak axial residual stress than the 2D model at the weld centreline. This is understandable considering the comments about the high stress gradients at this location made by Dong (2002, 2004).

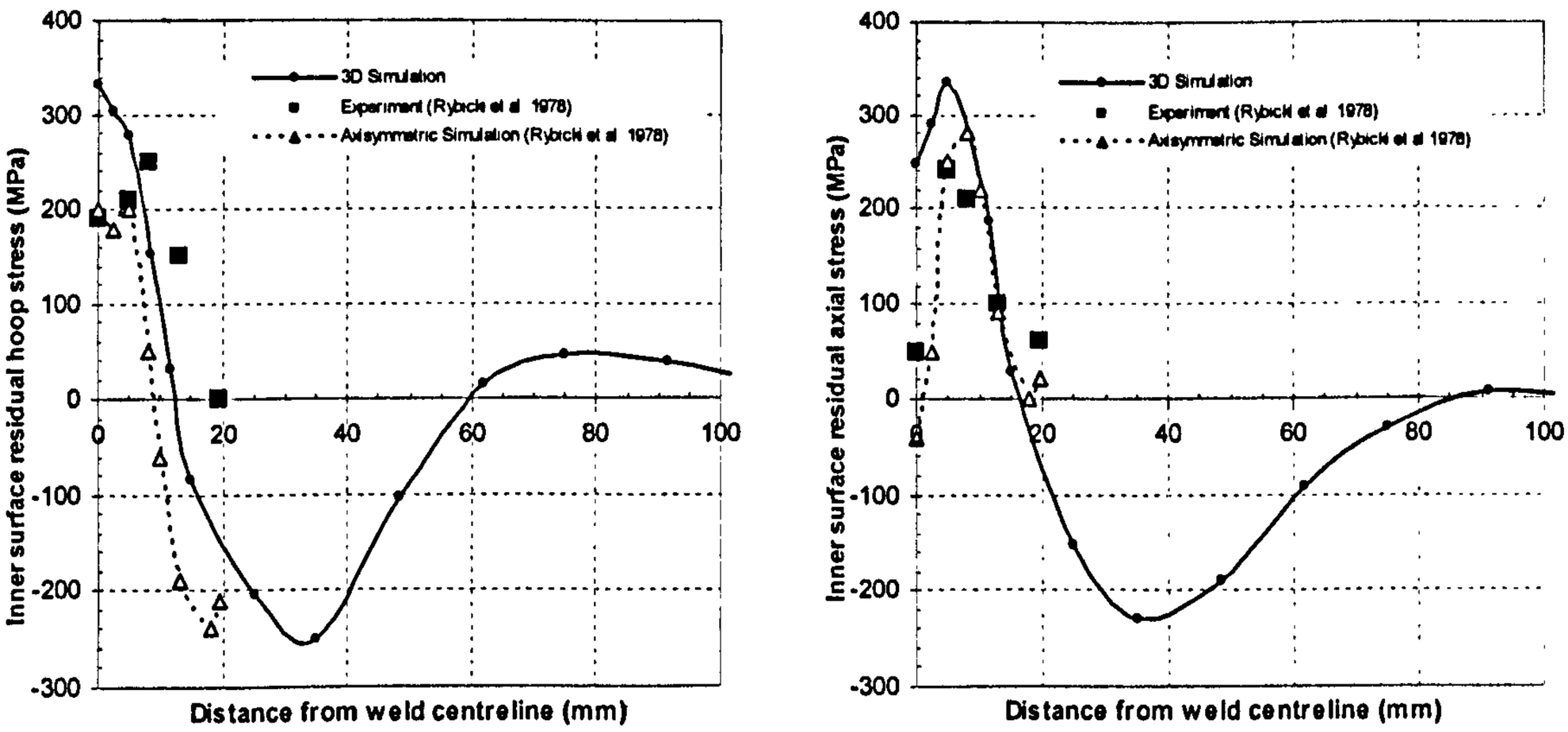

(a) Hoop residual stresses

(b) Axial residual stresses

Figure 6.12 Predicted vs. experimental residual stresses at the inner surface

The 3D predictions of hoop and axial residual stress on the outer surface of the pipe are compared with experimental data and the axisymmetric predictions in Figure 6.13. It can be clearly noticed in Figure 6.13(a) that the hoop residual stresses predicted by the 3D model agree with the experimental data much better than those obtained by the axisymmetric model. Both models under-predict the experimental result at the weld centreline. Also, in contrast to the 2D model, which clearly predicts a peak compressive stress at a distance of about 15mm from the weld centreline, both experimental data and the 3D predictions demonstrate uniform and almost negligible stress at and beyond this distance, bearing in mind that experimental data is only available up to a distance of 20mm from the weld centreline.

The axial residual stress distributions on the outer surface are shown in Figure 6.13(b). The predictions by the axisymmetric and 3D models are comparable in terms of both pattern and magnitude. For the case of the experimental results, while compressive stresses were measured within a distance of about 20mm from the weld centreline, the stress distribution pattern, unlike the FE data, is not clearly defined.

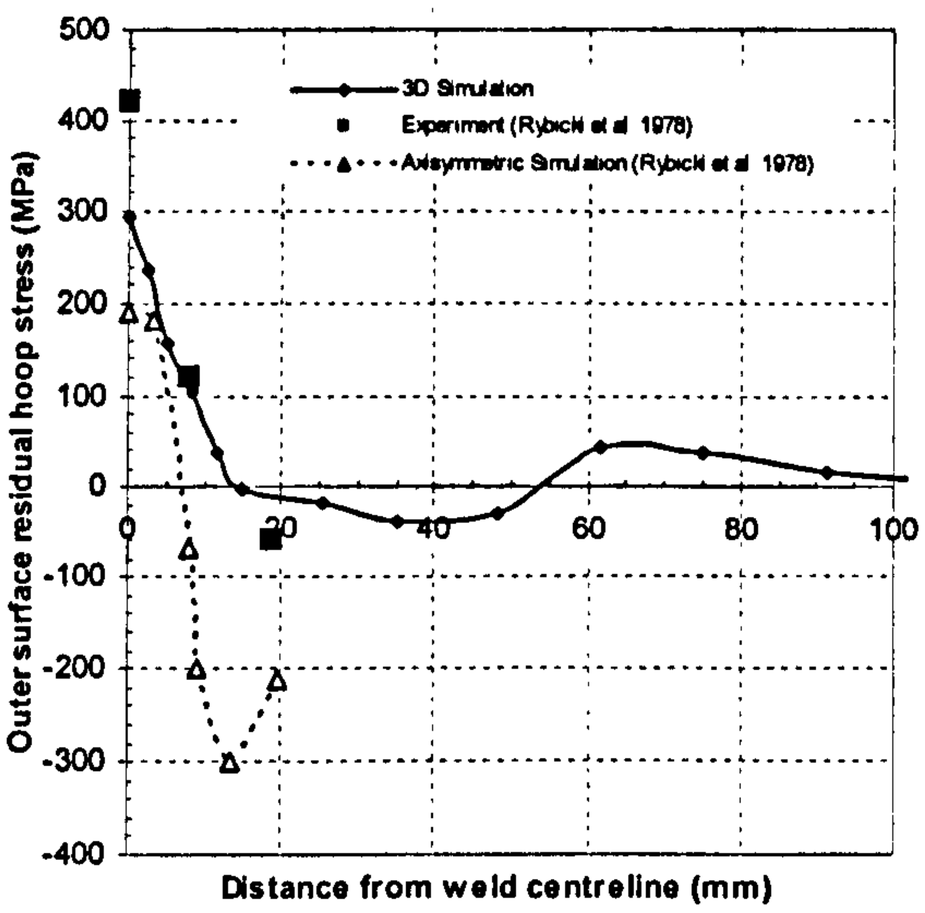

(a) Hoop residual stresses

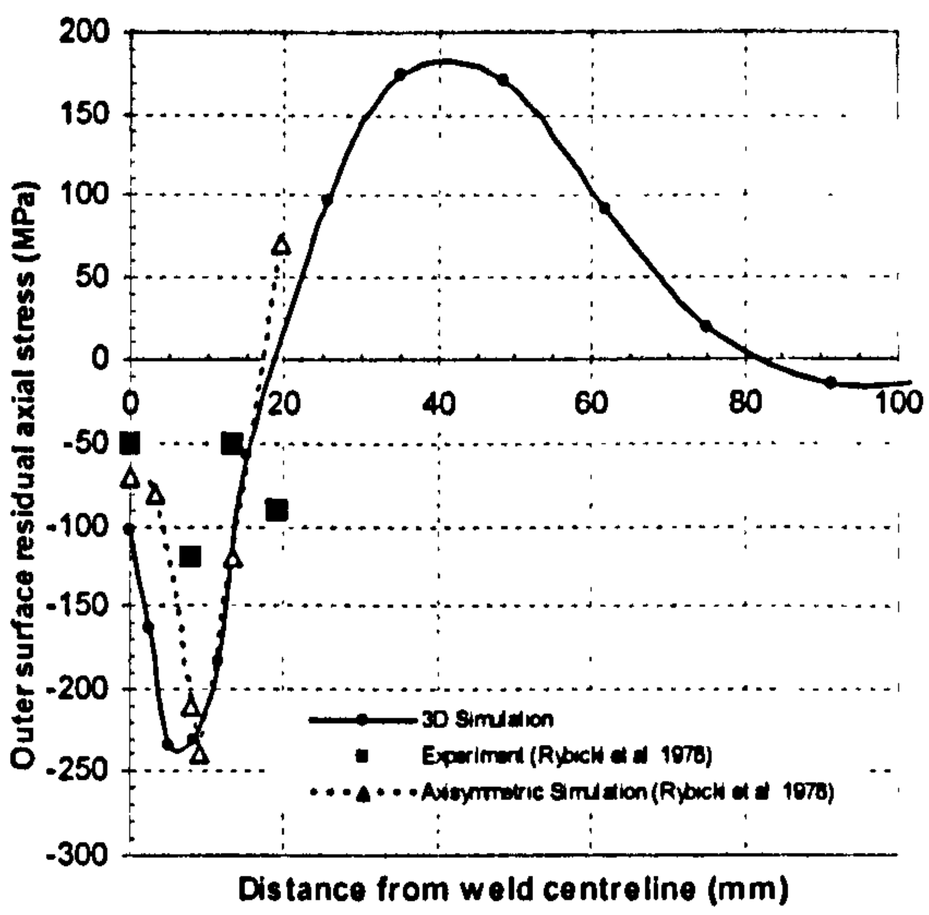

(b) Axial residual stresses

Figure 6.13 Predicted vs. experimental residual stresses at the outer surface

The overall good agreements between the FE predictions and independent experimental measurements for the multipass welded plate and pipe are highly encouraging. As the current full 3D FE model needs no geometric simplifications, it has the potential to be applied to other multipass welded complex geometries for residual stress prediction. In fact, modelling simplifications are impossible for some real pressure retaining components such as the tee branch junction to be considered next. The application of the current model to the thick-walled tee branch junction can minimize assumptions and reflect the realistic welding process as closely as possible.

6.3 Welded tee branch junction

6.3.1 Specimen and welding parameters

The thick-walled tee branch junction described in Chapter 5 is supposed to be welded by six passes. Each pass is completed by the uphill welding method from the same start/stop point. That is, welding starts at the flank centre on each side, and the

tie-in of the bead is made at the crotch corner (Rampaul 1973). The first pass is welded by tungsten inert gas arc welding (TIG) and the subsequent passes by manual metal arc welding (MMA). The simulation parameters, as is common industry practice as reported by Brickstad and Josefson (1998) and Rybicki *et al.* (1982), are listed in Table 6.6. For the stainless steel welds considered in this study, arc efficiencies equal to 0.5 and 0.7 have been assumed for the TIG and MMA, respectively. An interpass temperature of 120°C is assumed between the sequential passes. After the final pass, the component is allowed to cool down for 6000s to ambient temperature.

Table 6.6 Welding parameters used in the simulation (Brickstad and Josefson 1998 and Rybicki *et al.* 1982)

Pass number	Welding method	Voltage (V)	Current (A)	Speed (mm/s)	Heat input (kJ/mm)
1	TIG	9.6	75-120	1.00	0.48
2	MMA	17.3	85-140	1.33	1.09
3-6	MMA	17.6	150-190	1.83	1.14

For the convenience of discussion, this tee branch junction is assumed to be divided into four quadrants. A symmetrical welding sequence in the order of Quadrant *I, III, IV* and *II* is employed for all passes to minimize distortion, as shown in Figure 6.14. The numbers in the figure indicate the welding sequence. Within each quadrant, each pass is further divided into four sectors, i.e. each sector is a fractional pass. A total of 16 sectors are needed to complete a pass of a full circumferential weld. The times needed to complete welding a sector in each pass, which are also the step times used in the analysis, depend on the welding speed and are listed in Table 6.7.

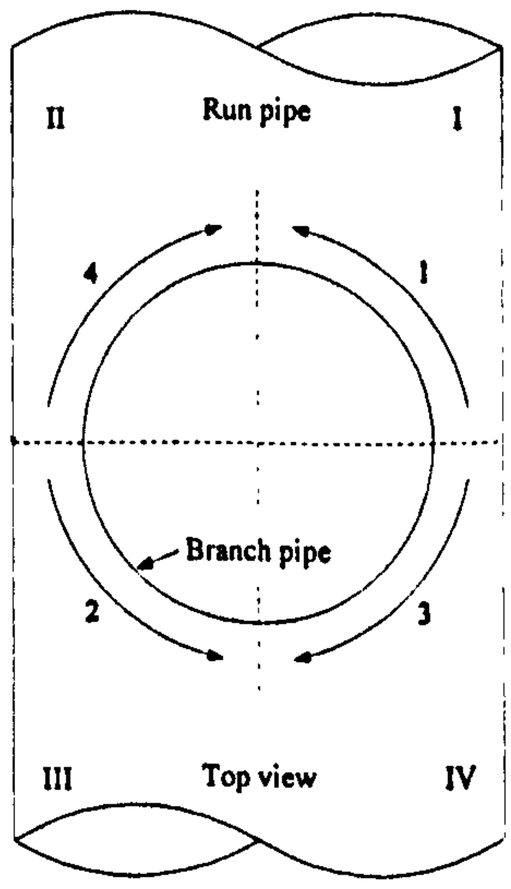

Figure 6.14 Welding sequence of the tee branch junction

Table 6.7 Step time of each pass

	Step time (s)	Subtotal time (s)	Total time (s)
Pass 1	56.0	896.0	896.0
Pass 2	43.2	691.2	1587.2
Pass 3	32.6	521.6	2108.8
Pass 4	33.7	539.2	2648.0
Pass 5	34.7	555.2	3203.2
Pass 6	35.8	572.8	3776.0
Cooling		6000	9777.0

6.3.2 Transient temperature fields

It is well known that a reliable evaluation of residual stress requires an accurate estimation of temperature fields. A thorough understanding of temperature distributions generated during the execution of complex welds and subsequent cooling can give a clear insight into how welding residual stresses build up during the operation. Such understanding will help in formulating recommendations, regarding the weld execution itself, towards reducing the severity of the 'as-welded' residual stress distributions and ensuring the formation of reliable joints that are most effective in service.

6.3.2.1 Output locations

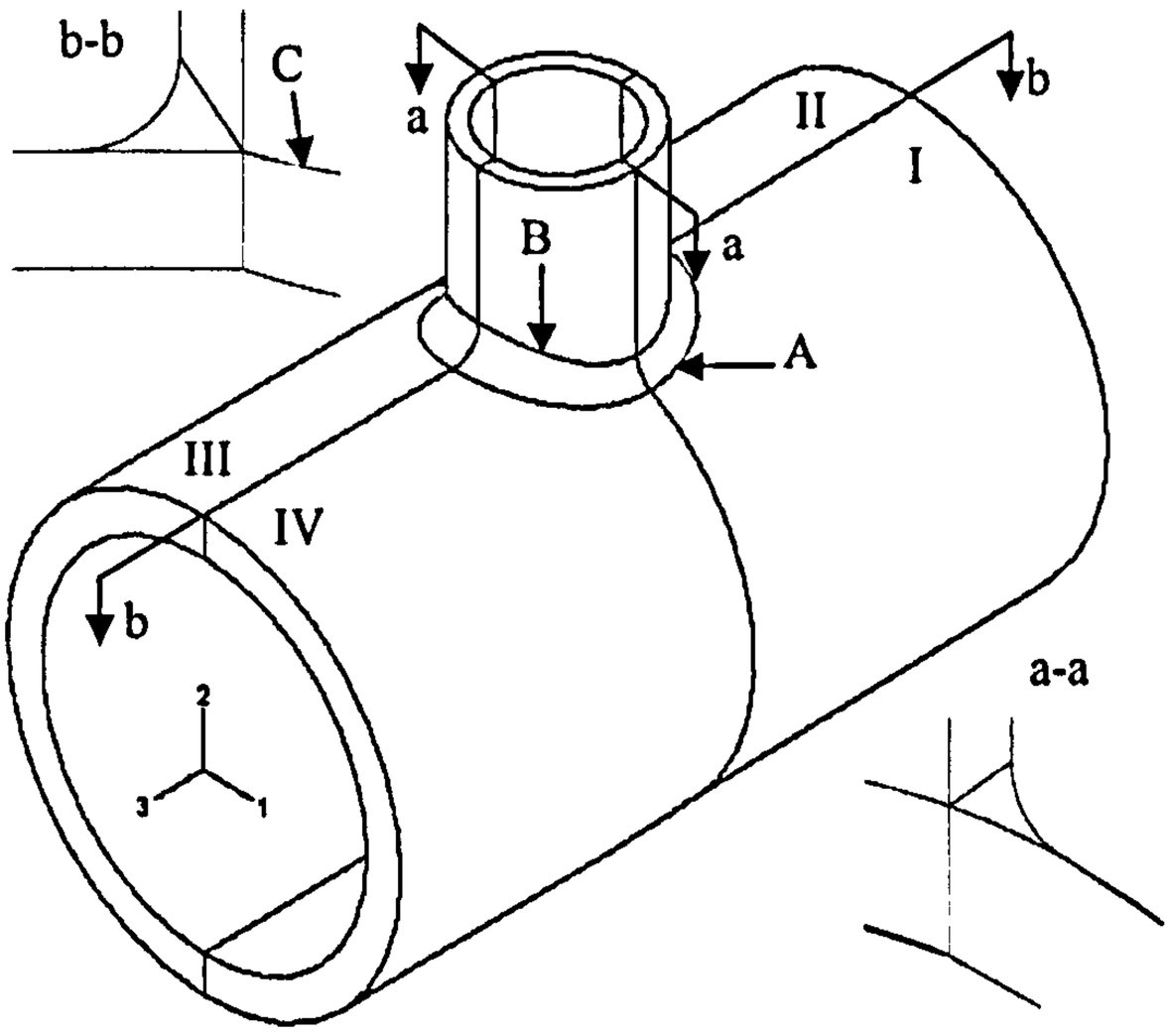

Figure 6.15 Temperature and stress output locations of the tee branch junction

To convey the whole and precise picture of temperature and stress distributions of interest to the welding industry, temperature and stress distributions in the following areas are of major concern (see Figure 6.15):

Branch cross section *a-a*

Run cross section *b-b*

Curve *A*: around the weldline on the outer surface of the run pipe

Curve *B*: around the weldline on the outer surface of the branch pipe

Curve *C*: around the weldline on the inner surface of the branch pipe

6.3.2.2 Temperature contour plots in Quadrant *I*

Table 6.8 presents temperature contour plots at times t=56s, 112s, 168s and 224s respectively after deposition of the first four sectors in Quadrant *I* during welding the first pass. The left column shows the temperature contour plots for Quadrant *I* viewed from the inside, while in the right column the contours are viewed from the outside. The times in the table are counted from the start of welding the first pass.

At time 56s, which corresponds to the time shortly after deposition of the first sector, the temperature appears to be highly localized and the highest temperature reaches 558°C ($0.4T_m$). As the heat source moves towards the crotch corner in Quadrant *I*, the peak temperatures after deposition of each sector do not change much. This is probably because at the early stage of welding, the component is at ambient temperature. The heat supplied by the heat source conducts quickly to the nearby regions. The highly localized temperature distribution and heat source movements can be clearly noticed from these four pairs of figures.

The first four pairs of figures in Table 6.9 present temperature contour plots at the end of deposition of the first four sectors during welding of the last pass. The times are counted from the start of welding the sixth pass. The material deposition and the heat source movement can be observed clearly. A gradual increase in the peak temperature can be noticed from these four figures. High temperature gradients first appear in the region close to the deposited pass. The temperature gradient ahead of the heat source becomes much greater than that behind it. This suggests that the heat transfers much faster in the direction of the heat source movement than it would behind it. A nonuniform temperature distribution can clearly be noticed in the intersection area.

Table 6.8 Temperature distributions in Quadrant *I* during deposition of the first pass

Welding Quadrant *I*	Inside	Outside
t=56s	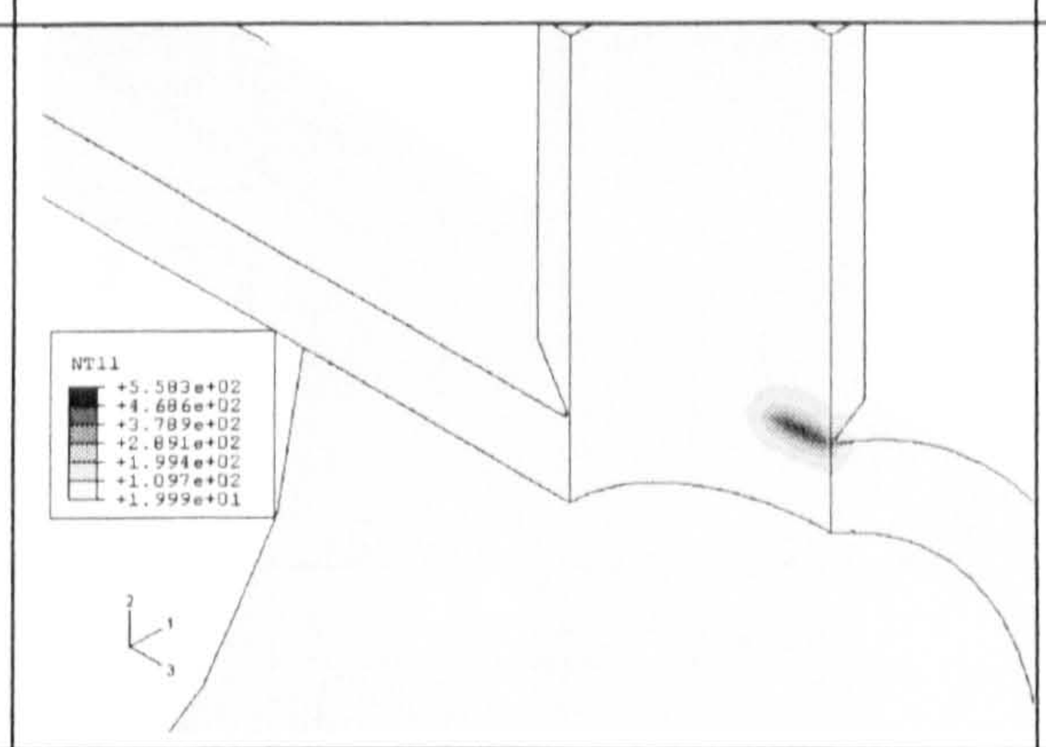	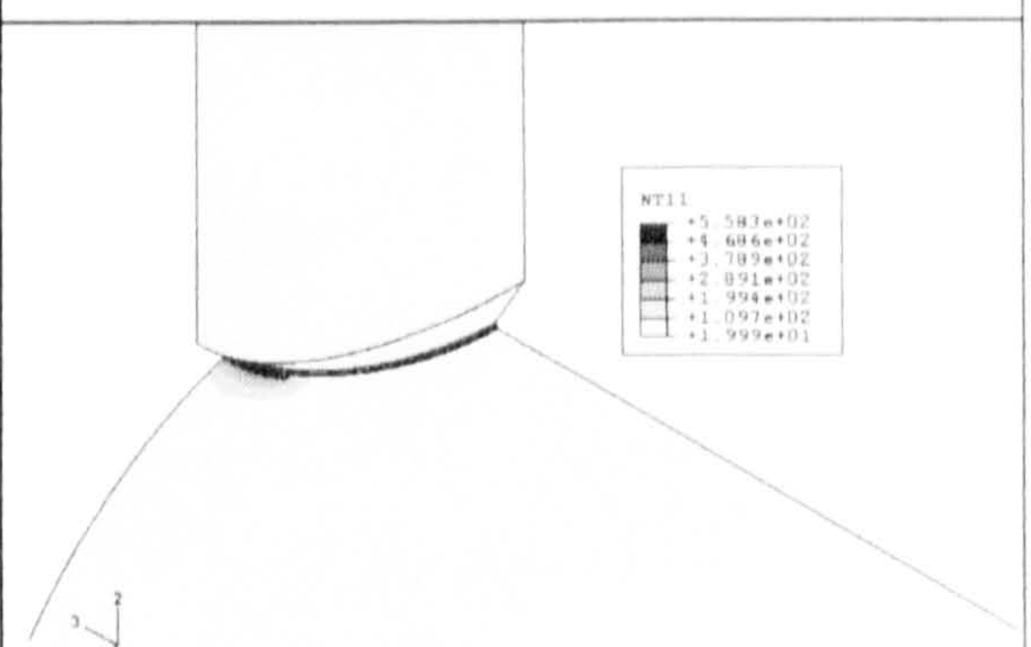
t=112s	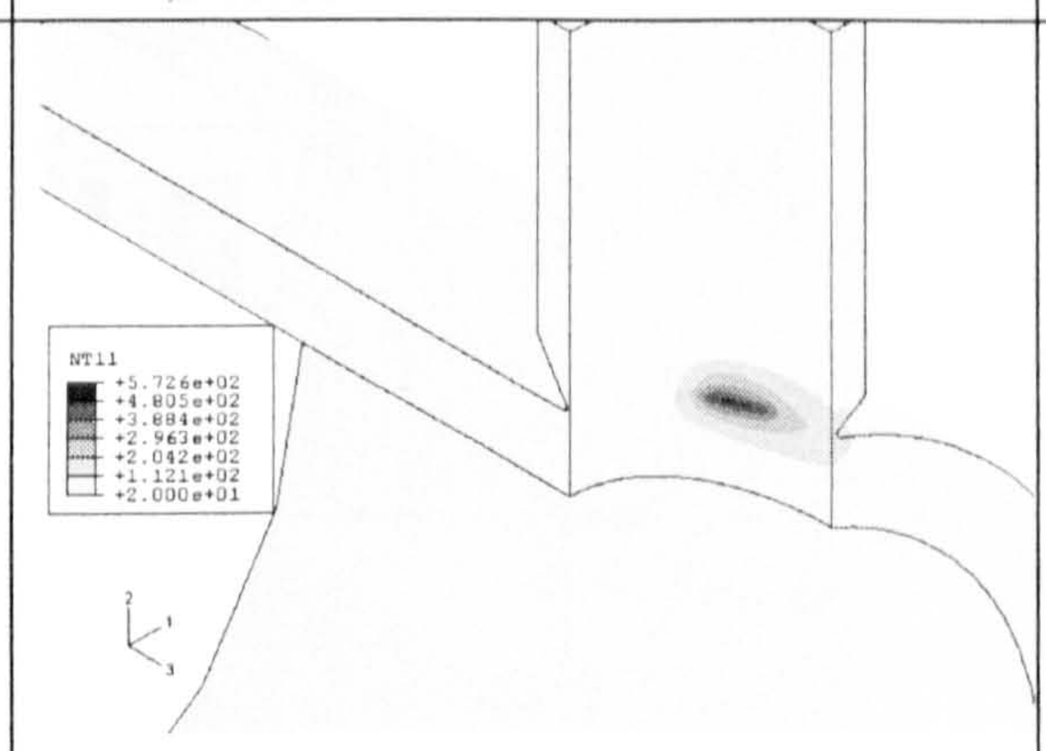	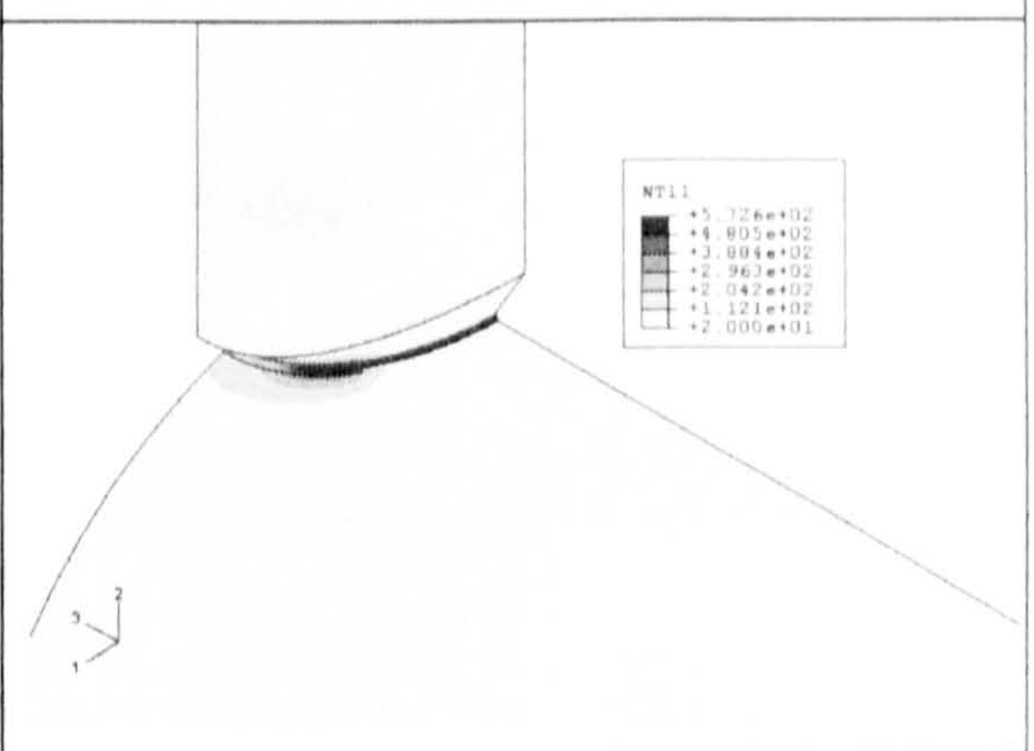
t=168s	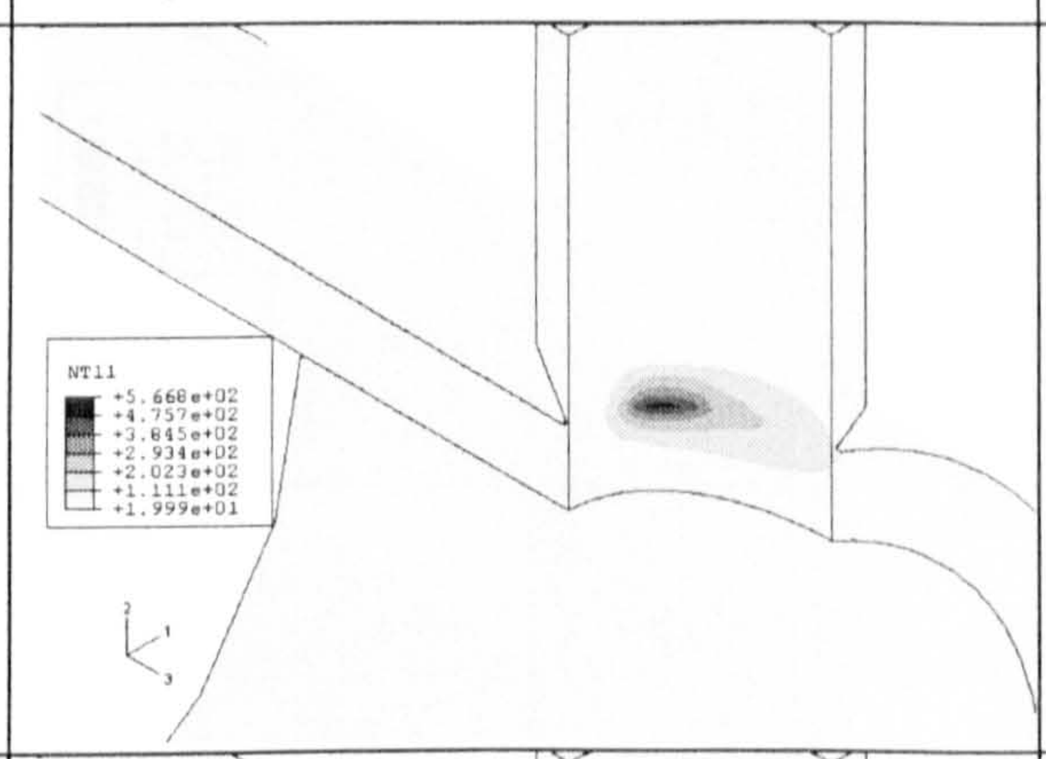	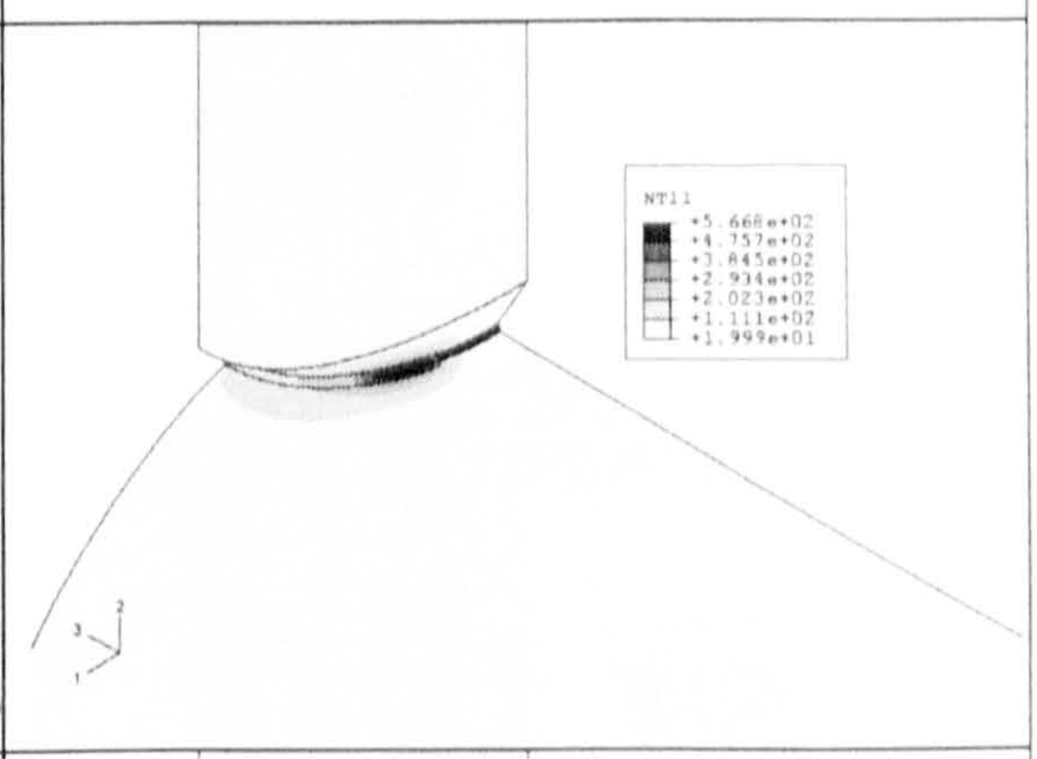
t=224s	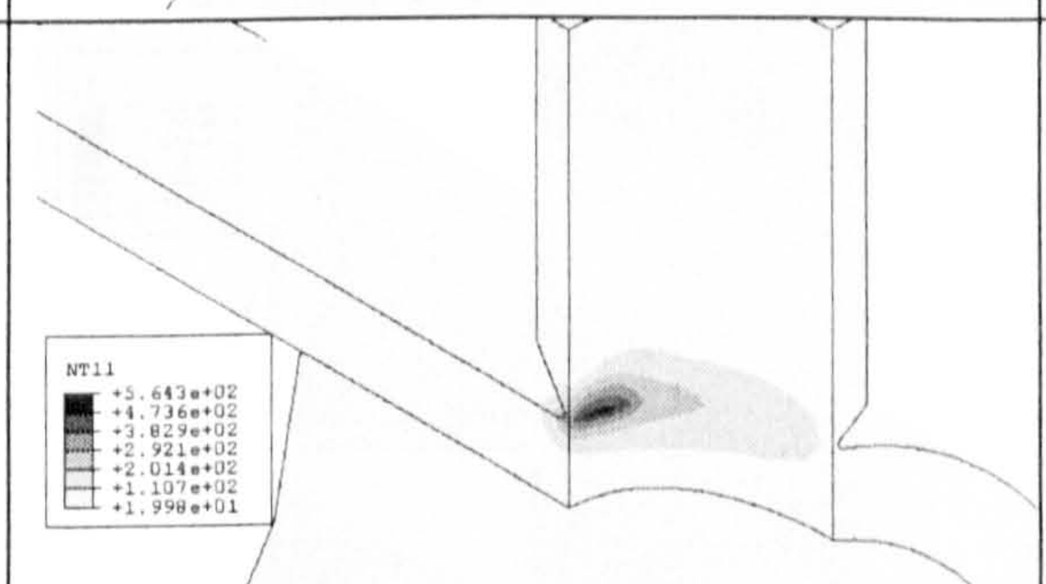	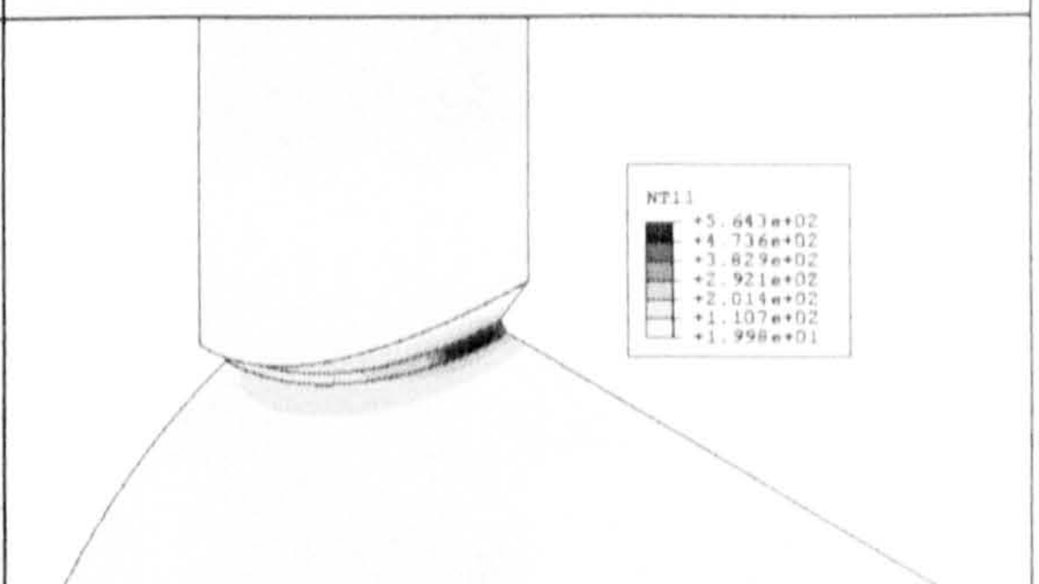

Table 6.9 Temperature distributions in Quadrant *I* during deposition of the sixth pass

Welding Quadrant *I*	Inside	Outside
t=35.8s	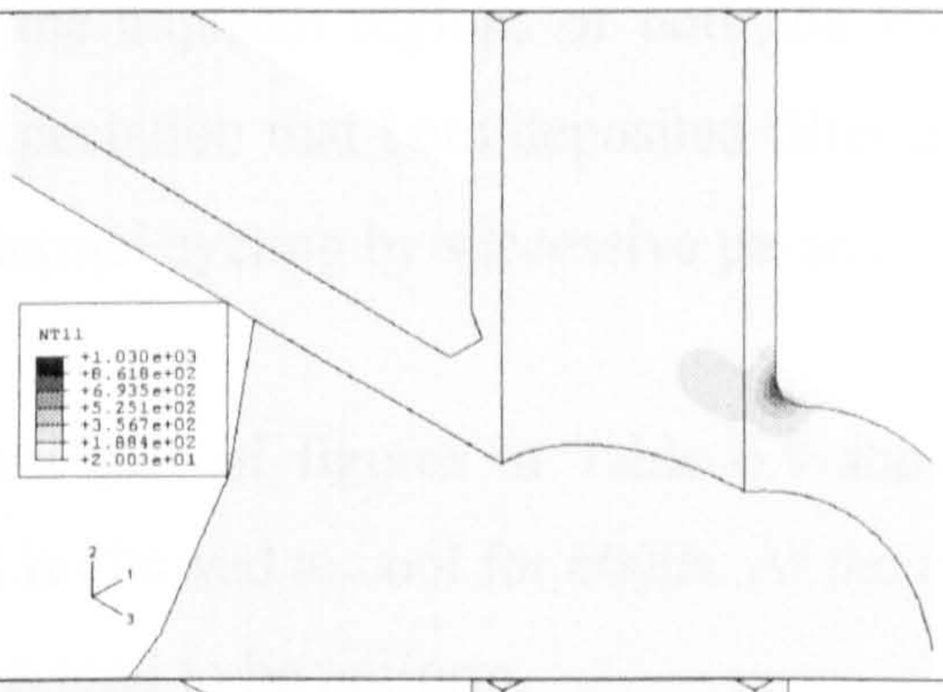	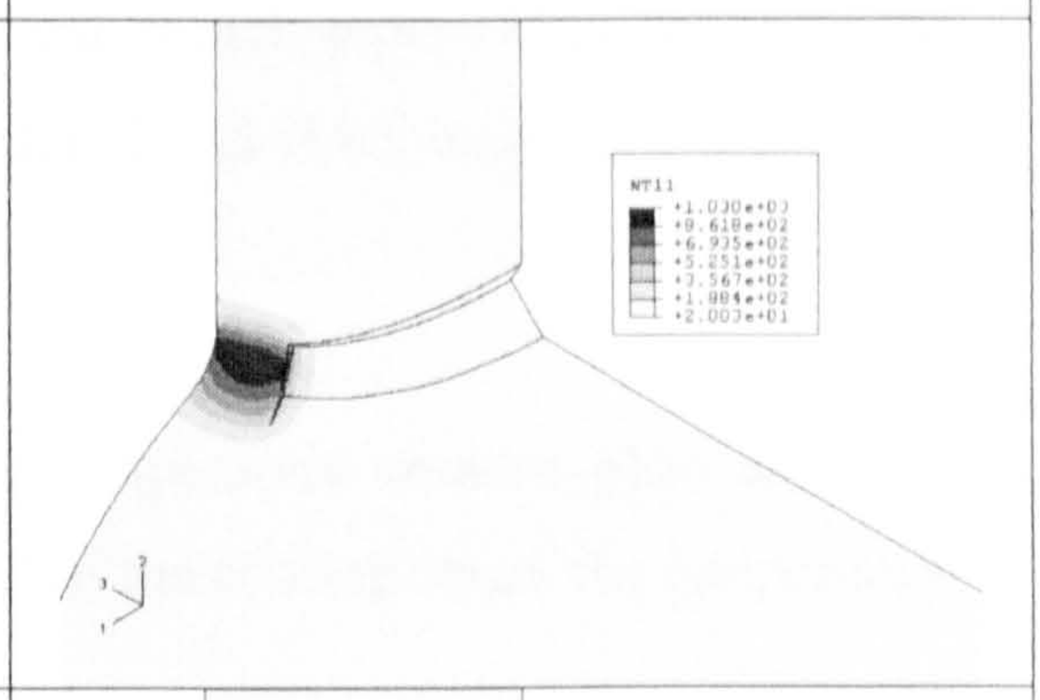
t=71.6s	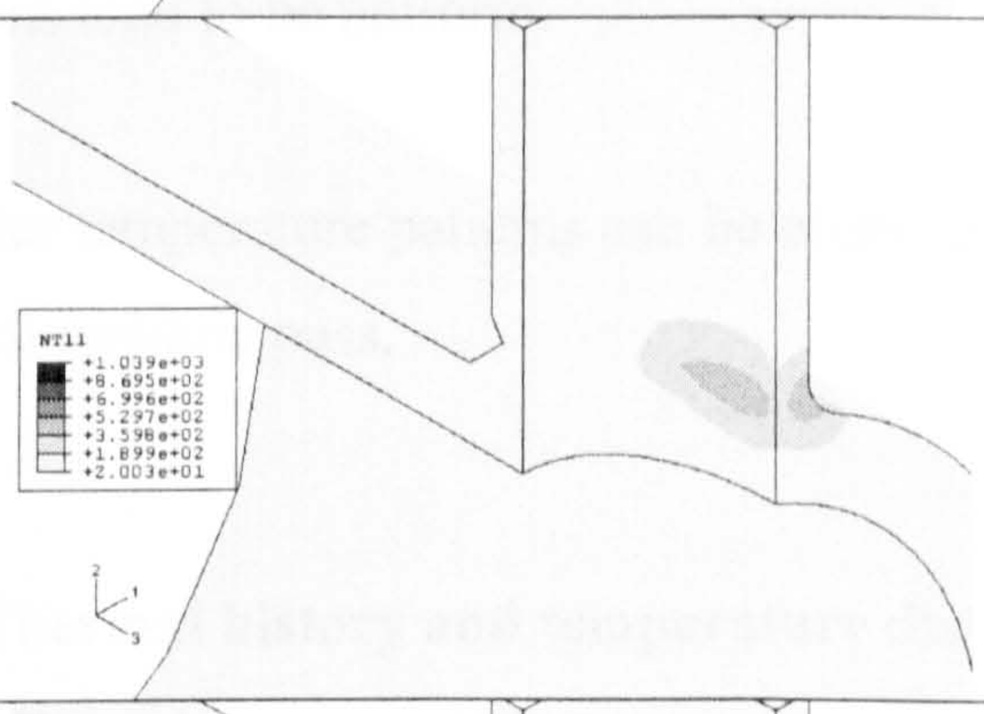	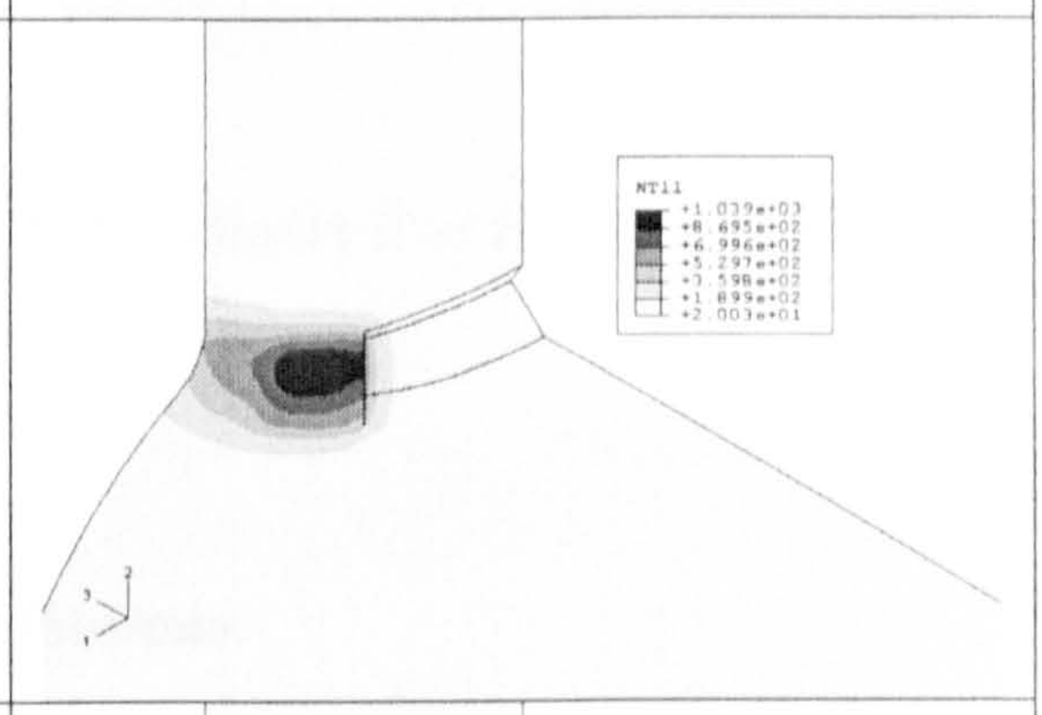
t=107.4s	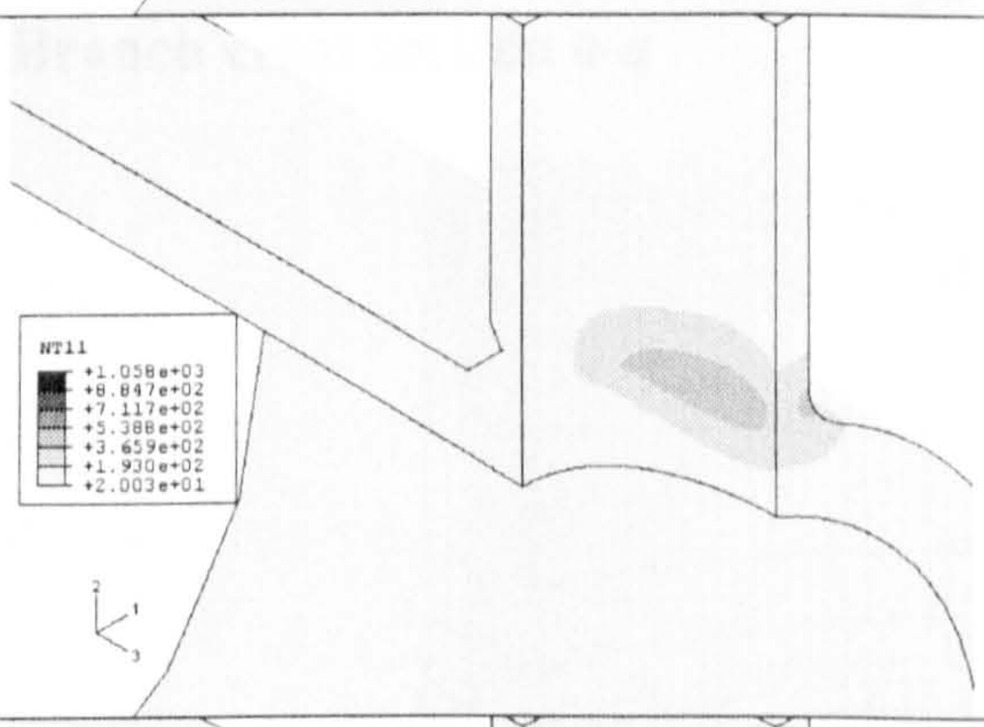	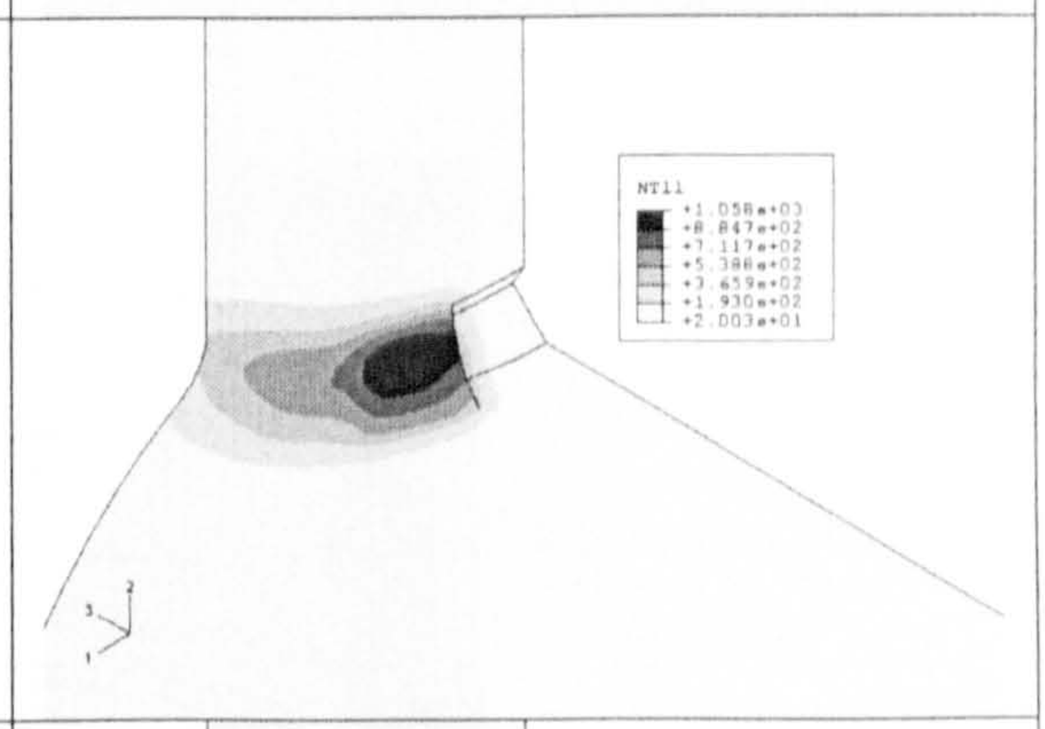
t=143.2s	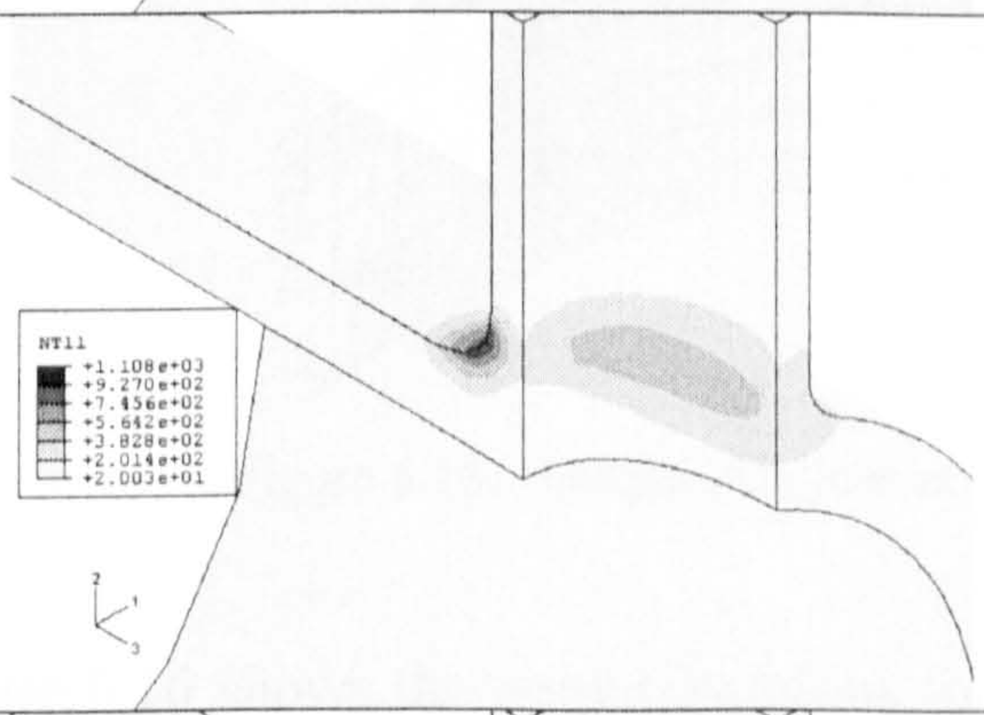	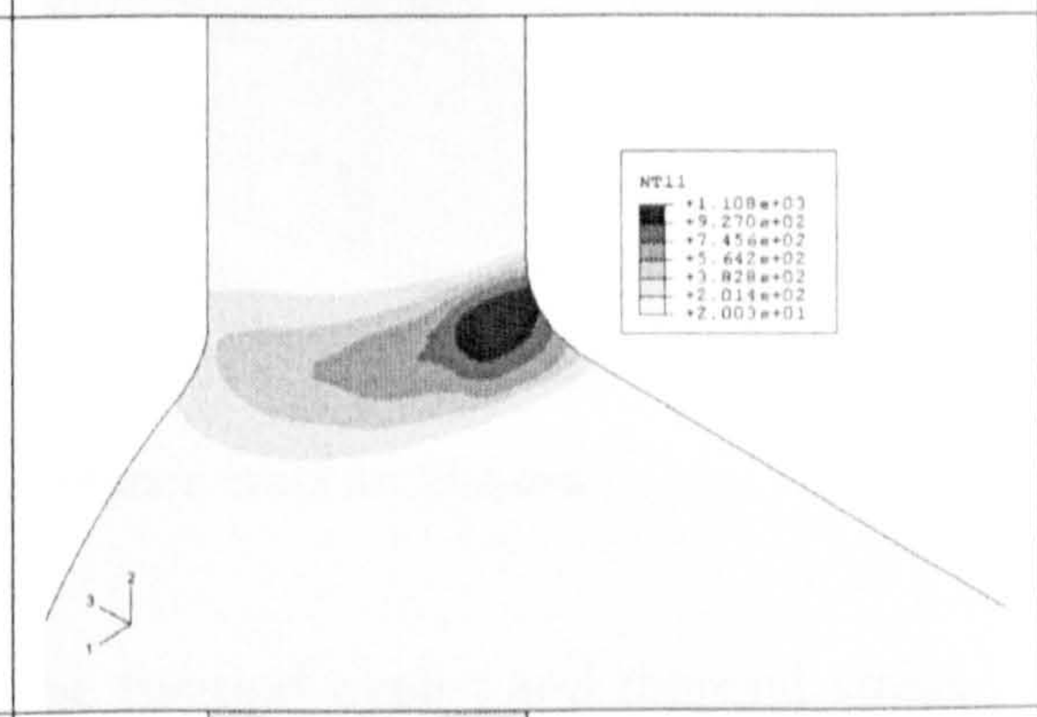
Cooling for 6000s	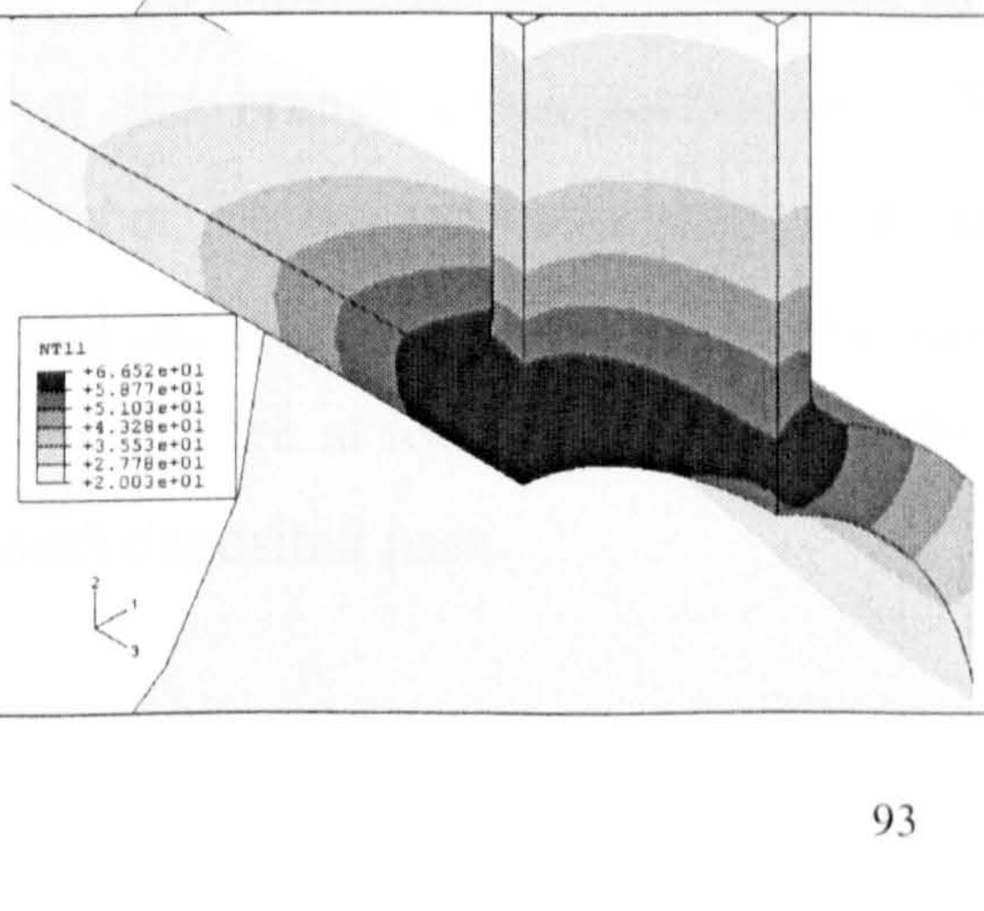	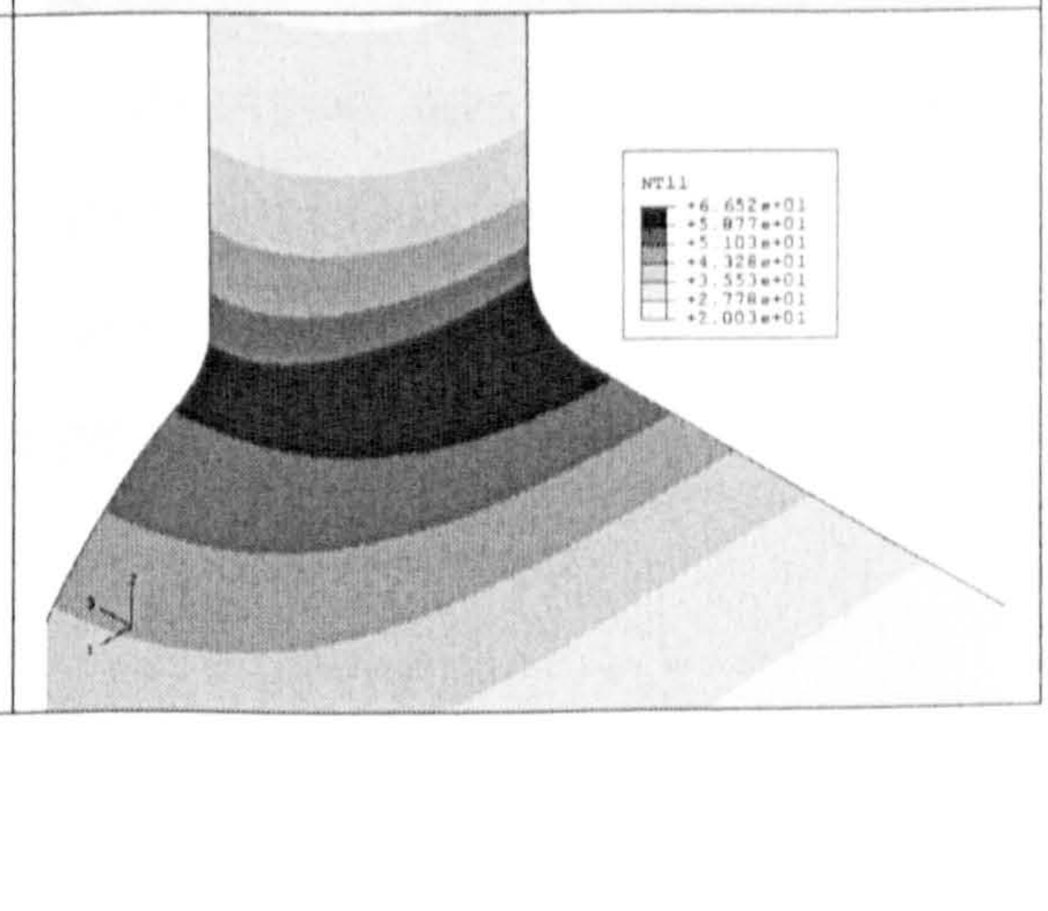

Also noticeable is that the heat conducted to the previously deposited passes as well as to the adjacent regions of both the run and branch pipes. This confirms the intuitive expectation that both deposited filler material and HAZ undergo a process of complex thermal cycling by successive passes.

The last pair of figures in Table 6.9 shows temperature contour plots after the component is allowed to cool for 6000s. At the end of the cooling stage, the temperature distributions tend to be uniform.

Similar temperature patterns can be observed in Quadrants *II* to *IV* at various times during each welding pass.

6.3.2.3 Thermal history and temperature distributions

6.3.2.3.1 Branch cross section *a-a*

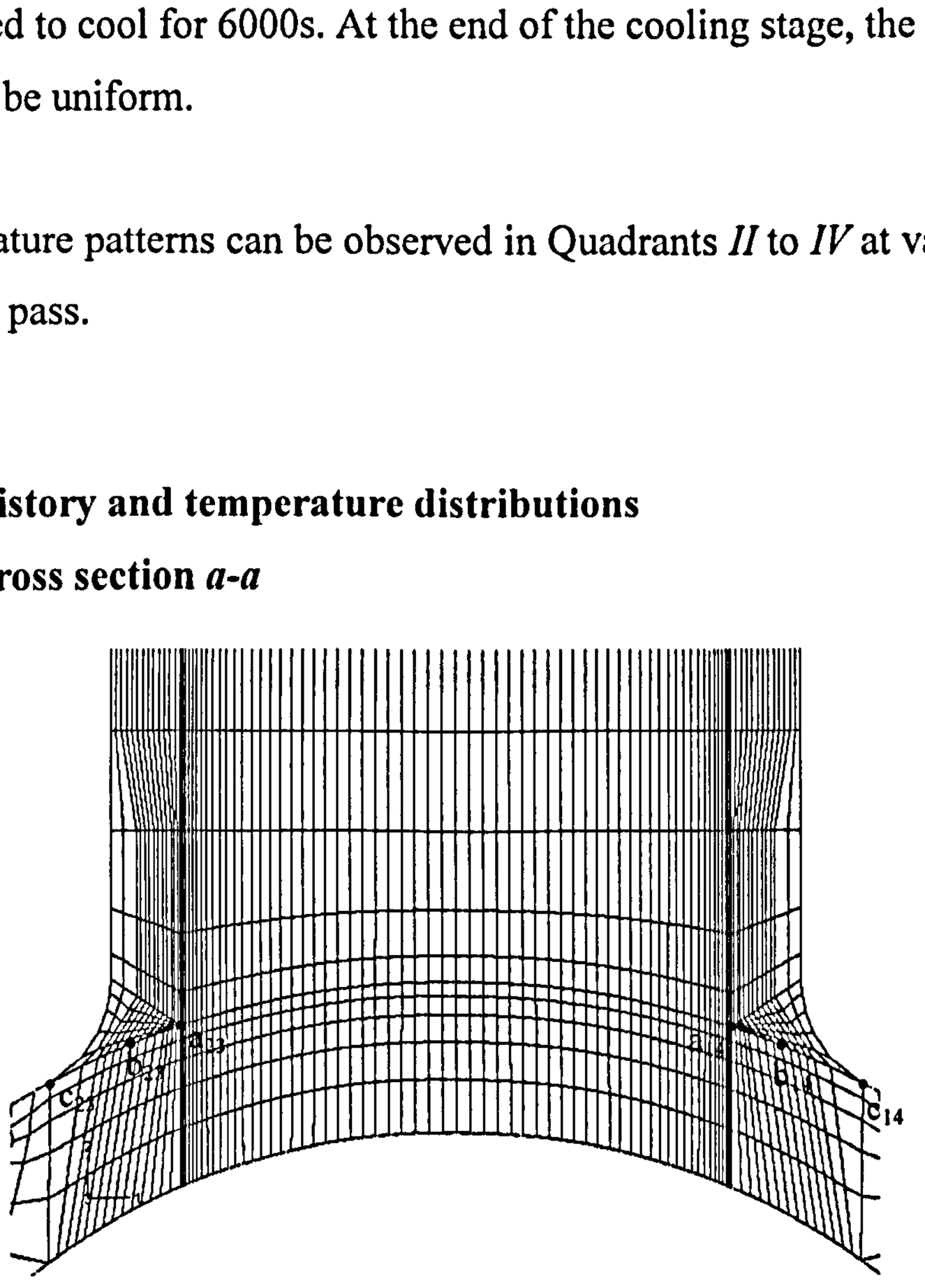

Figure 6.16 Output locations at the branch cross section *a-a*

Figure 6.16 shows the output locations for the thermal cycles and thermal stress evolutions at the branch cross section *a-a*. The subscripted numbers indicate the quadrant number, i.e. a_{14} indicates point *a* at the interface of Quadrants *I* and *IV*, etc. Points a_{14} and a_{23} are located on the intersection corner of the branch and run pipes. Points b_{14} and b_{23} are at locations where the third pass is deposited. Points c_{14} and c_{23} are at the sixth deposited pass.

Figure 6.17(a) shows the temperature cycle Point a_{14} experiences during welding. Two peak temperatures are evident within each pass. The first depicts the temperature after deposition of the first sector while welding Quadrant *I*, and the second after deposition of the first sector while welding Quadrant *IV*. Both sectors are welded from the start point a_{14}. Within each pass, it is interesting to note that the second peak temperature is always higher than the first one. This could be explained by the fact that the temperature at the start of each pass when welding Quadrant *I* is relatively lower compared to the moment when the heat source moves back to Point a_{14} to start welding Quadrant *IV*.

It can also be seen from Figure 6.17(a) that the temperature at Point a_{14} reaches a maximum value on deposition of the first pass followed by gradual cooling. The cooling rate is initially steep and become less so towards the end of the pass. Point a_{14} reaches its peak temperature each time the subsequent passes are deposited. However, the peak values decrease as the distances between each subsequent passes and Point a_{14} increase.

It is also noticed that the first pass has a relatively smaller interpass temperature compared with other passes. Two reasons might account for this: firstly, at the beginning of welding, the component is at lower temperature, even if it has been preheated to 65°C; secondly, the welding speed of the first pass is the slowest amongst all passes, which give the component enough time to cool down.

The interpass temperatures show a trend of steady increase as pass number increases. In practice, interpass temperatures are controlled to a certain level to provide adequate mechanical properties. In this simulation, the above value is artificially fixed to a constant value of 120°C, as indicated in each figure.

Figure 6.17(b) shows the temperature cycles that Point a_{23} experiences. Since a_{14} and a_{23} are symmetrical points, similar thermal cycles are observed.

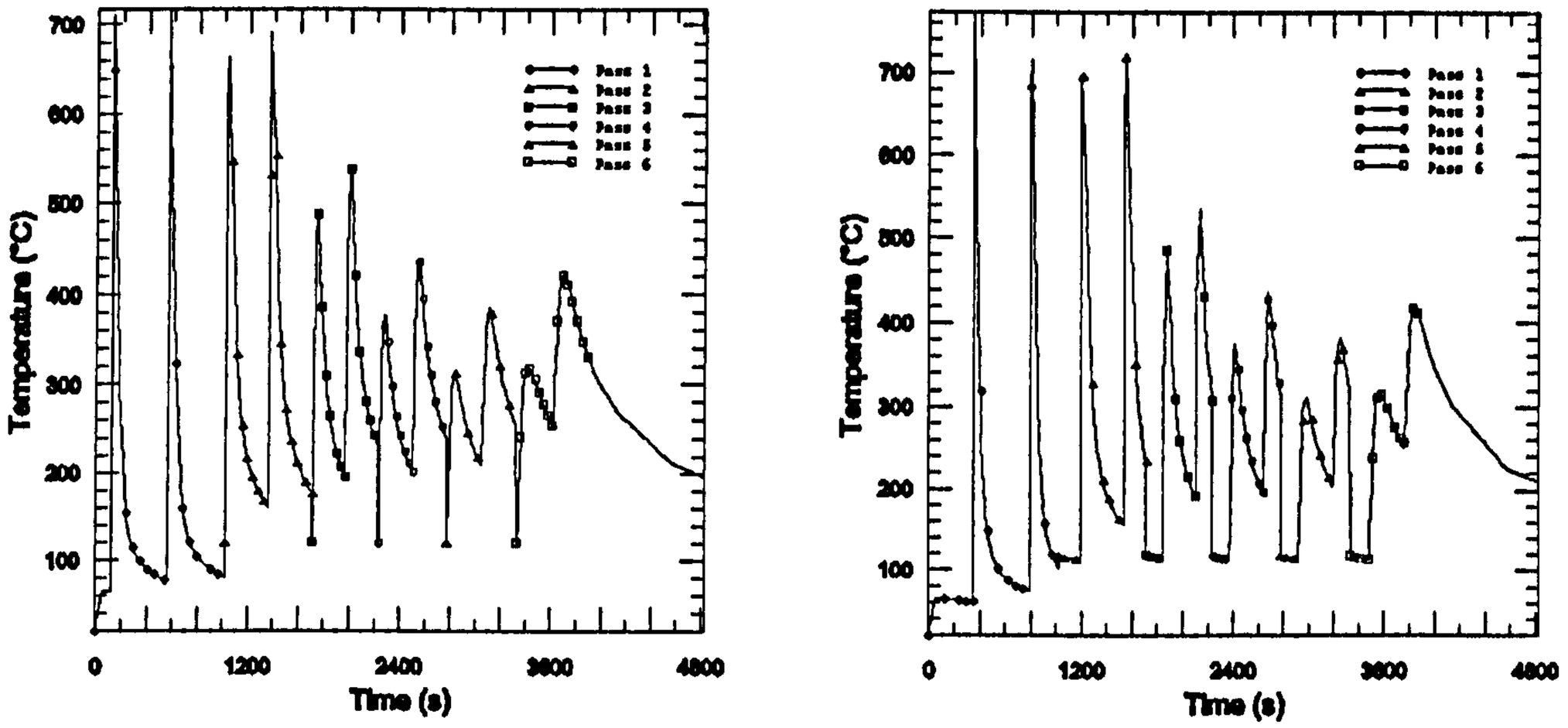

(a) (b)

Figure 6.17 Thermal cycles at (a) Point a_{14} (b) Point a_{23}

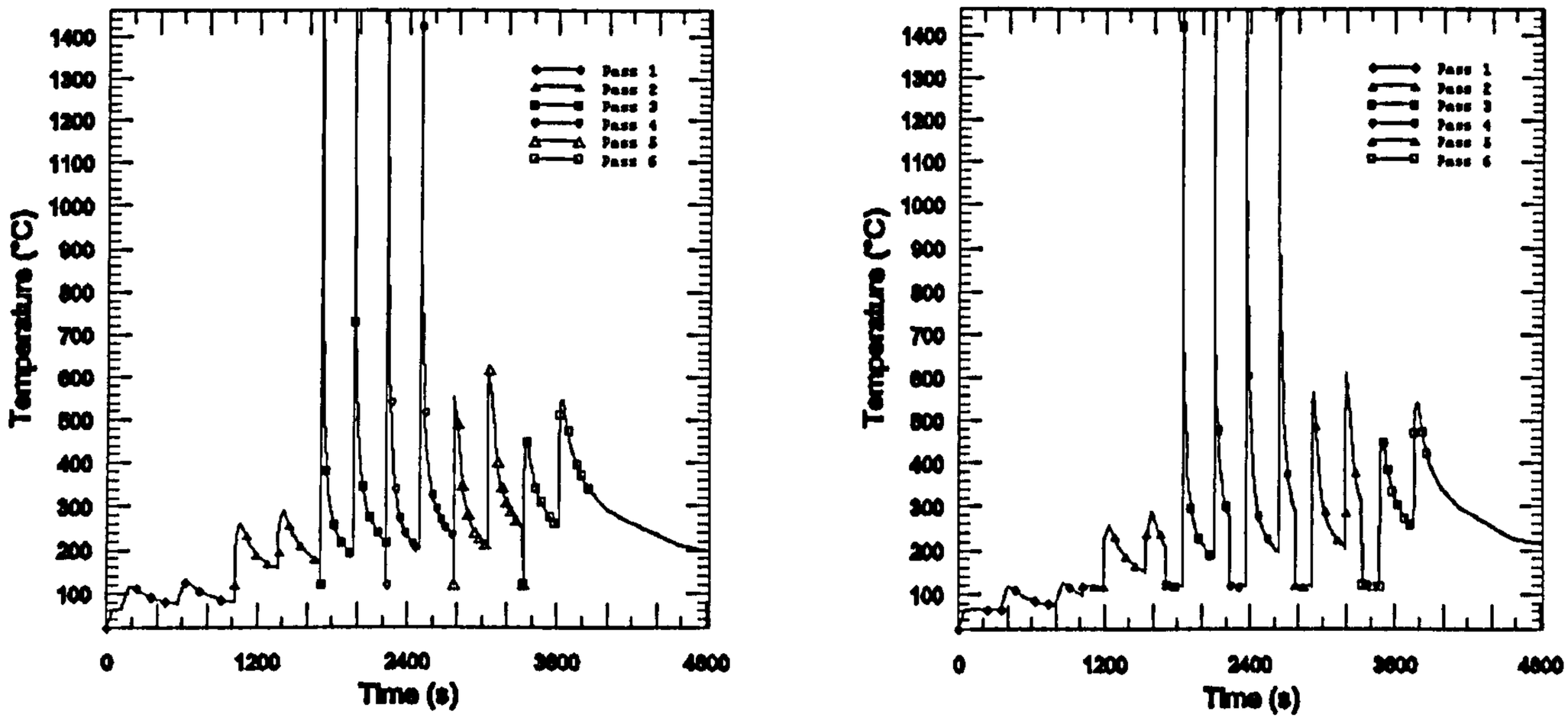

(a) (b)

Figure 6.18 Thermal cycles at (a) Point b_{14} (b) Point b_{23}

Figure 6.18(a) shows the temperature cycles that Point b_{14} experiences. Point b_{14} experiences heating each time the lower numbered passes are deposited. A maximum temperature of 1460°C is reached when the third pass is deposited. The temperature at Point b_{14} continues to reach a peak value each time the subsequent passes are deposited. The peak value depends on the distance between individual passes and Point b_{14}. Similar thermal cycles are observed for Point b_{23}, as shown in Figure 6.18(b).

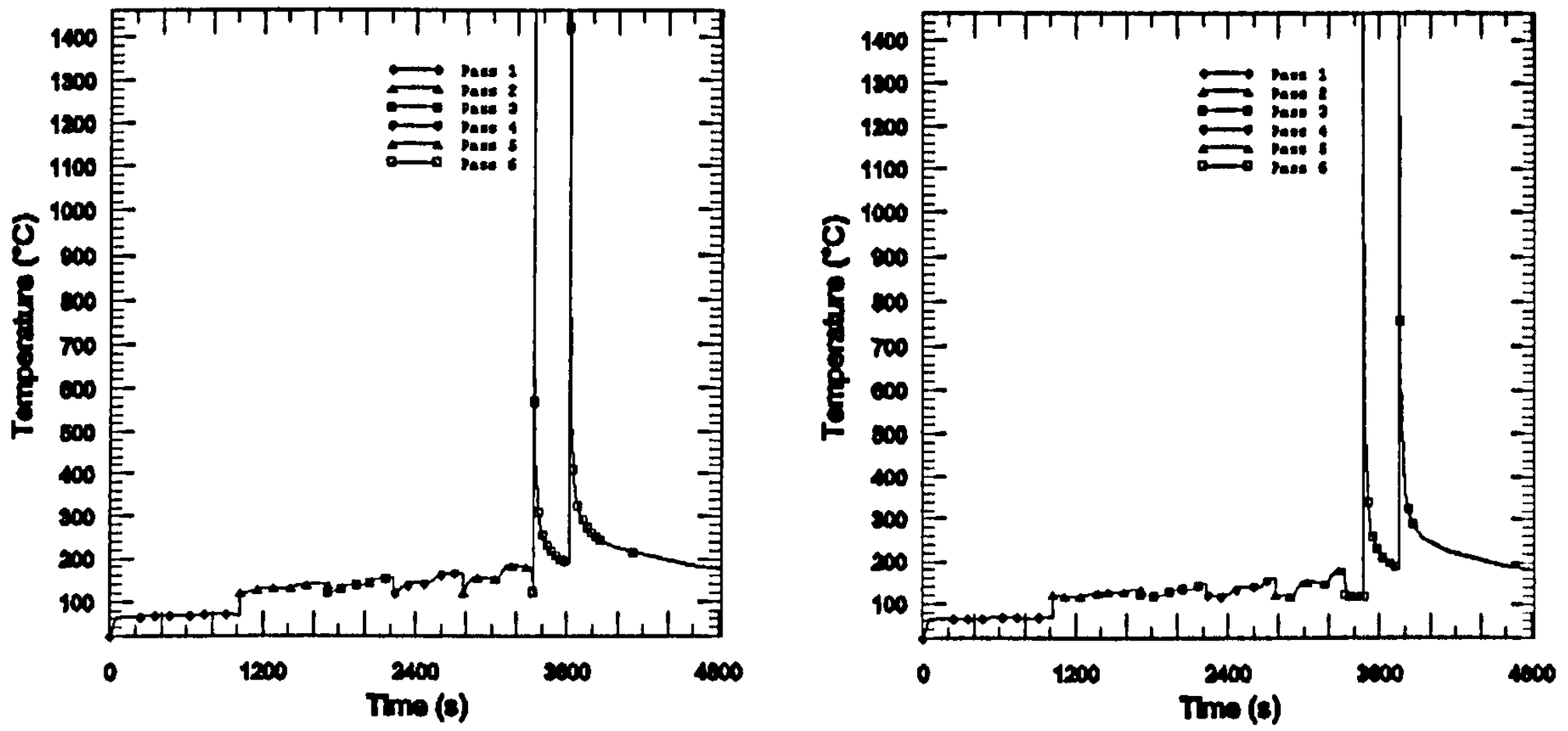

Figure 6.19 Thermal cycles at (a) Point c_{14} (b) Point c_{23}

Points c_{14} and c_{23} experience similar temperature cycles, as observed from Figures 6.19(a)-(b). A peak temperature of 1460°C is reached when the sixth pass is deposited.

From the above presentation, it is noticed that Points a_{23}, b_{23} and c_{23} experience similar thermal cycles to those of their symmetrical points. Therefore, the following section will only present results at Points a_{14}, b_{14} and c_{14} to avoid repetition.

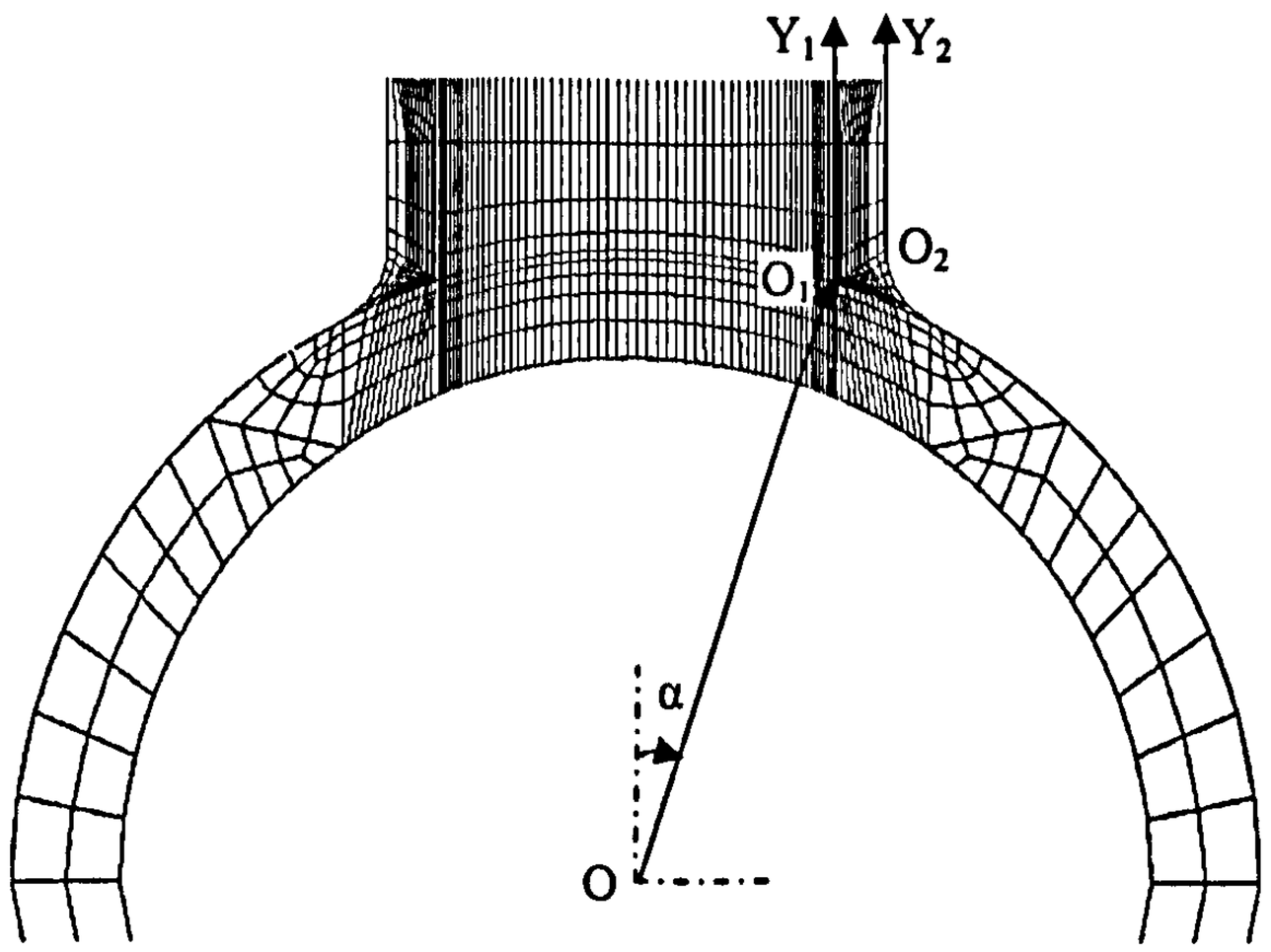

Figure 6.20 Local coordinate systems at the branch cross section *a-a*

The locations of the origins and local coordinate systems for depicting temperature and stress distributions at the branch cross section *a-a* are shown in Figure 6.20. The origins O_1 and O_2 are selected at the edge of the branch pipe that intersects the weld seam. The Y_1 and Y_2 axes are located axially along the branch inner and outer surfaces,

respectively. The centre of the run pipe *O* is selected as the origin to establish local coordinate system to present results along the outer surface of the run pipe. Results are presented within a range of α (between 18° and 90°). The output locations will be further demonstrated by thick lines in each inserted geometrical diagram. In these figures, the solid lines represent the temperature distributions at 1s after deposition of the first sector during welding the first and last pass. The dashed lines display the temperature distributions after deposition of these sectors.

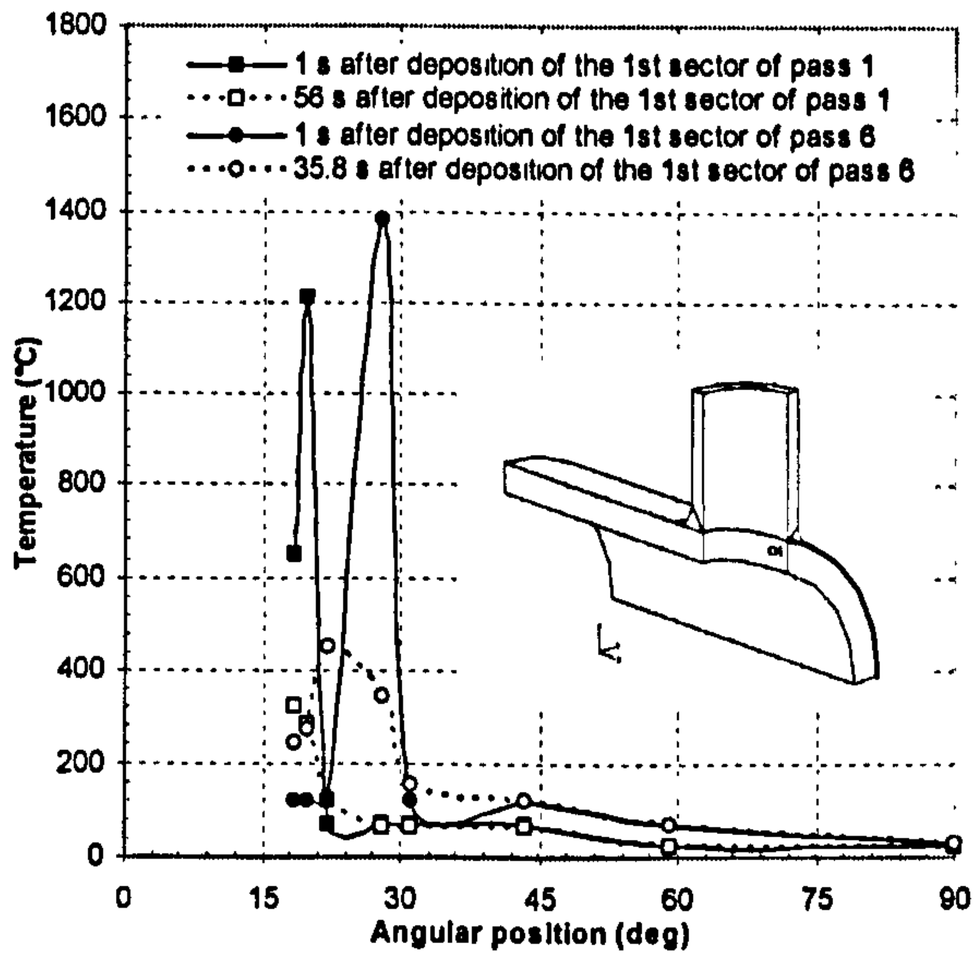

Figure 6.21 Temperature vs. angular position on the run pipe outer surface

Figure 6.21 shows temperature versus angular position circumferentially along the outer surface of the run pipe. High temperatures are mainly concentrated in the region spanning 18° to 30°, where the weld groove is located. The region beyond 30° seems to be hardly affected by welding. The two peak temperatures indicate the maximum temperature experienced by the material on the fusion line at 1s after deposition of the first sector of the first and last pass, respectively. Steep temperature gradients can be clearly observed. The material within the region spanning 18° to 30° experiences intense heating-cooling thermal cycles.

Figure 6.22 shows temperature distributions in the Y_1-direction. The locations of the origin O_1 and Y_1 axis are shown in the inserted figure. The peak temperature at 1s after deposition of the first sector of the first pass is 650°C ($0.45T_m$), and is localized at the origin O_1. At the end of deposition of this sector, heat is noted to conduct to the nearby regions and the highest temperature reduces to 320°C ($0.2T_m$). The last pass has

almost no effect on the inner surface temperature at the moment of deposition, probably because this pass is at some distance away from the branch inner surface. However, at the end of the deposition, heat eventually conducts to the inner surface of both branch and run pipes; the highest temperature being 250°C ($0.17T_m$) at the origin O_1.

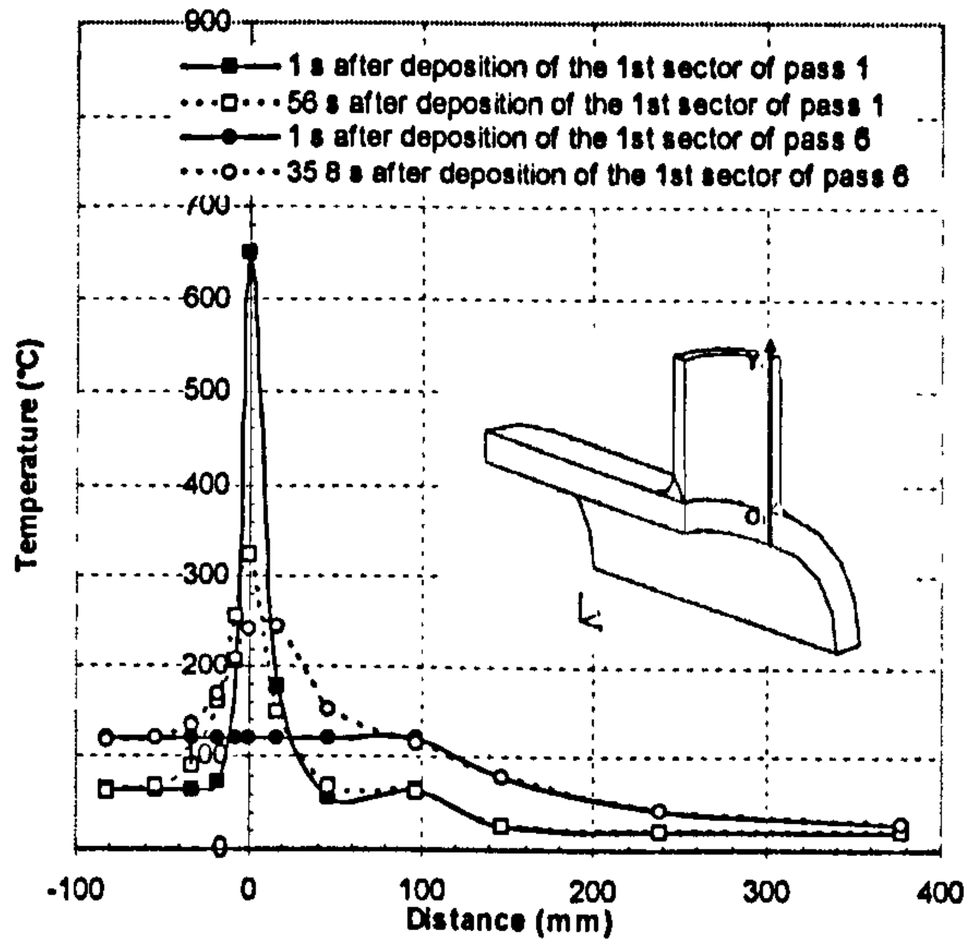

Figure 6.22 Temperatures in the Y_1-direction on the branch inner surface

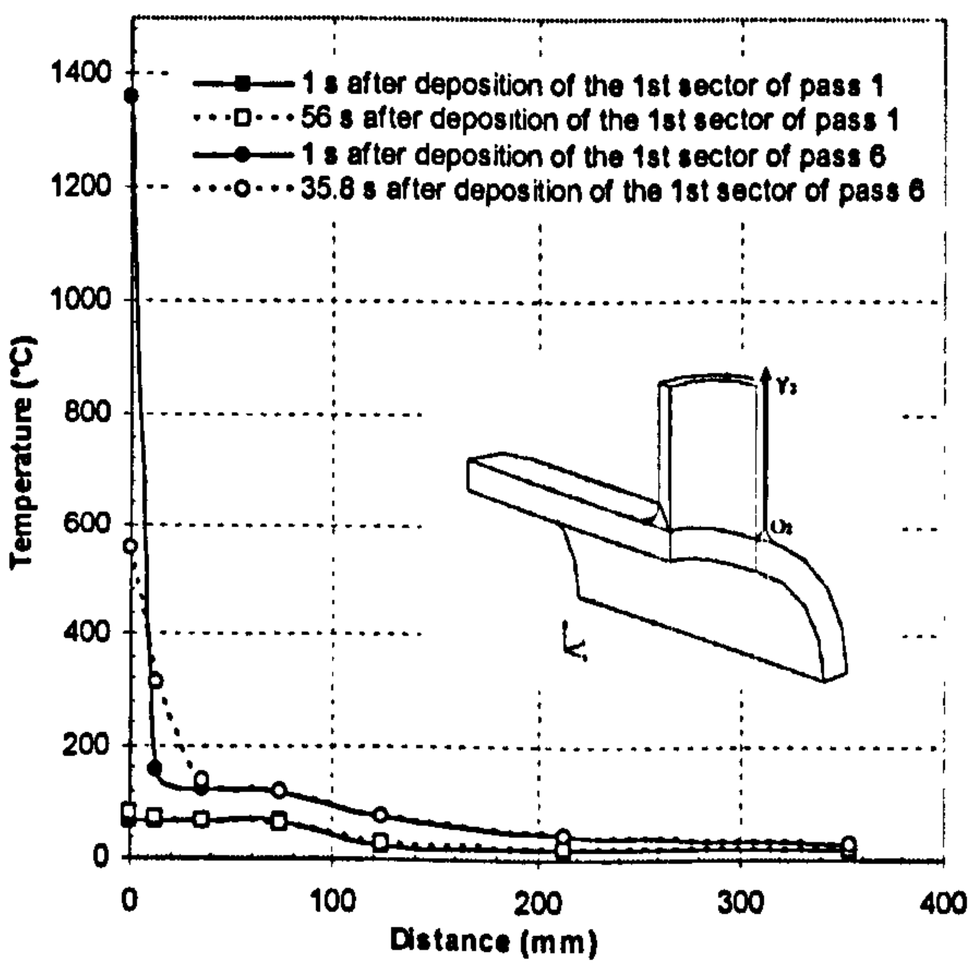

Figure 6.23 Temperatures in the Y_2-direction on the branch outer surface

Figure 6.23 shows temperature distributions along Y_2-direction. It is noticed that the first pass has hardly any effects on the temperature changes on the branch outer surface. At 1s after deposition of the first sector of the last pass, the region localized to the heat source reaches 1360°C ($0.93T_m$). The temperature rapidly decreases to 155°C ($0.1T_m$) at a distance of about 13mm away from the origin O_2. At the end of deposition

of this sector, the highest temperature reaches 557°C ($0.38T_m$) at the origin O_2.

6.3.2.3.2 Run pipe cross section *b-b*

Figure 6.24 shows the output locations for the thermal cycles and stress evolutions at the run pipe cross section *b-b*. Points a_{12} and a_{34} are located at the intersection corner of the branch and run pipe. Points b_{12} and b_{34} correspond to the locations where the third pass is deposited. Points c_{12} and c_{34} are at the sixth deposited pass.

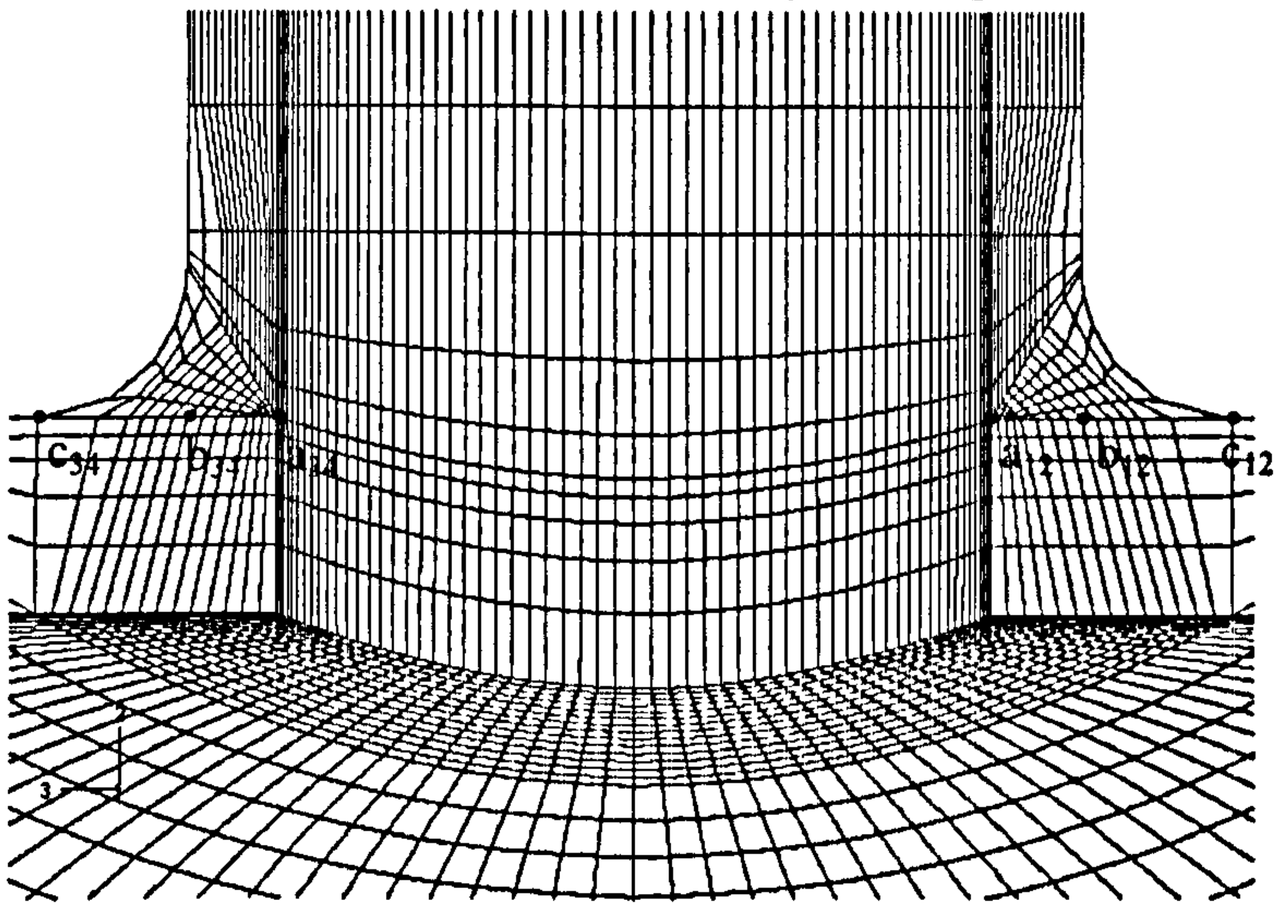

Figure 6.24 Output locations at the run pipe cross section *b-b*

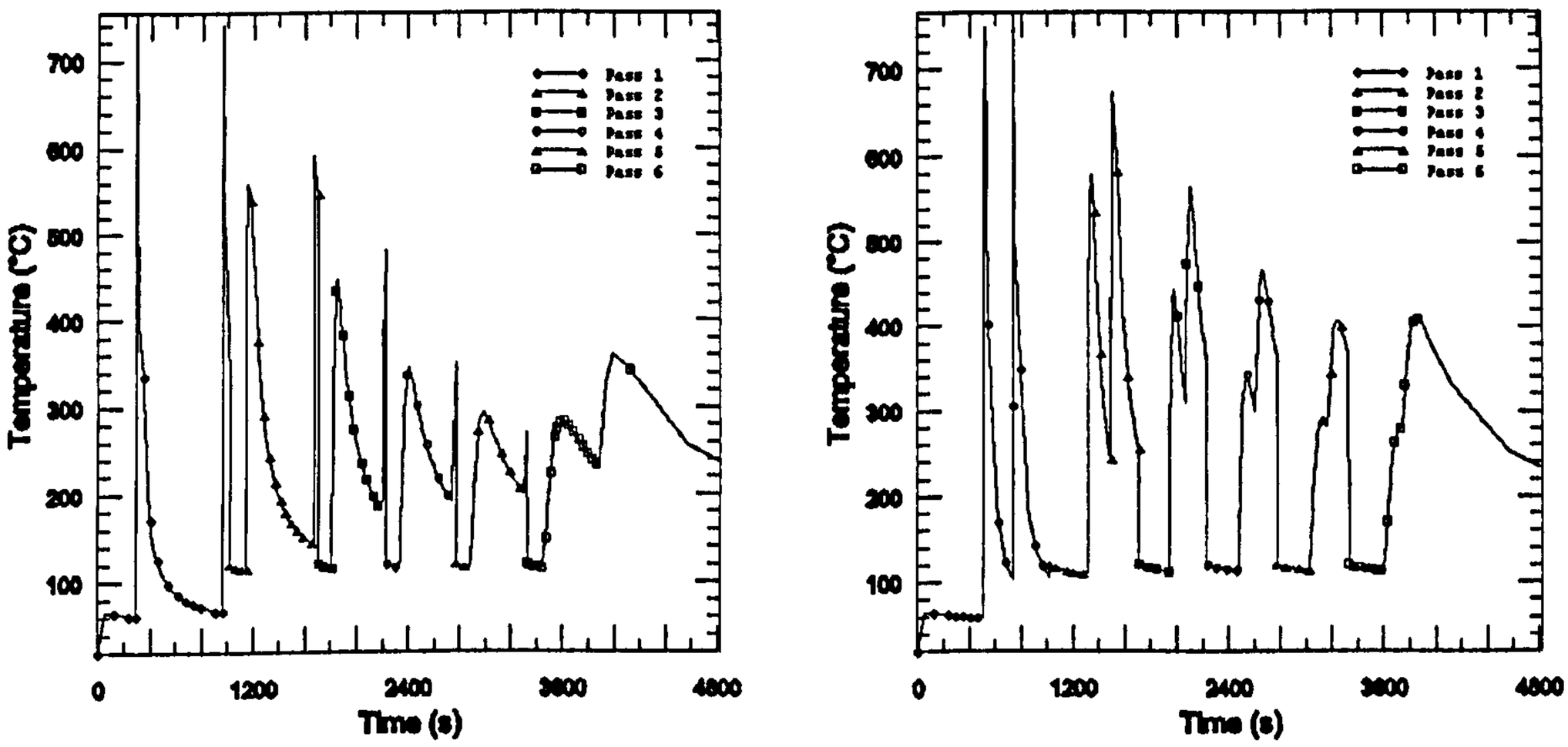

(a) (b)

Figure 6.25 Thermal cycles at (a) Point a_{12} (b) Point a_{34}

Figure 6.25(a) shows the thermal cycle that Point a_{12} experiences. It is noticed again that each pass has two peak temperatures; the first indicates the temperature after deposition of the last sector when welding Quadrant *I*, and the second is after deposition

of the last sector when welding Quadrant *II*, i.e. the last sector before the completion of circumferential welding of the pass under consideration. The temperature at Point a_{12} decreases gradually after the first peak value. It then drops rapidly after the second peak value because of the imposed interpass temperature. As the distances between the heat source and Point a_{12} increase, the peak temperatures decrease.

Figure 6.25(b) shows the temperature cycles that Point a_{34} experiences. Within each pass except the first one, Point a_{34} is kept at an interpass temperature of 120°C before it reaches the first peak temperature. Each pass has two peak temperatures. However, as the pass numbers increase, these two peaks are not as markedly obvious as at the smaller numbered passes.

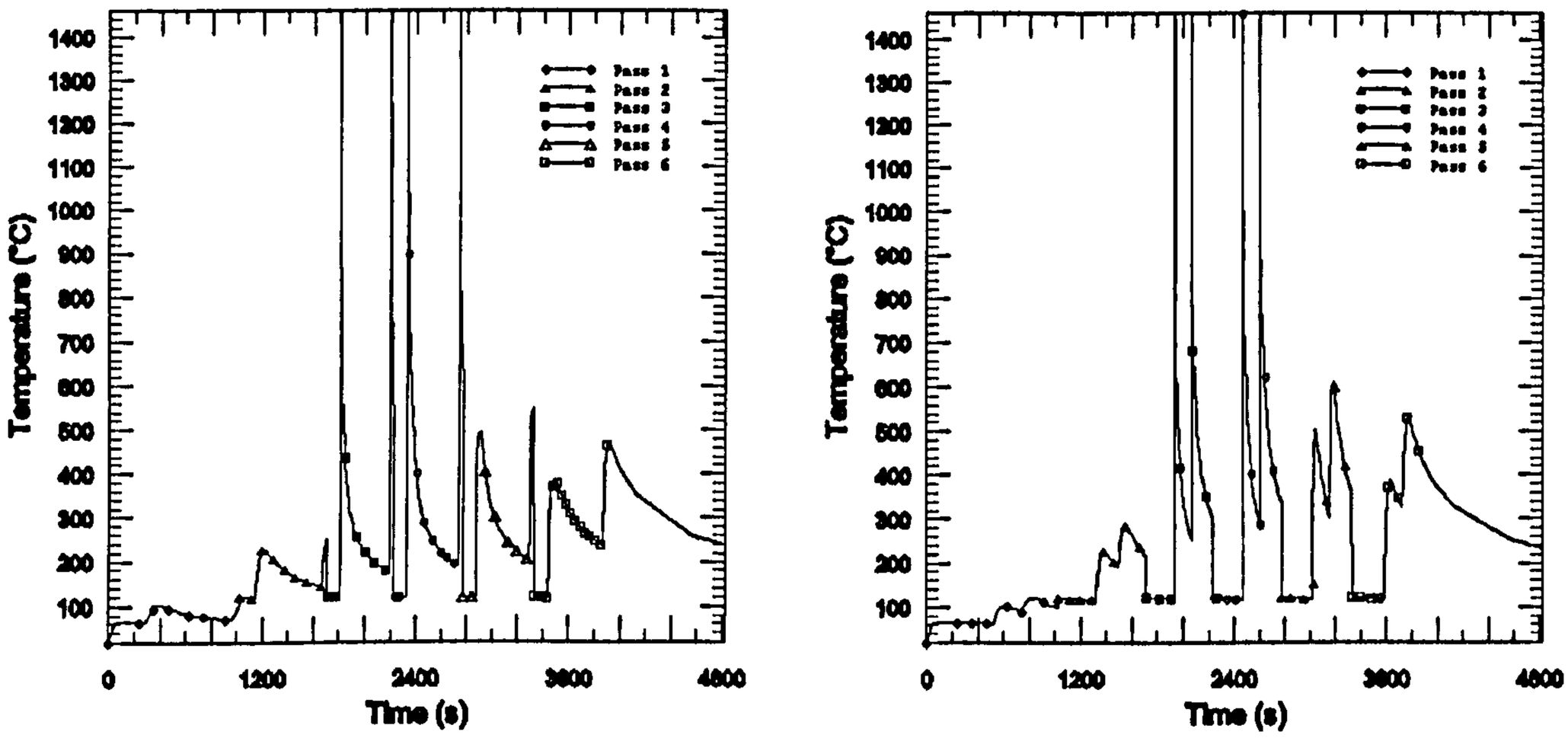

(a) (b)

Figure 6.26 Thermal cycles at (a) Point b_{12} (b) Point b_{34}

Figures 6.26(a)-(b) show the temperature cycles that Points b_{12} and b_{34} experience. A similar pattern is observed for both points. A peak temperature of 1460 °C is reached.

Point c_{12} shows a similar thermal cycle pattern to that of Point c_{34}, as shown in Figures 6.27(a)-(b), except that the time between the two peak temperatures in Figure 6.27(b) is shorter than that in Figure 6.27(a).

Since Points a_{12}, b_{12} and c_{12} show similar thermal cycles to those of their symmetrical Points a_{34}, b_{34} and c_{34}, the following section will present results at one side only.

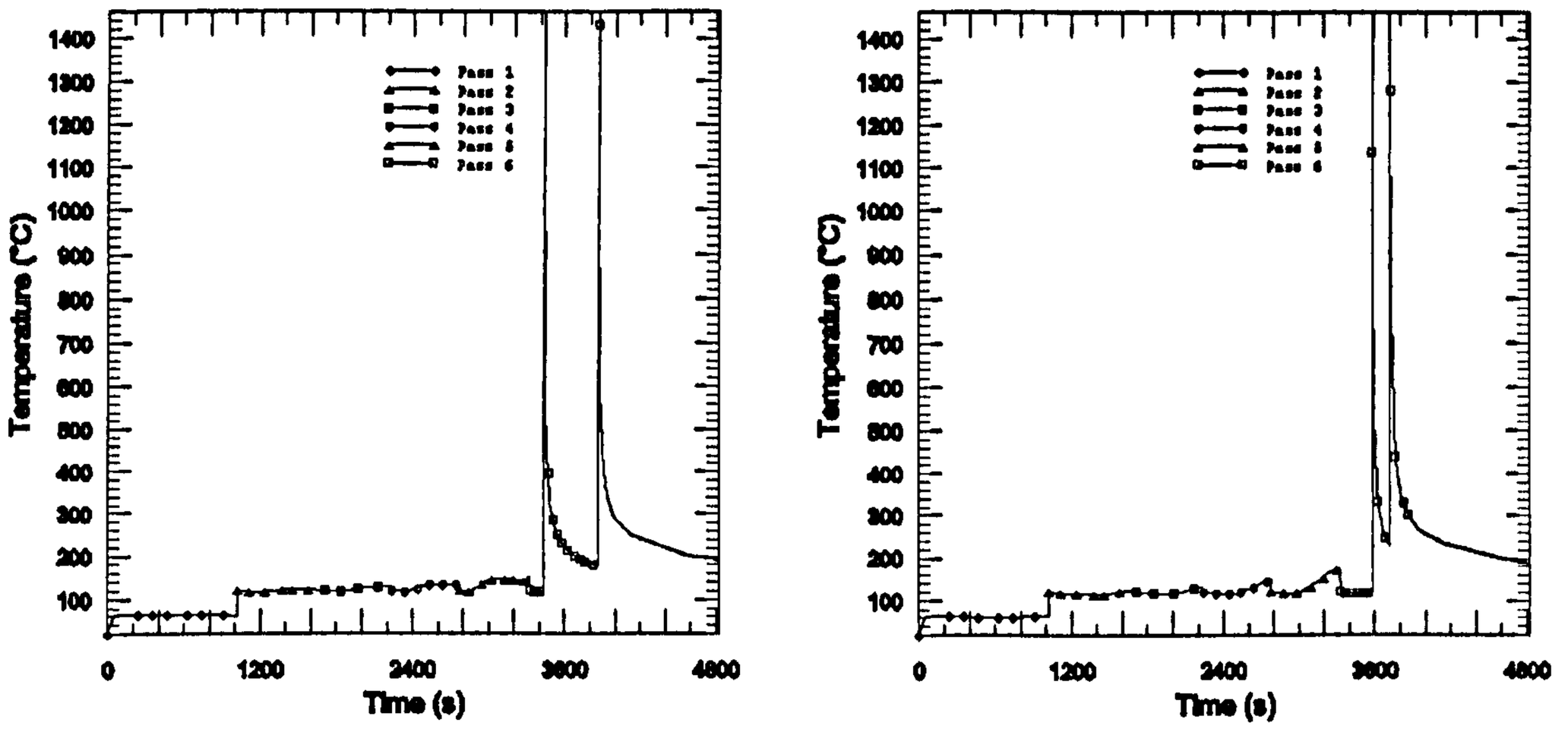

Figure 6.27 Thermal cycles at (a) Point c_{12} (b) Point c_{34}

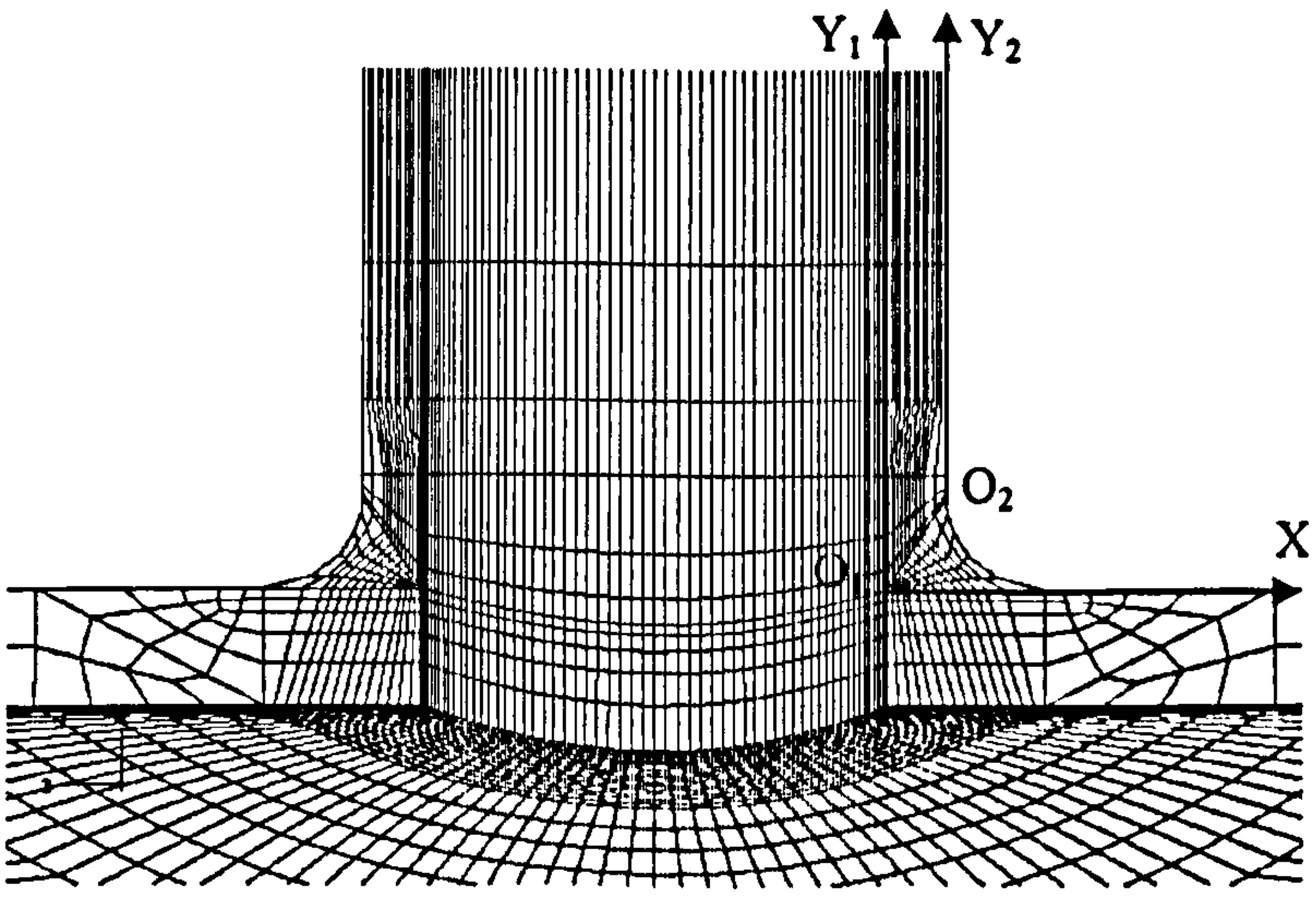

Figure 6.28 Local coordinate systems at the run cross section *b-b*

The locations of the origins and local coordinate systems at the run pipe cross section *b-b* are shown in Figure 6.28. The origins O_1 and O_2 were selected to be at the edge of the branch pipe that intersects the weld seam. The X axis locates axially along the outer surface of the run pipe, while the Y_1 and Y_2 axes locate axially along the branch inner and outer surfaces, respectively. These output locations are also indicated by thick lines in the inserted diagrams in each of the following figures.

Figure 6.29 shows temperature versus distance in the X-direction. At 1s after the deposition of the fourth sector of the first pass, the peak temperature reaches 1300°C ($0.9T_m$). High temperatures are localized within a relatively narrow area of the

deposited pass. At the end of deposition of this sector, the peak temperature decreases to 340°C ($0.23T_m$) at the origin O_1. The peak temperature is seen to reach 1420°C ($0.97T_m$) at 1s after deposition of the fourth sector of the last pass. A steep temperature gradient is noticed in front of the deposited pass. At the end of deposition of this sector, heat is noted to conduct to the previously deposited passes. A relatively uniform temperature of 400°C ($0.27T_m$) is noticed between 50 and 100mm.

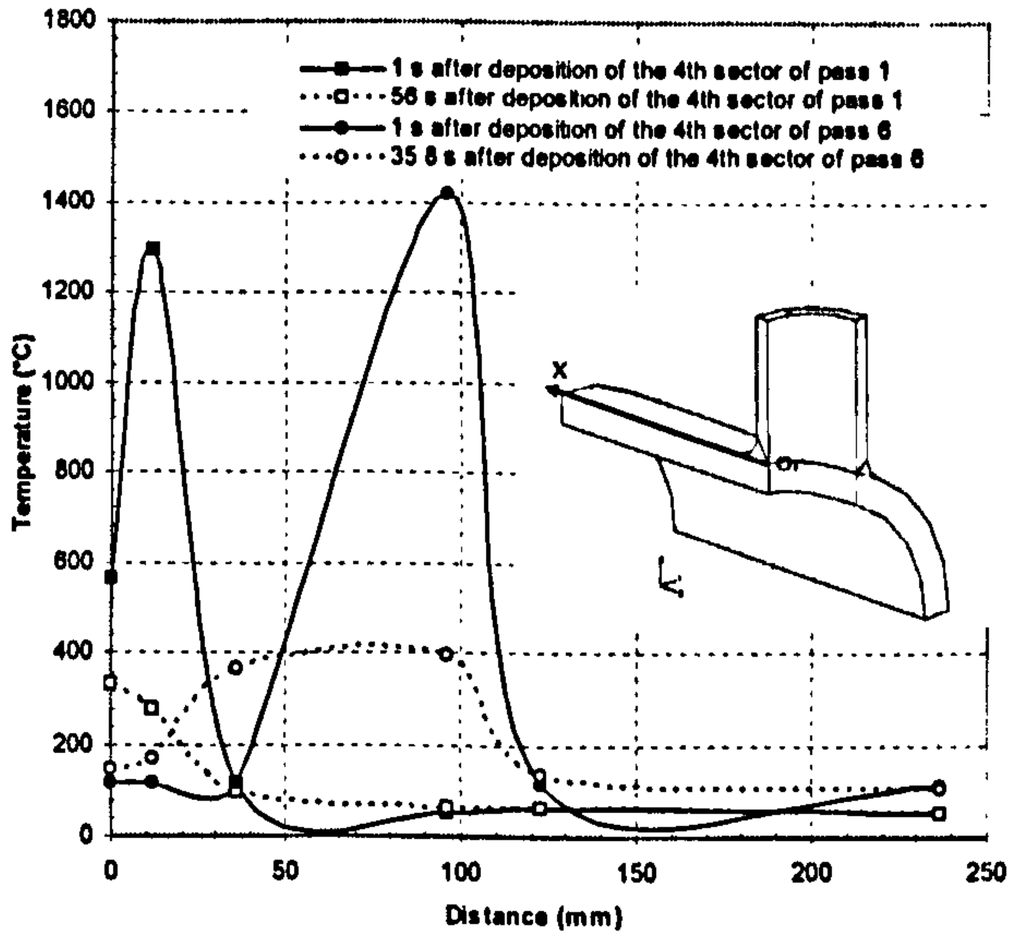

Figure 6.29 Temperatures in the X-direction on the run pipe outer surface

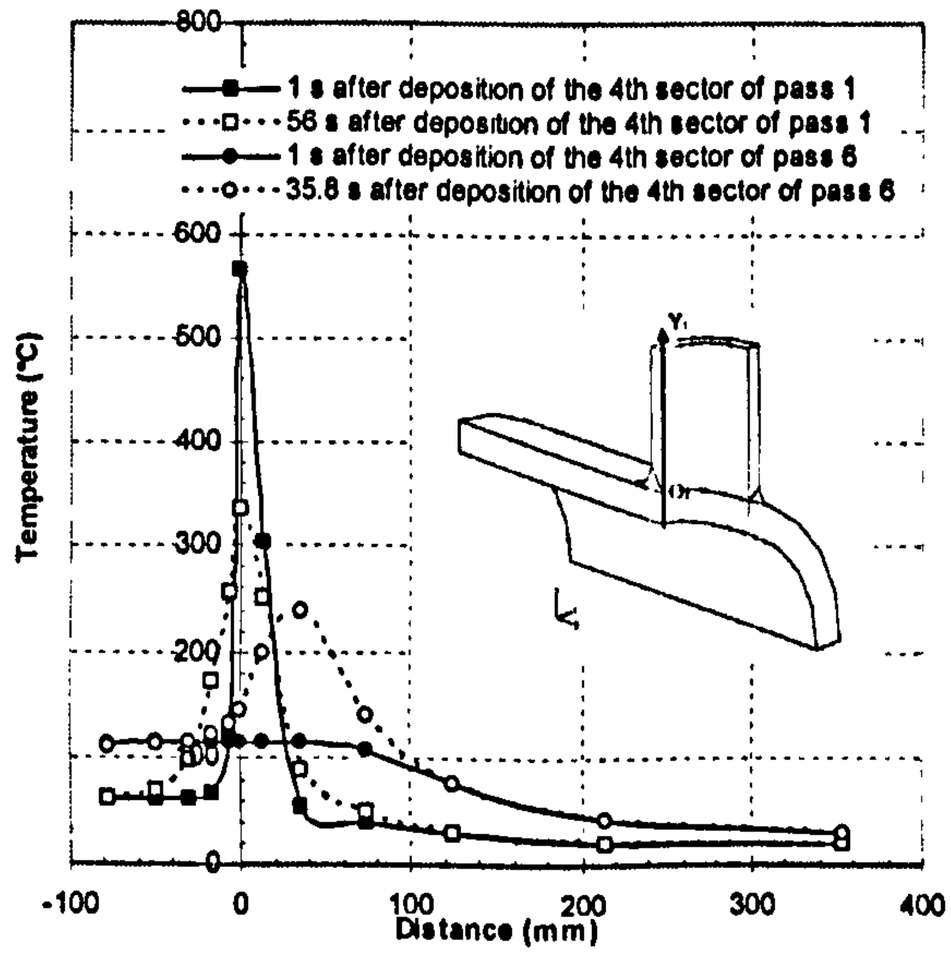

Figure 6.30 Temperatures in the Y_1-direction on the branch inner surface

Figure 6.30 shows temperature distributions along Y_1-direction. The origin O_1 reaches a peak temperature of 570°C ($0.39T_m$) at 1s after deposition of the fourth sector of the first pass. As the last pass is at some distance away from the inner surface, it

appears to have less effect on the temperature changes on the inner surface at the moment of deposition.

Combined with the observation from Figure 6.22, it could be concluded that the thermal cycles generated on the inner surface of the branch pipe are mainly caused by the first few passes. The effects of the higher numbered passes are quite small at the moment of deposition. Their effects on the branch inner surface are primarily due to heat conduction after deposition.

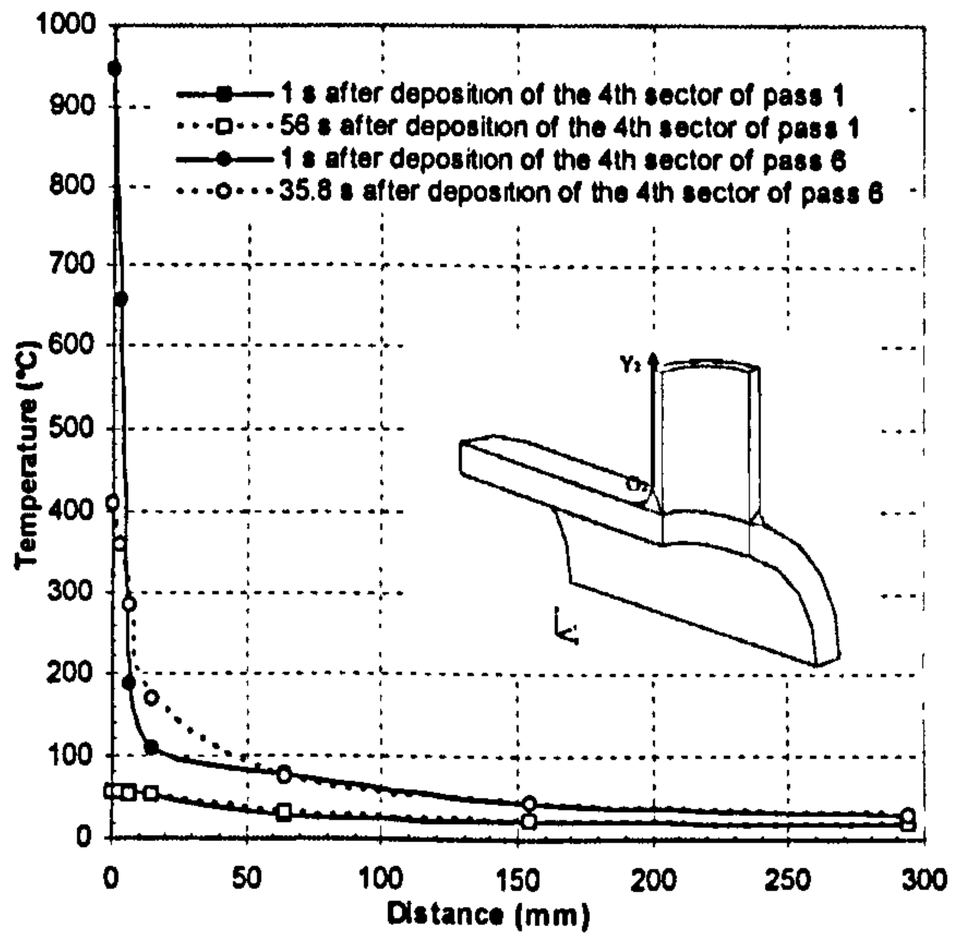

Figure 6.31 Temperatures in the Y_2-direction on the branch outer surface

Temperature distributions along Y_2-direction are shown in Figure 6.31. At 1s after deposition of the fourth sector of the last pass, the peak temperature reaches 950°C ($0.65T_m$), then decreases to 410°C ($0.28T_m$) at the end of deposition of this sector. The first pass has negligible effects on the temperature distributions on the branch outer surface.

In view of the above remarks, together with observations from Figure 6.23, it could be concluded that the thermal cycling on the outer surface of the branch pipe is mainly caused by the last few passes. Based on this, it could be further concluded that the lower numbered passes have a negligible effect on the temperature distribution along the circumferential fusion line on the outer surface of both run and branch pipes (i.e. Curves *A* and *B*).

6.3.2.3.3 Circumferentially along Curve *A*

Figures 6.32 to 6.36 show temperature distributions along Curves *A*, *B* and *C* during deposition of the selected passes. In these figures, angular positions are measured anticlockwise from the welding start point at the flank centre between Quadrants *I* and *IV*. Times, listed in the figures, are counted from the start of each pass. As the lower numbered pass does not appear to affect much the temperature distributions along Curves *A* and *B*, as discussed in the previous sections, the temperature distributions along them are only presented during welding of the last pass.

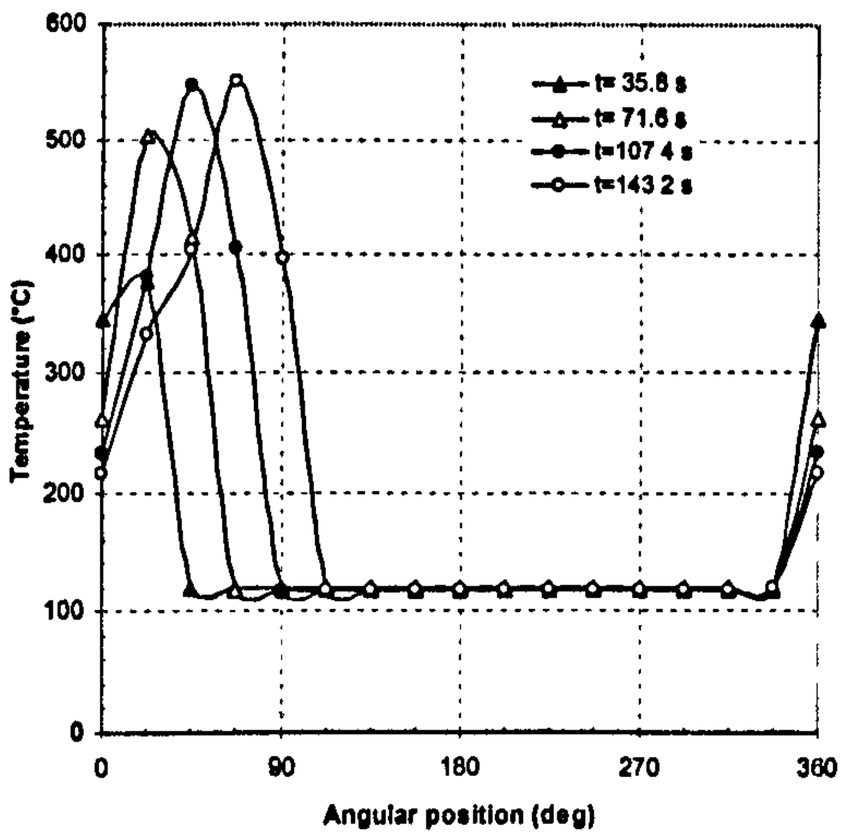

(a) Welding Quadrant *I*

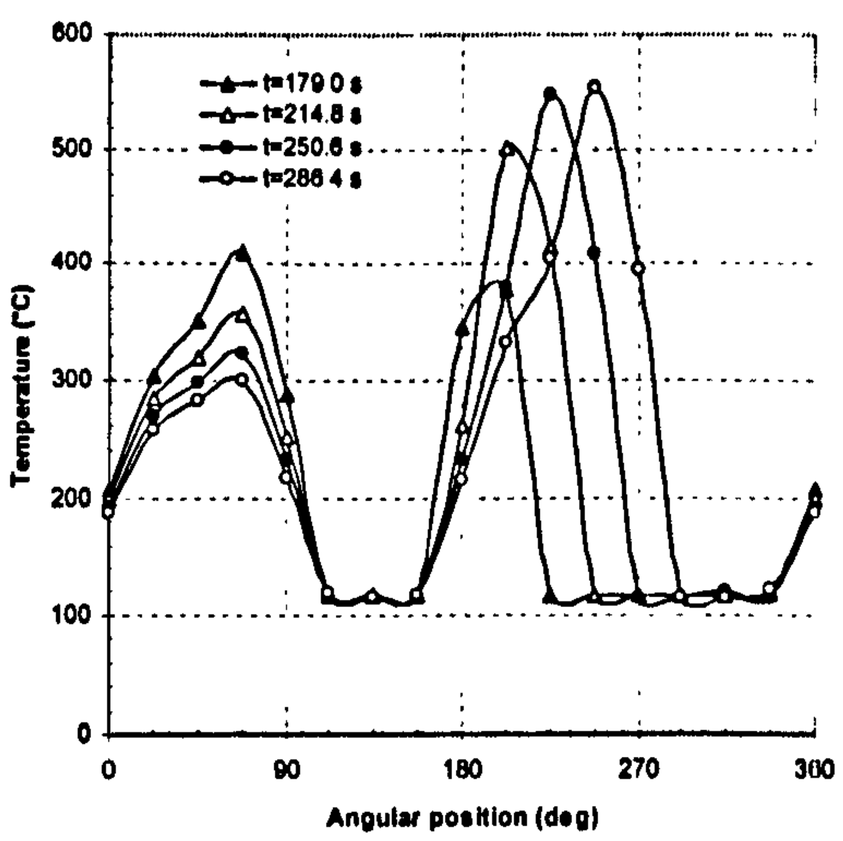

(b) Welding Quadrant *III*

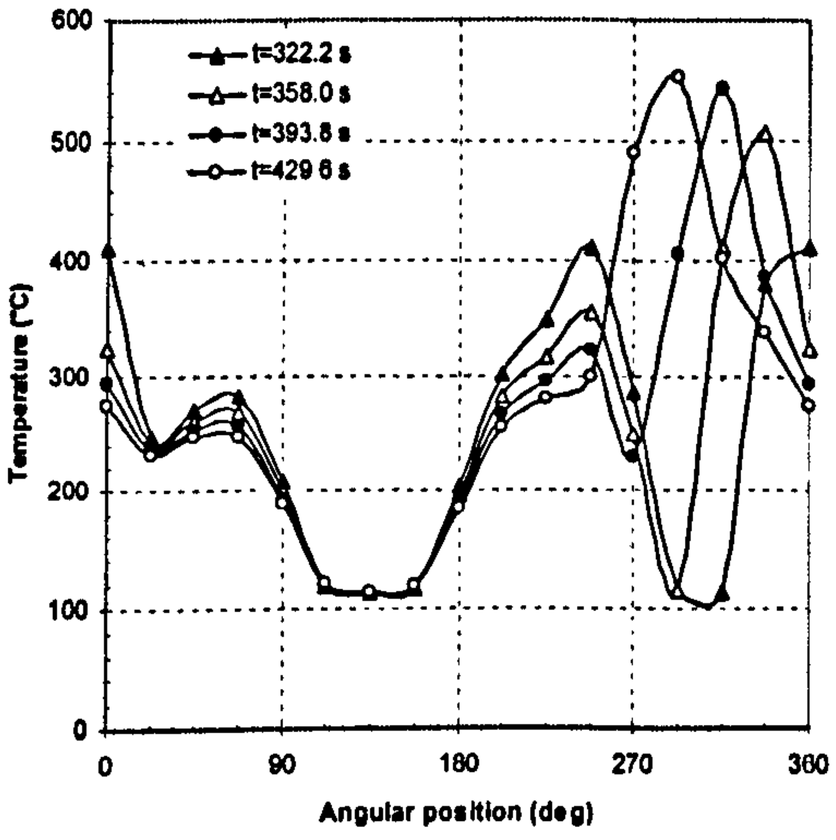

(c) Welding Quadrant *IV*

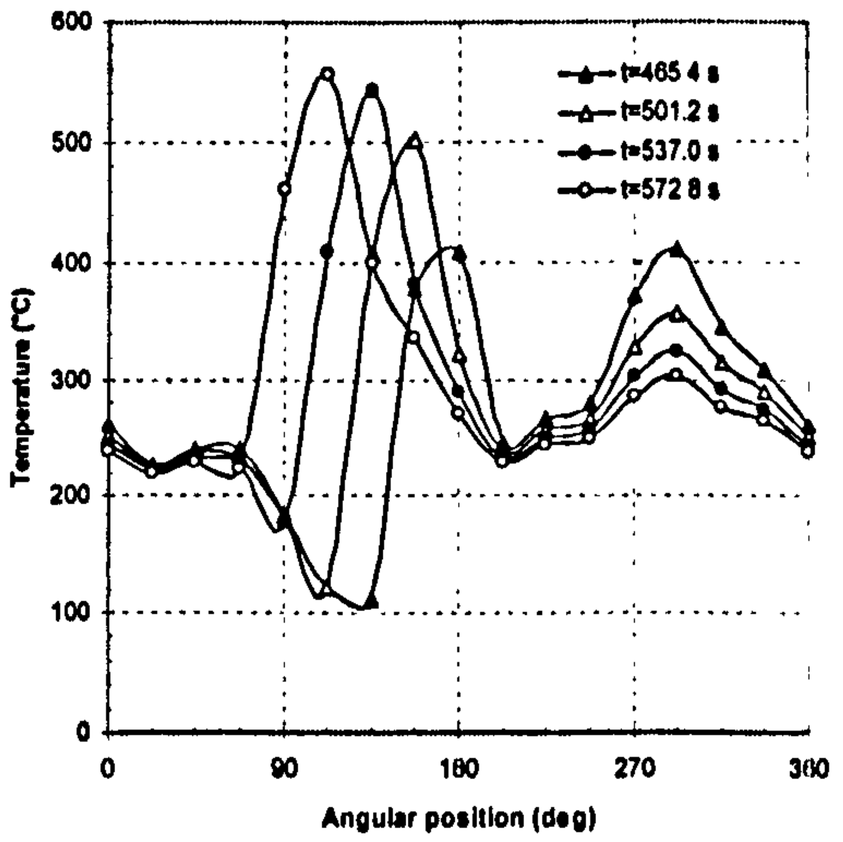

(d) Welding Quadrant *II*

Figure 6.32 Temperature distributions along Curve *A* at the end of deposition of each sector of the sixth pass

It can be seen from Figure 6.32(a) that at the end of deposition of the first sector, i.e. at t=35.8s, a peak temperature of 380°C ($0.26T_m$) is reached within the deposited sector. The remaining regions of the circumference are at the interpass temperature of

120°C. As the heat source moves towards the second sector, this sector reaches a peak temperature of 500°C ($0.34T_m$) while the first sector cools down to 250°C ($0.17T_m$). Similar temperature distributions appear while welding the subsequent sectors, except that the peak temperature gradually increases to 550°C ($0.38T_m$).

As the heat source moves between 180° and 270°, similar temperature patterns appear in Quadrant *III*. At the same time, Quadrant *I* is seen to cool down gradually. The quadrants that have not been welded yet remain at the interpass temperature, as shown in Figure 6.32(b). When welding proceeds to Quadrants *IV* and *II*, high temperatures concentrate in these two quadrants. As expected, the temperatures in the previously welded regions gradually cool down. Overall, the temperature distribution is quite uneven as the heat source moves along Curve *A*.

6.3.2.3.4 Circumferentially along Curve *B*

Similar temperature patterns to those of Curve *A* can be noticed along Curve *B* while welding the sixth pass, as shown in Figure 6.33. The only difference is that the peak temperature increases to about 700°C ($0.48T_m$) after the deposition of the second sector in each quadrant. This is because, at the 'saddle like' intersection, the distance between Curve *B* and the centre of the deposited second sector is smaller than those of the third and fourth sectors; while the heat input of the second sector, which relates to the deposited volume, is relatively larger compared to that of the first sector.

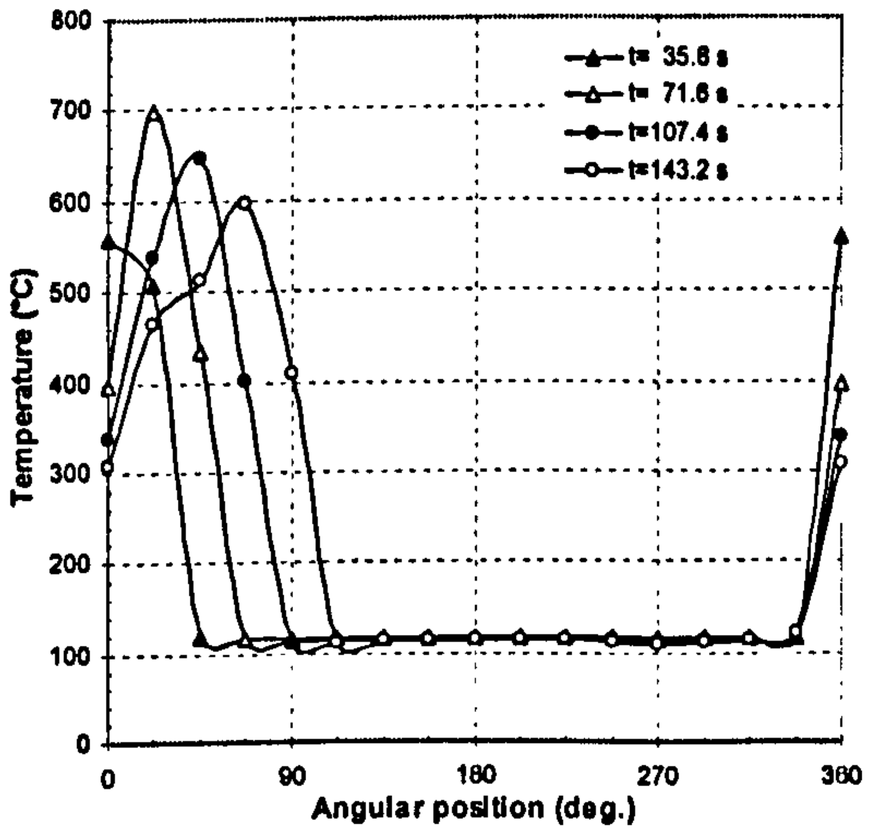

(a) Welding Quadrant *I*

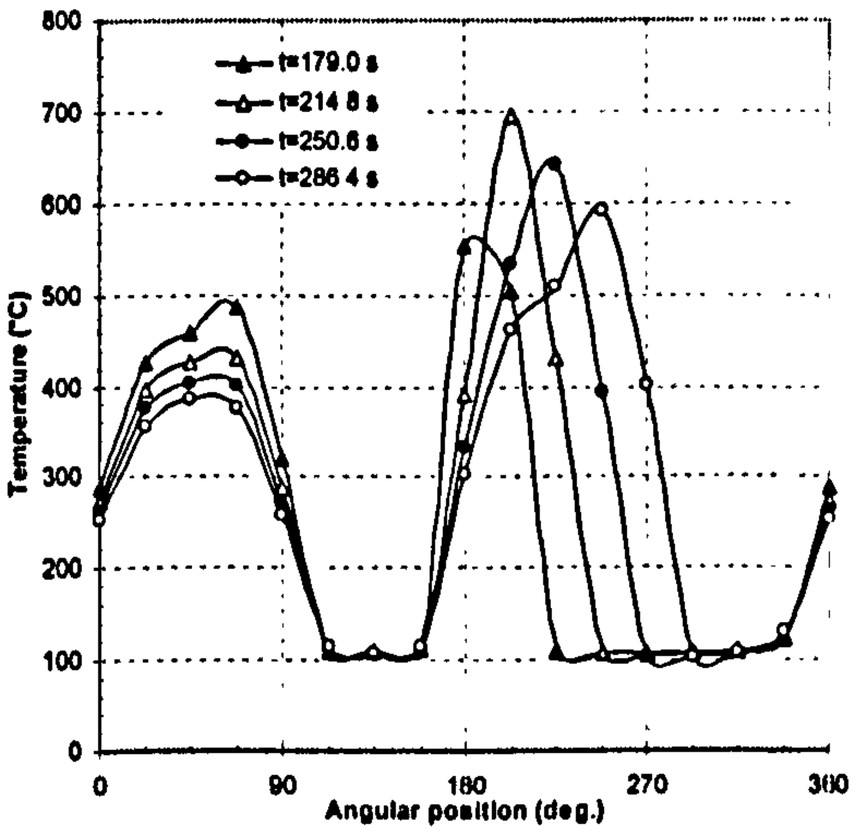

(b) Welding Quadrant *III*

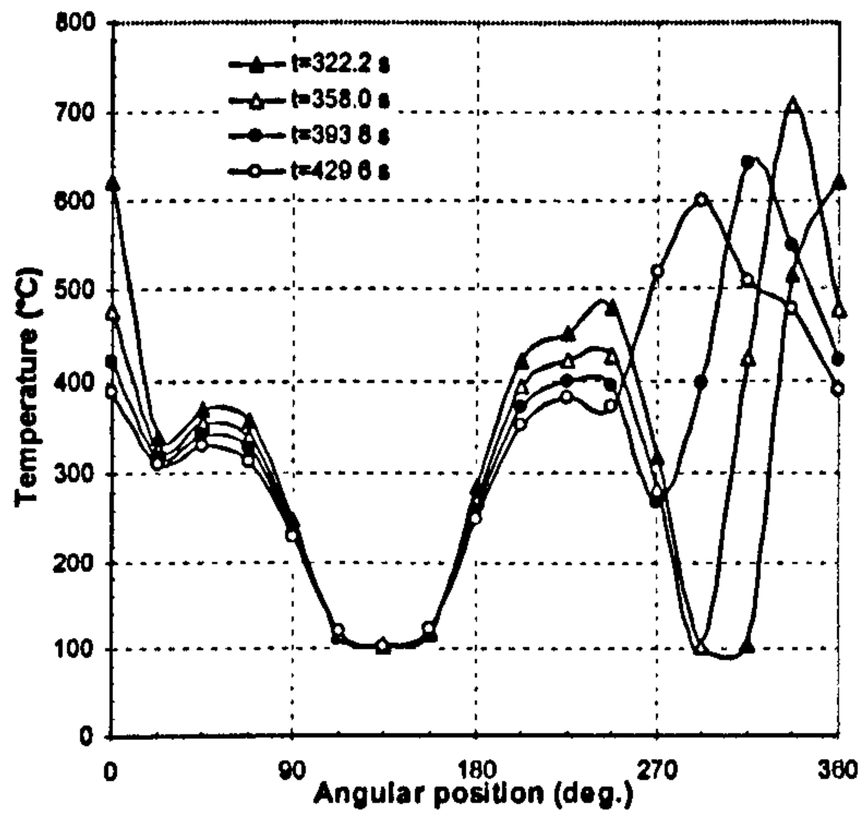

(c) Welding Quadrant *IV*

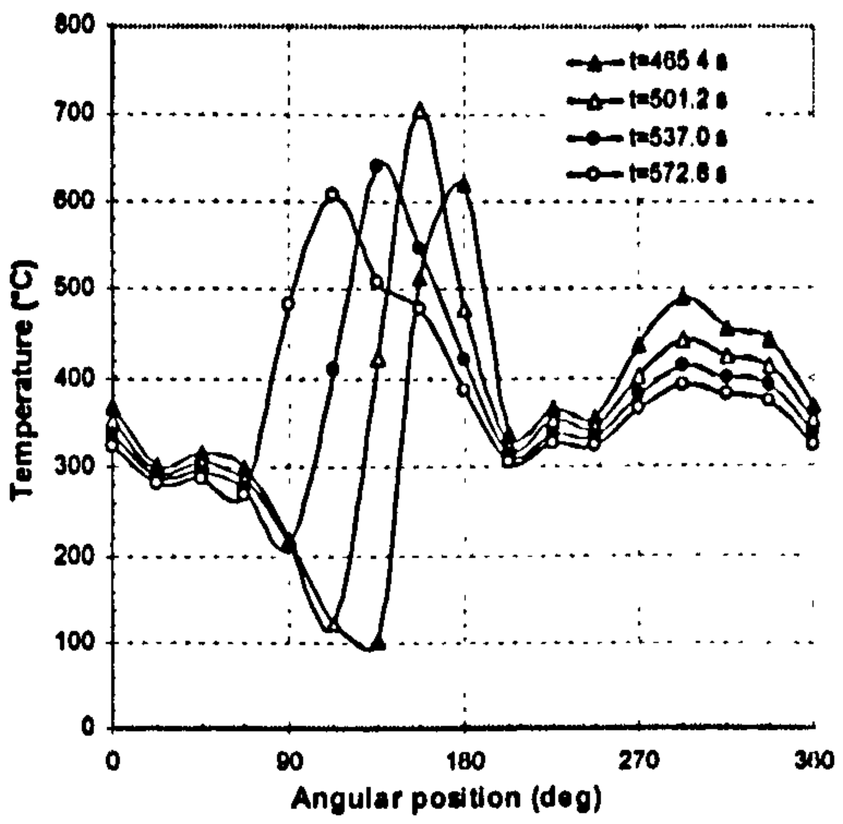

(d) Welding Quadrant *II*

Figure 6.33 Temperature distributions along Curve *B* at the end of deposition of each sector of the sixth pass

6.3.2.3.5 Circumferentially along Curve *C*

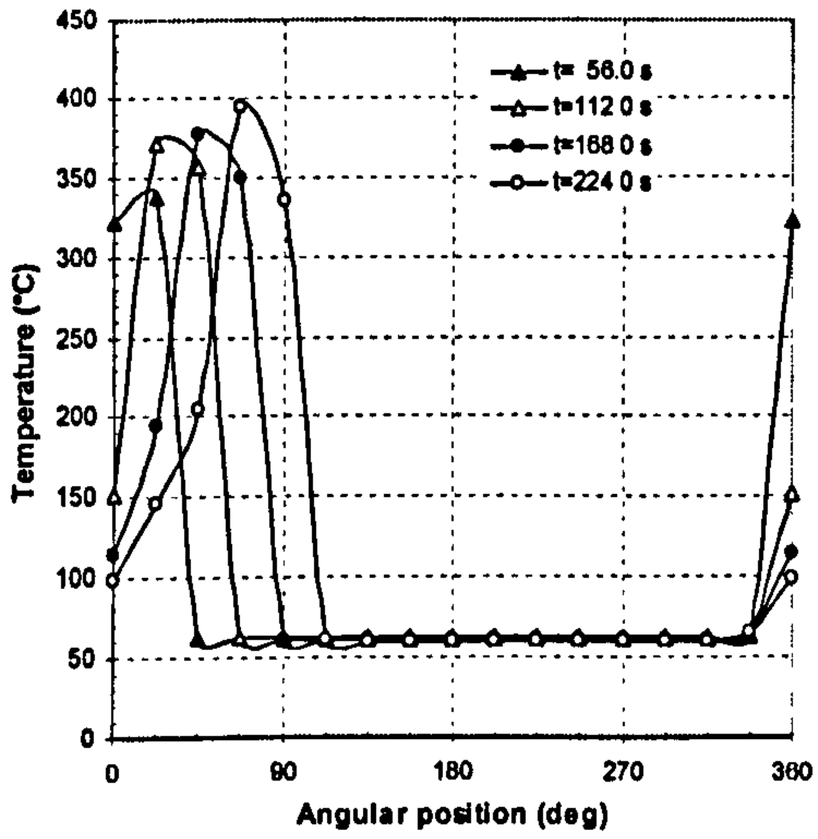

(a) Welding Quadrant *I*

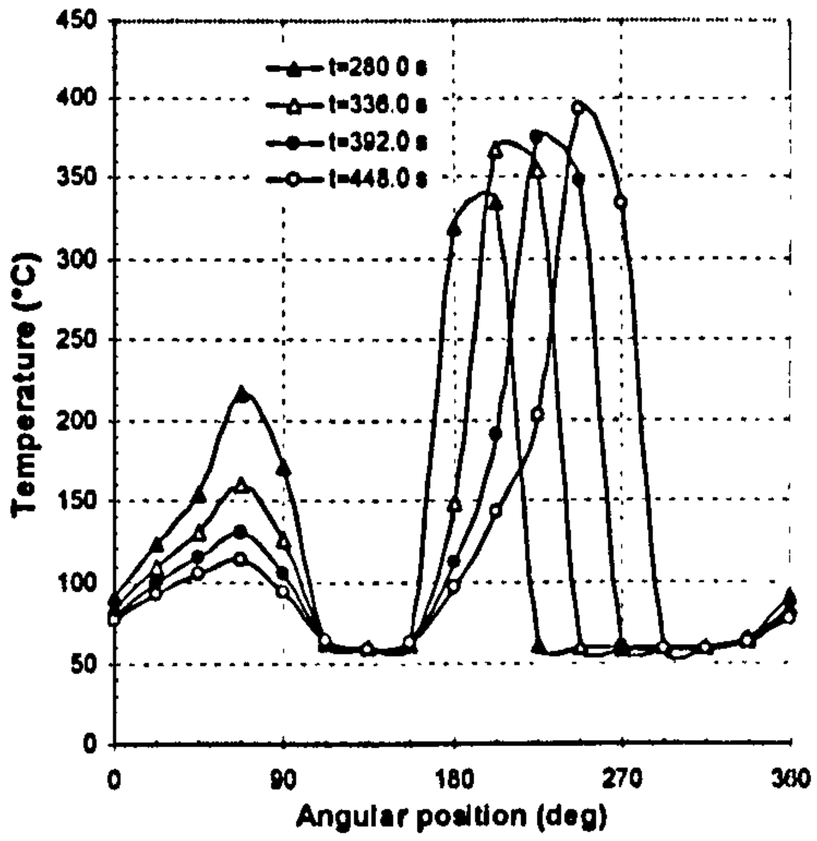

(b) Welding Quadrant *III*

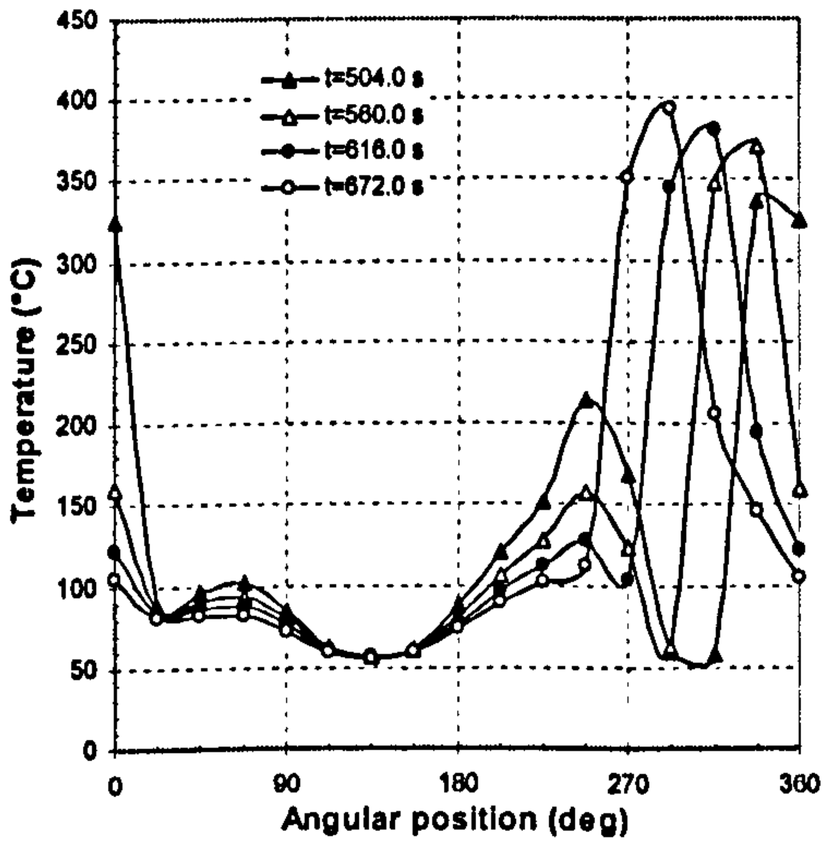

(c) Welding Quadrant *IV*

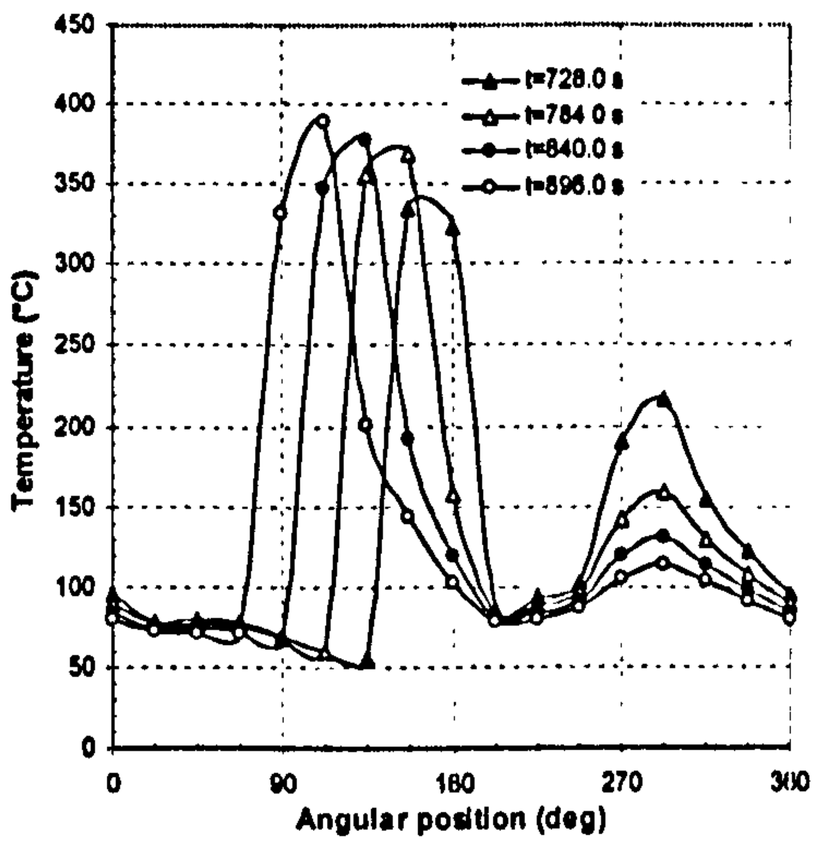

(d) Welding Quadrant *II*

Figure 6.34 Temperature distributions along Curve *C* at the end of deposition of each sector of the first pass

Figure 6.34(a) shows temperature distributions along Curve *C* while welding Quadrant *I* in the first pass. After the deposition of the first sector, the peak temperature in this sector is 340°C ($0.23T_m$). The remaining areas along Curve *C* stay at the preheating temperature of 65°C. The peak temperature increases to 400°C ($0.27T_m$) within the fourth sector when welding this sector, while the temperature in the first sector decreases to 100-150°C. Similar temperature distribution patterns to those in Quadrant *I* in Figure 6.34(a) are noticed as welding proceeds to Quadrants *III*, *IV* and *II*, as shown in Figures 6.34(b)-(d). The temperatures in the previously welded quadrants gradually cool down.

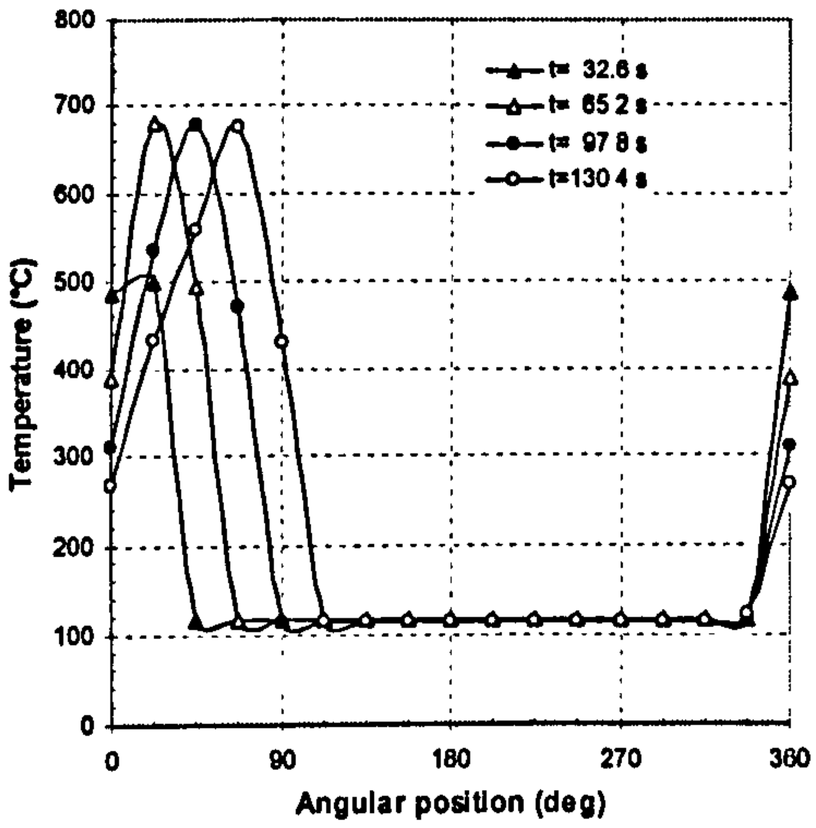

(a) Welding Quadrant *I*

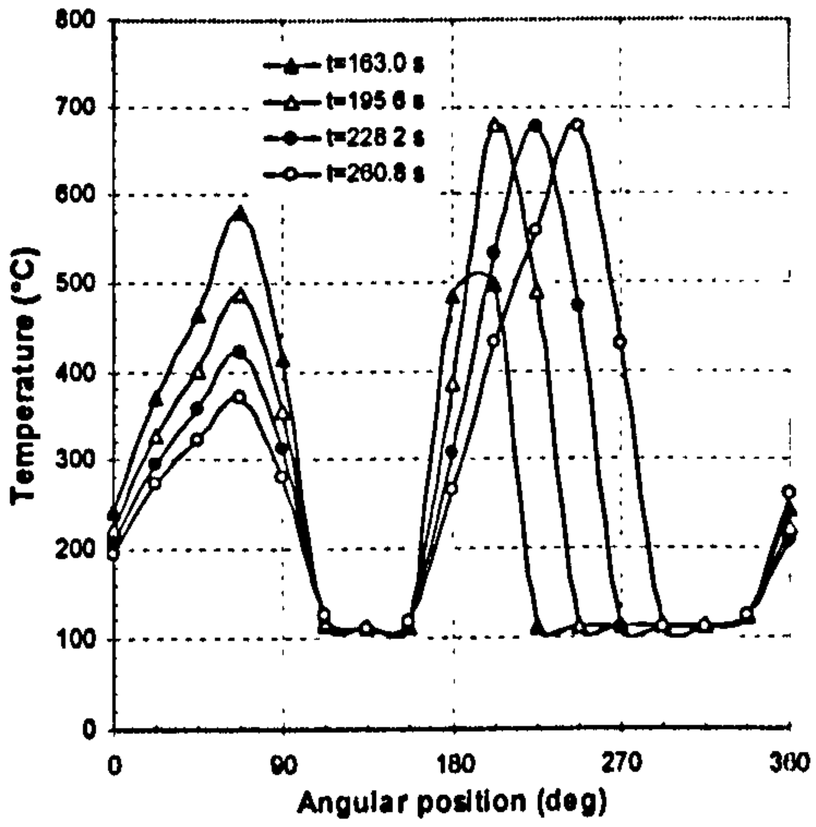

(b) Welding Quadrant *III*

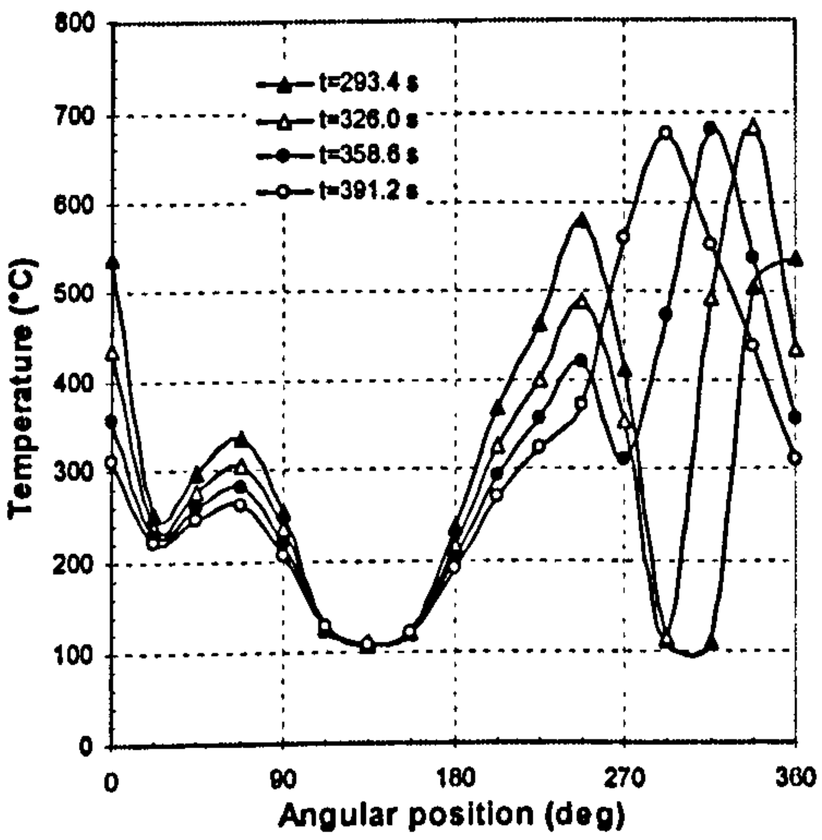

(c) Welding Quadrant *IV*

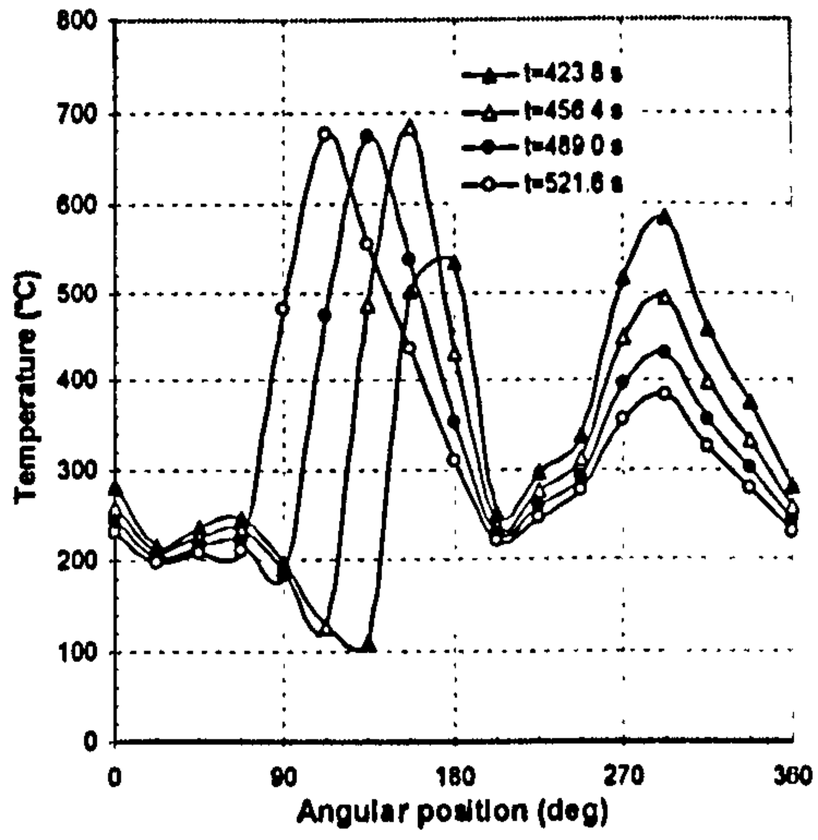

(d) Welding Quadrant *II*

Figure 6.35 Temperature distributions along Curve *C* at the end of deposition of each sector of the third pass

Figure 6.35(a) shows that the peak temperature after the deposition of the first sector of the third pass is about 500°C ($0.34T_m$), and increases to 680°C ($0.47T_m$) while welding the next sectors. Between the angular span of 112° and 338°, the temperatures

along Curve *C* remain at the interpass temperature. Similar temperature distribution patterns are observed for Quadrants *III*, *IV* and *II* as welding proceeds in these quadrants. The temperatures in the previously deposited sectors are seen to decrease, as shown in Figures 6.35(b)-(d).

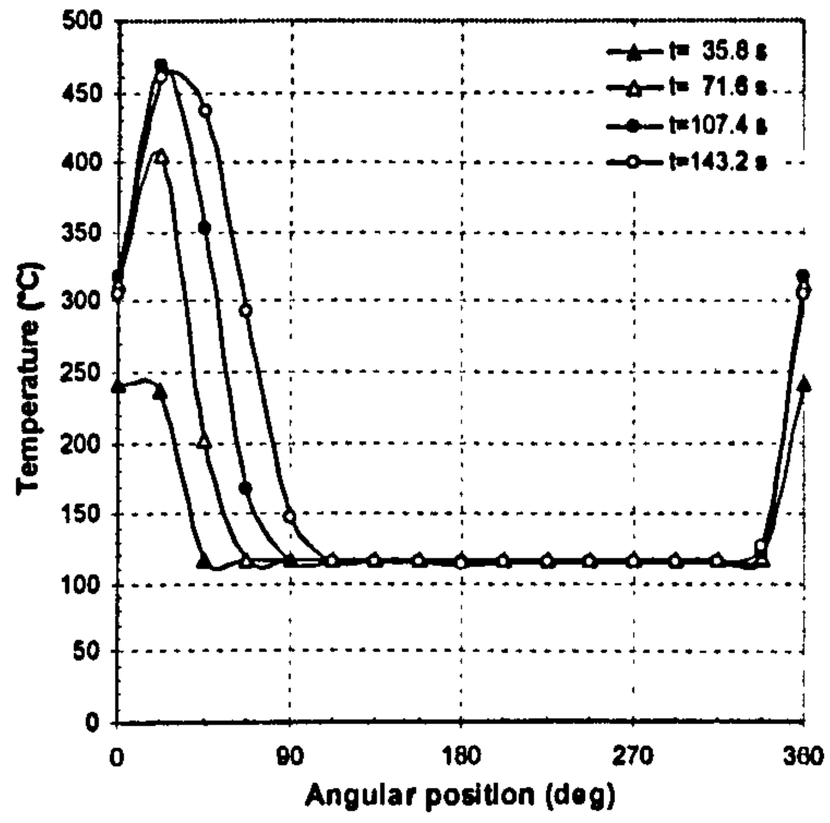

(a) Welding Quadrant *I*

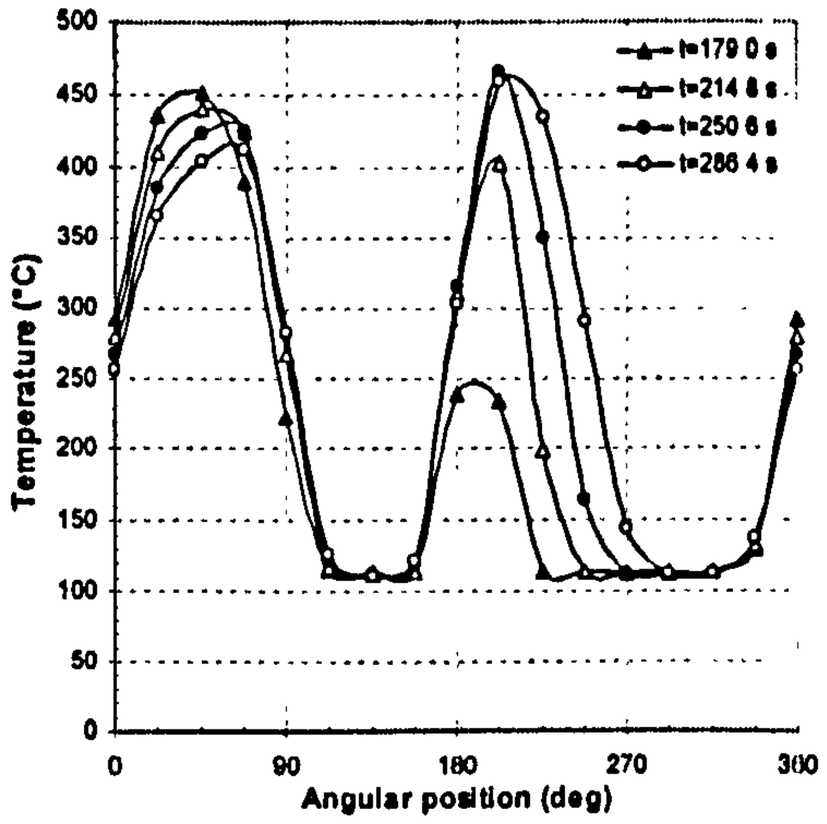

(b) Welding Quadrant *III*

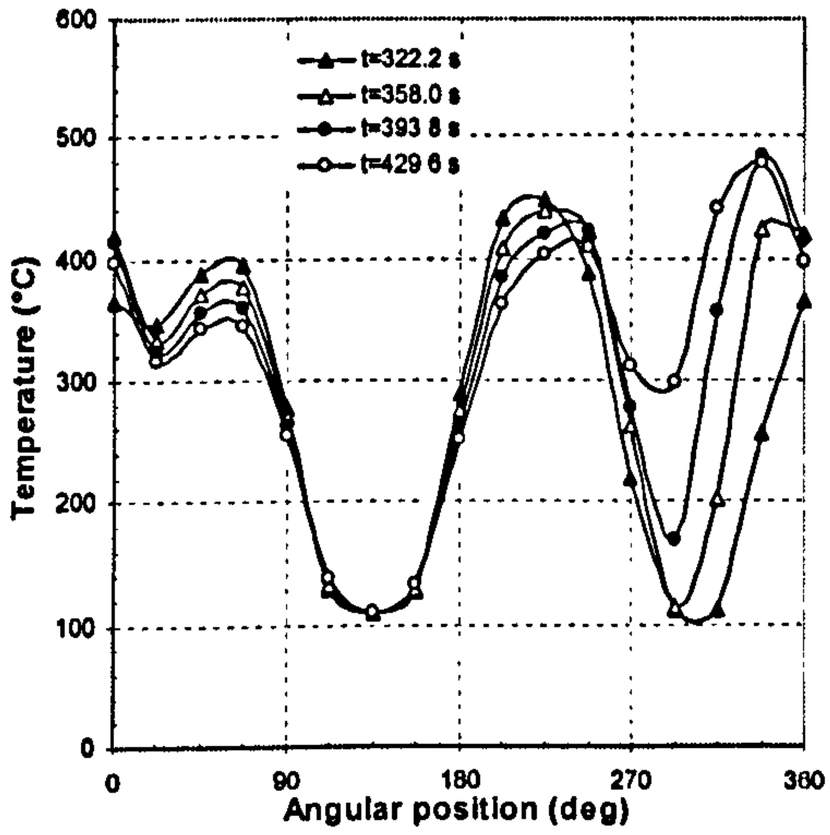

(c) Welding Quadrant *IV*

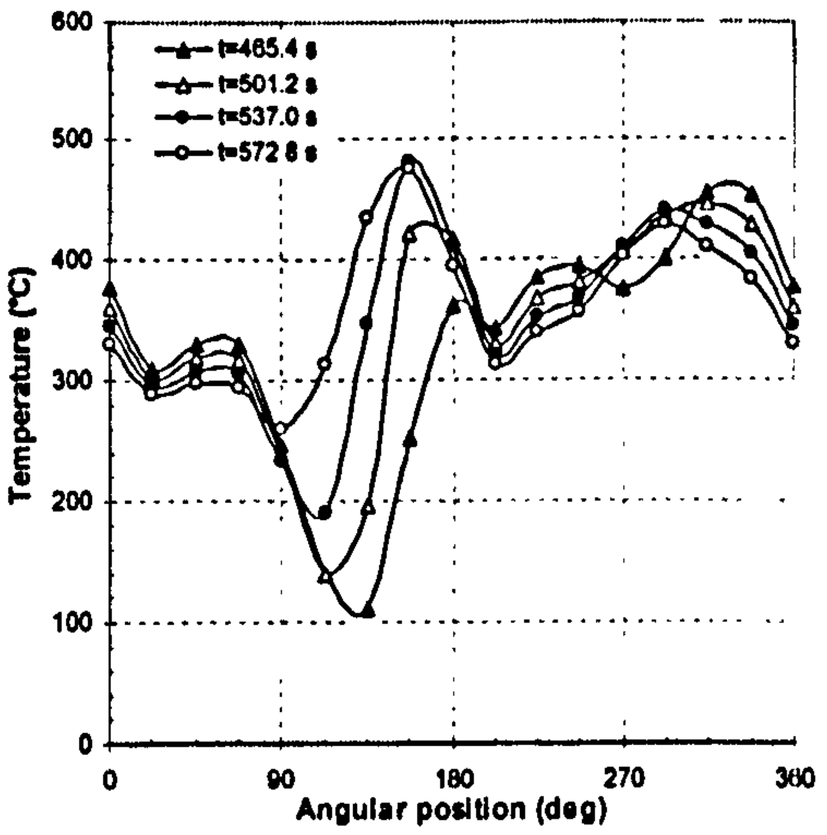

(d) Welding Quadrant *II*

Figure 6.36 Temperature distributions along Curve *C* at the end of deposition of each sector of the sixth pass

Figure 6.36 shows temperature distributions along Curve *C* at the end of deposition of each sector during welding of the last pass. As the last pass is at some distance away from the inner surface, it does not have much effect on the peak temperatures along Curve *C*. The peak temperature, in this case, is under 500°C ($0.34T_m$), compared with those of about 700°C ($0.48T_m$) during welding of the third pass. It is also noticed that the previously deposited quadrants do not cool down as rapidly as those happen when welding lower numbered passes. The temperatures along Curve *C* after welding of the last pass tend to be uniform, varying from 260°C to 480°C ($0.18\text{-}0.33T_m$).

6.3.3 Transient and residual stress fields

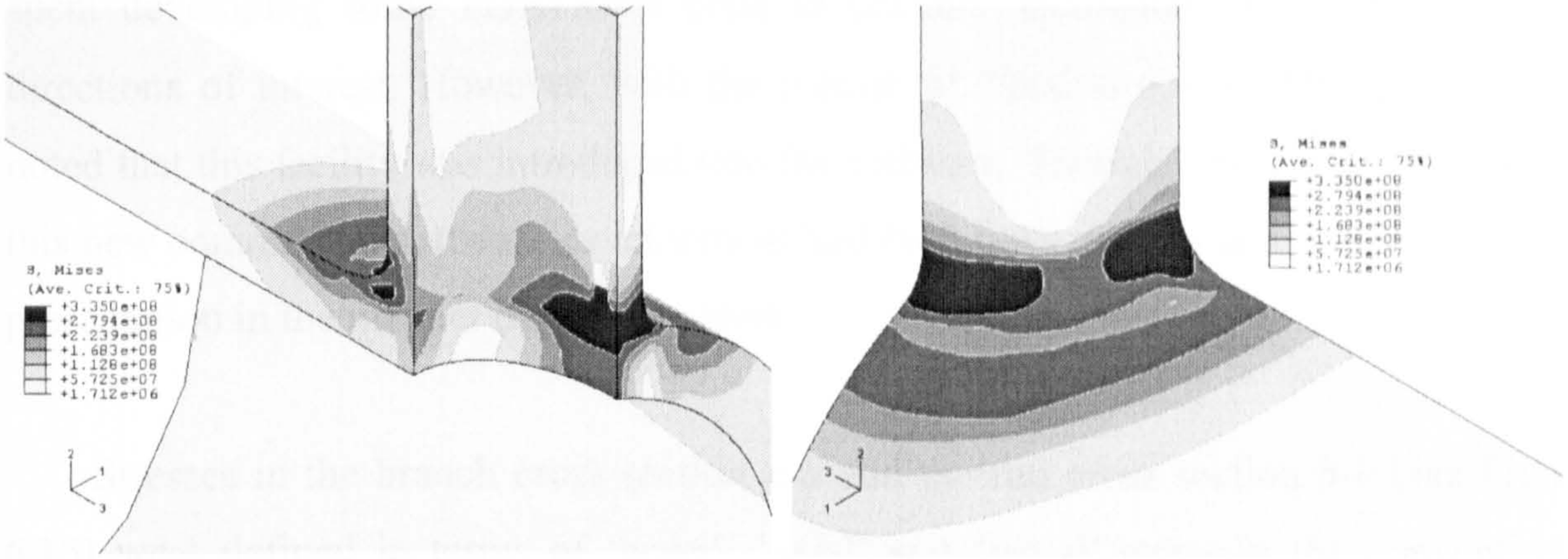

(a) Inside (b) Outside

Figure 6.37 Residual stress distribution contour plots

Figure 6.37 gives overall contour plots of residual stress distributions in Quarter *I* of the tee branch junction. From these figures, it is noticed that high von Mises stress locates in the areas of the crotch corner, flank centre and along the weld seam. From this brief observation, it is decided that stresses in the areas of the branch cross section *a-a*, run cross section *b-b*, Curves *A*, *B* and *C* are of major concern (see Figure 6.15).

6.3.3.1 Stress directions

Unlike simple geometries such as plates and pipes, stress directions in the region of interest of the tee branch junction are quite complicated to define, as stresses at different locations follow different definitions.

When using commercial software, stresses are normally output in the default global Cartesian coordinate system. For uniform geometries, facilities such as *TRANSFORM or *ORIENTATION in ABAQUS can be used to output meaningful data that can be easily interpreted by the analyst. However, for the junction under consideration, neither stress output in the usual coordinate system nor globally transformed stresses are of any use. At the saddle-like juncture, the stress directions of interest continuously change as we move along the weldline. From a practical standpoint, it is argued that the stress directions of most interest to the structural integrity analyst are those that are 'normal'

and 'tangential' to the weld. When tensile, the former has the potential to open crack-like defects if they develop (Fracture Mechanics mode I) while the latter causes a mode II type of concern. In view of the above consideration, some initial effort was spent developing some FORTRAN code to convert 'elemental' stress output to the directions of interest. However, with the release of Version 6.4 of ABAQUS, it was noted that this facility was introduced into the software. Though time consuming to use, this new commercial software development had facilitated matters and permitted results presentation in the manner described below.

Stresses in the branch cross section *a-a* and the run cross section *b-b* (see Figure 6.15) were defined in terms of 'hoop', 'axial' and 'radial' stress in the conventional sense and defined with respect to either the run or branch pipe, depending on the location of interest. However, stresses along the three fusion lines on the outer surface of the run and branch pipe and on the inner surface, i.e. Curves *A*, *B* and *C*, were defined as normal and tangential to the fusion weldline. Stress parallel to the direction of the weldline is called tangential stress, while stress normal to the direction of the weldline is known as a normal stress.

To obtain stresses locally normal to the above weldline, a series of local coordinate systems on the selected points along the weld path have to be defined. There are three points used to define a local coordinate system, as shown in Figures 6.38 to 6.40. Two subsequent points on the weld path defines the welding direction *X*, which is always parallel to the weld. The direction *Y*, which is normal to the weldline, is defined by a point on the run or branch pipe surface and the base point on the weld path. By taking the cross product of the two vectors of *X* and *Y*, a third direction *Z* can be defined. With such definition, ABAQUS transforms stresses from a global coordinate system to these user-defined local coordinate systems mapping the weld path. These local coordinate systems can move with specified points as the model deforms.

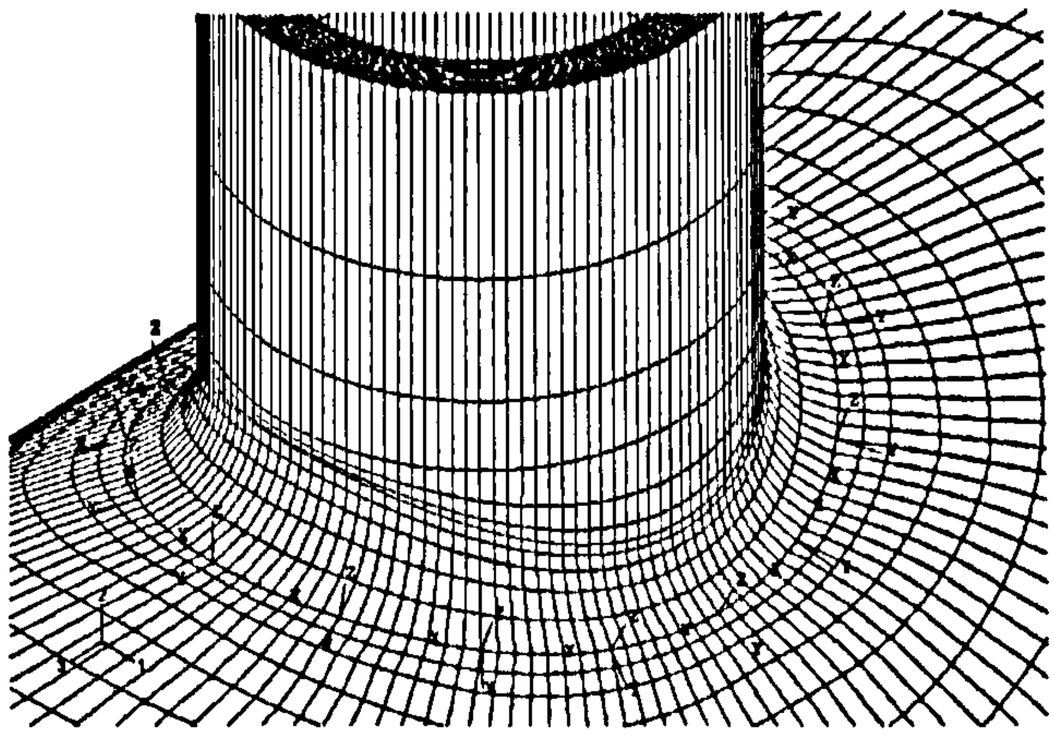

Figure 6.38 Local coordinate systems along Curve *A*

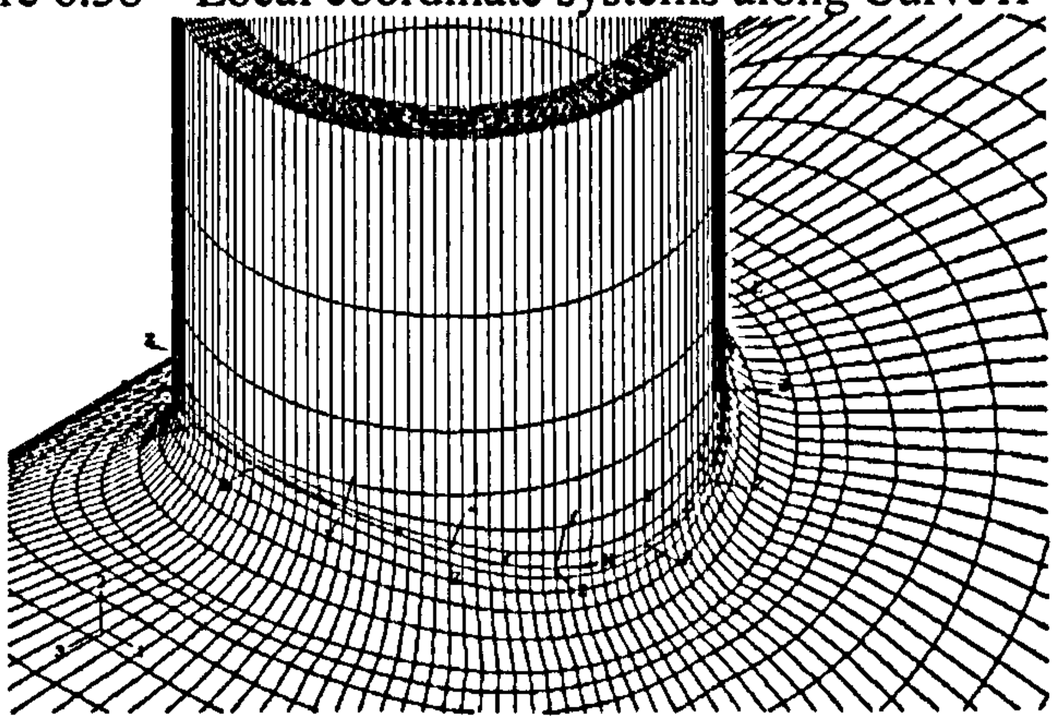

Figure 6.39 Local coordinate systems along Curve *B*

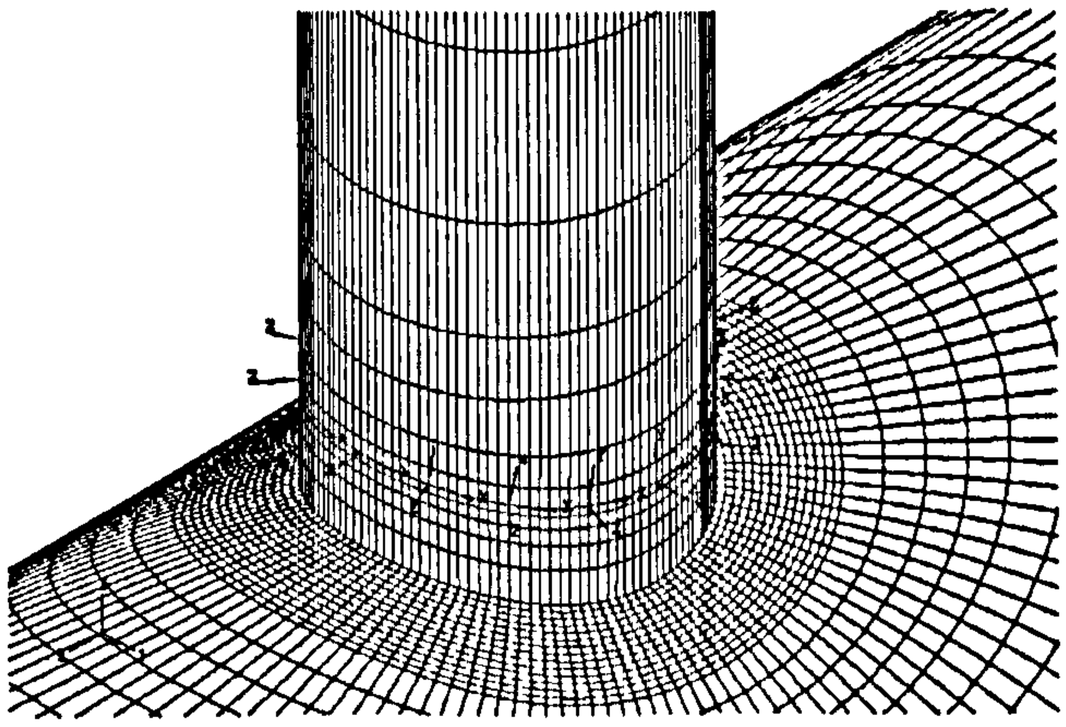

(a) Viewed with only inner surface depicted

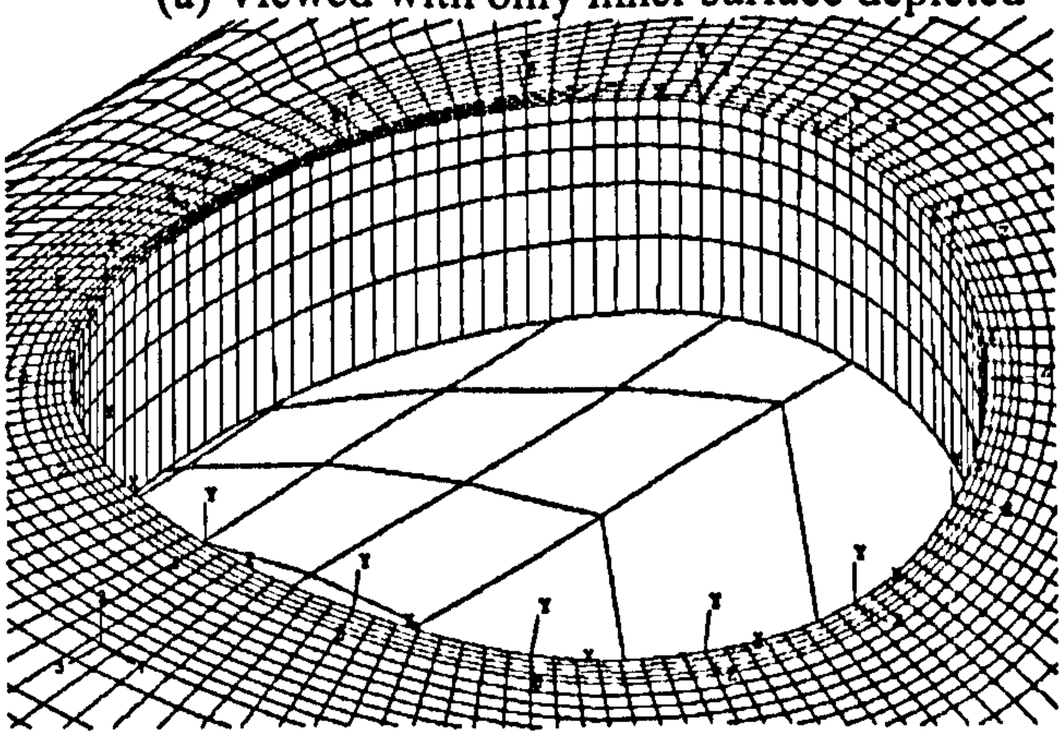

(b) Viewed without branch pipe

Figure 6.40 Local coordinate systems along Curve *C*

6.3.3.2 Branch cross section *a-a*

Stresses at the branch cross section *a-a* are defined in the conventional sense with respect to either the run or branch pipe. For the stresses on the run pipe outer surface, they are defined as S_{11} the radial stress, S_{22} the hoop stress and S_{33} the axial stress. While for the stresses on the branch pipe, e.g. in Y_1- and Y_2-direction, the stresses are defined as S_{11} the radial stress, S_{22} the axial stress and S_{33} the hoop stress.

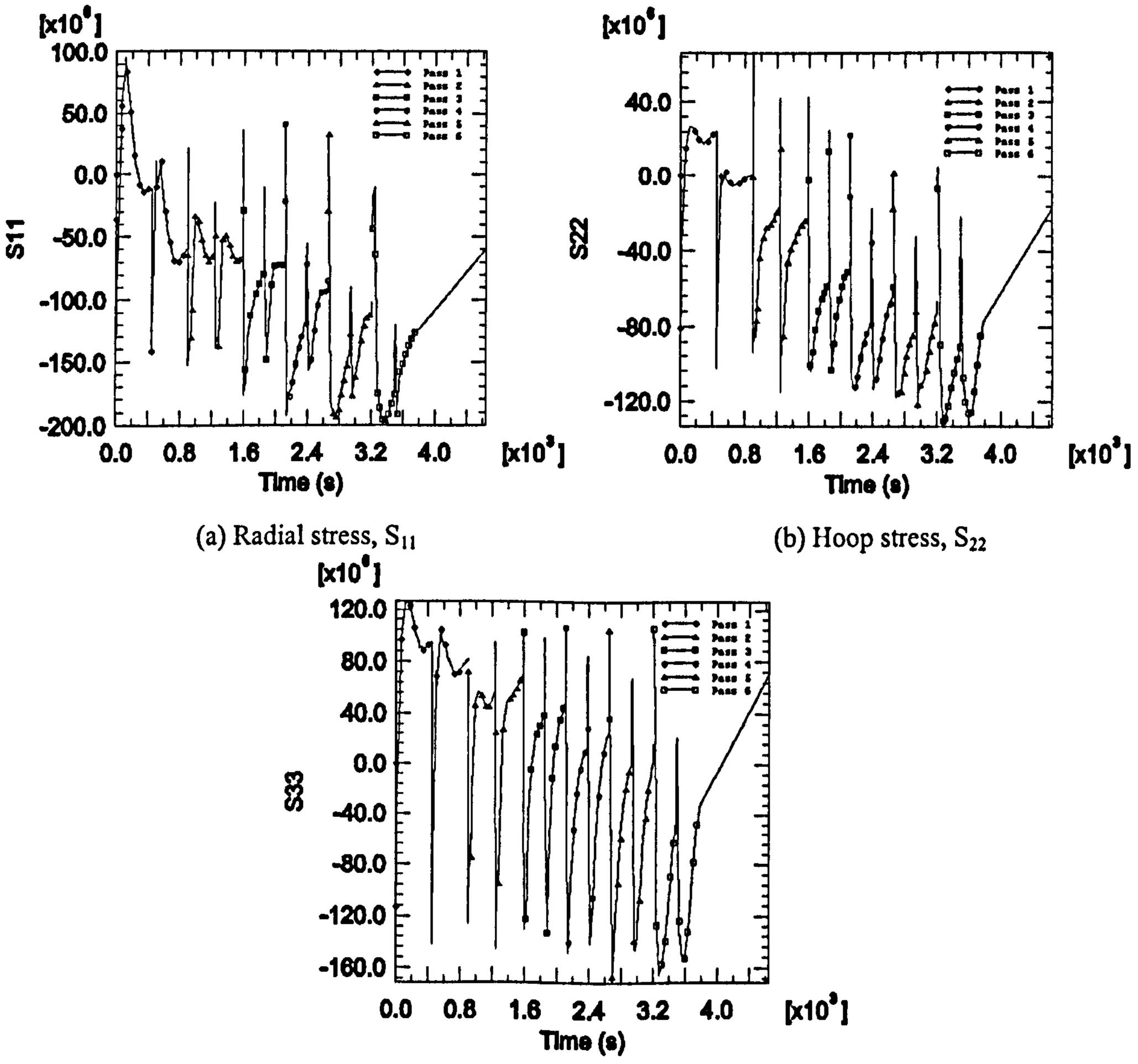

(a) Radial stress, S_{11} (b) Hoop stress, S_{22}

(c) Axial stress, S_{33}

Figure 6.41 Thermal stress evolution at Point a_{14}

It can be seen from Figure 6.41(a) that at the moment of deposition of the first pass, a compressive radial stress of 130MPa appears and then increases to a maximum tensile stress of 100MPa (36%σ_y). This tensile stress gradually decreases to become compressive while welding proceeds to Quadrants *I* and *III*. At the start of welding

Quadrant *IV*, the peak compressive radial stress decreases again to 150MPa and then increases to a small tensile stress. This stress pattern repeats itself for the following passes. In Figures 6.41(b)-(c), the hoop and axial stresses show similar evolution patterns to that of the radial stress, except with different peak tensile and compressive values. Another common phenomenon in these figures is the increase of stresses at the cooling stages. This is due to the recovery of the material yield stress when temperature decreases. The stress state at Point a_{14} is affected by all the passes.

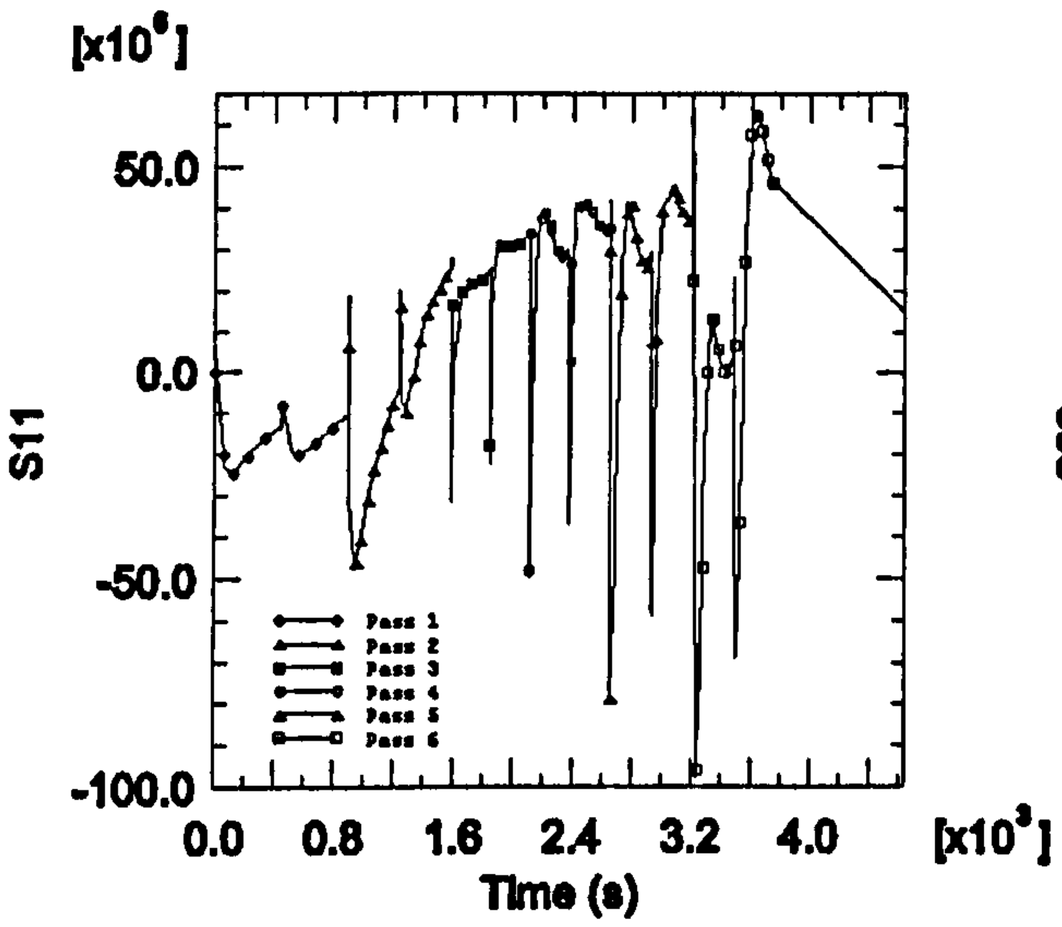

(a) Radial stress, S_{11}

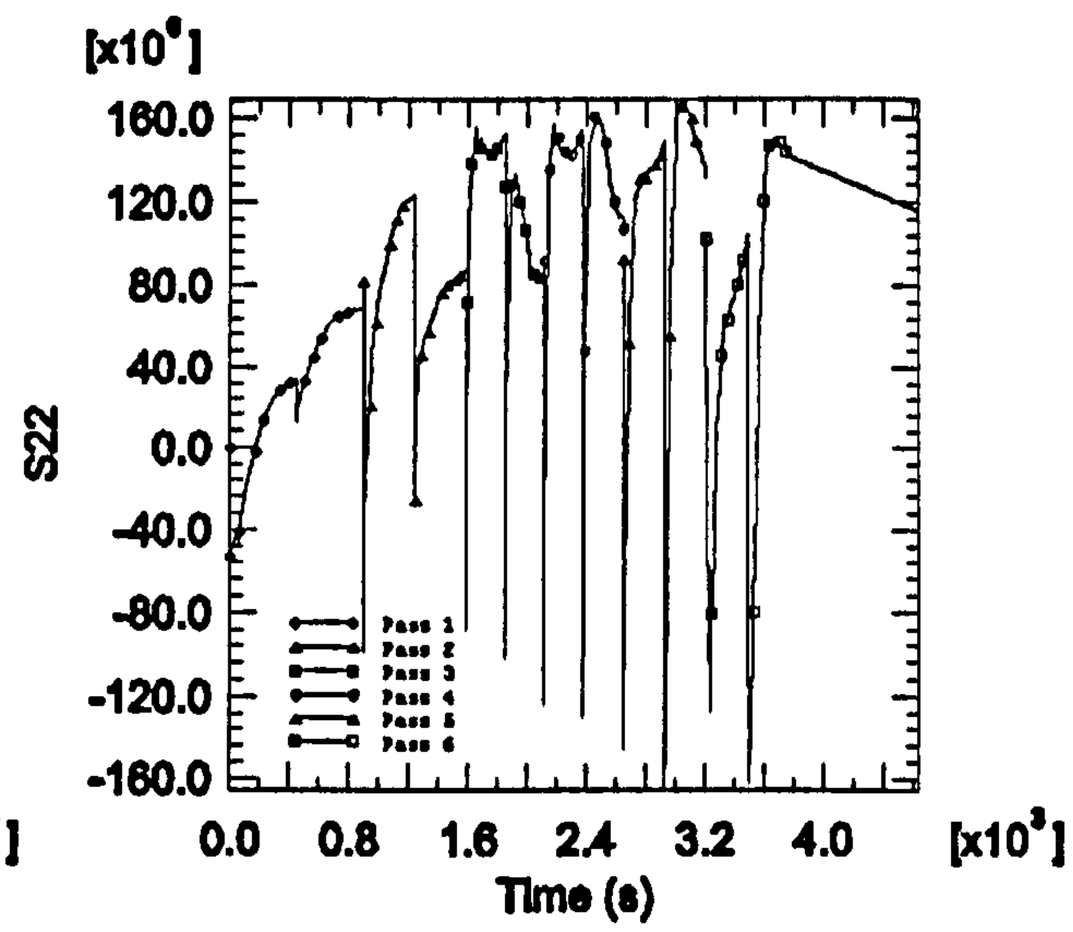

(b) Hoop stress, S_{22}

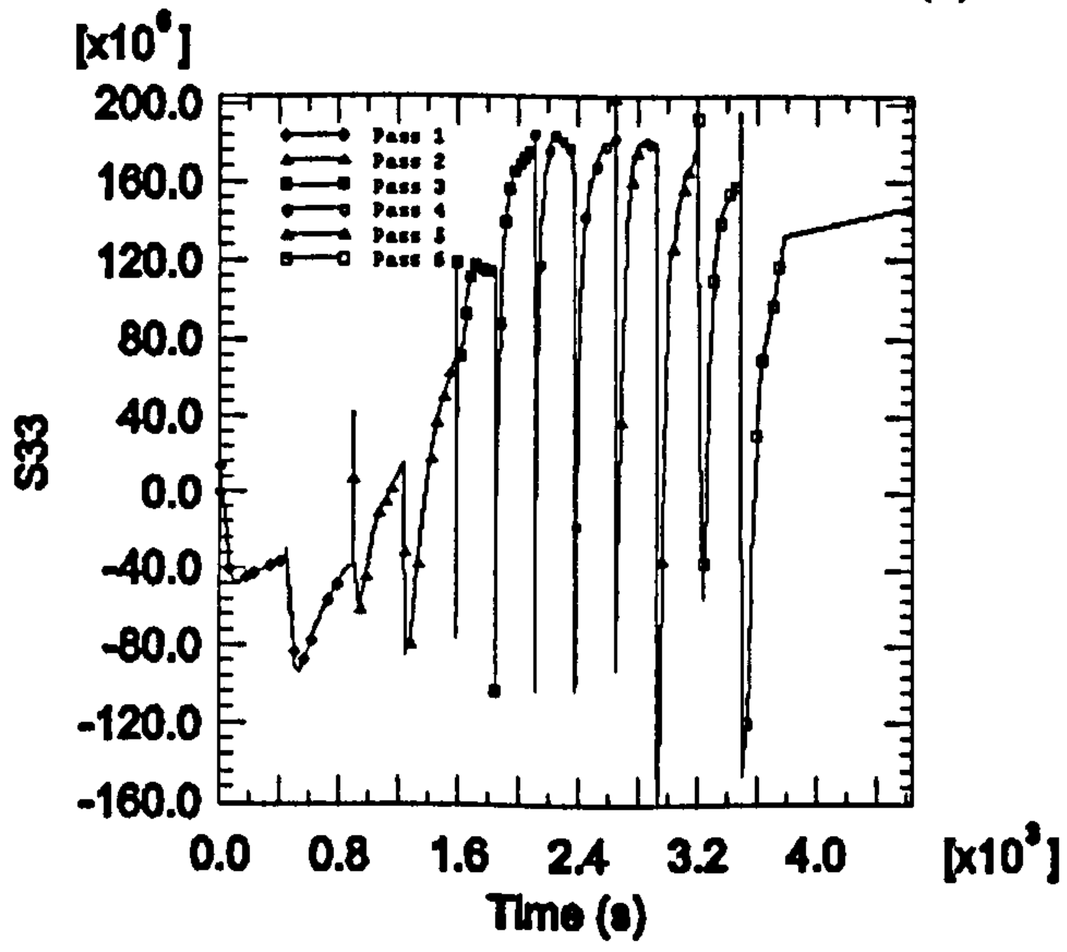

(c) Axial stress, S_{33}

Figure 6.42 Thermal stress evolution at Point b_{14}

Figure 6.42 presents the thermal stress evolution at Point b_{14}. It is observed again that stresses reach peak compression at the moment of deposition. The stress state at this point is mainly affected by the third and later passes.

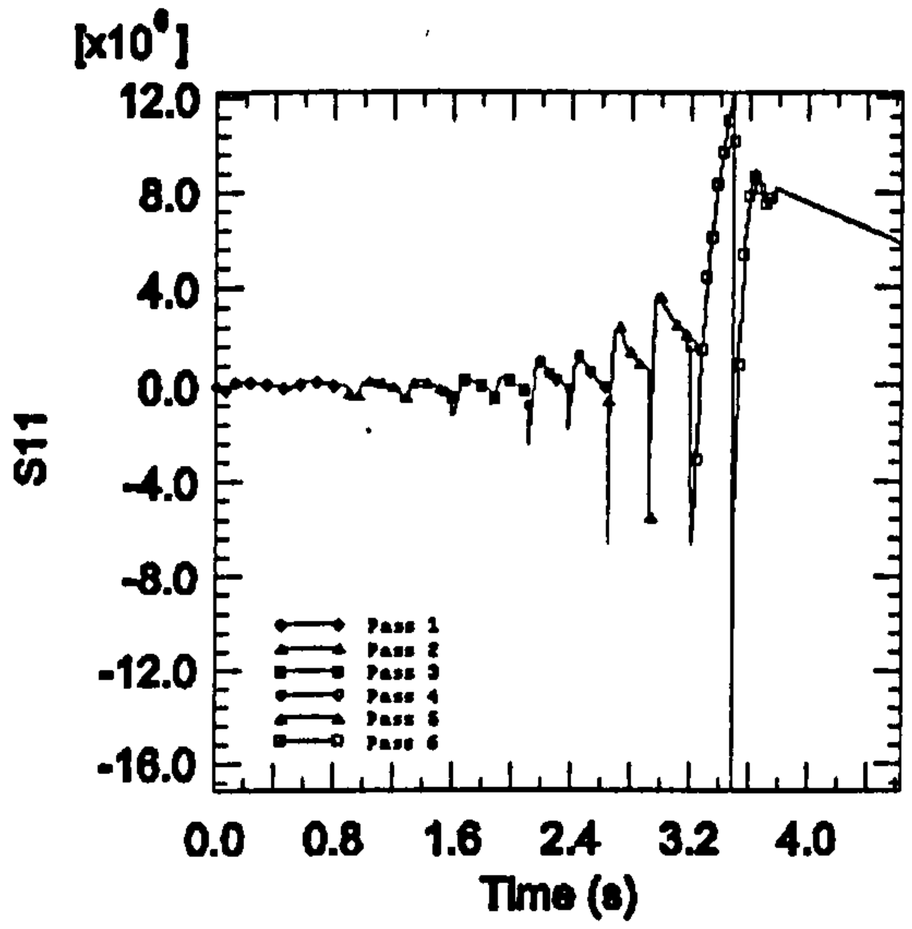

(a) Radial stress, S_{11}

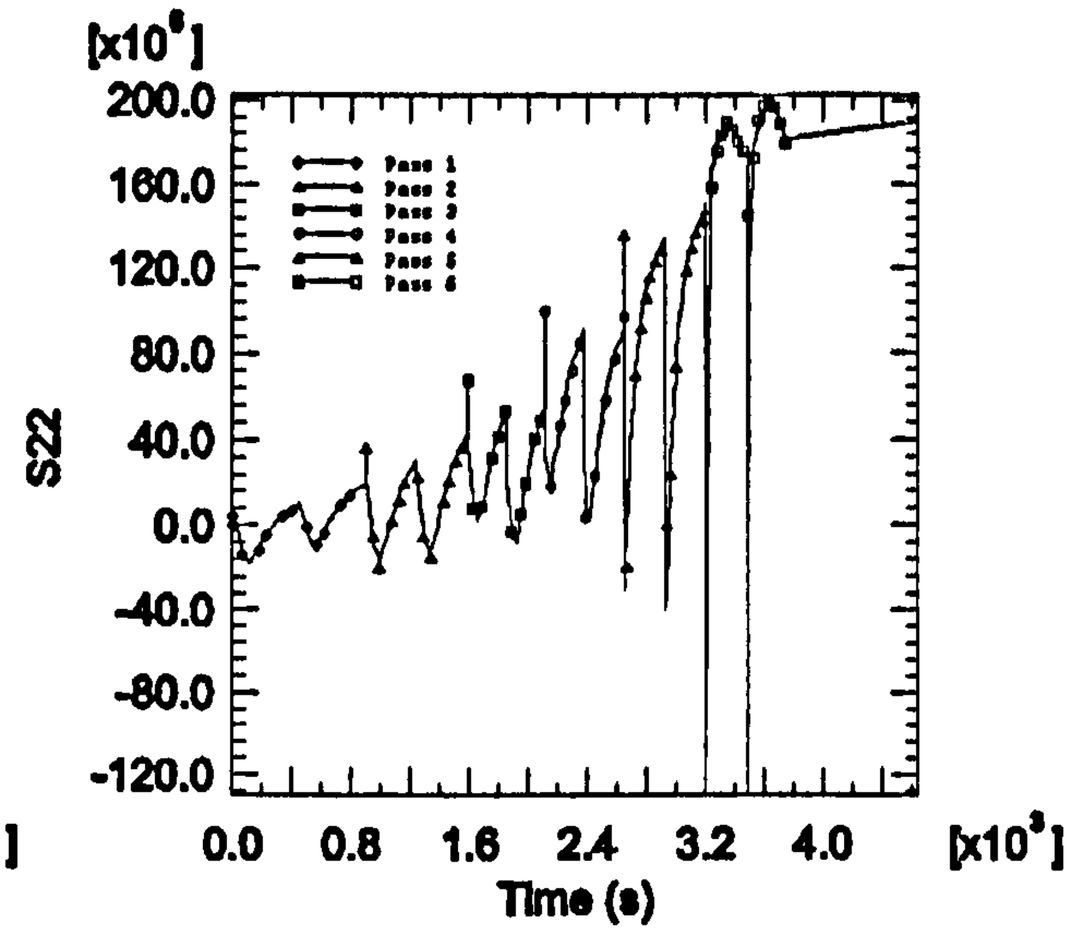

(b) Hoop stress, S_{22}

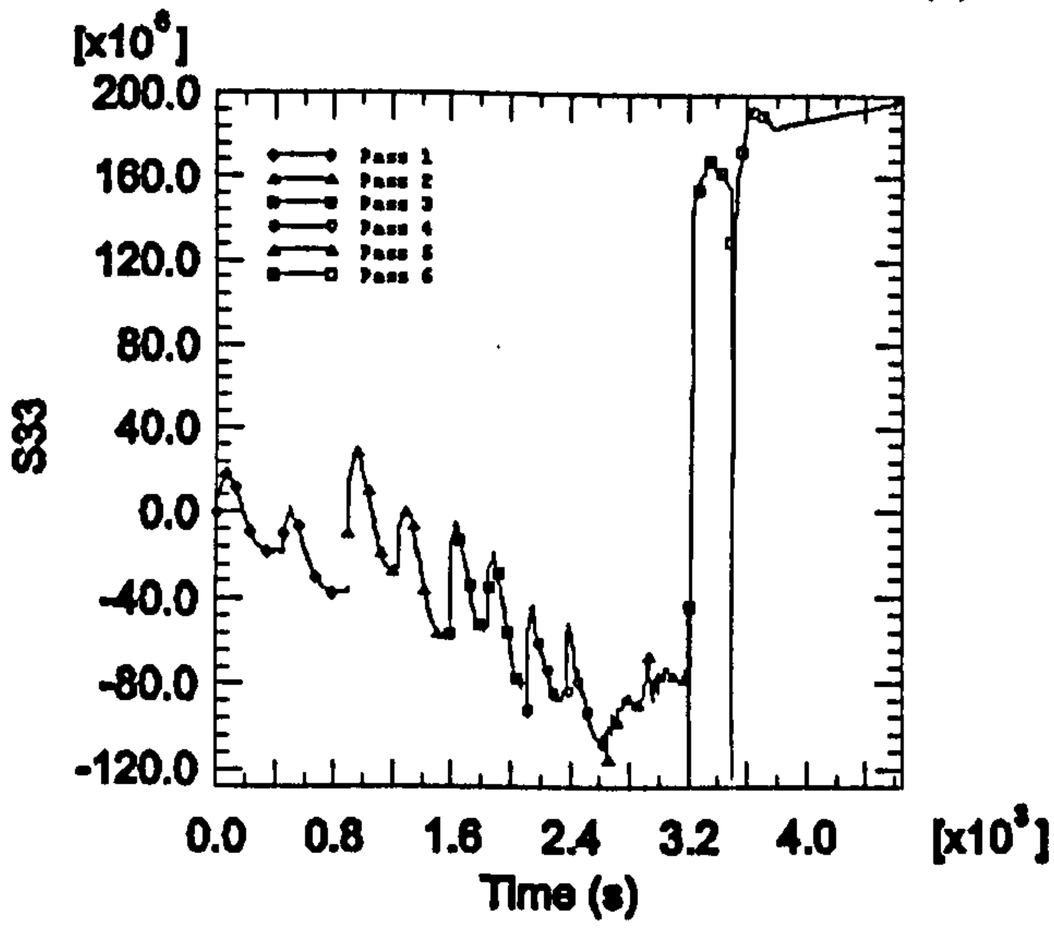

(c) Axial stress, S_{33}

Figure 6.43 Thermal stress evolution at Point c_{14}

As Point c_{14} is located at the further end of the last pass, from Figure 6.43, it is clearly noticed that those previous deposited passes have almost negligible effects on the stress state of Point c_{14}. The last pass decides the final stress state of Point c_{14}. Although this conclusion is valid for Point c_{14}, it can also be extended to other locations along the weldline.

Figure 6.44(a) shows the radial stress versus angular position on the outer surface of the run pipe. It can be noticed that the radial stresses are affected only within the region spanning 18° to 30°. The values vary within a range of $50\%\sigma_y$ in compression to $36\%\sigma_y$ in tension. Figures 6.44(b)-(c) present the hoop and axial stress distributions respectively. It is found that the locations, where the filler material is deposited,

experience compressive stress at 1s after deposition. They experience tensile stress at the end of material deposition. Large stress variations occur within the region spanning 18° to 45°. Beyond 45°, stresses tend to be zero.

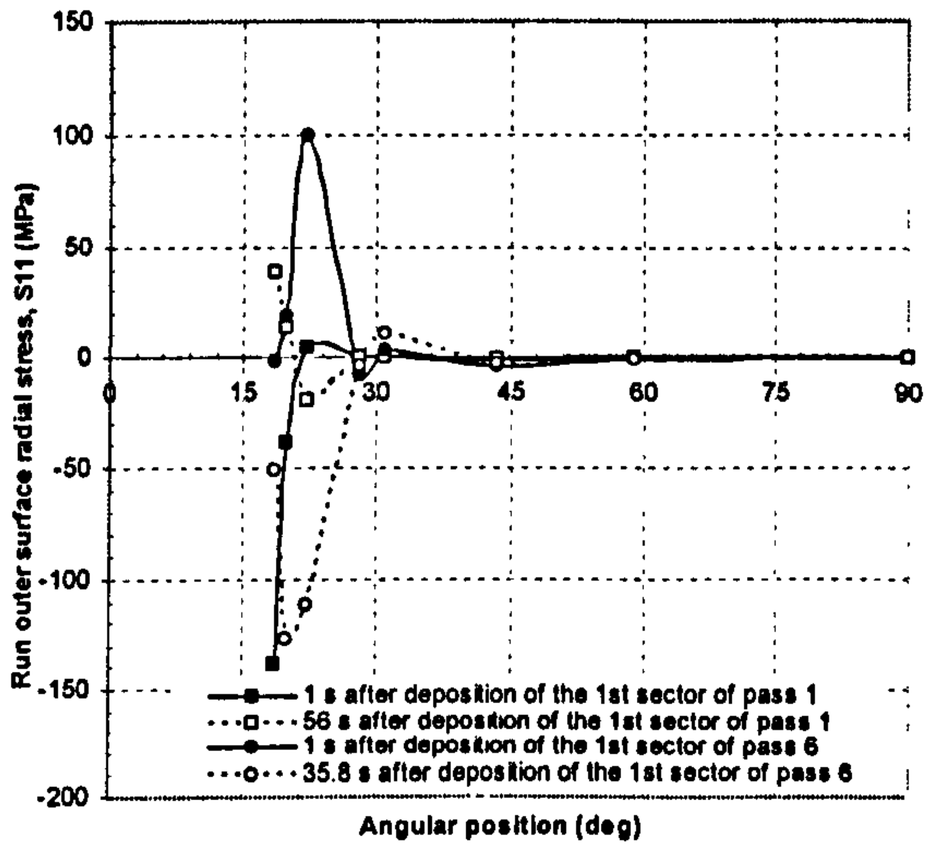

(a) Radial stress, S_{11}

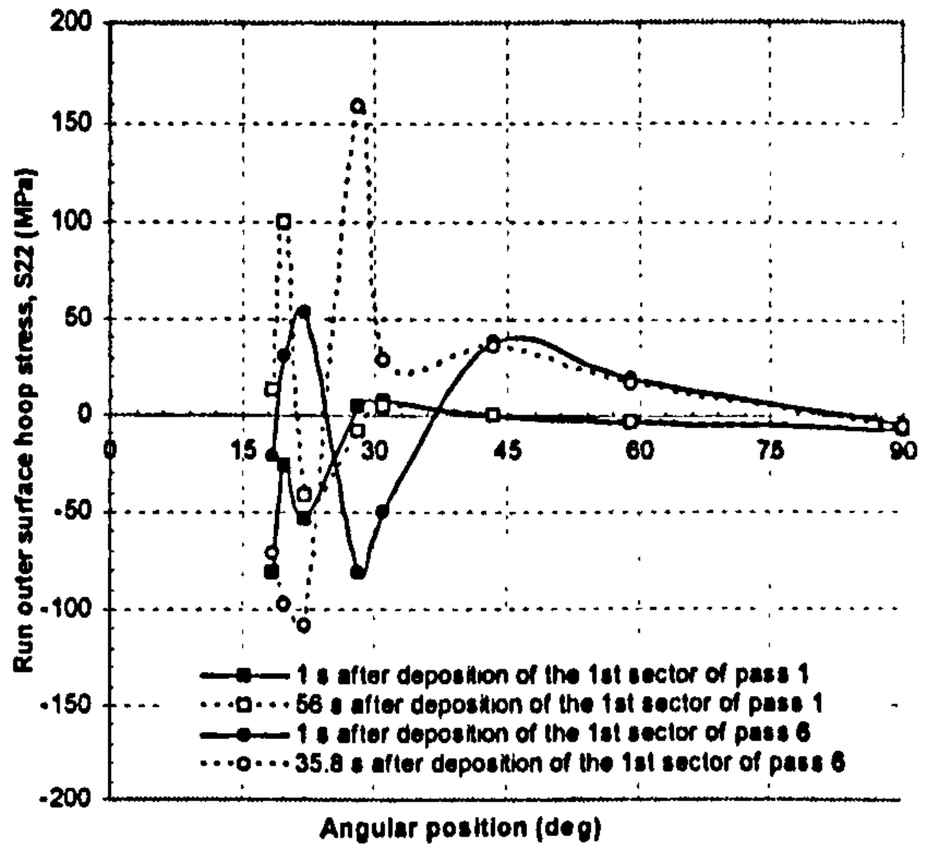

(b) Hoop stress, S_{22}

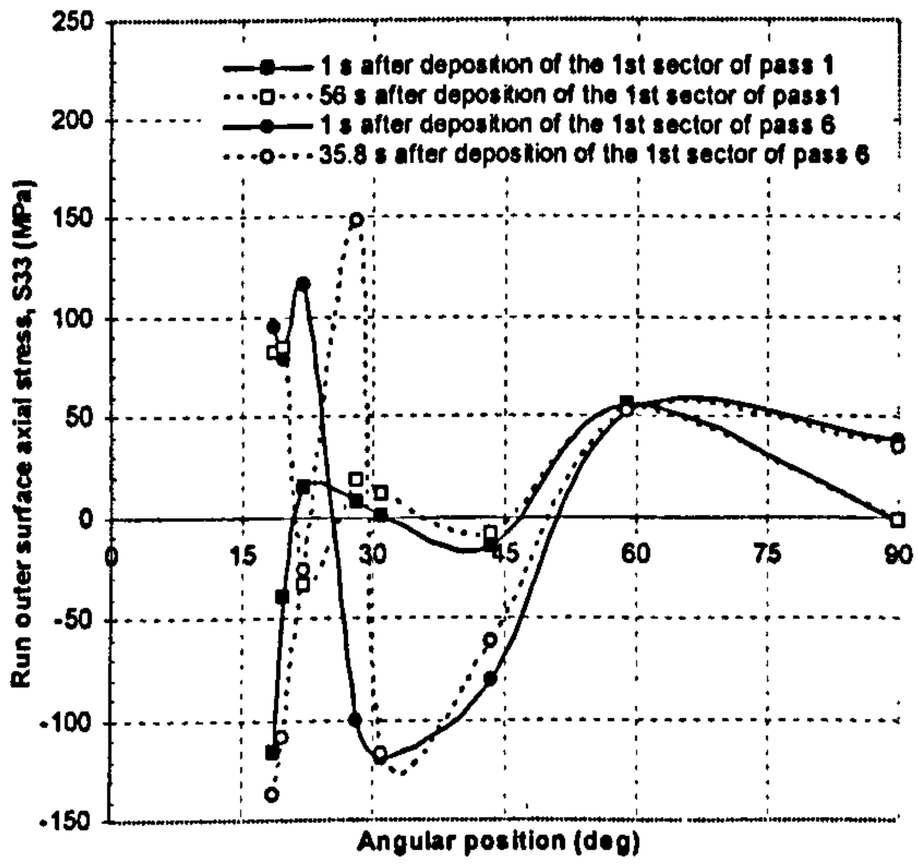

(c) Axial stress, S_{33}

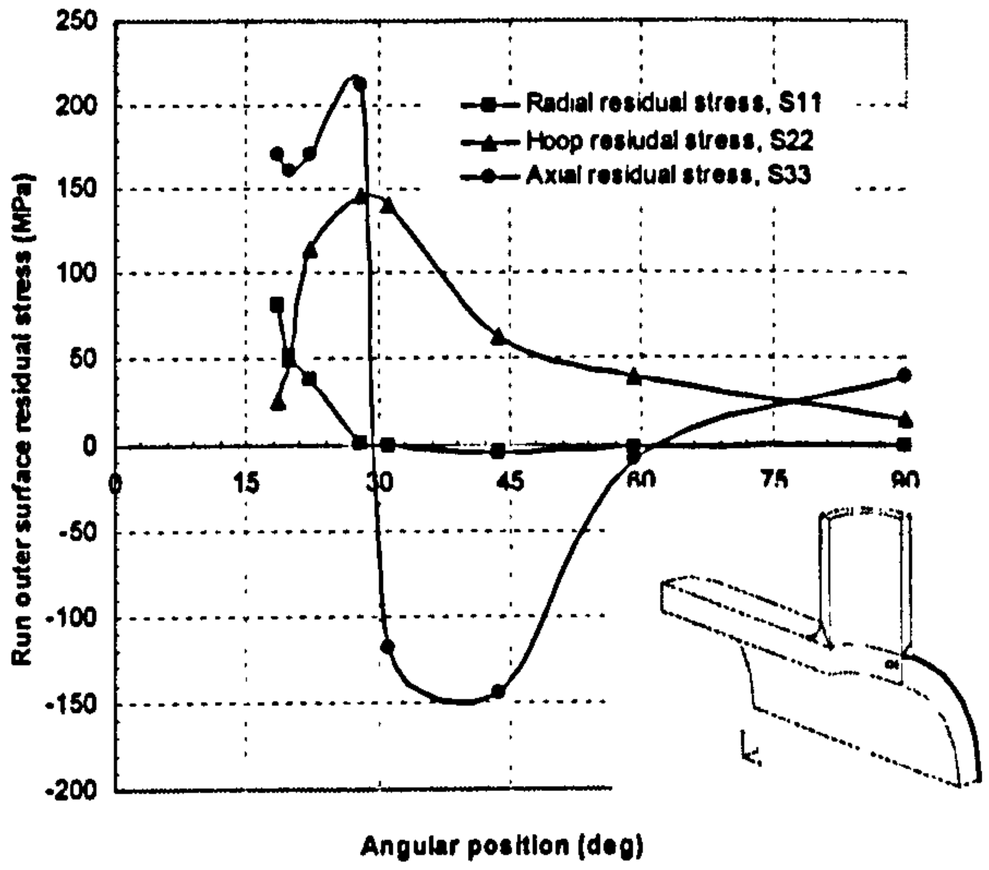

(d) Residual stresses

Figure 6.44 Stresses vs. angular position on the run pipe outer surface

Figure 6.44(d) summaries the stress versus angular position on the run pipe outer surface. The peak radial residual stress is approximately 29%σ_y at the origin. The peak hoop and axial residual stresses are 53%σ_y and 76%σ_y, respectively, at the weld toe. At some distance away from the weldline, the peak axial residual stress is compressive and can reach a magnitude of up to 54%σ_y. The tensile hoop residual stress decays away along the run pipe outer surface. As the distance from the weldline increases, the magnitudes of all three stresses tend to reduce significantly up to becoming negligible.

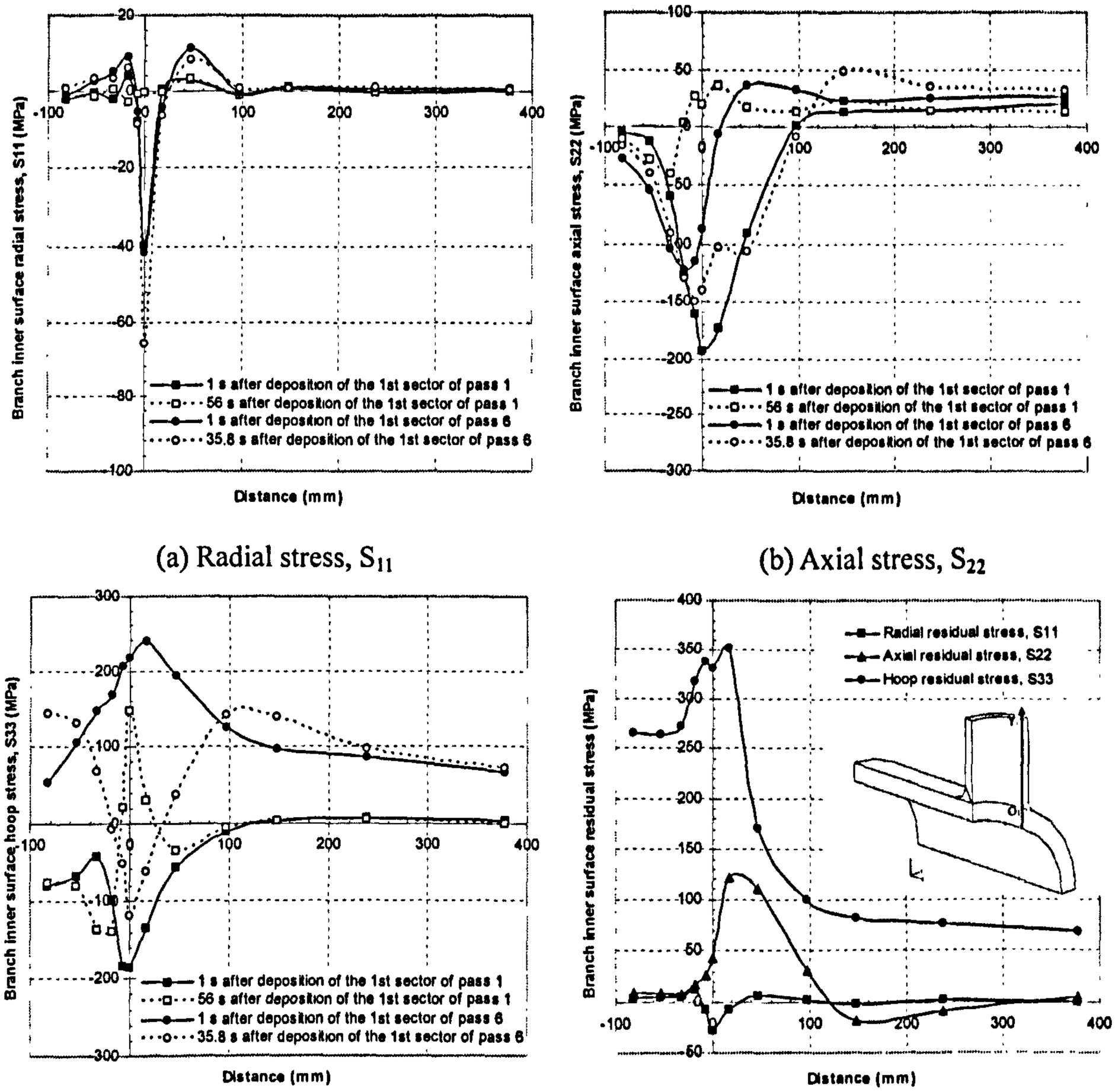

Figure 6.45 Stresses in the Y_I-direction on the branch inner surface

Figure 6.45 shows the stress distributions in the Y_I-direction at the moments shown in the figures. Figure 6.45(a) presents the radial stress distributions. It can be noticed that the peak compressive radial stresses are located at the origin O_I with a value of about 65MPa (23%σ_y). Figure 6.45(b) shows the axial stress distributions. Most areas adjacent to both sides of the origin experience compression. At some distance away from the origin, small tensile stresses are experienced. Figure 6.45(c) shows the hoop stress distributions. It can be seen that both peak tensile or peak compressive stresses are located near the origin.

Figure 6.45(d) shows the residual stress distributions in the Y_I-direction. The radial residual stresses are small and can be considered to have negligible effect. This stress will not be considered in the parametric studies to be discussed later. The stress

component that dominates the final stress state is the hoop stress. Both hoop and axial residual stress appear to peak at about the same distance of 17mm from the origin at the branch pipe side, with values of 126%σ_y and 44%σ_y, respectively. The hoop residual stresses on the run pipe side are about 95%σ_y. These observations demonstrate that the inner surface of the run pipe up to 20mm is a high stress area that should be given particular attention. Beyond a distance of about 100mm, i.e. in the branch pipe parent material away from the weld, both radial and axial stresses almost vanish while the hoop residual stress is well below 100MPa.

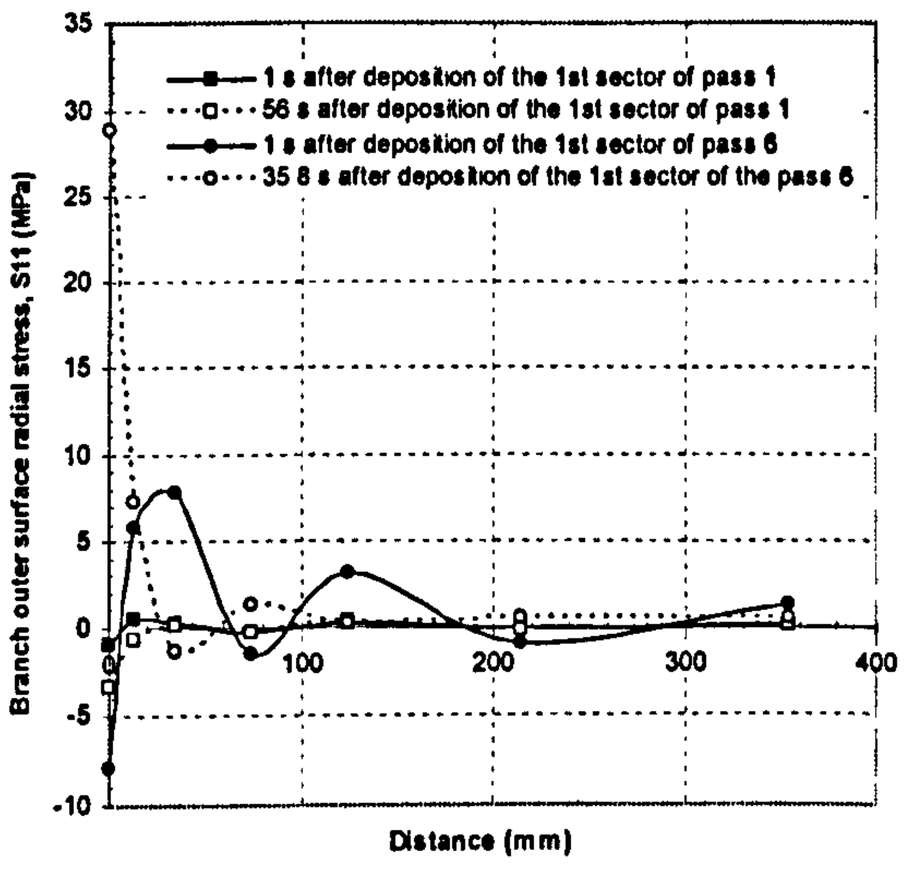

(a) Radial stress, S_{11}

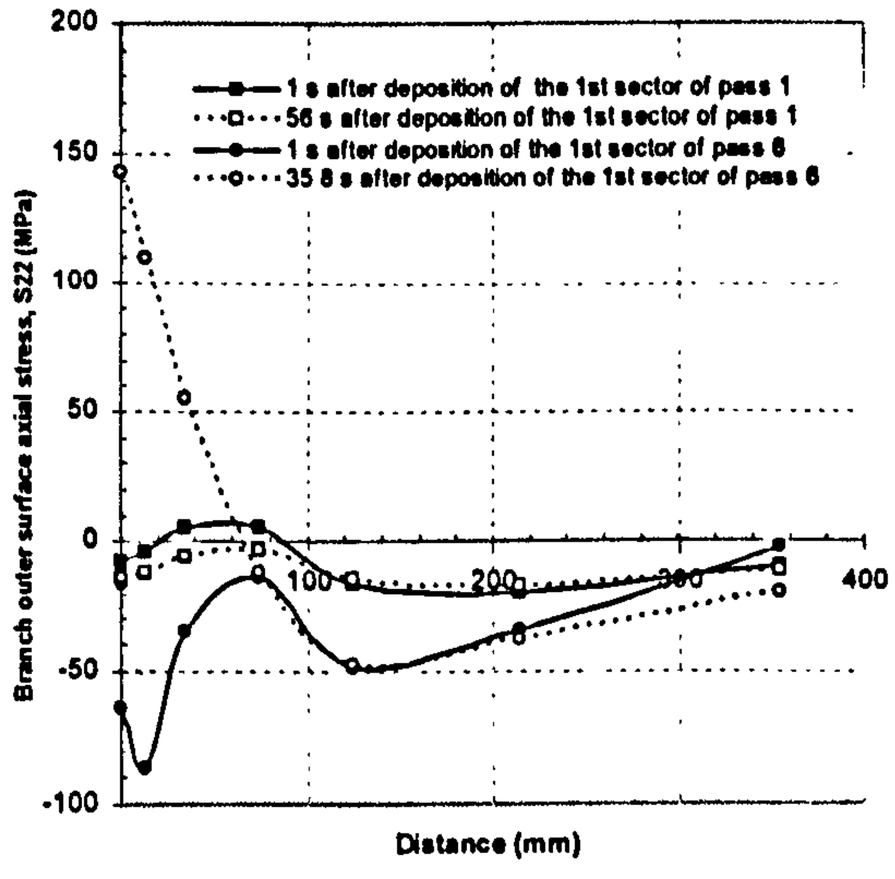

(b) Axial stress, S_{22}

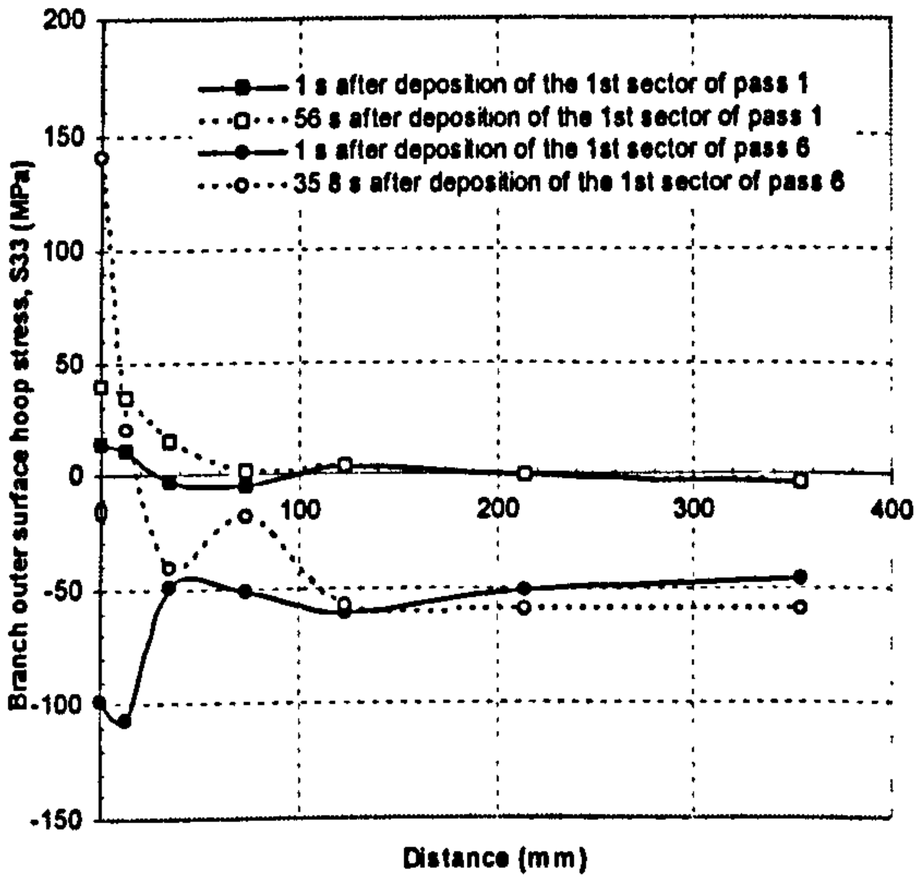

(c) Hoop stress, S_{33}

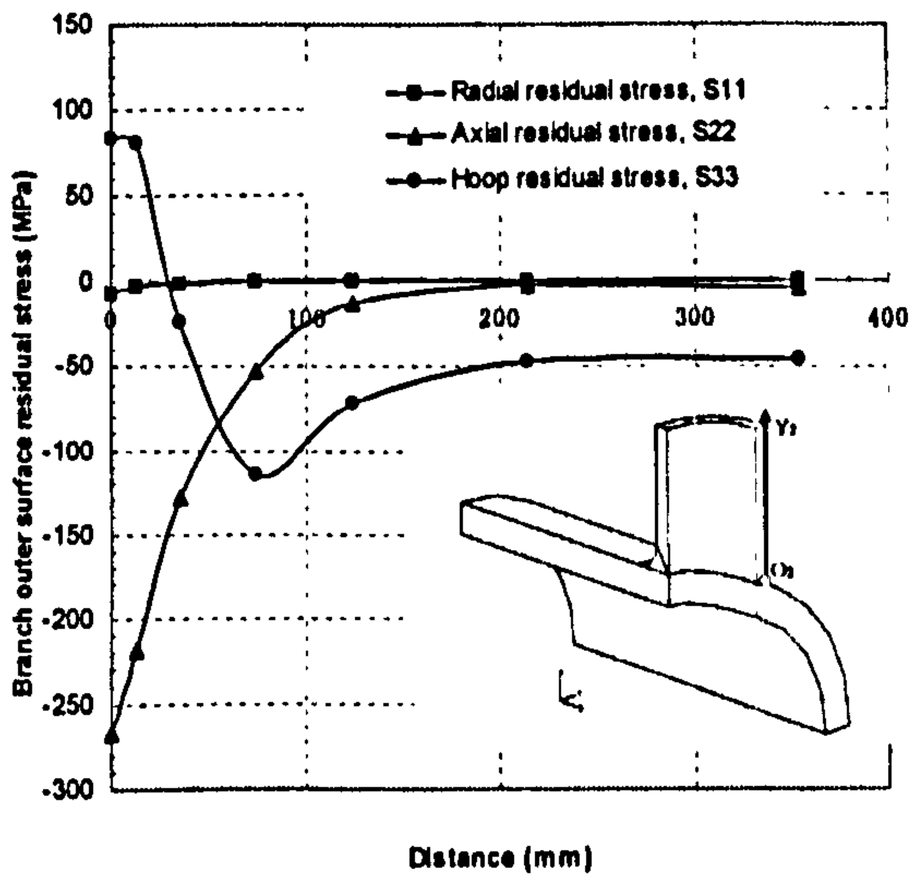

(d) Residual stresses

Figure 6.46 Stresses in the Y_2-direction on the branch outer surface

Figure 6.46 shows the stress distributions in the Y_2-direction. From Figures 6.46(a)-(c), it is noticed that the stresses after the deposition of the first pass are quite small. It could thus be concluded that the first few passes may not have much effect on the stress state at the branch outer surface. Figure 6.46(d) shows that the tensile hoop

residual stresses are located near the origin O_2, with a peak value of 85MPa (30%σ_y). Compressive axial residual stresses exist everywhere, with a peak magnitude of 270MPa at the weldline, increasing to zero as we move away from the weld region towards the branch pipe parent material. Radial stresses are almost non-existent.

6.3.3.3 Run pipe cross section *b-b*

Stresses at the run pipe cross section *b-b* are also defined in the conventional sense. For the stresses on the run pipe, e.g. in the *X*-direction, stresses are defined as S_{11} the hoop stress, S_{22} the radial stress and S_{33} the axial stress. Similarly, for the stresses on the branch pipe, e.g. in the Y_1- and Y_2-direction, the stresses are defined as S_{11} the hoop stress, S_{22} the axial stress and S_{33} the radial stress.

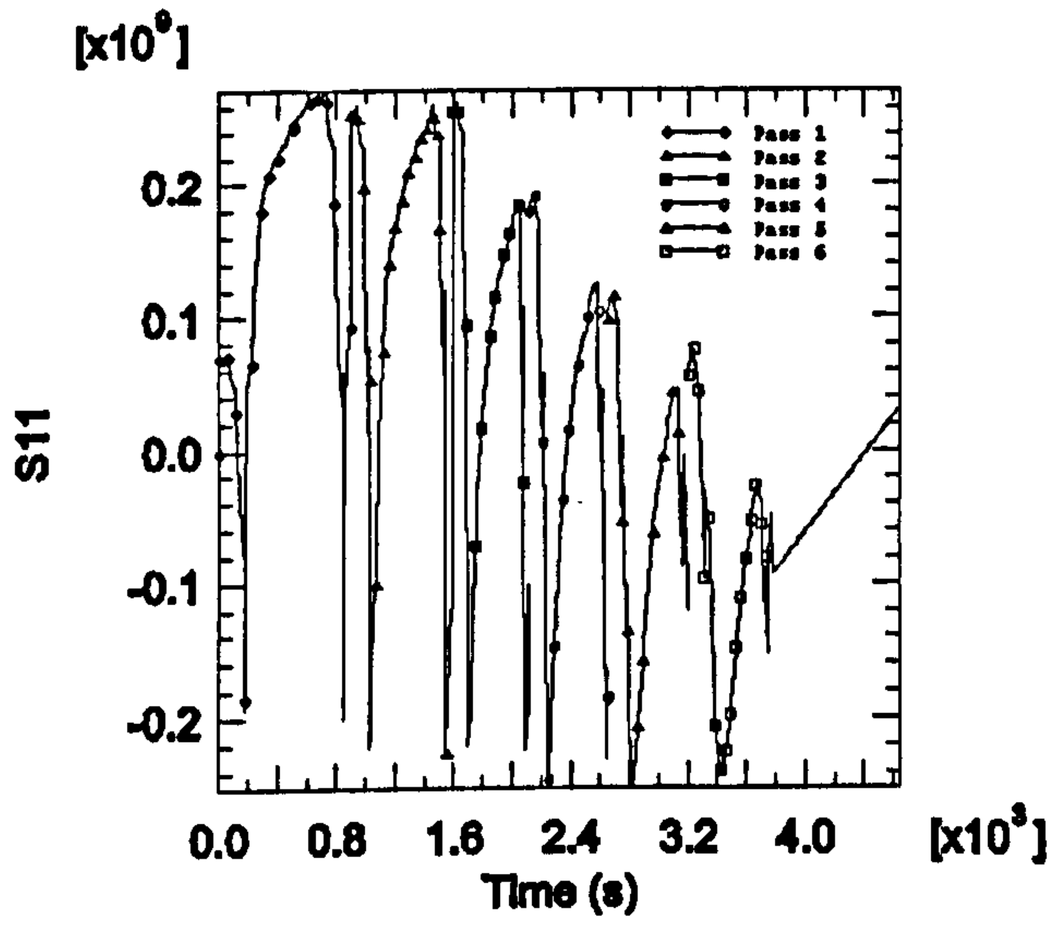

(a) Hoop stress, S_{11}

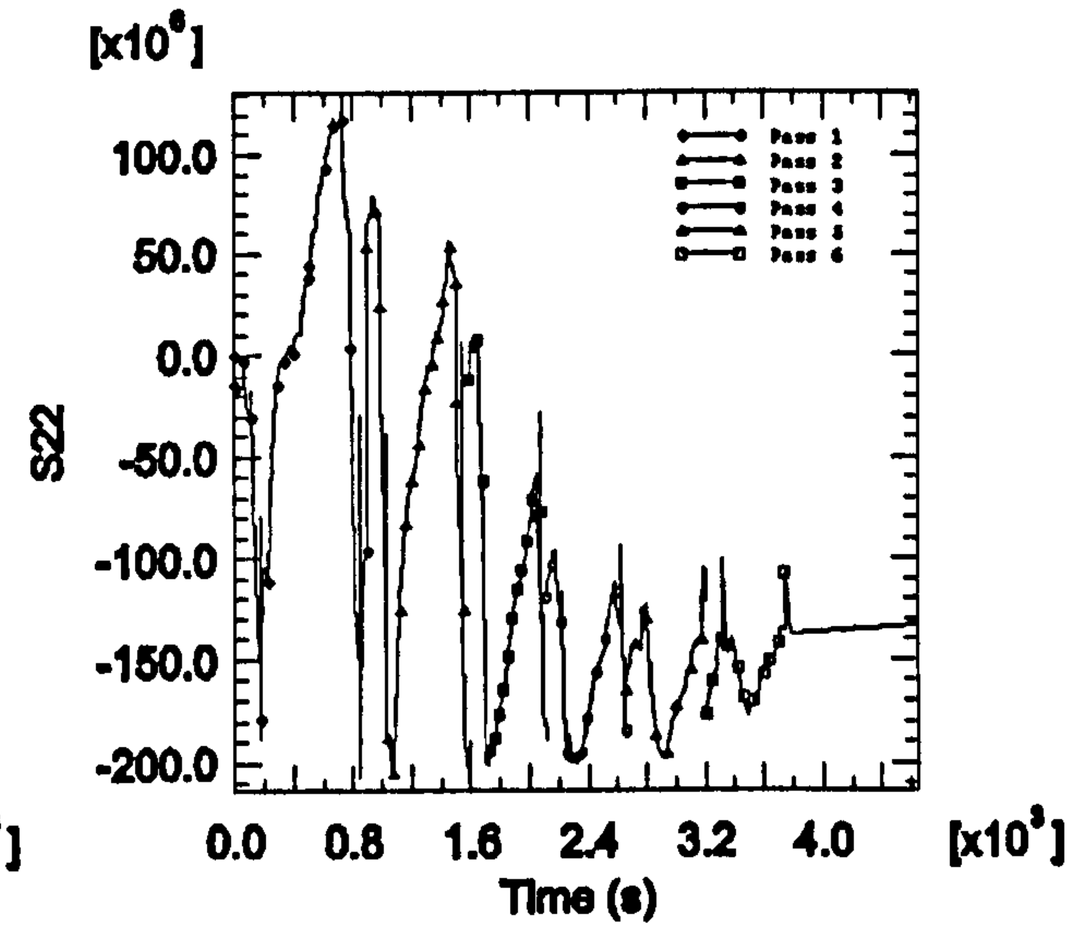

(b) Radial stress, S_{22}

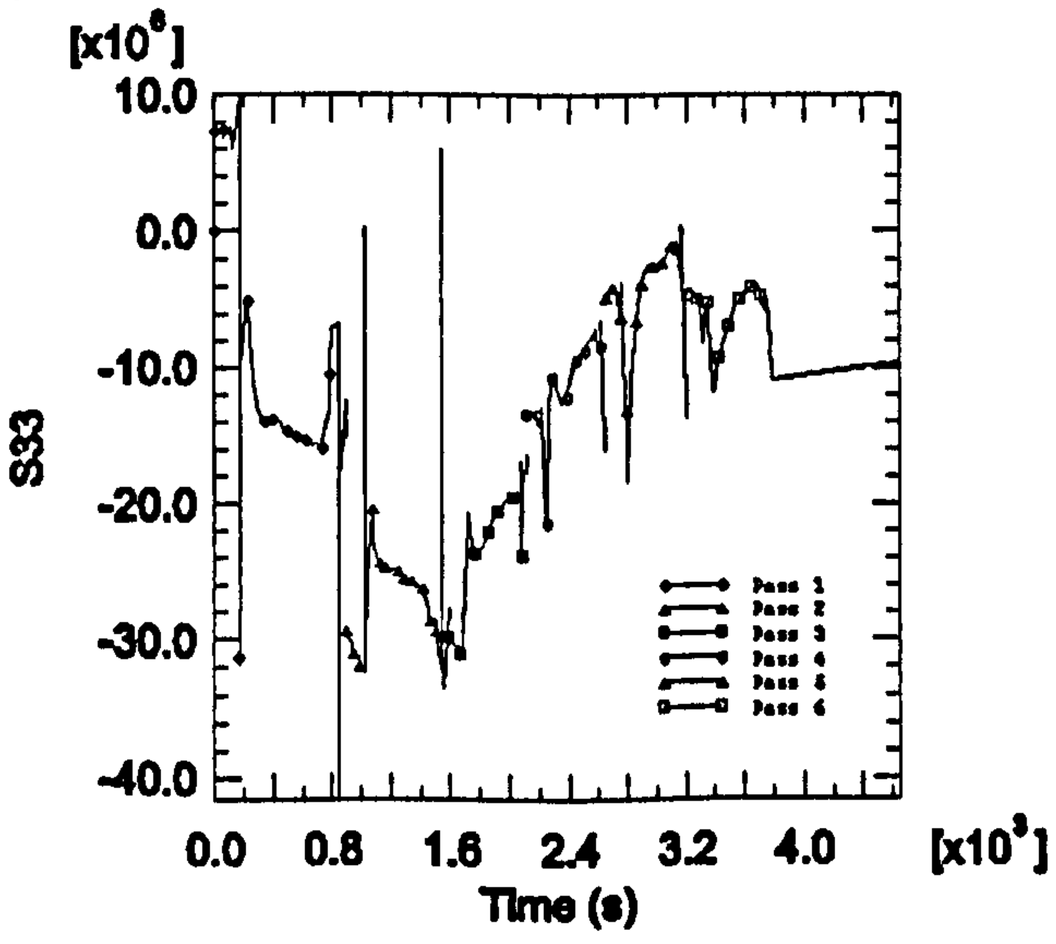

(c) Axial stress, S_{33}

Figure 6.47 Thermal stress evolution at Point a_{12}

In Figure 6.47(a), it can be seen that each pass has two peak compressive hoop stresses. The first indicates the stress when welding the last sector of Quadrant *I*, while the second shows the stress when welding the last sector of Quadrant *II*. When the heat source moves away, the stress gradually increases to being tensile. Similar phenomena can be observed in Figure 6.47(b), with smaller tensile radial stress, although the peak compressive stresses are almost the same as those in Figure 6.47(a). It can be noticed in Figure 6.47(c) that axial stresses at Point a_{12} are very small and do not have much effect on the stress state.

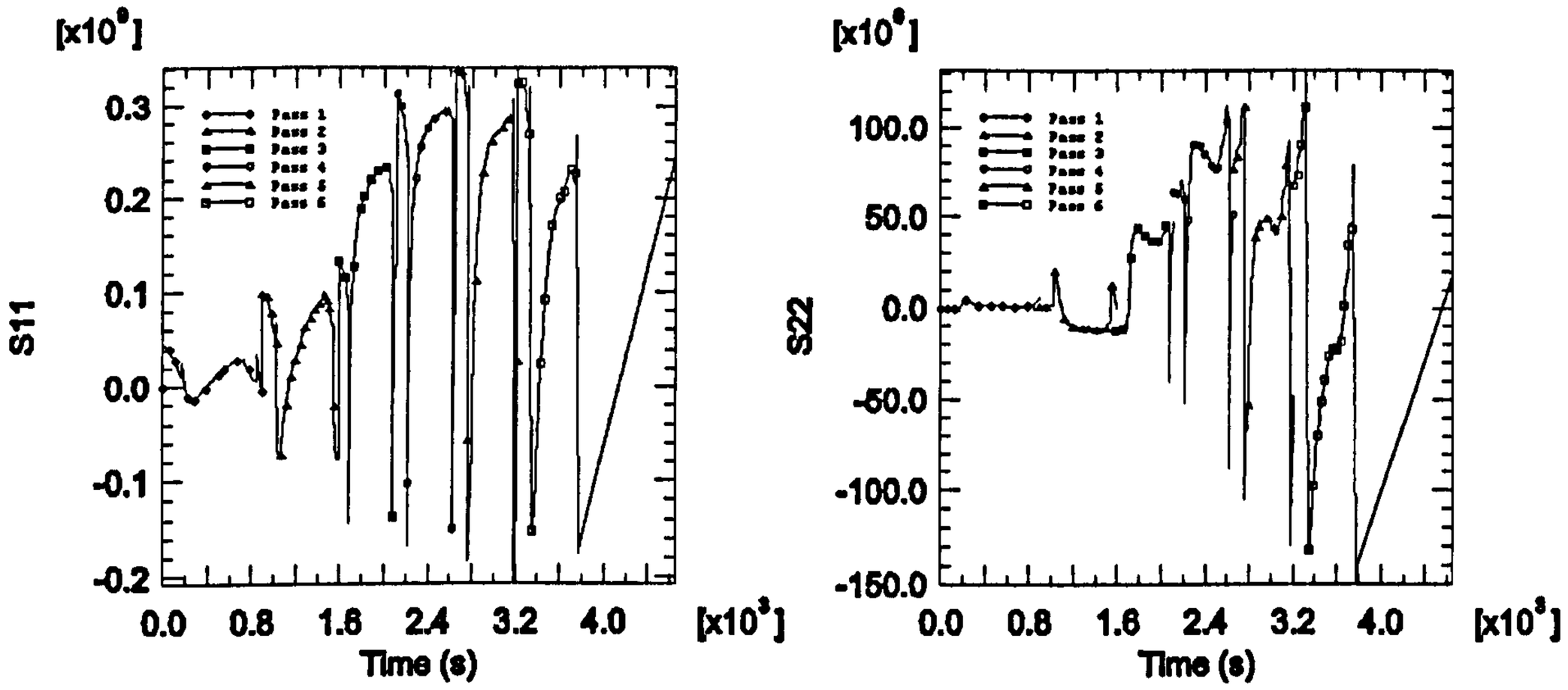

(a) Hoop stress, S_{11} (b) Radial stress, S_{22}

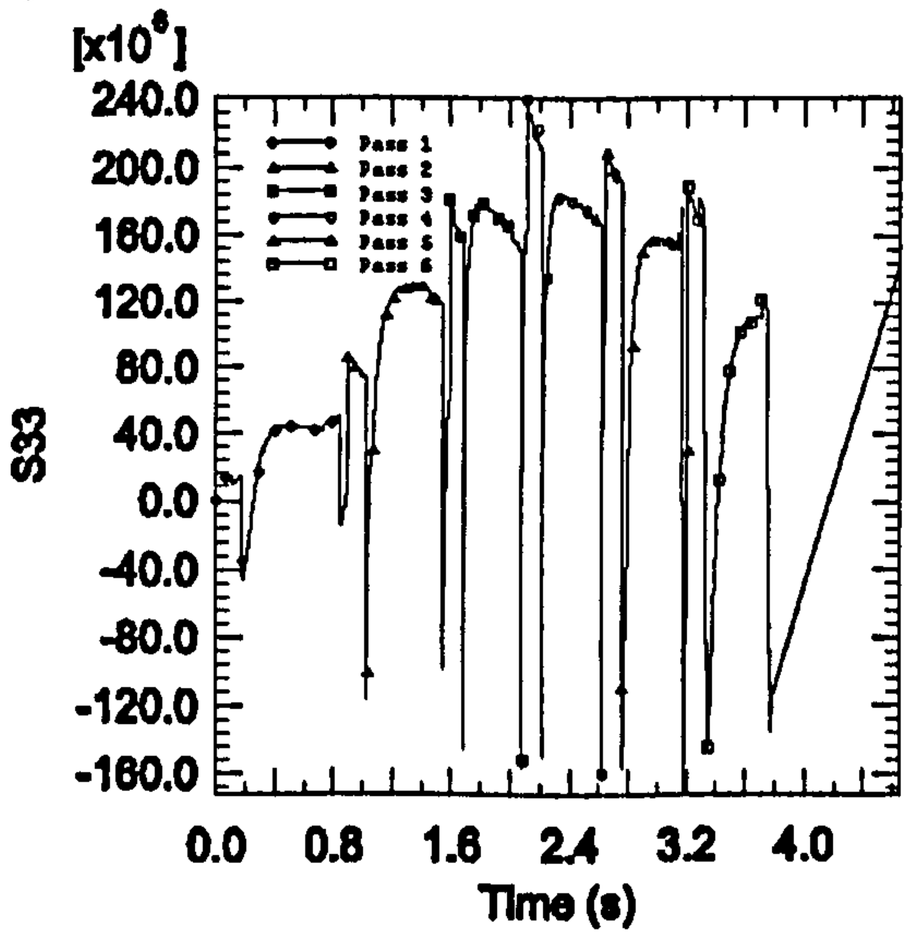

(c) Axial stress, S_{33}

Figure 6.48 Thermal stress evolution at Point b_{12}

Figure 6.48 shows the stress evolution that Point b_{12} experiences. As Point b_{12} is at the location where the third pass is deposited, the higher numbered passes have obviously some effects on its stress state. Worthy of mention is that a linear increase of

stress is noticed clearly at the cooling stage in all the three figures.

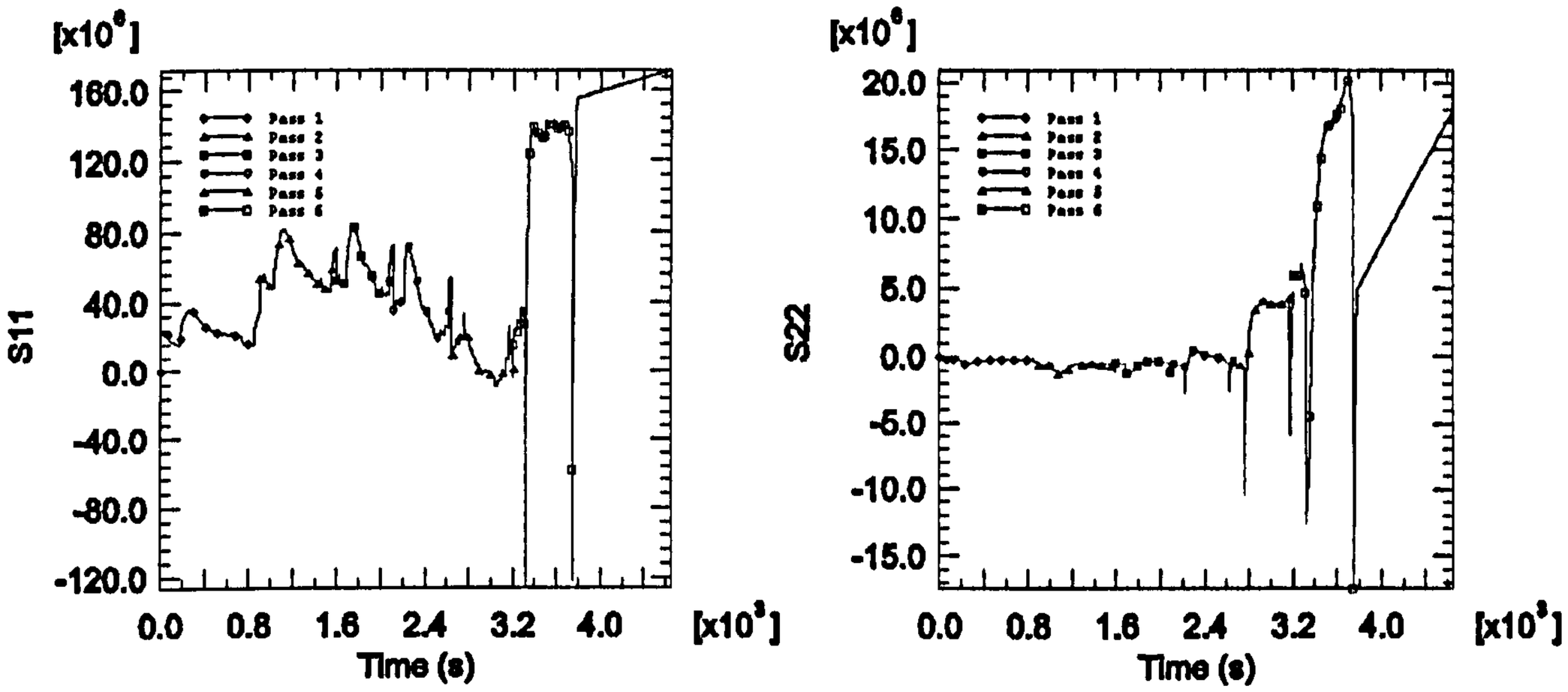

(a) Hoop stress, S_{11}

(b) Radial stress, S_{22}

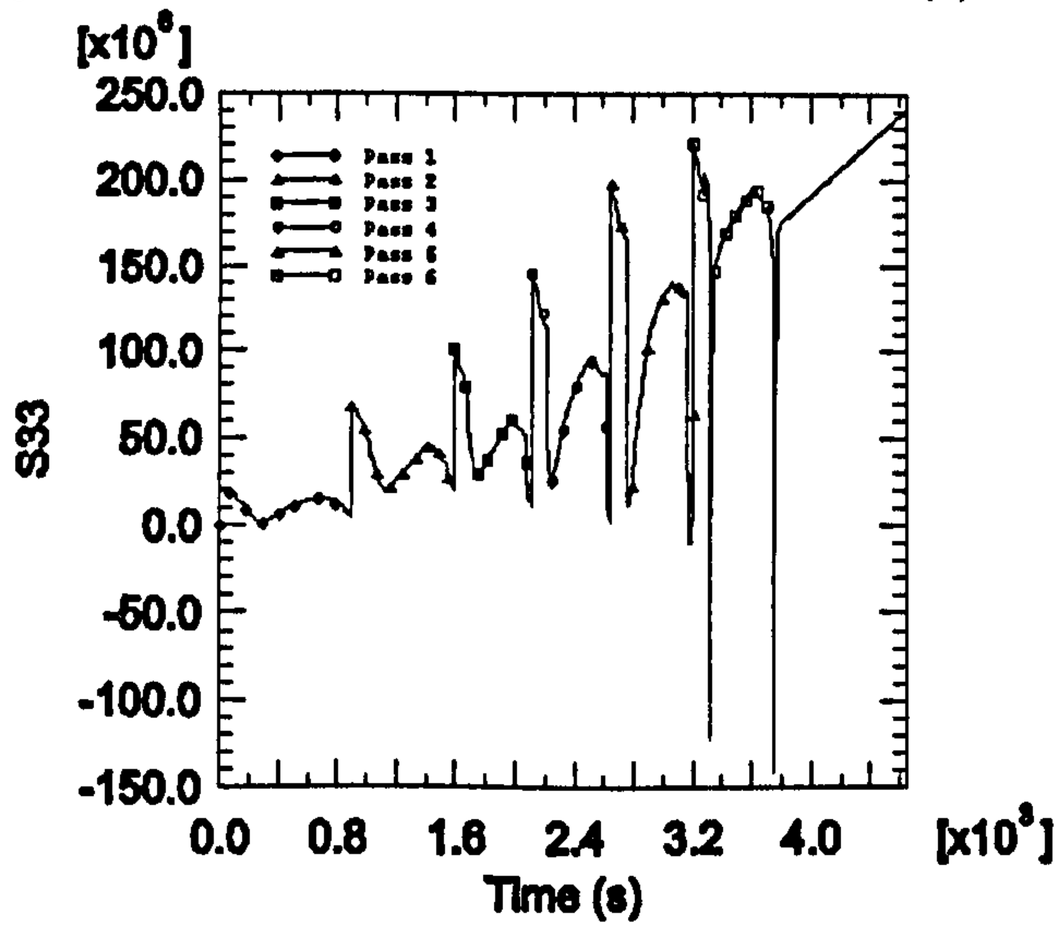

(c) Axial stress, S_{33}

Figure 6.49 Thermal stress evolution at Point c_{12}

Figure 6.49 shows the stress evolution at Point c_{12}. All the stresses are mainly affected by the last pass, although the radial stress is quite small.

Figures 6.50(a)-(c) show the stress distributions in the *X*-direction at various moments as indicated. It is observed again that, at the regions near x=0 and 96mm, where the first and last passes are deposited, the material experiences compressive hoop or axial stress at 1s after deposition, and experiences tensile stress at the end of the deposition of that sector. Stresses evolve mainly within the region between 0 and 100mm, i.e. under the weld seam. Beyond 100mm, they are hardly affected by welding and tend to be zero.

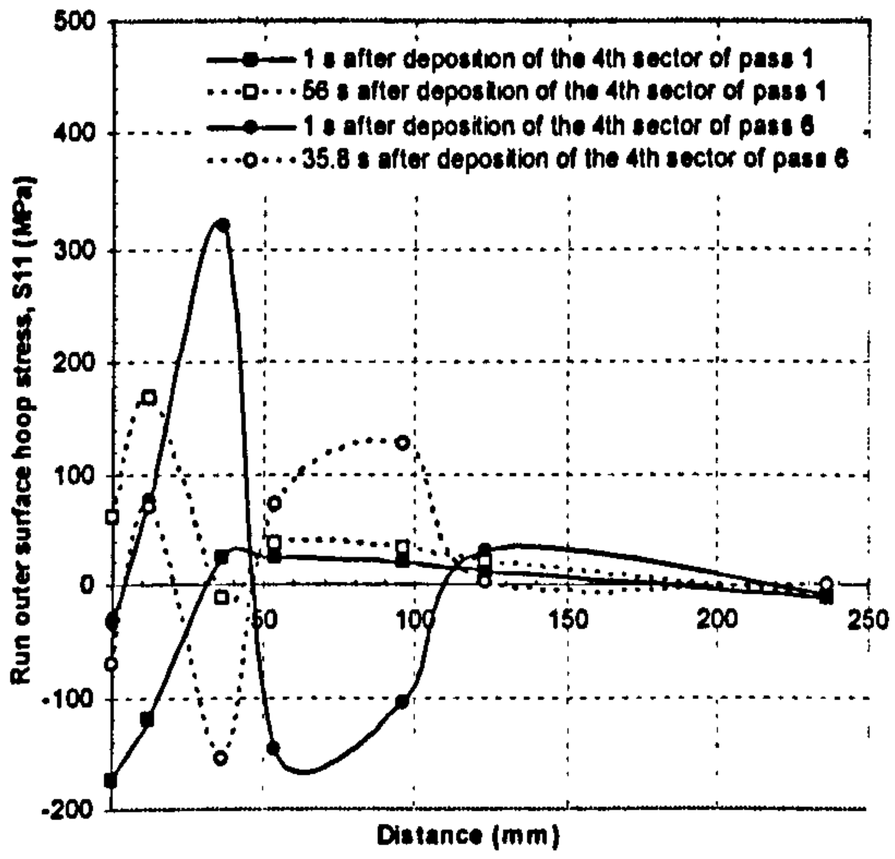

(a) Hoop stress, S_{11}

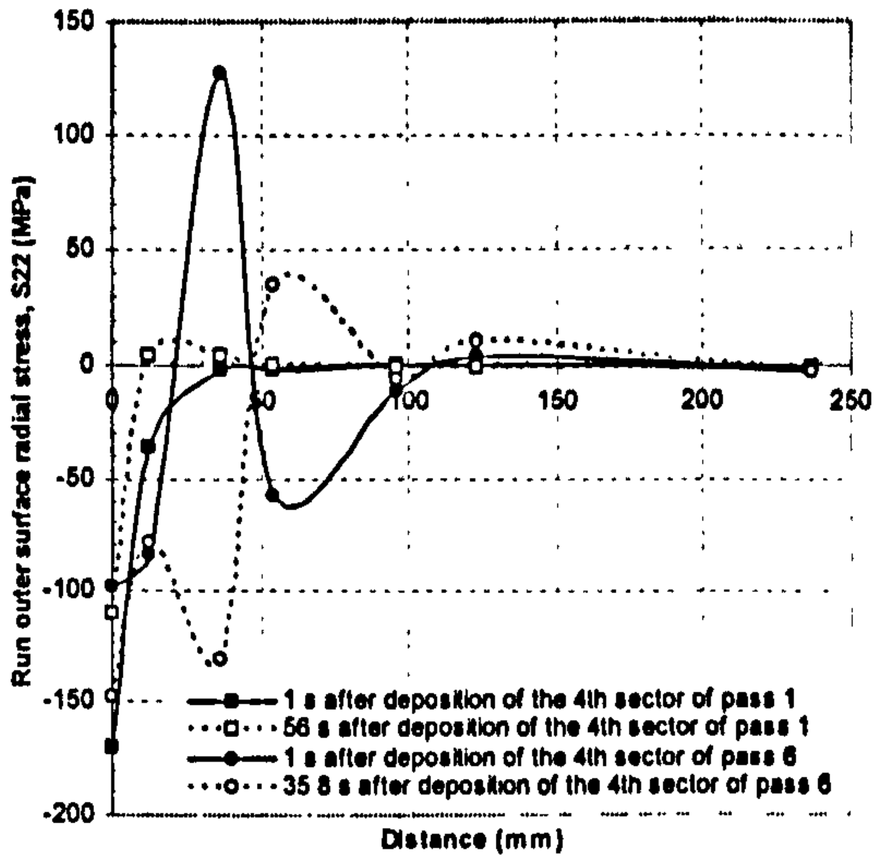

(b) Radial stress, S_{22}

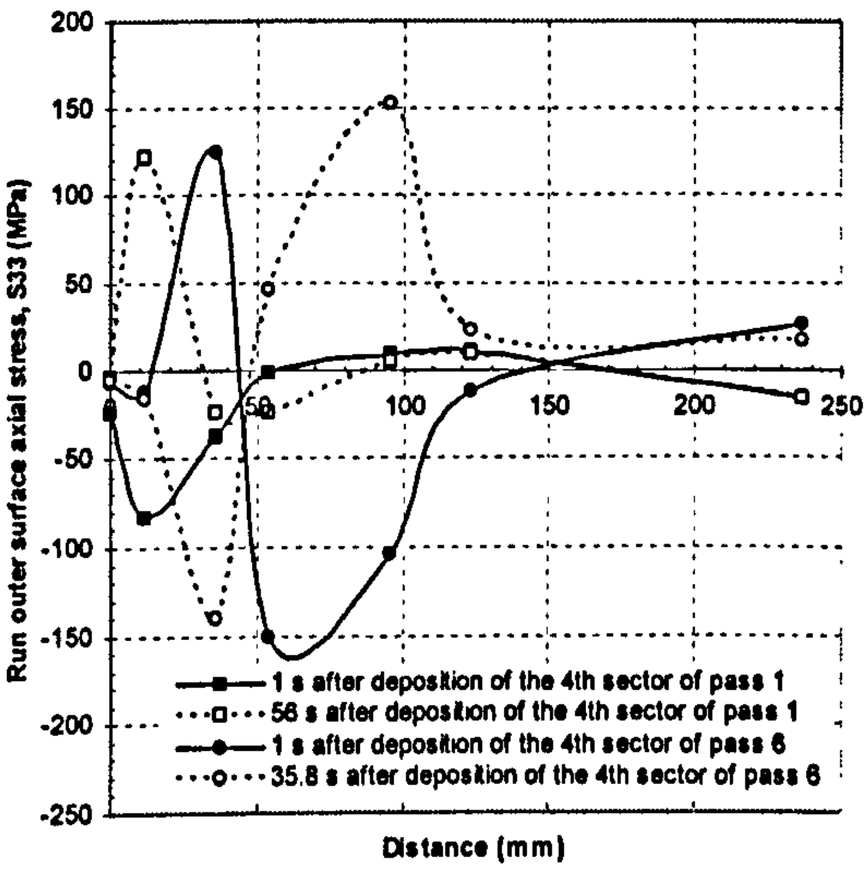

(c) Axial stress, S_{33}

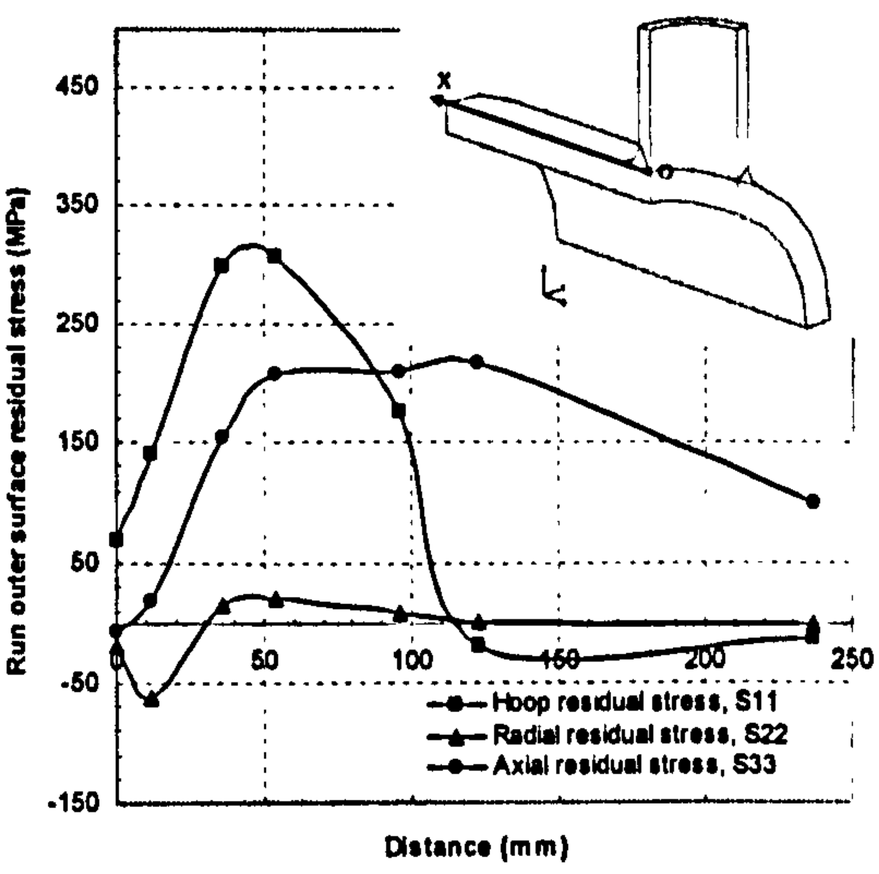

(d) Residual stress

Figure 6.50 Stresses in the *X*-direction on the run pipe outer surface

Figure 6.50(d) shows stress versus distance in the *X*-direction on the run pipe outer surface. It is noticed that high tensile hoop residual stresses are located within a distance of 100mm from the branch inner surface. A peak value of about 310MPa (112%σ_y) is located at roughly the centre of the weld seam, then decreases to zero at about 10mm away from the weld toe, and ultimately becomes somewhat compressive as distance increases. The entire outer surface along the *X*-direction, except the area around the origin O_1, experiences tensile axial residual stress with a peak value of about 79%σ_y near the weldline. Radial residual stresses are again rather small throughout the whole length along the *X*-direction.

Figure 6.51 shows the through-thickness residual stress at the weld toe of the run

cross section. The horizontal axis shows the radial distance from the inner surface of the run pipe to its outer surface. A typical through-thickness bending situation is depicted for the hoop residual stress in such that stress changes from tension on the outer surface to compression on the inner surface at about one third of the thickness from the outer surface. A similar pattern is exhibited for the axial residual stress as again it changes from tension on the outer surface to compression on the inner surface at about two thirds of the thickness from the outer surface. The maximum tensile hoop residual stress is on the outer surface, with a value of $63\%\sigma_y$. The peak axial residual stress is at a distance of 4% of the run pipe thickness from the outer surface with a value of $85\%\sigma_y$. The radial residual stress is again negligible throughout the thickness.

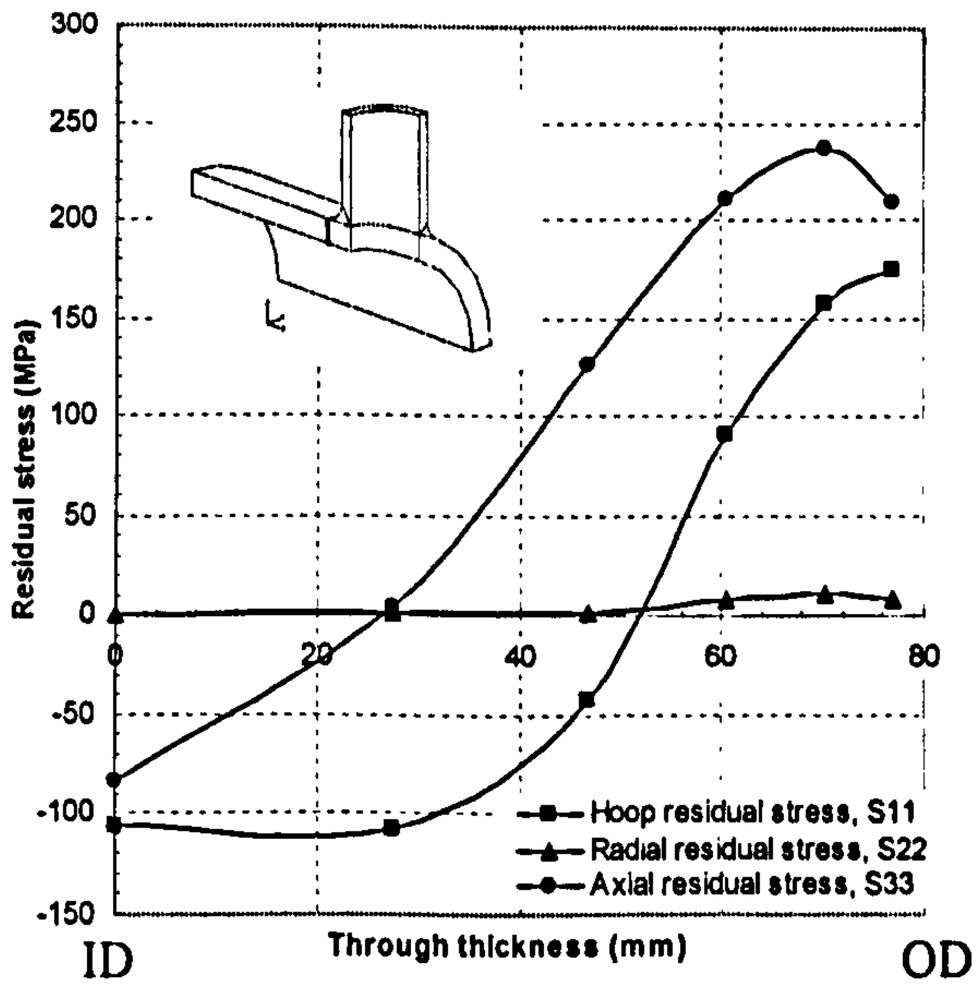

Figure 6.51 Through thickness residual stress at the weld toe of the run cross section

From Figures 6.52(a)-(c), it is noticed that most regions, especially the areas around the origin, experience compressive stresses during welding. Figure 6.52(d) shows the final residual stress distributions in the Y_1-direction. It is noted that high compressive hoop stresses are mainly located in the run pipe, with a peak magnitude of about 150MPa on the inner surface. It starts becoming tensile just below the weldline to reach a peak magnitude of 110MPa at a distance of 27% of the branch pipe thickness on the branch pipe side, beyond which it starts to decrease steadily to eventually become compressive again at a distance of 75mm. The axial residual stress is almost negligible around the origin on the run pipe side. It gradually increases to a peak value of 100MPa at a distance of 75mm. The radial stress is again negligible throughout. In summary, the stress component that dominates the final stress state within the vicinity of the weld area

is the hoop residual stress. The axial residual stress appears to be equally significant but it does not peak in the weld region itself but well into the parent material. Overall, the stress levels along this path are not significantly important as they just about exceed a magnitude of 100MPa (36%σ_y).

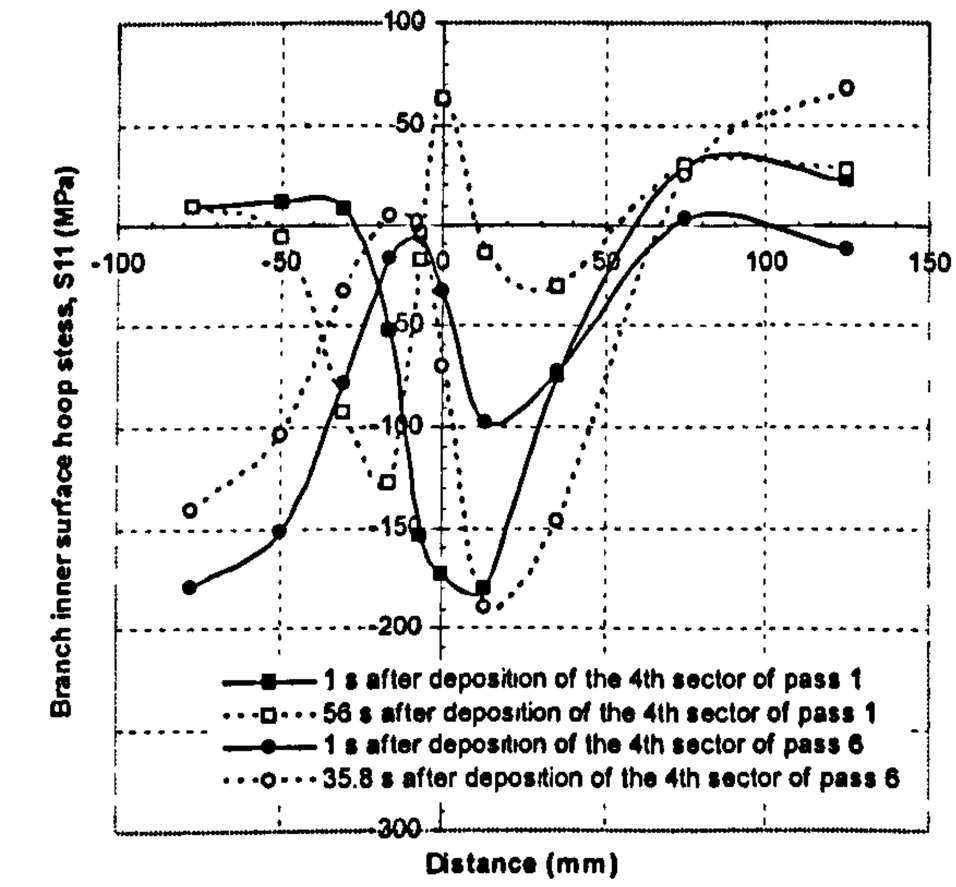

(a) Hoop stress, S_{11}

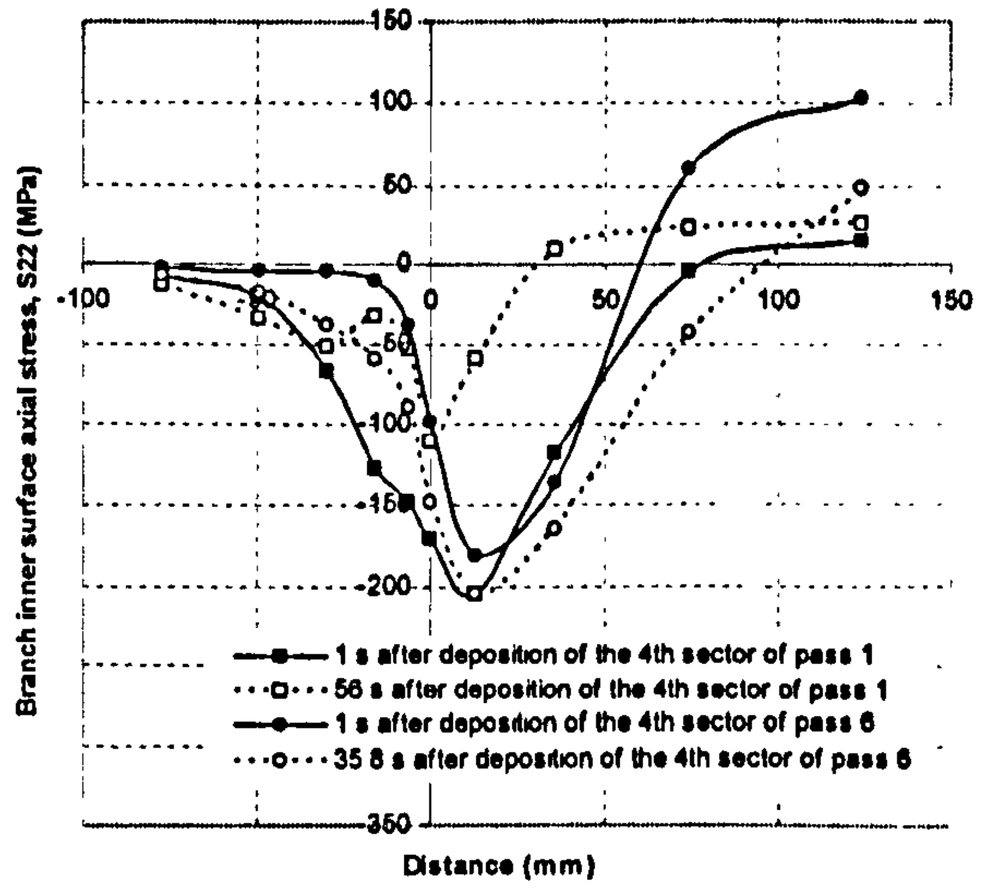

(b) Axial stress, S_{22}

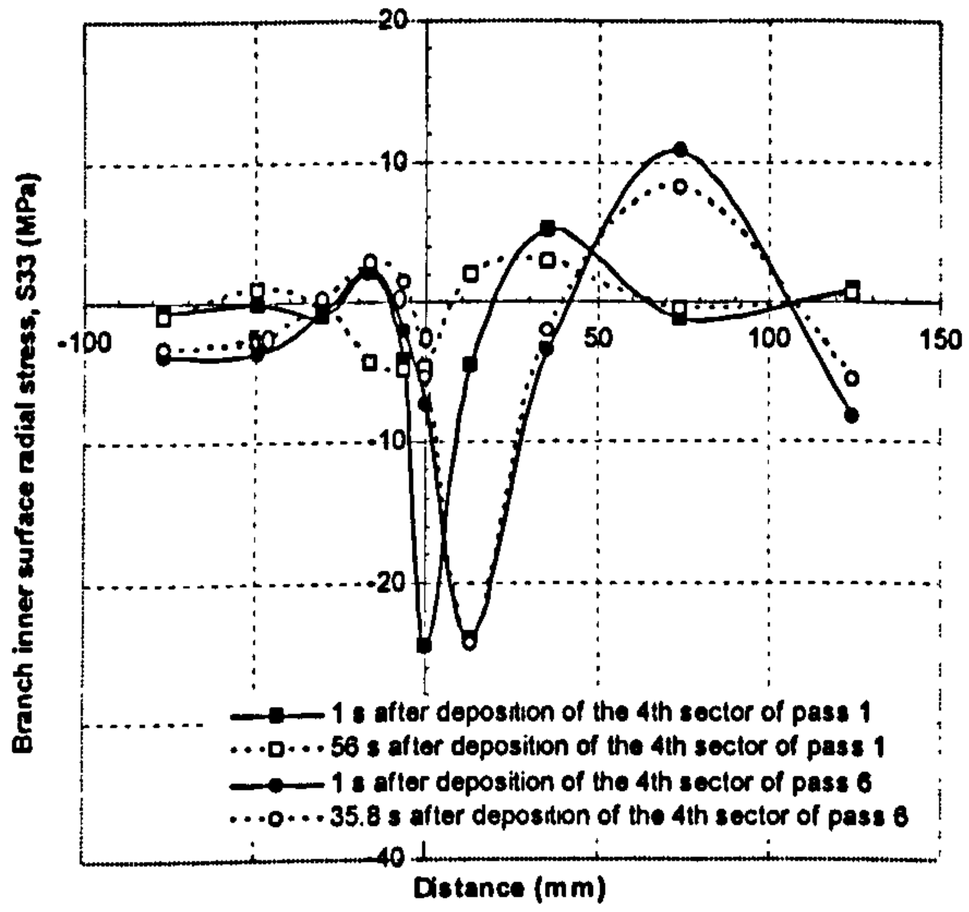

(c) Radial stress, S_{33}

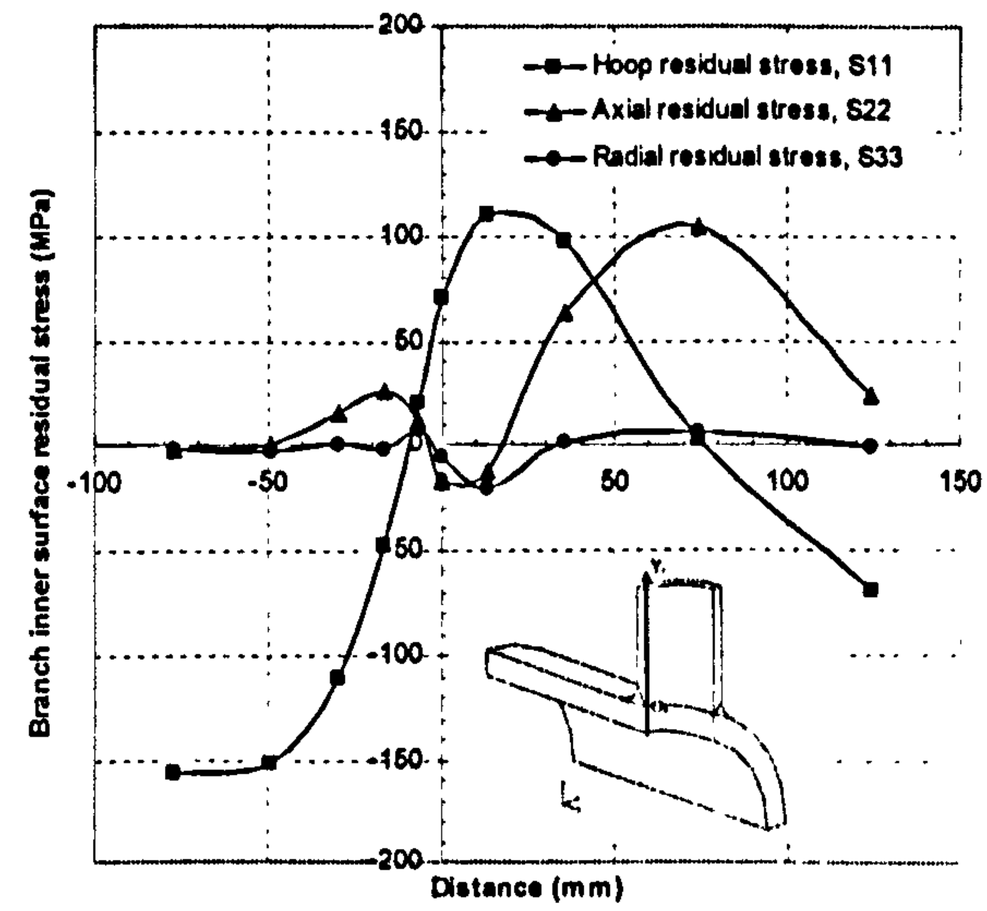

(d) Residual stress

Figure 6.52 Stresses in the Y_1-direction on the branch inner surface

Figures 6.53(a)-(c) show the stress distributions in the Y_2-direction. Similar to the observations regarding the results in Figure 6.46, it is noticed again that the first pass has negligible effect on the stress state on the outer surface of the branch pipe. Figure 6.53(d) shows residual stress distributions. Most regions, along this path, experience tensile hoop stress, with a peak value of 180MPa at the origin. Compressive axial residual stresses are limited to an area within 22% of the branch pipe thickness from the origin beyond which tensile axial residual stresses are shown to exist for the rest of the

region along the Y_2-direction. As noted earlier, radial residual stresses are rather small in magnitude and can again be considered as negligible.

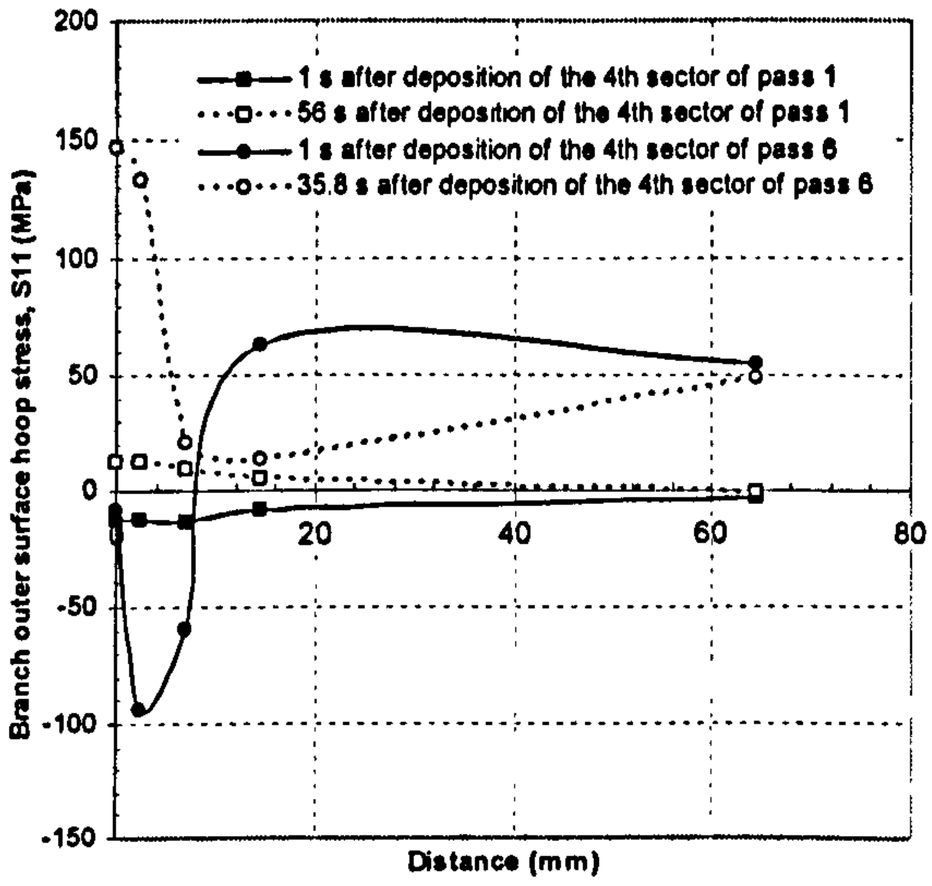

(a) Hoop stress, S_{11}

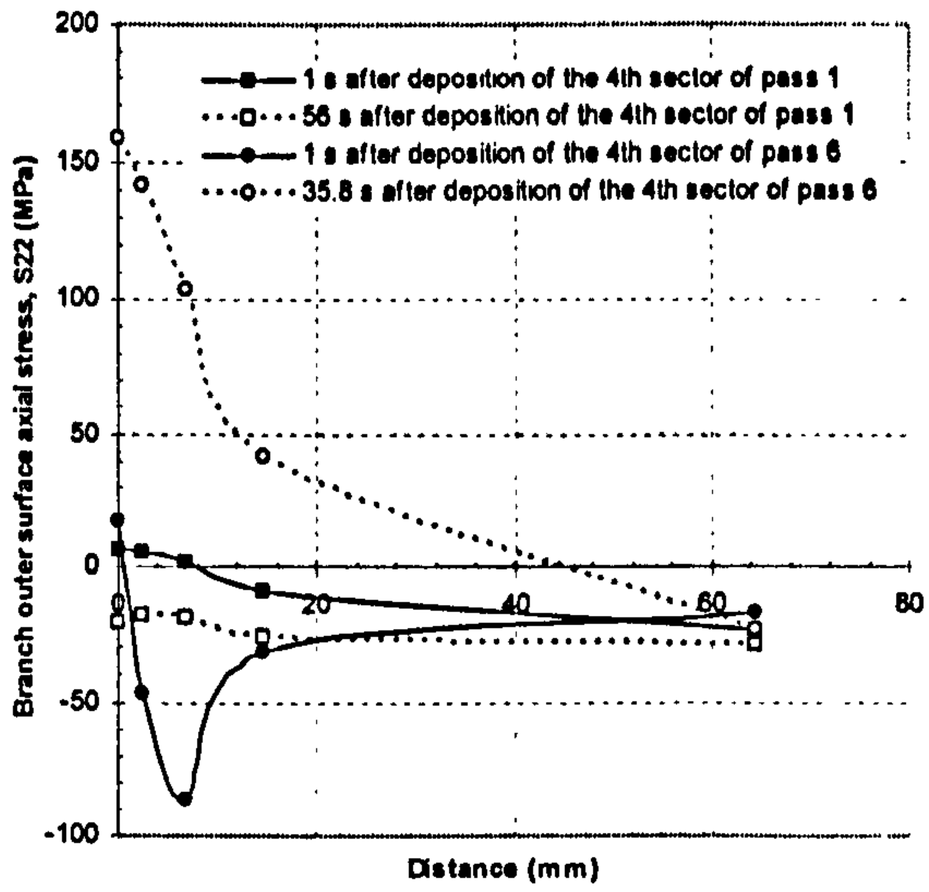

(b) Axial stress, S_{22}

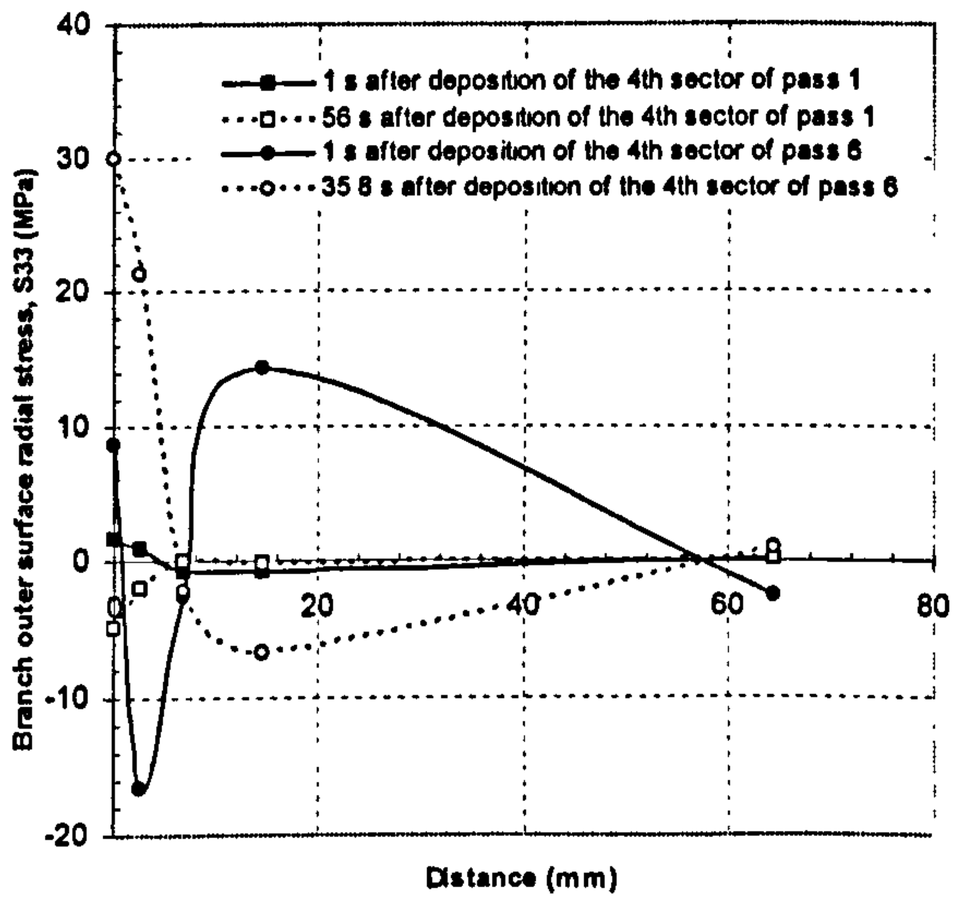

(c) Radial stress, S_{33}

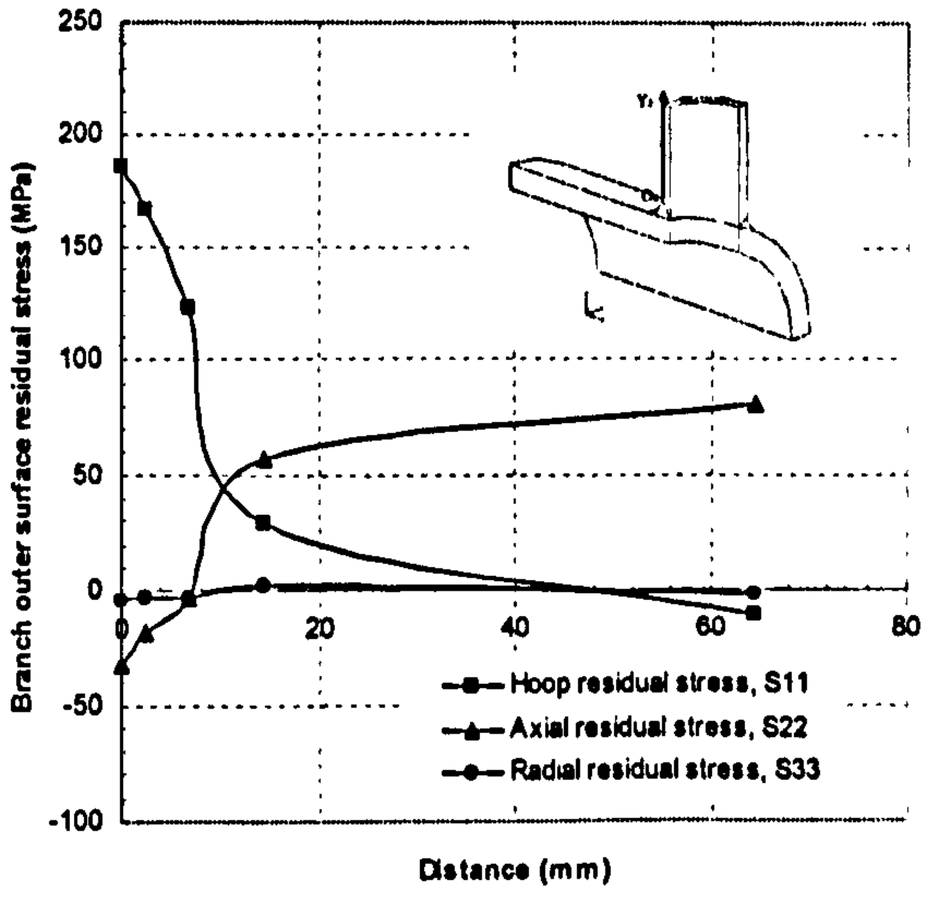

(d) Residual stress

Figure 6.53 Stresses in the Y_2-direction on the branch outer surface

6.3.3.4 Circumferentially along Curve *A*

The stresses along the weldline on the outer surface of the run (Curve *A*) and branch (Curve *B*) pipes and on the inner surface around the intersection (Curve *C*) in the tee branch junction during the deposition of the selected passes are presented in Figures 6.54 to 6.65. Each curve in the figures presents the transient thermal stress distribution along the weldline at the end of deposition of each sector.

Figure 6.54 shows the tangential stress distributions along Curve *A*. Since previous

passes have negligible effect on the stress state along Curves *A* and *B*, as discussed in Section 6.3.3.2 and 6.3.3.3, the stress evolutions during these passes are not presented.

It can be seen from Figure 6.54(a) that at the end of deposition of the first sector, i.e. at t=35.8s, a uniform tensile stress of 150MPa (54%σ_y) appears within the deposited sector and then decreases rapidly. A steep stress gradient is observed within the second sector. The tangential stresses vary between small tension and compression along the rest of the circumferential weldline. Similar stress distributions appear while welding the subsequent sectors. However, higher peak tensile stresses are observed in the previously deposited sectors as the heat source moves from 0° to 90°. High tensile stresses are mainly located within Quadrant *I*, with a peak value of 170MPa at 22.5°.

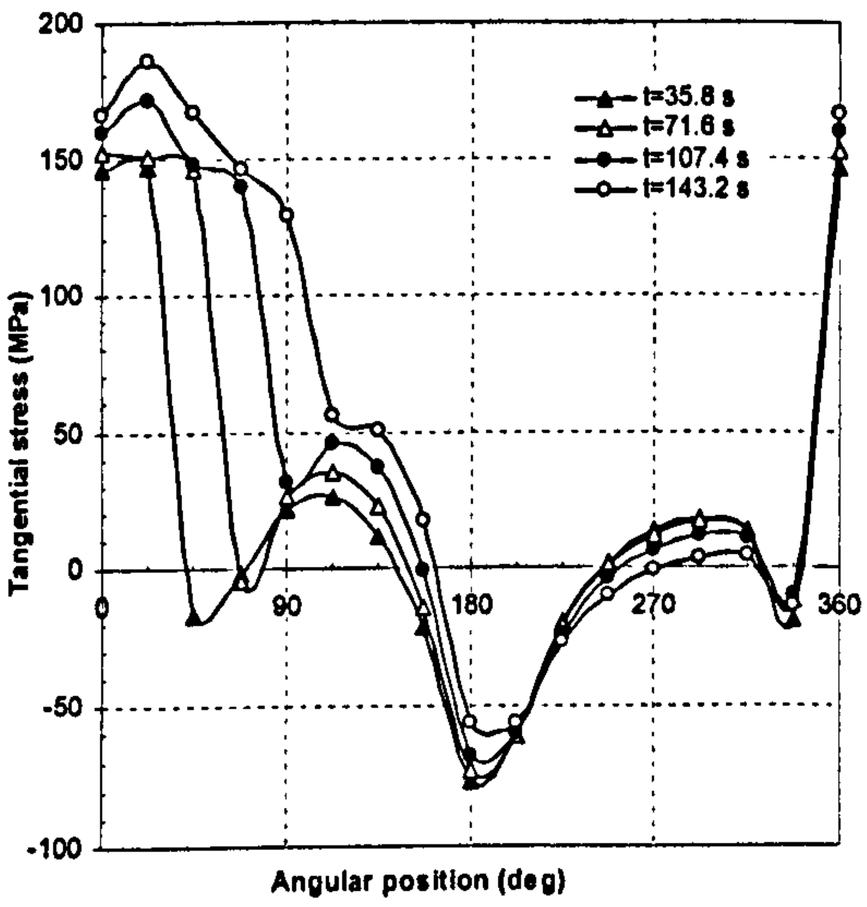

(a) Welding Quadrant *I*

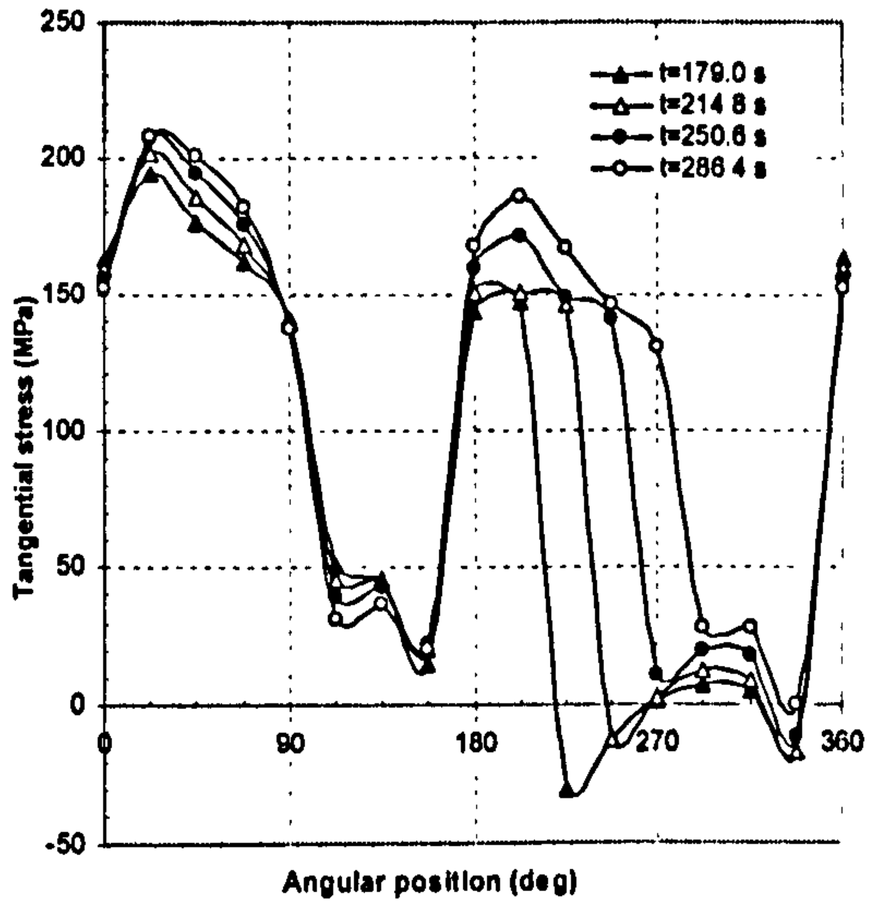

(b) Welding Quadrant *III*

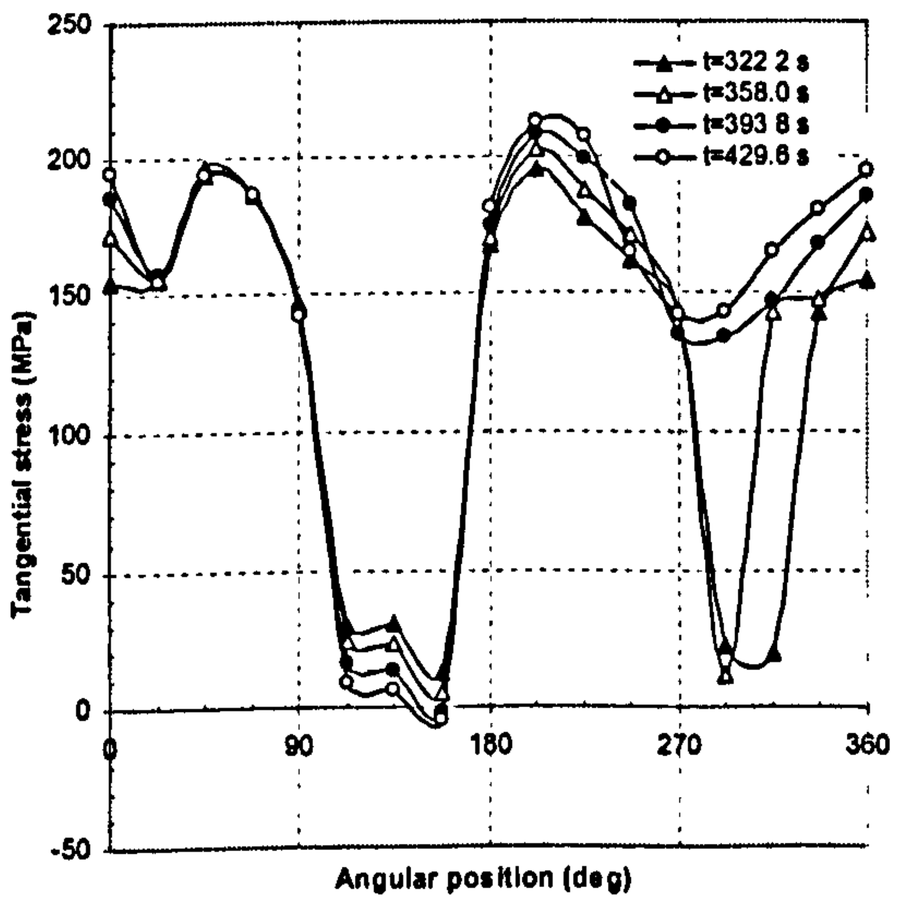

(c) Welding Quadrant *IV*

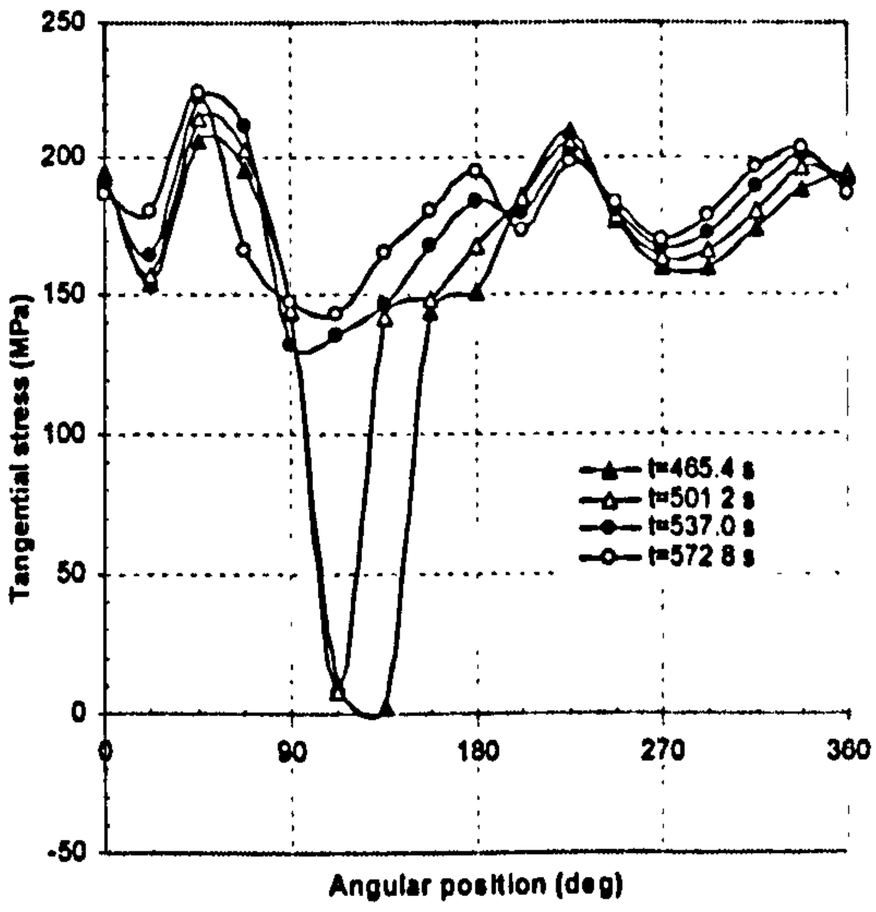

(d) Welding Quadrant *II*

Figure 6.54 Tangential stress distributions along Curve *A* at the end of deposition of each sector of the sixth pass

Figure 6.54(b) shows the stress distributions when welding proceeds to Quadrant *III*. The stress distribution patterns in Quadrant *III* are similar to those of Quadrant *I* in Figure 6.54(a). As the heat source moves in Quadrant *III*, the previously deposited sectors in Quadrant *I* cool down and the peak temperature gradually reduce to 300°C (See Figure 6.32). The tangential stress in Quadrant *I* then gradually increase up to the yield stress at the corresponding temperature. The peak tensile stress in Quadrant *I* is seen to increase to a value of 220MPa (80%σ_y) at 22.5°.

The stresses remain at high tensile levels in Quadrants *I* and *III* as welding proceeds to Quadrant *IV*, as shown in Figure 6.54(c). Stresses in Quadrant *II* are tensile and relatively small in magnitude. While welding the last quadrant, the tangential stresses in Quadrant *II* increase from small tensile to relatively high tensile. Stresses in the rest of the quadrants remain at high levels, varying from 47%σ_y to 83%σ_y.

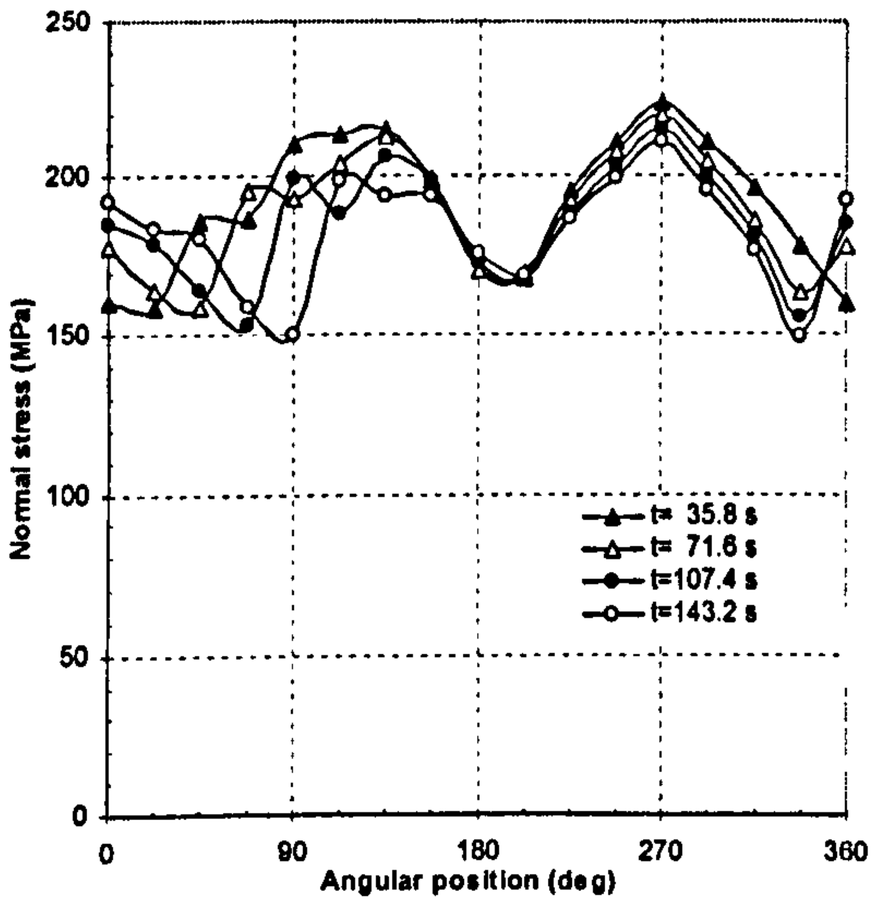

(a) Welding Quadrant *I*

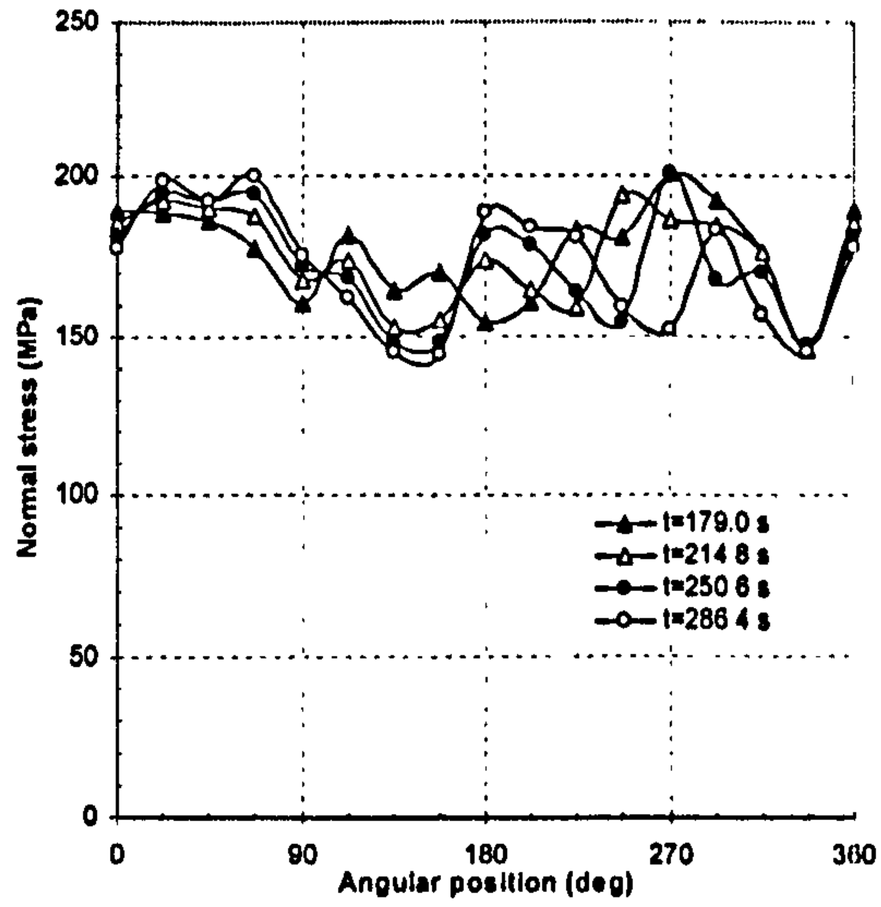

(b) Welding Quadrant *III*

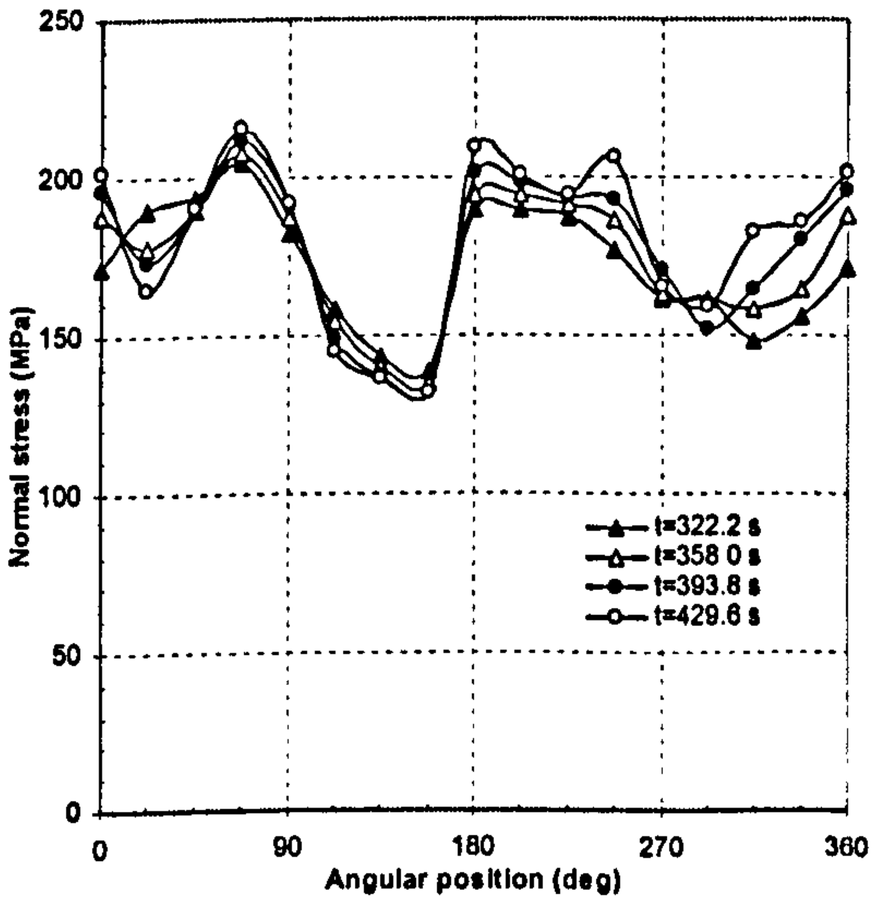

(c) Welding Quadrant *IV*

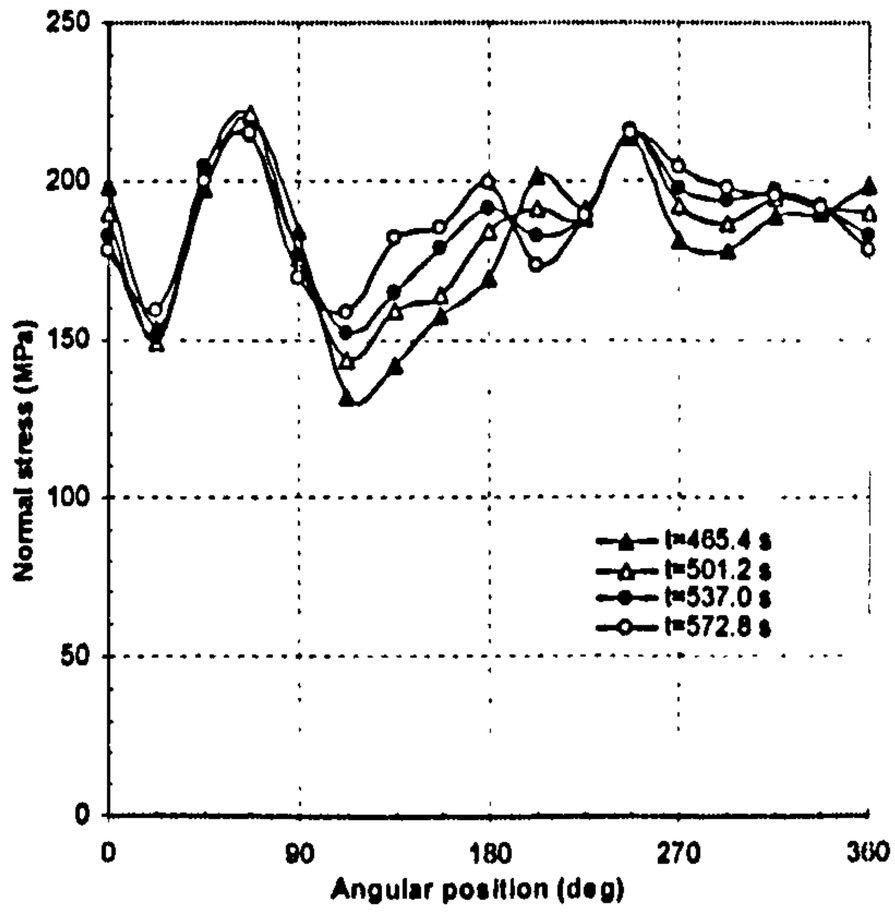

(d) Welding Quadrant *II*

Figure 6.55 Normal stress distributions along Curve *A* at the end of deposition of each sector of the sixth pass

Figure 6.55 shows the normal stress distribution on Curve *A*. These normal stresses vary between 130 (47%σ_y) and 220MPa (80%σ_y).

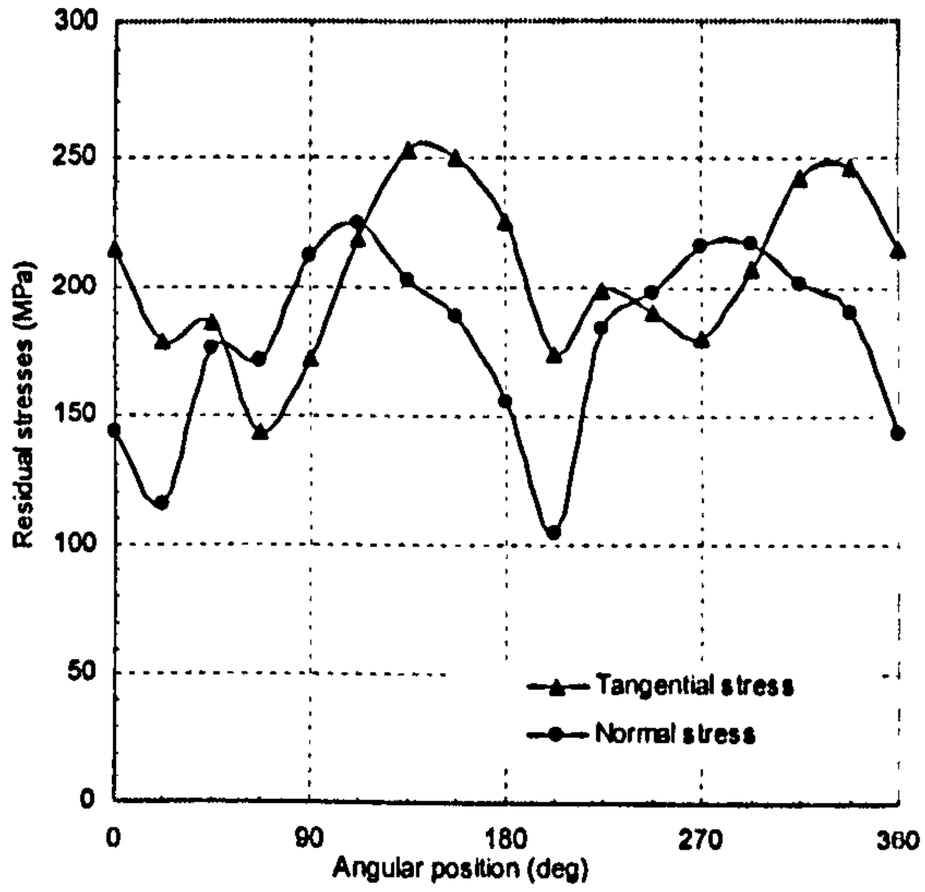

Figure 6.56 Residual stresses along Curve *A*

The residual stresses along Curve *A* are depicted in Figure 6.56. It is noticed that both the tangential and normal stresses along Curve *A* are in tension. Two regions of high stress levels are observed. The first region is within 90°-180°, with a peak tangential stress of 255MPa (92%σ_y) at 135° and a peak normal stress of 220MPa (80%σ_y) at 112.5°, respectively. The second region is within 270°-360°, with a peak tangential stress of 250MPa at 315° and a peak normal stress of 210MPa at 270°, respectively. There is no distinct symmetrical feature for these distributions.

6.3.3.5 Circumferentially along Curve *B*

Figure 6.57 presents the tangential stress distributions along Curve *B* after deposition of each sector during welding of the last pass. It is noticed that after deposition of the each sector, the deposited sector reaches tensile stresses between 150-180MPa. Stresses in the previously deposited quadrants increase to higher tensile stresses than those in the current quadrant. The peak tangential stress can be as high as 240MPa (86%σ_y).

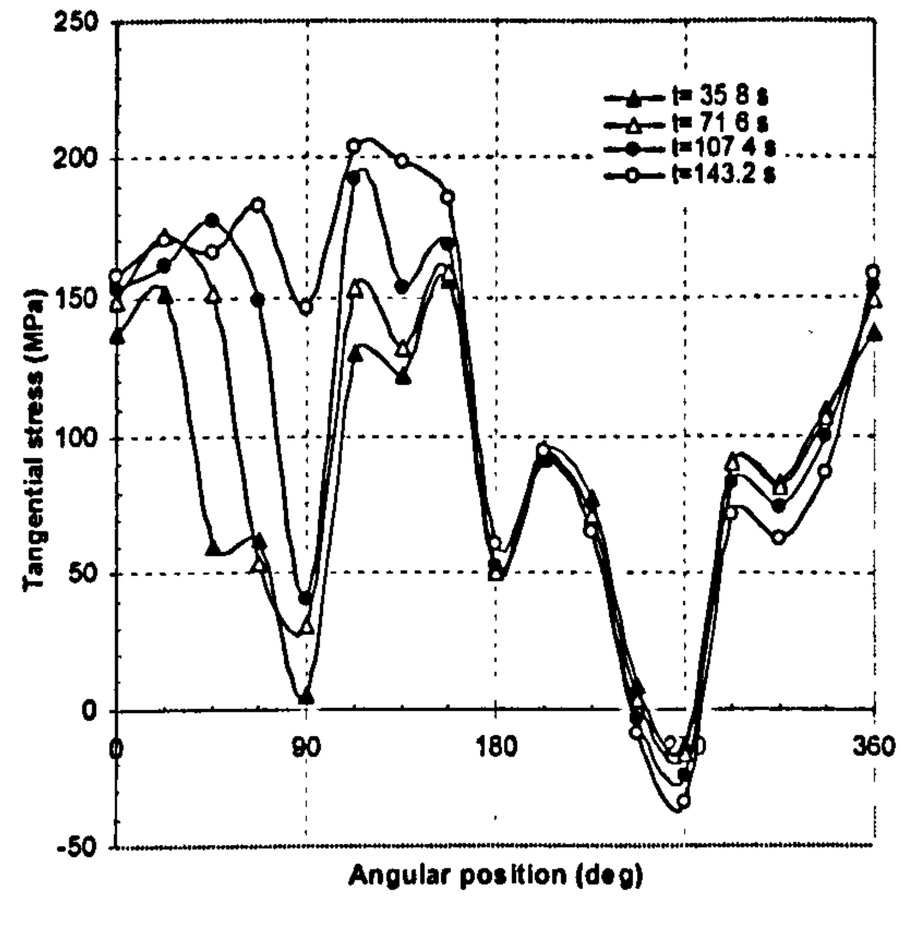

(a) Welding Quadrant *I*

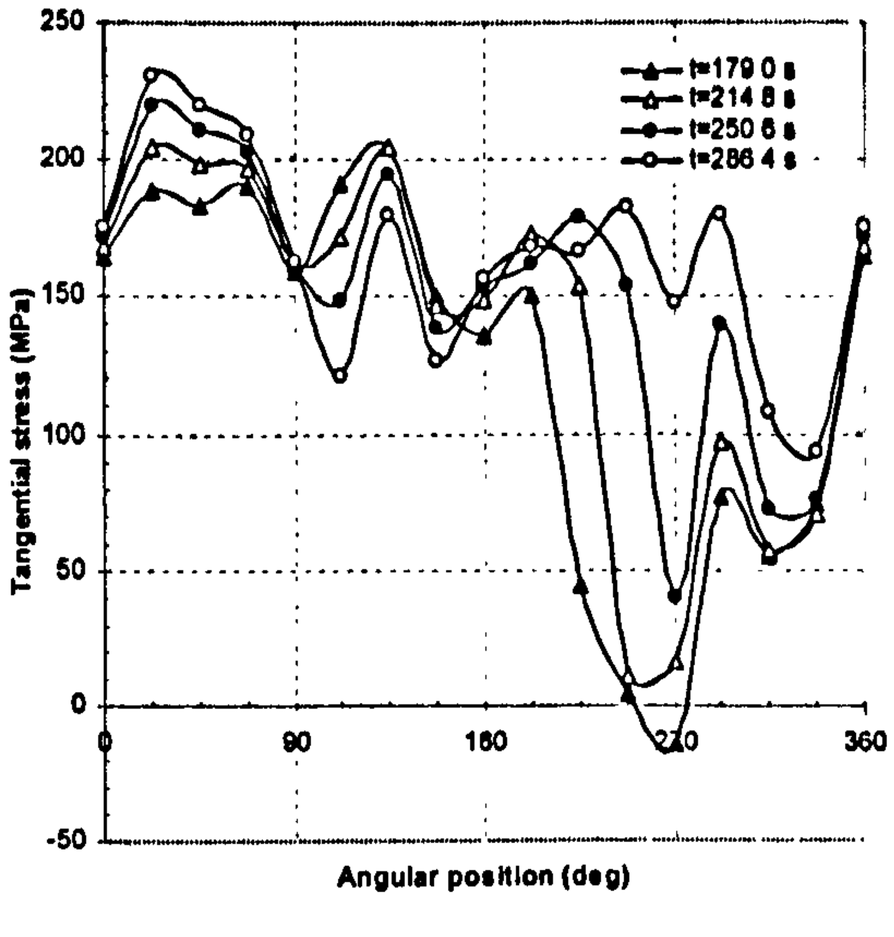

(b) Welding Quadrant *III*

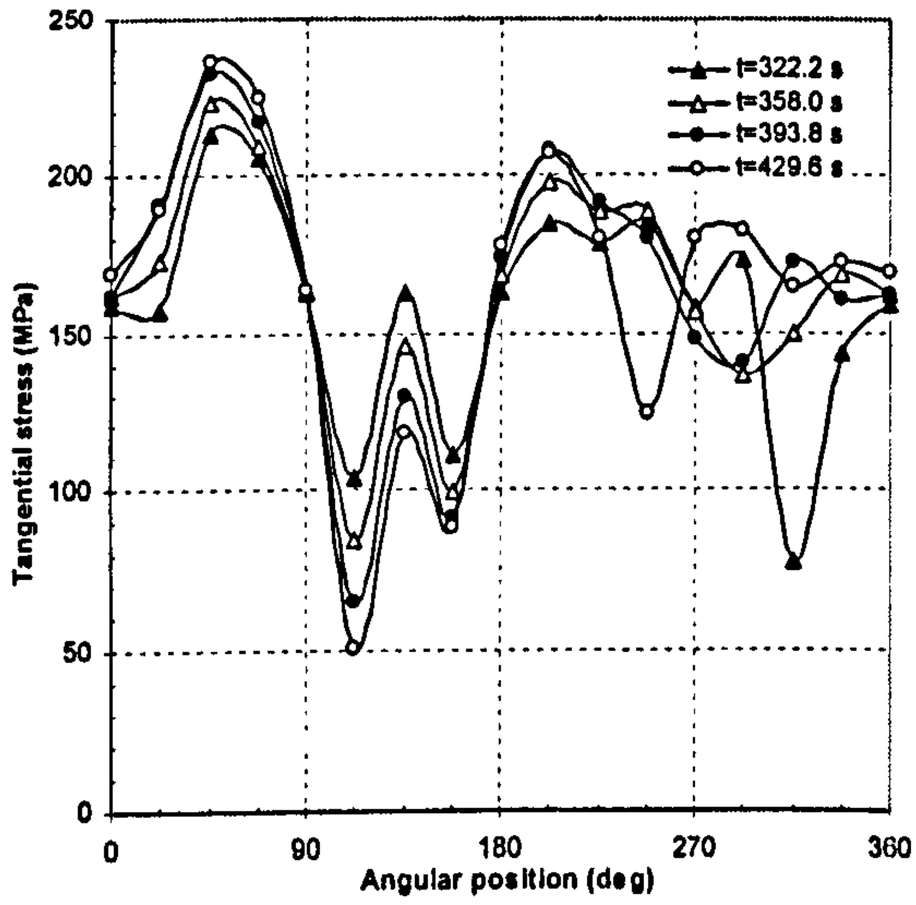

(c) Welding Quadrant *IV*

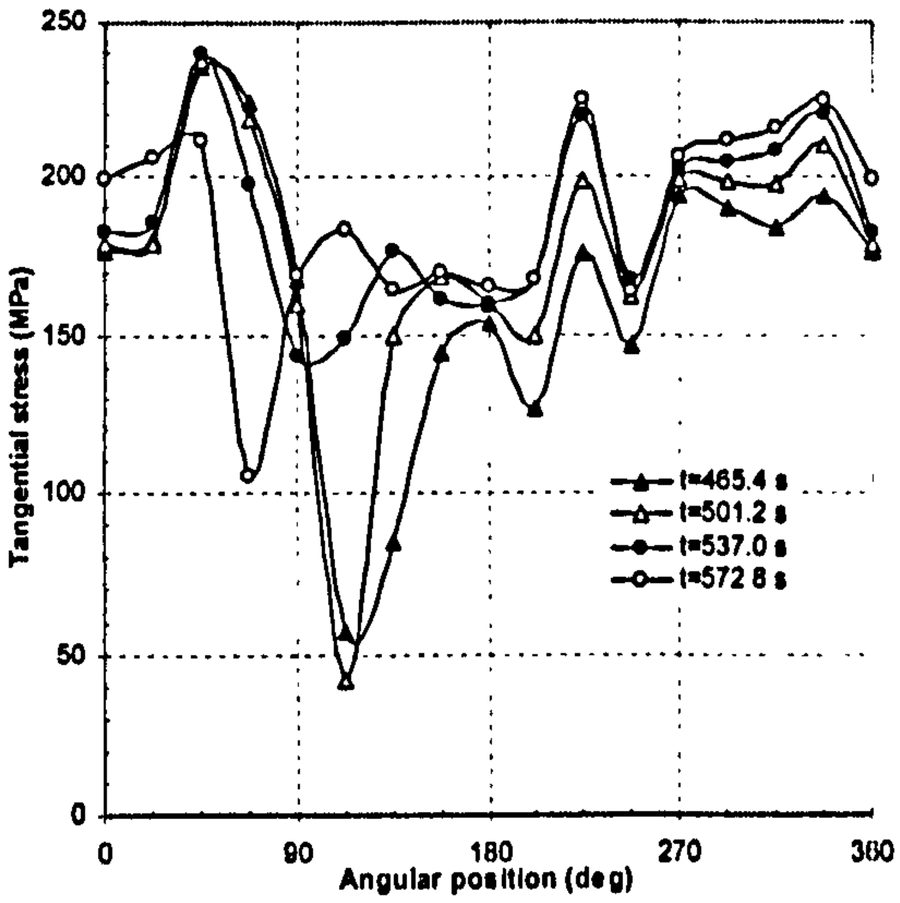

(d) Welding Quadrant *II*

Figure 6.57 Tangential stress distributions along Curve *B* at the end of deposition of each sector of the sixth pass

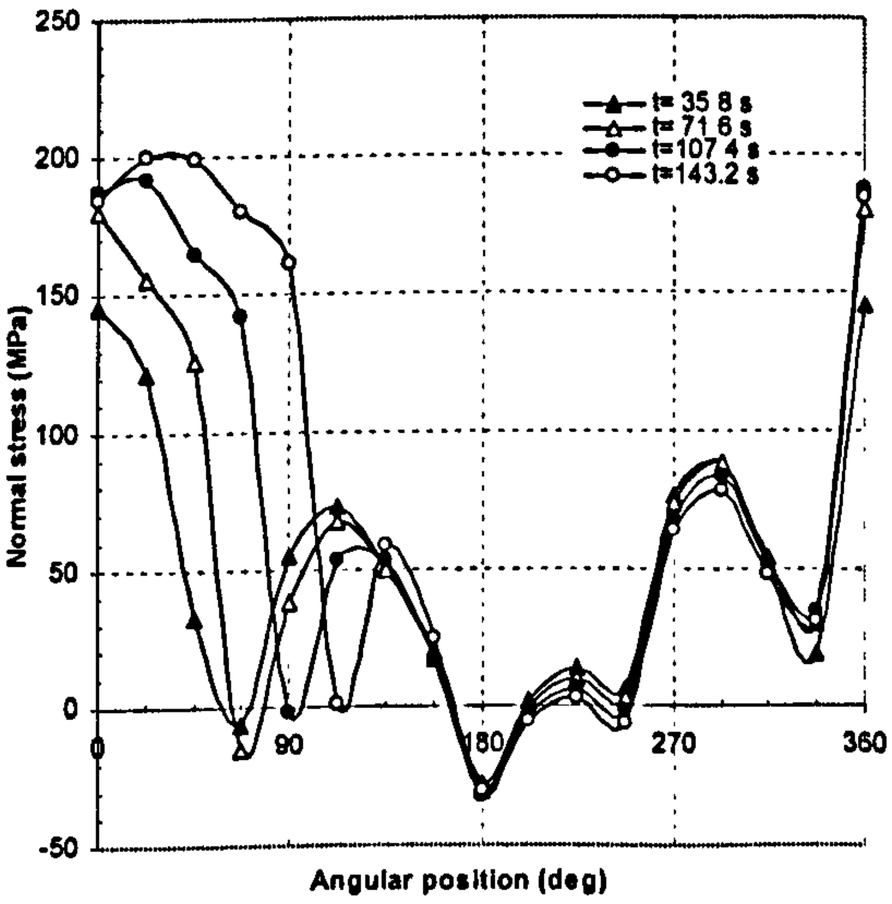

(a) Welding Quadrant *I*

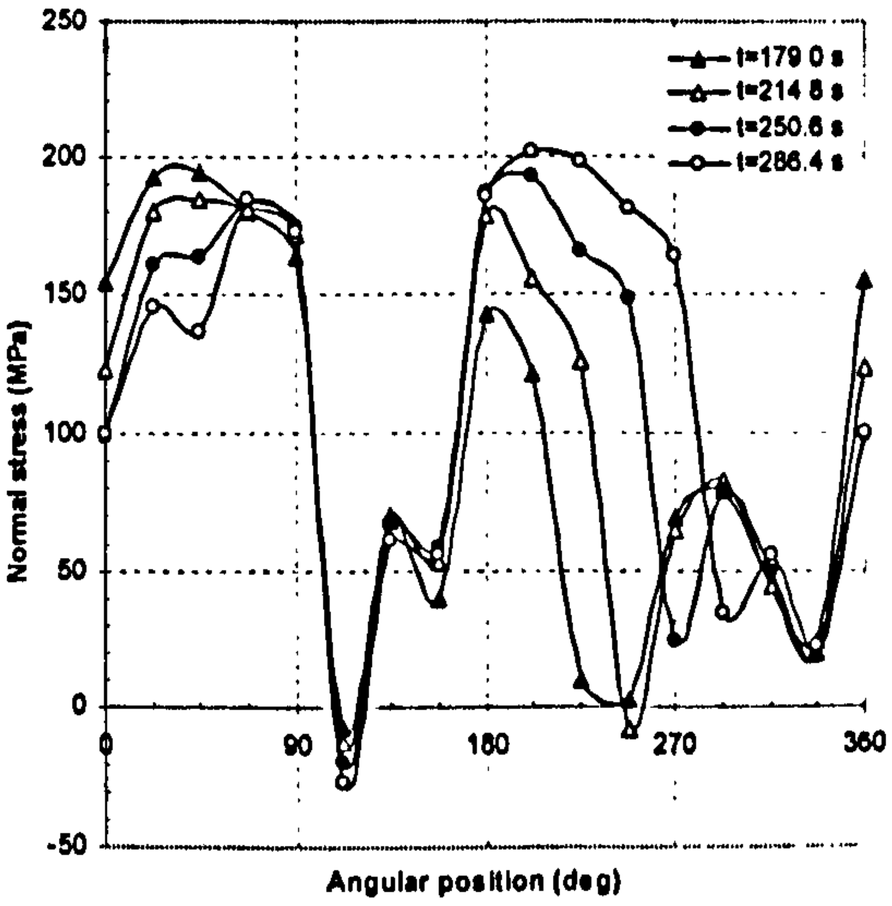

(b) Welding Quadrant *III*

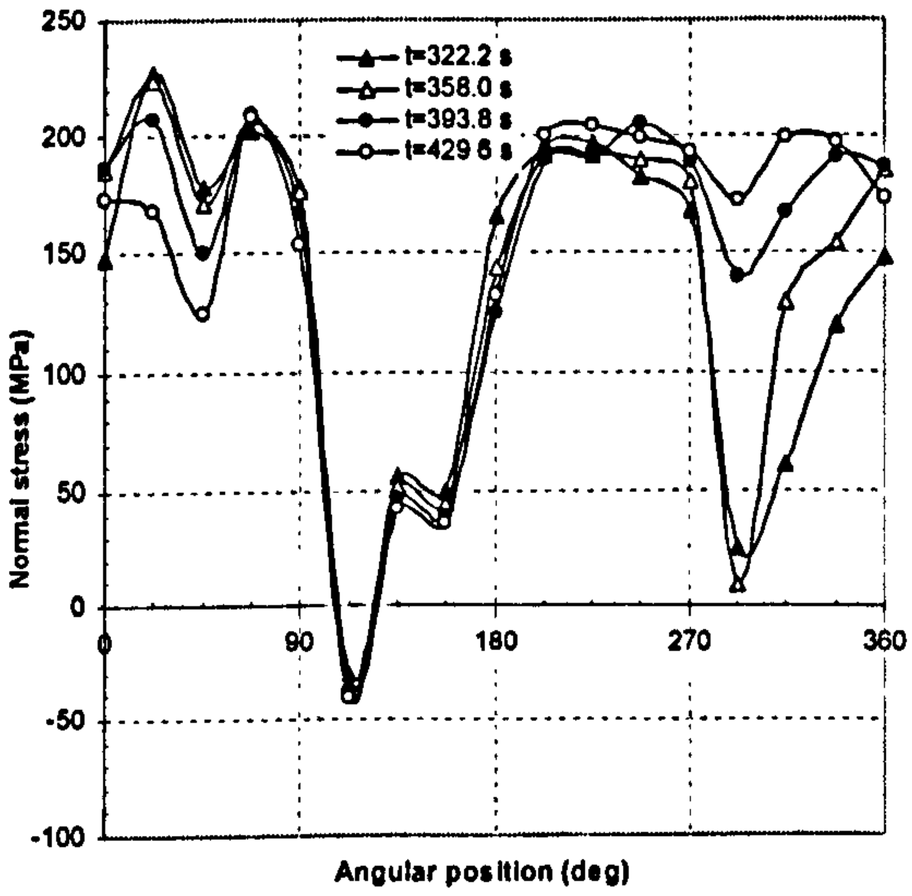

(c) Welding Quadrant *IV*

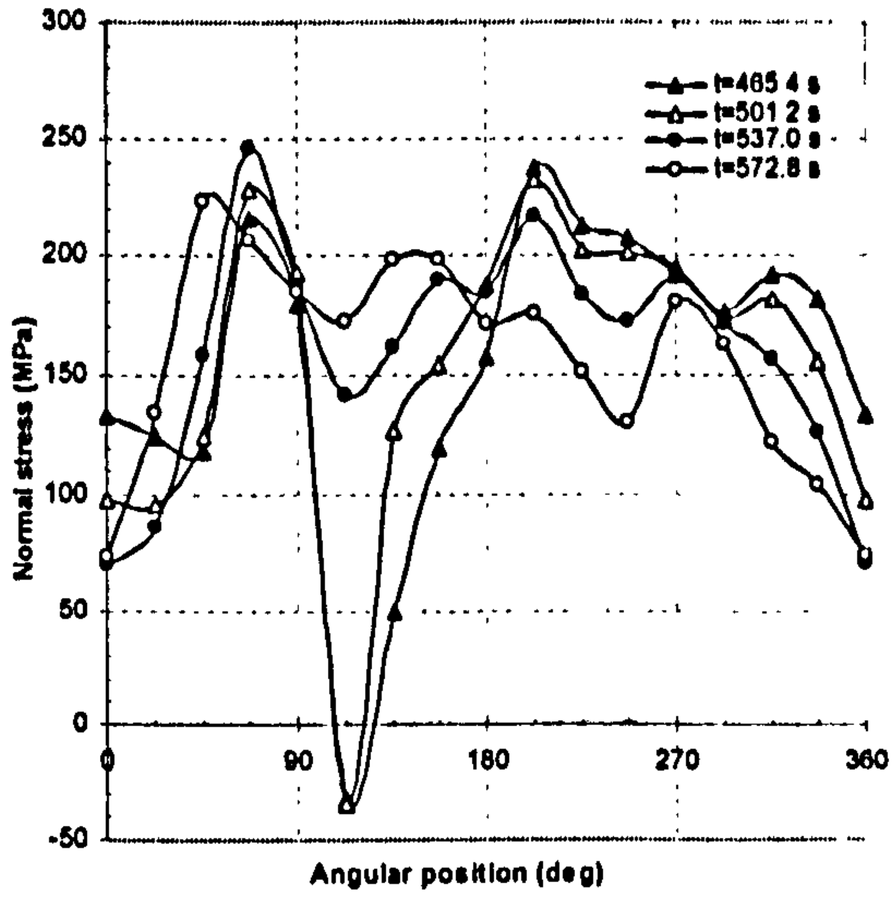

(d) Welding Quadrant *II*

Figure 6.58 Normal stress distributions along Curve *B* at the end of deposition of each sector of the sixth pass

Figure 6.58 shows the normal stress distributions along Curve *B*. Similar stress evolution patterns to those in Figure 6.54 are observed.

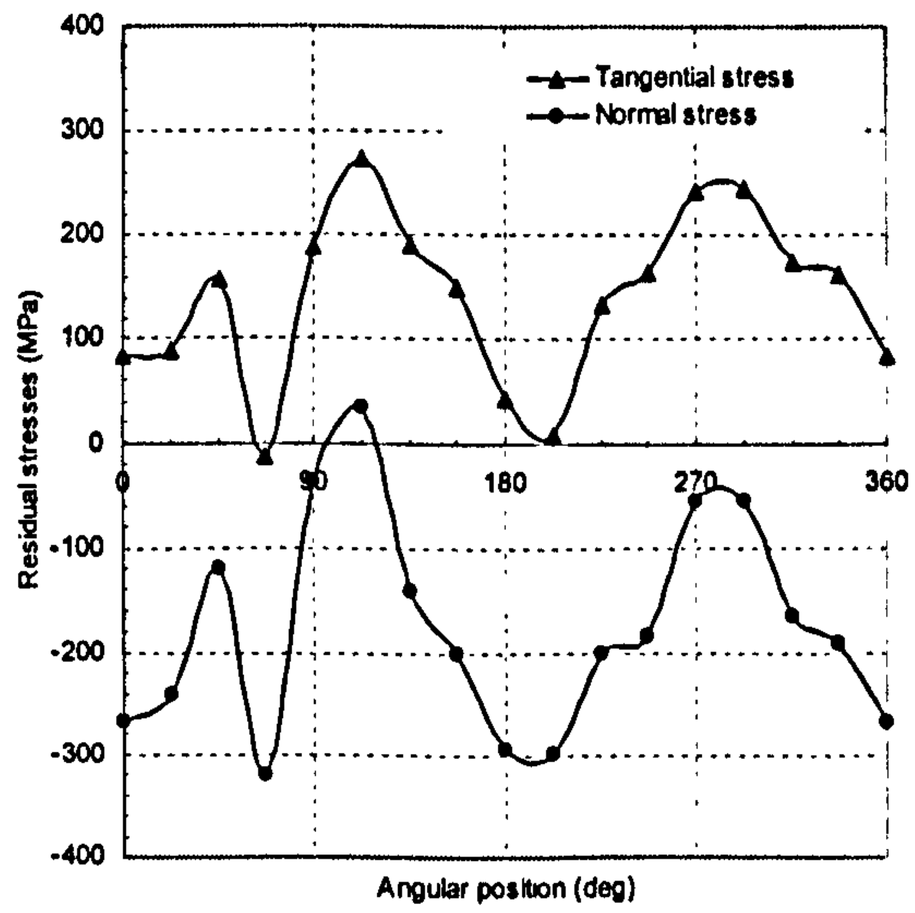

Figure 6.59 Residual stresses along Curve *B*

Figure 6.59 shows the residual stresses along Curve *B*. It is noticed that the tangential stresses along Curve *B* are mostly tensile with magnitudes varying between -10 to 275MPa. High tangential stresses are located within the regions between 90°-135° and 250°-300°, with a peak magnitude at 112.5° from the welding start point. A similar distribution pattern can be observed for the normal residual stresses. However, the normal stresses are mostly compressive. It can be concluded from the above observation that if a defect were to develop in this region, then a shearing type mode of failure would be of most concern to the structural analyst.

6.3.3.6 Circumferentially along Curve *C*

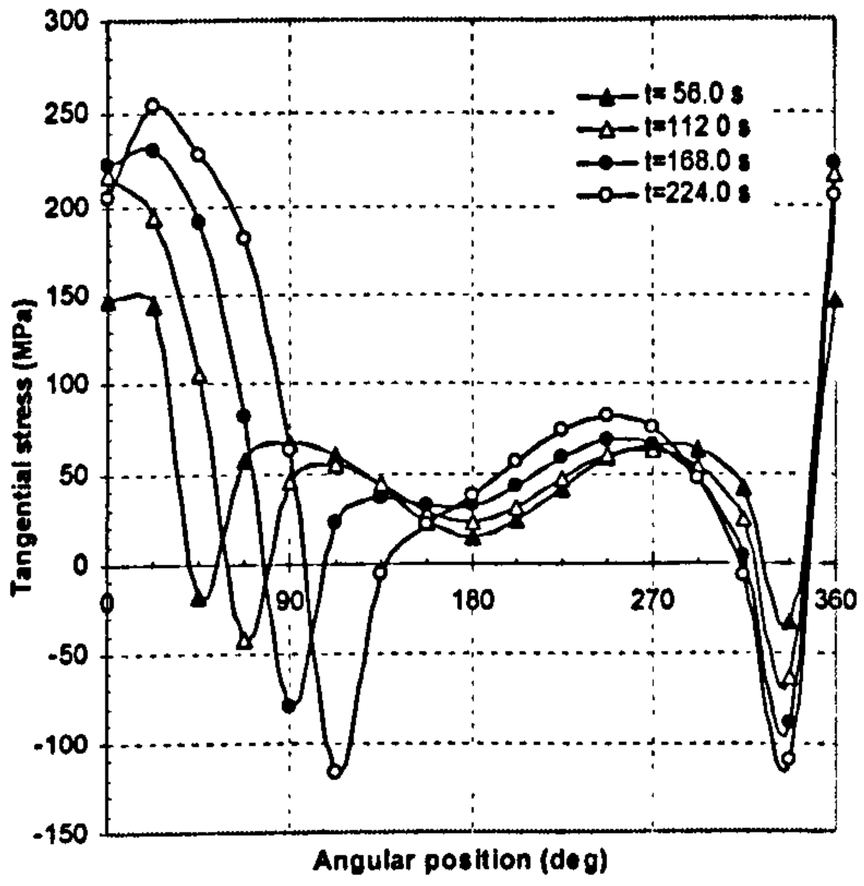

(a) Welding Quadrant *I*

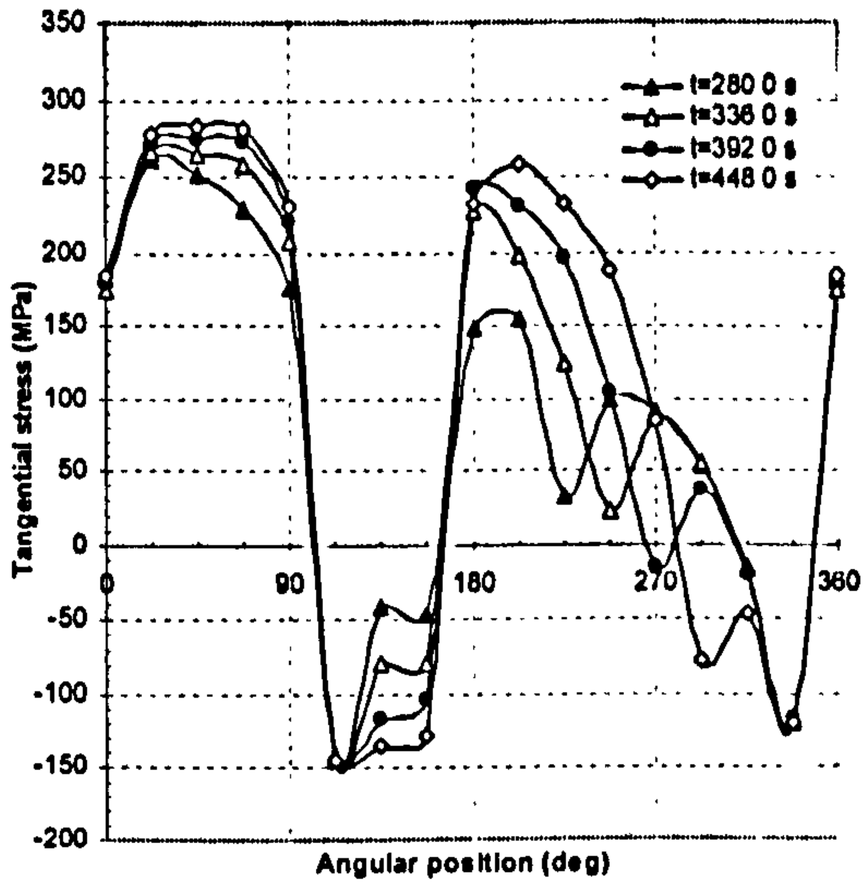

(b) Welding Quadrant *III*

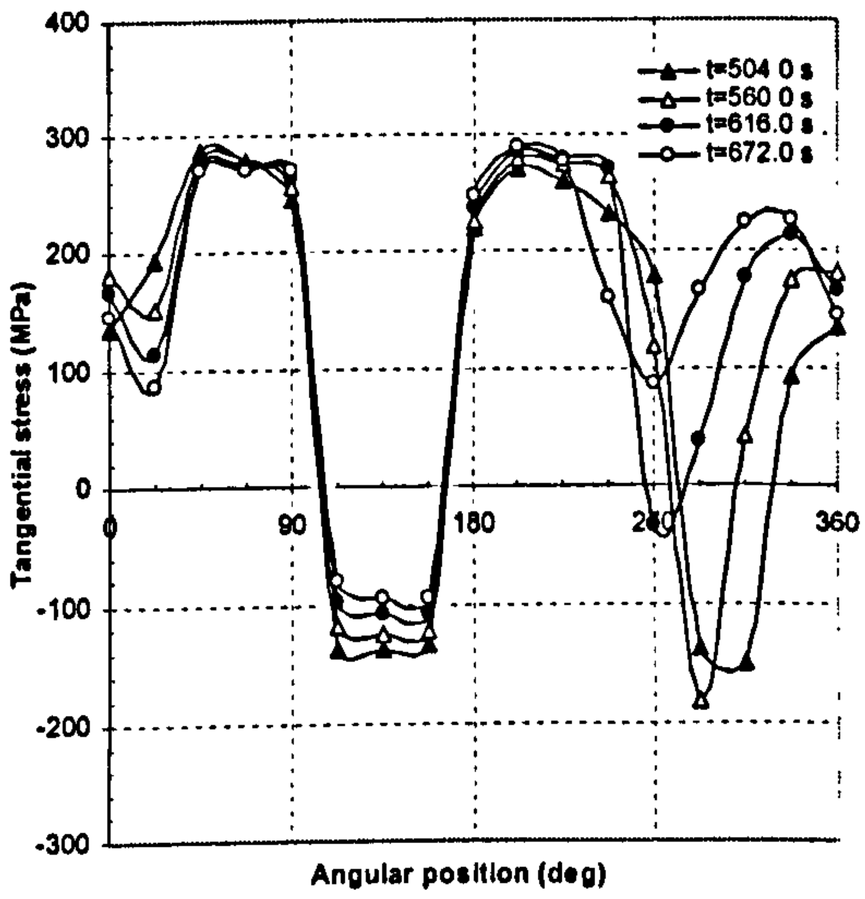

(c) Welding Quadrant *IV*

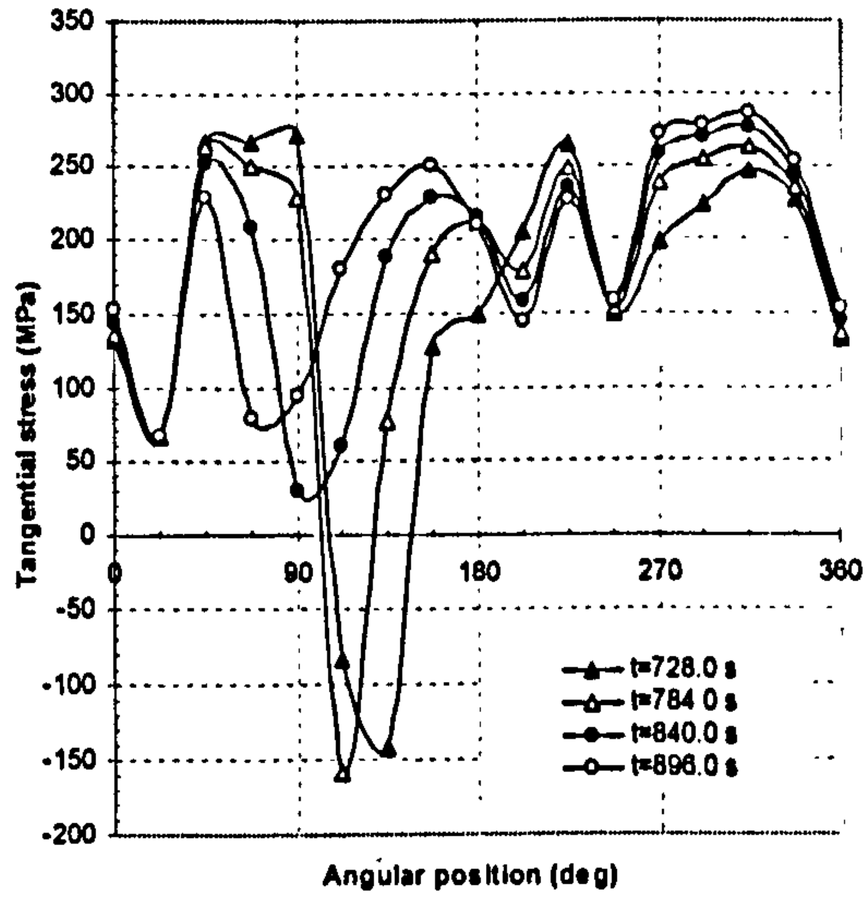

(d) Welding Quadrant *II*

Figure 6.60 Tangential stress distributions along Curve *C* at the end of deposition of each sector of the first pass

Figures 6.60 to 6.62 show the evolution of the tangential stress along Curve *C* after deposition of each sector during the first, third and sixth pass, respectively. It can be seen from Figure 6.60(a) that after deposition of the first sector, the peak tensile stress is 150MPa within the first sector. Small tensile and compressive stresses distribute along the rest of the circumference. Similar tangential stress distributions are observed for the following deposited sectors except that the peak tensile and compressive stresses show higher magnitudes. The reason for this may be explained by the fact that at the end of the deposition of the first sector, the deposited material does not have sufficient time to solidify. The temperature in the first sector is around 340°C (See Figure 6.34) and the

corresponding yield stress at this temperature is about 150MPa (See Figure 4.7). As the welding proceeds to the second sector, the temperature in the first sector decreases to 150-300°C, while the temperature in the second sector reaches 370°C (See Figure 6.34). Thus the tangential stress in the first sector increases to 200MPa, which corresponds to the yield stress at 150-300°C. As there is no material deposited beyond the first two sectors, stresses along the rest of the circumference of the weldline are quite small. These small tensile or compressive stresses are mainly in equilibrium with the high tensile stress in the deposited sectors.

Similar stress distributions to those of Quadrant *I* in Figure 6.60(a) are observed when welding proceeds to Quadrant *III*. At the end of welding of Quadrant *III*, the temperatures in Quadrant *I* cool down to about 100°C (See Figure 6.34), thus the tangential stresses in this quadrant increase to a magnitude close to the room temperature yield stress, i.e. 278MPa. As there is still no material deposited in Quadrants *II* and *IV*, stresses in these two quadrants remain small.

Similar stress distributions are observed as welding proceeds to Quadrants *IV* and *II*. Stresses near the interface of these two quadrants are slightly changed to keep stress continuity between the two adjacent quadrants.

Figure 6.61 shows the tangential stress distributions along Curve *C* after deposition of each sector during the third pass. Since an interpass temperature of 120°C is imposed before welding the third pass, tensile tangential stresses distribute along Curve *C*.

After the deposition of the first sector of the third pass, the temperature of the corresponding first sector on Curve *C* is 500°C while the remaining areas along Curve *C* are at 120°C (See Figure 6.35). The thermal expansion of the first sector on Curve *C* is restrained by the surrounding metal where the temperatures are lower. Consequently compressive stresses are generated in the first sector, as shown in Figure 6.61(a). Similar phenomena are observed while welding proceeds to the following sectors. At the end of deposition of the fourth sectors, the temperature of the corresponding fourth sector on Curve *C* reaches 680°C, while the temperature of the first sector on Curve *C* decreases to 270-450°C (See Figure 6.35). For the same reason, the expansion in the fourth sector is restrained and thus stresses are in compression. However, the metal in

the first sector contracts and stresses increase. At the end of welding Quadrant *I*, compressive or small tensile stress appear in Quadrant *I*, while the other quadrants remain in a high tensile stress state.

Similar tangential stress distribution patterns are observed as welding proceeds to Quadrants *III*, *IV* and *II*. The previously deposited quadrants gradually cool down and thus tensile stresses are generated there.

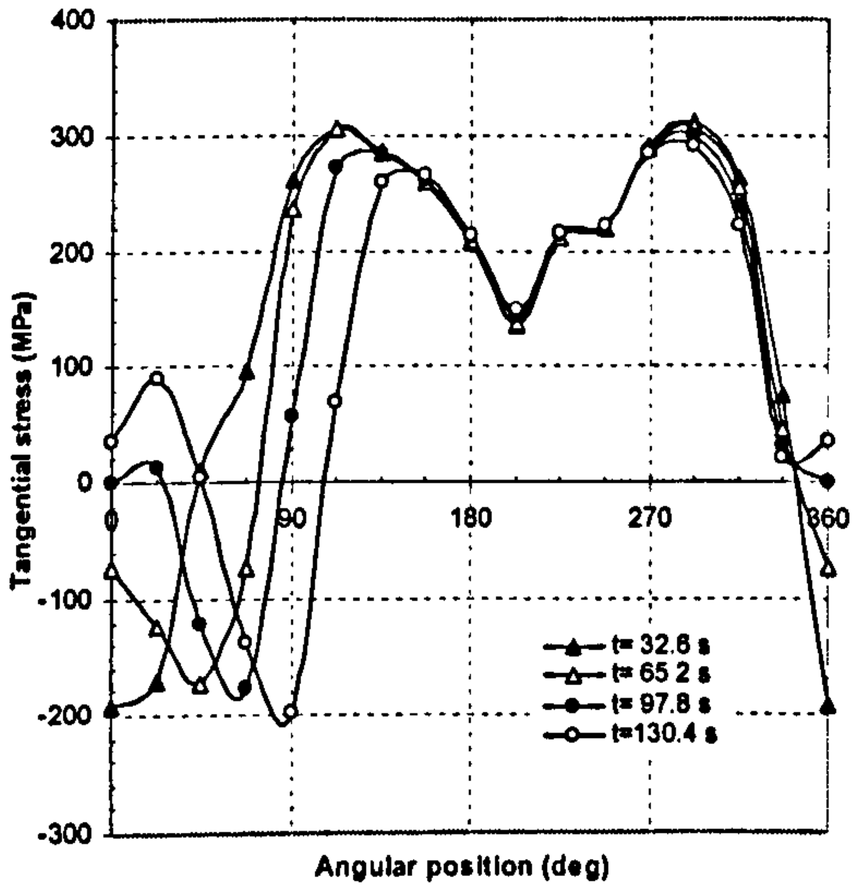

(a) Welding Quadrant *I*

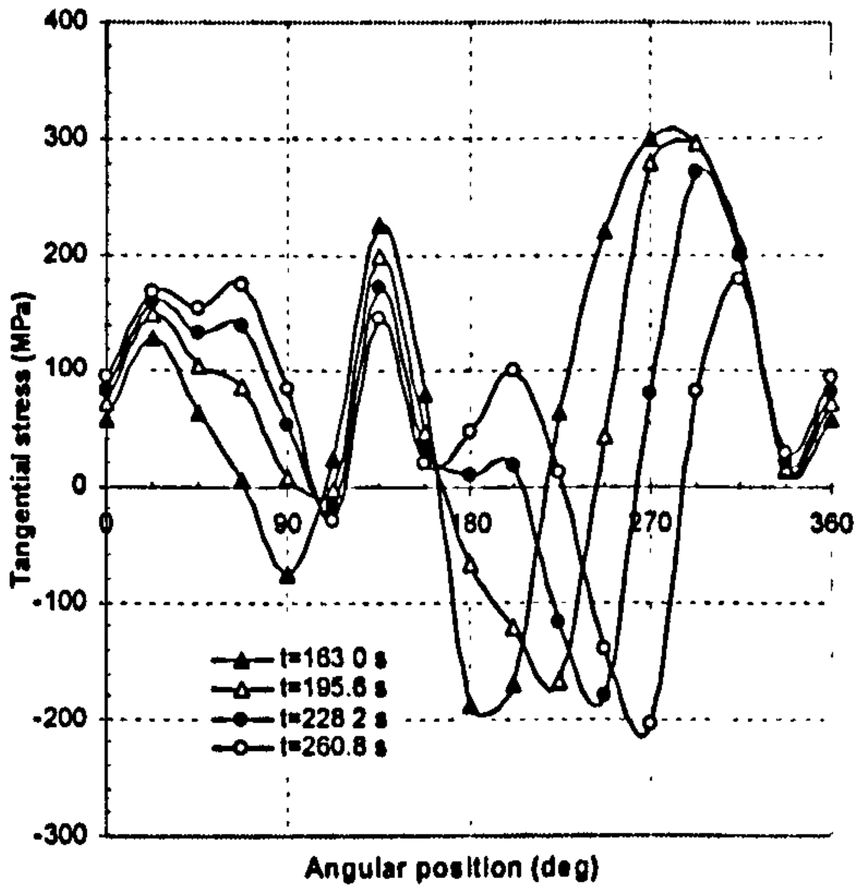

(b) Welding Quadrant *III*

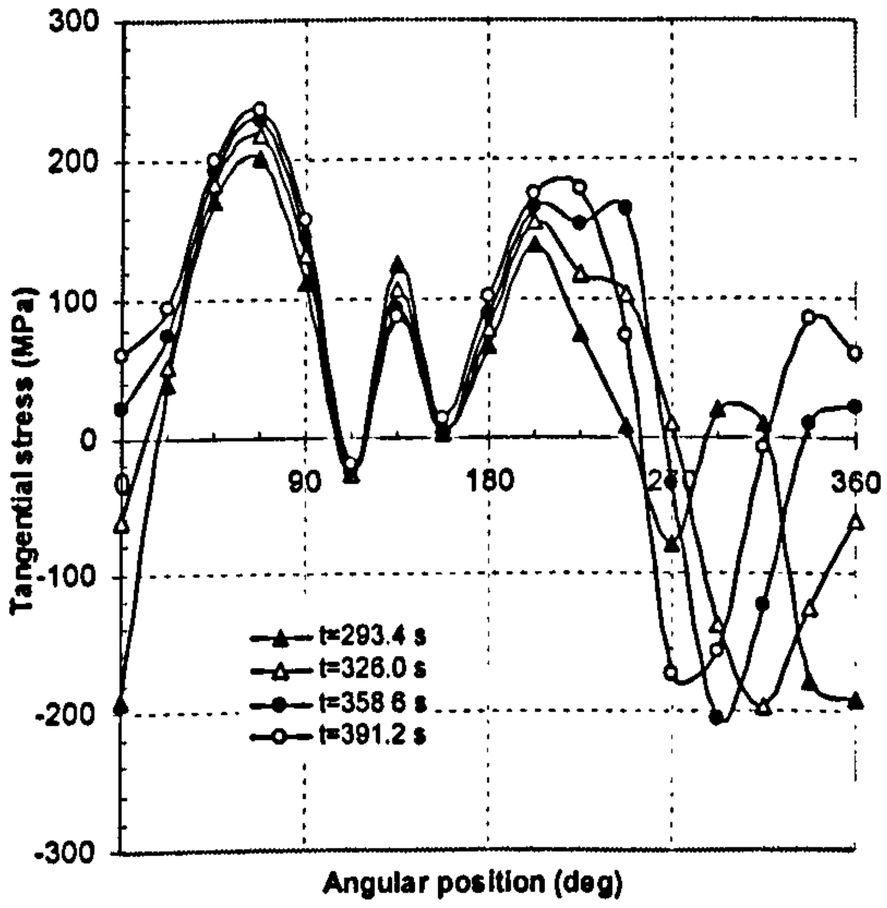

(c) Welding Quadrant *IV*

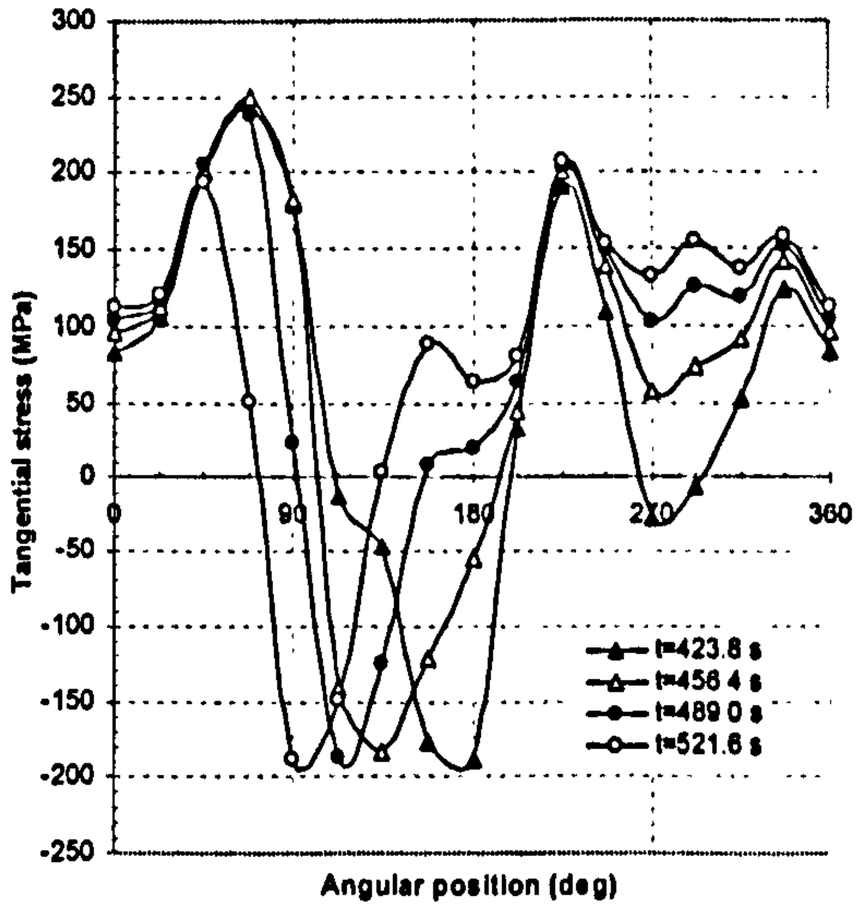

(d) Welding Quadrant *II*

Figure 6.61 Tangential stress distributions along Curve *C* at the end of deposition of each sector of the third pass

A similar tangential stress evolution to that in Figure 6.61 is observed in Figure 6.62 after the deposition of each sector during welding of the sixth pass. After welding the last pass, the temperatures in the regions along Curve *C* vary between 260 and 480°C (See Figure 6.36). These regions have a tendency to experience expansion and

are restrained by the surrounding already welded material. Thus most areas along Curve *C* are in compression.

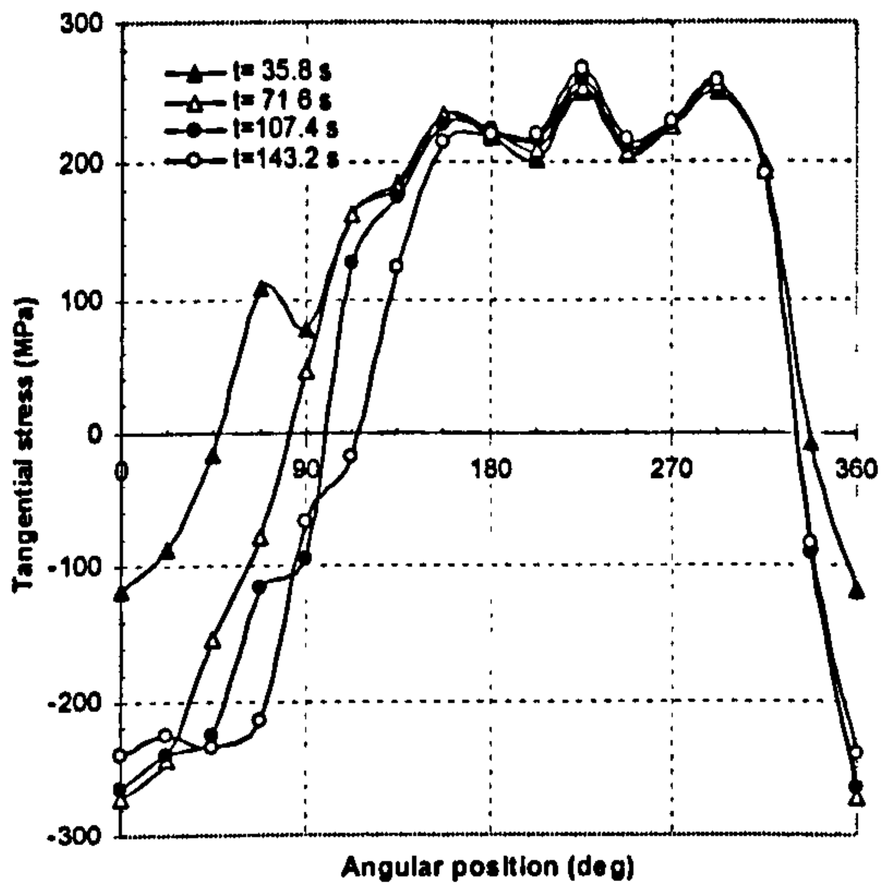

(a) Welding Quadrant *I*

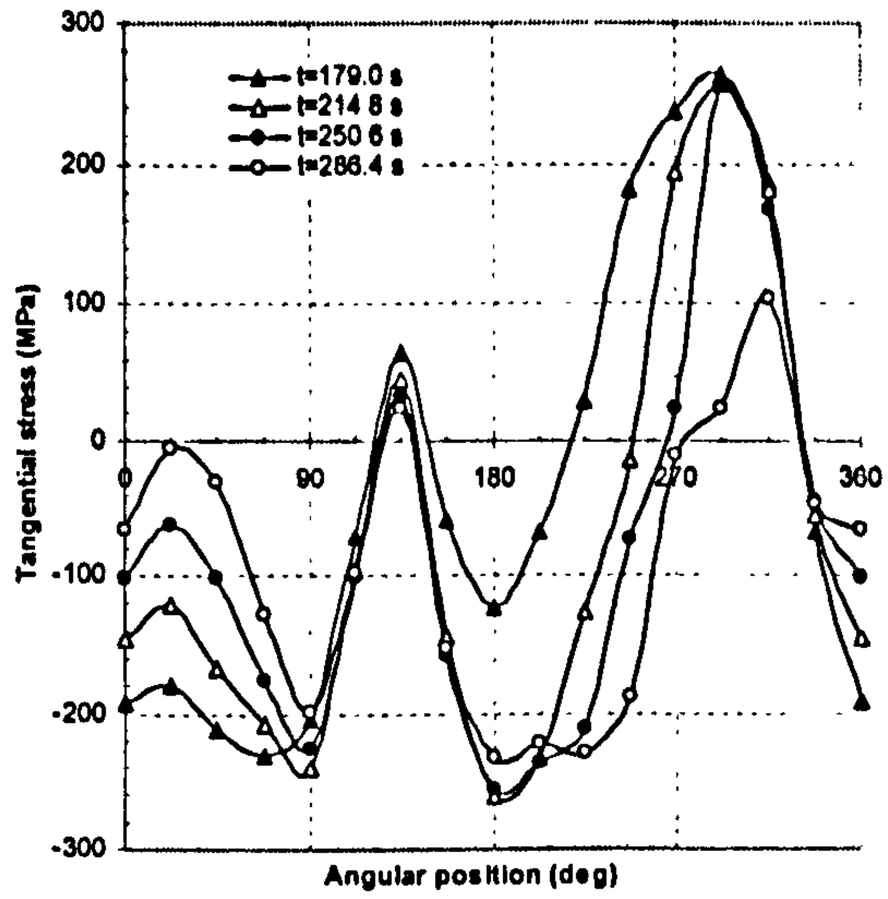

(b) Welding Quadrant *III*

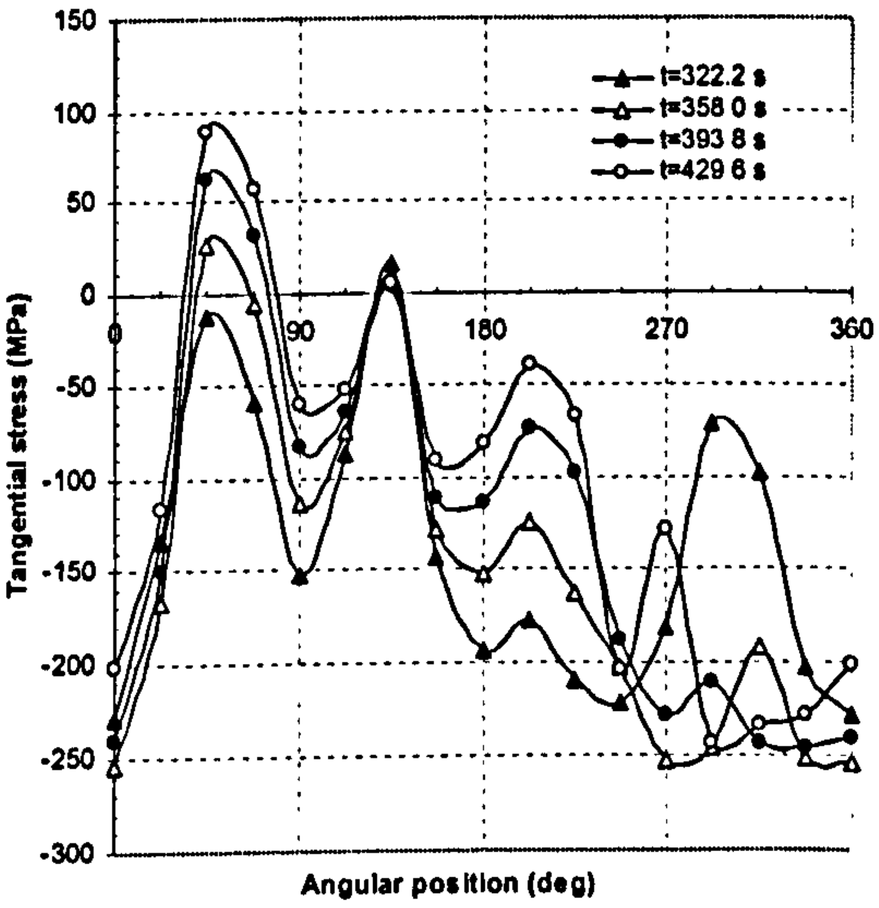

(c) Welding Quadrant *IV*

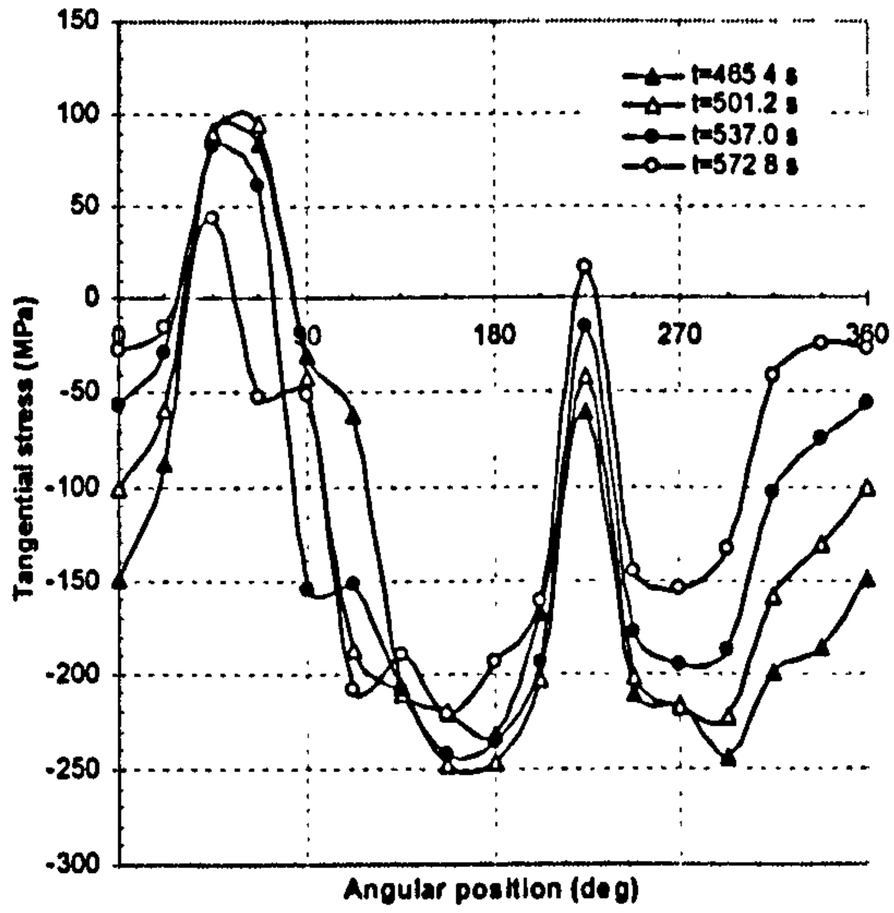

(d) Welding Quadrant *II*

Figure 6.62 Tangential stress distributions along Curve *C* at the end of deposition of each sector of the sixth pass

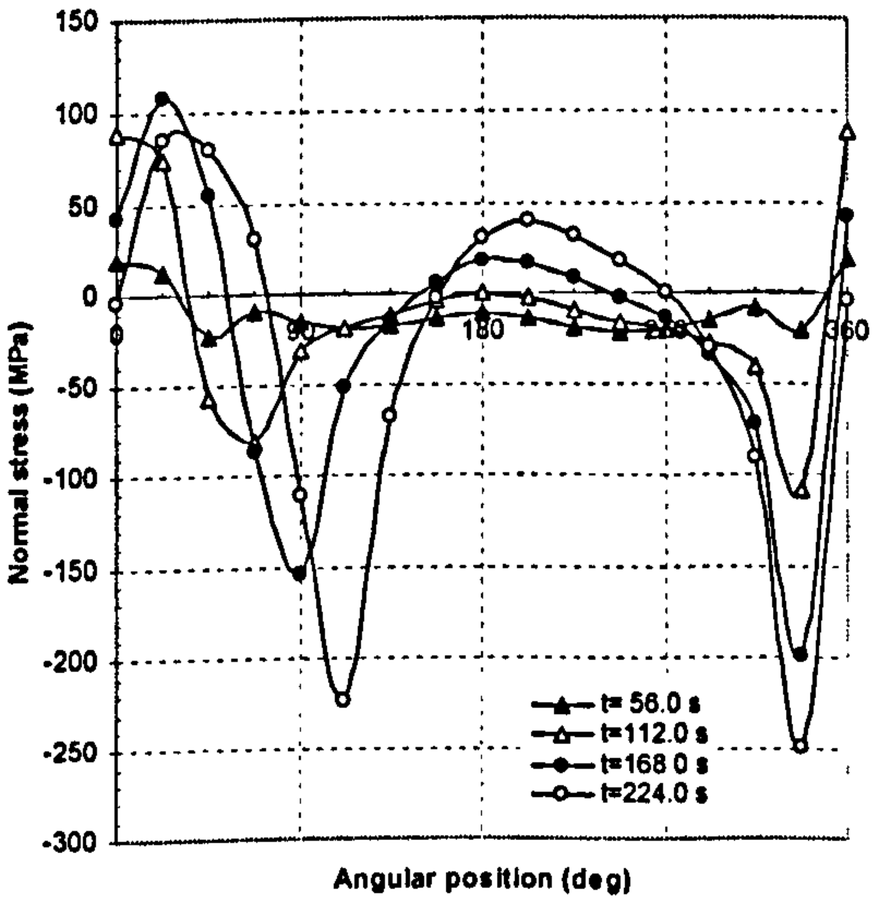

(a) Welding Quadrant *I*

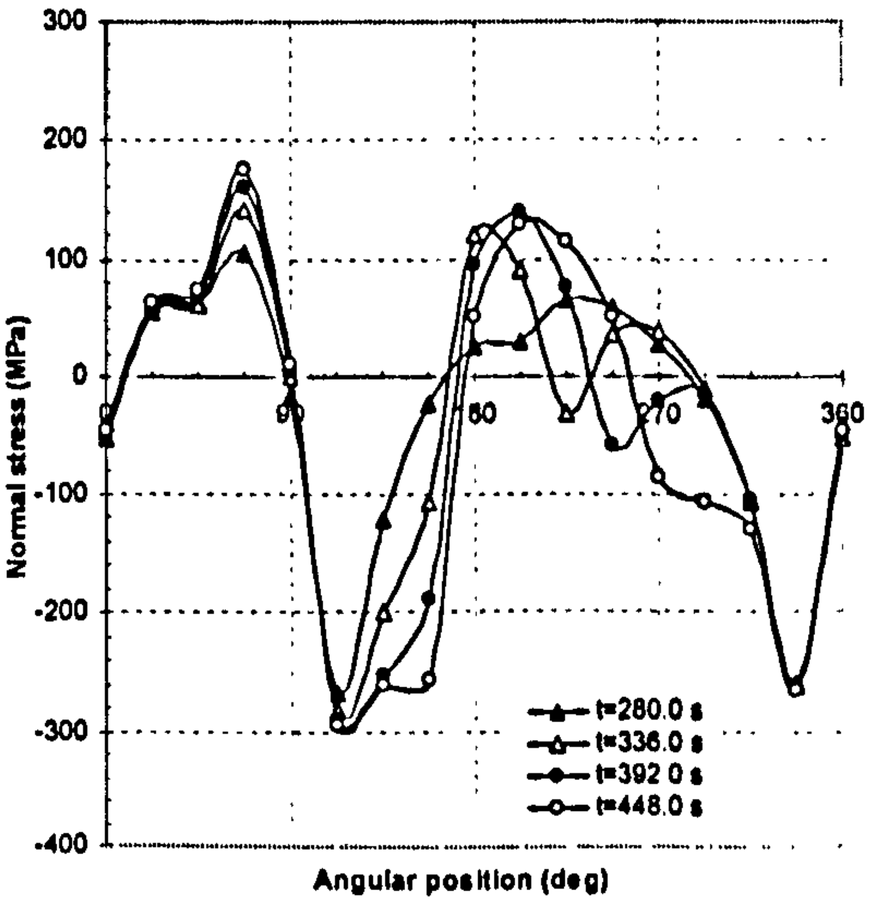

(b) Welding Quadrant *III*

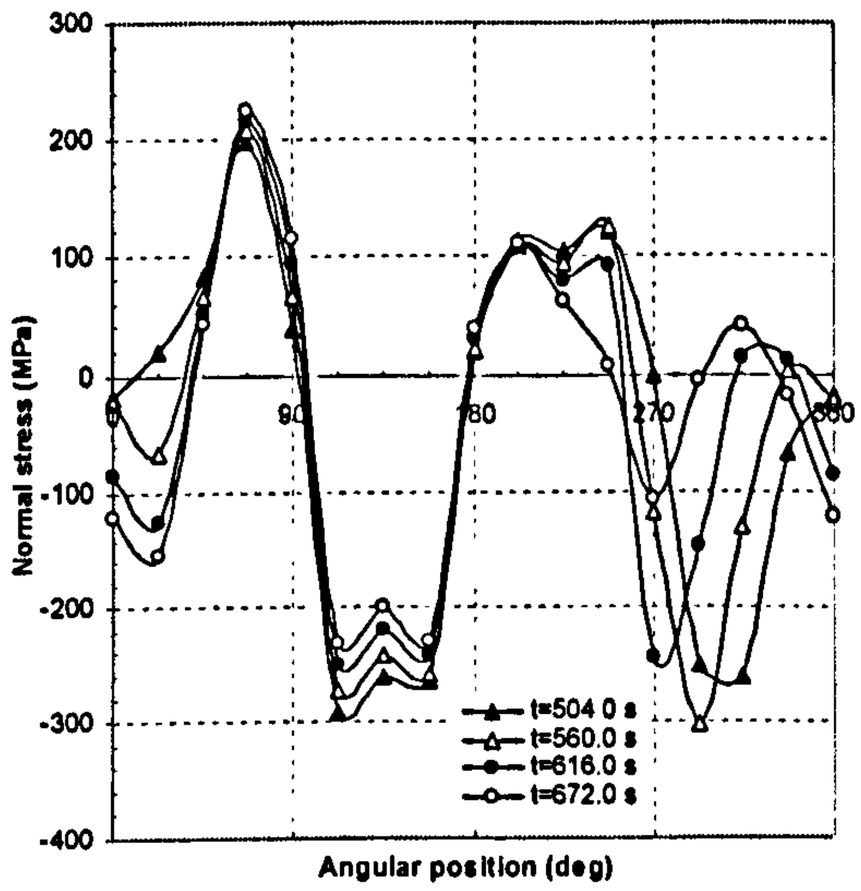

(c) Welding Quadrant *IV*

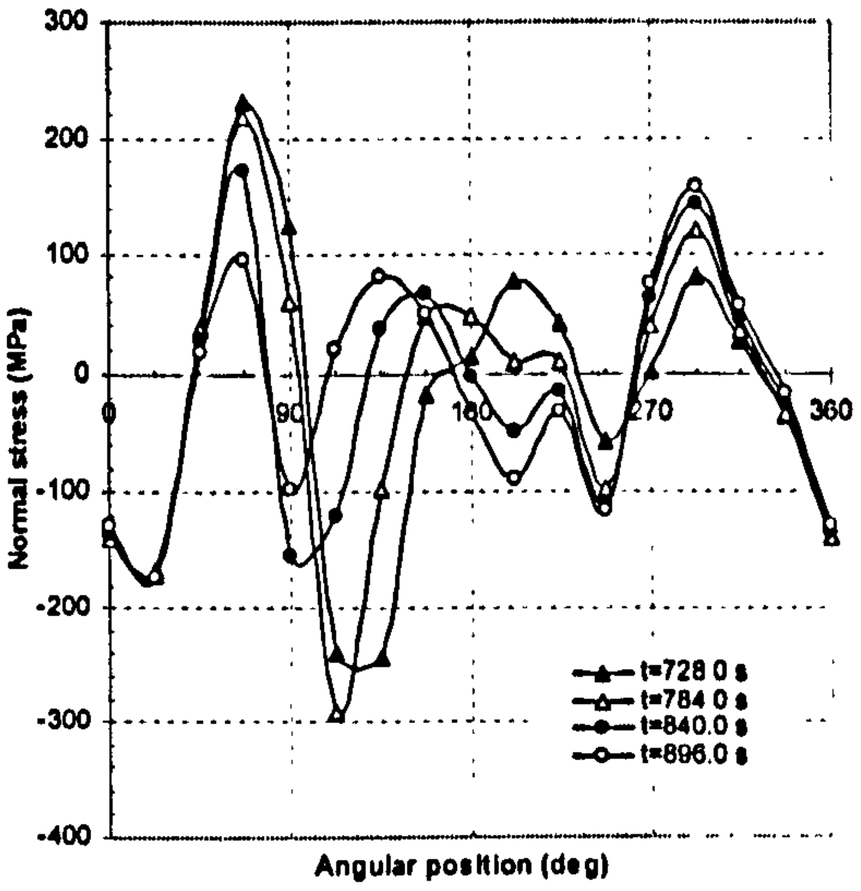

(d) Welding Quadrant *II*

Figure 6.63 Normal stress distributions along Curve *C* at the end of deposition of each sector of the first pass

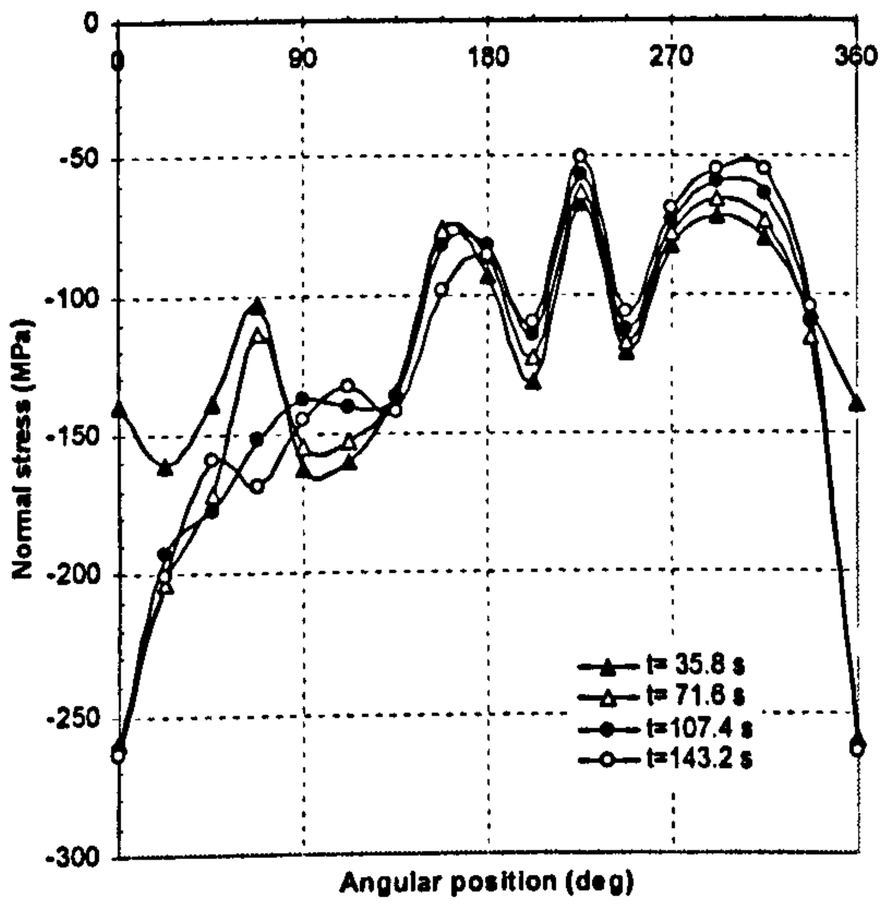

(a) Welding Quadrant *I*

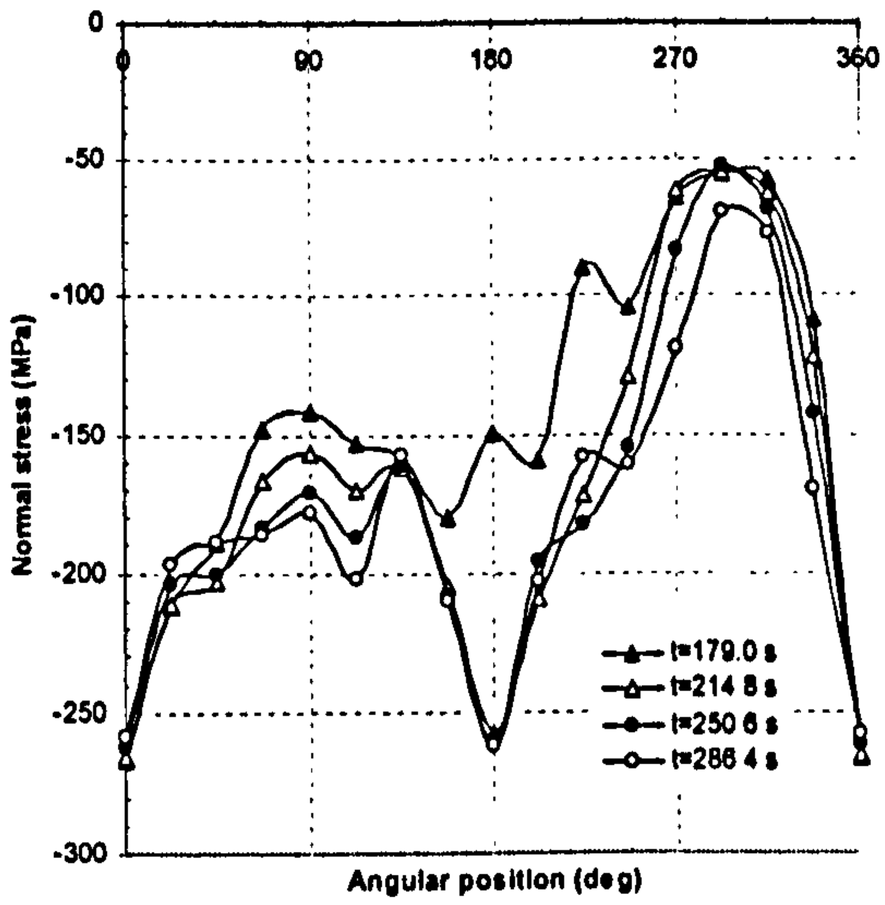

(b) Welding Quadrant *III*

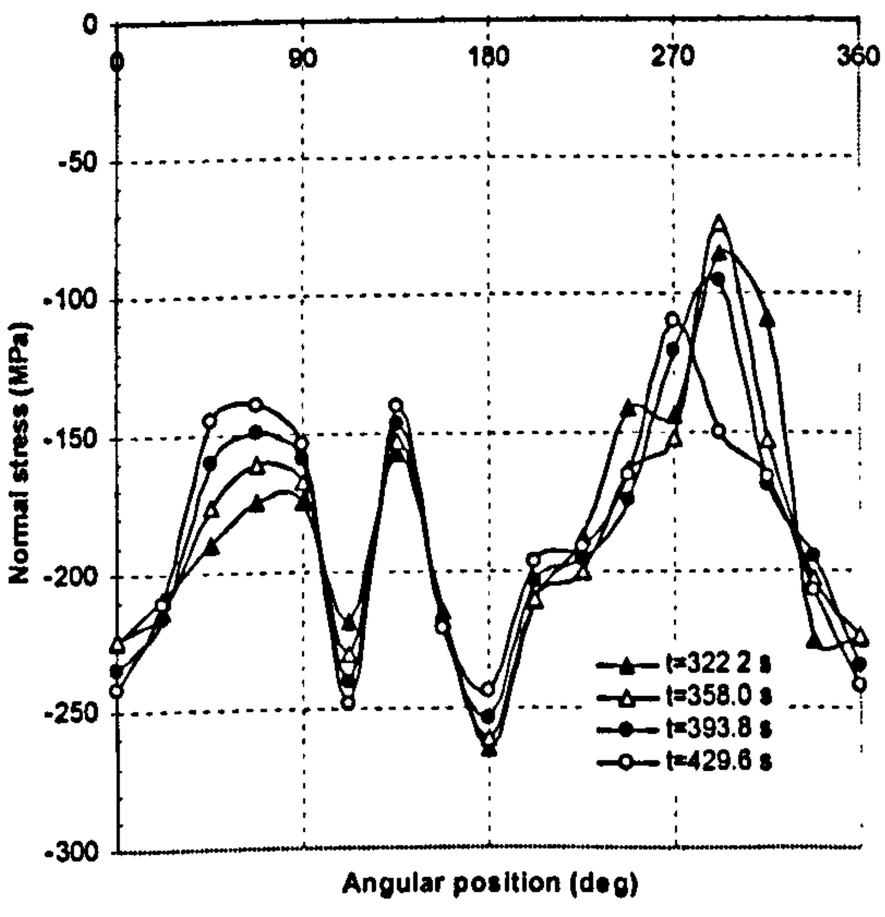

(c) Welding Quadrant *IV*

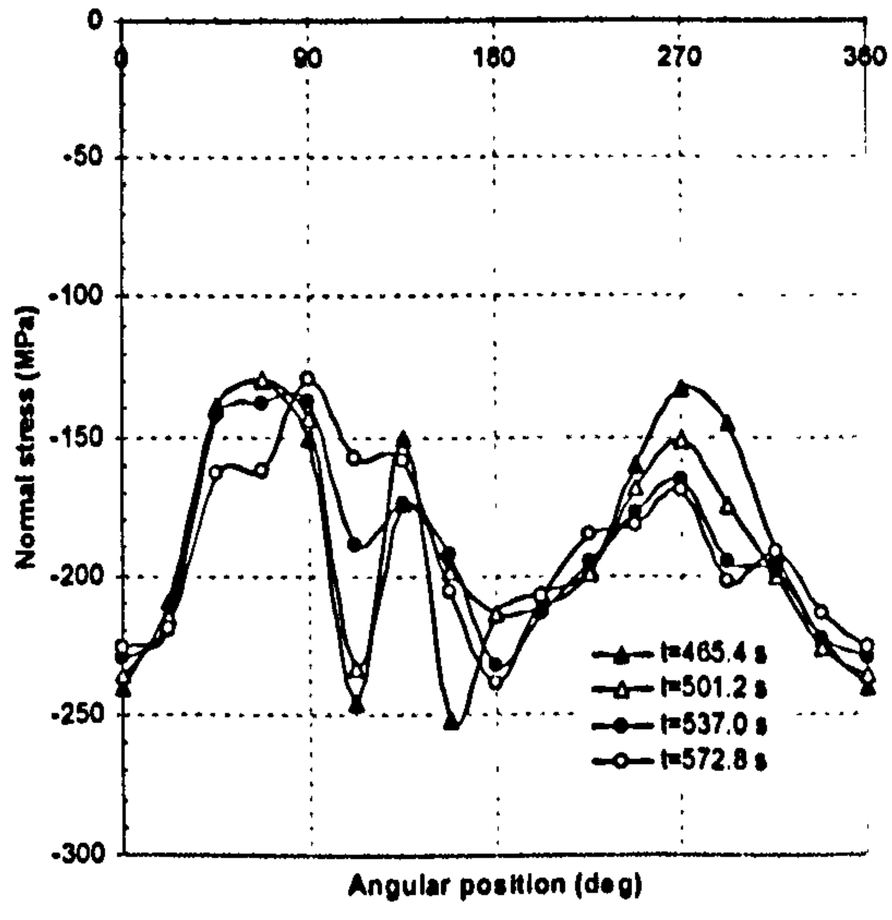

(d) Welding Quadrant *II*

Figure 6.64 Normal stress distributions along Curve *C* at the end of deposition of each sector of the sixth pass

Figures 6.63 to 6.64 show the normal stress distributions along Curve *C* after deposition of each sector during welding of the first and sixth pass, respectively. Similar normal stress distribution patterns to those of the tangential stress in Figures 6.60 to 6.62 are observed. The explanations given previously remain applicable to the evolution of the normal stresses, except that the thermal expansions are restrained by the materials in the direction normal to Curve *C*. At the end of deposition of the last pass, compressive normal stresses distribute along Curve *C*.

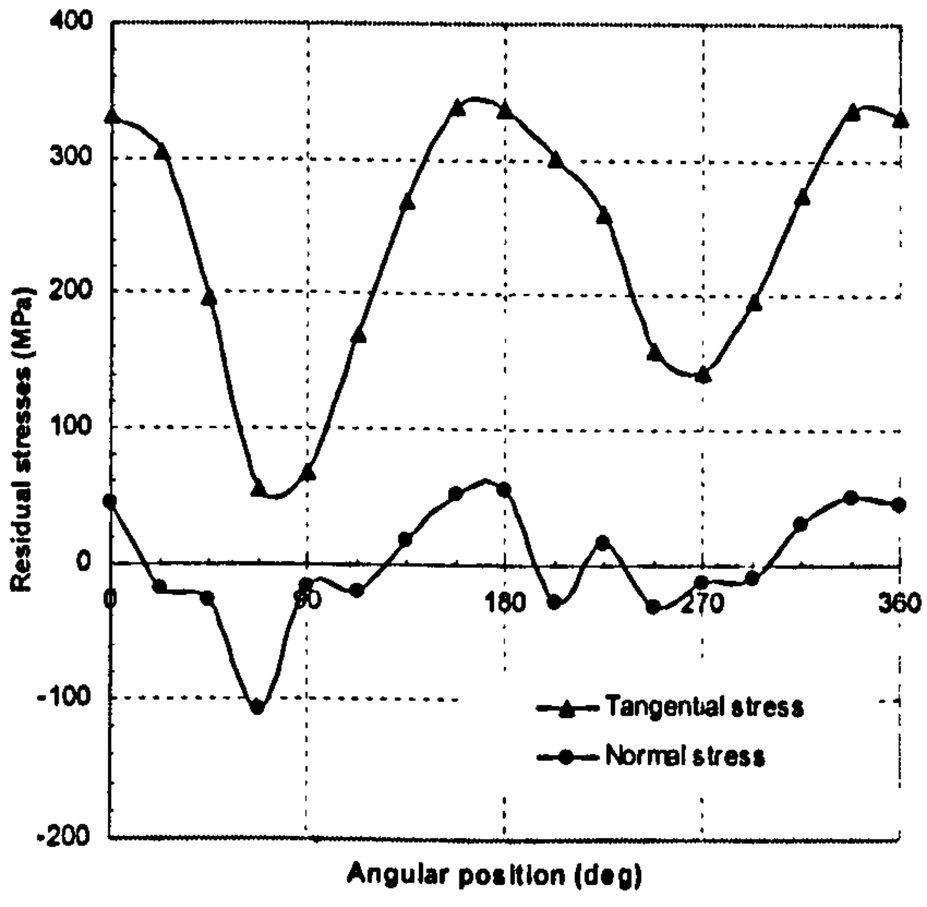

Figure 6.65 Residual stresses along Curve *C*

Figure 6.65 depicts the residual stress distributions along Curve *C*. The peak tangential residual stress reaches 340MPa (122%σ_y) at the regions around the two flank centres. On the other hand, the peak tensile normal residual stresses along Curve *C* are about 50MPa in magnitude and are relatively small. By comparison, they can be considered as not being important as the tangential residual stresses. Consequently, the latter should be of particular interest to the structural integrity analyst as they appear to peak in the regions where the least material is deposited during welding.

6.4 Conclusions

6.4.1 Model validation

The full 3D FE model involving a moving heat source and continuous filler material deposition in multipass welding was firstly developed and applied to multipass butt-welded plates and pipes for validation.

As a general comment, FE runs have shown that the temperature predictions from the thermal analyses respond to expectation when some parameters are slightly varied. Indeed temperature profiles and detailed thermal histories can be consistently reproduced with ease as has been reported in reference (Jiang *et al.* 2004) as well as in Section 6.1.3.1 and 6.2.2.1.

However, for the case of resultant stresses, the simulation results appear to be sensitive to parameters such as the yield stress of the material, similar to the conclusion drawn by Zhu (2002). The numerically obtained residual stress results from the current 3D analyses were compared with existing experimental data and 2D predictions on the surfaces of the weldments. Both 2D and 3D models provided acceptable residual stress results, however, the predictions from the 3D model were noted, in general, to agree better with the experimental data than those from the 2D models.

6.4.2 Simulation results of the tee branch junction

6.4.2.1 Temperature field

The temperature simulation results can be summarised as follows:

Firstly, from the contour plots, it is observed that high temperatures and steep thermal gradients appear in the region close to the deposited passes. Peak temperatures are, as expected, limited to the region surrounding the heat source, from which lower temperature zones fan out into both run and branch pipes as well as the previously deposited material.

Secondly, from the results of the thermal cycles experienced by the selected points at both the branch and run pipe cross sections, it is found that the thermal history experienced by each point depends on its geometric locations at the weld seam. For the points near the lower numbered pass, the thermal cycle is affected by all passes; while for the points close to the higher numbered pass, the thermal cycle is mainly affected by higher numbered passes. The peak temperature each point undergoes depends on the distance between the point and the heat source. Interpass temperature steadily increases

as the pass number increases. Symmetrical points experience similar thermal cycles.

Thirdly, from the temperature distributions on the inner and outer surfaces of both the run and branch pipes, it is found that the thermal cycles generated on the inner surface of the branch pipe are mainly caused by the first few passes. The effects of the higher numbered passes are quite small at the moment of deposition. Their effects on the inner surface are mostly due to heat conduction after the deposition. The thermal cycle on the outer surface of the branch pipe are mainly caused by the last few passes.

Finally, it is observed that the transient temperature distributions along Curves *A*, *B* and *C* continuously change as welding proceeds circumferentially along the weldline. Highly non uniform temperature distributions are observed during each welding pass. The temperature each point experiences depends on both time and its relative position with respect to the heat source. The continuous changes of the transient temperature fields play an important role in the formation of residual stresses along the circumferential weldline.

6.4.2.2 Transient and residual stress field

The thermal and residual stress simulation results can be summarised as follows:

Firstly, from the thermal stress evolution at the selected points, it is observed that peak compressive stresses appear at the moment of deposition, and gradually increase to higher stress as the heat source moves away. At the cooling stage, an obvious stress increase can be noticed for almost all the stress components. For the points near the lower numbered pass, the thermal stresses are affected by all passes; while for the points close to the higher numbered pass, they are mainly affected by higher numbered passes. As expected, this conclusion follows the observations made for the thermal cycles.

Secondly, the transient and residual stress distributions on the inner and outer surfaces of both the run and branch pipes are reported. As expected, the stresses mainly evolve in the regions around the weld. The residual stresses drop rapidly with increasing distance from the weld. The stresses on the outer surface of the branch pipe are mainly

affected by last few passes. At the branch cross section *a-a*, the critical region is at the inner surface and is located at a distance of about 55% of the branch pipe thickness from the origin on the branch side, with a peak hoop residual stress of 126%σ_y. At the run pipe cross section *b-b*, the critical area is roughly at the centre of the weld with a peak hoop residual stress of 112%σ_y. A typical through-thickness bending situation is observed for both the hoop and axial residual stresses at the weld toe at the run pipe cross section. Radial residual stresses have been shown to be the stresses that exhibit the least variations and are, in general, almost negligible.

Finally, the transient and residual stress distributions along Curves *A*, *B* and *C* are reported. The peak tangential and normal stresses are 90%σ_y and 80%σ_y respectively on Curve *A* under the current welding conditions. Should the welding parameters not be controlled properly, both mode I and mode II types of failure would be of concern if a defect were to be present or initiate in the regions represented by Curve *A*. Tensile tangential stress becomes dominant on both Curves *B* and *C*, with peak value being 97%σ_y and 122%σ_y, respectively. This makes mode II type of failure more important in the regions represented by Curve *C* than on those represented by Curve *B*. This is especially so because the peak tensile tangential stress is located near the two flank centres where the least material is deposited. Overall the radial stresses are not very important, consequently mode III type of failure is of least concern in welded cylinder-to-cylinder junctions.

Since the model take into account the heat source movement, although a symmetrical welding sequence is employed for all passes, the residual stress distributions along Curves *A*, *B* and *C* do not exhibit any obvious symmetry. High residual stresses are mainly located in the regions near either flank centres or crotch corners in Quadrants *II* and *IV*.

Chapter 7 Parametric Studies and Optimization

This chapter investigates the correlations between welding parameters and residual stresses and subsequently addresses optimization of residual stress profiles in a multipass welded tee branch junction. The parameters that affect residual stress generation are firstly discussed and grouped into design-related, material-related and manufacture-related in Section 7.1. The design-related and material-related parameters are then discussed briefly in Section 7.2. Finally, detailed parametric studies of the manufacture-related parameters as well as residual stress optimization are reported in Section 7.3 .

7.1 Overview

Fusion welding is a highly nonlinear, multivariable process which inevitably induces residual stresses. Before considering ways to optimise these stresses, it is worth reviewing the factors that cause them.

Fusion welding can be carried out in many ways, as will be described in Section 7.3.1. However, all of them involve deposition of a small amount of molten material within a gap between the components to be joined. When the filler material solidifies, the weld joins the parts together. Good bonding between the base and the filler metal can occur only when the edges of the joint have melted and blended into the weld pool as the filler metal is being added. The heat source is used to supply sufficient heat to prevent premature solidification.

The success of a welding operation depends on the heat input to the joint. As soon as the heat is supplied to the area to be welded, it starts to flow away into the metal on either side. In order to achieve melting, the rate at which heat is supplied to the joint must be greater than the rate at which it is flowing into the base metal.

It follows that thermal conductivity of the base metal, as well as the thermal

conditions like cooling rate, are important factors when choosing welding conditions. Preheating can assist in reaching the melting point rapidly by reducing the temperature difference between the filler and base metals. Finally, the cross sectional area of the groove is also important. Normally thickness is more important than the cross sectional area, and, in general, the thicker the component being welded, the faster the heat is conducted away from the weldline (Gourd 1995, Davies 1989, Lancaster 1986). Besides, thickness also relates to the number of passes.

Successful welding not only means joining parts together, but also means that the joint must have adequate strength. In other words, the joint should ideally have minimum tensile residual stresses. It is a well accepted fact that the magnitude and distribution of residual stresses are the results of complex interactions between the welding parameters, the material's response at high temperature and the joint design.

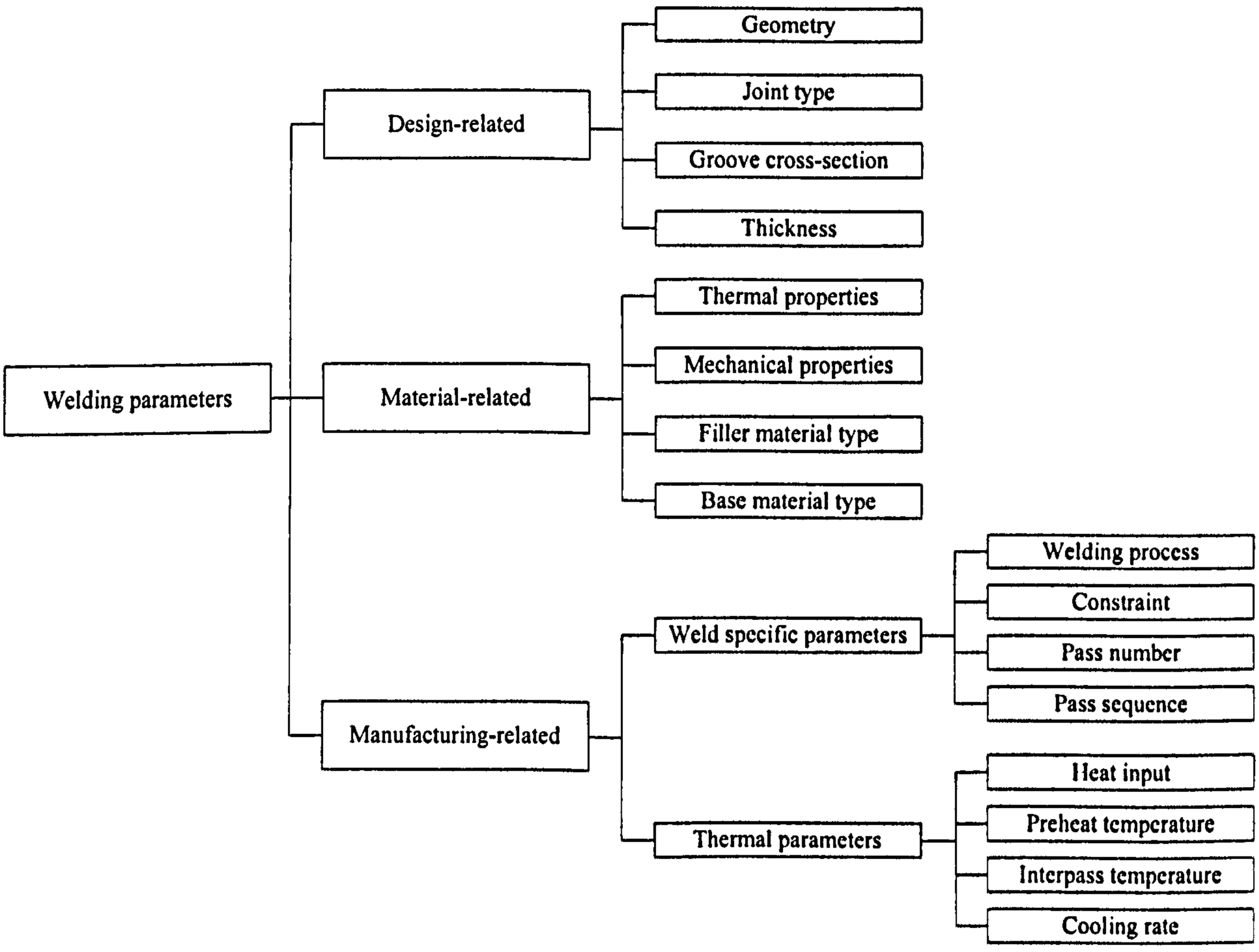

Figure 7.1 Welding parameters

As a summary, welding parameters can be grouped as design-related, material-related and manufacture-related parameters (Radaj 1992), as shown in Figure

7.1. The design-related parameters include component geometry, joint type, groove cross-section and thickness. These parameters are defined at design stage. The material-related parameters involve physical and mechanical properties of both filler and base materials. The manufacture-related parameters consist of process type, welding procedure, constraint conditions, welding current, voltage, speed and efficiency, as well as thermal conditions like preheat, interpass temperature and cooling rate.

Historically, welding procedures were developed empirically. The selection of welding procedures was basically based on experimental results, trial-and-error and experience. There is no specific methodology for the selection and optimization of welding procedures. With recent advances in computational hardware and software, modelling and optimization by FE method has become increasingly important in obtaining high quality welds in industry. Nowadays, it is possible to undertake computationally intensive optimization schemes that embody realistic 3D numerical residual stress prediction to help understand the effect of parameters on the magnitude and distribution of critical stresses over a wide range of values.

7.2 Welding parameters

7.2.1 Design-related

Plates and pipes are the most commonly used geometries for welded structures. When fabricating them, five basic types of joint, i.e. butt, tee, corner, lap and edge joints, can be selected. The selection of joint type depends on the assembly position of the components to be welded (American Welding Society, 1963, 1967).

The thickness of a welded component relates closely not only to the number of passes but also to the groove shapes. Thinner plates are usually welded by single V or single U joints, while thicker plates are usually prepared as double V or double U joints.

Generally speaking, a single U shape groove is more favourable and requires less filler metal than a single V groove when welding heavy sections. Double V groove joints require approximately one-half the amount of filler metal used to produce the single V groove joint for the same plate thickness. Symmetrical weld grooves permit

easier welding and reduce angular shrinkage while residual stresses are increased in heavy sections (Radaj 1992).

The thick-walled, fillet-welded tee branch junction, as described in the previous chapters, was used in the following parametric studies.

7.2.2 Material-related

The thermal and mechanical properties of both the base and filler metals affect the resultant residual stresses. The melting temperature and coefficient of thermal expansion act in the same direction on welding residual stresses. With a higher thermal diffusivity, the heat dissipates at a faster rate from the weld region. In general, the higher the thermal diffusivity, the larger the resulting stresses (Radaj 1992).

The elastic modulus, Poisson's ratio, as well as yield stress, act in the same direction on welding residual stresses. Residual stress induced by welding can reach as high a value as that of the yield strength of the base metal (Masubuchi 1982, Brickstad 1998).

Many welding processes include adding consumable filler metal. The choice of filler metal is based on providing adequate mechanical strength and corrosion resistance. Rybicki and McGuire (1982) found that, while increasing the yield stress of the filler metal lowered the stresses in the weld deposited area; this generally has very little effect on the outside of the weld area. Furthermore, since the yield stress of the weld deposit is not known accurately, the base and filler metal are usually represented by the same material properties.

The final factor within the material-related parameters is about weldability of the base metal. The suitability for welding is assessed essentially on the basis of the material characteristic values, such as melting temperature, coefficient of thermal expansion, thermal diffusivity, elastic modulus and yield stress, as suggested by Radaj (1992). In the current parametric studies, stainless steel was considered for both the filler and base material.

7.2.3 Manufacture-related

A large number of manufacture-related parameters affect the magnitude and distribution of the welding residual stresses. These parameters can be grouped as thermal and weld specific, as shown in Figure 7.1, and will be discussed in detail in the following section.

7.3 Parametric studies and optimization

A welding process is governed by a multitude of process parameters that influence, to various extents, the residual stresses. While residual stresses can sometimes be beneficial, they are usually undesirable in most cases. They can even be more critical when tensile and present in structures that will have deteriorated and developed defects after prolonged service. It is therefore desirable to optimise welding residual stress profiles, in particular, to reduce the maximum tensile stress and/or to decrease the zones with high tensile residual stresses.

Due to the large amount of parameters involved in the welding process, complete parametric studies for residual stress optimization in the multipass welded tee branch junction would be impracticable for one investigator. In order to reduce the parameters to a manageable number, it is assumed that the design and material related parameters are already defined. Therefore, the present investigation will focus on the manufacture-related parameters only. Hence, the parameters to be investigated include the number of passes, pass sequences, heat input, preheat temperature, interpass temperature and cooling rate.

A total of fifteen cases were investigated, as listed in Table 7.1. The highlighted Case 3 in Table 7.1 was selected as a benchmark case for the purpose of comparison. In the following sections, these manufacture-related parameters are firstly described in detail. Then, each parameter is investigated considering low, medium and high values. The ranges of the parameters were obtained from the literature and welding practice. Residual stresses under different cases are compared with those of Case 3 at the branch

cross section *a-a*, the run cross section *b-b* and Curves *A, B, C* (see Figure 6.15). Finally, the underlying trends of the effects of these parameters are summarised at the end of each section.

Table 7.1 Parametric study cases

Case number	Number of welders	Pass number	Preheating temperature (°C)	Interpass temperature (°C)	Convection heat transfer coefficients ($W/m^2°C$)	Heat input *
1	1	6	65	120	30	Medium
2	2	6	65	120	30	Medium
3	**4**	**6**	**65**	**120**	**30**	**Medium**
4	4	3	65	120	30	Medium
5	4	2	65	120	30	Medium
6	4	6	100	120	30	Medium
7	4	6	65	67	30	Medium
8	4	6	65	240	30	Medium
9	4	6	65	120	Inside 1000	Medium
10	4	6	65	120	Outside 1000	Medium
11	4	6	65	120	Both 1000	Medium
12	4	6	65	120	30	Low
13	4	6	65	120	30	High
14	4	6	65	120	30	Highest
15	4	6	65	240	Inside 500	Medium

* Quantification of the heat input is given in great detail in Table 7.2.

7.3.1 Welding process

The commonly used method to permanently join metallic plates and pressure vessels is fusion welding, including tungsten inert-gas (TIG) or gas tungsten arc welding (GTAW), manual metal arc (MMA) welding or shielded metal arc welding (SMAW), metal inert gas (MIG) or gas metal arc welding (GMAW) and submerged arc welding (SAW). The current research will focus on the general feature of fusion welding and not on any particular process. The physics of these processes can be found in the general literature on welding, e.g. Gourd (1995) and the American Welding Society (1963).

7.3.2 Welding constraint

There are usually two types of constraint involved in welding. One is to constrain the parts to be welded by tacking/clamping and the other is to allow the parts to deform freely.

Welding residual stresses and distortions, to a large extent, behave in an adverse way. A component rigidly fixed when being welded develops high residual stresses. If, by contrast, it is welded without constraint, the distortions will be large and residual stresses will be relatively small. It is not, therefore, readily possible to fabricate a component which is at same time low in both residual stresses and distortions, as is often desired in practice. Consequently, it is necessary to distinguish between measures which keep residual stresses low and those which keep distortion low. Many of these measures relate simultaneously to residual stress and distortion by way of a compromise (Radaj 1992).

Another fact, which is worth mentioning, is that distortion is a problem associated primarily with thin structures, because they are unable to support weld induced stresses. In this case, rather rigidly clamped constraints are applied in order to achieve desired geometrical specifications. As welded sections become thicker, they are able to support larger stresses without significant distortion, and residual stresses become increasingly important. In many cases, load from the weight of thick connected parts is sufficient to ensure such requirement without any special constraint.

In the current research, the large geometry, especially the high stiffness or rigidity associated with the thick-walled tee branch junction, provides a high degree of internal constraint. The significant 3D residual stresses in this component are basically local and mainly caused by this constraint. The external constraints applied on the run pipe in the FE model are for preventing rigid body movement only. Considering the conclusions of Abid and Siddique (2005) that residual stresses had weak dependence on constraints, together with the general practice in relation to welding such heavy components, it is assumed that constraint is not as important as the other parameters and consequently its effects cannot be considered to be of much importance.

7.3.3 Effect of number of passes

7.3.3.1 Introduction

Three multipass welding schemes, i.e. two, three and six passes, are proposed here to investigate the effect of number of passes on the residual stresses in the tee branch

junction. The six-pass scheme simulated each pass individually. The two-pass scheme was conducted by grouping the first five passes together as one layer and the last pass as another layer; while the three-pass scheme was performed by grouping each of two successive passes together sequentially, as shown in Figures 7.2(a)-(c). The numbers in the figure indicate the pass numbers.

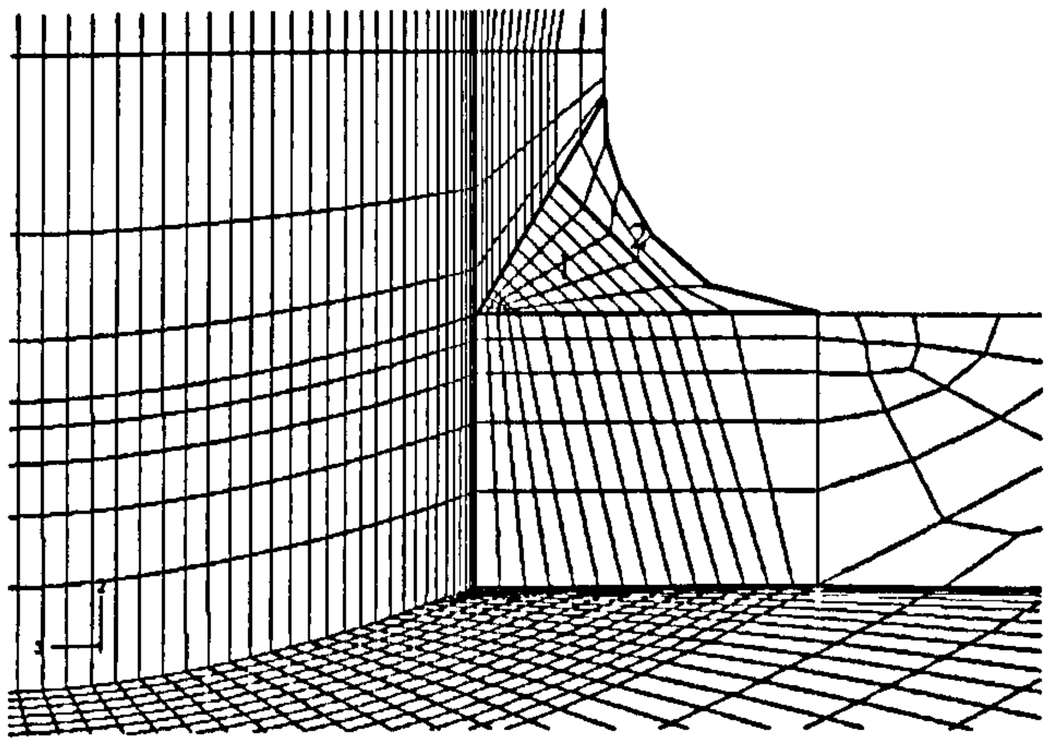

(a) Two passes

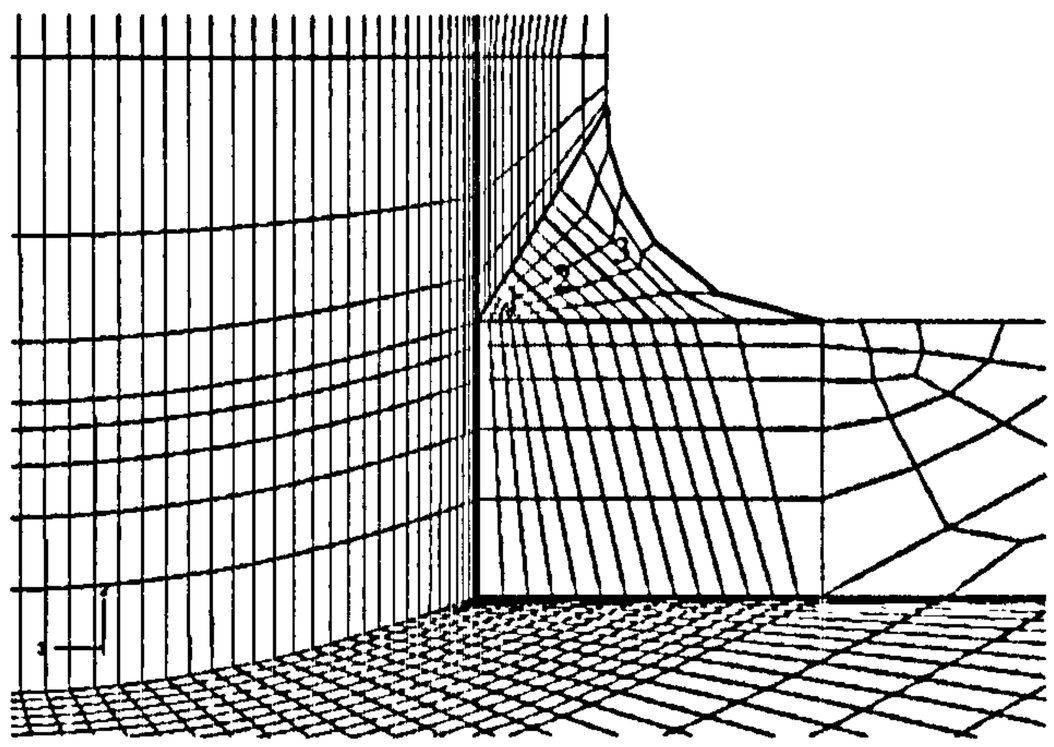

(b) Three passes

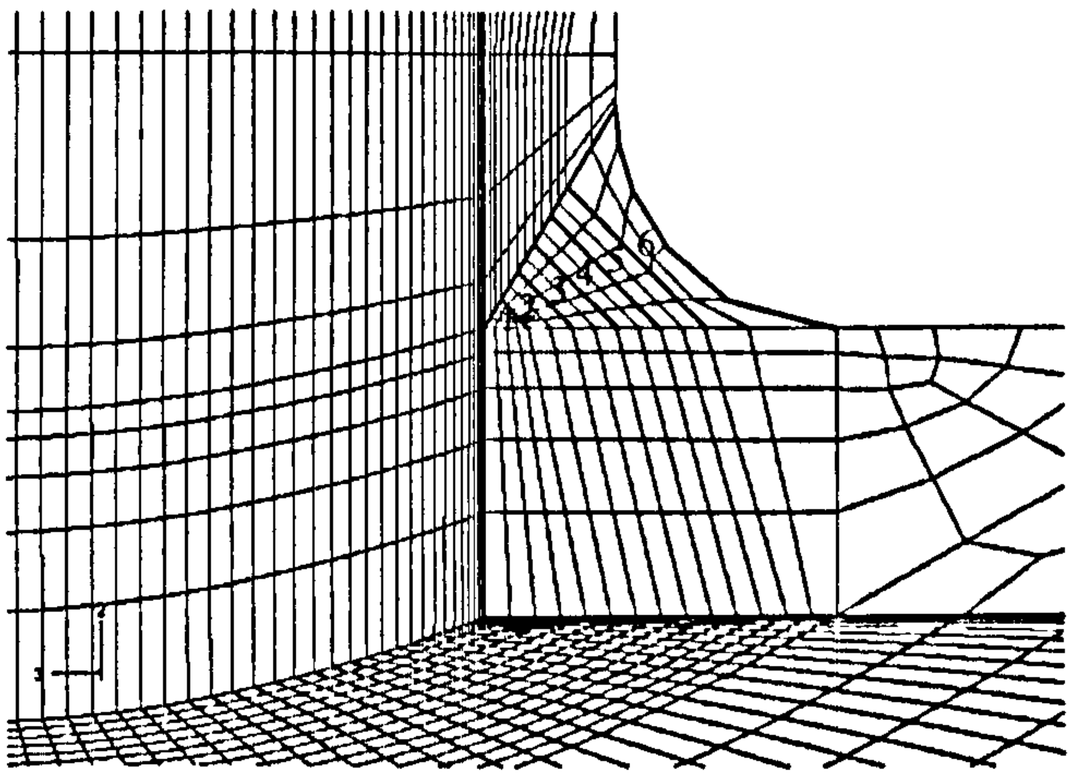

(c) Six passes

Figure 7.2 Number of passes

The welding schemes for the two- and six-pass models, as compared to the three-pass model, show that the last deposited layer for the first two models are similar, and rather different from the three-pass model, as shown in Figure 7.2. As will be explained later, this has an important bearing on the final residual stress distributions.

7.3.3.2 Results and discussion

Since the branch cross section *a-a*, the run cross section *b-b*, Curves *A*, *B* and *C* are high stress regions, as discussed in Chapter 6, the following parametric studies will focus on understanding mechanisms to reduce residual stresses in these regions. The

output locations are indicated by a thick line on each geometrical model (as inserts in the figures). Radial residual stresses are generally not very important, as discussed in Chapter 6, and will not be presented in the following figures.

7.3.3.2.1 Branch cross section *a-a*

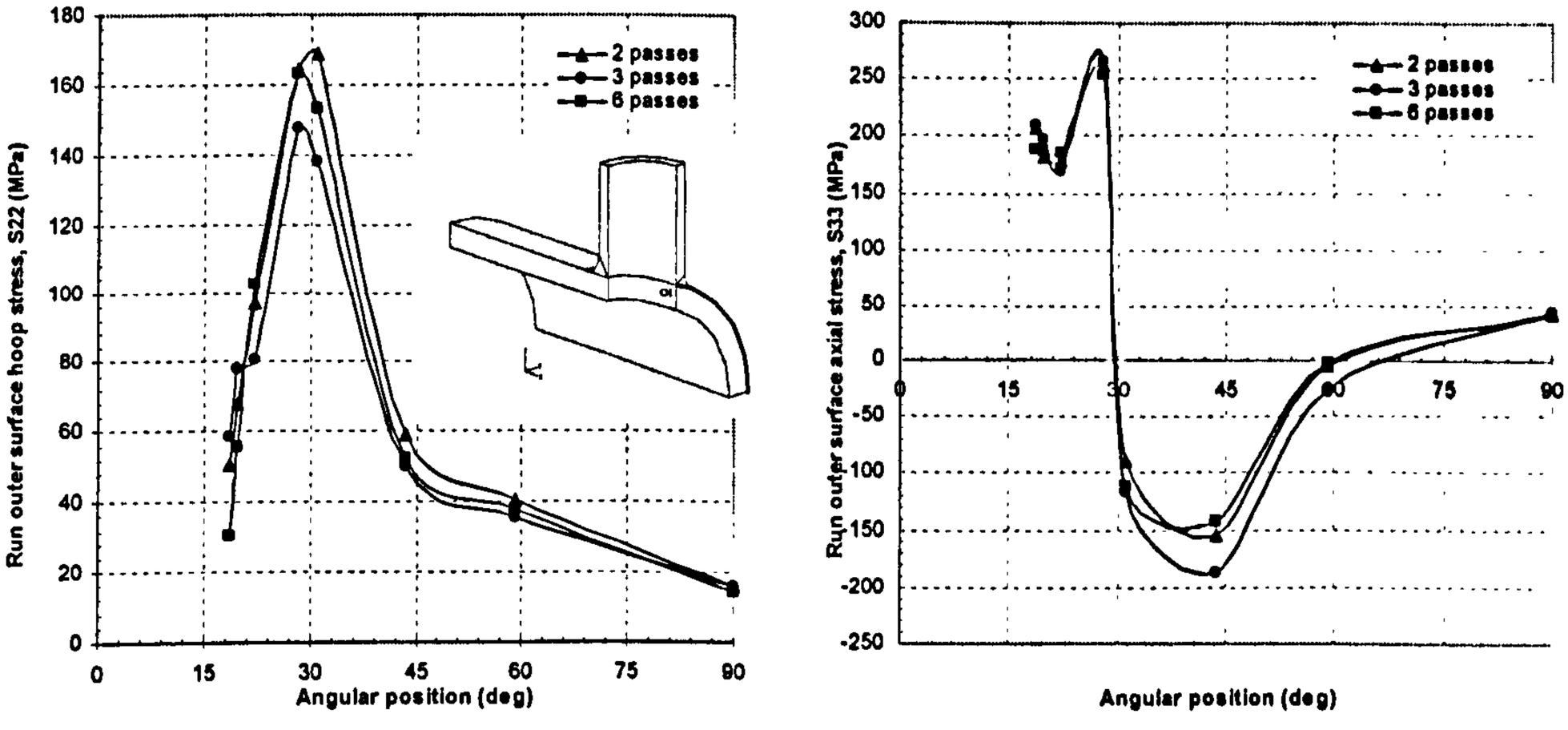

(a) Hoop stress

(b) Axial stress

Figure 7.3 Stress vs. angular position on the run pipe outer surface

Figure 7.3 shows the stress versus angular position on the outer surface of the run pipe. It can be noticed from Figure 7.3(a) that the peak tensile hoop stress is at the weld toe for the six-pass and three-pass models, with the three-pass model having the value 10% less than that of the six-pass model. The peak hoop stress for the two-pass model is at the HAZ with a value of 170MPa, which is comparable to that of the six-pass model. The dominant stress along this angular position is the axial stress, with a peak tensile value of 270MPa (97%σ_y). There is not much difference among the three models for the peak tensile axial stress; although some minor differences exist for the peak compressive axial stress, as can be noticed in Figure 7.3(b).

Figure 7.4 presents residual stress distributions along the Y_1-direction. It is noticed that the two-pass and six-pass models predict similar peak axial stress and distribution while the three-pass model predicts a highest value of 260MPa, which is about 58% more than that of the six-pass model, and a wider tension region, as shown in Figure 7.4(a). All the three models give similar hoop residual stresses from the run pipe side up

to 17mm branch pipe side, as demonstrated in Figure 7.4(b). Beyond this distance and up to 140mm, the three-pass model predicts higher tensile hoop stresses than the other two models. The two-pass model shows better agreement with the six-pass approach than the three-pass one. This is probably because the two-pass and six-pass models have the same heat input in the last pass.

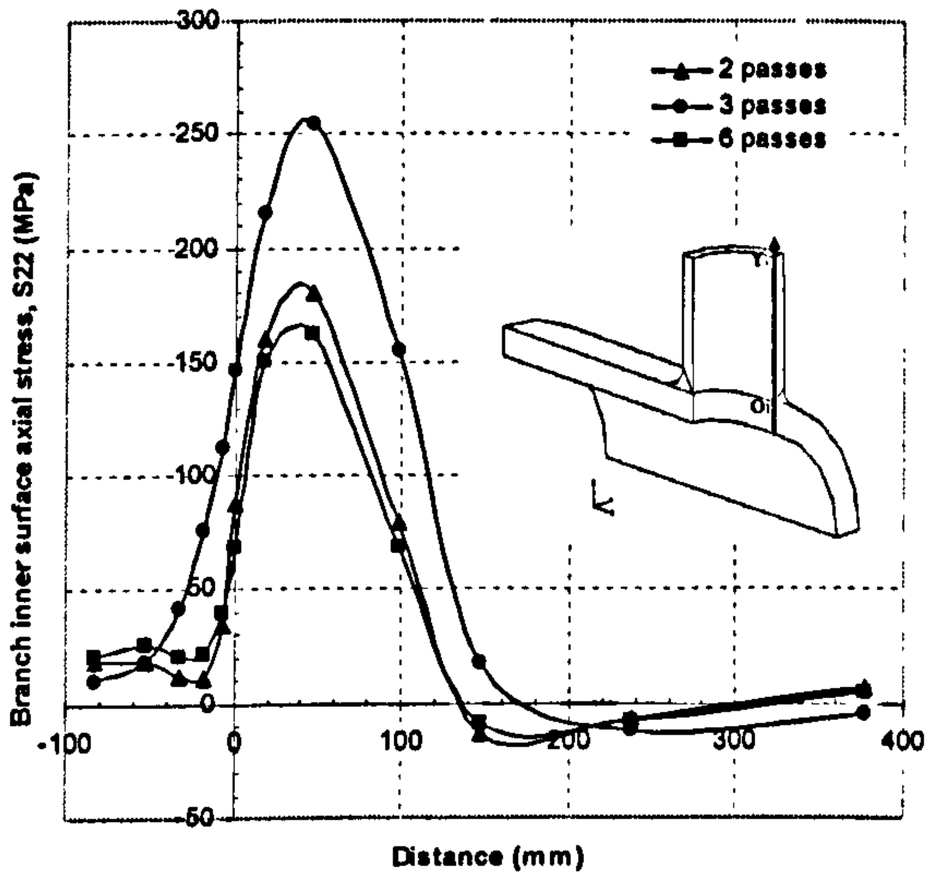

(a) Axial stress

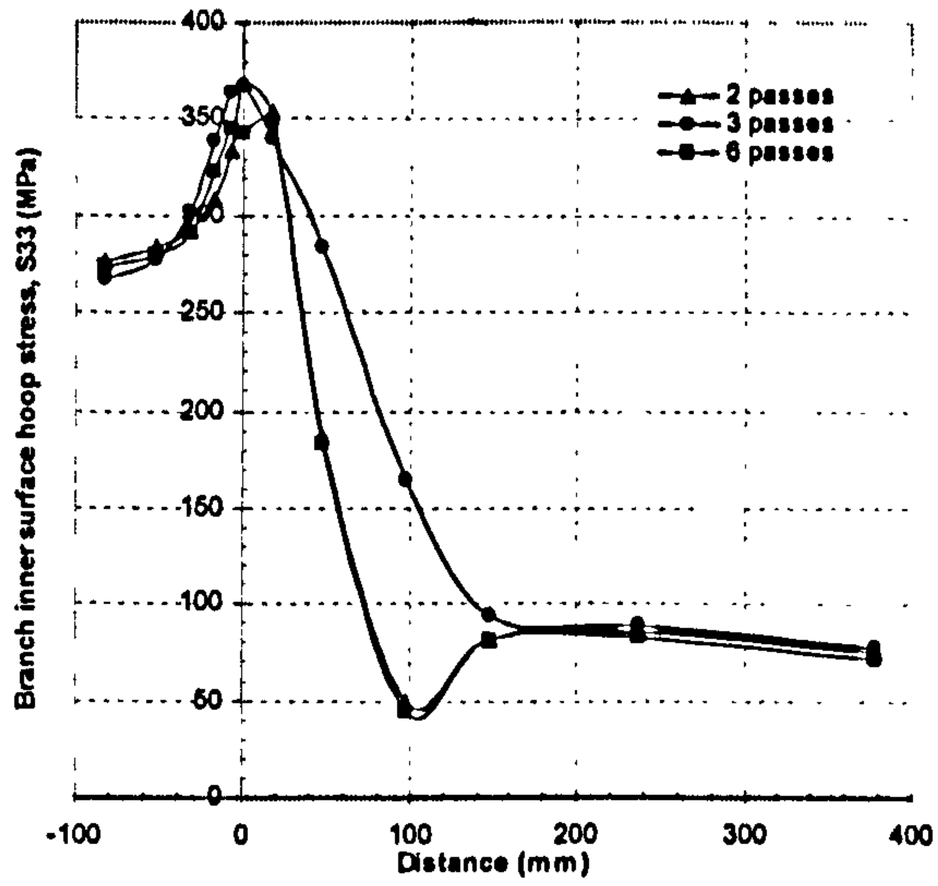

(b) Hoop stress

Figure 7.4 Residual stresses in the Y_1-direction on the branch inner surface

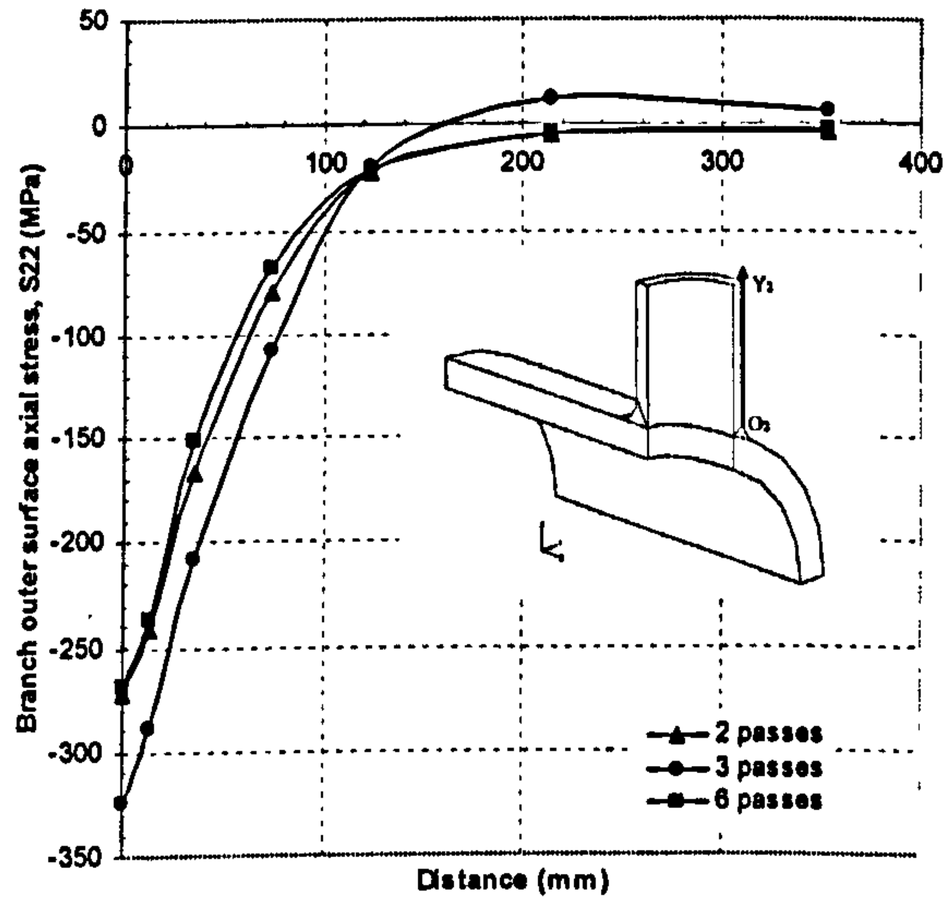

(a) Axial stress

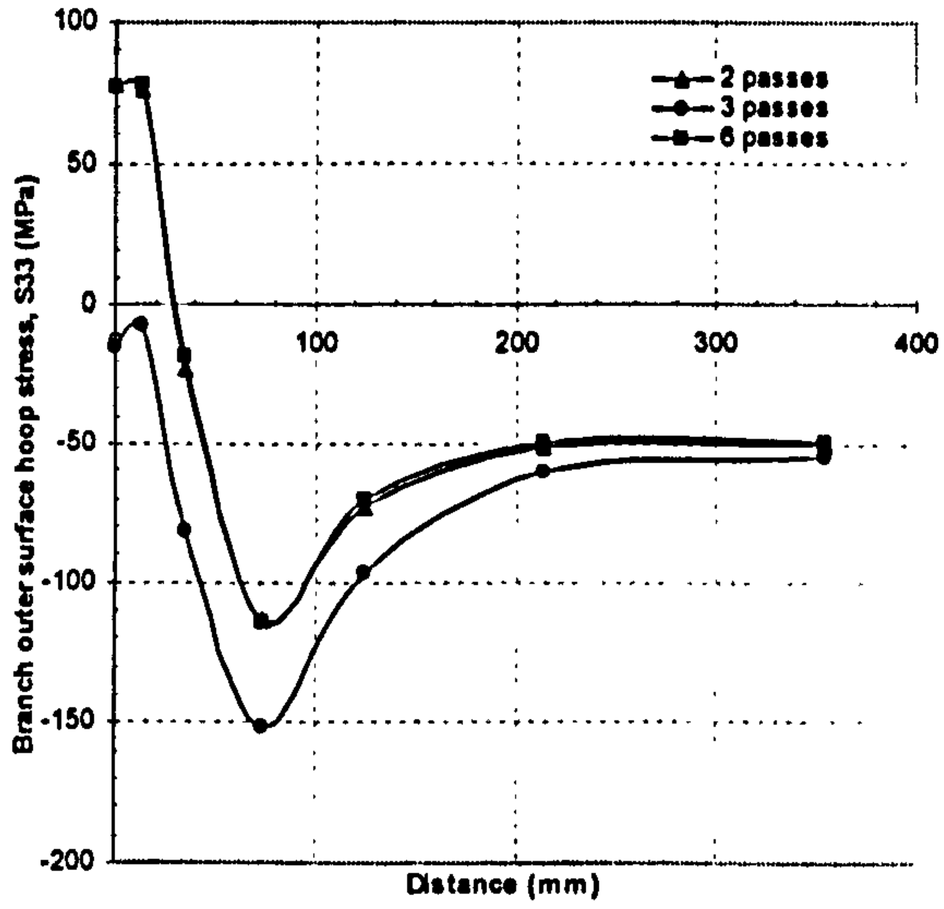

(b) Hoop stress

Figure 7.5 Residual stresses in the Y_2-direction on the branch outer surface

Figure 7.5 illustrates residual stress distributions along the Y_2-direction. The axial stresses are in compression. It is again noticed from Figure 7.5(b) that the two-pass and six-pass models provide almost identical hoop stress predictions, while the three-pass model gives a similar trend but smaller values, leaving the entire outer surface along Y_2

in compression.

7.3.3.2.2 Run pipe cross section *b-b*

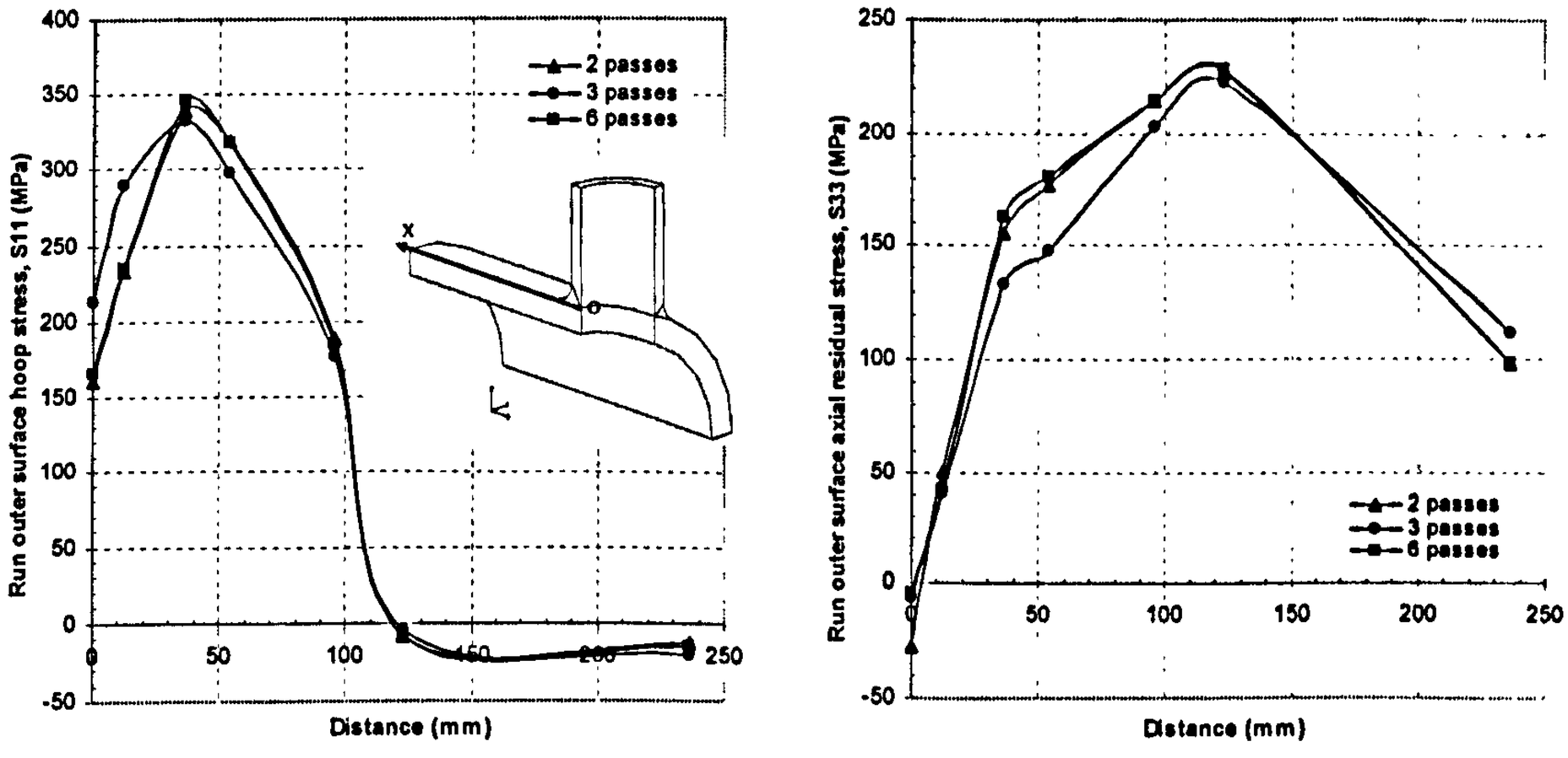

(a) Hoop stress (b) Axial stress

Figure 7.6 Residual stresses in the *X*-direction on the run outer surface

Figure 7.6 presents residual stress distributions in the *X*-direction. Similar trend of the hoop stress distributions can be noticed in Figure 7.6(a). The three models predict almost the same peak tensile hoop residual stress of 340MPa (122%σ_y) at the same location. Similar trends for the axial stress distributions are also observed, with the three-pass model giving slightly smaller values.

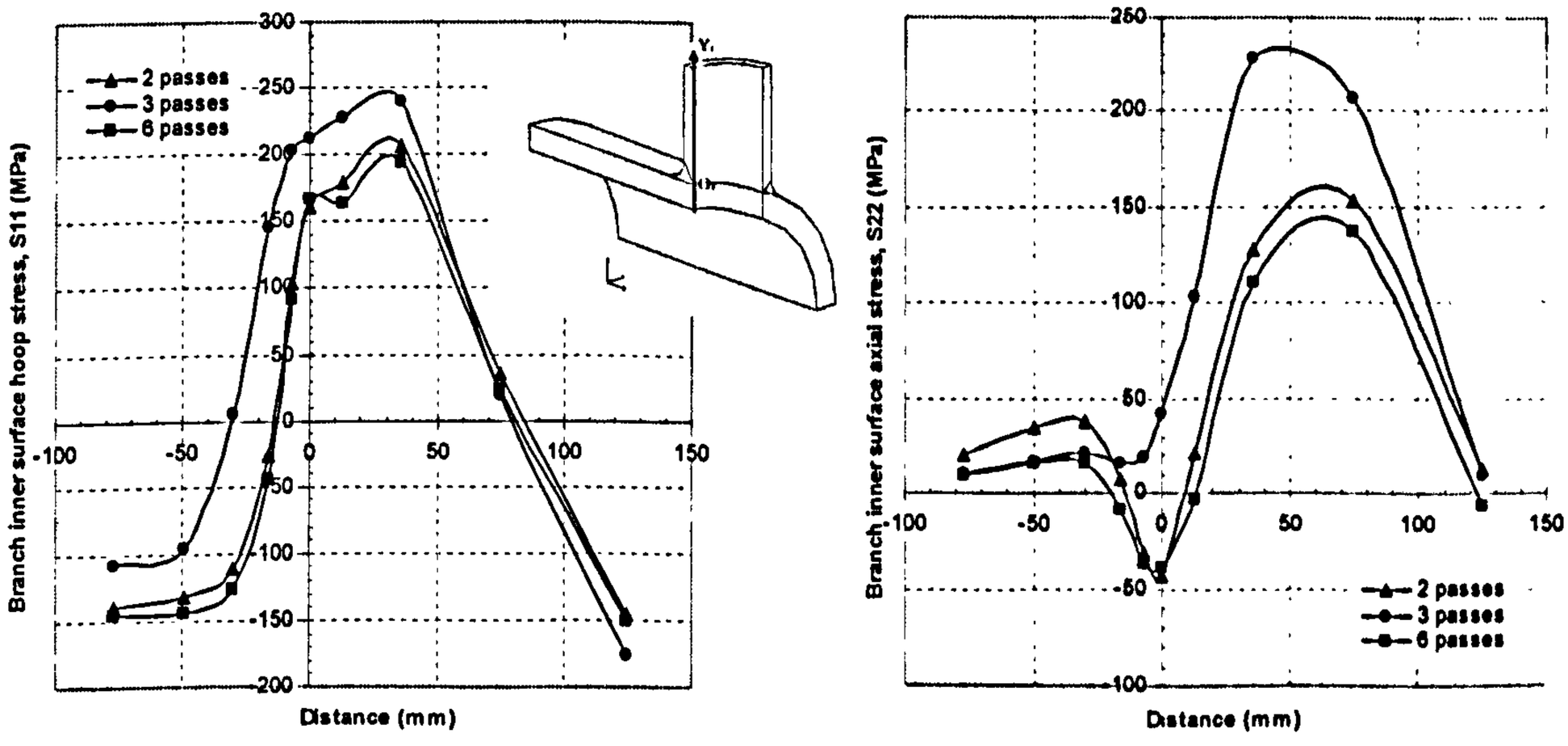

(a) Hoop stress (b) Axial stress

Figure 7.7 Residual stresses in the Y_1-direction on the branch inner surface

Figure 7.7 shows residual stress distributions in the Y_1-direction. Again the two-pass and six-pass models predict similar trends for both hoop and axial stresses, while the three-pass model appears to overestimate them. It predicts higher hoop stresses from the inner surface of the run pipe up to 60mm along the branch pipe side and higher axial stresses in the branch pipe side. The peak hoop and axial stresses are 20% and 64% more than those of the six-pass model, respectively. The three-pass models also give a wider tensile zone than the other two models. This is probably because the heat inputs of the last pass of the two- and six-pass models are the same.

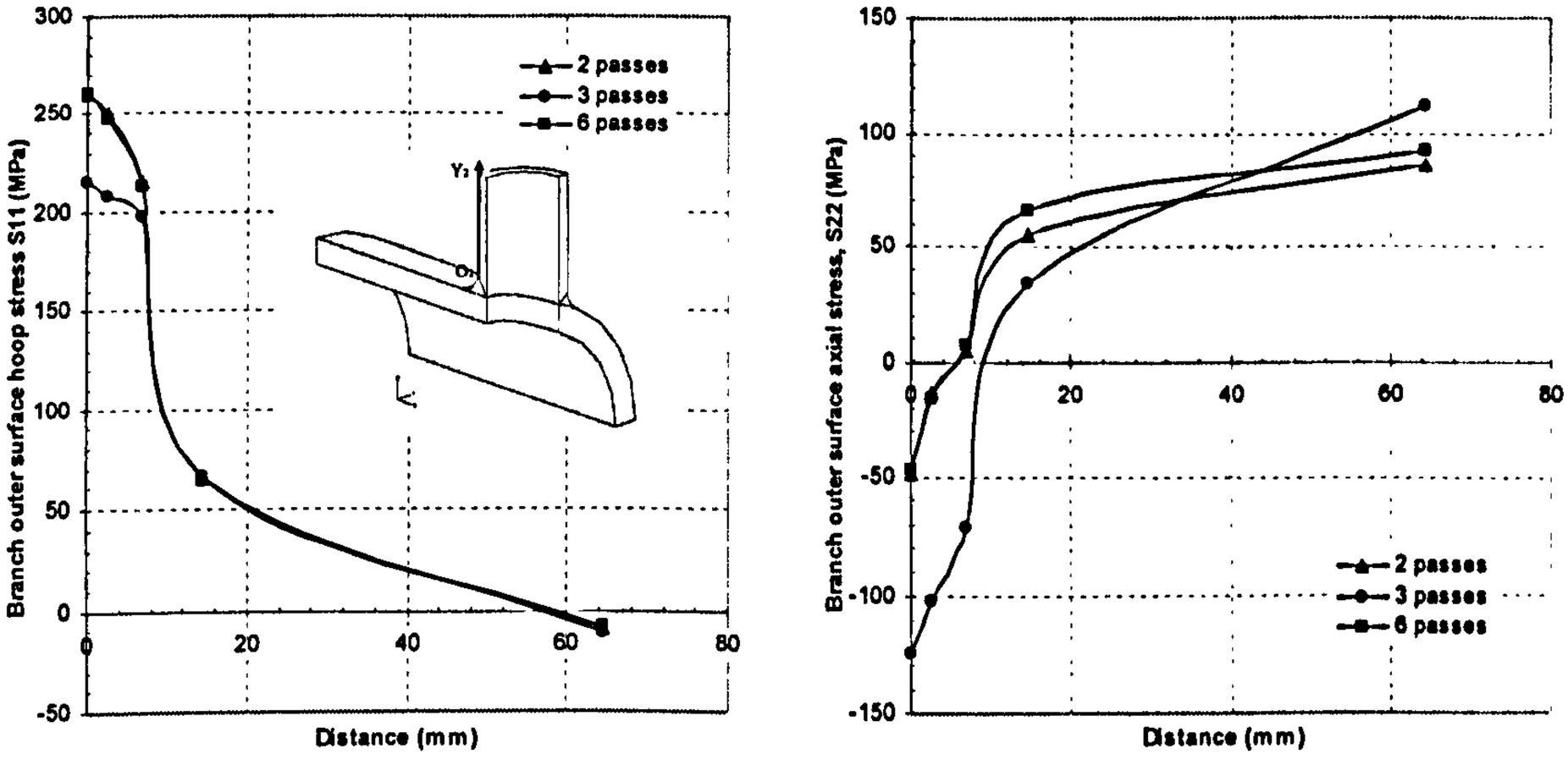

(a) Hoop stress (b) Axial stress

Figure 7.8 Residual stresses in the Y_2-direction on the branch outer surface

Figure 7.8 shows residual stress distributions in the Y_2-direction. The two-pass and six-pass models again predict almost identical hoop stress, while the three-pass model predicts slightly lower hoop stress within 8mm from the origin. The axial stresses predicted by the two-pass and six-pass models are more consistent than those by the three-pass model.

7.3.3.2.3 Circumferentially along Curve *A*

Figure 7.9 shows residual stress distributions along Curve *A*. Quite consistent distribution shapes and almost the same magnitudes of the tangential stress can be noticed in Figure 7.9(a), with a peak value of 270MPa at the flank centres. As for the normal stress, the two-pass and six-pass models give the same predictions, while the

three-pass model give a similar distribution but with slightly smaller magnitudes, as shown in Figure 7.9(b).

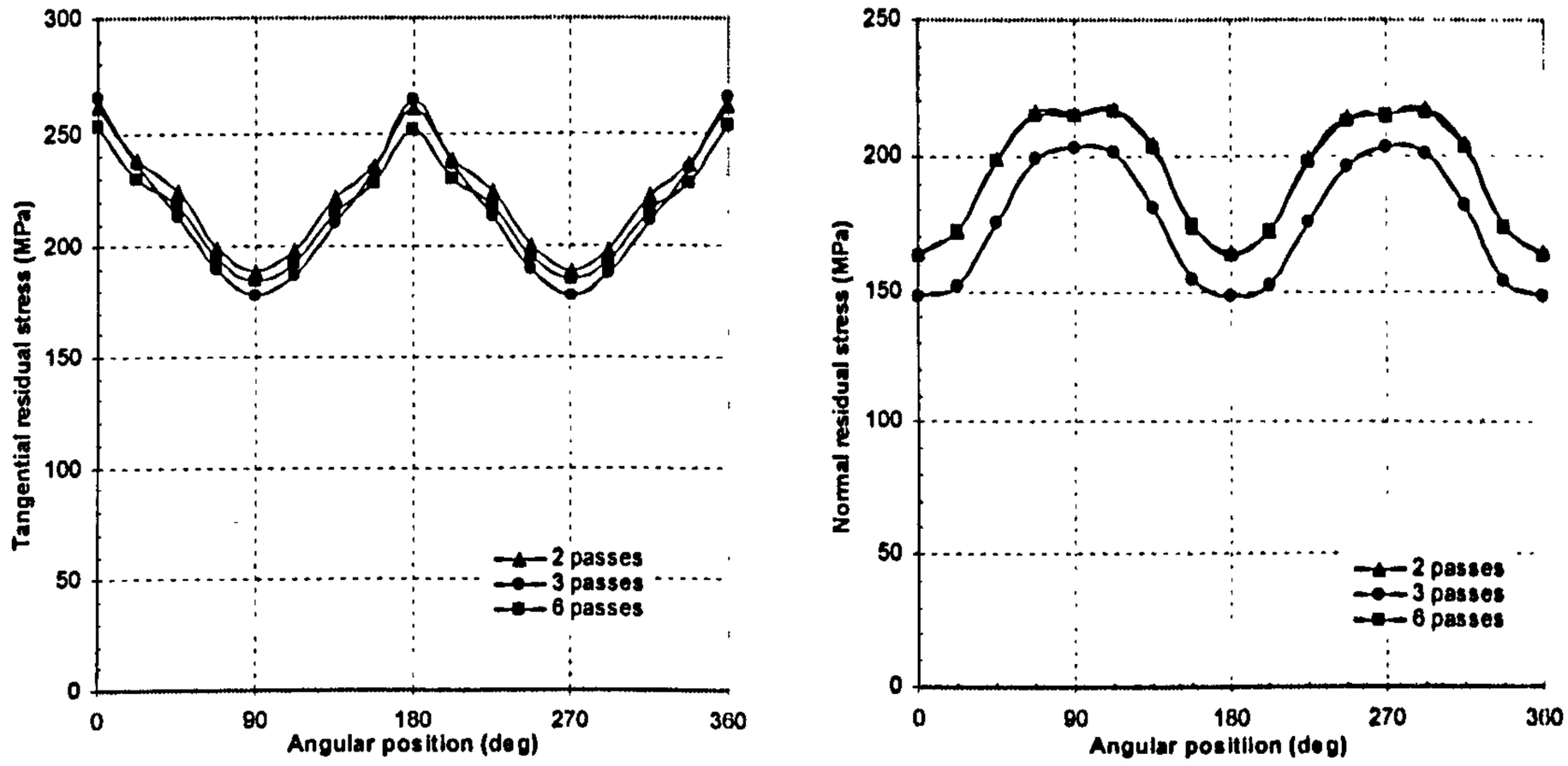

(a) Tangential stress (b) Normal stress

Figure 7.9 Residual stress distributions along Curve *A*

7.3.3.2.4 Circumferentially along Curve *B*

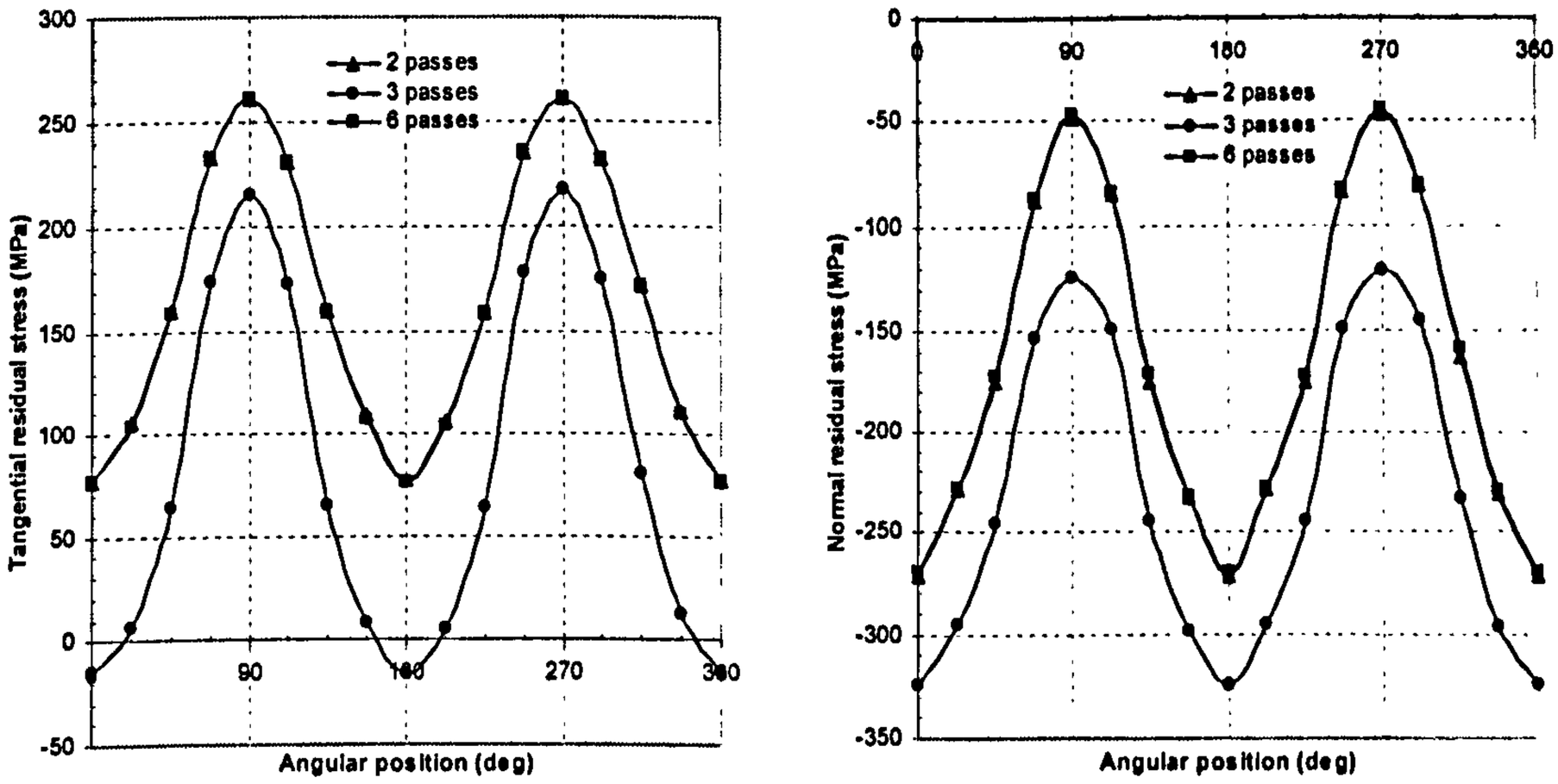

(a) Tangential stress (b) Normal stress

Figure 7.10 Residual stress distributions along Curve *B*

Figure 7.10 presents residual stress distributions along Curve *B*. Similar phenomena are observed again, i.e. the two-pass and six-pass models predict almost identical residual stresses. This is probably because the heat input of the last deposited pass of these two models is the same. The peak tangential and normal stresses predicted

by the three-pass model are 45MPa and 70MPa lower, respectively, than those by the six-pass models.

7.3.3.2.5 Circumferentially along Curve *C*

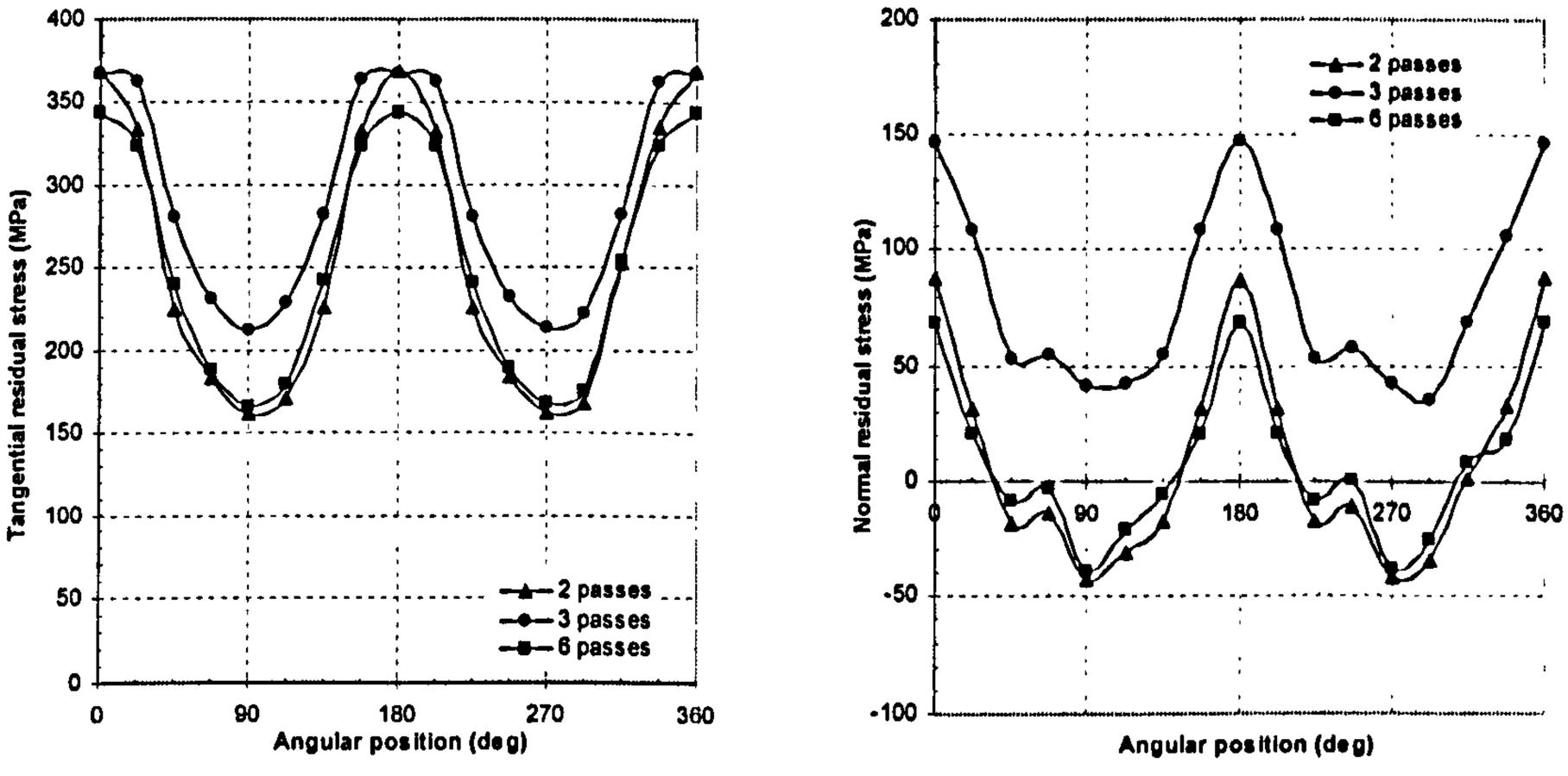

(a) Tangential stress (b) Normal stress

Figure 7.11 Residual stress distributions along Curve *C*

Figure 7.11 shows residual stress distributions along Curve *C*. Again, the two-pass and six-pass models predict similar tangential and normal residual stresses. The three-pass model seems to overestimate them, especially for the normal stress.

7.3.3.3 Summary

All the three models predict similar residual stress distributions. However, the two-pass model provides closer predictions to those of the six-pass model, compared with the three-pass model. This is probably because the two-pass and six-pass model have the same heat input for the last pass. It could be further concluded that the last pass is probably the most important pass in determining the final residual stresses in the multipass welding.

Form the point of view of the computational cost, the two-pass model requires less computational time and disk space than those of the six-pass simulation. It is therefore

suggested that multipass welding simulation can be performed in two layers. The first is one layer grouping all the previous passes together except the last, and the other layer containing the last pass only. This observation is coincident with the view expressed by Leung and Pick (1990). This conclusion is especially helpful for efficient prediction of weld induced residual stresses in thick components.

7.3.4 Effect of welding pass sequence

7.3.4.1 Introduction

As a general practice, the thick-walled tee branch junction is welded from the inside out. However, the circumferential welds of such large tee branch junction are usually executed simultaneously by several welders, symmetrically welding the component to reduce residual stresses and distortions.

In order to study the dependence of residual stresses on welding sequence, the weld path in the tee branch junction is divided into four quadrants; each quadrant is assumed to be welded from the flank centre (Rampaul 1973). To minimise uneven shrinkage, distortions and consequent residual stresses, three possible symmetrical welding sequences were proposed, as shown in Figure 7.12. The numbers in the figure indicate the welding sequences. The welding sequences investigated are summarised as follows:

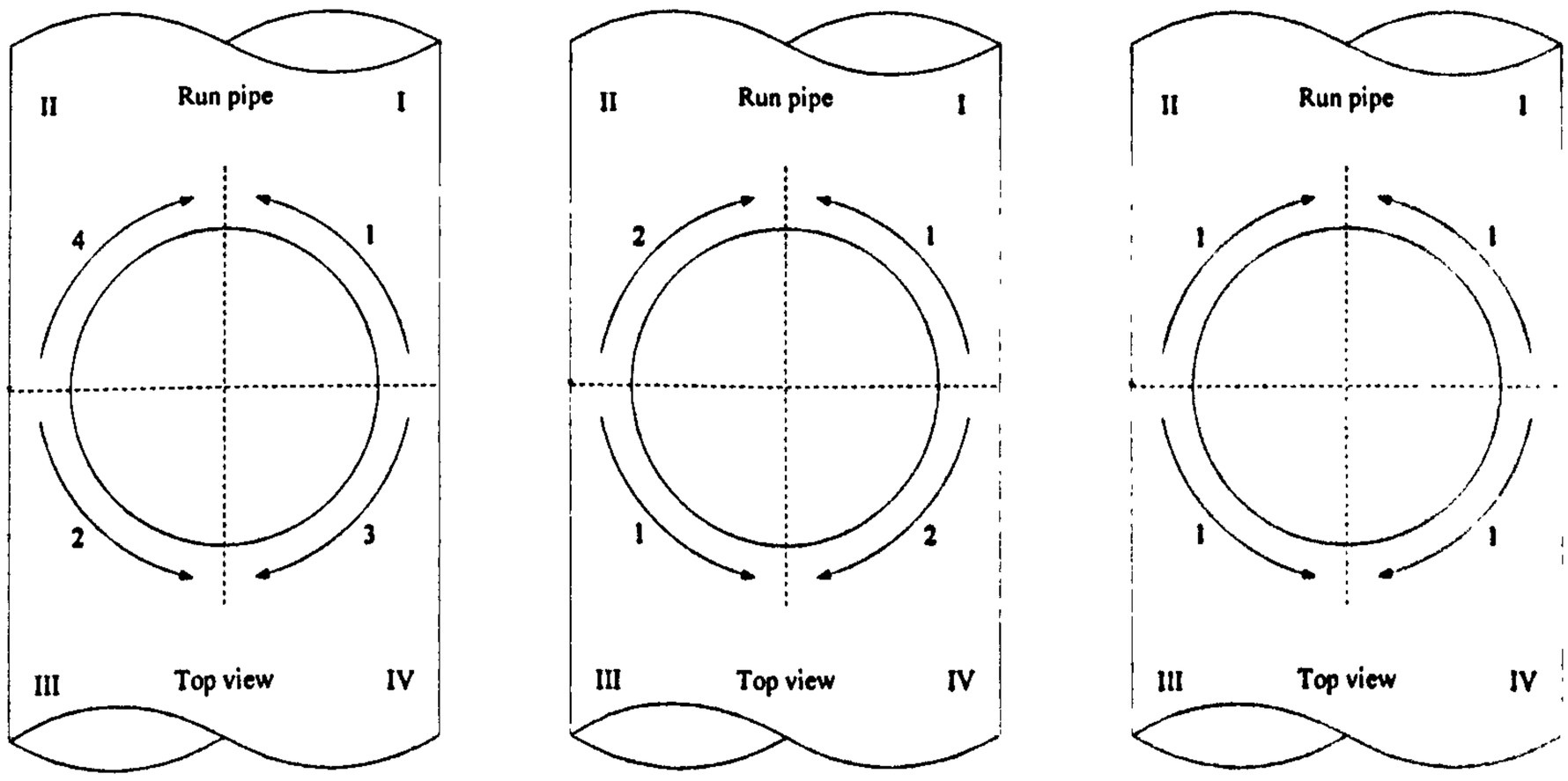

(a) One welder (b) Two welders (c) Four welders

Figure 7.12 Welding sequences of the tee branch junction

Case *A*: One welder to weld from the flank centre of the joint, in the order of

Quadrant *I, III, IV, II.*

Case *B*: Two welders starting at opposite flank centres, welding Quadrants *I* and *III* simultaneously, followed by Quadrants *IV* and *II.*

Case *C*: Four welders operating in each quadrant simultaneously from both the flank centres of the joint.

7.3.4.2 Results and discussion

7.3.4.2.1 Branch cross section *a-a*

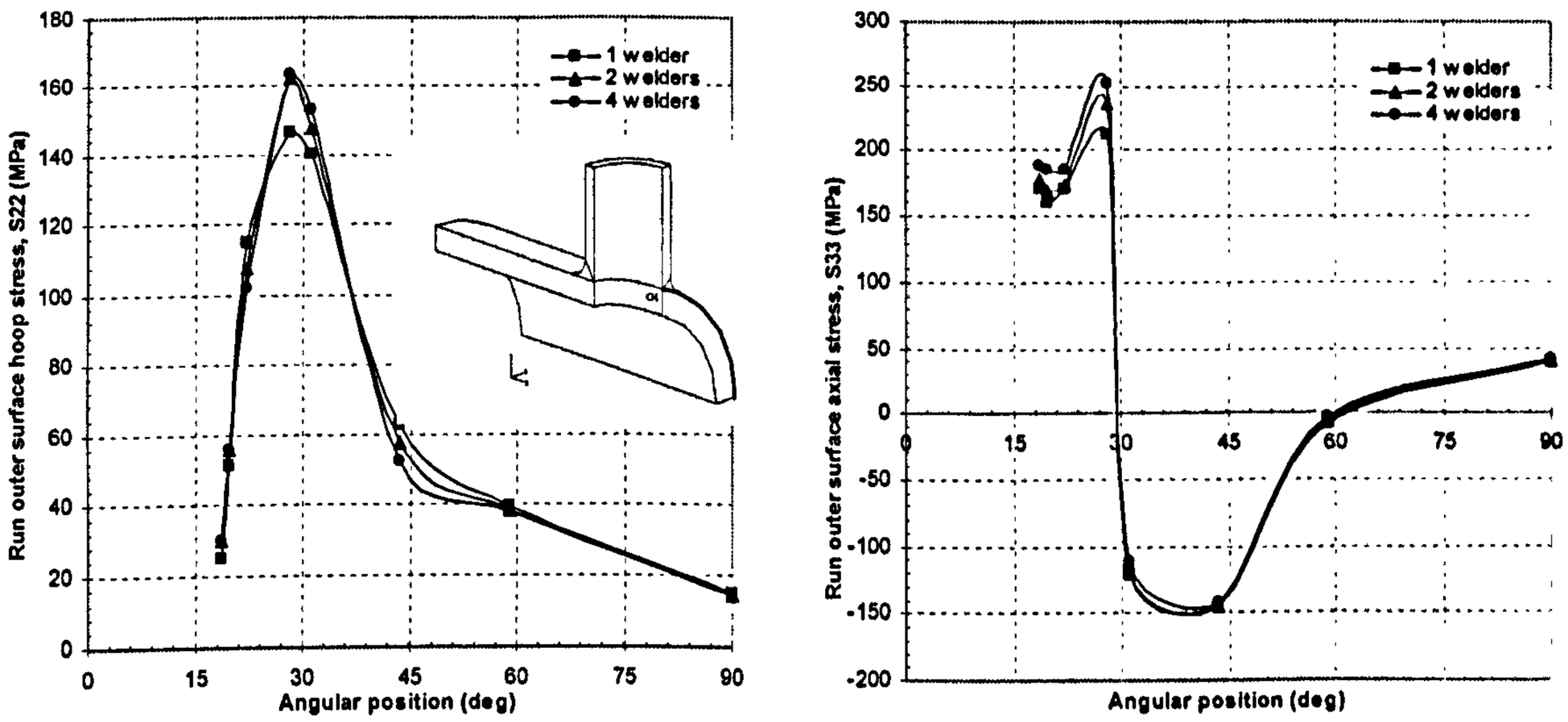

(a) Hoop stress (b) Axial stress

Figure 7.13 Stress vs. angular position on the run pipe outer surface

Figure 7.13 shows residual stress distributions versus angular position on the outer surface of the run pipe. Generally speaking, these three models predict similar patterns of the hoop and axial stress distributions. However, the peak hoop and axial stresses predicted by the one-welder model are 11% and 15% less than those by the four-welder model, respectively.

Figure 7.14 presents residual stress distributions in the Y_1-direction. In Figure 7.14(a), the one-welder model predicts a smaller tensile zone and the lowest peak tensile axial stress of 120MPa (43%σ_y), which is about 27% less than that by the four-welder model. These three models predict almost identical patterns and magnitudes of the hoop stresses, as shown in Figure 7.14(b).

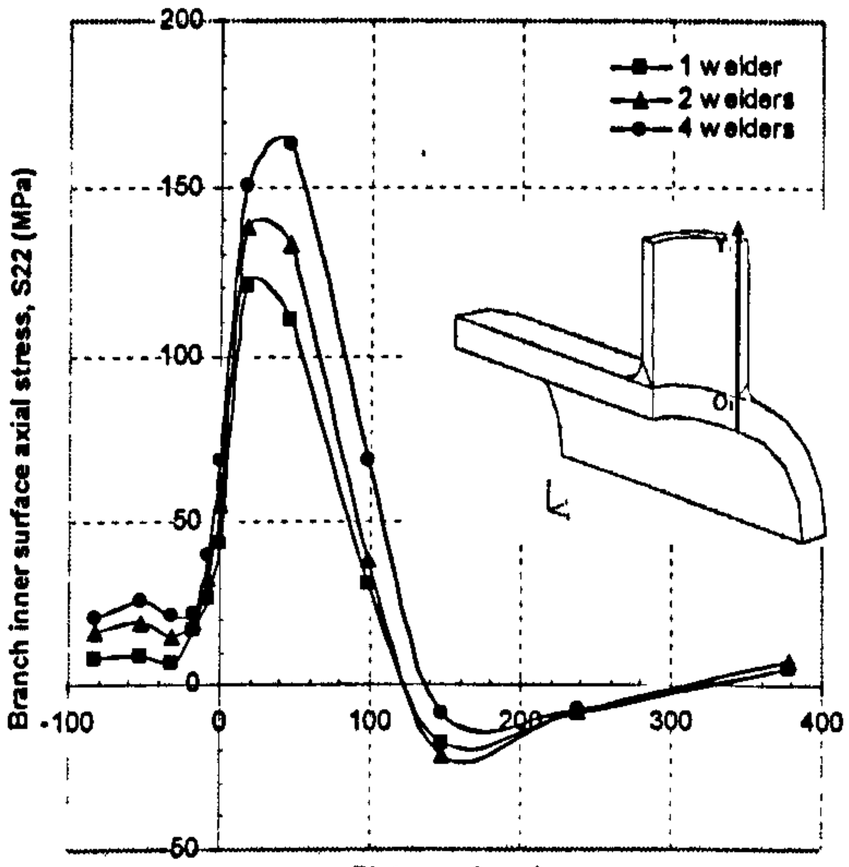

(a) Axial stress

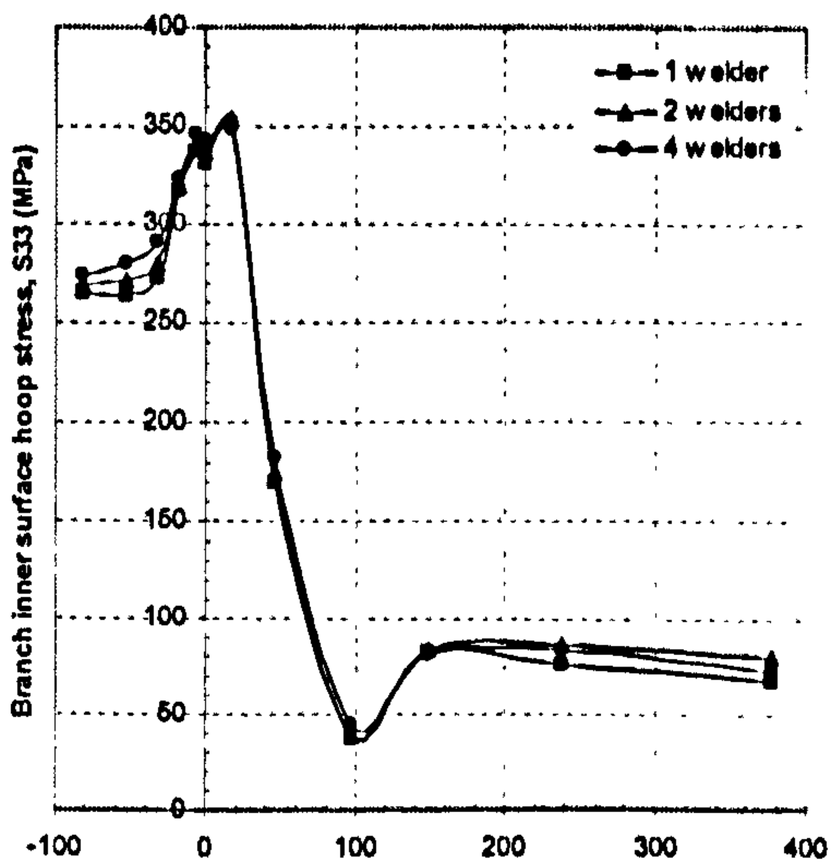

(b) Hoop stress

Figure 7.14 Residual stresses in the Y_1-direction on the branch inner surface

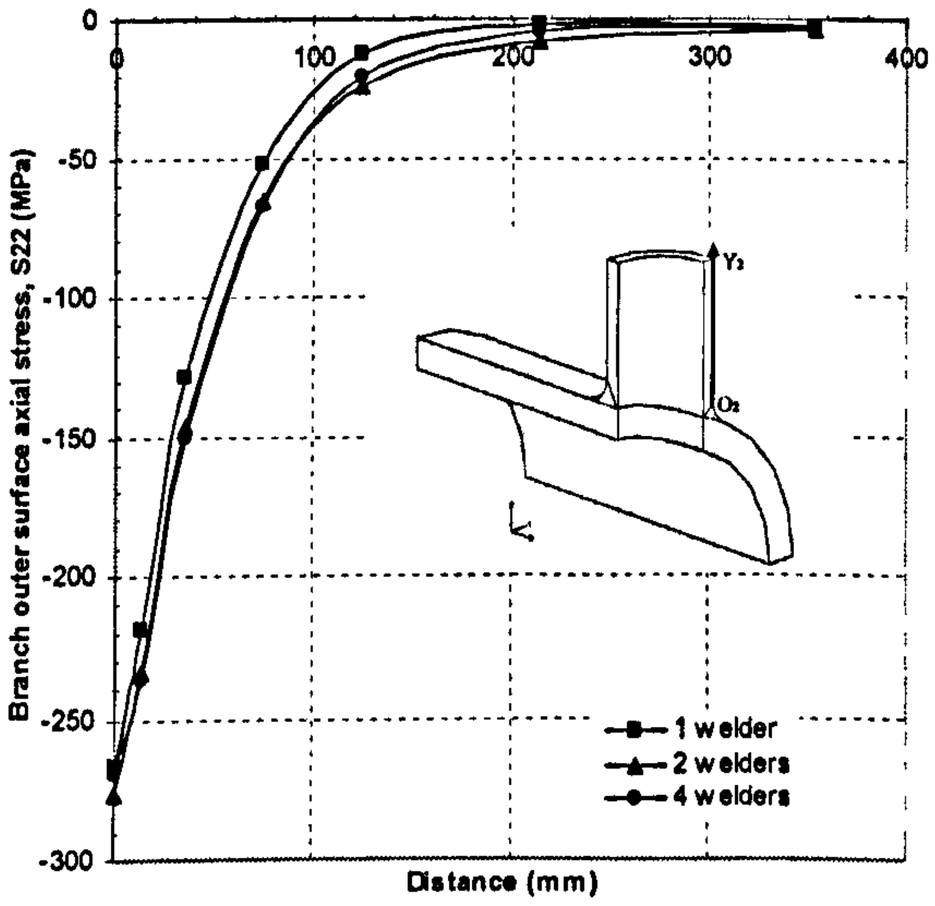

(a) Axial stress

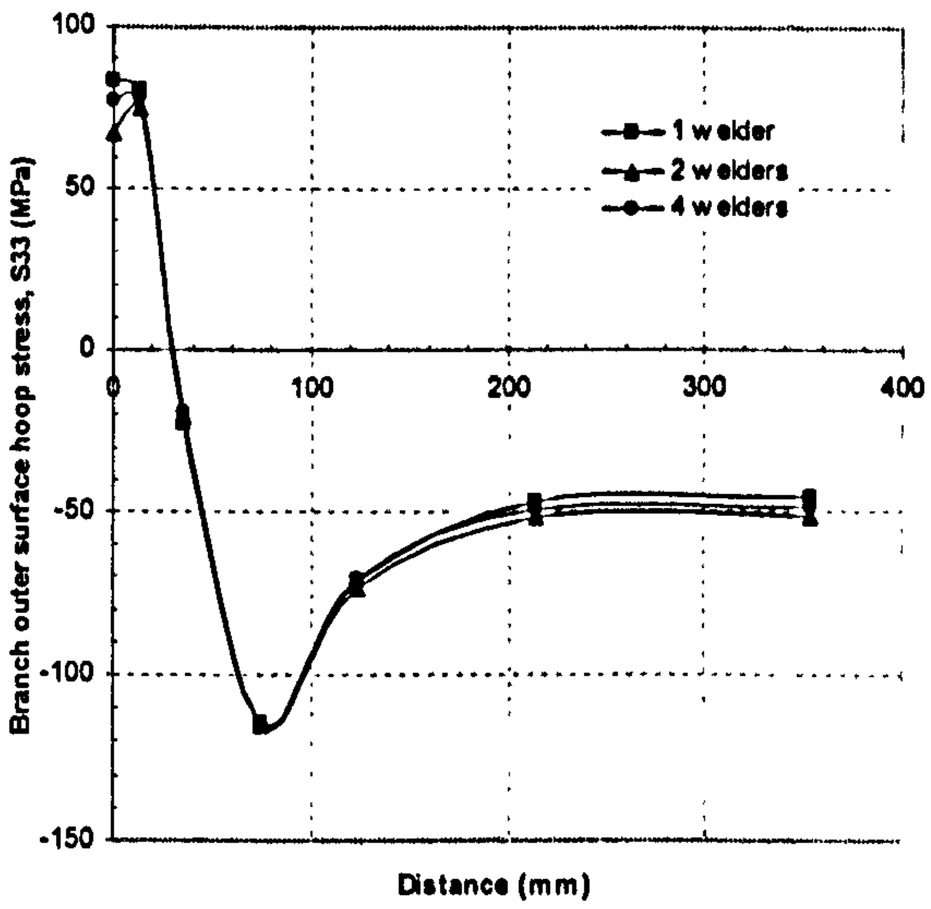

(b) Hoop stress

Figure 7.15 Residual stresses in the Y_2-direction on the branch outer surface

Figure 7.15 shows residual stress distributions in the Y_2-direction. The axial stresses are compressive along this path on the branch outer surface. The hoop stresses are mainly compressive, with only a small tensile zone with stresses well below 100MPa. Quite consistent residual stress distributions and almost the same magnitudes can be observed from the predictions of these three models.

7.3.4.2.2 Run pipe cross section *b-b*

Figure 7.16 shows the residual stress distributions in the X-direction. The hoop

residual stresses predicted by the three models agree quite well beyond 50mm. However, within 50mm, the four-welder model predicts a slightly higher hoop stresses while the one-welder model gives the lowest values. The predictions by the two-welder model are located closer to those by the four-welder model. The maximum hoop stress predicted by the four-welder model is 350MPa (126%σ_y) near the centre of the weld seam, which is 13% more than that by the one-welder model, as shown in Figure 7.16(a). From Figure 7.16(b), it is noticed that the axial stress predictions from the three models are quite similar, except within the distance from 50mm to 122mm, which represents both sides of the weld toe. Nevertheless, the differences are not very noticeable.

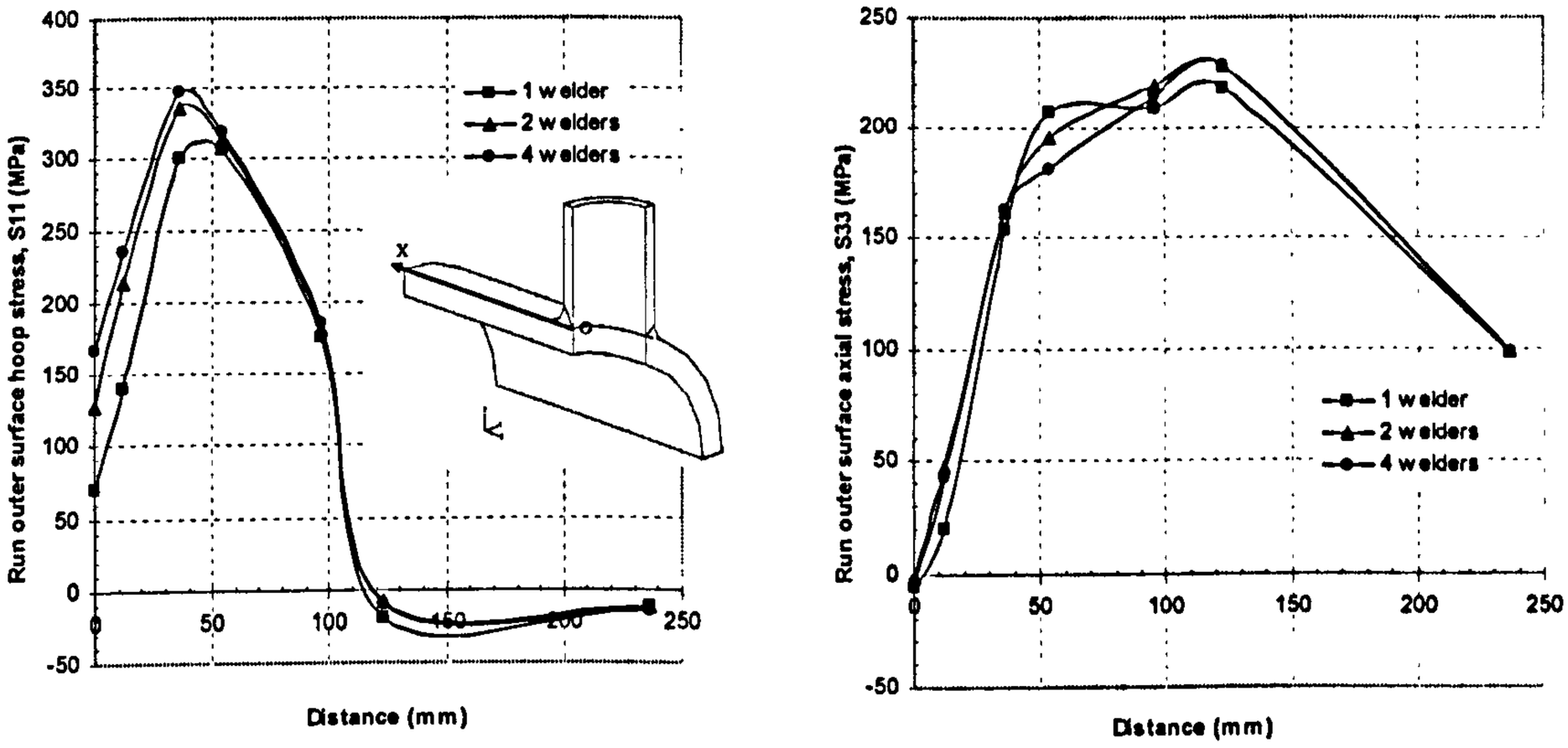

(a) Hoop stress (b) Axial stress

Figure 7.16 Residual stresses in the *X*-direction on the run outer surface

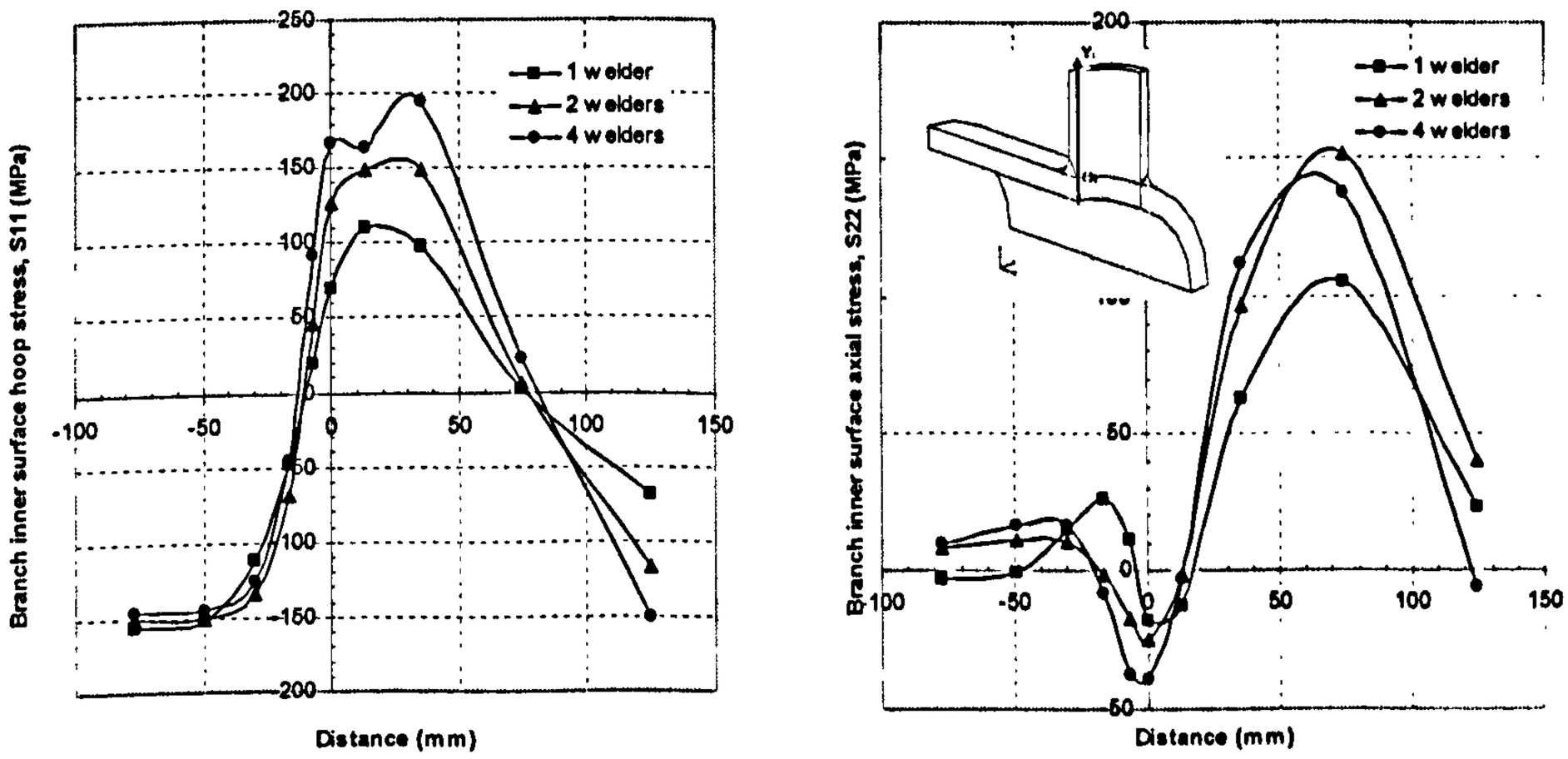

(a) Hoop stress (b) Axial stress

Figure 7.17 Residual stresses in the Y_l-direction on the branch inner surface

Figure 7.17 shows the residual stress distributions along the Y_1-direction. The one-welder model predicts the lowest peak hoop stress of 110MPa, while the four-welder model gives the highest magnitude of 200MPa, which nearly doubles the prediction of the one-welder model. Considering the axial stresses, it is noticed that all the three models predict similar patterns, with the one-welder model again giving the lowest peak axial stress. Both the hoop and axial stresses predicted by the two-welder model are located in between and closer to those of the four-welder model.

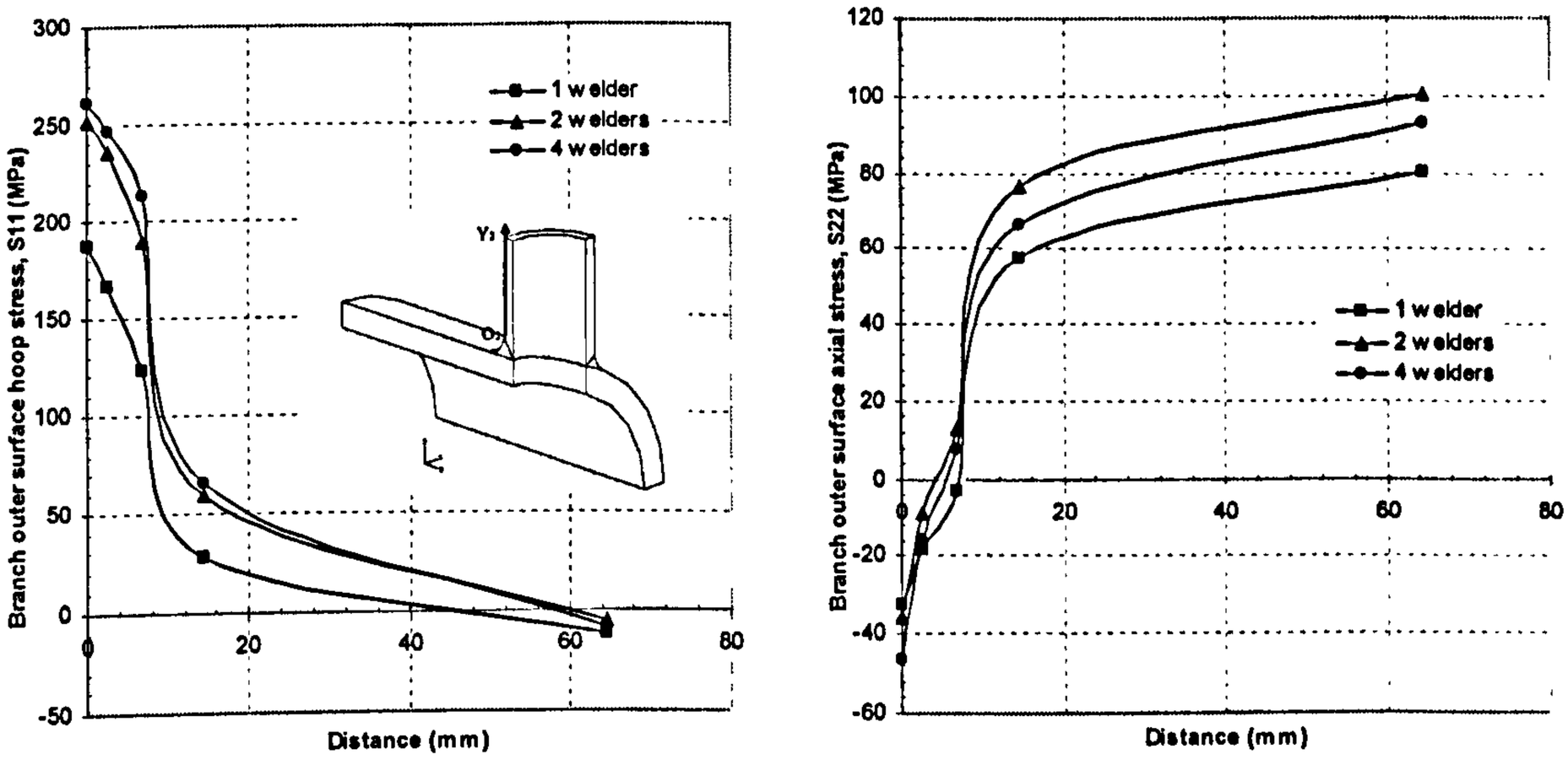

(a) Hoop stress (b) Axial stress

Figure 7.18 Residual stresses in the Y_2-direction on the branch outer surface

Figure 7.18 shows residual stress distributions in the Y_2-direction. It is again observed that the three models predict similar residual stress distributions, with the predictions by the two-welder model being closer to those of the four-welder model. The peak hoop and axial residual stresses predicted by the one-welder model are 27% and 11% less than those by the four-welder model, respectively.

7.3.4.2.3 Circumferentially along Curve *A*

Figure 7.19 shows the residual stress distributions along Curve *A*. Almost the same peak tensile tangential stress of 250MPa ($90\%\sigma_y$) is predicted by both the one-welder and four-welder models, however, at slightly different locations. For the four-welder model, it is at the flank centres, while for the one-welder model, it is at 135° away from the start of welding. The peak tensile tangential stress predicted by the two-welder

model is 240MPa at the flank centres and their surrounding areas. The predictions by the two-welder and four-welder models show symmetrical feature while those by the one-welder model do not. Similar observations can be made about the results presented in Figure 7.19(b), except that the peak tensile normal stress of 220MPa is located at the two crotch corners.

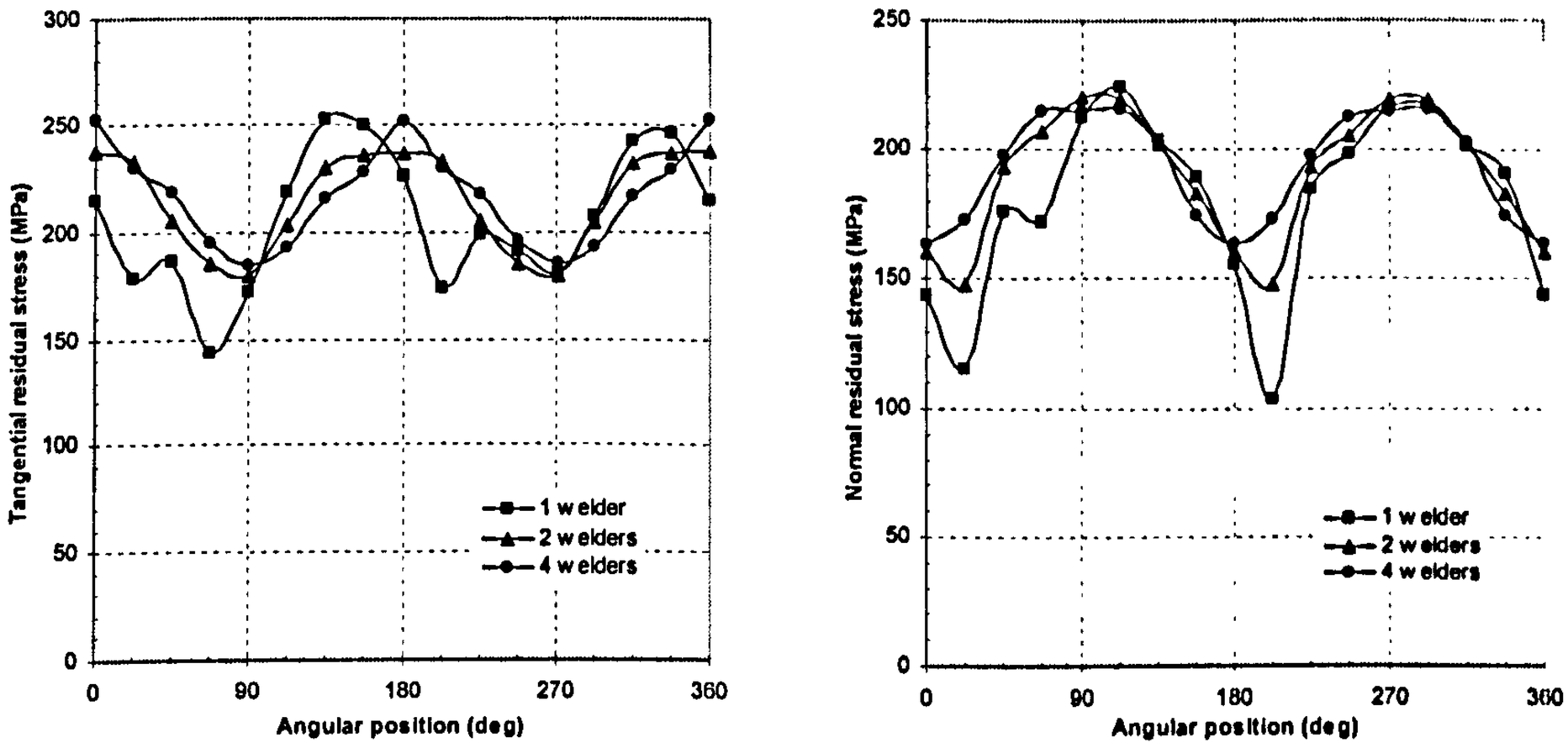

(a) Tangential stress (b) Normal stress

Figure 7.19 Residual stress distributions along Curve *A*

7.3.4.2.4 Circumferentially along Curve *B*

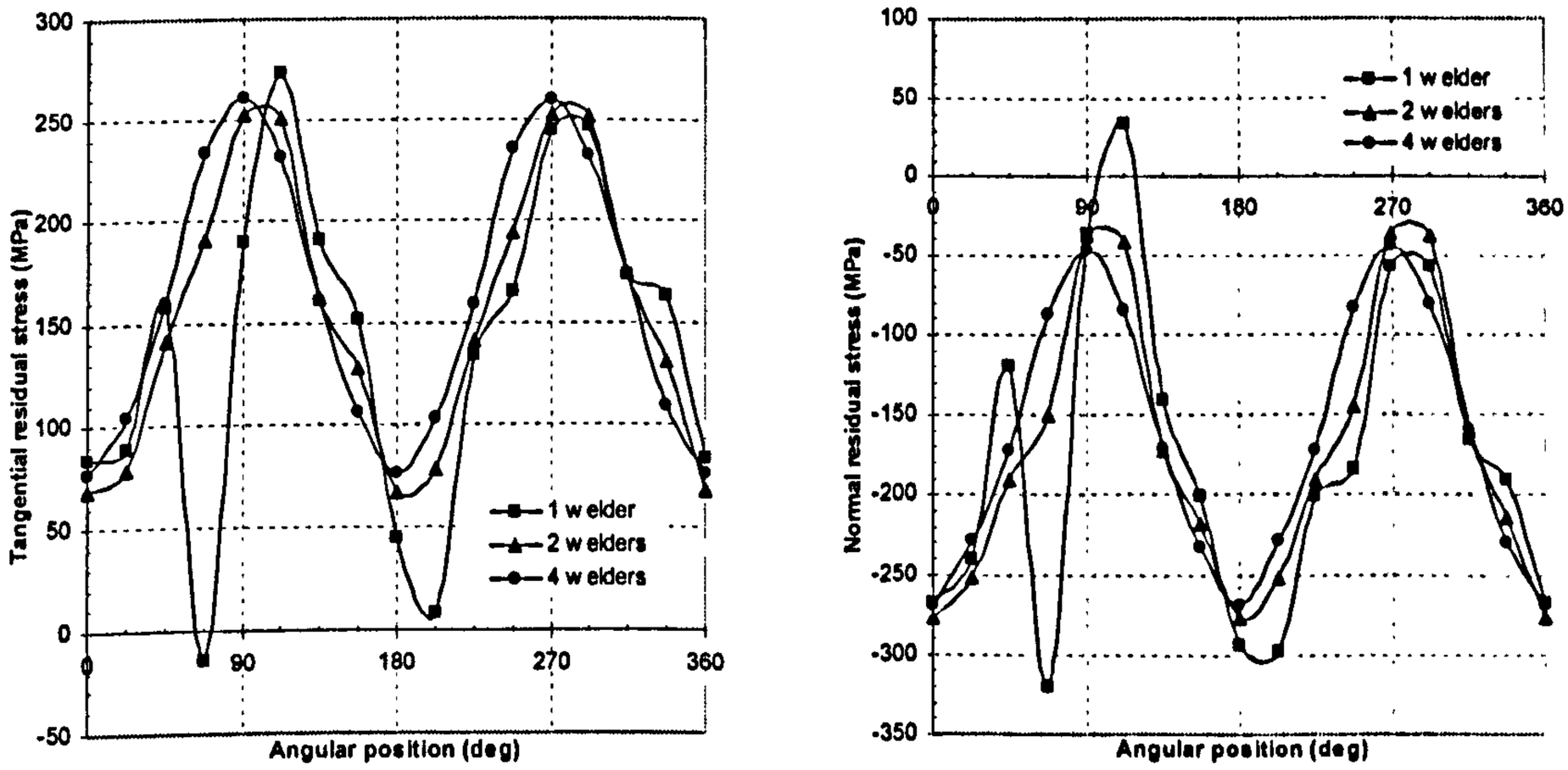

(a) Tangential stress (b) Normal stress

Figure 7.20 Residual stress distributions along Curve *B*

Figure 7.20 shows residual stress distributions along Curve *B*. Again, the predictions from both the two-welder and four-welder models show symmetrical

characteristics along the weldline. There is no symmetrical feature for the predictions by the one-welder model. The peak tensile tangential stresses are located at the two crotch corners. The normal stresses in most regions along Curve *B* are in compressive except near the 90° location from the start of welding, where a negligibly small tensile stress is predicted by the one-welder model.

7.3.4.2.5 Circumferentially along Curve *C*

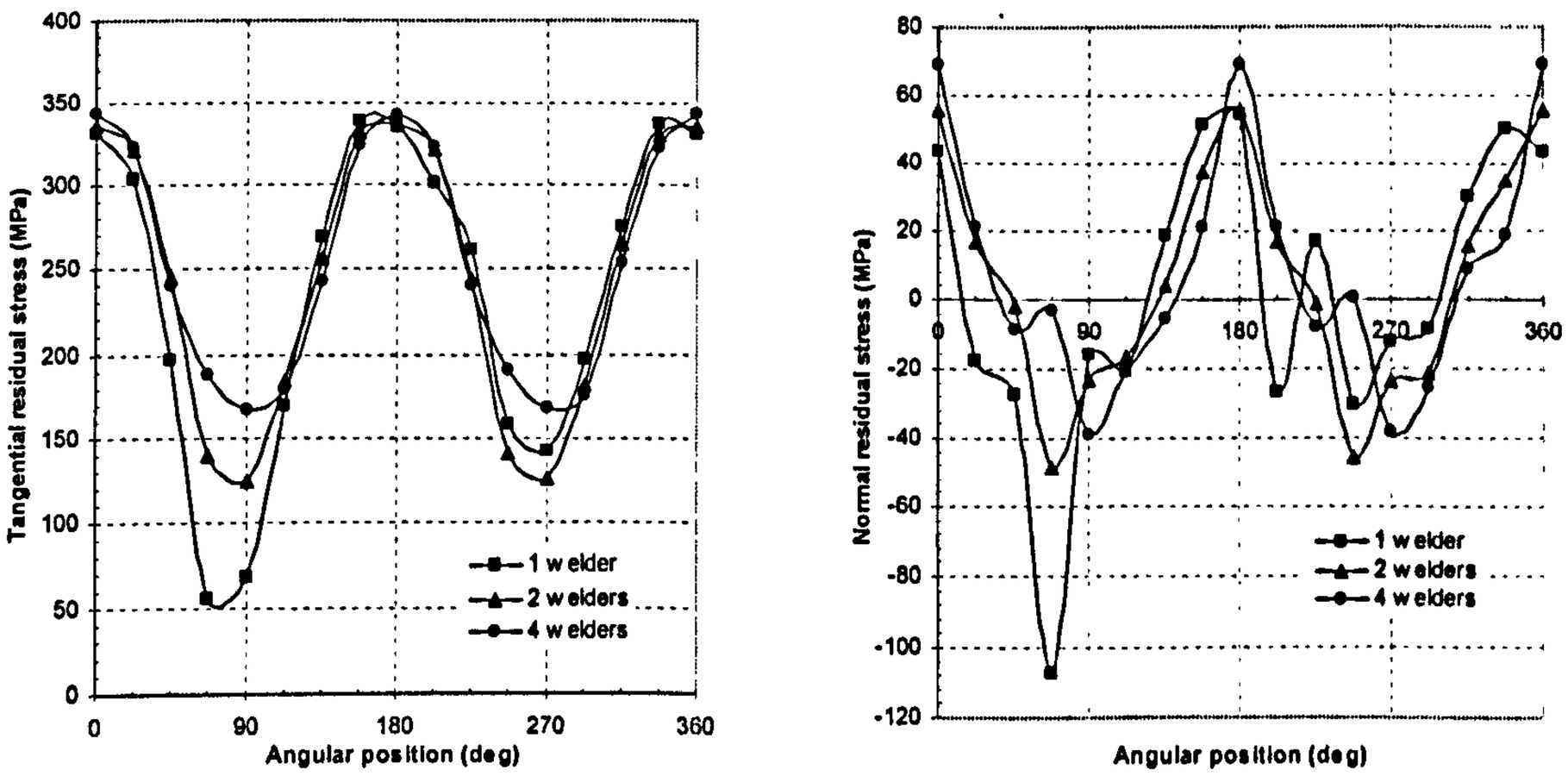

(a) Tangential stress (b) Normal stress

Figure 7.21 Residual stress distributions along Curve *C*

Figure 7.21 illustrates the residual stress distributions along Curve *C*. The tangential residual stress distributions along Curve *C* predicted by the three models demonstrate comparable trends, with the predictions of the two-welder and four-welder models show clear symmetry. All of the three models give a maximum tensile tangential stress of about 340MPa (122%σ_y) at the two flank centres, as can be noticed in Figure 7.21(a). No clear features can be noticed among the three models in the predicted normal stresses in Figure 7.21(b).

7.3.4.3 Summary

As a general comment, at both the branch and run cross section, the four-welder model predicts the highest peak stresses while the one-welder model gives the lowest

values; The predictions by the two-welder model are almost always located closer to those by the four-welder model.

There are not many differences for the predicted maximum stresses along Curves *A*, *B* and *C* between the three models. However, as would be expected, the stress distributions predicted by the four-welder and two-welder models show more symmetrical feature than those by the one-welder model.

7.3.5 Effect of heat input

7.3.5.1 Introduction

Heat input is a relative measure of the energy transferred per unit length during welding. It is a dominant factor governing all significant thermal events in welding (American Welding Society, 1963). Heat input serves to fuse the base and filler material in order to provide reliable bonding between them continuously throughout the total length of the joint. The maximum temperature a component can attain is dependent on the total heat input. It is thus important to control the heat input so that the edges of the base metal will melt sufficiently and at the same time no excessive penetration will happen.

To take into account the heat transfer to ambient air and radiation to the surroundings, heat input is typically calculated using the following expression:

$$Q=\eta UI/v \qquad \text{Equation 7.1}$$

Changes in individual parameters such as voltage, current, efficiency or travel speed have effects only in so far as heat input is changed. In other words, heat input is not the sole factor governing weld quality, but is a unique determinant of the thermal event as a whole (American Welding Society, 1963).

Brickstad and Josefson (1998) commented that, in weld specifications, the current, voltage and travel speed were generally given with wide limits. Thus the heat input could be easily varied with a factor of four and still be inside the limits of the given welding parameters. However, some combinations of the welding parameters were

clearly unrealistic, i.e. they corresponded to situations for which either the melting temperature could not be reached or a too large molten zone size was achieved.

In order to guarantee a realistic welding implementation, the combinations of welding parameters were chosen cautiously. Four cases (*A*, *B*, *C* and *D*, which corresponded to low, medium, high and highest amount of heat input respectively) were investigated, as indicated in Table 7.2. Based on the parameters listed in Table 6.6, the welding voltage and speed were kept the same for Cases *A*, *B* and *C*, while the welding current was changed from a minimum to a maximum value within the given limits. For Case *D*, the heat input of each pass was assumed to be twice that of Case *C*. In order to achieve this, the arc efficiencies were increased to 70% and 80% for the TIG and MMA, respectively. The welding speeds were slightly adjusted while weld voltage and current were kept the same as those of Case *C*. The heat input of each pass in each case was compared with corresponding passes of Case *B*. The relative values of heat input as well as simulation parameters are listed in Table 7.2. The evaluation was carried out by keeping the rest of the parameters at the same constant values.

Table 7.2 Weld parameters used in the simulation for evaluating heat input effect

Case No.	Heat input	Pass number	Welding method	Voltage (V)	Current (A)	Speed (mm/s)	Heat input (kJ/mm)	Relative heat input
A	Low	1	TIG	9.6	75	1.00	0.36	0.75
		2	MMA	17.3	85	1.33	0.774	0.71
		3-6	MMA	17.6	150	1.83	1.01	0.89
B	Medium	1	TIG	9.6	100	1.00	0.48	1
		2	MMA	17.3	120	1.33	1.09	1
		3-6	MMA	17.6	170	1.83	1.14	1
C	High	1	TIG	9.6	120	1.00	0.576	1.2
		2	MMA	17.3	140	1.33	1.274	1.16
		3-6	MMA	17.6	190	1.83	1.279	1.12
D	Highest	1	TIG	9.6	120	0.70	1.15	2.39
		2	MMA	17.3	140	0.76	2.55	2.33
		3-6	MMA	17.6	190	1.05	2.56	2.24

7.3.5.2 Results and discussion

7.3.5.2.1 Branch cross section *a-a*

Figure 7.22 shows residual stress distributions versus angular position on the outer surface of the run pipe. It is clearly noticed that all the four cases predict almost identical results.

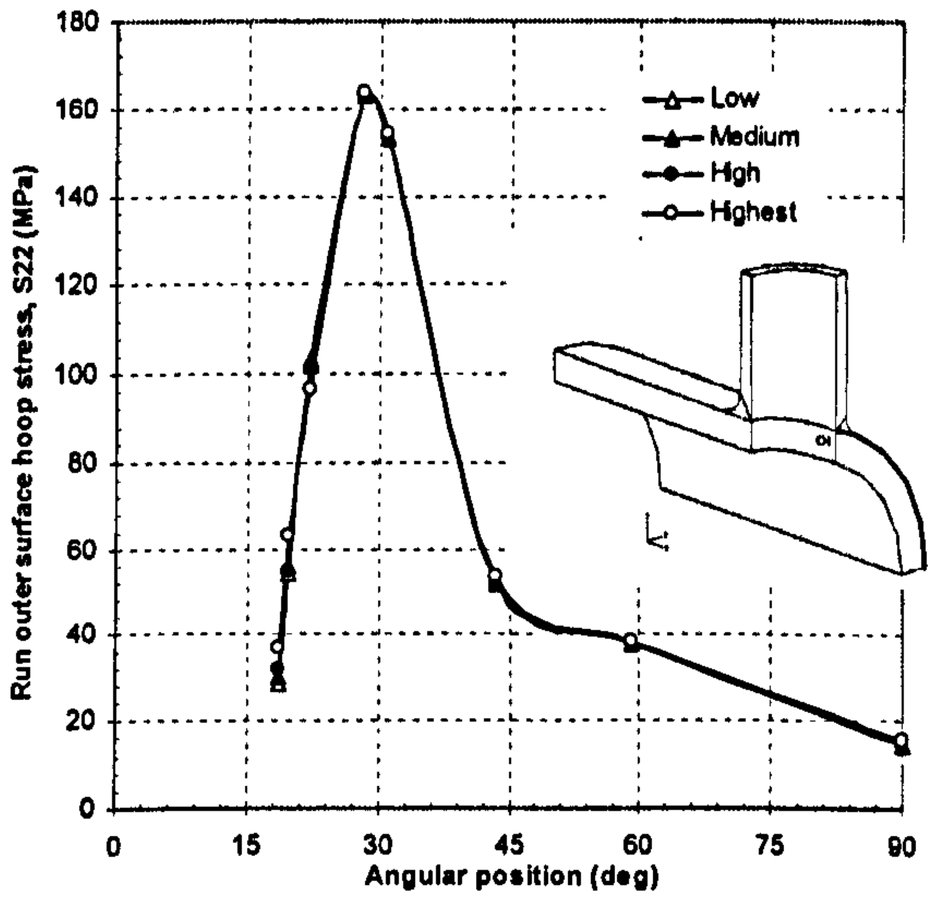

(a) Hoop stress

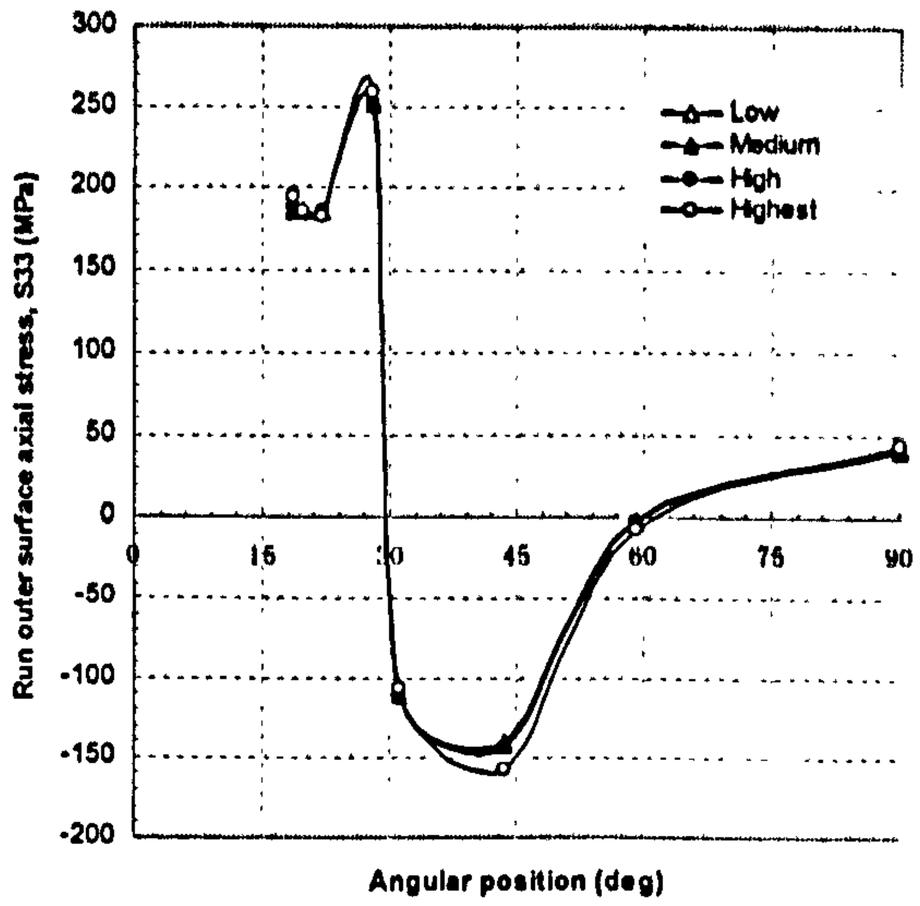

(b) Axial stress

Figure 7.22 Stress vs. angular position on the run pipe outer surface

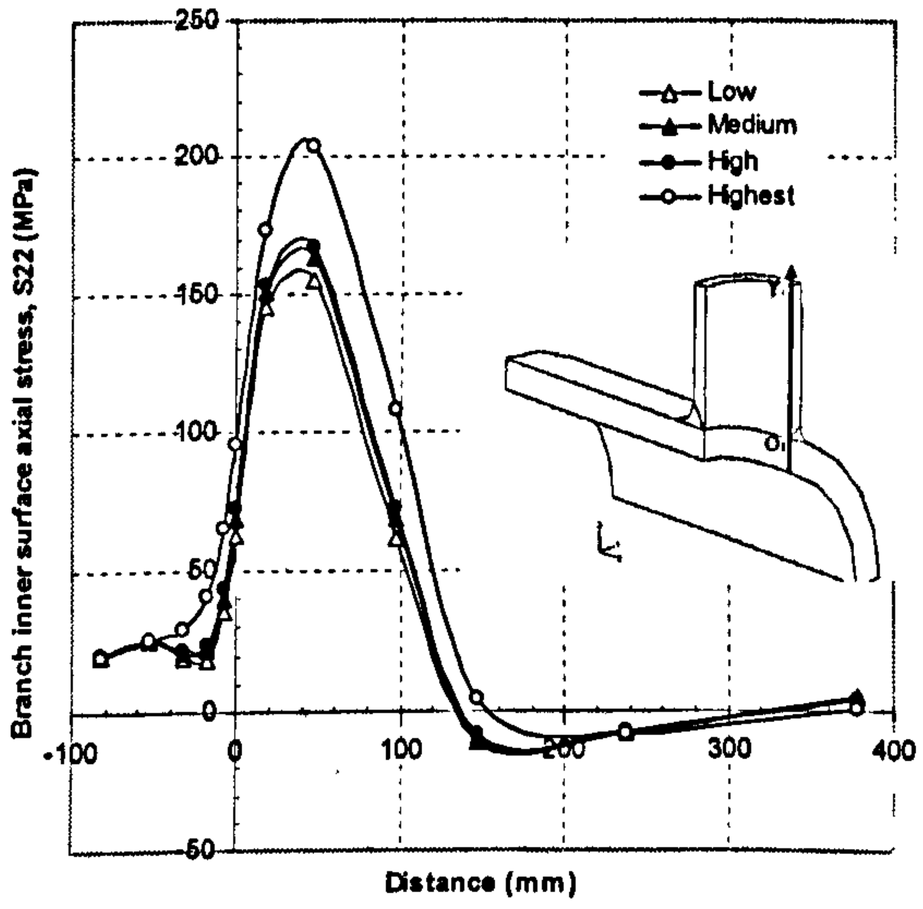

(a) Axial stress

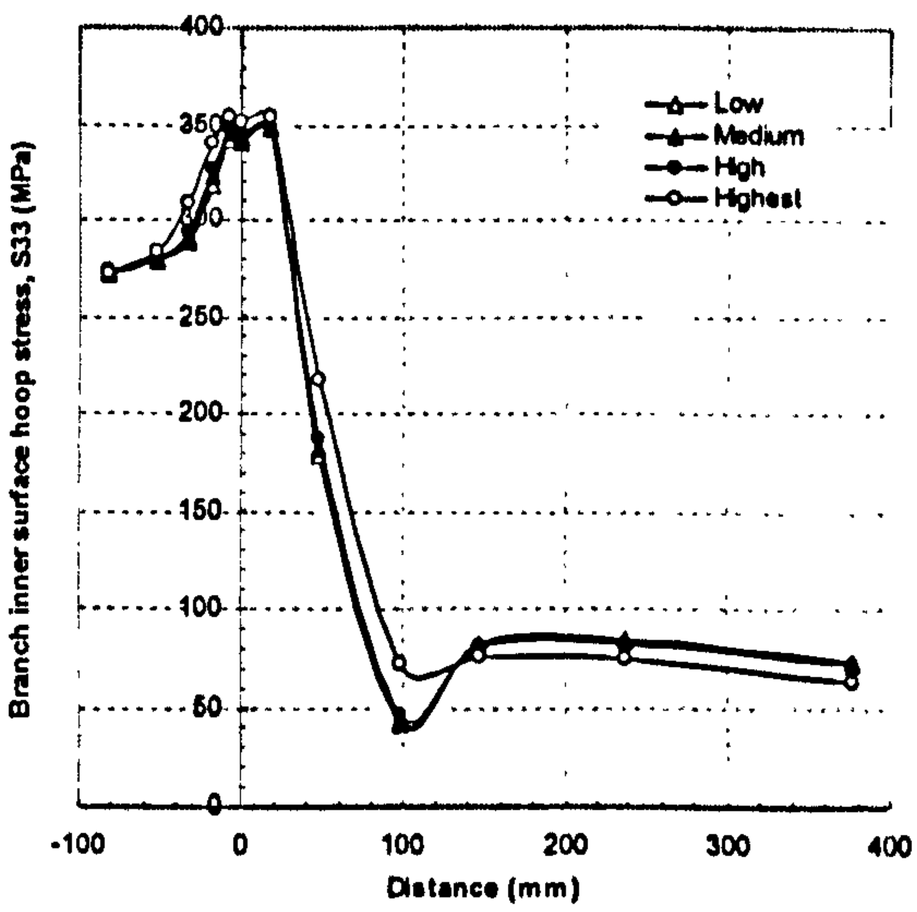

(b) Hoop stress

Figure 7.23 Residual stresses in the Y_1-direction on the branch inner surface

Figure 7.23 presents residual stress distributions in the Y_1-direction. With the heat input being doubled, the peak tensile axial stress increased by 23%, i.e. from 170MPa to 210MPa, and the axial tensile zone also widened. The hoop stresses from the inner surface of the run pipe up to 120mm on the branch side are also marginally increased.

Figure 7.24 presents the residual stress distributions in the Y_2-direction. It is noted that axial compressive stresses are throughout the Y_2-direction. Hoop stresses are mainly compressive except within a distance of 25mm from the origin, where they are tensile with magnitudes less than 75MPa. Overall, the heat input does not appear to affect

much the residual stress, except only slightly decreasing the hoop residual stress by about 20MPa at the origin.

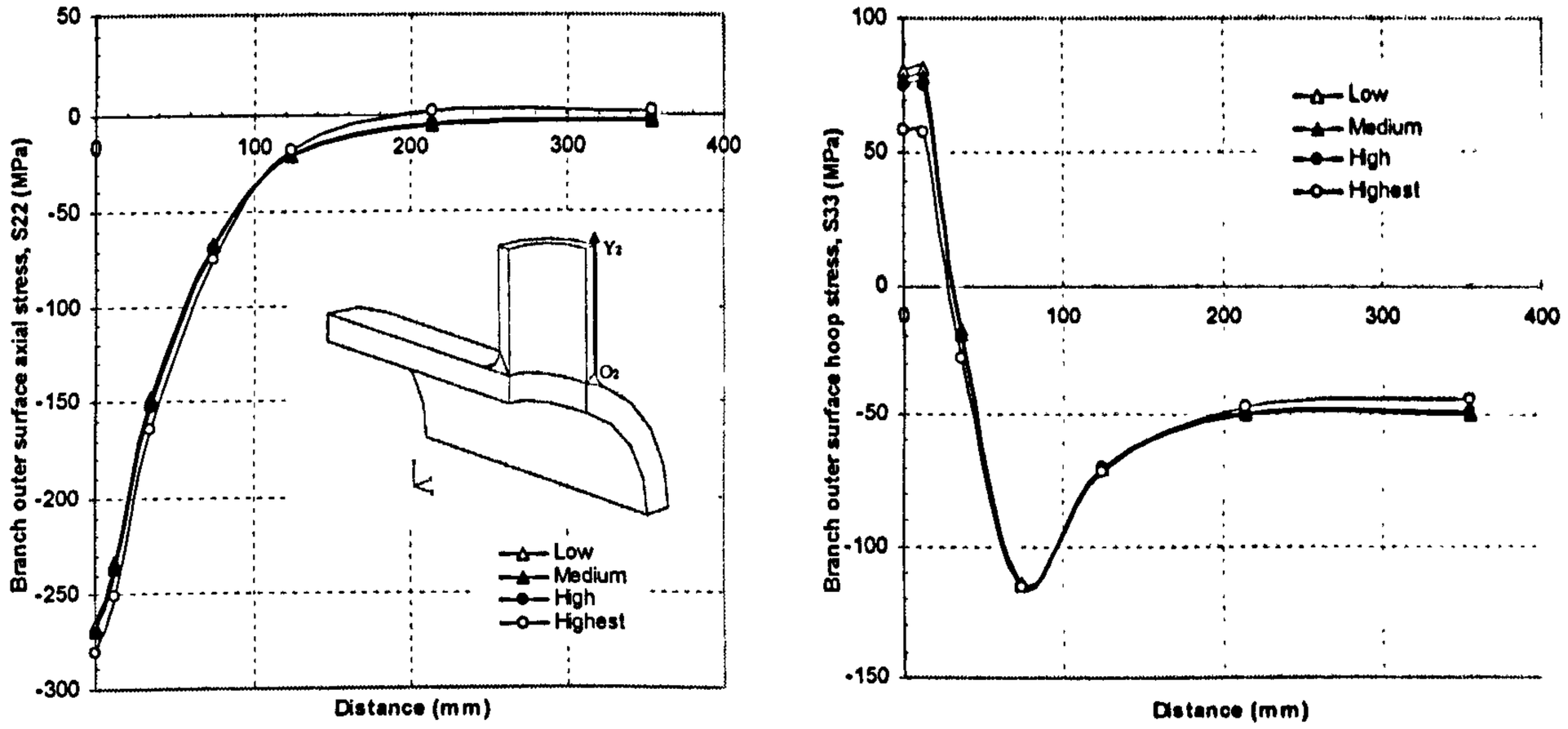

(a) Axial stress (b) Hoop stress

Figure 7.24 Residual stresses in the Y_2-direction on the branch outer surface

7.3.5.2.2 Run pipe cross section *b-b*

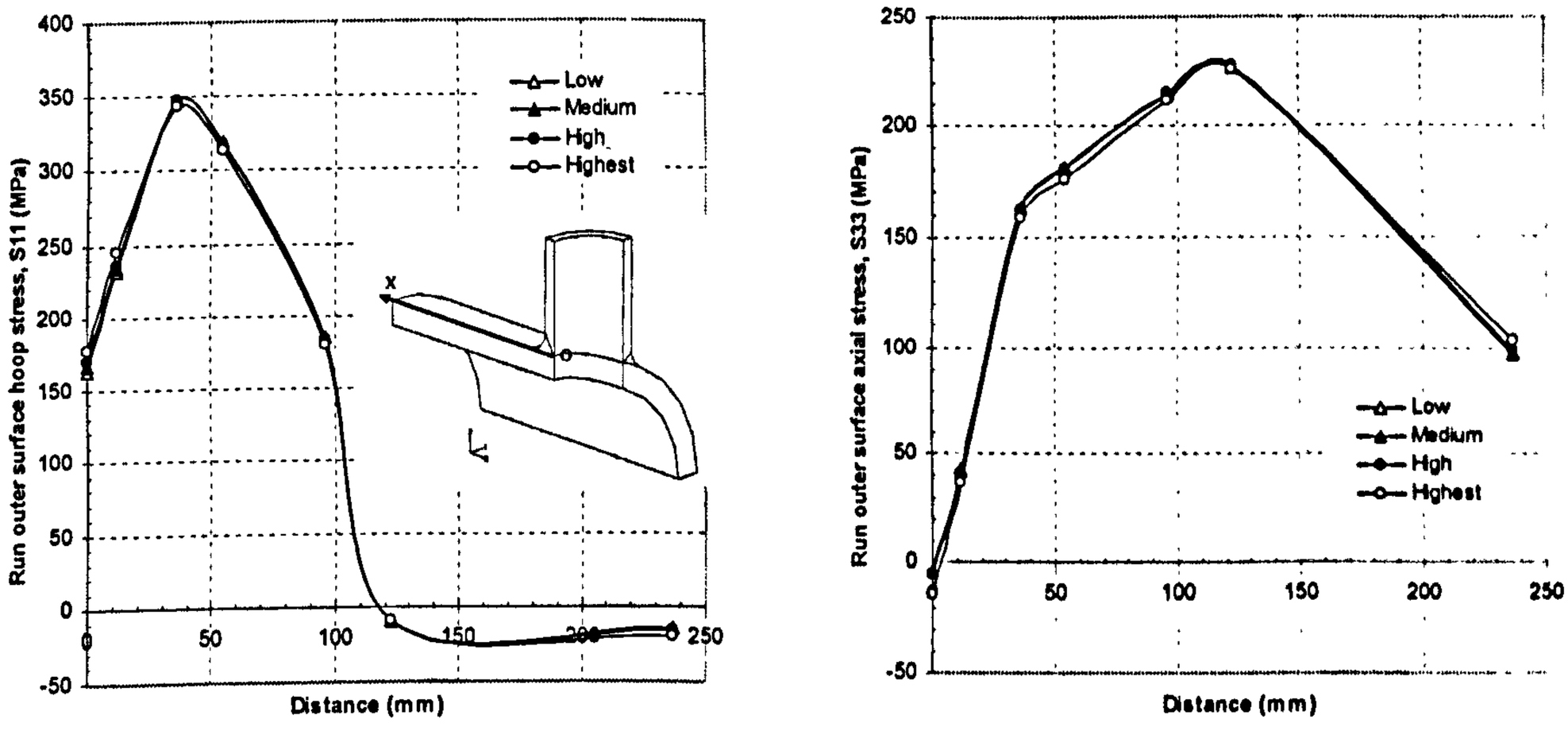

(a) Hoop stress (b) Axial stress

Figure 7.25 Residual stresses in the X-direction on the run outer surface

Figure 7.25 shows the residual stress distributions in the X-direction. The almost identical simulation results indicate that varying the heat input has almost no effects on the residual stresses.

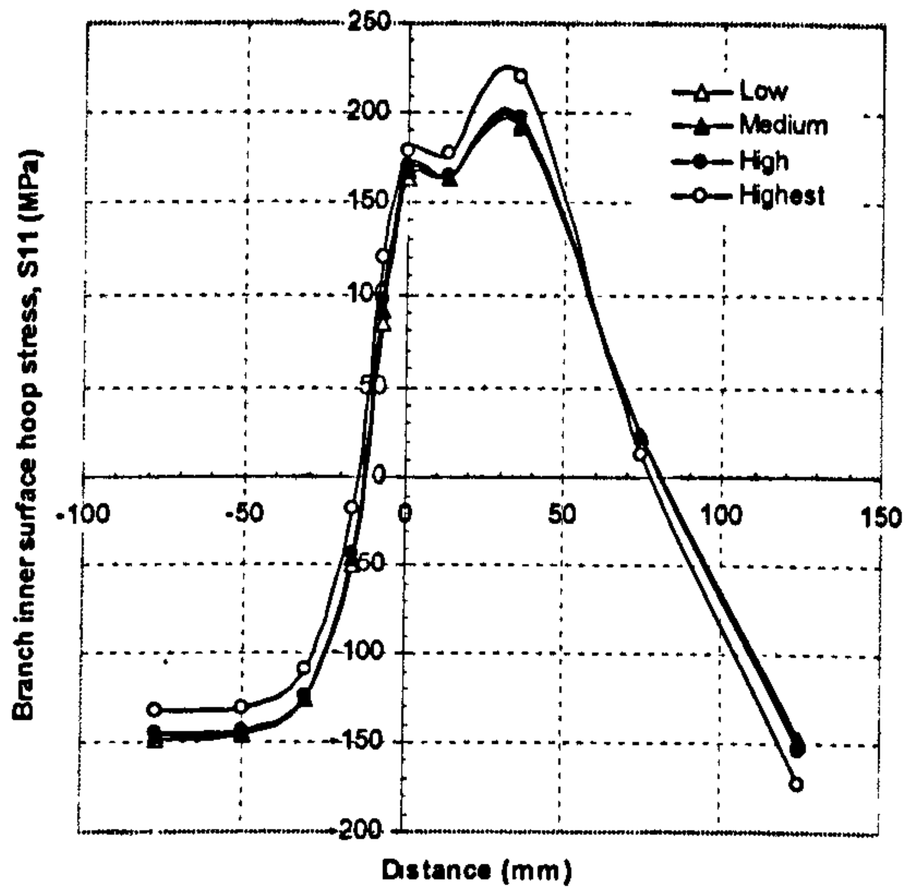

(a) Hoop stress

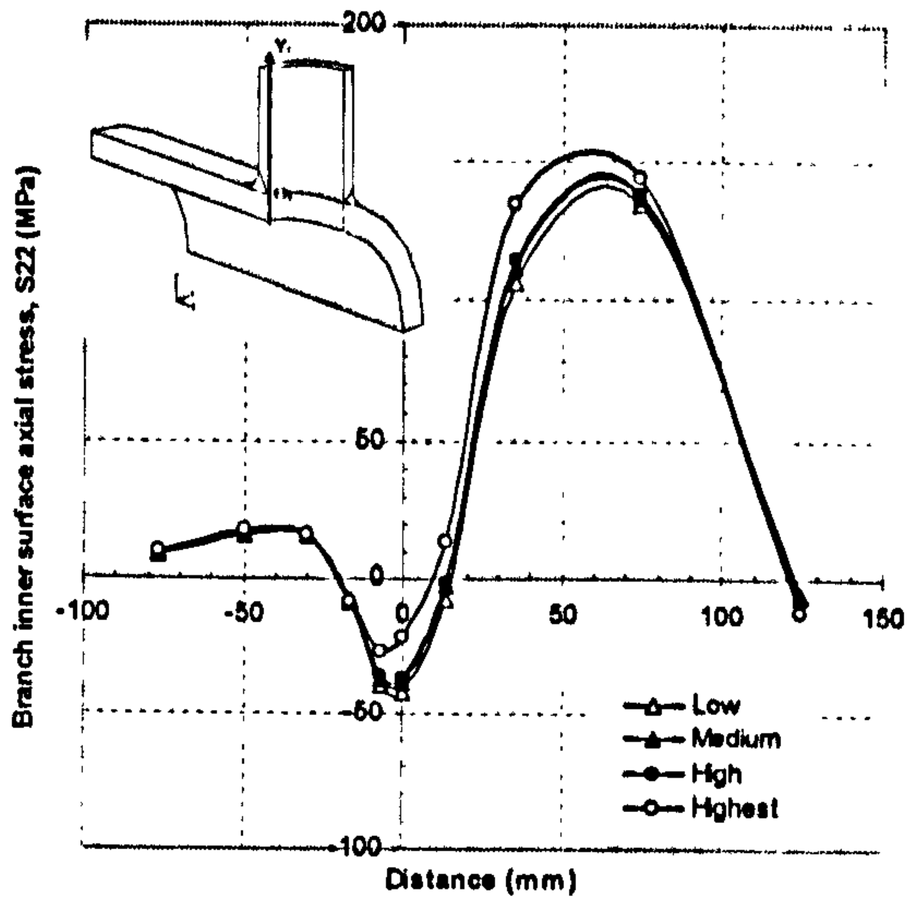

(b) Axial stress

Figure 7.26 Residual stresses in the Y_1-direction on the branch inner surface

Figure 7.26 shows residual stress distributions in the Y_1-direction. It is noticed that, by doubling the heat input in Case *D*, the peak hoop and axial residual stresses are increased only by 12% and 6%, respectively, compared to those of Case *B*.

Figure 7.27 shows the residual stress distributions in the Y_2-direction. Again, it is noticed that increasing the heat input has negligible effect on the residual stresses.

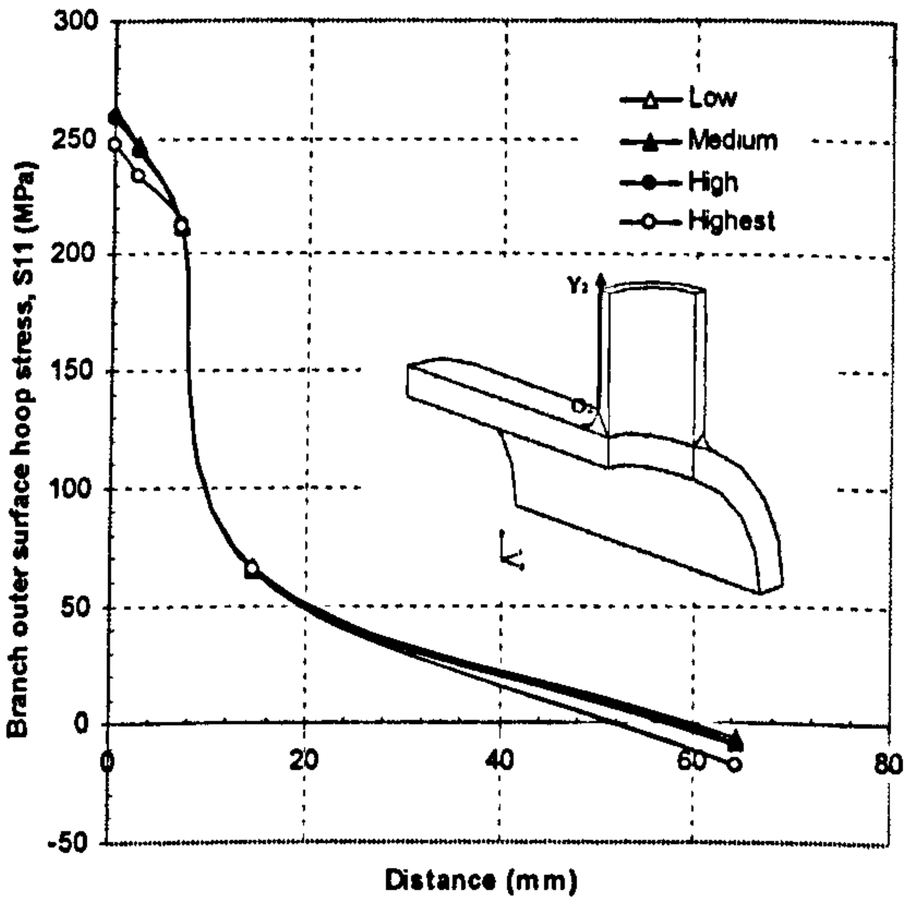

(a) Hoop stress

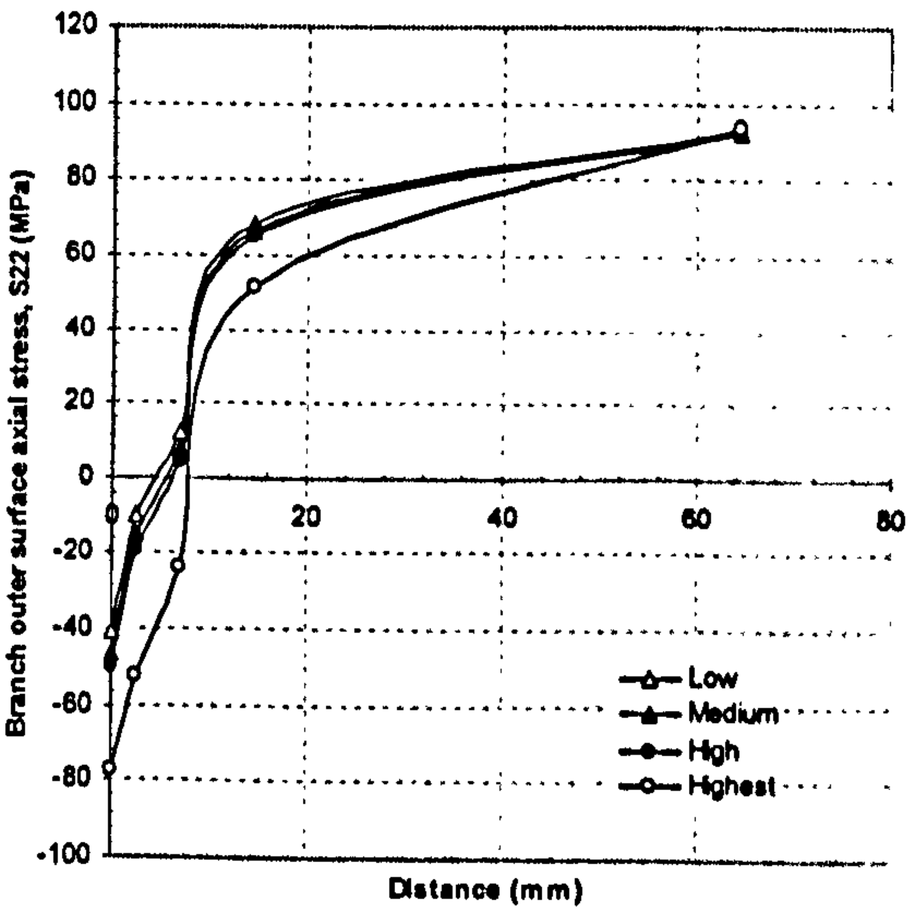

(b) Axial stress

Figure 7.27 Residual stresses in the Y_2-direction on the branch outer surface

7.3.5.2.3 Circumferentially along Curve *A*

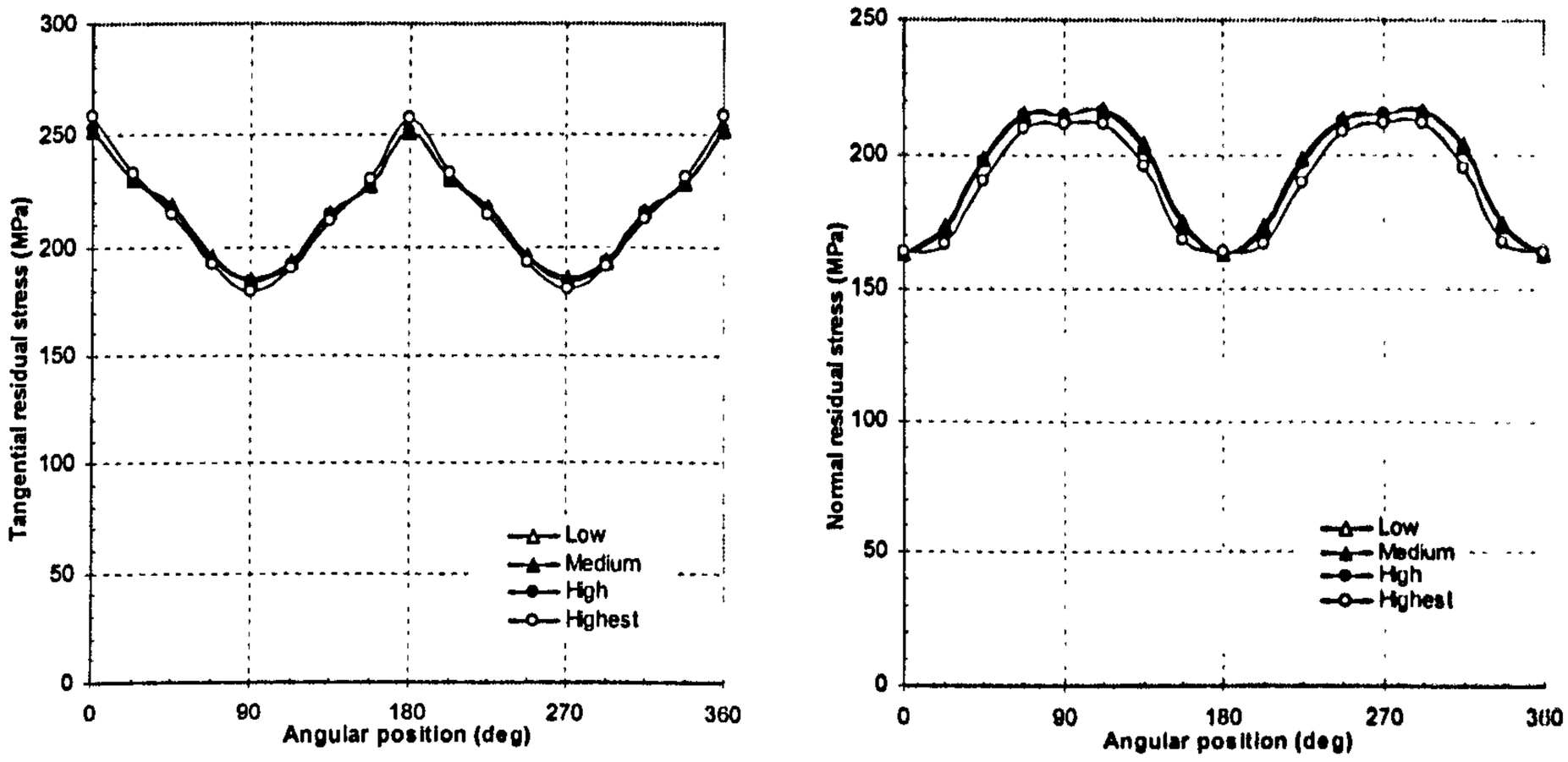

(a) Tangential stress (b) Normal stress

Figure 7.28 Residual stress distributions along Curve *A*

Figure 7.28 presents the residual stress distributions along Curve *A*. Increasing the heat input is shown again to have negligible effects on both tangential and normal residual stresses.

7.3.5.2.4 Circumferentially along Curve *B*

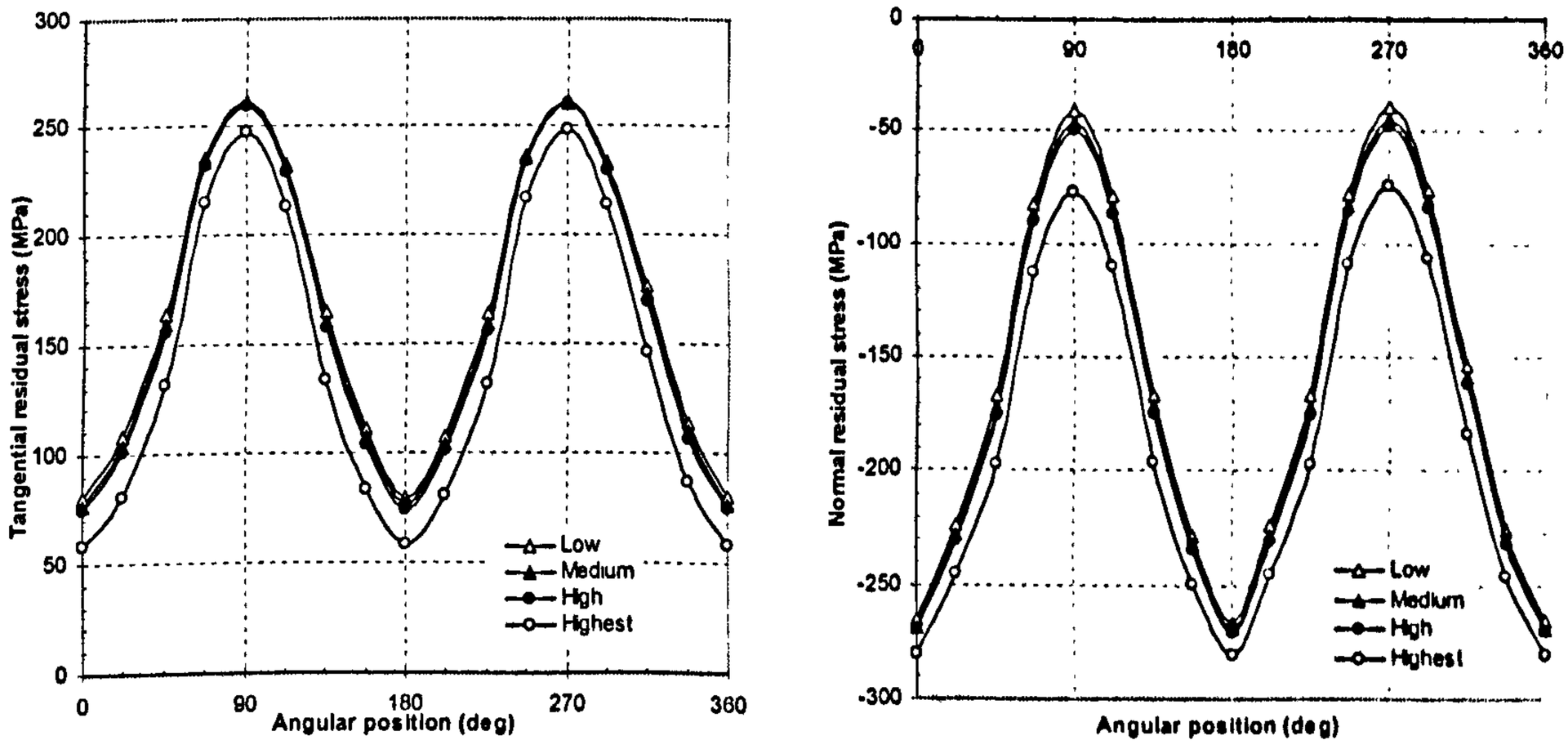

(a) Tangential stress (b) Normal stress

Figure 7.29 Residual stress distributions along Curve *B*

Figure 7.29 presents the residual stress distributions along Curve *B*. Although the

effect of the heat input on the residual stress distributions along Curve *B* is more visible than that on Curve *A*, by doubling the heat input in Case *D*, the tangential and normal residual stresses only marginally decreased.

7.3.5.2.5 Circumferentially along Curve *C*

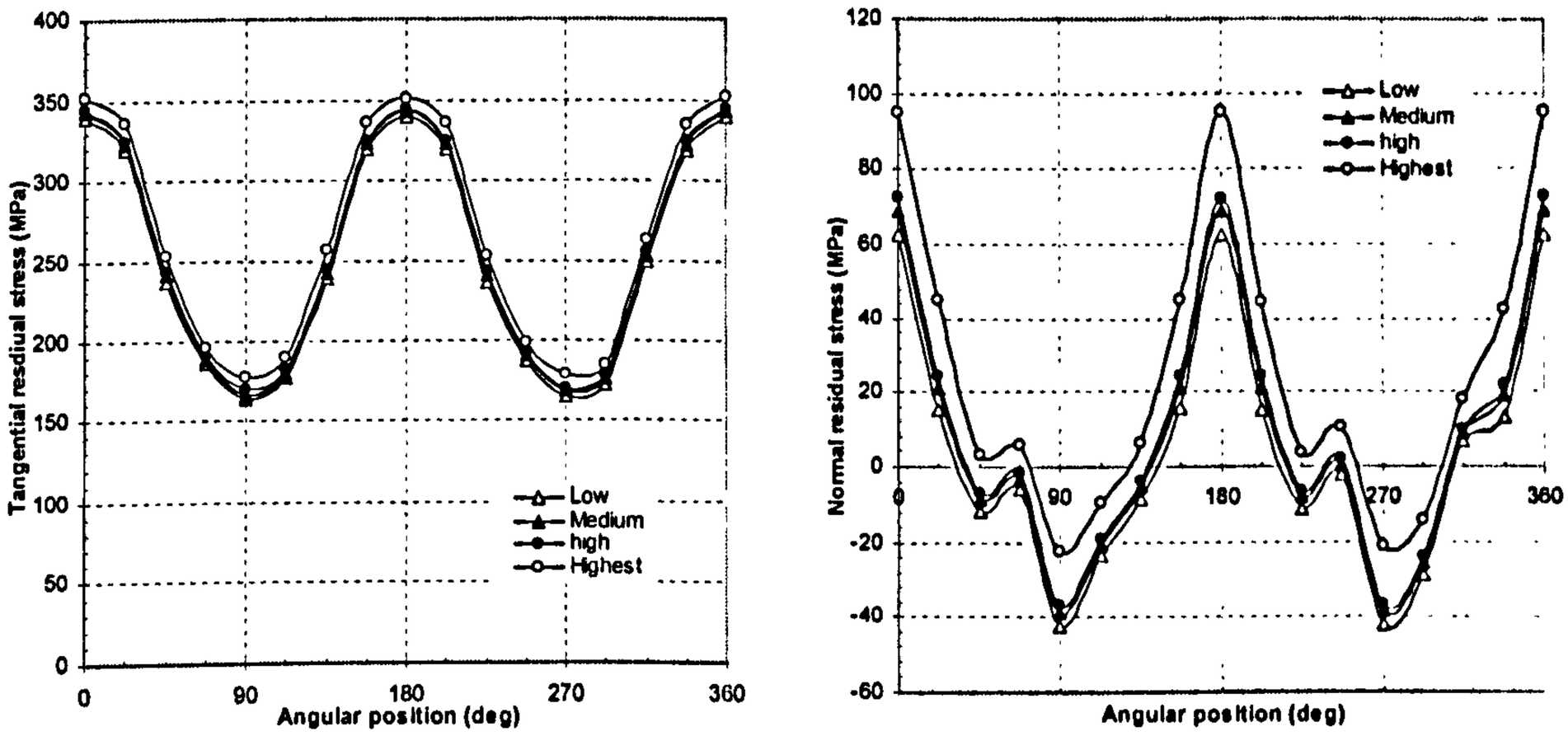

(a) Tangential stress

(b) Normal stress

Figure 7.30 Residual stress distributions along Curve *C*

Figure 7.30 illustrates the residual stress distributions along Curve *C*. By doubling the heat input in Case *D*, the peak tangential and normal residual stresses increase by 2% and 28% respectively.

7.3.5.3 Summary

Contrary to the widely held view that higher heat input will generate higher residual stresses, the simulation results show that heat input does not have much effect on the residual stresses. Even if the heat input were to be doubled, the variation of residual stress is still less than 30%. This is probably because in the thick component, heat conducts to the surrounding area more quickly than in the thinner parts. According to the result of this parametric study, when welding the present component, the weld current, voltage, travel speed and arc efficiency can be taken arbitrarily from the range given in the welding specification without concerns about any significant differences in

the resultant residual stresses. The effect of heat input on residual stresses in different thickness tee branch junction still needs further investigation.

7.3.6 Effect of preheat temperature

7.3.6.1 Introduction

Preheating involves raising the temperature of the base metal, either in its entirety or just in the region surrounding the joint, to a specific desired temperature prior to welding. Preheating can assist in reaching the melting point rapidly by reducing the temperature difference between the filler and the base metal. Heating may be continued during the welding process, but frequently the heat from welding is sufficient to maintain the desired temperature without a continuous application of the external heat source (Funderburk 1997).

The main beneficial effect of preheating is that it slows the cooling rate, producing a more ductile metallurgical structure with greater resistance to cracking. However, excessive preheating not only adds unnecessary discomfort to the welder, but also increases the extent of the HAZ (American Welding Society, 1963).

In the current model, preheat temperatures of 65°C and 100°C were maintained for a distance about 75mm in all directions from the point of welding, as suggested by the American Welding Society (1998). These regions were thoroughly heated so that the minimum temperature met the specified preheat temperature. The rest of the parameters were kept at their initial values.

7.3.6.2 Results and discussion

Residual stress distributions along Curve *A* are presented in Figure 7.31. It is clearly noticed that preheat temperatures have almost no effects on the magnitudes and distributions of residual stresses. This conclusion holds true for the residual stress distributions at other locations, which are omitted to avoid repetition.

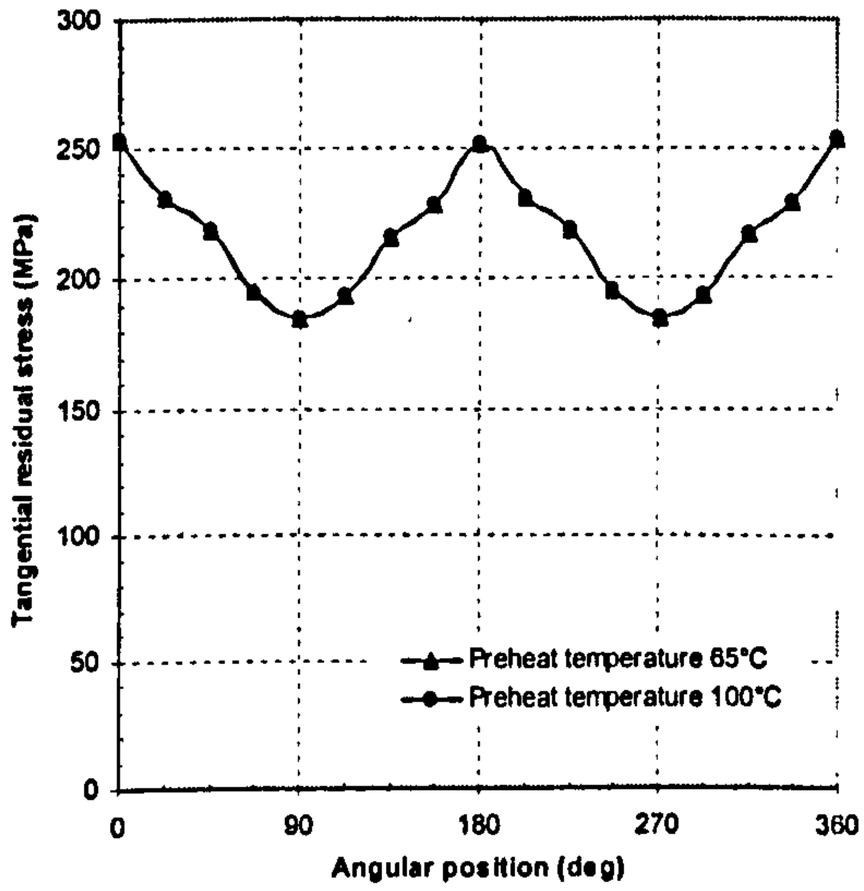

(a) Tangential stress

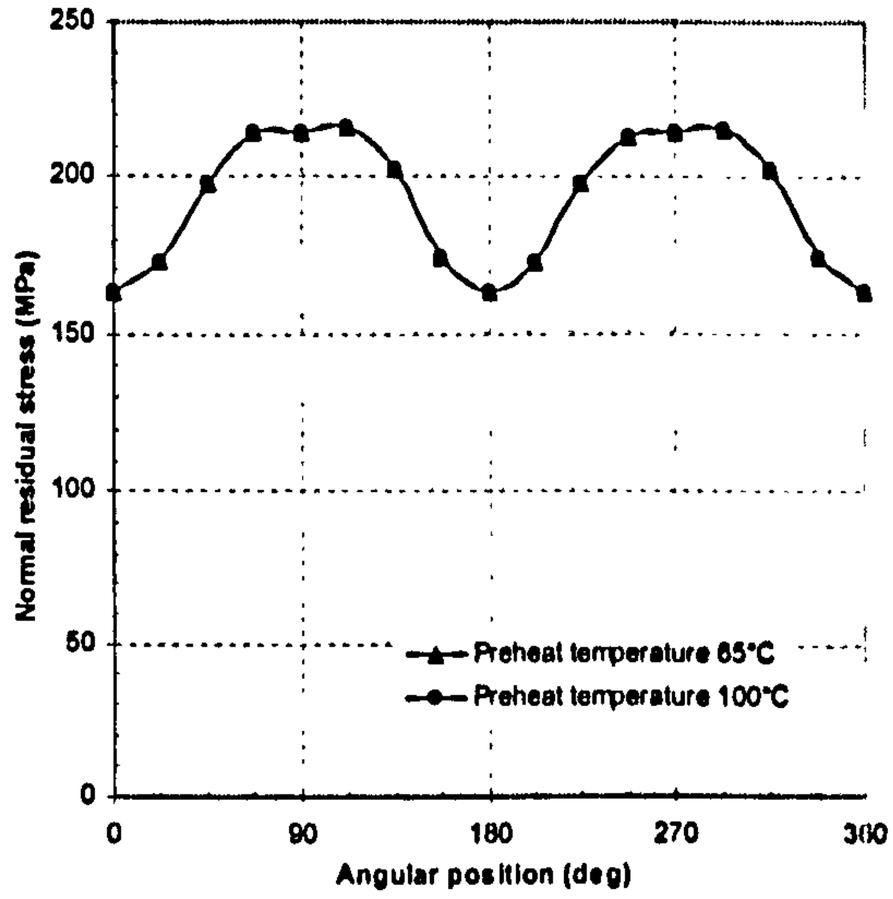

(b) Normal stress

Figure 7.31 Residual stress distributions along Curve *A*

7.3.6.3 Summary

Preheating elevates the equilibrium temperature and at the same time increases the heat input amount. The first is beneficial for reducing welding residual stress, while the second is detrimental. The cumulative effects result in the welding residual stress not being reduced significantly in the tee branch junction.

7.3.7 Effect of interpass temperature

7.3.7.1 Introduction

Interpass temperature refers to the temperature of the material in the weld area immediately before the second and each subsequent pass in a multipass weld. Welding should be performed within a specified range of minimum and maximum interpass temperatures.

There is a delicate balance between the minimum and maximum interpass temperatures. The minimum interpass temperature, normally equal to the minimum specified preheat temperature, must be sufficient to prevent cracking, while the maximum interpass temperature must be controlled to provide adequate mechanical properties and to prevent deterioration of the weld metal and HAZ properties

(Funderburk, 1998).

In the current study, the minimum and maximum interpass temperatures of 67°C and 240°C, as is commonly used by industry (American Welding Society 1998), were selected to investigate their effects on the magnitudes and distributions of residual stresses. The interpass temperatures were maintained throughout the full thickness of the base metal and approximately equal to 75mm away from the weld along both the run and branch pipe, as recommended by American Welding Society (1998). All the other variables in the FE model were kept at their initial values.

7.3.7.2 Results and discussion

7.3.7.2.1 Branch cross section *a-a*

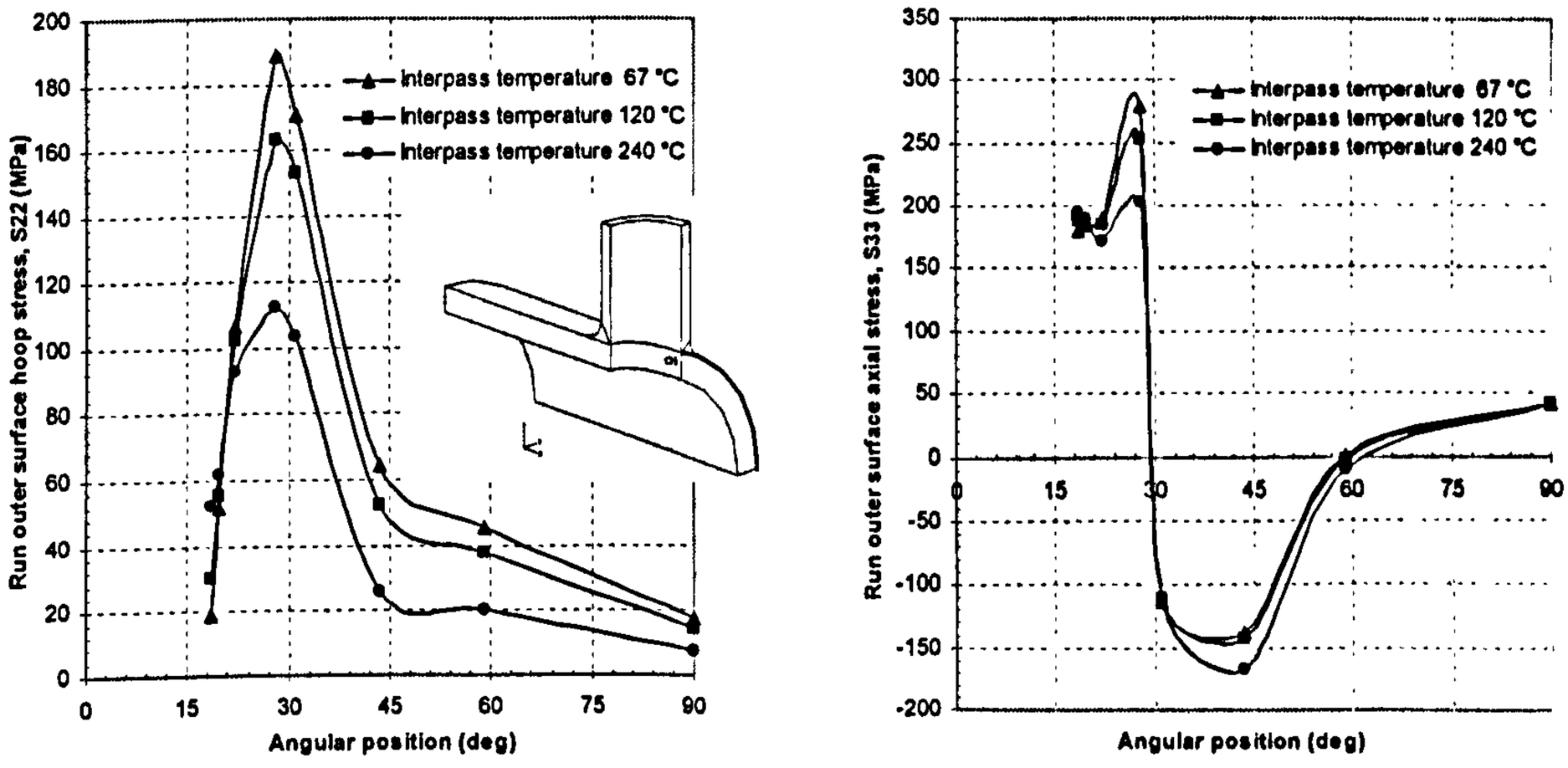

(a) Hoop stress

(b) Axial stress

Figure 7.32 Stress vs. angular position on the run pipe outer surface

Figure 7.32 shows the residual stress distributions versus angular position on the outer surface of the run pipe. The distribution patterns of the hoop and axial stresses predicted by the three models are similar. However, the magnitudes are different. When applying an interpass temperature of 67°C, the peak hoop and axial stresses reach values of 190MPa and 290MPa (68%σ_y and 104%σ_y), respectively, which are about 15% higher than those predicted by the model with an interpass temperature of 120°C. By elevating the interpass temperature to 240°C, the corresponding values decrease to 110MPa and 200MPa, which are about 25% lower than those obtained from the case

with 120°C interpass temperature.

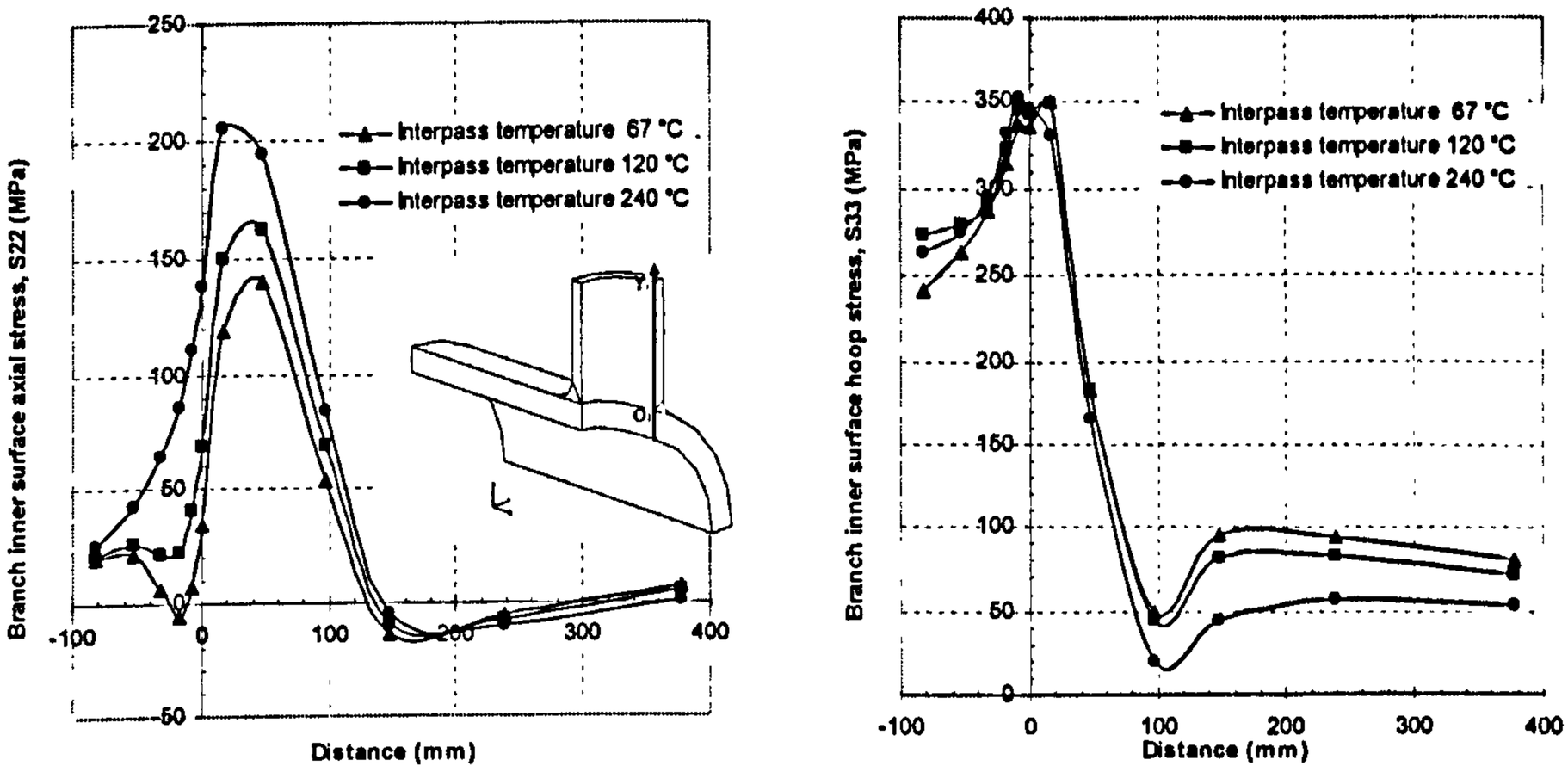

(a) Axial stress (b) Hoop stress

Figure 7.33 Residual stresses in the Y_1-direction on the branch inner surface

Figure 7.33 shows the residual stress distributions along the Y_1-direction. Compared with the case with 120°C interpass temperature, the peak axial stress decreases by 13% when reducing the interpass temperature to 67°C; it increases by 30% when increasing the interpass temperature to 240°C. The tensile zone also spreads slightly with a higher interpass temperature, as shown in Figure 7.33(a). From Figure 7.33(b), it is observed that the interpass temperature has almost no effect on the hoop residual stress from the run pipe to a distance up to 100mm on the branch pipe side. Stress variations of about 50MPa are noticed beyond this location.

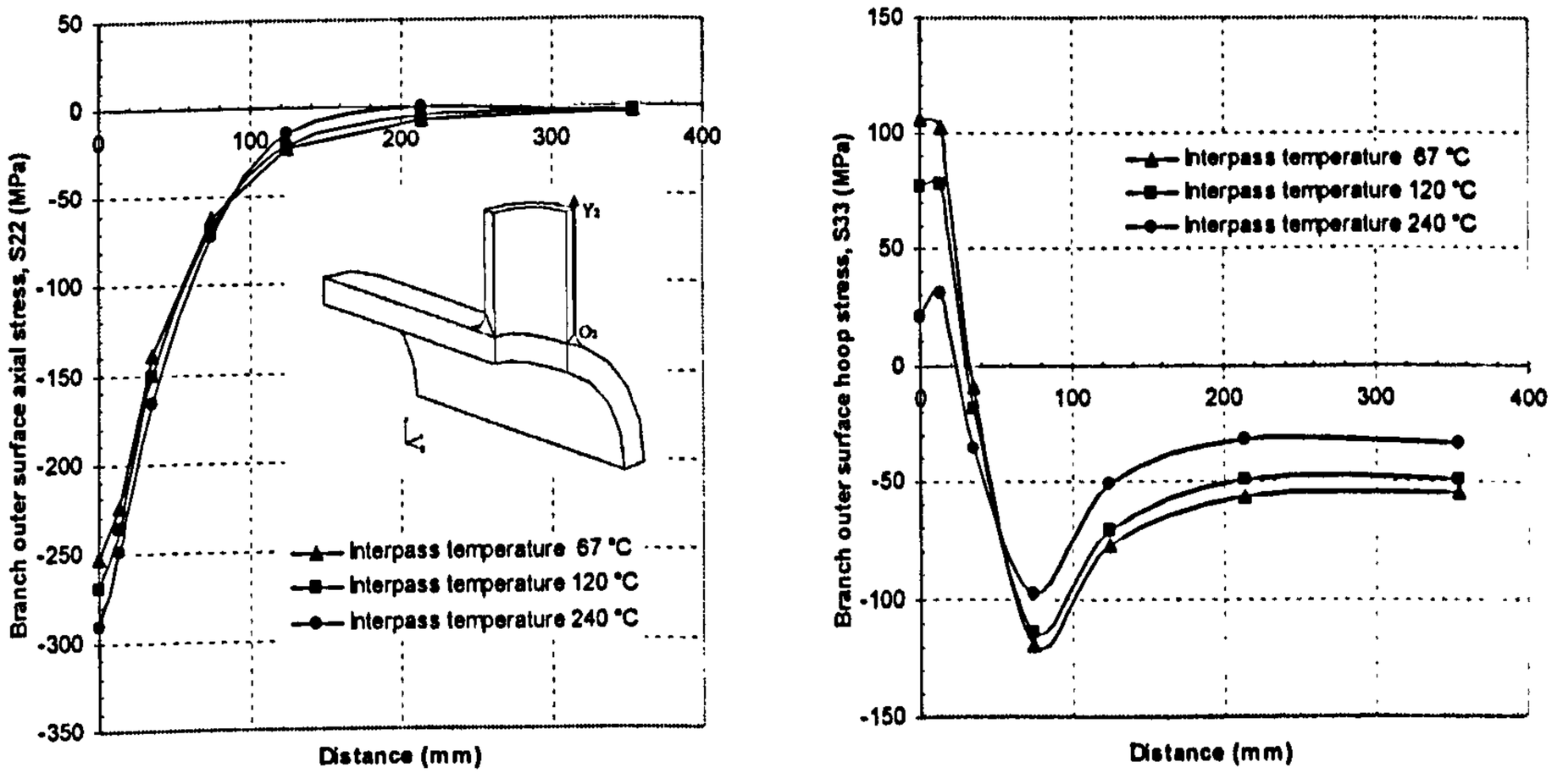

(a) Axial stress (b) Hoop stress

Figure 7.34 Residual stresses in the Y_2-direction on the branch outer surface

Figure 7.34 shows the residual stress distributions along the Y_2-direction. There are not many differences for the axial stress distributions under different interpass temperatures. The interpass temperature appears to affect the magnitudes of hoop stress near the origin, although the distribution patterns are similar. With an increasing interpass temperature, the peak tensile hoop stress decreases, as shown in Figure 7.34(b).

7.3.7.2.2 Run pipe cross section *b-b*

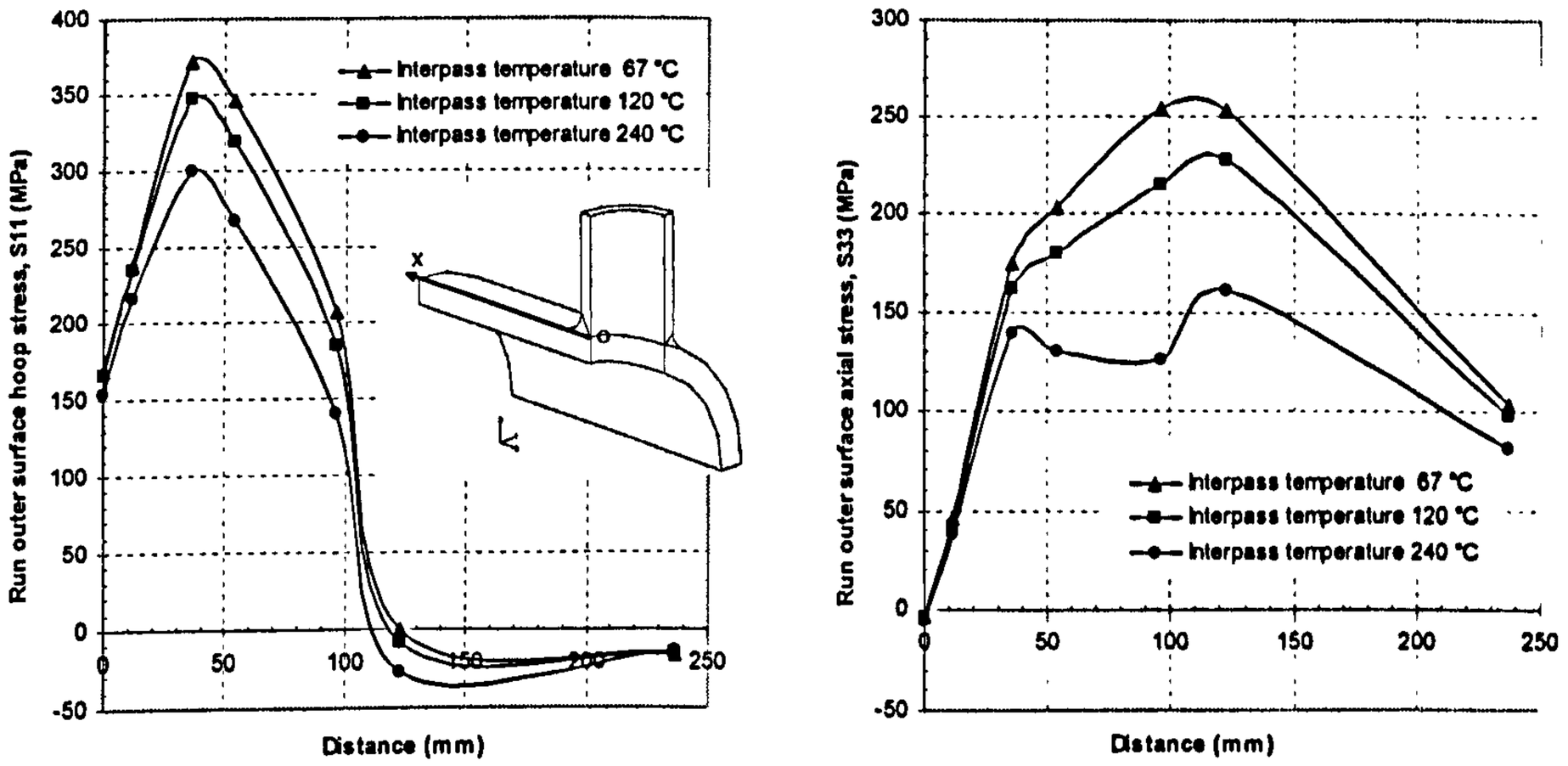

(a) Hoop stress

(b) Axial stress

Figure 7.35 Residual stresses in the *X*-direction on the run outer surface

Figure 7.35 shows the residual stress distributions in the *X*-direction. The hoop residual stresses predicted by the case with lower inperpass temperature are generally higher than those predicted by the case with higher interpass temperature, as shown in Figure 7.35(a). By increasing the interapss temperature from 67°C to 240°C, the peak hoop residual stress at the centre of the weld seam decreases from 370MPa (133%σ_y) to 300MPa (108%σ_y). A similar tendency can be noticed from Figure 7.35(b), i.e. the higher the interpass temperature, the lower the magnitudes of the axial stress. By increasing the interpass temperature by a factor of four, the maximum axial residual stress can reduce by up to about 38%.

Figure 7.36 shows the residual stress distributions in the Y_1-direction. There are not

many differences for the hoop stresses among the cases with different interpass temperatures, see Figure 7.36(a). However, an increase in interpass temperature increases the axial stresses on the branch inner surface. The increments of axial residual stress could be as large as 110-130MPa at the origin and its surrounding regions when the interpass temperature increased by a factor of four from its lowest value of 67°C. This can be clearly seen from Figure 7.36(b).

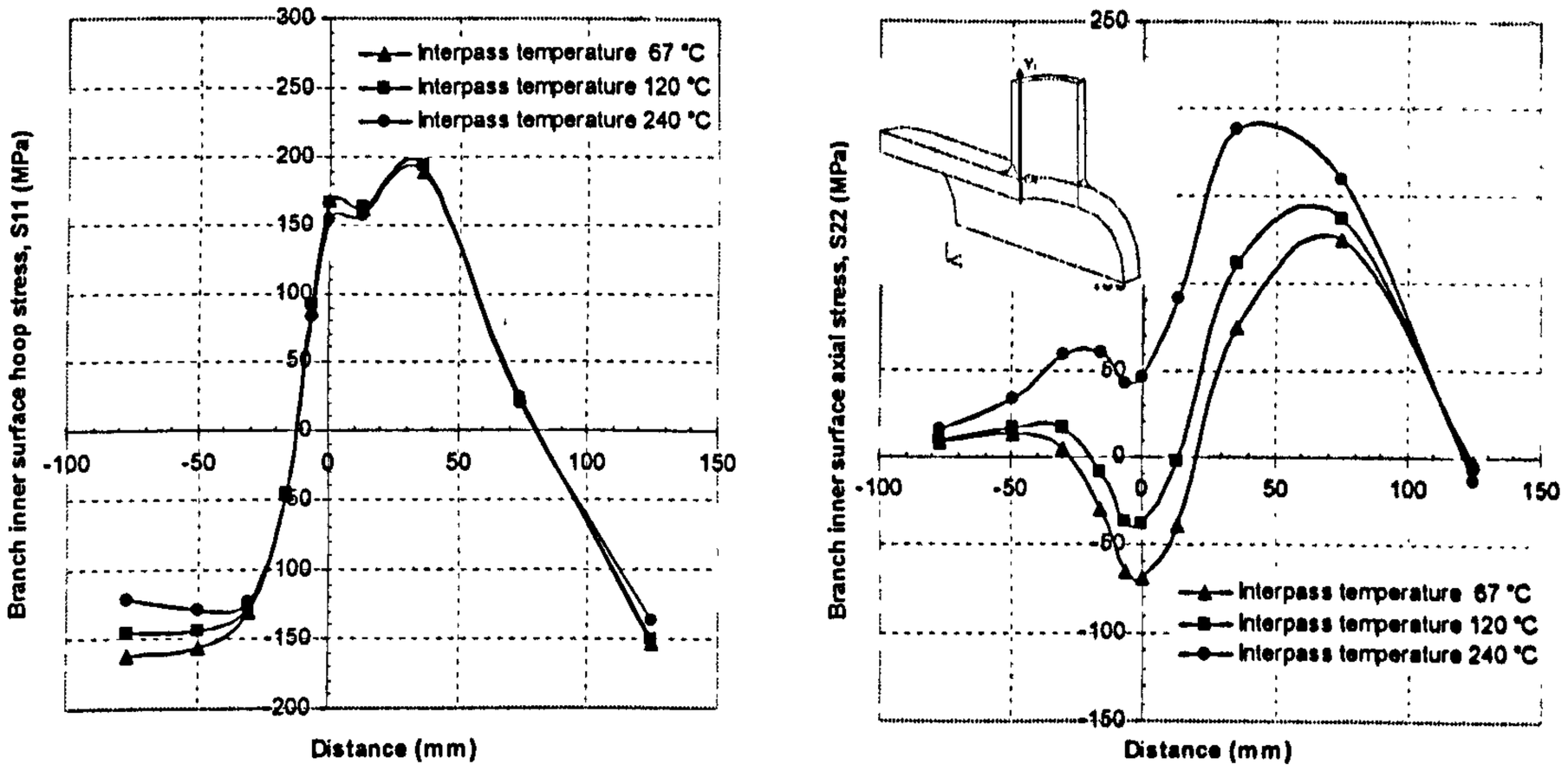

(a) Hoop stress (b) Axial stress

Figure 7.36 Residual stresses in the Y_1-direction on the branch inner surface

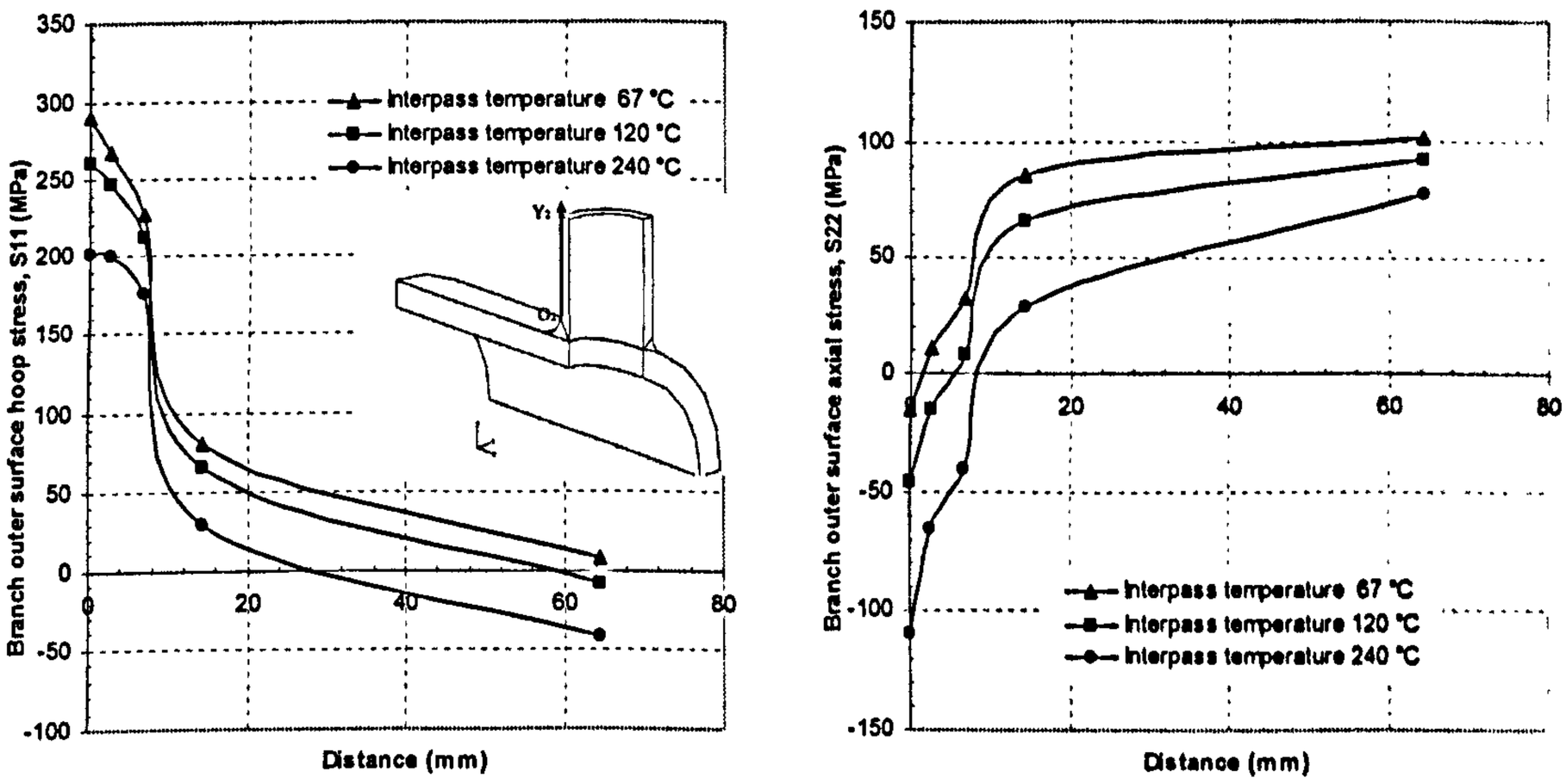

(a) Hoop stress (b) Axial stress

Figure 7.37 Residual stresses in the Y_2-direction on the branch outer surface

Figure 7.37 presents residual stress distributions in the Y_2-direction. It is observed that with an increasing interpass temperature, both the hoop and axial stresses decrease.

7.3.7.2.3 Circumferentially along Curve *A*

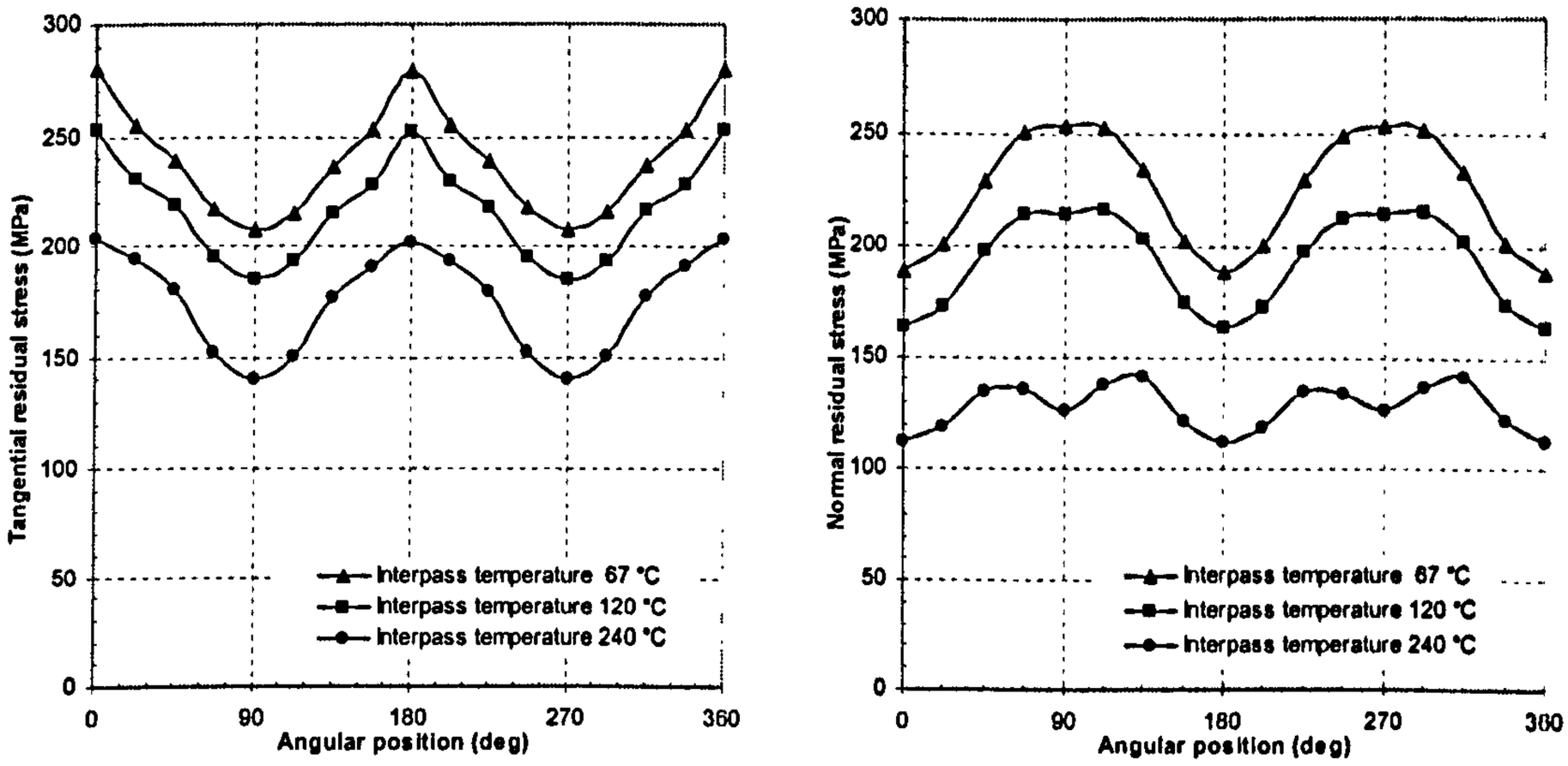

(a) Tangential stress (b) Normal stress

Figure 7.38 Residual stress distributions along Curve *A*

Figure 7.38 illustrates residual stress distributions along Curve *A*. With an increasing interpass temperature, both tangential and normal residual stresses decrease, however, to different extents. By increasing the interpass temperature from 67°C to 240°C, the tangential residual stress decreases by about 30% on average. The normal residual stress distribution along Curve *A* tended to be uniform and the maximum value decreased by about 50% at the crotch corners.

7.3.7.2.4 Circumferentially along Curve *B*

Figure 7.39 illustrates residual stress distributions along Curve *B*. By increasing the interpass temperature from 67°C to 240°C, the tangential residual stresses decrease by 80MPa on average. The decreases in the normal residual stress are not uniform along Curve *B*. The maximum reduction is 100MPa at the crotch corners and the minimum reduction is 40MPa at the flank centres. The normal residual stresses are all in compression.

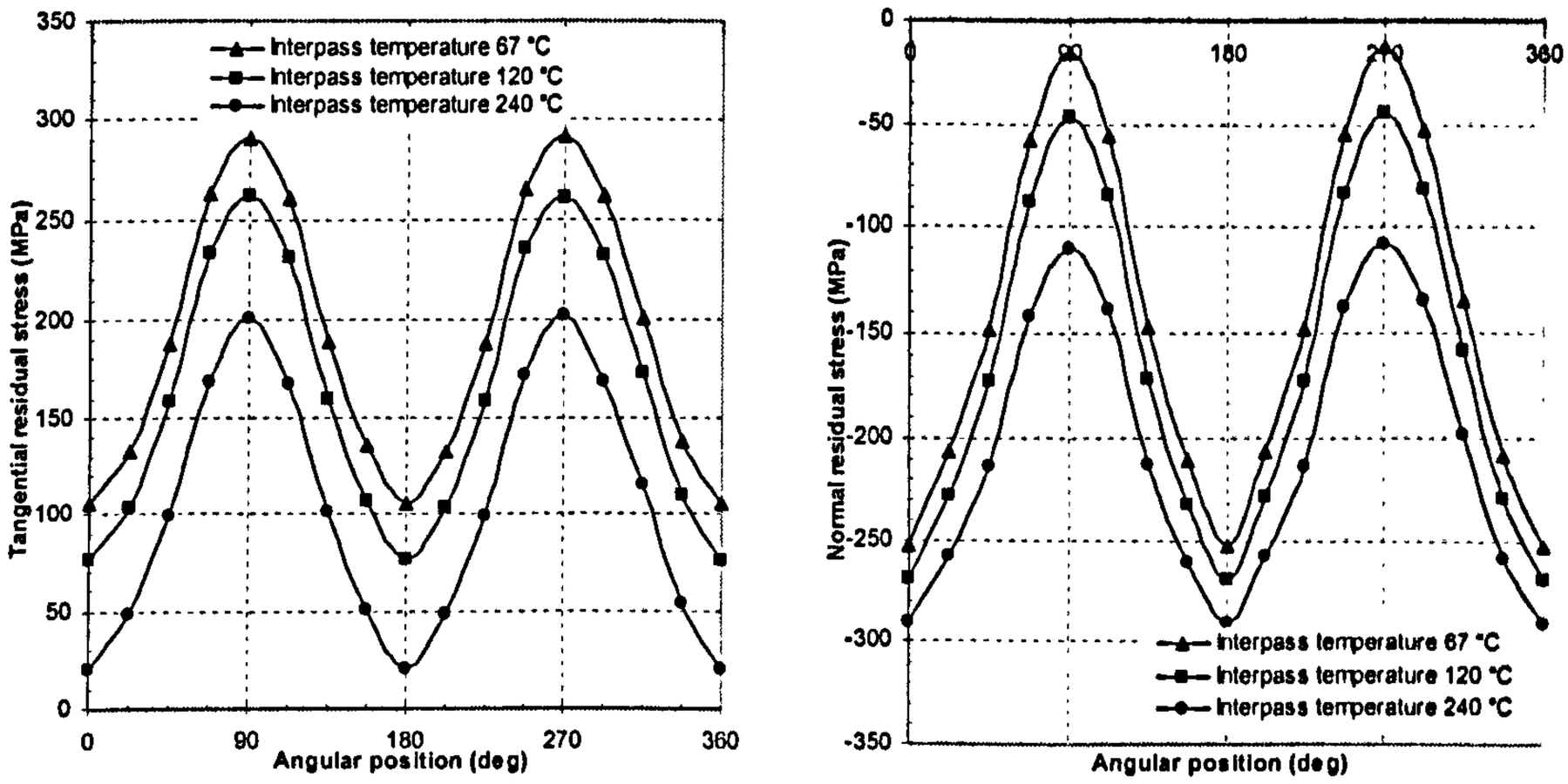

(a) Tangential stress

(b) Normal stress

Figure 7.39 Residual stress distributions along Curve *B*

7.3.7.2.5 Circumferentially along Curve *C*

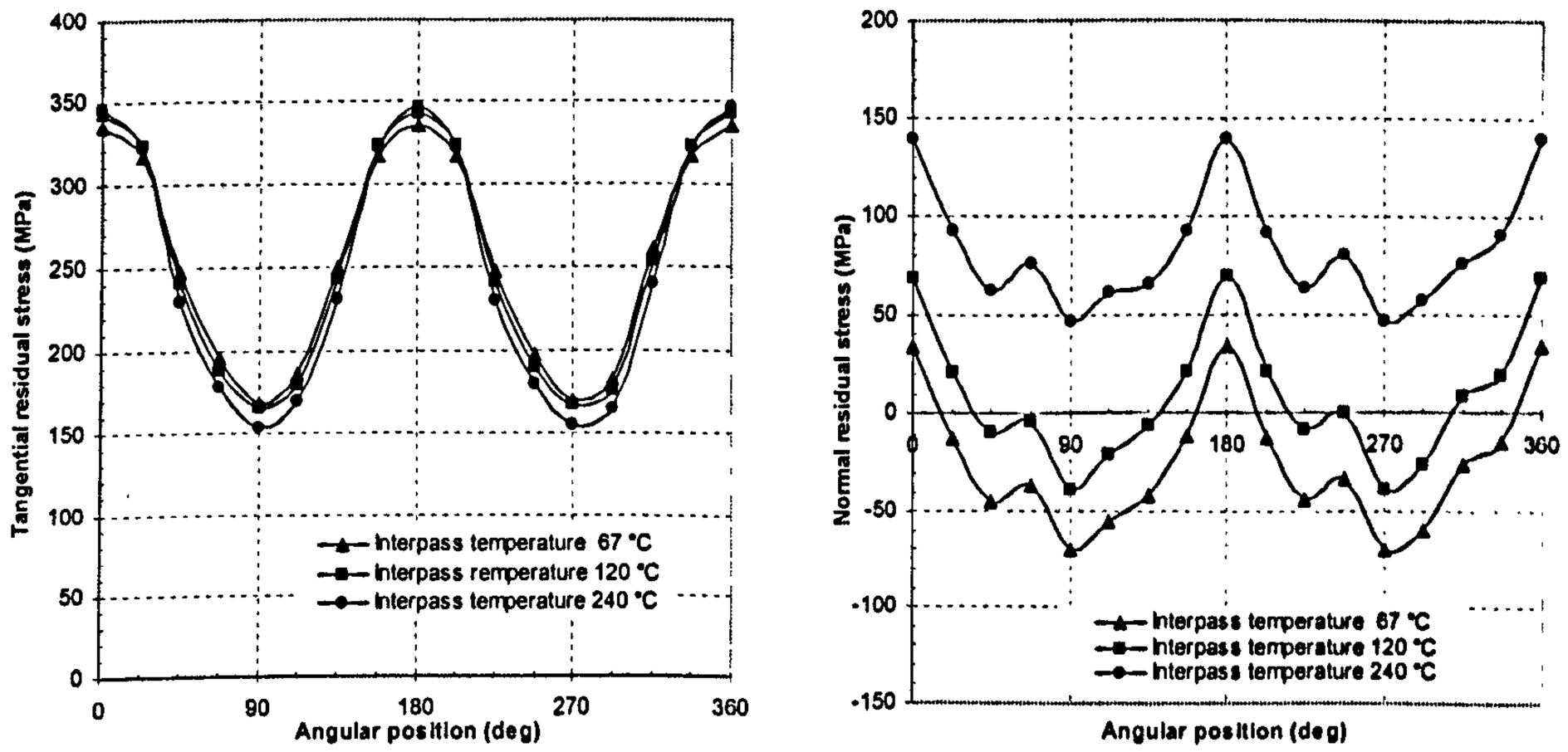

(a) Tangential stress

(b) Normal stress

Figure 7.40 Residual stress distributions along Curve *C*

Figure 7.40 illustrates residual stress distributions along Curve *C*. Although the interpass temperature has almost no effect on the tangential residual stresses along Curve *C*, they will affect the normal residual stresses. The higher the interpass temperature, the higher the normal residual stresses are observed. The average increase of the normal residual stress is 100MPa along Curve *C* when the interpass temperature increases from 67°C to 240°C, as shown in Figure 7.40(b). Nevertheless, the maximum

normal stress along Curve *C* is less than 150MPa in general.

7.3.7.3 Summary

Although interpass temperature has less influence on the residual stress distribution patterns, it is one of the most important parameters affecting the magnitudes of residual stresses. Generally speaking, increasing the interpass temperature helps reduce residual stresses at most locations investigated.

By increasing the interpass temperature to 240°C, the peak hoop and axial residual stresses on the outer surface of both the run and branch pipes decreased by 10-40%, compared to the corresponding stresses at 120°C interpass temperature. The tangential and normal stresses along Curves *A* and *B* were reduced by 20-60%. Increasing the interpass temperature did not affect the hoop residual stresses on the branch inner surface; but it increased the axial residual stresses. The normal residual stresses on Curve *C* also increased. Nevertheless, the increased residual stresses are well below the room temperature yield stress of 278MPa.

7.3.8 Effect of cooling rate

7.3.8.1 Introduction

Cooling rate is a primary factor that determines the final metallurgical structure and material properties of the weld and HAZ. A lower cooling rate usually means a more ductile microstructure (American Welding Society, 1963). However, besides this latter statement, there is no indication about the effect of cooling rate on the magnitude and distribution of residual stresses.

The cooling rate can be related to the convective heat transfer coefficients. In the current research, the cooling rate was varied by applying different convective heat transfer coefficients to different locations of the tee branch junction. Two kinds of media, i.e. air and water, were simulated. In the case of an 'air-steel' interface, the coefficient of convective heat transfer was assigned a value of $30 W/m^2°C$. When cooling by water flowing or being sprayed over the surface of the tee branch junction, the 'water-steel'

interaction was modelled by introducing a convective heat transfer coefficient of 1000W/m^2°C. Cooling was applied during all weld passes following the root pass. Four cases were investigated in this section:

Case *A*: air-steel (h=30W/m^2°C).

Case *B*: water-steel: Water flows or is sprayed on both the outer and inner surfaces of the component (h=1000W/m^2°C).

Case *C*: water-steel, inside: Water flows or is sprayed on the inner surface of the branch pipe only (h=1000W/m^2°C).

Case *D*: water-steel, outside: Water flows or is sprayed on the outer surface of both the run and branch pipe in the region near the weld seam (h=1000W/m^2°C).

7.3.8.2 Results and discussion

7.3.8.2.1 Branch cross section *a-a*

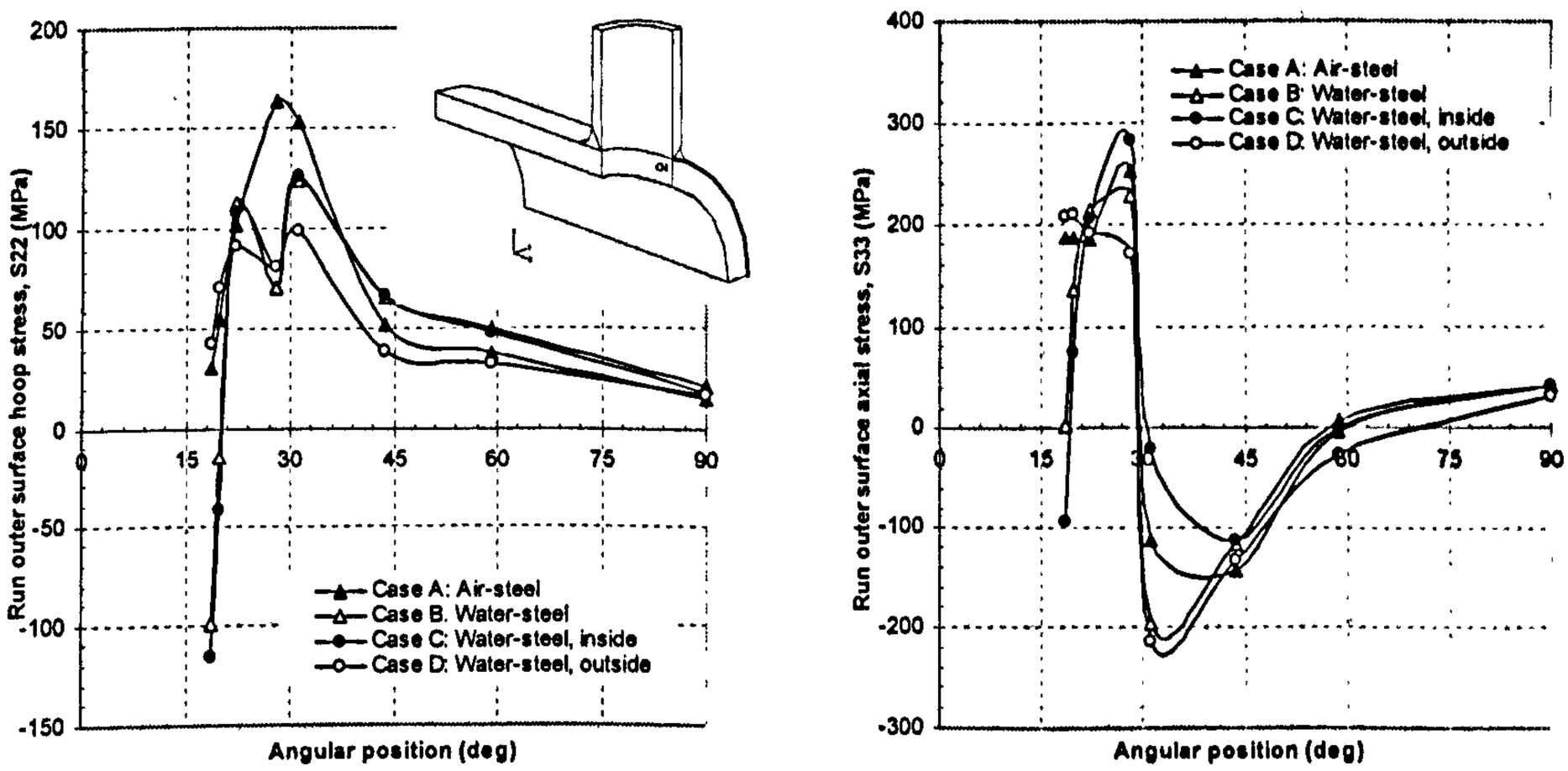

(a) Hoop stress

(b) Axial stress

Figure 7.41 Stress vs. angular position on the run pipe outer surface

Figure 7.41 shows residual stress distributions versus angular position on the outer surface of the run pipe. It is noticed from Figure 7.41(a) that the small tensile hoop stresses at the origin for Cases *A* and *D* change to compressive stresses for Cases *B* and *C*. Case *A* predicts the highest peak hoop stress of 160MPa. Again the axial residual stress near the origin changes from tension in Cases *A* and *D* to zero for Case *B* and to compression for Case *C*. By cooling the inner surface of the branch pipe with water in

Case *C*, the peak axial stress reaches nearly 300MPa (108%σ_y), while by cooling the outside as in Case *D*, the peak axial stress reduces to 200MPa (72%σ_y).

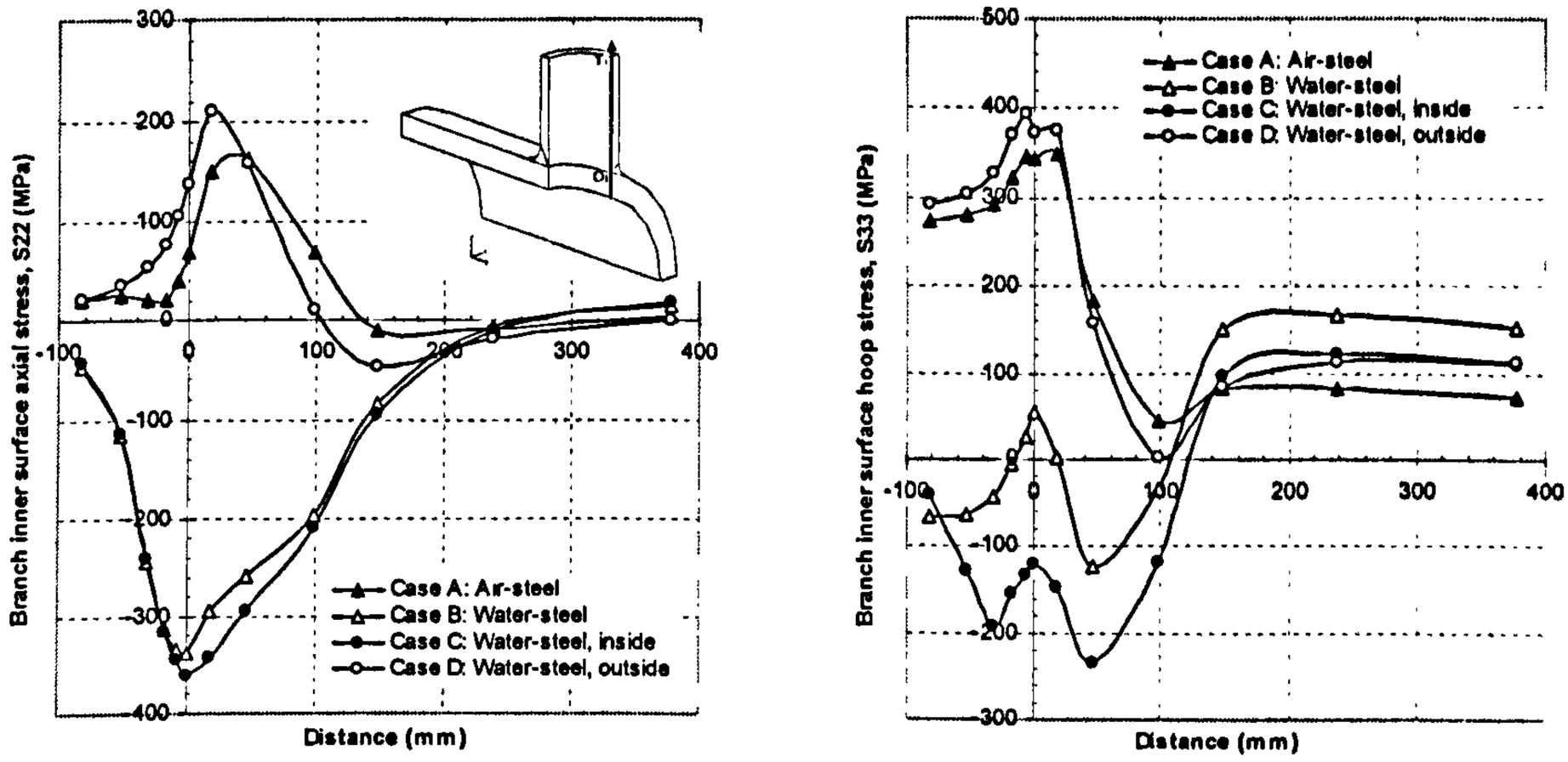

(a) Axial stress

(b) Hoop stress

Figure 7.42 Residual stresses in the Y_1-direction on the branch inner surface

Figure 7.42 shows residual stress distributions in the Y_1-direction. It is noticed that the cooling conditions substantially change the axial and hoop stresses around the origin. By cooling both the inner and outer surfaces as in Case *B* or only the branch pipe inner surface as in Case *C*, the peak axial stress dramatically changes from 210MPa tensile to 340MPa compressive. The axial stresses in the regions near the origin also change from tension to compression in these two cases. In Figure 7.42(b), the peak tensile hoop stress of 400MPa generated by cooling on the outer surface in Case *D* is dramatically changed to -110MPa in Case *C* and to 50MPa in Case *B*. The tensile hoop stresses near the origin are lowered as well for Cases *B* and *C*. The remote end of the branch pipe is not affected by the cooling conditions. These facts demonstrate that changing the cooling rate on the branch inner surface is an effective method in changing the stress states on the branch inner surface.

Figure 7.43 presents the residual stress distributions in the Y_2-direction. It is noticed that by cooling the outer surface in Case *D*, both the axial and hoop stresses on the branch pipe outer surface can decrease to becoming compressive; while by cooling the inner surface as in Case *C*, the predicted axial and hoop stresses are highest among the four cases.

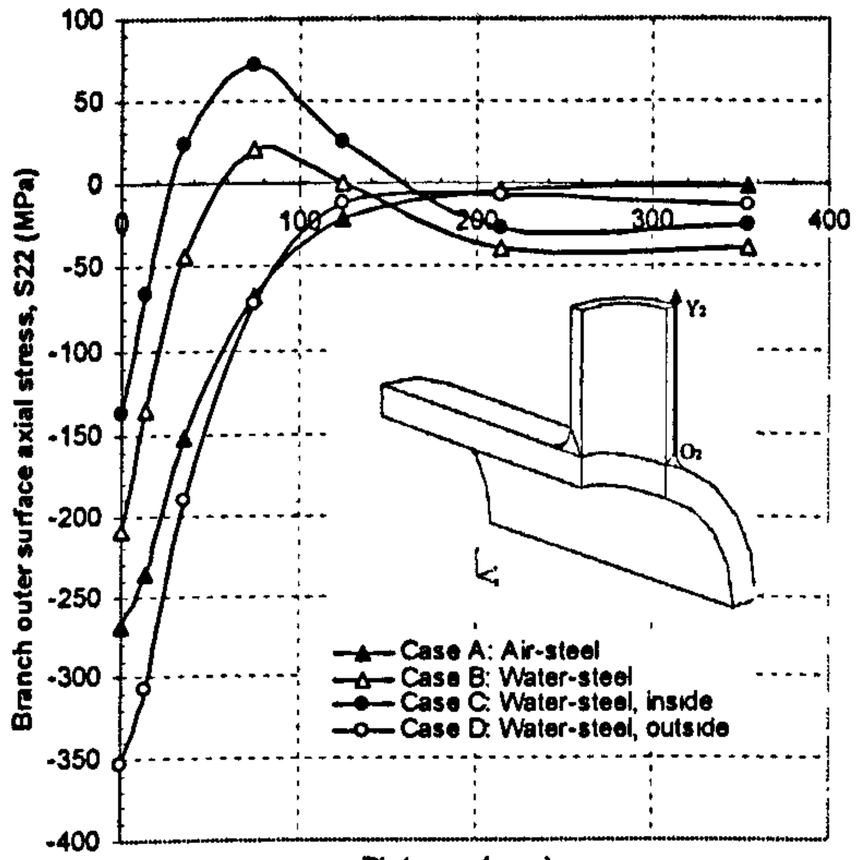

(a) Axial stress

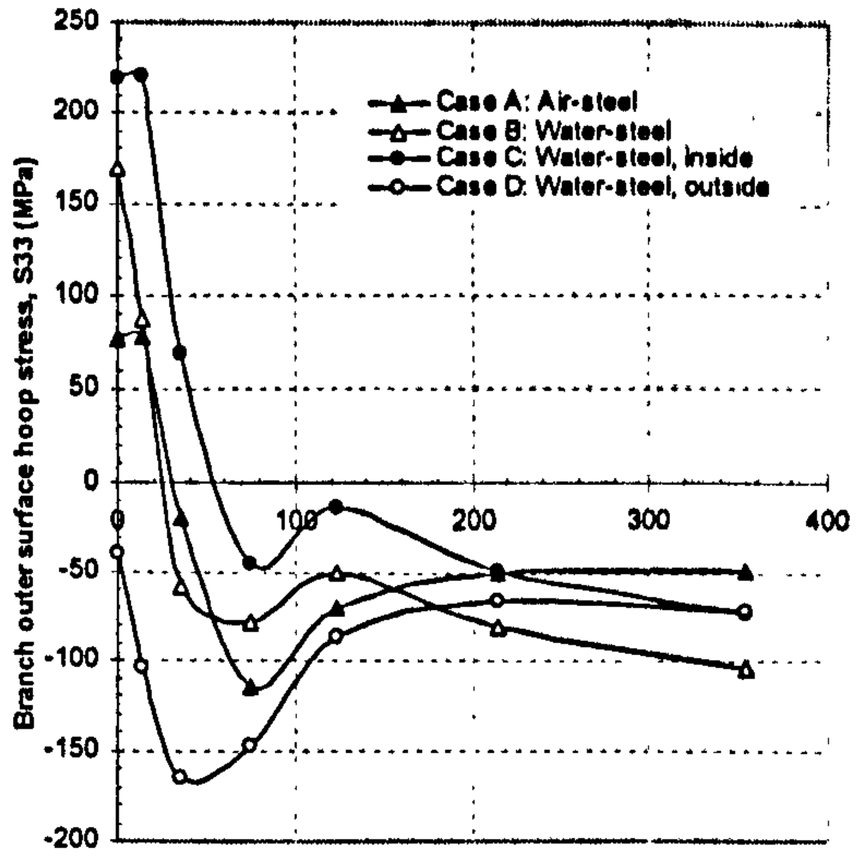

(b) Hoop stress

Figure 7.43 Residual stresses in the Y_2-direction on the branch outer surface

7.3.8.2.2 Run pipe cross section *b-b*

Figure 7.44 shows residual stress distributions in the *X*-direction. It is observed from Figure 7.44(a) that, although varying the cooling condition changes the hoop stress at the origin from tension to compression, the peak tensile hoop stress remains high, with a minimum value of 350MPa (126%σ_y) in Case *A*. The peak axial residual stress decreases by 26% from the peak value in Case *A* when cooling the branch inner surface as for Case *C*, as shown in Figure 7.44(b).

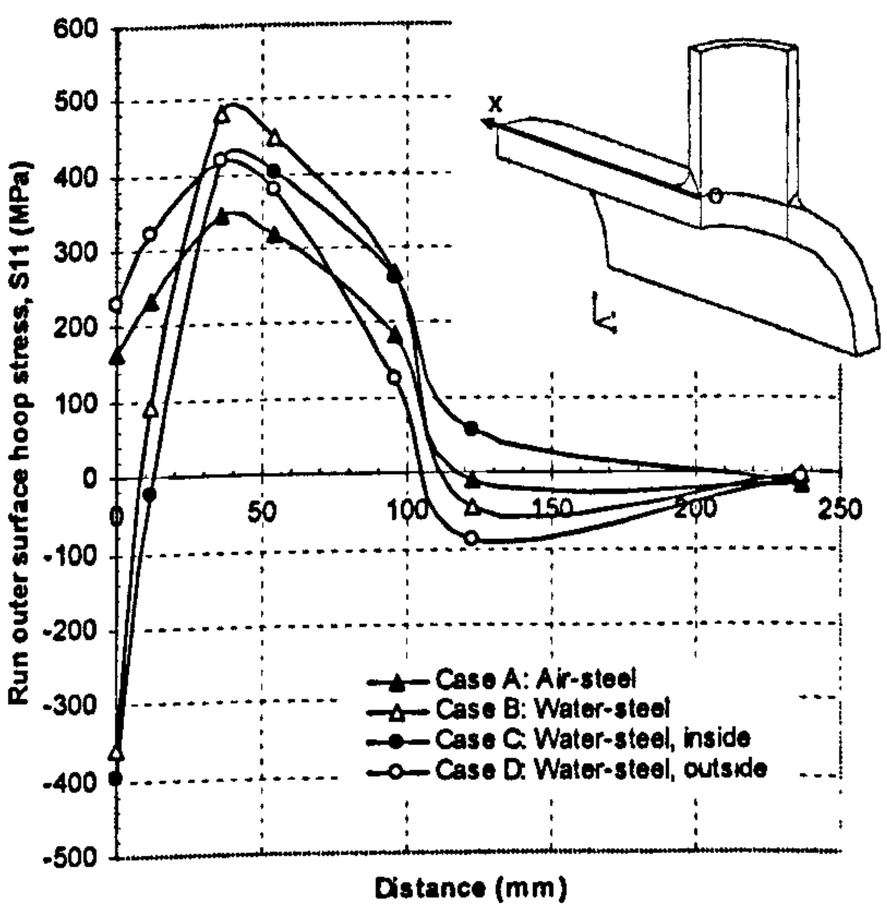

(a) Hoop stress

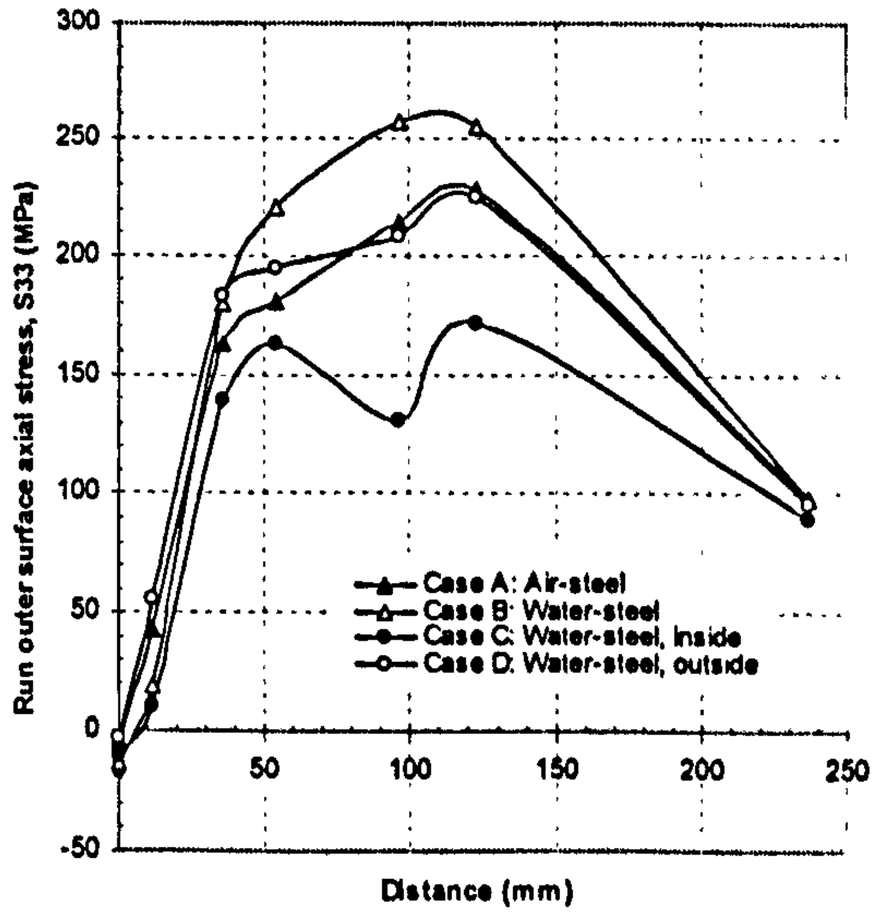

(b) Axial stress

Figure 7.44 Residual stresses in the *X*-direction on the run outer surface

Figure 7.45 shows the residual stress distributions in the Y_1-direction. It is again observed that for Cases *B* and *C*, both the hoop and axial residual stresses on the branch inner surface along the Y_1-direction are in compression.

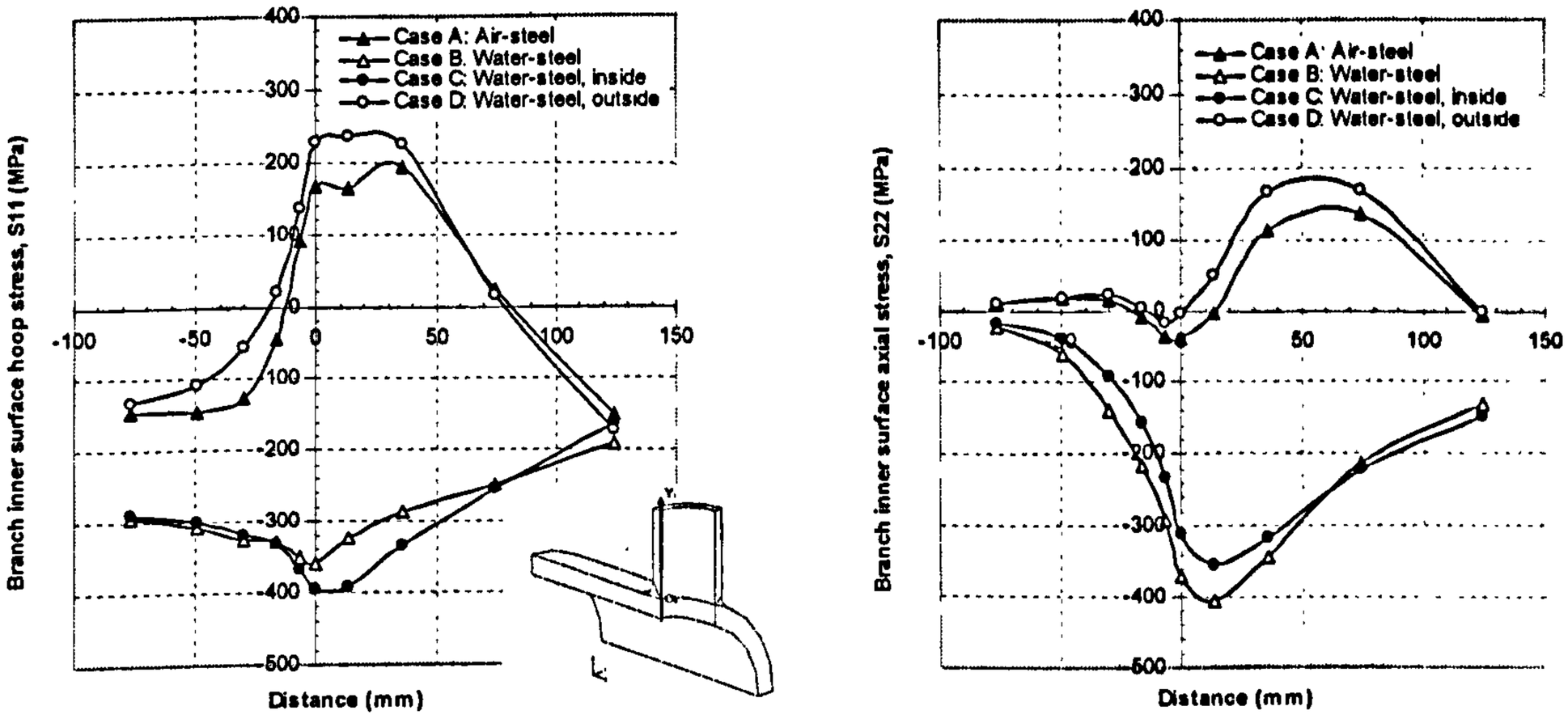

(a) Hoop stress

(b) Axial stress

Figure 7.45 Residual stresses in the Y_1-direction on the branch inner surface

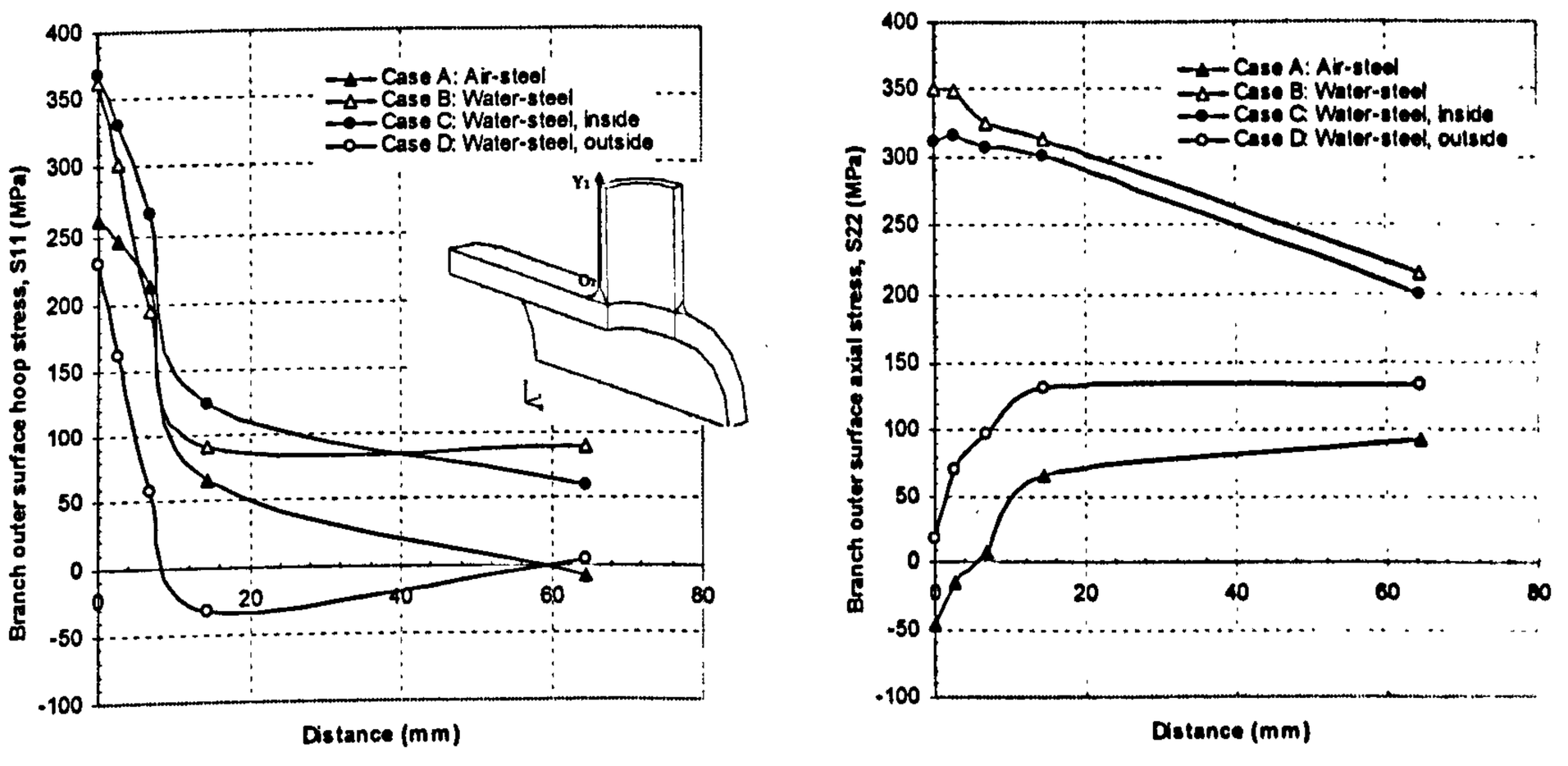

(a) Hoop stress

(b) Axial stress

Figure 7.46 Residual stresses in the Y_2-direction on the branch outer surface

Figure 7.46 shows the residual stress distributions in the Y_2-direction. It is again noticed that by cooling the outer surface as in Case *D*, both the hoop and axial residual stresses on the branch outer surface are greatly reduced. However, for Cases *B* and *C*, the peak hoop and axial stresses reach magnitudes as high as 350MPa ($126\%\sigma_y$) at the origin.

7.3.8.2.3 Circumferentially along Curve *A*

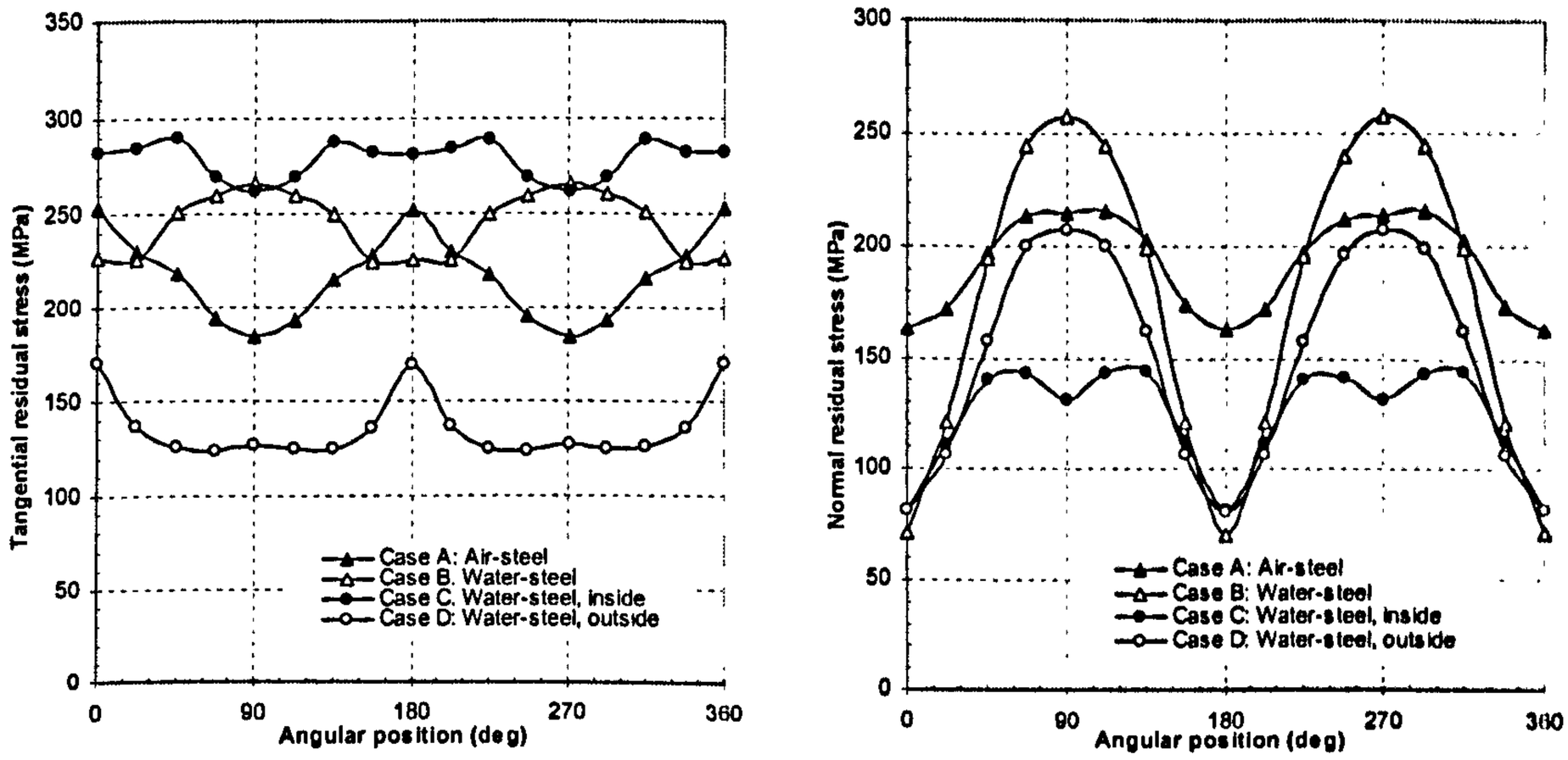

(a) Tangential stress

(b) Normal stress

Figure 7.47 Residual stress distributions along Curve *A*

Figure 7.47 shows the residual stress distributions along Curve *A*. The residual stress distributions show obvious symmetry under all cooling conditions. It is noticed that by cooling the outer surface as in Case *D*, the peak tangential stress reaches a minimum value of 170MPa, while the peak normal stress also reduces to about 210MPa. Although by cooling the branch inner surface as in Case *C*, the peak normal stress reduces to a minimum magnitude of 150MPa, the peak tangential stress reaches to a maximum magnitude of 290MPa. It is thus concluded that Case *D* is a more acceptable cooling scheme than Case *C* for reducing residual stresses along Curve *A*.

7.3.8.2.4 Circumferentially along Curve *B*

Figure 7.48 presents the residual stress distributions along Curve *B*. Compared with Case *A*, it is found that cooling the outer surface as in Case *D* helps with the residual stress reduction along Curve *B*. The peak tangential residual stress decreases from 260MPa to 220MPa. The peak normal residual stress slightly increases from -50MPa to 10MPa. For Cases *B* and *C*, however, the peak tangential and normal stresses increase to about 360MPa ($129\%\sigma_y$) and 340MPa ($122\%\sigma_y$), respectively. This observation suggests that cooling the outer surface adjacent to the weldline (Case *D*) is an effective measure for reducing residual stresses along both Curves *A* and *B*.

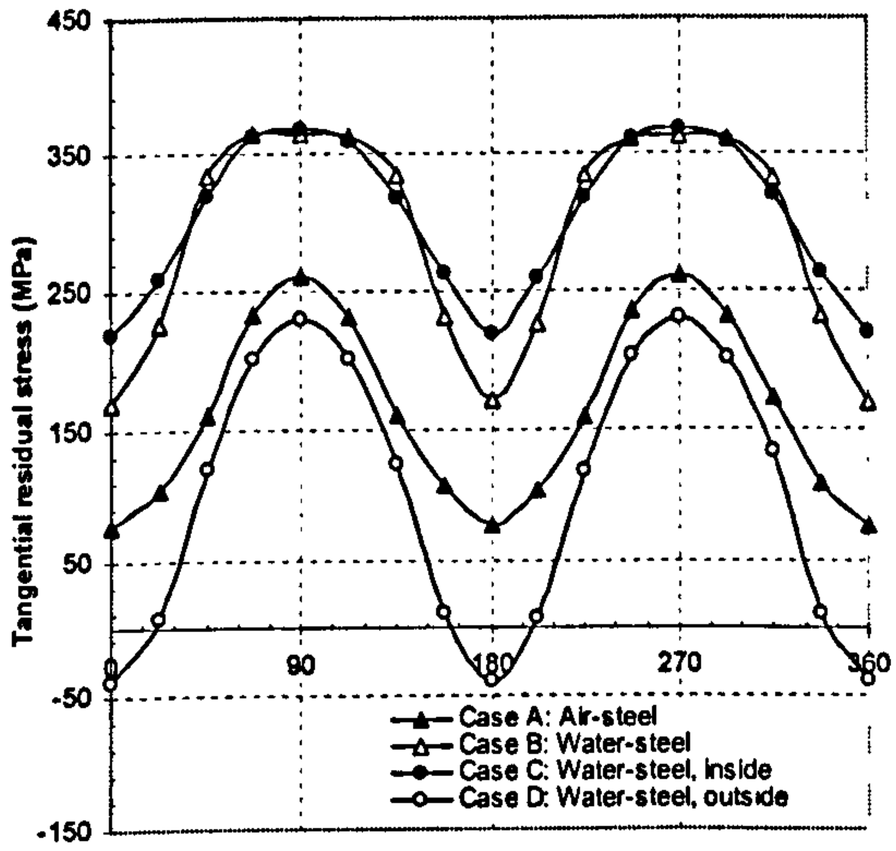

(a) Tangential stress

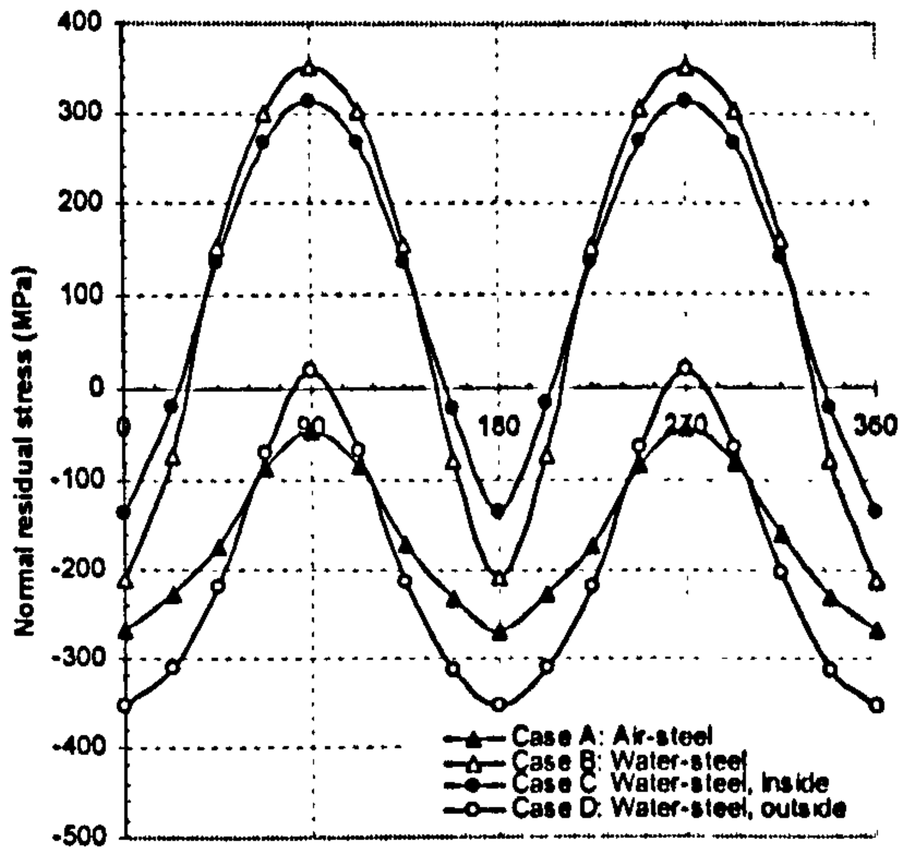

(b) Normal stress

Figure 7.48 Residual stress distributions along Curve *B*

7.3.8.2.5 Circumferentially along Curve *C*

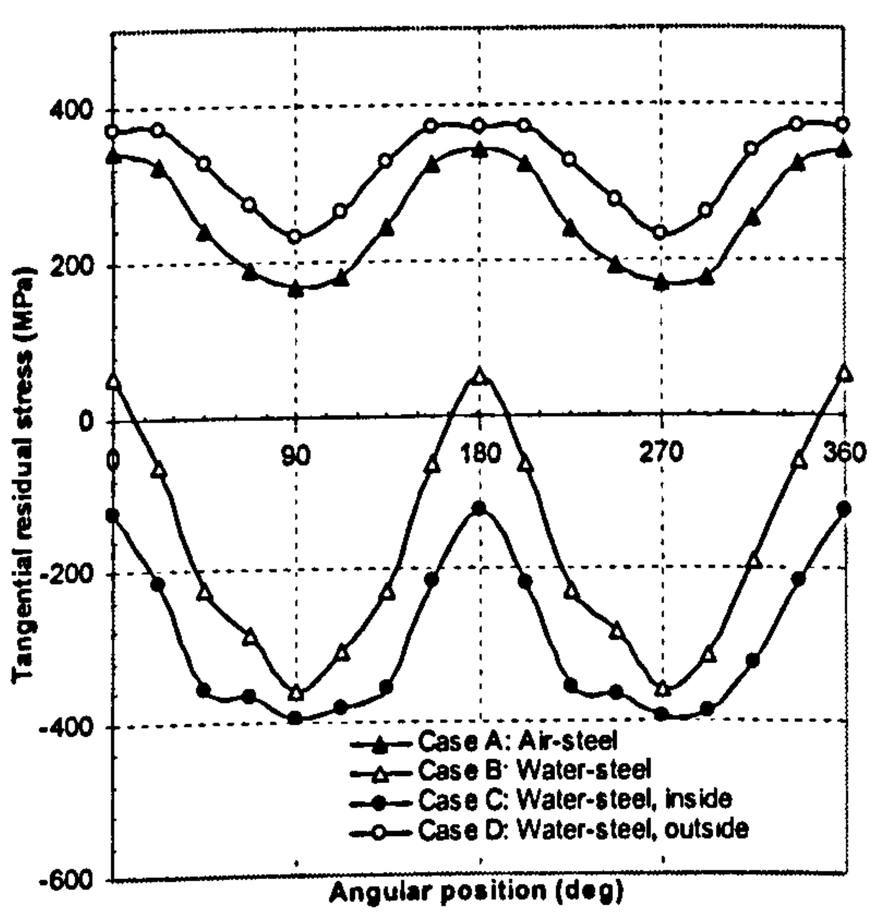

(a) Tangential stress

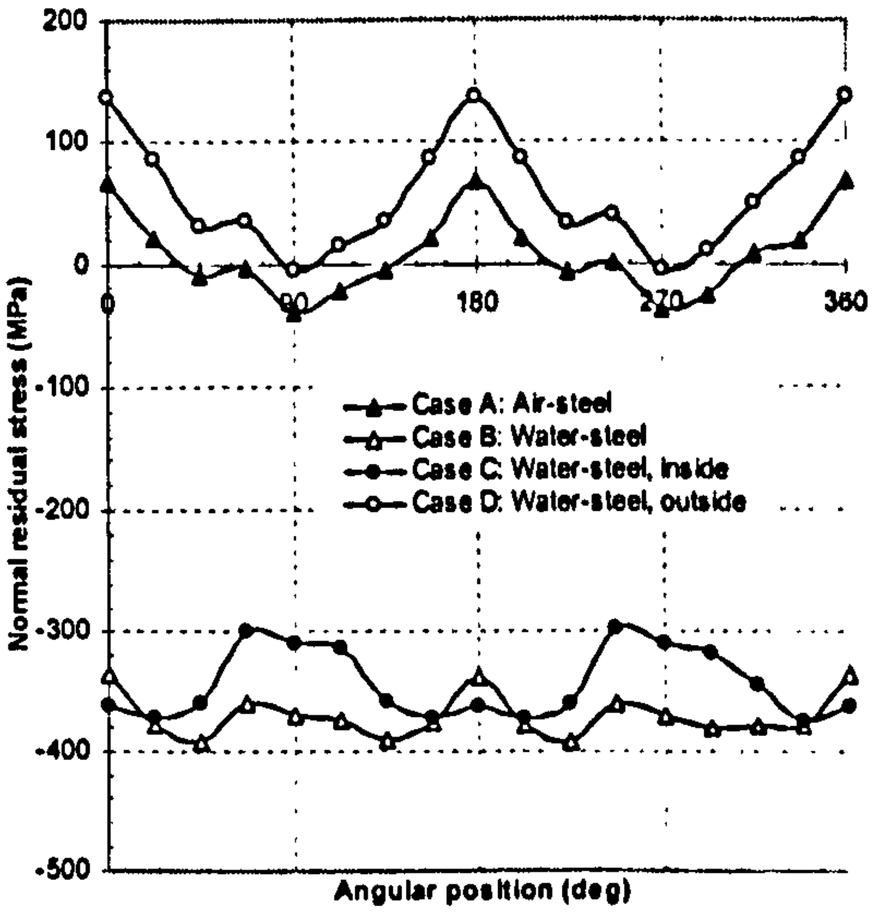

(b) Normal stress

Figure 7.49 Residual stress distributions along Curve *C*

Figure 7.49 illustrates the residual stress distributions along Curve *C*. Contrary to the previous observations, cooling the outer surface(Case *D*) causes the peak tangential residual stress to increase to 380MPa (137%σ_y); while for Cases *B* and *C*, both tangential and normal residual stresses are greatly reduced along Curve *C*.

7.3.8.3 Summary

The effects of different cooling schemes on residual stresses have been investigated. It is found that the cooling rate is the most important parameter that has significant effect on both the magnitudes and overall distribution patterns of the residual stresses.

An important observation is that cooling the outer surface can considerably reduce stresses on the outer surface. Similarly, cooling the inner surface can dramatically change stresses from tensile to compressive on the inner surface. However, it should also be noticed that the reduction of residual stresses at one location will undesirably increase stresses at another location. Careful evaluation and prediction are needed before applying appropriate cooling scheme.

The effect of cooling rate on the residual stress can be explained as follows. While applying cooling schemes, the material contract and cause tensile stresses. When welding is completed, the stress profile reverses so that the tensile stress become compressive and vice versa. The maximum stress relates closely to the temperature change, thus to the convective heat transfer coefficient. The convective heat transfer coefficient should be controlled within a certain range so that both peak tensile stress and peak compressive stress are within an acceptable range. The stress magnitudes can be adjusted by applying different convective heat transfer coefficient at various locations to control the cooling rate.

7.3.9 Optimization

7.3.9.1 Introduction

From the previous parametric studies, it is found that the interpass temperature and cooling rate are the most sensitive parameters affecting the magnitudes and distributions of the residual stress in the tee branch junction. To take into account the combined effect of these two parameters, a model was then proposed for optimising residual stress profiles, as described in Case *D*. Case *D* is based on the four-welder model, however, the interpass temperature is set to 240°C. It is also assumed that the convective heat transfer coefficient is 500W/m^2°C; while cooling the branch inner surface during

welding. The simulation results from Case *D* are compared with the predictions from the previously performed cases of *A*, *B* and *C*. The details of these cases are listed as follows.

Case *A*: Four-welder model.

Case *B*: Four-welder model and interpass temperature of 240°C.

Case *C*: Four-welder model, interpass temperature of 120°C, and convective heat transfer coefficient of 1000W/m^2°C (branch inner surface cooling).

Case *D*: Four-welder model, interpass temperature of 240°C, and convective heat transfer coefficient of 500W/m^2°C (branch inner surface cooling).

7.3.9.2 Results and discussion

7.3.9.2.1 Branch cross section *a-a*

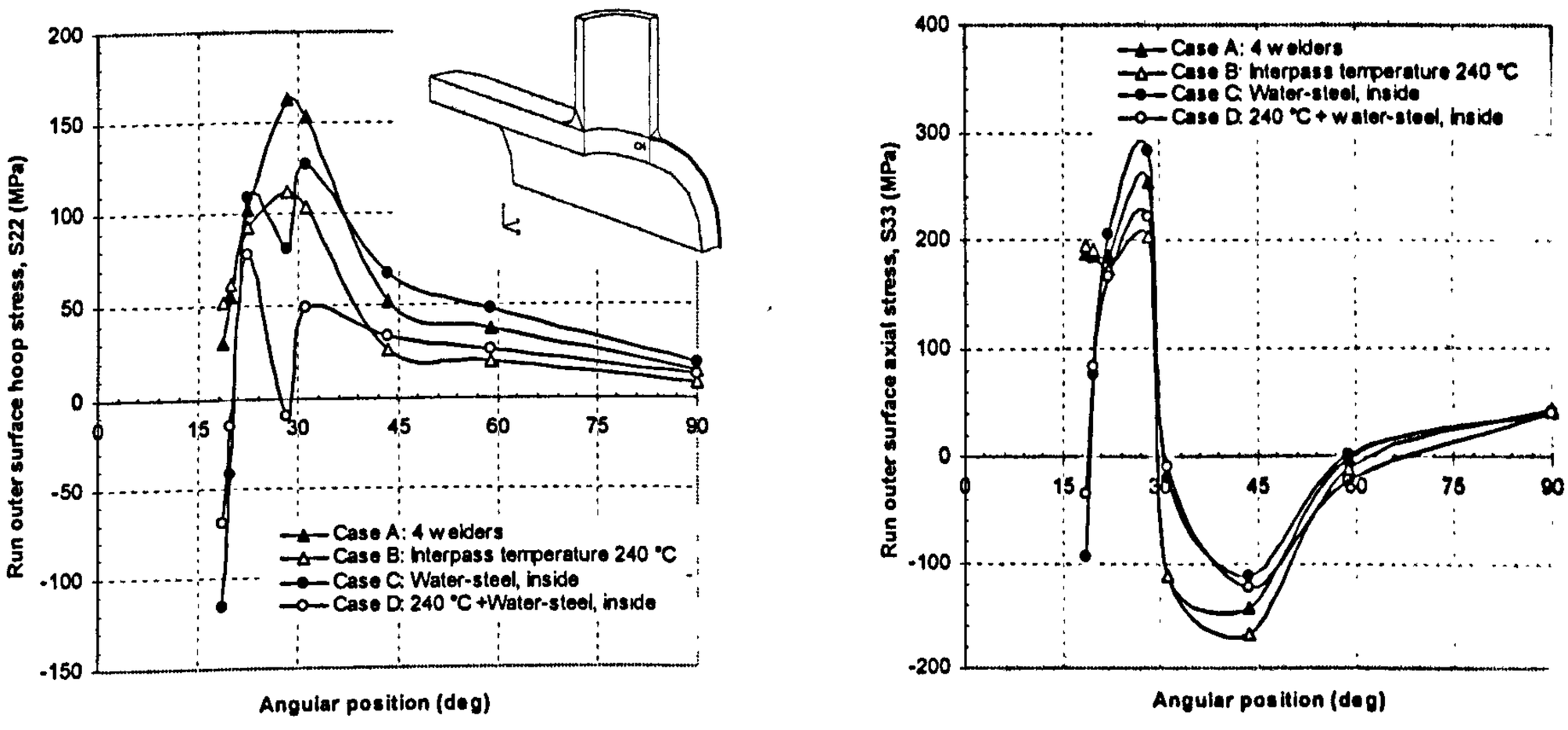

(a) Hoop stress

(b) Axial stress

Figure 7.50 Stress vs. angular position on the run pipe outer surface

Figure 7.50 shows the residual stress distributions versus angular position on the outer surface of the run pipe. Compared with other cases, Cases *C* and *D* change the hoop and axial residual stresses from tensile to compressive on the branch inner surface. Case *D* also reduces the peak hoop and axial tensile residual stresses to 80MPa and 210MPa, respectively. There are not many differences away from the weld seam amongst the four cases.

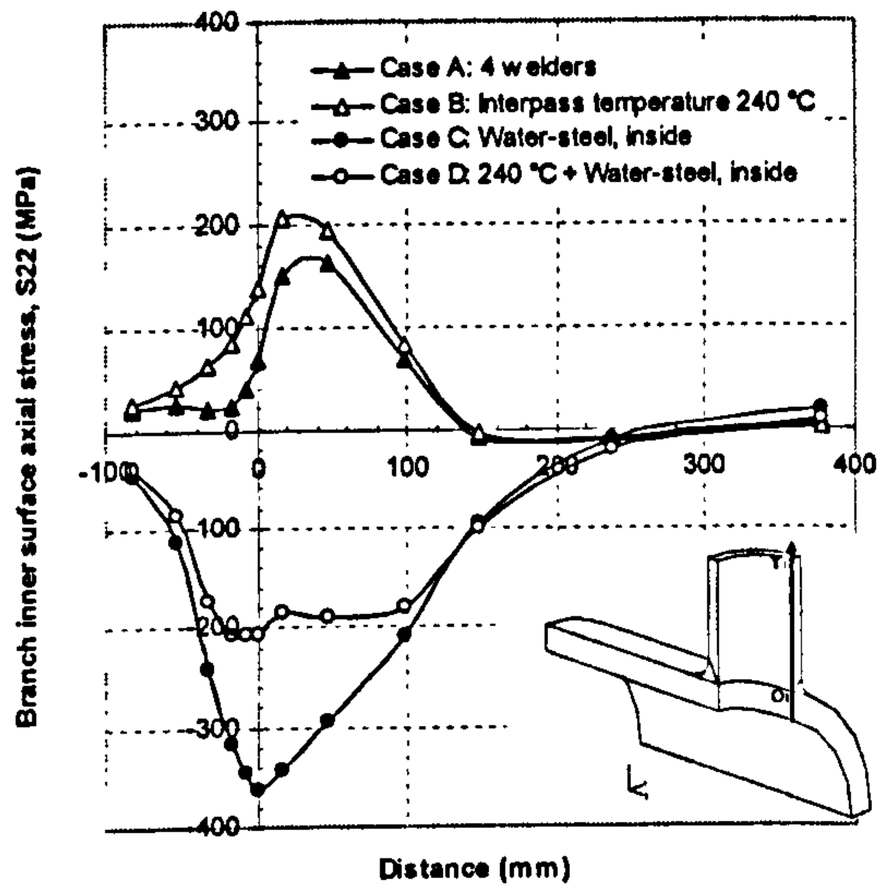

(a) Axial stress

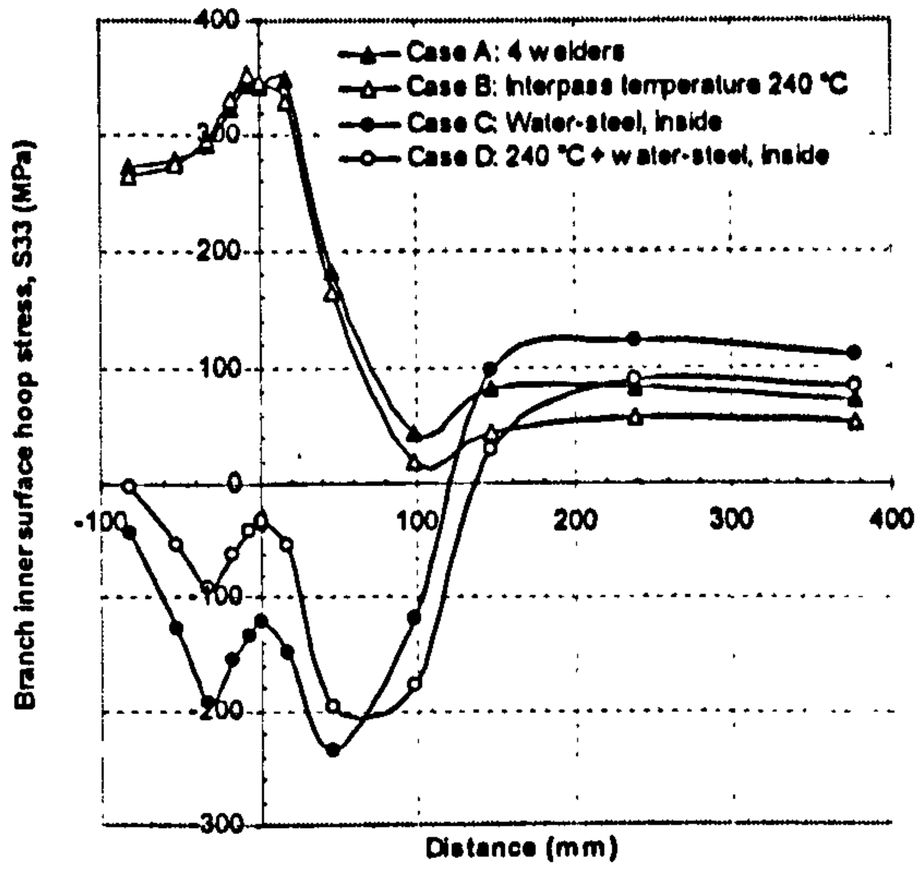

(b) Hoop stress

Figure 7.51 Residual stresses in the Y_1-direction on the branch inner surface

Figure 7.51 shows the residual stress distributions in the Y_1-direction. Both Cases *C* and *D* change the peak axial and hoop residual stress from tensile to compressive along the Y_1-direction on the branch inner surface. However, Case *D* gives a more acceptable compressive stress than Case *C*.

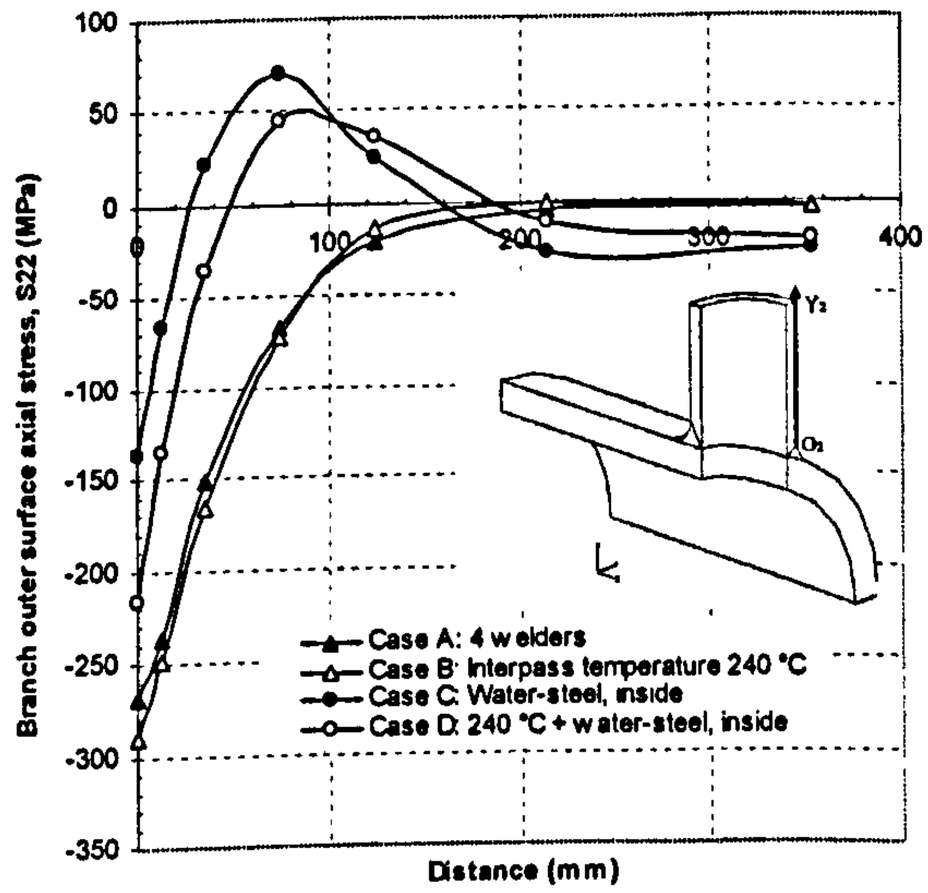

(a) Axial stress

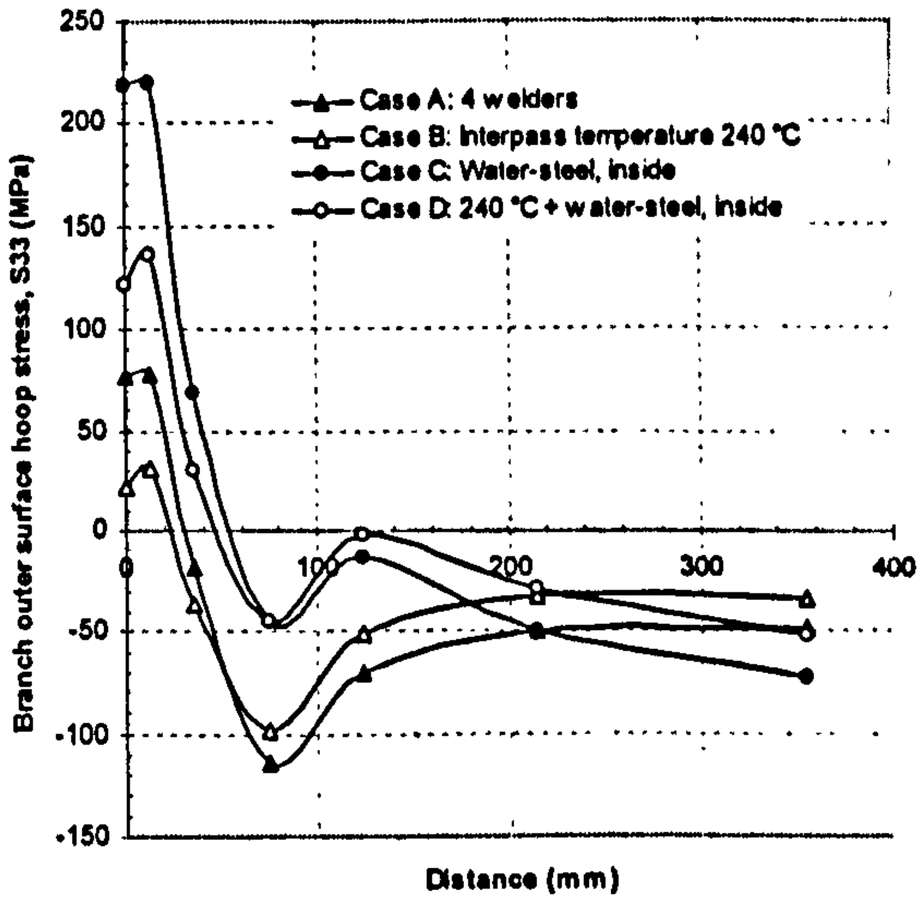

(b) Hoop stress

Figure 7.52 Residual stresses in the Y_2-direction on the branch outer surface

Figure 7.52 presents the residual stress distributions in the Y_2-direction. Although Case *D* increases both the peak axial and hoop residual stresses compared with those of Cases *A* and *B*, their magnitudes are below 150MPa.

7.3.9.2.2 Run pipe cross section *b-b*

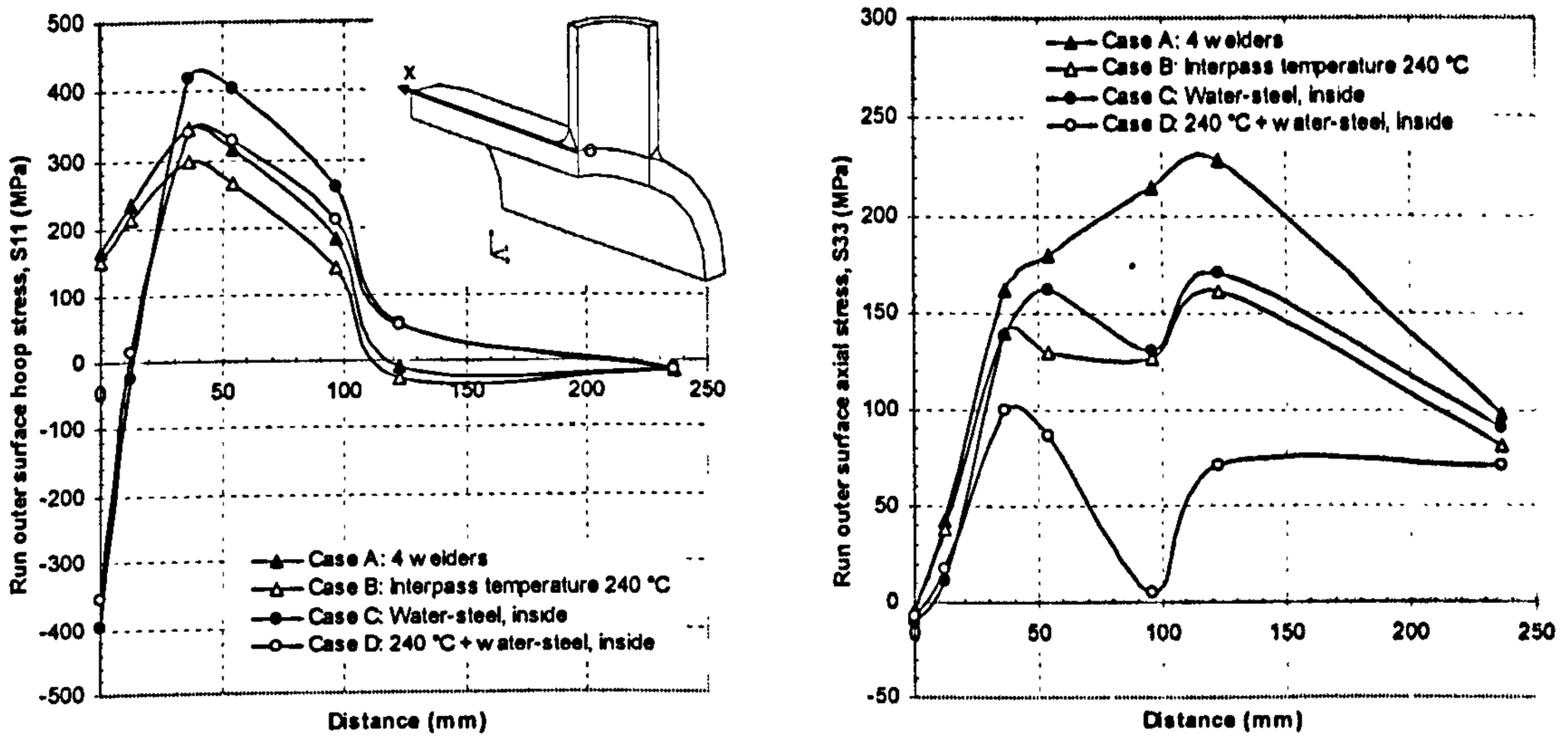

(a) Hoop stress (b) Axial stress

Figure 7.53 Residual stresses in the *X*-direction on the run outer surface

Figure 7.53 shows the residual stress distributions in the *X*-direction. Although Cases *C* and *D* change the hoop stress from tensile to compressive near the origin, the peak hoop stress in Case *D* is 350MPa(126%σ_y). The axial residual stresses on the run pipe outer surface are reduced dramatically in Case *D*.

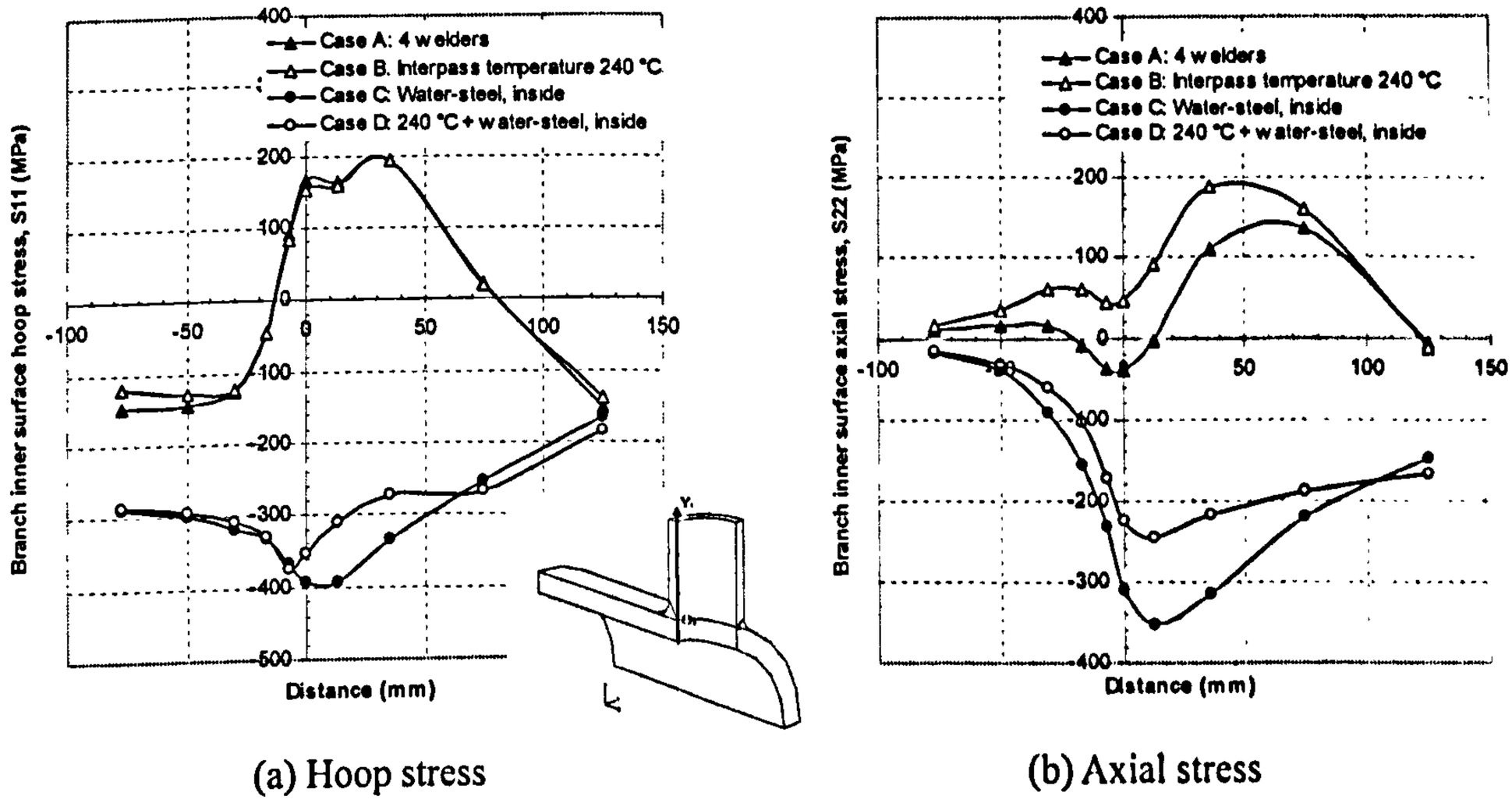

(a) Hoop stress (b) Axial stress

Figure 7.54 Residual stresses in the Y_1-direction on the branch inner surface

Figure 7.54 shows the residual stress distributions in the Y_1-direction. Cases *C* and *D* have significant effects in changing the tensile hoop and axial residual stresses to

compressive stresses on the branch inner surface.

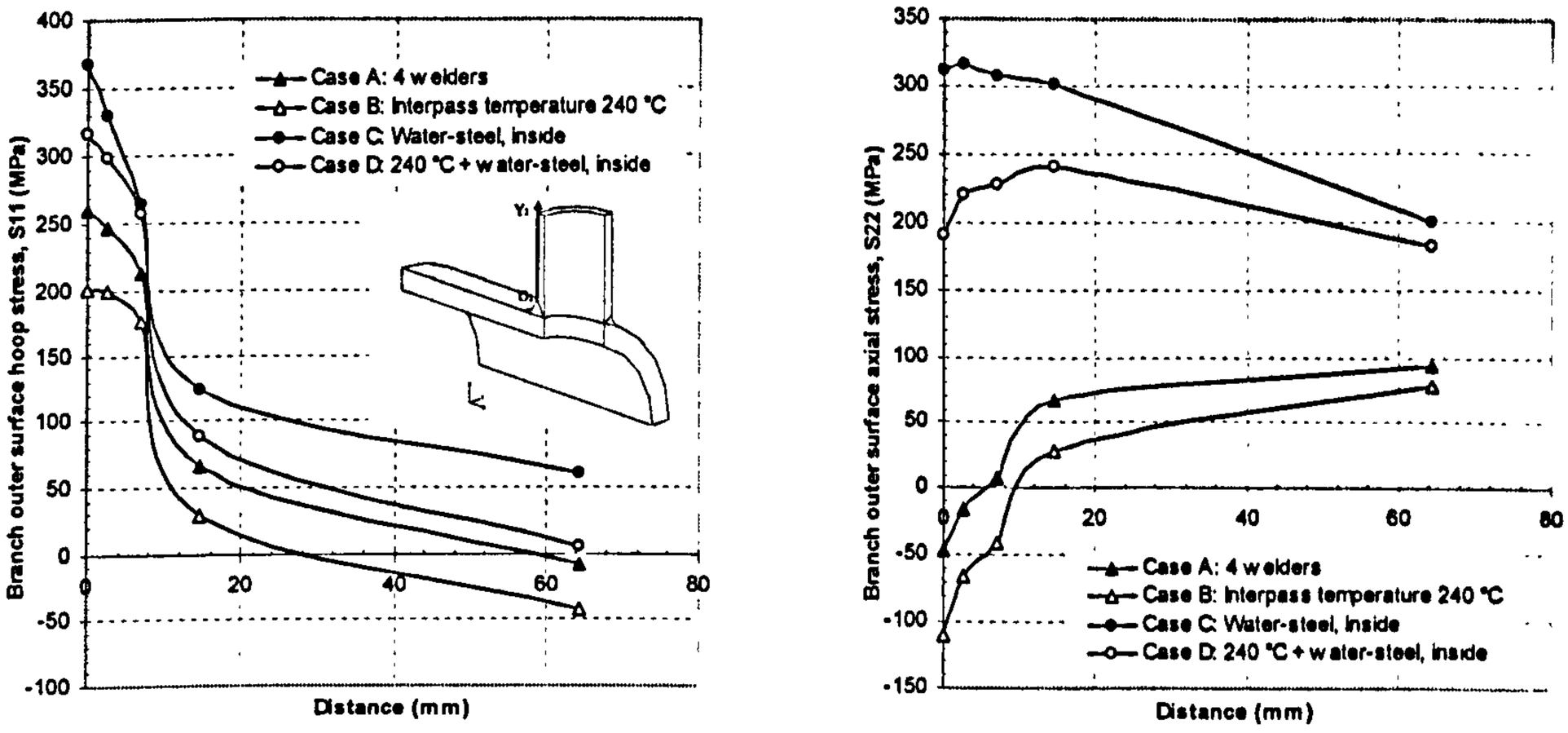

(a) Hoop stress

(b) Axial stress

Figure 7.55 Residual stresses in the Y_2-direction on the branch outer surface

Figure 7.55 shows the residual stress distributions in the Y_2-direction. Again it is noticed that cooling the branch inner surface can increase the hoop and axial residual stresses, while increasing interpass temperature produces an opposite effect. Overall, this makes the hoop and axial stress distributions in Case *D* locate between those predicted by Case *A* and *C*.

7.3.9.2.3 Circumferentially along Curve *A*

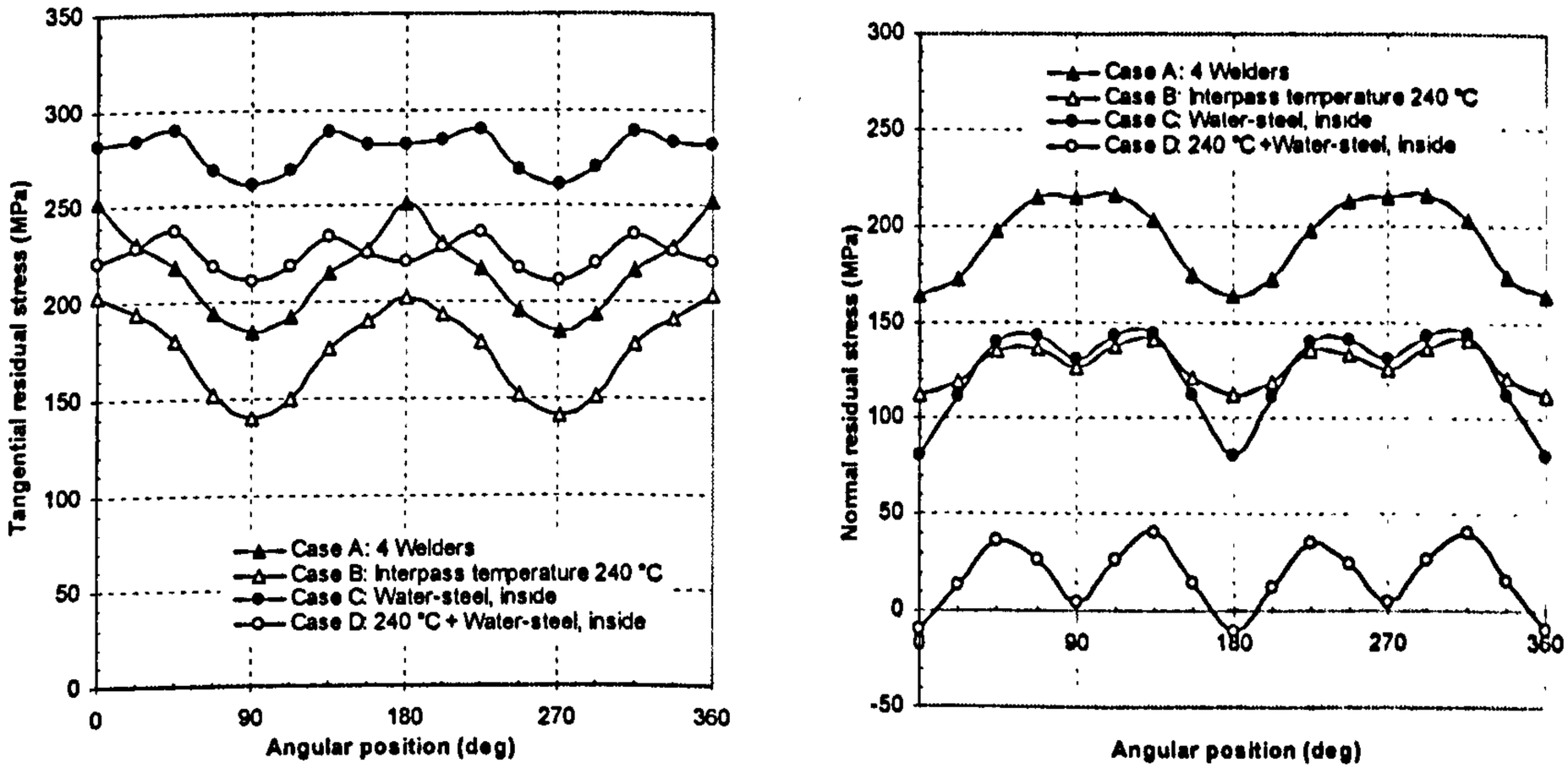

(a) Tangential stress

(b) Normal stress

Figure 7.56 Residual stress distributions along Curve *A*

Figure 7.56 displays the residual stress distributions along Curve *A*. It is noticed that in Case *D*, the tangential residual stresses along Curve *A* tend to be uniform, varying within the range 210 to 240MPa. The peak normal residual stresses are reduced greatly, from peak value of 220MPa (Case *A*) to only 40MPa (Case *D*). The normal stresses are also quite uniform, varying between -10 and 40MPa.

7.3.9.2.4 Circumferentially along Curve *B*

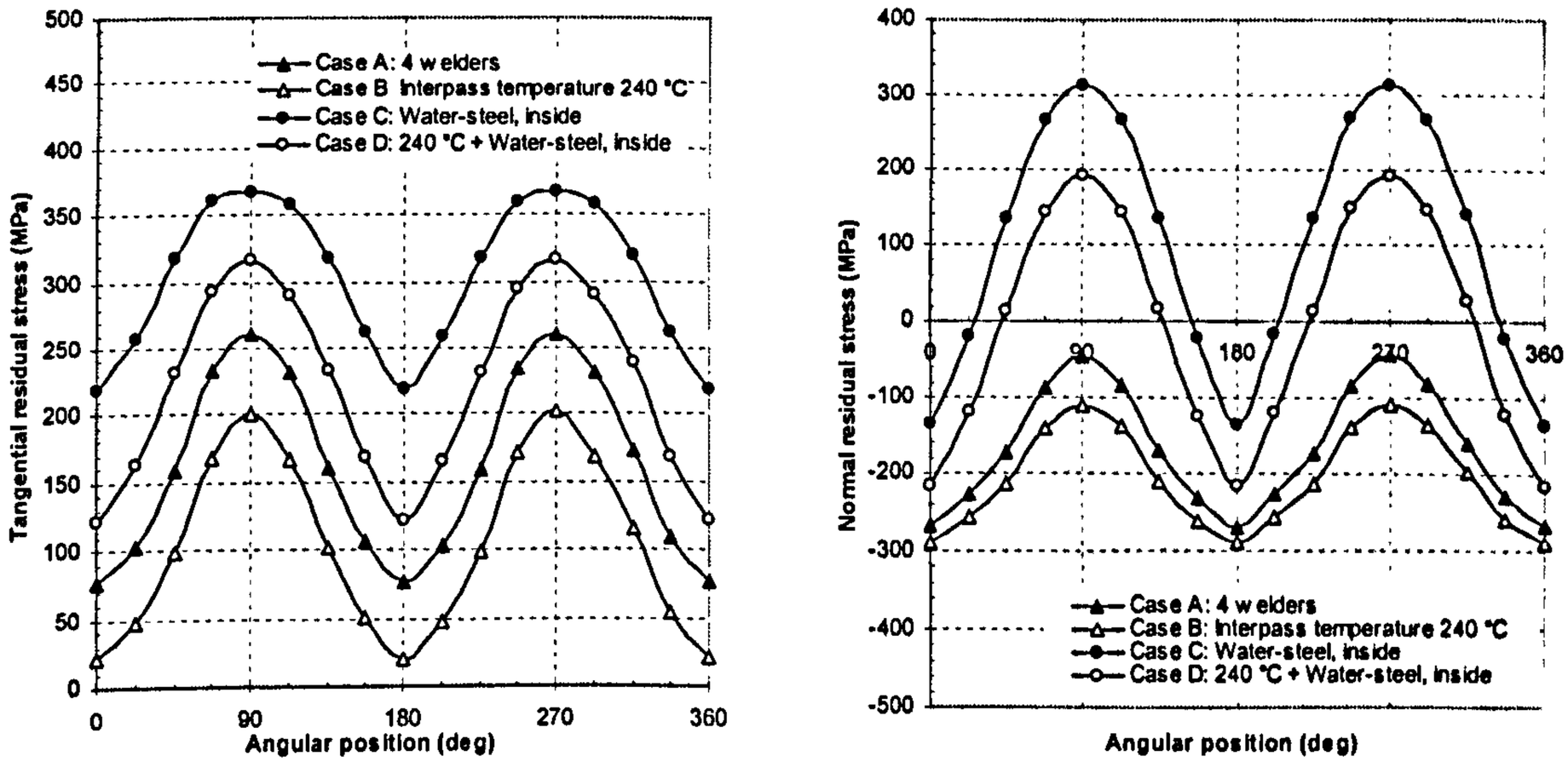

(a) Tangential stress (b) Normal stress

Figure 7.57 Residual stress distributions along Curve *B*

Figure 7.57 presents the residual stress distributions along Curve *B*. Although in Case *D*, both tangential and normal stresses are greatly reduced and tend to be uniform along Curve *A*, (see Figure 7.56), they are both increased along Curve *B*. The peak tangential residual stress is 310MPa (111%σ_y) at the crotch corners.

7.3.9.2.5 Circumferentially along Curve *C*

Figure 7.58 illustrates the residual stress distributions along Curve *C*. Case *D* produces acceptable residual stress distributions along Curve *C*. The peak tangential residual stress is greatly reduced from 350MPa to -20MPa. The normal residual stresses are changed to compression and the distribution is quite uniform along Curve *C*.

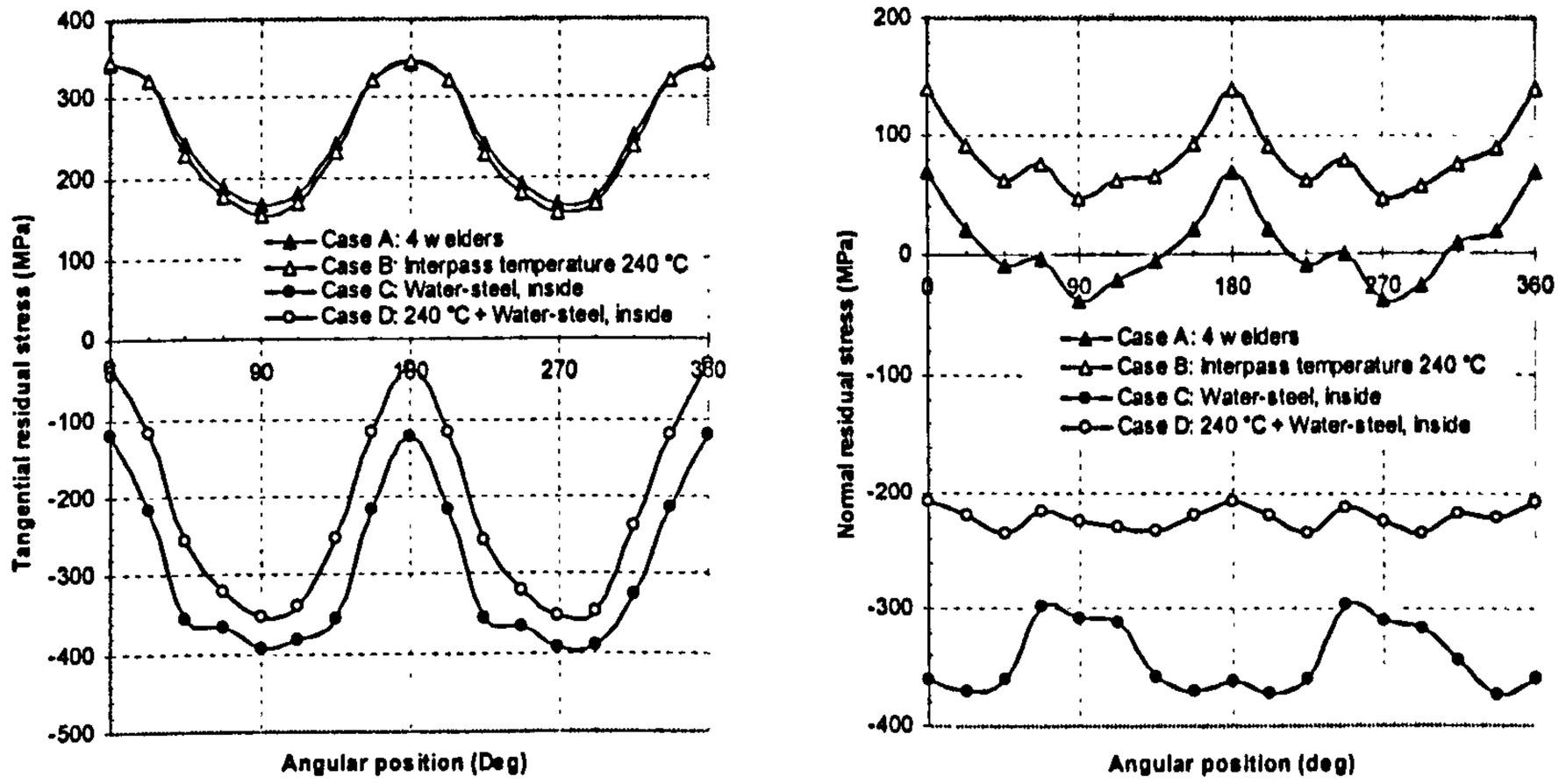

(a) Tangential stress (b) Normal stress

Figure 7.58 Residual stress distributions along Curve *C*

7.3.9.3 Summary

Based on the parametric studies in the previous sections, the most sensitive parameters appear to be the interpass temperature and the cooling rate. The latter is controlled by the convective heat transfer coefficient. They were selected for optimization.

Generally speaking, the proposed optimization scheme of Case *D* was quite effective in optimizing the residual stresses profiles at most locations, especially on the branch inner surface. Both the hoop and axial residual stresses were dramatically reduced or changed from tensile to compressive. However, it is again noticed that due to the complexity of geometry, the reduction of residual stresses at one location undesirably increases stresses at another location.

7.4 Conclusions

In this chapter, the validated 3D FE model was used to investigate the sensitivity of the manufacturing-related parameters on the weld induced residual stresses in the tee branch junction. The relative importance of the welding parameters and their influence on the final residual stress build-up has been identified. The intricacies of how the

various variables interact are now well understood and attempts to control them to optimize residual stress profiles have been addressed. The parameters investigated included pass number, weld sequence, heat input, preheat temperature, interpass temperature and cooling rate.

It was found that different parameters affect the magnitudes and overall distributions of residual stresses in different ways. Residual stresses are influenced significantly by the cooling rate, and, to a lesser extent, by other parameters, such as the interpass temperature. Tensile residual stress on the inner surface of the tee branch junction can be dramatically changed to compressive by controlling and applying different convective heat transfer coefficient to the branch inner surface. Interpass temperature also has an important effect. It generally reduces the residual stresses when it is increased. The effect of heat input is not so evident. A 100% increase of heat input has little effect on the magnitudes of stresses. Preheating is usually expensive to apply and has less effect. The effect of welding sequence is not very significant. Assigning four/two welders to fabricate the tee branch junction gives a symmetrical residual stress distribution. Finally, an effective method for multipass welding simulation was proposed from the results of the effect of pass number on the residual stress.

Based on these conclusions, a set of optimum welding parameters has been proposed for minimizing residual stresses in several critical regions when multipass welding thick-walled tee branch junctions. Quite effective optimization results have been obtained, especially on the branch inner surface.

Chapter 8 Conclusions and Future Work

8.1 Conclusions

A novel full 3D thermomechanical FE model, together with all-hexahedral meshing technique, has been developed to predict residual stresses in a thick-walled tee branch junction. The correlations between welding parameters and residual stresses have been established and issues concerning residual stress profile optimization have been addressed. The main work and conclusions are as follows:

A generalized plain strain model was first developed. Modelling techniques, such as contact versus standard boundary conditions, sequentially versus fully coupled model, have been investigated. For the first case, it was found that both contact and standard boundary conditions gave similar results. However, analyses involving contact were noted to require more computer resources and were consequently more expensive.

For the second case, the coupling between the thermal and mechanical field was confirmed to be somewhat weak by comparing residual stresses predicted by the sequentially and fully coupled models. As a consequence, a standard boundary condition, in conjunction with a sequentially coupled model, were deemed adequate in the further model development.

A full 3D model was then developed and applied to multipass butt-welded plates and pipes for validation. The moving heat source and filler material deposition were simulated by assigning reactivated elements moving along the weld path with volumetric heat flux. Temperature and residual stress simulation results were compared with existing experimental data. Good agreements have been obtained.

A novel all-hexahedral meshing technique has been developed and employed to mesh the complex 'saddle like' geometry with well graded mesh suitable for multipass simulation. Combined with the validated 3D modelling technique, the model was finally applied to the multipass welded tee branch junction. The thermal cycles and temperature distributions, as well as thermal stress evolutions and residual stress distributions at the

branch and run cross section and along the weldline circumferentially around the run and branch pipe have been reported.

The thermal analysis revealed that, as expected, the peak temperatures and steep thermal gradients are always limited to the domain of the heat source. Temperature distributions on the inner surface of the branch pipe are affected by the heat input of the first few passes, while temperature distributions on the branch outer surface are mainly decided by the last few passes. Transient temperature distributions along the weldline on the outer surface of the run (Curve *A)* and branch (Curve *B*) pipe and on the inner surface of the branch pipe (Curve *C*) continuously change as welding proceeds circumferentially along the weldline. The continuous change of the transient temperature fields plays an important role in the formation of residual stresses along the circumferential weldline.

The stress analysis revealed that peak compressive stresses appear at the moment of deposition, and gradually increase to higher stress as the heat source moves away. Steep stress gradients appear near the weld toe. The stresses on the outer surface of the branch pipe are mainly affected by last few passes. At the branch cross section *a-a*, the critical region is at the branch inner surface, with a peak hoop residual stress 26% above the room temperature yield stress. At the run pipe cross section *b-b*, the critical area is roughly at the centre of the weld, with a peak hoop residual stress 12% above the room temperature yield stress. A typical through-thickness bending situation is observed for both the hoop and axial residual stresses at the weld toe at the run pipe cross section *b-b*. The peak tangential and normal stresses are 90% and 80% respectively of the room temperature yield stress on Curve *A*. Tangential stress becomes dominant on both Curves *B* and *C*, with peak value being 97% and 122% of the room temperature yield stress, respectively.

Extensive parametric studies have been carried out. The parameters investigated included the number of passes, welding sequence, heat input, preheat temperature, interpass temperature and cooling rate. It was found that different parameters affect the magnitudes and overall distributions of residual stresses in different ways. Cooling rate, which is in the form of convective heat transfer coefficient, is the most important parameter influencing residual stress profiles. Stress magnitudes can be adjusted by

varying convective heat transfer coefficient and applying cooling on different locations. Interpass temperature is another important parameter. It usually reduces the residual stresses when increased. The predicted residual stress fields for the tee branch junction are found to be fairly insensitive to the heat input and preheat temperature. Several welders working symmetrically and simultaneously gives a symmetrical residual stress distributions. Proper grouping (i.e. grouping all the passes except the last as one layer, and the last pass as another layer) is an effective method in multipass welding simulation.

Finally, based on these conclusions, a set of optimum welding parameters has been proposed for minimizing residual stresses in several critical regions in the thick-walled tee branch junctions. Quite effective optimization results have been obtained.

The dissertation as a whole illustrates the predictive potential of FE modelling for realistic multipass welding. Through parametric studies, it will not only improve welding procedures and prolong the service life of irregular heavy welded constructions, but also will dramatically reduce the time and expense associated with developing new welding procedures for complex thick-walled components or components where specific weld properties are required. The use of simulation techniques will provide a wide-range of information critical for proposing recommendations to improve design and welding procedures. The work will also contribute towards the improvement of techniques for *repairing* defected welded structures; the latter being particularly relevant to the 'offshore' oil and power industries.

8.2 Suggestions for future work

The applications of the current FE model to several geometries demonstrate that the model is effective in predicting and optimising residual stresses induced by welding. Although the parametric studies in the current research focused on manufacturing-related parameters, in the future work, it is hoped to include the important geometrical features of a tee branch junction, such as various thicknesses and branch-to-run outside diameter ratios. It is also hoped to consider different and realistic parent weld and HAZ material properties in the model. Finally, more cases of various

manufacturing parameters, such as different start/stop points for various passes, should be performed. With improved resources, the future work could also include using quadratic elements, reducing angular deposition to below 22.5°, as well as increasing the number of welding passes.

Bibliography

Abid, M. and Siddique, M. (2005) Numerical simulation of the effect of constraints on welding deformations and residual stresses in a pipe–flange joint. *Modelling and Simulation in Materials Science and Engineering*, **13** (6), pp. 919–933.

Agapakis, J.E. and Masubuchi, K. (1984) Analytical modeling of thermal stress relieving in stainless and high strength steel weldments. *Welding Journal*, **63** (6), pp. 187-196.

American Welding Society (1963) *Welding handbook: Section 1, Fundamentals of welding*. 5th ed., Cleaver-Hume: American Welding Society.

American Welding Society (1967) *Welding handbook: Section 5, Applications of welding*. 5th ed., Macmillan: American Welding Society.

American Welding Society (1998) *Structural welding code: steel.* 16th ed., Miami: American Welding Society.

Andersson, B.A.B. (1978) Thermal stresses in a submerged-arc welded joint considering phase transformations. *Journal of Engineering Materials and Technology, Transactions of the ASME*, **100** (4), pp. 356-362.

Andersson, B. and Karlsson, L. (1981) Thermal stresses in large butt-welded plates. *Journal of Thermal Stresses*, **4** (3-4), pp. 491-500.

Argyris, J.H., Szimmat, J. and William, K.J. (1982) Computational aspects of welding stress analysis. *Computer Methods in Applied Mechanics and Engineering*, **33** (1-3), pp. 635-666.

ASM International Handbook Committee. (1990) *Metals handbook: vol.1 Properties and selection: irons, steels, and high-performance alloys.* 10th ed., Materials park, Ohio: ASM International.

Bednar, H. H. (1981) *Pressure vessel design handbook.* London: Van Nostrand Reinhold.

Benzley, S.E., Perry, E., Merkely, K., Clark, B. and Sjaardama, G. D. (1995) A comparison of all hexagonal and all tetrahedral finite element meshes for elastic and elasto-plastic analysis. *Proceedings of the 4th International Meshing Roundtable: October 16-17, 1995,* Albuquerque, New Mexico: Sandia National Laboratories, pp.179-191.

Bhadeshia, H. K. D. H. (1995) Possible effects of stress on steel weld microstructures. In Cerjak, H. and Bhadeshia, H.K.D.H. (eds.), *Mathematical Modelling of Weld Phenomena 2.* London: The Institute of Materials, pp. 71-118.

Boley, B. A. and Weiner, J. H. (1960) *Theory of thermal stresses.* London: John Wiley & Sons.

Boyer, H.E. (ed.) (1987) *Atlas of stress-strain curves.* 2nd ed., Metals Park, Ohio: ASM International.

Brickstad, B. and Josefson, B. L. (1998) A parametric study of residual stresses in multi-pass butt-welded stainless steel pipes. *International Journal of Pressure Vessels and Piping,* **75** (1), pp. 11-25.

Brown, S. and Song, H. (1992a) Finite element simulation of welding of large structures, *Journal of Engineering for Industry, Transactions of the ASME,* **114** (4), pp. 441-451.

Brown, S. and Song, H. (1992b) Implications of three-dimensional numerical simulations of welding of large structures. *Welding Journal,* **71** (2), pp. 55-62.

Brust, F. W. and Kanninen, M. F. (1981) Analysis of residual stresses in girth welded type 304 stainless pipes. *Journal of Materials for Energy Systems, Transactions of the ASME*, **3** (3), pp. 56–62.

Brust, F. W. and Rybicki, E. F. (1981) A computational model of backlay welding for controlling residual stresses in welded pipes. *Journal of Pressure Vessel Technology, Transactions of the ASME*, **103** (3), pp. 226-232.

Cañas, J., Picón, R., París, F., Blazquez, A. and Marín, J. C. (1996) A simplified numerical analysis of residual stresses in aluminum welded plates. *Computers & Structures*, **58** (1), pp. 59-69.

Carslaw, H.S. and Jaeger, J.C. (1947) *Conduction of heat in solids*. Oxford: Clarendon press.

Chandra, U. (1985) Determination of residual stresses due to girth-butt welds in pipes. *Journal of Pressure Vessel Technology, Transactions of the ASME*, **107** (2), pp. 178-184.

Chang, P.H. and Teng, T.L. (2004) Numerical and experimental investigations on the residual stresses of the butt-welded joints. *Computational Materials Science*, **29** (4), pp. 511-522.

Chen G, Xu X, Poon C.C. and Tam A.C. (1999) Experimental and numerical studies on microscale bending of stainless steel with pulsed laser. *Journal of Applied Mechanics, Transactions of the ASME*, **66** (3), pp. 772–779.

Chuse, R. (1977) *Pressure vessels: the ASME code simplified*. 5th ed., New York: McGraw-Hill.

Davies, A.C. (1989) *The science and practice of welding*. 9th ed., Cambridge University Press.

Dong, Y., Hong, J.K., Tsai, C.L. and Dong, P. (1997) Finite element modeling of residual stresses in

austenitic stainless steel pipe girth welds. *Welding Journal,* **76** (10), pp. 442-449.

Dong, P., Zhang, J. and Li, M. V. (1998) Computational modelling of weld residual stresses and distortions-an integrated framework and industrial applications. *Proceedings of the 1998 ASME/JSME Joint Pressure Vessels and Piping Conference, Fatigue, Fracture, and Residual Stresses, PVP,* **373**, Rahman, S. (ed.), *July 26-30, 1998, San Diego, CA, USA.* pp. 311-335.

Dong, P.S. (2000) Recent progress in analysis of residual welding stresses – Report1: Modeling of weld residual stresses and distortion: computational procedures and applications. *Welding Research Council Bulletin,* **455**, pp. 1-11.

Dong, P., Zhang, J., Hong, J. K., Bell, W. and McDonald, E. J. (2000) Recent progress in analysis of residual welding stresses –Report 3: Finite element and experimental study of residual stresses in a multi-pass repair weld. *Welding Research Council Bulletin,* **455**, pp. 22-28.

Dong, P. and Brust, F.W. (2000) Welding residual stresses and effects on fracture in pressure vessel and piping components: A millennium review and beyond. *Journal of Pressure Vessel Technology, Transactions of the ASME,* **122** (3), pp. 329-338.

Dong, P. (2001) Residual stress analysis of a multi-pass girth weld: 3D special shell versus axisymmetric models. *Journal of Pressure Vessel Technology, Transactions of the ASME,* **123** (2), pp. 207-213.

Dong, P. (2002) Recommendations for determining residual stresses in fitness-for-service applications. *Welding Research Council Bulletin,* **476**, pp. 1-61.

Dong, P. (2004) On the mechanics of residual stresses in girth welds. *Proceedings of the 2004 ASME/JSME Pressure Vessels and Piping Conference, Residual Stress, Fracture, and Stress Corrosion Cracking, PVP,* **479**, Wang, Y.Y. (eds.), *Jul 25-29, 2004, San Diego, CA, USA.* pp.

119-124.

Engelhard, G., Habip, L. M., Pellkofer, D. and Schmidt, J. (2000) Optimization of residual welding stresses in austenitic steel piping: prooftesting and numerical simulation of welding and postwelding processes. *Nuclear Engineering and Design,* **198** (1-2), pp.141-151.

Fanous, I. F. Z., Younan, M. Y. A. and Wifi, A.S. (2003) Study of the effect of boundary conditions on residual stresses in welding using element birth and element movement techniques. *Journal of Pressure Vessel Technology, Transactions of the ASME*, **125** (4), pp. 432-439.

Free, J.A. and Goff, R.F.D.P. (1989) Predicting residual stresses in multi-pass weldments with the finite element method. *Computers & Structures,* **32** (2), pp. 365-378.

Friedman, E. (1975) Thermomechanical analysis of the welding process using the finite element method. *Journal of Pressure Vessel Technology, Transactions of the ASME,* **97** (3), pp. 206-213.

Funderburk, R. S. (1998) The importance of interpass temperature. *Welding Innovation,* **15** (1).

Funderburk, R. S. (1997) Fundamentals of Preheat. *Welding Innovation*, **14** (2).

Goff, R.F.D. P. (1979) Simplified analysis of the residual tangential stresses and strain due to the gas-cutting and welding of thin steel plate. *International Journal of Mechanical Sciences*, **21** (5) pp. 287-300.

Goldak, J., Chakravarti, A. and Bibby, M. (1984) A new finite element model for welding heat sources. *Metallurgical Transactions B-Process Metallurgy,* **15** (2), pp. 299-305.

Goldak, J., Bibby, M., Moore, J., House, R. and Patel, B. (1986a) Computer modeling of heat flow in welds. *Metallurgical Transactions B-Process Metallurgy,* **17** (3), pp. 587-600.

Goldak, J., McDill, M., Oddy, A., House, R., Chi, X. and Bibby, M. (1986b) Computational heat transfer for weld mechanics. American Welding Society, Welding Research Council, *Advances in Welding Science and Technology - TWR '86: Proceedings of an International Conference on Trends in Welding Research: 18-22 May, 1986, Gatlinburg, Tennessee, USA*. New York: ASM International, pp. 15-20.

Goldak, R. J. and Gu, M. (1995) Computational weld mechanics of the steady state. In Cerjak, H. and Bhadeshia, H.K.D.H. (eds.), *Mathematical Modelling of Weld Phenomena 2*. London: The Institute of Materials, pp. 207-225.

Gordon, J. R. (1996) Modeling of residual stress and distortion in welded structures: an overview of selected U.S. research initiatives. *Proceedings of the 1996 ASME Pressure Vessels and Piping Conference, Residual Stresses in Design, Fabrication, Assessment and Repair, PVP*, **327**, Warke, R.W. (ed.), *Jul 21-26, 1996, Montreal, Canada*. pp. 1-8.

Gourd, L.M. (1995) *Principles of welding technology.* 3rd ed., London: Edward Arnold.

Grong, Ò. (1994) *Metallurgical modelling of welding.* London: The Institute of Materials.

Gunnert, R. (1955) Residual welding stresses. Stockholm: Almqvist & Wiksell.

Hansen, J.L., Hattel, J. and Lorentzen, T. (2001) Numerical and experimental analyses of residual stresses in submerged arc welding of mild steel plates. In Cerjak, H. and Bhadeshia, H.K.D.H. (eds.), *Mathematical Modelling of Weld Phenomena 5*. London: The Institute of Materials, pp. 581-596.

Hibbitt, H.D. and Marcal, P.V. (1973) Numerical thermo-mechanical model for the welding and subsequent loading of a fabricated structure. *Computers & Structures,* **3** (5), pp. 1145-1174.

Hibbitt, Karlsson & Sorensen, Inc. (2002) ABAQUS/Standard User's Manual, version 6.3.

Hibbitt, Karlsson & Sorensen, Inc. (2003) ABAQUS/CAE User's Manual, version 6.4.

Hong, J. K., Tsai, C. L. and Dong, P. (1998) Assessment of numerical procedures for residual stress analysis of multipass welds. *Welding Journal*, 77 (9), pp. 372-382.

Inoue, T. (1998) Residual stresses and distortion metallo-thermo-mechanics: simulation of engineering processes incorporating phase transformation. In Cerjak, H. and Bhadeshia, H.K.D.H. (eds.), *Mathematical Modelling of Weld Phenomena 4.* London: The Institute of Materials, pp. 547-575.

Ji, S. D., Fang, H. Y., Liu, X. S. and Meng, Q. G. (2005) Influence of a welding sequence on the welding residual stress of a thick plate. *Modelling and Simulation in Material Science and Engineering*, **13** (4), pp. 553-565.

Jiang, W., Yahiaoui, K., Wang, C.J., Hall, F.R. and Laoui, T. (2004) FE predictions of temperature distributions in a multipass welded piping branch junction. *Proceedings of the 2004 ASME/JSME Pressure Vessels and Piping Conference, High Pressure Technology: Innovations and Advances in High Pressure Technology, PVP,* **473**, Pfeifer, J. (eds.), *Jul 25-29, 2004, San Diego, CA, USA.* pp. 93-99.

Jiang, W., Yahiaoui, K. and Hall, F.R. (2005) Finite element predictions of temperature distributions in a multipass welded piping branch junction. *Journal of Pressure Vessel Technology, Transactions of the ASME,* **127** (1), pp. 7-12.

Jiang, W., Yahiaoui, K., Hall, F.R. and Laoui, T. (2005a) Comparison of sequentially and fully coupled generalized plane strain finite element modelling of multipass welding. *National Agency for Finite Element Methods and Standards, NAFEMS World Congress 2005, 17-21 May, 2005, Malta.*

pp. 92.

Jiang, W., Yahiaoui, K., Hall, F.R. and Laoui, T. (2005b) Finite element simulation of multipass welding: full three dimensional versus generalized plane strain or axisymmetric model. *Journal of Strain Analysis for Engineering Design*, **40** (6), pp. 587 – 598.

Jonsson, M., Karlsson, L. and Lindgren, L.E. (1985) Deformations and stresses in butt-welding of large plates with special reference to the mechanical properties. *Journal of Engineering Materials and Technology, Transactions of the ASME,* **107** (4), pp. 265-270.

Josefson, B.L. (1982) Residual stresses and their redistribution during annealing of a girth-butt welded thin-walled pipe. *Journal of Pressure Vessel Technology, Transactions of the ASME,* **104** (3), pp. 245-250.

Kadivar, M.H., Jafarpur,K. and Baradaran, G.H. (2000) Optimizing welding sequence with genetic algorithm. *Computational Mechanics,* **26** (6), pp. 514-519.

Karlsson, C. T. (1989) Finite element analysis of temperatures and stresses in a single-pass butt-welded pipe - influence of mesh density and material modelling, *Engineering Computations,* **6** (2), pp. 133-141.

Karlsson, R.I. and Josefson, B.L. (1990) Three-dimensional FE analysis of temperatures and stresses in a single-pass butt welded pipe. *Journal of Pressure Vessel Technology, Transactions of the ASME,* **112** (1), pp. 76-84.

Lancaster, J.F. (Ed.) (1986) *The physics of welding.* 2nd ed., Oxford: Pergamon.

Leung, C.K., Pick, R.J. and Mok, D.H.B. (1990) Finite element modeling of a single pass weld. *Welding Research Council Bulletin,* **356**, pp.1–10.

Leung, C.K. and Pick, R.J. (1990) Finite element analysis of a multipass weld. *Welding Research Council Bulletin*, **356**, pp. 11–33.

Lewis, R.W., Morgan, K., Thomas, H. R. and Seetharamu, K.N. (1996) *The finite element method in heat transfer analysis*. Chichester: Wiley and Sons.

Lin, Y. C. and Lee, K.H. (1997a) Effect of preheating on the residual stress in type 304 stainless steel weldment. *Journal of Materials Processing Technology,* **63** (1-3), pp. 797-801.

Lin, Y. C. and Lee, K.H. (1997b) Effect of welding parameters on the residual stress by the parallel heat welding. *International Journal of Pressure Vessels and Piping*, **71** (2), pp. 197-202.

Lin, Y.C. and Perng, J.Y. (1997) Effect of welding parameters on residual stress in type 420 martensitic stainless steel. *Science and Technology of Welding and Joining*, **2** (3), pp. 129-132.

Lindgren, L.E. and Karlsson, L. (1988) Deformations and stresses in welding of shell structures. *International Journal for Numerical Methods in Engineering,* **25** (2), pp. 635-655.

Lindgren, L.E., Haggblad, H.A., McDill, J. M. J. and Oddy, A. S. (1997) Automatic remeshing for three-dimensional finite element simulation of welding. *Computer Methods in Applied Mechanics and Engineering,* **147** (3-4), pp. 401-409.

Lindgren, L. E., Runnemalm, H. and Nasstrom, M.O. (1999) Simulation of multipass welding of a thick plate. *International Journal for Numerical Methods in Engineering,* **44** (9), pp. 1301-1316.

Lindgren, L.E. (2001a) Finite element modeling and simulation of welding. Part I: Increased complexity. *Journal of Thermal Stresses,* **24** (2), pp. 141–192.

Lindgren, L.E. (2001b) Finite element modeling and simulation of welding. Part II: Improved material modeling. *Journal of Thermal Stresses*, **24** (3), pp. 195–231.

Lindgren, L.E. and Hedblom E. (2001) Modelling of addition of filler material in large deformation analysis of multipass welding. *Communications in Numerical Methods in Engineering*, **17** (9), pp. 647-657.

Mackerle, J. (1996) Finite elements in the analysis of pressure vessels and piping, A bibliography (1976–1996). *International Journal of Pressure Vessels and Piping*, **69** (3), pp. 279-339.

Mackerle, J. (1999) Finite elements in the analysis of pressure vessels and piping, an addendum (1996–1998). *International Journal of Pressure Vessels and Piping*, **76** (7), pp. 461-485.

Mackerle, J. (2001) FEM and BEM analysis and modelling of residual stresses: A bibliography (1998–1999). *Finite Elements in Analysis and Design*, **37** (3), pp. 253-262.

Mackerle, J. (2002) Finite elements in the analysis of pressure vessels and piping, an addendum: a bibliography (1998–2001). *International Journal of Pressure Vessels and Piping*, **79** (1), pp. 1-26.

Mackerle, J. (2005) Finite elements in the analysis of pressure vessels and piping, an addendum: A bibliography (2001-2004). *International Journal of Pressure Vessels and Piping*, **82** (7), pp. 571-592.

Masubuchi, K. (1980) *Analysis of welded structures: residual stresses, distortion and their consequences*. Oxford: Pergamon Press.

Marcal, P. (1974) *Weld problems, structural mechanics programs*. Charlottesville: University Press, pp. 191-206.

McDill, J.M.J., Oddy, A.S., Goldak, J.A. and Bennisson, S. (1990) Finite Element analysis of weld distortion in carbon and stainless steels. *Journal of Strain Analysis for Engineering Design*, **25** (1), pp. 51-53.

Michaleris, P., Tortorelli, D. A. and Vidal, C.A. (1995) Analysis and optimization of weakly coupled thermoelastoplastic systems with applications to weldment design. *International Journal for Numerical Methods in Engineering*, **38** (8), pp. 1259-1285.

Michaleris, P. (1996) Residual stress distributions for multi-pass welds in pressure vessel and piping components. *Proceedings of the 1996 ASME Pressure Vessels and Piping Conference, Residual Stresses in Design, Fabrication, Assessment and Repair, PVP,* **327,** Warke, R.W. (ed.), *Jul 21-26, 1996, Montreal, Canada.* pp. 17-27.

Michaleris, P., Feng Z. and Campbell, G. (1997) Evaluation of 2D and 3D FEA models for predicting residual stress and distortion. *Proceedings of the 1997 ASME Pressure Vessels and Piping Conference, Approximate Methods in the Design and Analysis of Pressure Vessels and Piping Components, PVP,* **347,** Bees, W. J. (ed.), *Jul 27-31, 1997, Orlando, FL, USA.* pp. 91-102.

Mochizuki, M., Hayashi, M. and Hattori, T. (2000) Residual stress distribution depending on welding sequence in multi-pass welded joints with X-shaped groove. *Journal of Pressure Vessel Technology, Transactions of the ASME*, **122** (1), pp. 27-32.

Murthy, Y.V.L.N., Rao, G. V. and Iyer, P. K. (1996) Numerical simulation of welding and quenching processes using transient thermal and thermo-elasto-plastic formulations. *Computers & Structures,* **60** (1), pp. 131-154.

Murugan, S., Kumar, P.V., Raj, B.and Bose, M.S.C. (1998) Temperature distribution during multipass welding of plates. *International Journal of Pressure Vessels and Piping,* **75** (12), pp. 891-905.

Murugan, S., Rai, S.K., Kumar, P.V., Jayakumar, T., Raj, B. and Bose, M.S.C.(2001) Temperature distribution and residual stresses due to multipass welding in type 304 stainless steel and low carbon steel weld pads. *International Journal of Pressure Vessels and Piping,* **78** (4), pp. 307-317.

Nayama, M., Sakamoto, N., Takano, G. and Murase, K. (1997) Effects of a double sided heating method and its controlling parameters: Development of a residual stress control method for butt-welded pipe joints. *Welding International*, **11** (1), pp. 31-40.

Nguyen, N.T., Ohta, A., Matsuoka, K., Suzuki, N. and Maeda,Y.(1999) Analytical solutions for transient temperature of semi-infinite body subjected to 3D moving heat sources. *Welding Journal,* **78** (8), pp.265-274.

Peckner, D. and Bernstein, I.M. (1977) *Handbook of stainless steels.* New York: McGraw-Hill.

Radaj, D. (1992) *Heat effects of welding temperature field, residual stress, distortion.* Berlin: Springer-Verlag.

Rampaul, H. (1973) *Pipe welding procedures.* New York: Industrial Press.

Roelens, J.B. (1995a) Numerical simulation of some multipass submerged arc welding-Determination of the residual stresses and comparison with experimental measurements. *Welding in the World,* **35** (2), pp. 110-117.

Roelens, J.B. (1995b) Determination of residual stresses in submerged arc multi-pass welds by means of numerical simulation and comparisons with experimental measurements. In Cerjak, H. and Bhadeshia, H.K.D.H. (eds.), *Mathematical Modelling of Weld Phenomena 2.* London: The Institute of Materials, pp. 226-241.

Ronda, J. and Oliver, G. J. (1998) Comparisons of applicability of various thermo-viscoplastic constitutive models in modelling of welding. *Computer Methods in Applied Mechanics and Engineering,* **153** (3-4), pp. 195-221.

Rose, L.J. (1973) *Questions and answers on pipework and pipe welding.* London: Newnes-Butterworths.

Rosenthal, D. (1941) Mathematical theory of heat distribution during welding and cutting. *Welding Journal,* **20** (5), pp. 220-234.

Rosenthal, D. and Cambridge, M. (1946) The theory of moving sources of heat and its application to metal treatments. *Transactions of the ASME,* **68** (11), pp. 849-866.

Runnemalm, H. and Hyun, S. (2000) Three-dimensional welding analysis using an adaptive mesh scheme. *Computer Methods in Applied Mechanics and Engineering,* **189** (2), pp. *515-523.*

Rybicki, E. F., Schmueser, D. W., Stonesifer, R. B., Groom, J. J. and Mishler, H.W. (1978) A finite element model for residual stresses and deflections in girth-butt welded pipes. *Journal of Pressure Vessel Technology, Transactions of the ASME,* **100** (10), pp. 256-262.

Rybicki, E. F. and Stonesifer, R. B. (1979) Computation of residual stresses due to multipass welds in piping systems. *Journal of Pressure Vessel Technology, Transactions of the ASME,* **101** (2), pp. 149-154.

Rybicki, E. F. and McGuire, P. A. (1982) The effects of induction heating conditions on controlling residual stresses in welded pipes. *Journal of Engineering Materials and Technology, Transactions of the ASME,* **104** (4), pp. 267-273.

Sarkani, S., Tritchkov,V. and Michaelov, G. (2000) An efficient approach for computing residual

stresses in welded joints. *Finite Elements in Analysis and Design,* **35** (3), pp. 247-268.

Shi, Q.Y., Lu, A.L., Zhao, H.Y. and Wu, A.P. (2002) Development and application of the adaptive mesh technique in the three-dimensional numerical simulation of the welding process. *Journal of Materials Processing Technology*, **121** (2-3), pp. 167-172.

Shim, Y., Feng, Z., Lee, S., Kim, D., Jaeger, J., Papritan, J.C. and Tsai, C.L. (1992) Determination of residual stresses in thick-section weldments. *Welding Journal*, **71** (9), pp. 305-312.

Smith, D.J., Bouchard, P.J. and George, D. (2000) Measurement and prediction of residual stresses in thick-section steel welds. *Journal of Strain Analysis for Engineering Design*, **35** (4), pp.287-305.

Stouffer, D.C. and Dame, L. T. (1996) *Inelastic deformation of metals: models, mechanical properties, and metallurgy.* Chichester: Wiley and Sons.

Tall, L. (1964) Residual stresses in welded plates - a theoretical study. *Welding Journal,* **43** (1), pp.10-23.

Tautges, T.J. (2001) The generation of hexahedral meshes for assembly geometry: Survey and progress. *International Journal for Numerical Methods in Engineering*, **50** (12), pp. 2617-2642.

Tekriwal, P. and Mazumder, J. (1988) Finite element analysis of three-dimensional transient heat transfer in GMA welding. *Welding Journal,* **67** (7), pp.150-156.

Tekriwal, P. and Mazumder, J. (1991) Transient and residual thermal strain-stress analysis of GMAW. *Journal of Engineering Materials and Technology, Transactions of the ASME*, **113** (3), pp. 336-343.

Teng,T.L. and Chang, P.H. (1997) *A* study of residual stresses in multi-pass girth-butt welded pipes. *International Journal of Pressure Vessels and Piping,* **74** (1), pp. 59-70.

Teng, T. L., Chang, P.H. and Ko, H.C. (2000) Finite element analysis of circular patch welds. *International Journal of Pressure Vessels and Piping,* **77** (11), pp. 643-650.

Teng, T. L., Chang, P. H. and Tseng, W. C. (2003) Effect of welding sequences on residual stresses. *Computers & Structures*, **81** (5), pp. 273–286.

Ueda, Y. and Yamakawa, T. (1971) Analysis of thermal elastic-plastic stress and strain during welding by finite element method. *Transactions of JWRI (Japanese Welding Research Institute)*, **2** (2), pp. 90-100.

Ueda, Y., Takahashi, E., Fukuda, K., Sakamoto, K. and Nakacho, K. (1976) Transient and residual stresses from multipass welding in very thick plates and their reduction from stress relief annealing. *Transactions of JWRI (Japanese Welding Research Institute)*, **5** (2), pp. 179-187.

Wen, S.W. and Farrugia, D.C.J. (2001) Finite element modeling of submerged arc welding process. *Journal of Material Processing Technology,* **119** (1-3), pp. 203-209.

Wen, S.W., Hilton, P. and Farrugia, D.C.J.(2001) Finite element modeling of residual stress in pipe welds. *Journal of the British Society for Strain Measurement*, **37** (1), pp. 15-18.

Wikander, L., Karlsson, L., Nasstrom, M. and Webster, P. (1994) Finite element simulation and measurement of welding residual stresses. *Modelling and Simulation in Materials Science and Engineering*, **2** (4), pp.845-864.

Zacharia, T., Vitek, J.M., Goldak, J.A., Debroy, T.A., Rappaz, M. and Bhadeshia, H.K.D.H. (1995) Modeling of fundamental phenomena in welds. *Modelling and Simulation in Materials Science and Engineering,* **3** (2), pp. 265-288.

Zhang, J., Dong, P., Brust, F. W., Shack, W. J., Mayfield, M.E. and McNeil, M. (2000) Modeling of weld residual stresses in core shroud structures. *Nuclear Engineering and Design,* **195** (2), pp. 171-187.

Zhu, X. K. and Chao, Y. J. (2002) Effects of temperature-dependent material properties on welding simulation. *Computers & Structures,* **80** (11), pp. 967-976.

Publications

Note: The following publications are based on the thesis and the work completed in the research program.

1. Jiang, W., Yahiaoui, K., Wang, C.J., Hall, F.R. and Laoui, T. (2004) FE predictions of temperature distributions in a multipass welded piping branch junction. *Proceedings of the 2004 ASME/JSME Pressure Vessels and Piping Conference, High Pressure Technology: Innovations and Advances in High Pressure Technology, PVP*, **473**, Pfeifer, J. (eds.), *Jul 25-29, 2004, San Diego, CA, USA.* pp. 93-99. (This paper was awarded a Certificate of Recognition by the Senate of the American Society of Mechanical Engineers (ASME) Pressure Vessels and Piping Division)

2. Jiang, W., Yahiaoui, K. and Hall, F.R. (2005) Finite element predictions of temperature distributions in a multipass welded piping branch junction. *Journal of Pressure Vessel Technology, Transactions of the ASME*, **127** (1), pp. 7-12.

3. Jiang, W., Yahiaoui, K., Hall, F.R. and Laoui, T. (2005a) Comparison of sequentially and fully coupled generalized plane strain finite element modelling of multipass welding. *National Agency for Finite Element Methods and Standards, NAFEMS World Congress 2005, 17-21 May, 2005, Malta.*

4. Jiang, W., Yahiaoui, K., Hall, F.R. and Laoui, T. (2005b) Finite element simulation of multipass welding: full three dimensional versus generalized plane strain or axisymmetric model. *Journal of Strain Analysis for Engineering Design*, **40** (6), pp.587 – 598.

5. Jiang, W. and Yahiaoui, K. (2006) Finite element predictions of residual stress distributions in a multipass welded piping branch junction. (Accepted for the 2006 ASME Pressure Vessels and

Piping/Eleventh International Conference on Pressure Vessel Technology, ICPVT-11, 25-27 July, 2006, Vancouver, Canada).

6. Jiang, W. and Yahiaoui, K. Finite element predictions of residual stress distributions in a multipass welded piping branch junction. (Submitted to *Journal of Pressure Vessel Technology, Transactions of the ASME*).

7. Jiang, W. and Yahiaoui, K. Techniques for all-hexahedral mesh Generation for three-dimensional multipass welding simulation in complex geometries. (Under revision).

8. Jiang, W. and Yahiaoui, K. Predictions of residual stresses in a thick welded piping intersection: relative importance of welding parameters.(To be submitted)

9. Jiang, W. and Yahiaoui, K. Effect of interpass temperature on predicted residual stress distributions in a multipass welded piping branch junction. (To be submitted)

10. Jiang, W. and Yahiaoui, K. Effect of cooling rate on predicted residual stress distributions in a thick welded piping intersection. (To be submitted).

Finite Element Predictions of Temperature Distributions in a Multipass Welded Piping Branch Junction

Wei Jiang
e-mail: w.jiang@wlv.ac.uk

Kadda Yahiaoui
e-mail: k.yahiaoui@wlv.ac.uk

Frank R. Hall
e-mail: f.r.hall@wlv.ac.uk

School of Engineering and the Built Environment,
University of Wolverhampton,
Telford, TF2 9NT, United Kingdom

This contribution deals with the complex temperature profiles that are generated by the welding process in the intersection region of thick walled, cylinder-cylinder junctions. These affect material microstructure, mechanical properties and residual stresses. Knowledge of the thermal history and temperature distributions are thus critical in developing control schemes for acceptable residual stress distributions to improve in-service component behavior. A comprehensive study of three-dimensional temperature distributions in a stainless steel tee branch junction during a multipass welding process is presented. A newly developed partitioning technique has been used to mesh the complex intersection areas of the welded junction. Various phenomena associated with welding, such as temperature dependent material properties, heat loss by convection and latent heat have been taken into consideration. The temperature distribution at various times after deposition of certain passes and the thermal cycles at various locations are reported. The results obtained in this study will be used for on-going and future analysis of residual stress distributions. The meshing technique and modeling method can also be applied to other curved, multipass welds in complex structures. [DOI: 10.1115/1.1845450]

Keywords: Multipass Welding, Temperature Distribution, Finite Element Analysis, Tee Branch Junction

1 Introduction

Welded, thick walled, cylinder-cylinder intersections are piping components commonly used in the power industry and in oil or gas transport systems, amongst others. Owing to the relatively large wall thickness in such piping systems, the weldments are often constructed in several passes. The heat supplied by each welding pass produces complex thermal cycles, which greatly affect the material microstructure, mechanical properties, and residual stress distributions. It is therefore important to predict the temperature history to develop control schemes for acceptable residual stress distributions to improve in-service behavior of components.

Thus far, the thermal cycle and temperature distributions of the welding process have been studied analytically, experimentally, and numerically. The most significant analytical solution was proposed by Rosenthal [1]. It is a heat conduction analysis of a moving point heat source in an infinite solid. Rybicki et al. [2,3] developed a computational model, based on the analytical solution presented by Rosenthal, as a thermal load for the prediction of residual stresses during multipass girth-butt welding of 304 stainless steel pipes. However, the models ignored temperature dependent material properties and the effect of latent heat of fusion.

Very limited experimental data regarding the temperature distribution during multipass welding is available in the literature. Murugan et al. [4,5] reported experimentally obtained temperature distributions during multipass welding of low carbon steel and AISI type 304 stainless steel plates with thicknesses of 6, 8, and 12 mm. These experimental results will be used for comparison with data obtained from the numerical model developed in the current study.

Compared with analytical and experimental studies, numerical simulation has attracted a lot of attention because of its capability to deal with complex geometries, nonlinear behavior, and various boundary conditions [6]. To predict residual stresses in thick walled pipe, Scaramangas [7] simplified the analysis by assuming the heat flow to be axisymmetric, that is, heat was assumed to flow radially and axially but not circumferentially. The finite difference method was used, with a specified temperature distribution at the start of welding, corresponding to the melting temperature over the molten pool area and the preheat temperature over the pipe. The thermal properties were assumed to be temperature independent and heat loss from all exposed surfaces was taken into account. Brickstad and Josefson [8] used two-dimensional axisymmetric models to numerically simulate a series of multipass circumferential butt-welds of stainless steel pipes up to 40 mm thick in a nonlinear thermomechanical finite element (FE) analysis. The rotational symmetry assumption was invoked in their analysis. Wen et al. [9] also used a two-dimensional axisymmetric FE model to simulate three-pass pipe girth welding, with wall thickness of 19 mm. In the thermal analysis, the heat input and filler metal deposition were simulated by the definition of a moving heat source with a uniform body heat flux. The element reactivation technique was used to simulate weld deposition.

Although many studies have been conducted for circumferential butt weld simulation, most of the results were based on axisymmetric assumptions. In addition, research has been limited to relatively thin pipes. There is a paucity of reliable information about thermal cycles and temperature distributions in thick steel weldments. No attempt has been made yet to simulate three-dimensional (3D) temperature distribution of multipass welding of thick cylinder-cylinder intersections.

This paper presents a comprehensive study of 3D temperature distributions in a thick, stainless steel tee branch junction during a multipass welding process. The complexity of this weld geometry, together with the multipass process involved, is a particularly challenging FE weld simulation.

A newly developed meshing technique has been used for mesh

Contributed by the Pressure Vessels and Piping Division for publication in the JOURNAL OF PRESSURE VESSEL TECHNOLOGY. Manuscript received by the PVP Division August 24, 2004; revision received September 4, 2004. Review conducted by: S. Zamrik.

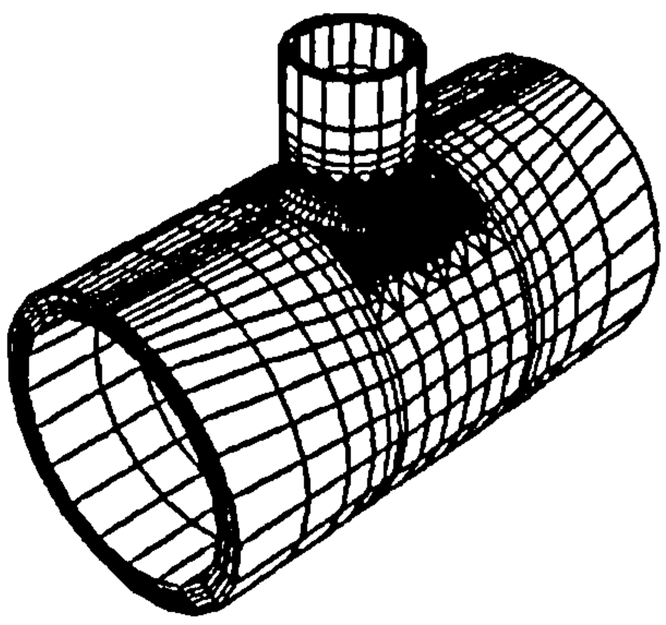

Fig. 1 FE mesh of a tee branch junction component

generation of the complex intersection areas of the welded junction. An element remove/reactivate technique has been employed to simulate the deposition of filler material. In addition, material nonlinearities, i.e., latent heat and temperature dependent thermal properties, have been taken into account.

2 Analysis Procedure

2.1 Geometry and FE Model. The component chosen for this simulation is an AISI 316L stainless steel tee branch junction. The outside diameter of the run pipe is 891 mm with a thickness of 77 mm. The outside diameter of the branch pipe is 356 mm with a thickness of 36 mm. This configuration gives branch-to-run outside diameter and thickness ratios of 0.40 and 0.468, respectively. The direct branch on pipe requires welding along the "saddle-like" intersection between run and branch-pipe fittings and modeling a full circumferential fillet weld. This complex geometry, coupled with multipass welding, presents a challenging and tedious mesh generation task.

In order to produce a well-graded finite element mesh, the geometrical model was partitioned into different regions. Each region consists of meshes of different element density. In the critical fusion regions near the intersection area of the joint, where temperature gradients are expected to be the most severe, fine meshes are generated. On the other hand, in the regions remote from the joint, the meshes are rather coarse. Between the refined and the far field regions, transition regions with tetrahedral elements were used. Figure 1 shows the finite element model. It consists of 26,682 eight-noded, 3D heat transfer brick elements (type DC3D8), 21,599 four-noded, 3D heat transfer tetrahedron elements (type DC3D4), and 34,954 nodes [10]. Figures 2(*a*) and 2(*b*) show details of the mesh at the flank and crotch corner locations, respectively. Figure 2(*c*) gives an indication of the elements representing the individual passes required to fill the groove.

The ABAQUS element removal/reactivation technique was applied in the thermal analysis. In this technique, the element sets representing each weld pass in the weld metal area were generated along with the FE meshes for the parent material. During analysis, elements associated with higher numbered passes were first removed and then reactivated at a time corresponding to the time at which the molten weld metal was deposited. When a group of weld pass elements were activated, a specified initial temperature was imposed for all nodes associated with the weld pass elements.

In order to reduce the computational requirement, a pragmatic approach to model the multipass weld deposits was adopted. The entire weld was represented by ten layers of filler metal, sequentially added to the model, one layer at a time. However, each layer can generally represent more than one weld pass.

2.2 Material Properties. The finite element heat transfer analysis requires accurate values of the thermal conductivity, specific heat, material density and latent heat of fusion up to the melting point. Temperature dependent thermal physical properties,

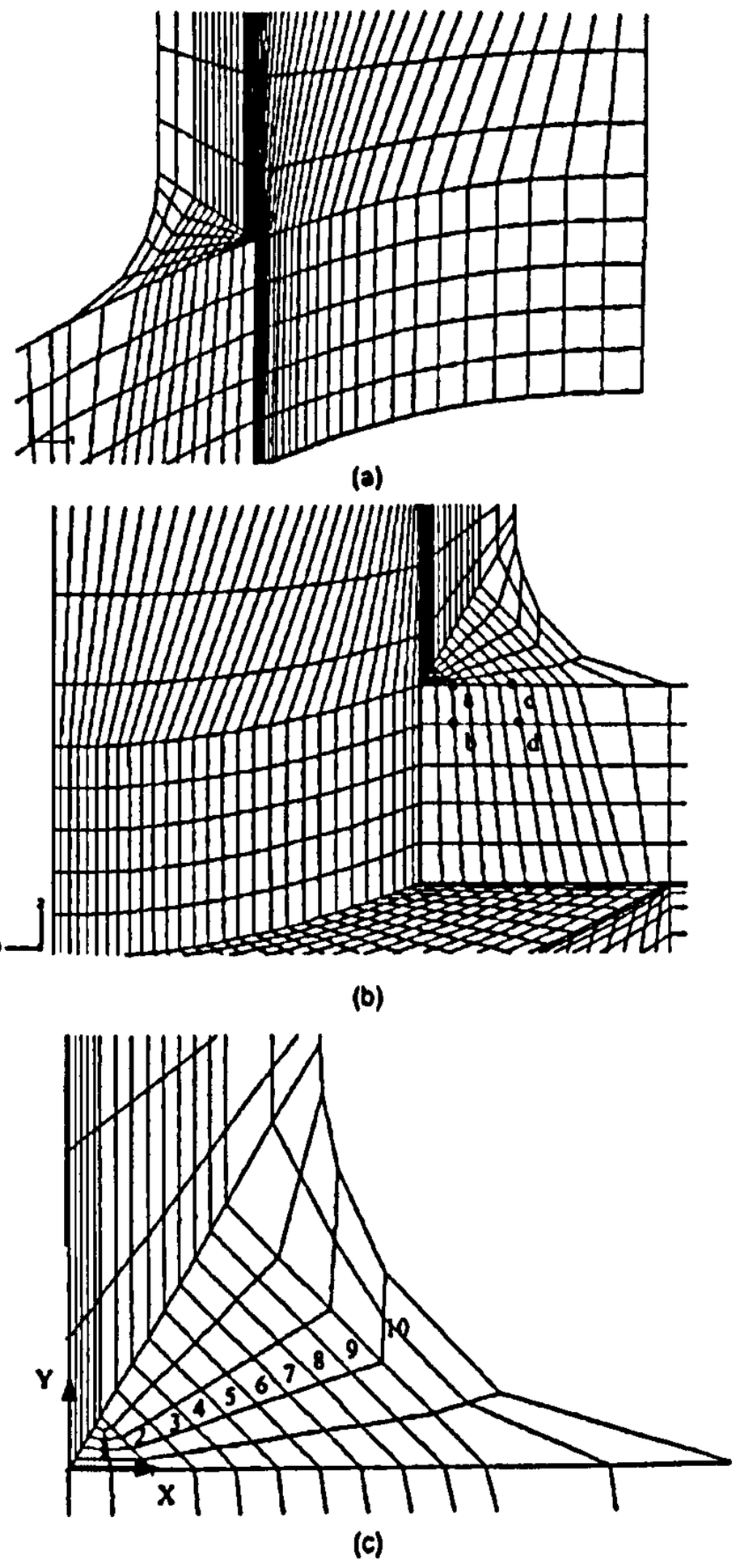

Fig. 2 Detailed FE mesh near weld metal region: (*a*) flank area mesh detail, (*b*) crotch corner detail and location ID's for temperature distribution plots, and (*c*) weld pass numbers and local coordinate system

which were assumed to be the same for both parent and weld materials up to the melting point of 1420°C [8,11], were used in the transient thermal analysis. These are shown in Fig. 3. Above the melting temperature, the properties were held constant, except for the thermal conductivity. The latter was doubled to compensate for the effect of heat transfer due to convection stirring in the molten weld pool material [8,11]. Latent heat effects were assigned a value of 300 kJ/kg between the solidus temperature of 1420°C and the liquidus temperature of 1460°C.

Both temperature-dependent material properties and latent heat effects introduce nonlinearities in the heat transfer analysis, although the former has a lesser effect than the latter.

2.3 Heat Transfer Analysis. The most significant heat transfer mechanisms in welding are the heat input from the heat source and the heat losses due to conduction, convection, and radiation from the weld surfaces. In the present investigation, the radiation mode of heat transfer was ignored.

There are two types of heat input in metal welding: one is the heat flux and the other is the heat content of filler metal droplets. In the current thermal FE analysis, the first part of heat input was

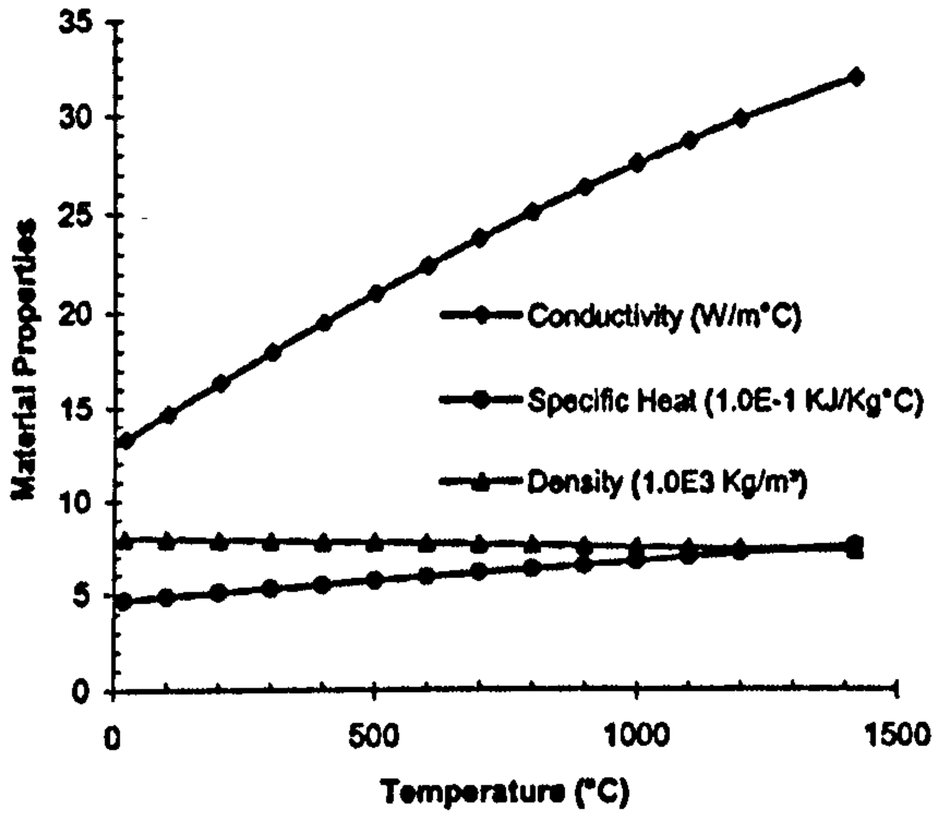

Fig. 3 Material properties of 316L stainless steel [11]

arranged as a column of elements with specified body heat flux instead of an infinitely thin line as used in analytical models. This heat input was imposed onto the specified newly activated elements representing a deposited pass at a given time. Body heat flux was uniformly distributed over the length of each weld layer. The simulation technique consists of: (*a*) a kind of ramp with linearly increasing heat input from the approaching heat source, (*b*) constant heat input when the elements are melted, and (*c*) linearly decreasing heat input when the heat source is leaving the element. Heat input was modeled by a distributed heat flux working on individual elements. In ABAQUS [10], distributed heat fluxes are coded with the option called DFLUX. The second part of heat input, i.e., the heat content of filler metal droplets, was assumed to be deposited at melting temperature and additional solution steps in the thermal analysis were needed to account for this.

The heat loss by free convection was modeled by Newton's cooling law. Boundary conditions were applied to all free surfaces of the component except for the successive boundaries created after each new weld pass. The surfaces exposed to the environment were subjected to the same convective boundary conditions, using a heat transfer convection coefficient of $h = 30\ \mathrm{W/m^2°C}$ to ambient air. The ambient temperature for both parent and weld metal was set at 20°C. The regions near the weld bead were assumed to be preheated before weld execution.

The heat input was applied by assigning each element in the weld pass an initial temperature and body flux. Subsequent cooling, as the heat conducted into the parent material and was lost through surface convection, was analyzed up to 1180, 800, and 600 s time periods for the first, second, and third pass onward after welding deposition. The cooling time is dependent on pipe circumference and welding speed and includes a gradual start and finish. After these times, the model was reset to an assumed interpass temperature using a steady state heat transfer step, before applying the next pass.

After the final pass has been analyzed, the model was allowed

Table 1 Weld parameters used in the simulation [8,12]

Pass No.	Welding method	Weld voltage (V)	Weld current (A)	Weld speed (mm/min)	Heat input (kJ/mm)
1	TIG	9.6	75–120	60	0.48
2	MMA	17.3	85–140	80	1.09
3–10	MMA	17.6	150–190	110	1.14

to cool down for 6000 s to ambient temperature. Automatic time stepping was used for the solution of this nonlinear transient heat transfer problem.

The tee branch junction component was assumed to be welded by tungsten inert gas arc welding (TIG) for the first pass and manual metal arc welding (MMA) for the subsequent passes. The simulation parameters, as is common industry practice as reported by Brickstad and Josefson [8] and Rybicki [12], are listed in Table 1. For the stainless steel welds considered in this study, arc efficiencies equal to 50% and 70% have been assumed for the TIG and MMA, respectively.

3 Verification

In order to check the predictions of the present analysis method, a pilot simulation to reproduce the experimental results reported by Murugan et al. [4] was performed. In the latter experiment, a low carbon steel specimen butt weld was produced using a multipass manual metal arc welding technique. The length, width, and thickness of the plate used are 150, 282.5, and 8 mm, respectively (see Fig. 4). The location of the measurement points are also indicated in Fig. 4.

For proper comparison, pass sequences and welding parameters, used in the simulation, were identical to those for the 8-mm-thick plate experiment, as shown in Table 2.

The calculated and measured temperature history at distance of $a = 11.5$ mm and $c = 21.5$ mm on the right side of the weld cen-

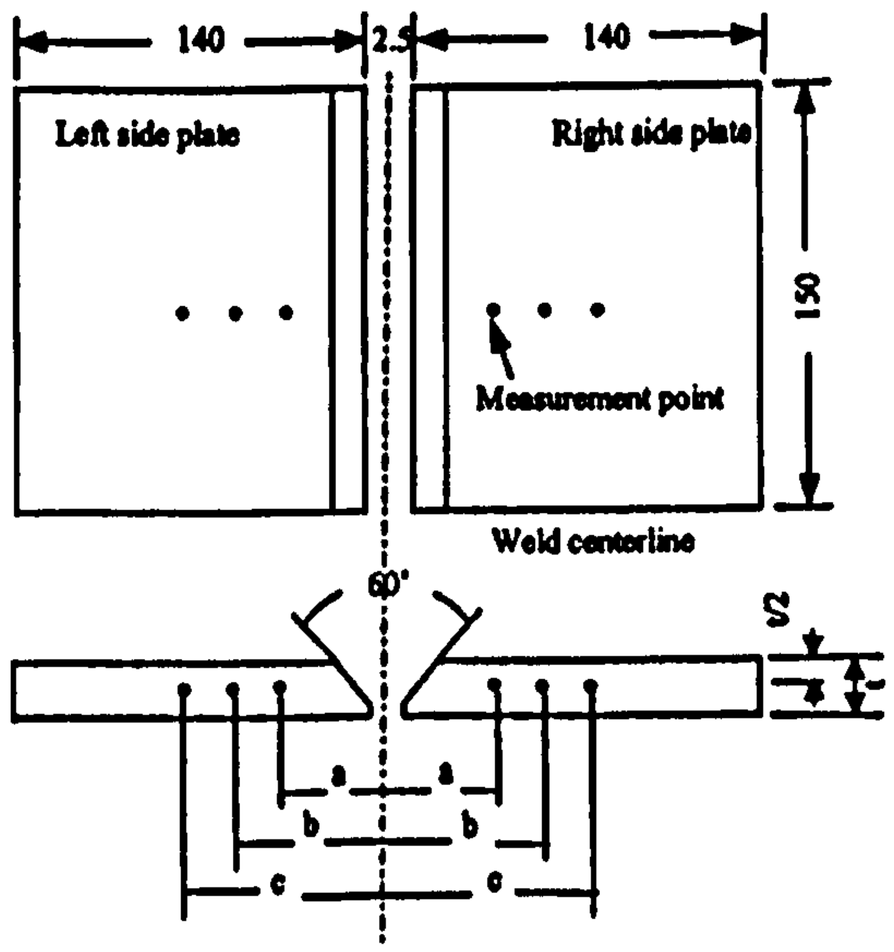

Fig. 4 Dimensional details of experimental specimen [4,5]

Table 2 Weld parameters during welding of low carbon steel 8-mm-thick plates [4]

Pass No.	Electrode diameter (mm)	Weld voltage (V)	Weld current (A)	Weld speed (mm/s)	Heat input (kJ/mm)
1	2.5	21	65–75	1.68	0.656
2	4	24	170–180	2.88	1.094
3	4	22	175–185	2.08	1.427

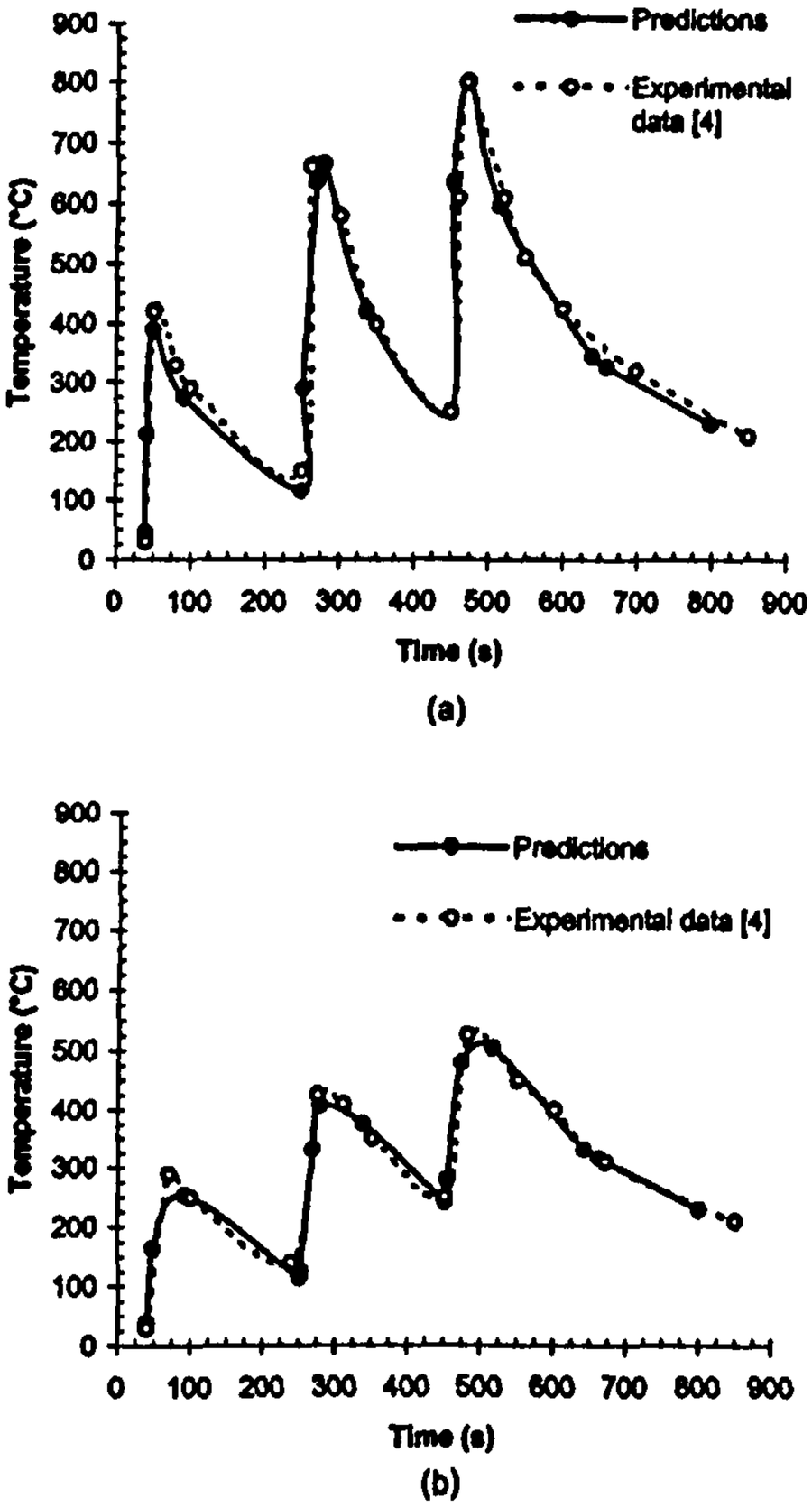

Fig. 5 Comparison of experimental and calculated temperature distributions: (*a*) predicted *v* measured temperature distributions at location *a* (11.5 mm from weld centerline) and (*b*) predicted *v* measured temperature distributions at location *c* (21.5 mm from weld centerline)

terline are shown in Figs. 5(*a*) and 5(*b*), respectively. As the figures indicate, the temperature distribution results obtained by the present simulation method closely match those obtained experimentally. Similar comparisons are also evident for location *b* = 16.5 mm shown in Fig. 4. A full description of the simulation technique and a detailed comparison with experimental data will be presented elsewhere. For the present purpose, it will suffice to conclude that in reproducing experimental results to this level of accuracy, the simulation method can be considered to be acceptable. Therefore, the procedure adopted here is considered suitable for the analysis of temperature distributions during multipass welding of tee branch junctions.

4 Results and Discussion

A thorough understanding of the temperature patterns that are generated during execution of complex welds and subsequent cooling rates can give a clear insight into how welding residual stresses buildup during the operation. Such understanding will help in formulating recommendations, regarding the weld execution itself, towards reducing the severity of "as-welded" residual stress distributions.

Figure 6(*a*) shows the temperature patterns at times $t = 1.018$, 20.8, 280.2, and 1180 s, respectively, on a quarter of the model after deposition of the first pass. It can be seen from the graph that, as expected, the peak temperature and high gradient first appear in the area close to the deposited pass ($t = 1.018$ s) after which heat gradually conducts to the nearby area of both run and branch pipe ($t = 20.8$ s). At time 280.2 s, which is about a quarter of the first pass welding time, a nonuniform temperature distribution can clearly be noticed in the intersection area.

The crotch area is shown to experience relatively higher temperature than that of the flank. This is explained by the fact that, while the welding parameters do not change during the process, the crotch area needs more metal deposition. Therefore, more heat has been brought in at the crotch area than at flank area. At the end of the first pass, i.e., at time 1180 s, the temperature distribution near the first pass area tends towards being uniform.

Figure 6(*b*) shows the temperature distribution at times $t = 1.042$, 20.52, 122.4, and 600 s after deposition of the fifth pass, respectively. At time 1.042 s, which corresponds to the time shortly after deposition, the temperature appears to be highly localized. As time elapses, heat conducts almost uniformly to both run and branch pipe. The crotch area again shows higher temperatures than those experienced by the flank area ($t = 20.52$, 122.4, and 600 s). Also noticeable is the heat conduction to the previously deposited passes. This confirms the intuitive expectation that both deposited weld material and heat affected zone undergo a process of thermal cycling by successive weld passes. This kind of thermal cycling will affect microstructure, mechanical properties and residual stress buildup.

Figure 6(*c*) shows the temperature distribution at times $t = 1.052$, 20.14, 169, and 600 s after depositing of the last pass, respectively. At this stage the groove is fully filled and temperature patterns are similar to those observed at pass 5.

In summary, because of the locally concentrated heat source, high temperature, and large gradients appear at the area close to individual passes and rapidly change with the distance from the center of the heat source. The highest temperature is limited to the domain of the heat source, from which lower temperature zones fan out into both run and branch pipes. This causes large through thickness temperature gradients.

For an appreciation of the thermal cycle as successive weld passes are deposited, Figs. 7(*a*) and 7(*b*) are presented. These depict the thermal cycles for the locations indicated in Fig. 2(*b*). These locations were arbitrarily chosen to represent typical critical regions, i.e., weld/parent fusion line and parent material away from the heat affected zone in the run pipe.

Points *a* and *c* are located on the fusion line of the first and fifth deposited pass on the run pipe side, respectively. Points *b* and *d* are located at about 15.4 mm below points *a* and *c* in the thickness direction.

It is seen from Fig. 7(*a*) that the temperature at point *a* reaches a maximum value on deposition of the first pass followed by a gradual cooling. The cooling rate is initially steep and less so towards the end of the pass. Point *a* reaches peak temperature each time the subsequent passes are deposited. However, the peak value decreases as the distance between subsequent passes and point *a* increases.

Although the thermal cycle is similar, the peak temperature experienced by point *b* is much less than that at point *a*. The rates of heating and cooling are also not as high compared to those noted for point *a*.

Figure 7(*b*) shows similar plots for locations *c* and *d*. Point *c* experiences heating each time the lower numbered passes are deposited and the maximum temperature is reached when the fifth pass is completed. The temperature at point *c* continues to reach peak value each time the subsequent passes deposit and the peak value depends on the distance between individual passes and point *c*.

The same behavior as that experienced by point *b* is noted for point *d*, with the peak temperatures being much lower than those recorded at location *c*.

Similar thermal cycles have been obtained for corresponding locations on the branch pipe side.

The interpass temperatures are 72, 216, and 330°C for the first,

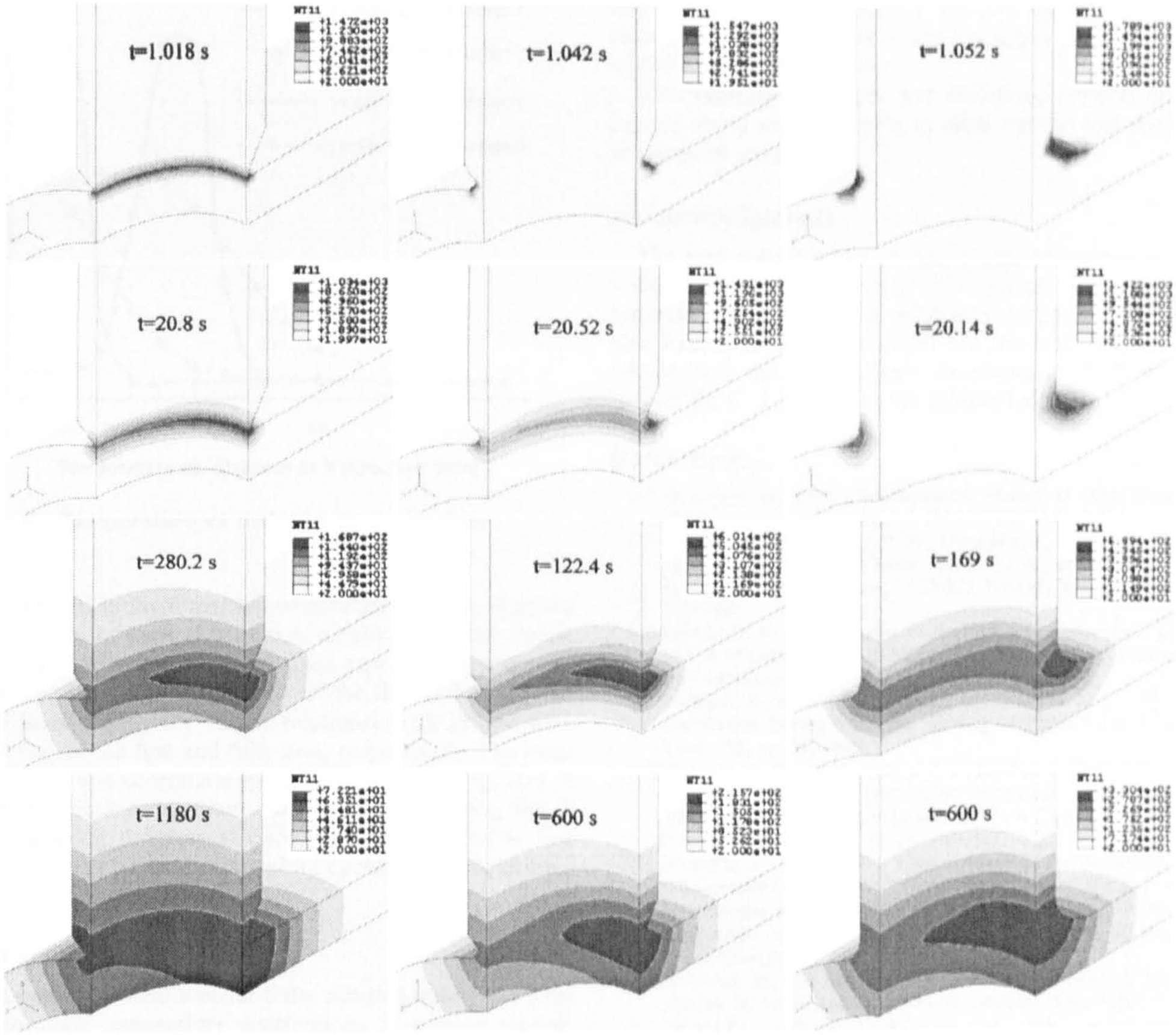

Fig. 6 Temperature distributions at various times after deposition of (*a*) pass 1, (*b*) pass 5, and (*c*) pass 10

fifth, and last pass, respectively. As expected, it shows a trend of steady increase. Its influence on residual stress buildup remains to be investigated.

In practice interpass temperatures are controlled to a certain level to provide adequate mechanical properties. In this simulation, the earlier reported value had to be artificially reduced to a constant value of 120°C as indicated by the dashed line in Fig. 7.

To present a full set of temperature distributions of interest to the welding industry would make this contribution rather lengthy and is therefore considered to be beyond its scope. To convey the whole picture will require plots of temperature distributions around the weldline, axially along and circumferentially around both branch and run pipes through the thickness at various locations. Temperature distributions versus distance from the center of

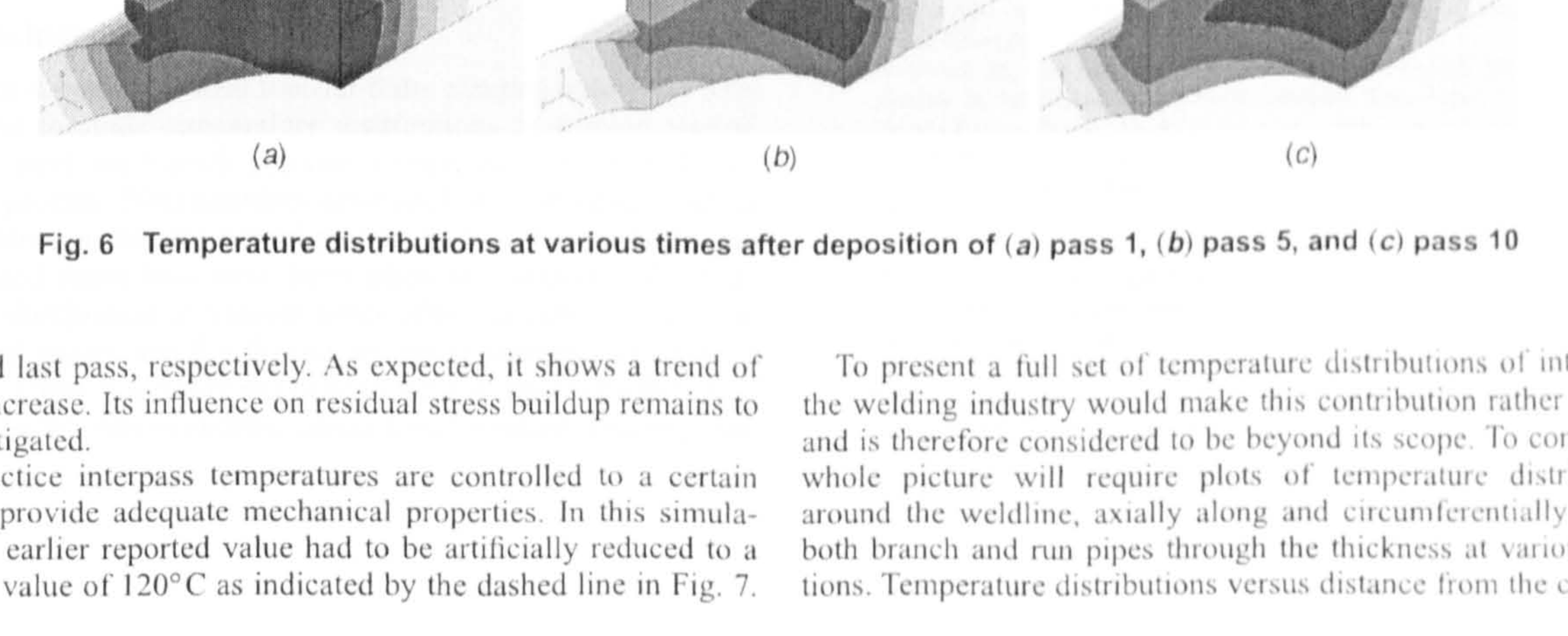

Fig. 7 Temperature cycles at various times and positions: (*a*) temperature cycle at point *a* and *b* and (*b*) temperature cycle at point *c* and *d*

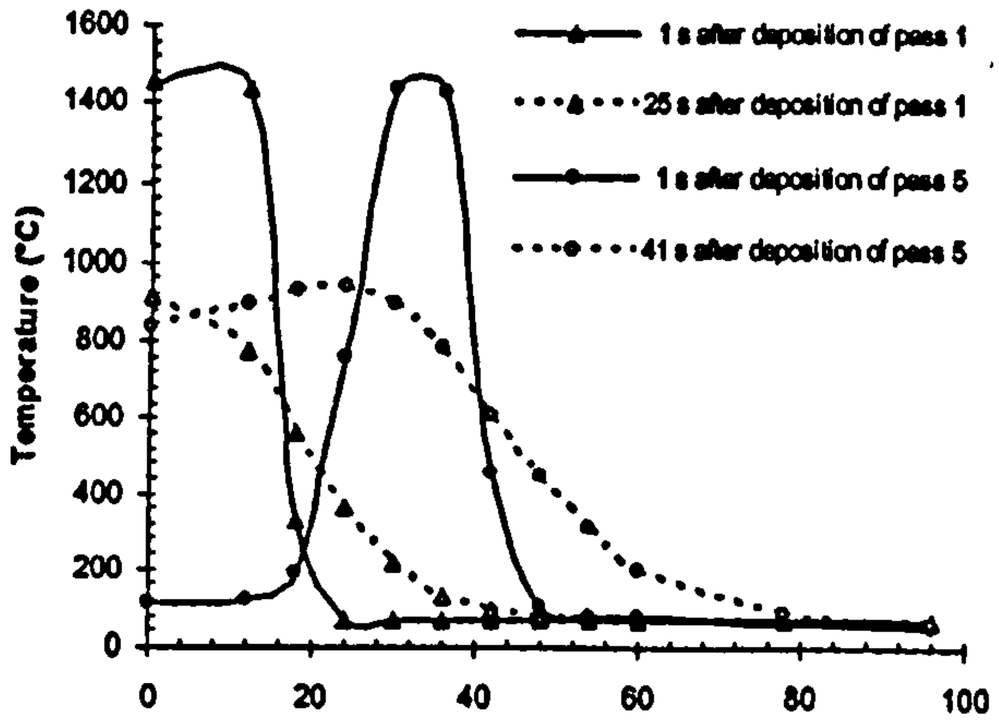

Fig. 8 Temperature vs distance in *X* direction

the weld are critical to the formation of residual stresses. Figure 8 shows an example of such distribution axially along the fusion line in the run pipe side. The solid lines represent temperature versus distance at 1 s after deposition of the first and fifth pass. The dashed lines display the earlier relationship at 25 and 41 s after completion of the first and fifth pass, respectively. The locations of the origin and coordinate system are shown in Fig. 2(*c*). It is observed that peak temperature and HAZ move along the X direction as welding progresses. Each point on the fusion line experiences complex heating and cooling cycles which determine the buildup of residual stresses.

5 Conclusions

A three-dimensional heat transfer finite element model has been developed to study temperature distributions in a thick walled, stainless steel tee branch junction component during multipass welding process. Nonlinearities associated with welding, such as temperature dependent material properties, heat loss through convection and latent heat have been taken into account. The temperature distribution at various times after deposition of a given number of passes and the thermal cycles at various locations are reported. These results are not only useful for estimating the likely changes in the microstructure, phase transformation and degradation in mechanical properties but also for the assessment of residual stress distributions which can affect the in-service behavior of the welded connection.

The meshing technique and modeling method utilized in the current study are applicable to other curved and multipass welds in complex structures.

Acknowledgments

The lead author acknowledges financial support, in the form of a studentship, by the School of Engineering and the Built Environment of the University of Wolverhampton. The authors would also like to thank Steve Boyle for his technical assistance. The advice from the lead author's cosupervisor Dr. T. Laoui and colleague Dr. C. J. Wang is also acknowledged.

References

[1] Rosenthal, D., 1941, "Mathematical Theory of Heat Distribution During Welding and Cutting," Weld. J. (Miami, FL, U.S.), **20**(5), pp. 220–234.
[2] Rybicki, E. F., Schmueser, D. W., Stonesifer, R. B., Groom, J. J., and Mishler, H. W., 1978, "A Finite Element Model for Residual Stresses and Deflections in Girth-Butt Welded Pipes," ASME J. Pressure Vessel Technol., **100**(10), pp. 256–262.
[3] Rybicki, E. F., and Stonesifer, R. B., 1979, "Computation of Residual Stresses Due to Multipass Welds in Piping Systems," ASME J. Pressure Vessel Technol., **101**(5), pp. 149–154.
[4] Murugan, S., Kumar, P. V., Raj, B., and Bose, M. S. C., 1998, "Temperature Distribution During Multipass Welding of Plates," Int. J. Pressure Vessels Piping, **75**, pp. 891–905.
[5] Murugan, S., Rai, S. K., Kumar, P. V., Jayakumar, T., Raj, B., and Bose, M. S. C., 2001, "Temperature Distribution and Residual Stresses Due to Multipass Welding in Type 304 Stainless Steel and Low Carbon Steel Weld Pads," Int. J. Pressure Vessels Piping, **78**, pp. 307–317.
[6] Mackerle, J., 1996, "Finite Element Analysis and Simulation of Welding: A Bibliography (1976–1996)," Modell. Simul. Mater. Sci. Eng., **4**, pp. 501–533.
[7] Scaramangas, A., 1984, "Residual Stresses in Girth Butt-Welded Pipes," Technical report no. CUED/D-struct/TR107, Department of Engineering, Cambridge University.
[8] Brickstad, B., and Josefson, B. L., 1998, "A Parametric Study of Residual Stresses in Multi-Pass Butt-Welded Stainless Steel Pipes," Int. J. Pressure Vessels Piping, **75**, pp. 11–25.
[9] Wen, S. W., Hilton, P., and Farrugia, D. C. J., 2001, "Finite Element Modeling of Residual Stress in Pipe Welds," Strain J. Brit. Soc. Strain Measurement, **37**(1), pp. 15–18.
[10] ABAQUS, User's Manual 6.3, 2002, Hibbitt, Karlsson and Sorensen, Inc.
[11] Dong, P., 2001, "Residual Stress Analysis of a Multipass Girth Weld: 3D Special Shell Versus Axisymmetric Models," ASME J. Pressure Vessel Technol., **123**(2), pp. 207–213.
[12] Rybicki, E. F., McGuire, P. A., Merrick, E., and Wert, J., 1982, "The Effect of Pipe Thickness on Residual Stresses Due to Girth Welds," ASME J. Pressure Vessel Technol., **104**(3), pp. 204–209.

Finite element simulation of multipass welding: full three-dimensional versus generalized plane strain or axisymmetric models

W Jiang*, K Yahiaoui, F R Hall, and T Laoui
School of Engineering and the Built Environment, University of Wolverhampton, Telford, UK

The manuscript was received on 15 October 2004 and was accepted after revision for publication on 11 February 2005.

DOI: 10.1243/030932405X16061

Abstract: A full three-dimensional (3D) thermo-mechanical finite element (FE) model has been developed to simulate the step-by-step multipass welding process. Non-linearities associated with welding, such as a moving heat source, material deposition, temperature-dependent material properties, latent heat, and large deformations, were taken into account. The model was applied to multipass butt-welded mild steel plate and girth butt-welded stainless steel pipe for validation. The simulation results were compared with independently obtained experimental data and numerical predictions from two-dimensional (2D) generalized plane strain and axisymmetric models. Good agreements between the 3D predictions and experimental data have been obtained. The computational model has the potential to be applied to multipass welded complex geometries for residual stress prediction.

Keywords: three-dimensional finite element (3D FE) thermo-mechanical model, multipass welding, residual stresses, plate, pipe

1 INTRODUCTION

Multipass welding is a reliable and efficient joining process for thick metal sections which is widely used in most engineering fields, including shipbuilding, power, and oil industries. However, this process inevitably induces complex residual stresses. When tensile, these stresses can be a serious cause for concern as they can have adverse effects on the in-service performance of weldments, decreasing life expectancy and leaving structures prone to catastrophic failure when defects or flaws are present. It is thus desirable to predict residual stress distributions well in advance of welding execution.

Previously, welding residual stresses were only assessed by experimental methods [1–3]. However, experimental residual stress measurements have practical limitations. First, they are expensive and require special equipment. Methods, such as the hole-drilling technique, are also destructive. Second, even when non-destructive (e.g. diffraction technique), residual stresses are measured only at discrete locations near the weld surface, and such data not only tend to show significant scatter but also spatial variations. Consequently, it is impossible for any experimental technique to give a complete mapping of three-dimensional (3D) residual stress distributions. Moreover, the results obtained from one particular weldment may not be directly applicable to other weldments.

With modern computing facilities, the finite element technique has become an effective method for prediction and assessment of welding residual stress. However, the accurate prediction of residual stresses and distortions induced by multipass welding is extremely difficult. This is so not only because the thermal and mechanical behaviours in welding include highly localized temperatures, temperature-dependent material properties, large deformation, and a moving heat source, but also because each successive weld pass alters the temperatures, stresses, and distortions caused by previous passes. Nevertheless, despite these complications, multipass welding has received a lot of attention in recent years and significant progress has been made in this field.

*Corresponding author: RIATec, School of Engineering and the Built Environment, University of Wolverhampton, Telford Campus, Telford TF2 9NT, UK. email: w.jiang@wlv.ac.uk

Recent advances in the study of the multipass welding process by the finite element (FE) method have, as would be expected, concentrated on simple geometries where modelling approximations can be justified. Hence the large number of publications covering plate and pipe welding where generalized plane strain conditions or axisymmetry can be invoked. When dealing with real complex geometries as used in industry, model simplifications may not be universally considered acceptable. For example, in dealing with a real geometrically complex welded configuration involving a common cylinder-to-cylinder connection, Smith *et al.* [3] had to be innovative. Besides the useful experimental results reported in their paper, in their FE simulation they assumed the header cylinder in the cylinder-to-nozzle junction to be spherical in order to justify the axisymmetric assumption. They stated that 'Full three-dimensional modelling of the welding process for this structure was judged to be impracticable'. Consequently, the purpose of this paper is to compare FE predicted results using modelling simplifications and experimental data with predictions using a full 3D model, since ultimately the objective of this research is to apply the simulation technique to assess residual stresses in welded 3D piping branch junctions.

In the current 3D thermo-mechanical FE model, all non-linearities associated with welding, such as the moving heat source, material deposition, temperature-dependent material properties, latent heat, and large deformations, were taken into account in order to simulate the real-life multipass welding process. The model was applied to multipass butt-welded mild steel plate and girth butt-welded stainless steel pipe, which are two simple but typical components commonly used in shipbuilding and the power and oil industries, for validation. Good agreements between 3D predictions and experimental data have been obtained. However, while there exists a great deal of confidence in the modelling technique itself, the final results need always to be treated with caution: this was demonstrated by the recent work of Bouchard and Bradford [4], where drastically different residual stress distributions were reported for the same joint configuration and welding conditions for a stainless steel pipe girth weld. The inconsistencies, as reported by Dong [5], can be attributed to the following:

1. Existing residual stress profiles are based on limited experimental data.
2. Depending on size, geometry, and weld parameters, weld axial residual stresses can range from the 'self-equilibrating' to the 'through-thickness bending' type.
3. Earlier measurements of such stresses have focused on the weld area where large scatter in data can be expected due to the high stress gradients there.
4. Residual stress measurement techniques, such as the blind hole technique, are similar to the use of strain gauges. They tend to give averaged data that can hardly be comparable with FE data obtained at integration points or even averaged in a finite element, especially in regions where high stress gradients exist.
5. Data obtained by the FE method can also be strongly dependent on the model, material properties, boundary conditions, and other assumptions.

Finally, despite the comments listed above, the computational model described here has the potential to be applied to multipass welded complex geometries for residual stress prediction.

2 PREVIOUS FE MODELLING TECHNIQUES

2.1 Plane strain and generalized plane strain models

Multipass welding simulation began with two-dimensional (2D) FE models. In 1989, Free and Porter Goff [6] used 2D plane strain elements for residual stress simulation in welded plates. However, the use of these elements resulted in higher stress predictions, as these elements could not accommodate any thermal expansion in the longitudinal direction. This important observation led other researchers [7–9] to favour instead the use of generalized plain strain elements to account for straining in the welding direction, which dramatically improved the predicted results.

Apart from using generalized plane strain elements in the analysis, several other modelling techniques were also employed to simulate various aspects of multipass welding phenomena. Leung and Pick [7] investigated a method of grouping the build-up of many weld passes into fewer layers with an envelope of combined temperature histories in the stress analysis. It was found that the method of grouping passes in a layer into two analyses (one involving all passes in the layer except the last one and the other involving the last pass only) gave results that were identical to a complete simulation.

Shim *et al.* [8] developed an uncoupled lumped pass model to reduce the computational time and cost when predicting through-thickness residual stress distribution during multipass welding of thick plates. In the thermal model, each layer of the weld bead was assumed as one lumped pass. The heat input for every pass in that layer was added and applied on the top surface of the layer. To model the heat input to the cross-section, a ramp heat input

was used to avoid numerical instability and to include the effect of a moving heat source. The generalized plane strain assumption was used in the stress analysis. The results by the lumped model showed good agreement with experimental data, however, the selection of the ramp time was quite arbitrary, i.e. based on trial and error.

In order to include the effect of the addition of filler material in each welding pass, Lindgren *et al.* [9] investigated two approaches when modelling multipass welding of two 200 mm thick plates. In the first approach, the model was generated with all elements making up the weld defined at the initial mesh creation stage. In the second, the topology of the weld elements was adjusted to accommodate previous deformation. It was found that both techniques gave the same results and the predictions agreed well with the experimentally obtained transient temperature and residual stress values.

2.2 Axisymmetric models

Another kind of 2D model, i.e. axisymmetric, has been used to simulate residual stress distribution in multipass girth butt-welded pipes. Rybicki *et al.* [10] developed an axisymmetric FE model by using the analytical solution presented by Rosenthal [11] as a thermal load to predict residual stresses in a two-pass girth butt-welded pipe. The model was based on a FE representation recognizing individual passes, temperature-dependent elastic–plastic constitutive behaviour, elastic unloading for material in the non-linear stress–strain range, and changes in geometry due to the deformation of each weld pass. Load incrementation and incremental stress–strain relations were also used. The limitations of the model were in the use of approximate analytical solutions for the thermal history and the neglect of the effects of the latent heat of fusion. Good agreement between numerical and experimental results was obtained for the axial residual stress at the inner surface. For the axial residual stress at the outer surface and the hoop residual stress at both inner and outer surfaces, the agreement was not so good.

Michaleris [12] implemented a residual stress simulation in multipass-welded girth welds on both thin- and thick-walled pipes with various radius–thickness ratios and validated their results by experiment. The heat generated by the welding process was modelled with a 'double ellipsoid' heat source model. Quasi-static FE stress analyses followed the heat transfer analyses and the computed temperature was used as thermal loading. Multipoint constraints were employed in a consistent element activation approach in the axisymmetric model. This method ensured that all elements were activated in a stress-free state at the beginning of the deposition of each weld pass in order to eliminate the errors introduced by stretching the elements to fit the deformed geometry produced by the previous passes. Elastic–plastic material response was assumed with kinematic work hardening. The computed and measured axial and hoop residual stresses at the inside surface agreed rather well considering the limitations of the blind hole drilling technique used in the experiments. The outside surface results were not reported.

2.3 Three-dimensional models

By modelling a typical cross-section, whether assuming generalized plane strain or axisymmetric conditions, it is assumed that welds are formed instantaneously. As such, the results obtained tend to reflect average values of residual stress distribution. Although these models yield useful information, the thermal and stress–strain responses of all weldments under a moving heat source are transient and 3D in nature. 3D modelling is of great importance in reflecting the reality of residual stress distribution, especially for complex geometries where no geometric simplification can be assumed.

With recent advances in computational power, it has gradually become feasible to conduct full 3D FE multipass welding simulation for transient temperature and residual stress distributions and at the same time include material non-linearities together with complex thermal and mechanical boundary conditions. However, until quite recently, 3D investigations were limited to relatively coarse meshes, rather small dimensions, and single-pass welding of simple geometries such as plates or pipes.

Tekriwal and Mazumder [13] performed a 3D uncoupled thermal and residual stress analysis of a single-pass butt weld of two 5.8 mm thick plates. The thermo-mechanical model employed the gradual element addition technique to simulate realistically the metal transfer in a gas metal arc welding process (GMAW). The model incorporated all the thermophysical and mechanical properties of the material as functions of temperature. A cut-off temperature lower than the melting point was used to reduce the analysis cost; however, this resulted in up to a 15 per cent overestimation of the transverse residual stress in the melt-pool zone.

Karlsson and Josefson [14] analysed a single-pass weld of an 8 mm thick pipe with an outer diameter of 114.3 mm. In the uncoupled thermo-mechanical analyses, the whole pipe in the hoop direction and the complete welding sequence of one revolution and subsequent cooling were covered. Although a thermo-elastoplastic material formulation with a von Mises' yield criterion, an associated flow rule, and temperature-dependent material properties were used, the small strain and displacement

assumption resulted in deviations of residual stresses in the weld region between the simulation results and experimental data. Nevertheless, these analyses confirmed the 3D nature of the temperature and stress fields developed during welding.

3 PRESENT 3D FE MODEL

In this paper, a full 3D thermo-mechanical model that simulates weld filler material being added continuously with a moving heat source is described. The ABAQUS element removal/reactivation technique was employed to simulate the addition of filler metal. This technique 'can be used to simulate removal of part of the model, either temporarily or for the remainder of the analysis'. It 'allows reactivation of elements strain-free or with strain' [15]. In the present work, the region representing the weld is partitioned comprehensively and meshed with the rest of the model initially. Elements representing each weld pass are then grouped in sets and disactivated at the start of the analysis. As the analysis progresses, element sets representing consecutive passes are reactivated strain-free to simulate material deposition.

A strain-free, reactivated element in large-displacement analysis 'fits into whatever configuration is given by its nodes at the moment of reactivation... Warnings are printed in the message file if the elements seem inappropriately distorted...' [15].

3.1 Geometry and meshing

The geometrical dimensions of both the butt-welded plate and pipe were identical to those used by Shim *et al.* [8] and Rybicki *et al.* [10], respectively. Since both the butt-welded plate and pipe used were symmetrical about the weld centre-line, only half of the components were modelled. In order to produce well-graded finite element meshes, the geometrical models were partitioned into various regions. Each region consisted of meshes of different density. In the critical fusion region near the joint intersection area, where temperature gradients were expected to be the most severe, fine meshes were generated. On the other hand, in the regions remote from the joint, the meshes were rather coarse. Between the refined and the far field regions, transition regions were used.

In the 3D plate model, the linear elements gave almost the same results as the quadratic elements; however, the running time was much shorter. In the 3D pipe model, the quadratic elements may be more suitable for the curved surfaces of the welded pipes but the linear elements could equally give good results if the meshes were fine enough. As can be seen from Fig. 1, the meshes were made fine enough in the current model.

Figure 1 shows 3D finite element meshes for the welded joints, along with the refined meshes in the weld toe. The detailed element design with mesh refinement near and within the weld area in both models proved to be adequate for such analysis

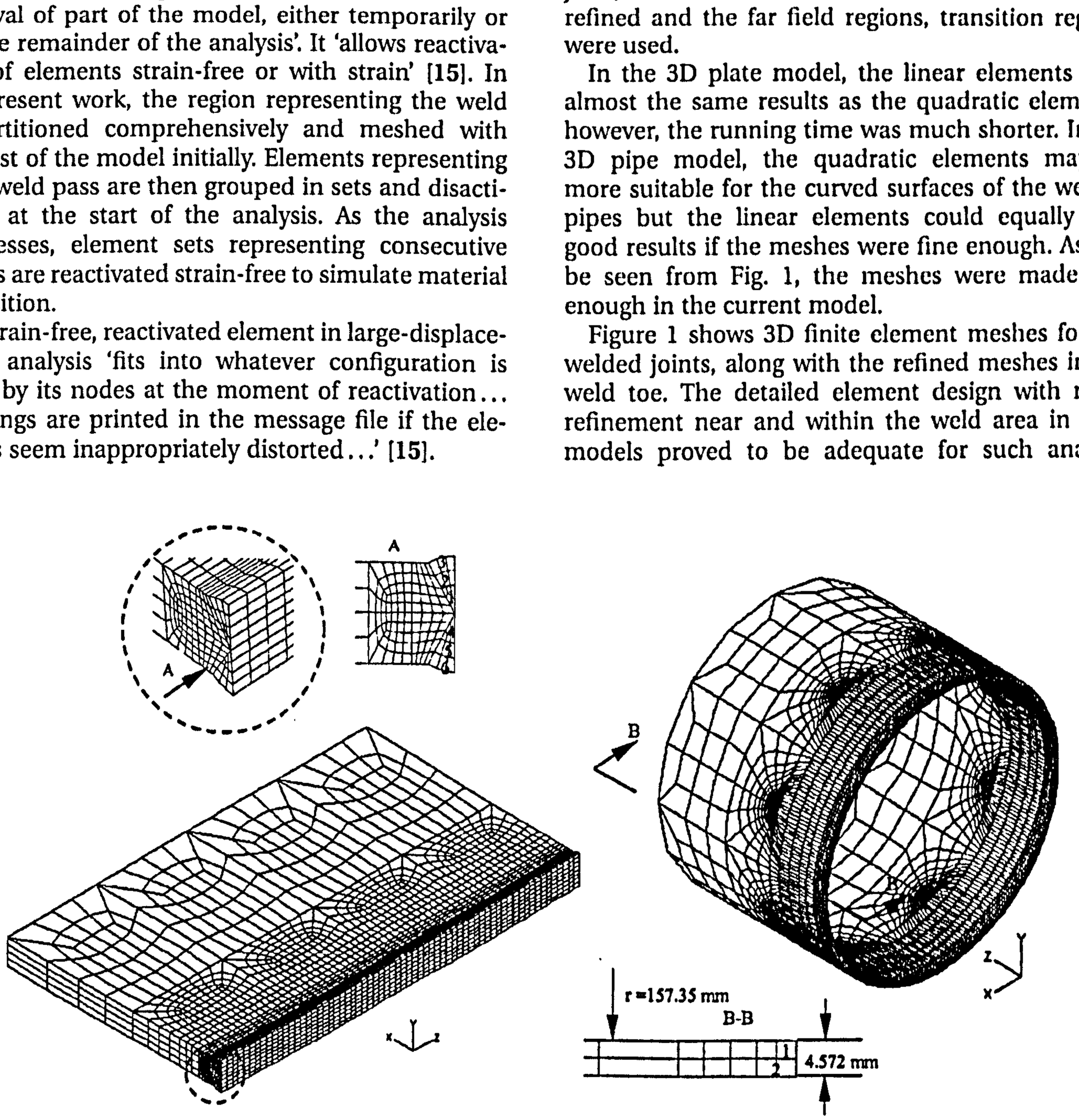

Fig. 1 Finite element meshes: (a) multipass butt-welded plate; (b) multipass butt-welded pipe

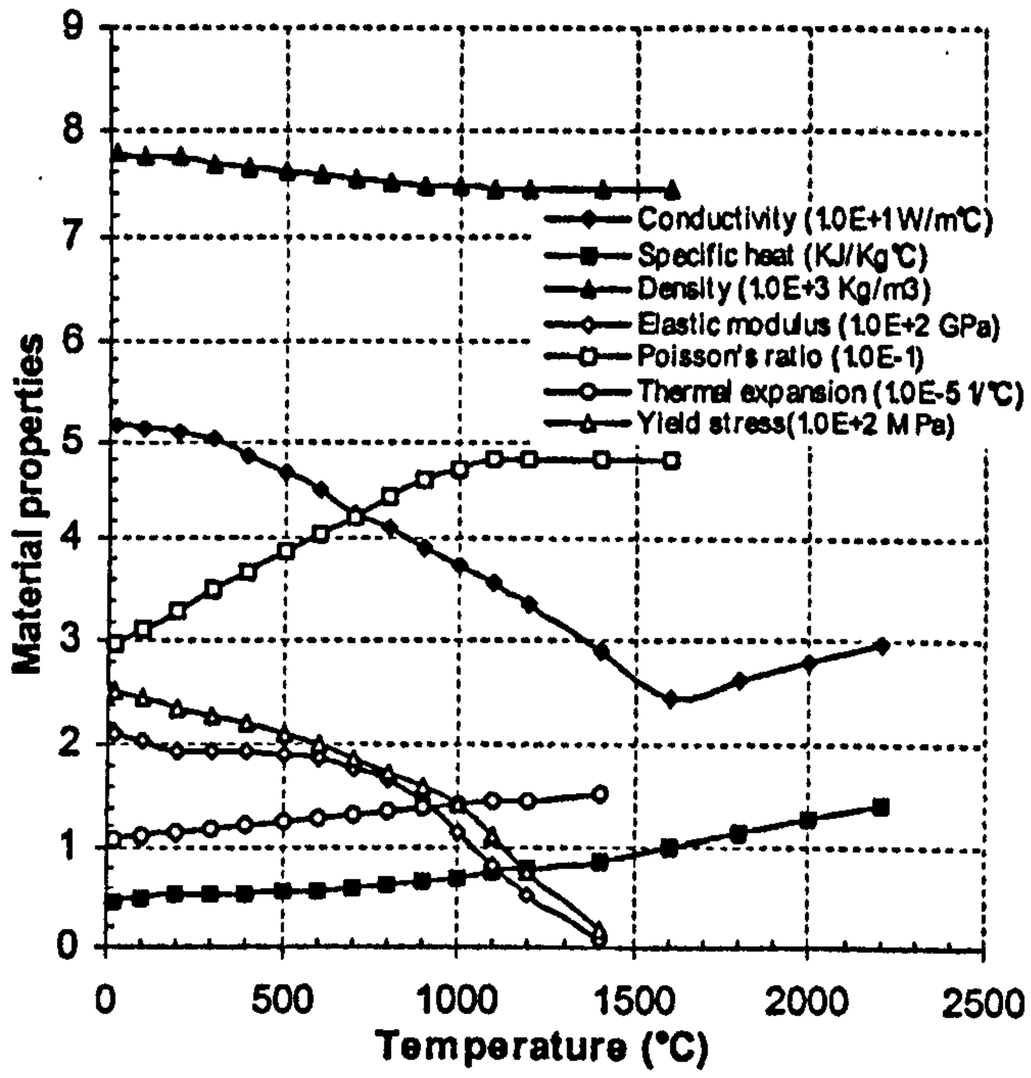

Fig. 2 Material properties of (a) ASTM A36 [8, 17] and (b) 304 stainless steel [10, 17]

based on a preliminary mesh sensitivity study. The symmetrical plate model [Fig. 1(a)] has 10 240 eight-node linear hexahedral elements and 12 195 nodes, while the symmetrical pipe model [Fig. 1(b)] has 7 776 eight-node linear hexahedral elements and 12 123 nodes. Eight-noded 3D hexahedral elements of the ABAQUS type DC3D8 [15] were used in the heat transfer analysis, while the continuum elements with reduced integration, C3D8R, were used in the stress analysis.

3.2 Material properties

Temperature-dependent thermo-physical properties, i.e. thermal conductivity, specific heat, and density, which were assumed to be the same for both parent and weld materials up to the melting point, were used in the transient thermal analysis. Above the melting temperature, the properties were held constant, except for the thermal conductivity. The latter was doubled to compensate for the effect of heat transfer due to convection stirring in the molten weld-pool material as was proposed in reference [16]. Latent heat effects were assigned a value of 247 kJ/kg between the solidus temperature of 1465 °C and the liquidus temperature of 1544 °C for ASTM A36 mild carbon steel and 300 kJ/kg between the solidus temperature of 1420 °C and the liquidus temperature of 1460 °C for 304 stainless steel, respectively [16, 17].

Temperature-dependent mechanical properties, i.e. elastic modulus, Poisson's ratio, coefficient of thermal expansion, and yield stress were also needed for the stress analysis. The material was assumed to be thermo-elastoplastic using rate-independent plasticity. The von Mises yield criterion and the associated flow rule were used. Linear isotropic hardening was assumed. The material properties required for the current simulation are shown in Fig. 2. All of these introduced material non-linearities in the thermo-mechanical analysis.

3.3 Boundary conditions

The heat losses by free convection were modelled by Newton's cooling law. Boundary conditions were applied to all free surfaces of the components except for the successive boundaries created after each new weld pass. The surfaces exposed to the environment were subjected to the same convective boundary conditions, using a heat transfer convection coefficient of $h = 30\,\mathrm{W/m^2\,°C}$ to ambient air. The ambient temperature for both parent and weld metal was set at 25 °C.

Boundary conditions were also applied to prevent rigid body motion of the plate and the pipe in the mechanical model. In the plate model, the nodes under the root pass were constrained in the y direction. One node at the bottom of one corner of the plate was constrained in the y and z directions and the corresponding node at the other corner of the plate was constrained in the y direction only. In the pipe model, two symmetric nodes at the end of the pipe were restrained in both the radial and tangential directions. In either case, reaction forces were output to assess whether they represented unrealistic

constraints as compared with what would be expected in a typical welding execution.

Symmetrical boundary conditions were imposed along the weld centre-line in both the plate and the pipe models since only half of the components were analysed.

3.4 Analysis procedure

A sequentially coupled thermo-mechanical analysis was conducted to simulate the multipass welding process. In the thermal model, two types of heat input were considered. One was heat flux and the other was heat content of filler metal droplets. The first part of heat input was arranged as a column of elements with specified body heat flux progressing along the weld path. This heat input was imposed on to the specified newly activated elements representing a deposited pass at a given time. Body heat flux was uniformly distributed over the volume of each weld droplet. The second part of heat input, i.e. the heat content of filler metal droplets, was assumed to be deposited at melting temperature and additional solution steps in the thermal analysis were needed to account for this. After the final pass had been analysed, the model was allowed to cool down to the ambient temperature. Automatic time stepping was used for the solution of this non-linear transient heat transfer problem.

The same meshes were used for both heat transfer and residual stress analysis. Creep strains were not included in the stress analysis because the time spent at high temperature was deemed to be very short. The fusion zone elements were incrementally activated in strain-free states to model the continuous deposition of filler material. Large deformation and thermo-elastoplastic material formulation were considered. The most important factors when calculating residual stresses introduced by thermal strains in welds are the effects of temperature and the thermal history on the mechanical properties. These temperature histories were obtained from the thermal analysis and were used as thermal loading on to the structural model to calculate thermal strains and stresses for each time increment. The thermal strains and stresses were then accumulated to produce the final state of residual stresses.

4 TEST CASES

4.1 Multipass butt-welded plate

A butt-welded plate from the paper of Shim *et al.* [8] was chosen for the validation of the current 3D FE plate model. This was the only model for which full information was available in that paper. This

Table 1 Parameters for welding 25.4 mm thick ASTM A36 carbon steel plate [8]

Pass no.	Weld voltage (V)	Weld current (A)	Weld speed (mm/s)	Heat input (kJ/mm)
1	25	190	3.34	1.21
2–5	26	215	4.7	1.01
6	25	190	3.34	1.21
7–9	26	220	4.7	1.03
10–11	27	250	4.7	1.22

consisted of two ASTM A36 mild steel plates of thickness 25.4 mm with a double V groove, which were welded by the GMAW method. The component was fabricated by 11 passes. The welding parameters are shown in Table 1. An arc efficiency of 0.85 was chosen, as was reported in reference [8]. Free boundary conditions were applied to all free surfaces. The blind hole-drilling method was used to determine experimentally the surface residual stresses in the weldment.

4.2 Circumferentially multipass butt-welded pipe

The circumferentially butt-welded pipe from the paper of Rybicki *et al.* [10] was chosen for the validation of the current 3D FE pipe model. It was a 304 stainless steel pipe, 457.2 mm in length, 323.85 mm outer diameter by 4.572 mm wall thickness, which was cut in half before the cut edges were weld prepared. The weld required two passes. Both passes started at the same point and proceeded in the same direction. The root pass was made by gas tungsten arc (GTA) welding and the second pass by gas metal arc (GMA) welding. The arc efficiencies were 0.687 and 0.81 for the GTA weld of pass 1 and the GMA weld of pass 2, respectively [10]. No filler metal was added to the root pass. An elapsed time of 30 min and 35 s occurred between the completion of the root pass and the start of the second pass. An insert ring was tack-welded to one of the pipes. The two pieces of pipe were then mounted on a spider frame to maintain joint alignment. The welding parameters are listed in Table 2.

5 COMPARISON AND DISCUSSION

As a general comment, FE runs have shown that the temperature predictions from the thermal analyses respond to expectation when some parameters are slightly varied. Indeed temperature profiles and detailed thermal histories can be consistently reproduced with ease as has been reported in reference [18]. However, for the case of resultant stresses, the simulation results appear to be sensitive to parameters such as the yield stress of the material. In

Table 2 Parameters for welding 4.572 mm thick 304 stainless steel pipe [10]

Pass no.	Welding method	Weld voltage (V)	Weld current (A)	Weld speed (mm/s)	Heat input (kJ/mm)
1	GTA	9	115	1.27	0.559
2	GMA	22	220	8.47	0.462

some cases, not only stress magnitude is affected as expected but also the shape of the stress profile.

5.1 Multipass butt-welded plate

5.1.1 Thermal results

Figure 3 shows the temperature versus time plots for the first pass at distances of 12.7 mm and 19.1 mm from the weld centre-line on the top surface of the mid-section of the plate. The experimental results from the thermocouples and the simulation results from Shim's 2D model are also plotted for comparison.

As shown in Fig. 3(a), at a distance of 12.7 mm from the weld centre-line, the temperature profiles from the current 3D model show a good correlation with the experimental data, both at the heating stage and at peak temperature. As for the cooling stage, the temperatures predicted by the 3D model agreed better with the experimental data than those by the 2D model.

At the location 19.1 mm from the weld centre-line, the experimental results appeared to be over-predicted by the 3D model and under-predicted by the 2D model at most locations, as shown in Fig. 3(b). However, the experimental results appear to be closer to those predicted by the 3D model than those obtained using the 2D model. It is speculated that the 2D model underestimates might be due to the introduction of the ramp heat input to the cross-section that was intended to take account of the moving arc effect in the 2D model.

Overall, both the 2D and 3D models gave similar temperature distribution patterns at both selected experimental locations. However, the 3D model provided better simulation results than the 2D model, especially at a distance near to the weld centre-line, where high temperatures at these critical locations usually result in large plastic strains and residual stresses.

5.1.2 Residual stress results

Figure 4 shows the longitudinal and transverse stress distributions at the top surface of the mid-section of the plate. The experimental measurement and simulation results from Shim's 2D generalized plane strain lumped pass model are also plotted. The current 3D model employed the same lumping technique as the model of Shim *et al.*, i.e. a total of 11 passes were lumped into six passes, as shown in Fig. 1(a).

As shown in Fig. 4(a), a similar peak tensile longitudinal stress is noted around the weld centre-line. Within a distance of 30 mm from the weld centre-line, the

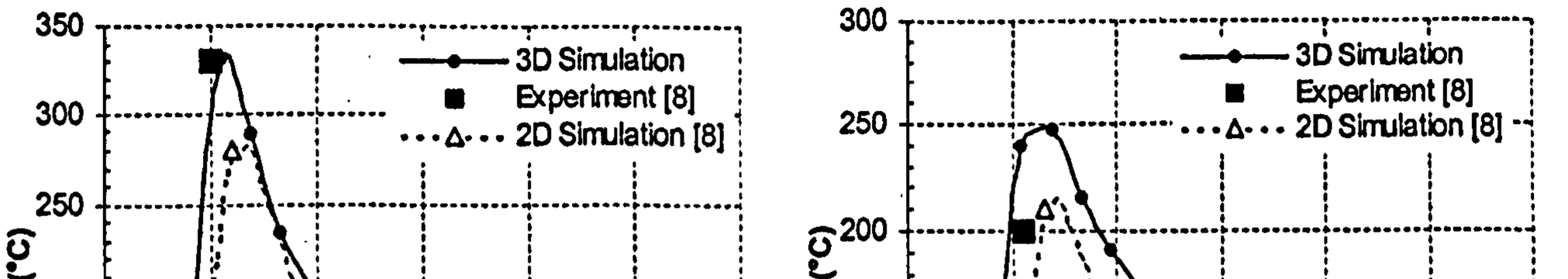

Fig. 3 Top surface temperature profiles for the first pass at (a) 12.7 mm and (b) 19.1 mm from the weld centre-line

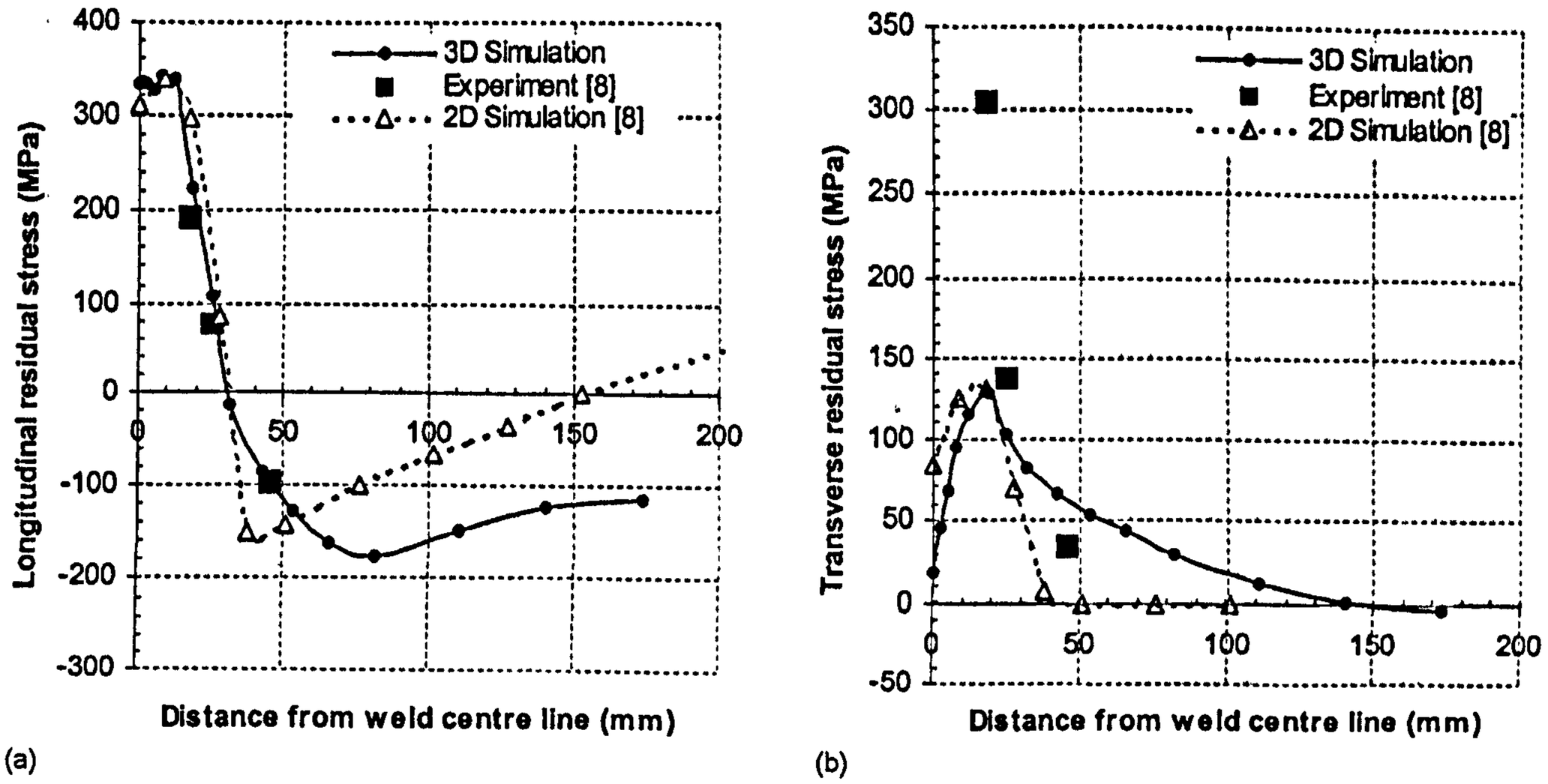

Fig. 4 Comparison of simulated and experimental residual stresses at the top surface: (a) longitudinal residual stresses; (b) transverse residual stresses

predicted results from the 3D model agreed extremely well with both the experimental data and the 2D model's results. Besides, the 3D model gave the same tensile zone as that of the 2D model. In the compressive zone, the 3D model agreed with experimental results better than the 2D model. The 3D model showed slightly higher peak longitudinal compressive stress than that of the 2D model.

The transverse residual stress distributions from both models showed similar patterns and peak tensile transverse residual stress values were almost the same, as shown in Fig. 4(b). The 3D model resulted in a wider tensile transverse stress zone than the 2D model. As regards the lone experimental data point at a stress level of 300 MPa, although it appears at this stage like a 'rogue' point, this may not be truly the case. There is a possibility that, since both FE simulations used the lumped pass method, they could be under-predicting the stress level at this location and such an experimental data point can prove invaluable if there is a need for the lumping technique to be improved.

In summary, both the 2D and 3D models gave not only nearly the same peak value but also similar distribution patterns for both longitudinal and transverse residual stress. However, the predicted results from the 3D model showed better agreement with the experimental data than the 2D generalized plane strain model. Ignoring the above statement about the lumping technique, it is also noted that the transverse stresses may be more sensitive than the longitudinal stress to the lumping technique.

5.2 Circumferentially multipass butt-welded pipe

5.2.1 Thermal results

Figure 5 shows the temperature distributions obtained from the current 3D model. The results from the axisymmetric model and thermocouple measurements are also provided. The reference time in the figures corresponds to the time at which the thermocouple nearest the weld centre-line reached its maximum temperature. It can be seen that the agreement between predictions from both models and the experimental values are quite good.

5.2.2 Residual stress results

Figure 6 gives the 3D prediction of axial and hoop residual stresses at the inner surface of the two-pass welded pipe. The results obtained from the experiment and the axisymmetric model of Rybicki *et al.* are also plotted for comparison. As can be noted from the figures, the latter results are rather limited. They only cover a distance of about 20 mm from the weld centre-line.

It is noticed from Fig. 6(a) that the predicted hoop residual stress from the current 3D model shows a similar pattern to that from the axisymmetric model within a distance of about 20 mm from the weld centre-line except at the centre-line itself. Both have almost the same peak compressive stress value, which does not occur at exactly the same distance from the weld centre-line for the two models. The 3D predicted hoop stresses also fall between the axisymmetric predictions and the experimental

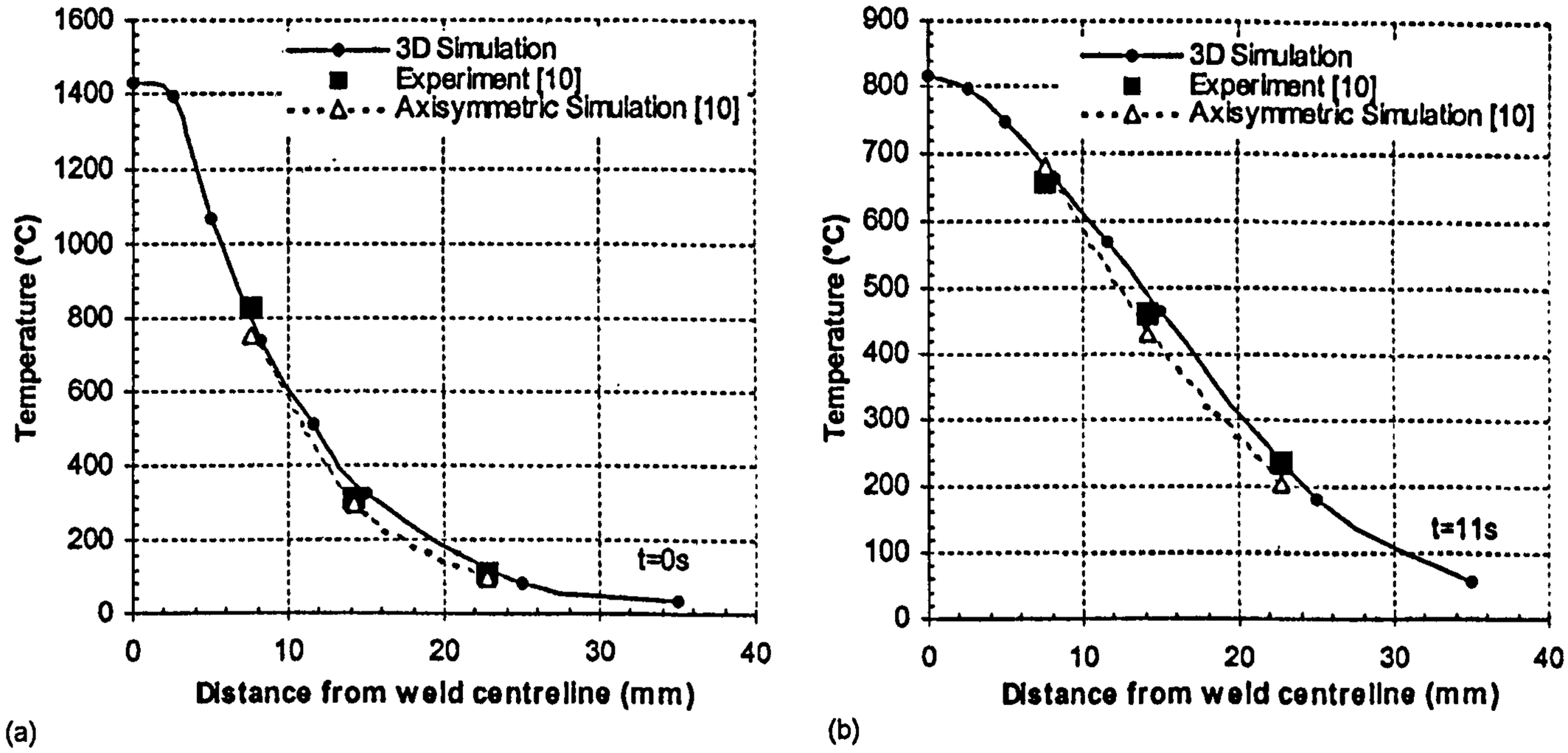

Fig. 5 Comparison of simulated and experimental temperature for the root pass at (a) $t = 0$ s and (b) $t = 11$ s

measurements at a distance from the weld centre-line between 8 and 20 mm. For the weld centre-line location, it is surprising to note that both the axisymmetric model and experimental results show a 'trough' in the hoop stress distribution, which is not depicted by the 3D model.

The 3D prediction of axial residual stresses shows a similar trend to that obtained by the axisymmetric model, as can be noticed in Fig. 6(b), except again at the weld centre-line. Both give almost the same tensile zone. However, the 3D model predicts higher peak axial residual stress than the 2D model at the weld centre-line. This is understandable considering the comments about the high stress gradients at this location made by Dong [5] and mentioned in the introduction.

The 3D predictions of hoop and axial residual stress at the outer surface of the two-pass welded pipe are compared with experimental data and the axisymmetric model of Rybicki *et al.* in Fig. 7. It can be clearly noticed in Fig. 7(a) that the outer surface hoop residual stresses predicted by the 3D model agree with the experimental data much better than those obtained by the axisymmetric model. Both FE

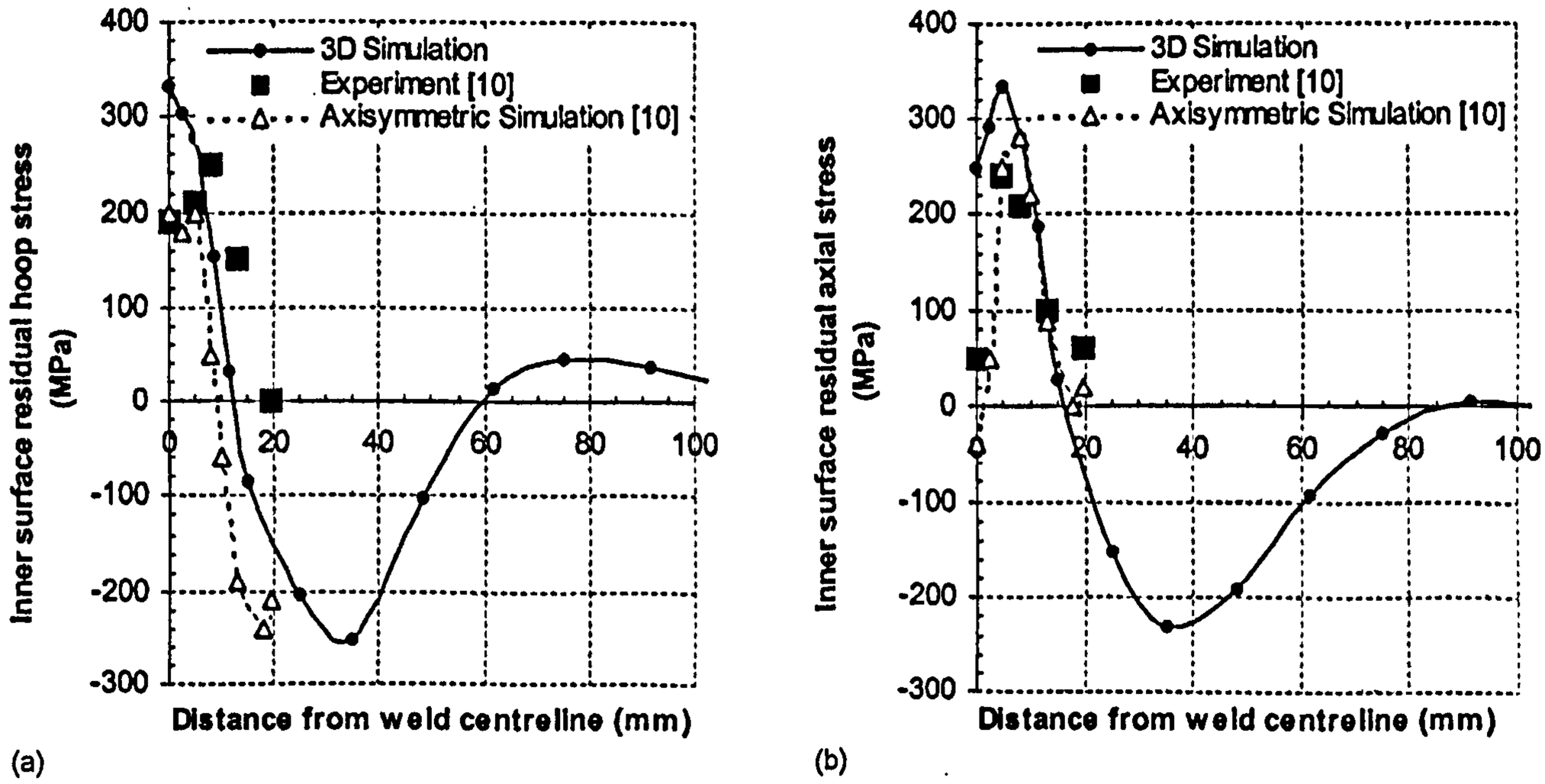

Fig. 6 Comparison of simulated and experimental residual stresses at the inner surface: (a) hoop residual stresses; (b) axial residual stresses

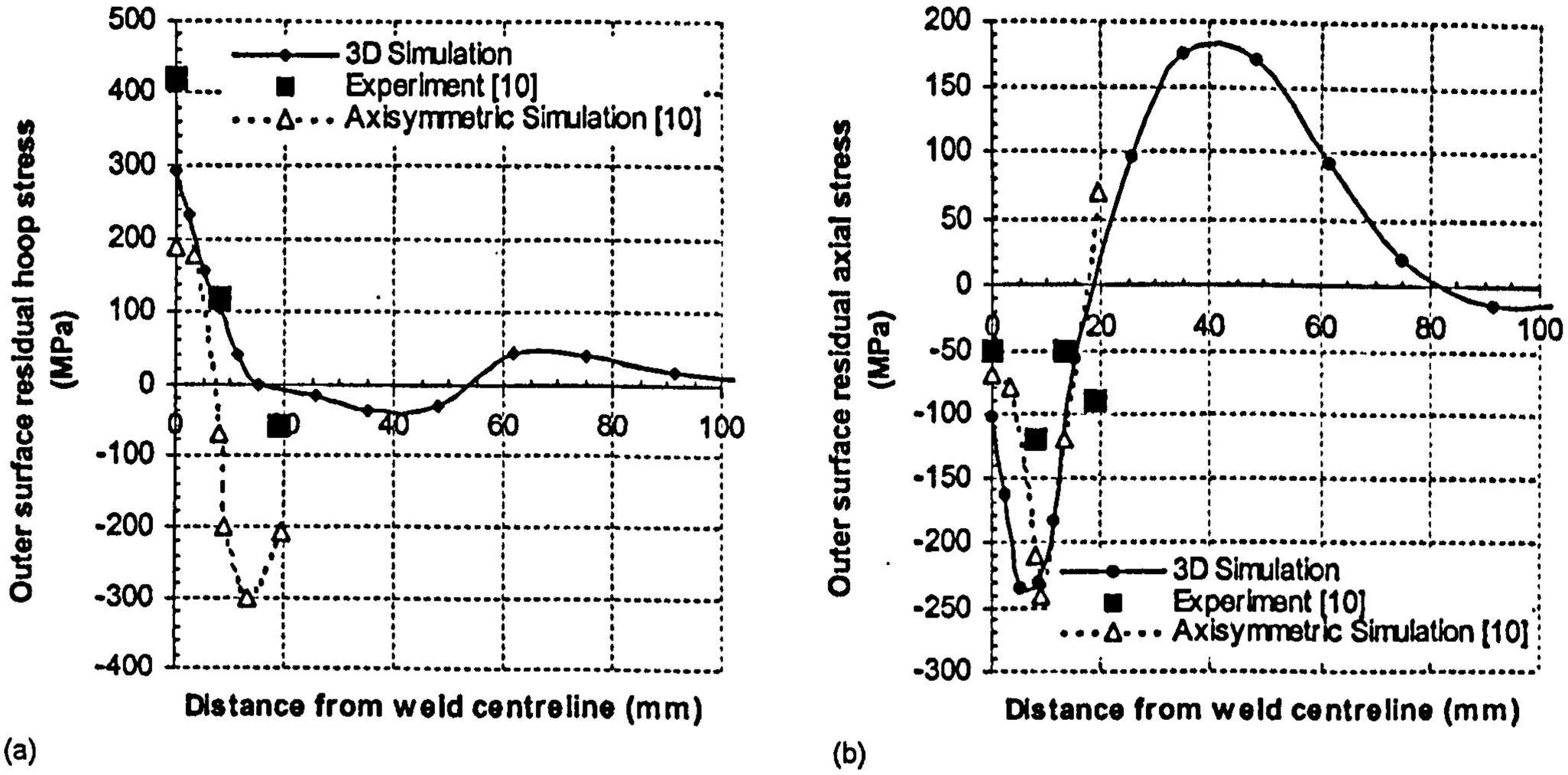

Fig. 7 Comparison of simulated and experimental residual stresses at the outer surface: (a) hoop residual stresses; (b) axial residual stresses

models under-predict the experimental result at the weld centre-line. Also, and in contrast to the 2D model, which clearly predicts a peak compressive stress at a distance of about 15 mm from the weld centre-line, both experimental data and the 3D model predictions demonstrate uniform and almost negligible stress at and beyond this distance, bearing in mind that experimental data are only available up to a distance of 20 mm from the weld centre-line.

The axial residual stress distributions on the outer surface are shown in Fig. 7(b). The predictions by the axisymmetric and 3D FE models are comparable in terms of both pattern and magnitude. For the case of the experimental results, while compressive stresses were measured within a distance of about 20 mm from the weld centre-line, the stress distribution pattern, unlike the FE data, is not clearly defined.

6 CONCLUSIONS

The objective of this study was to develop a versatile 3D computational model for predicting multipass welding residual stresses on the basis of known material behaviour and welding process parameters with little concern as regards geometric simplifications.

A full 3D FE model involving moving heat source and continuous filler material addition in connection with body flux in multipass welding has been developed. The model has been applied to a multipass butt-welded plate and pipe for validation. The numerically obtained temperature and residual stress results from the current full 3D thermo-mechanical analyses were compared with existing experimental data and predictions from the 2D generalized plane strain and axisymmetric models at the surfaces of the weldments. Both 2D and 3D models can provide acceptable temperature and residual stress results; however, the predictions from the full 3D model were noted, in general, to agree better with the experimental data than those from the 2D models.

As the current full 3D FE model needs no geometric simplifications, it has the potential to be applied to other multipass welded complex geometries for residual stress prediction. In fact, modelling simplifications are impossible for some real pressure-retaining components such as cylinder-to-cylinder connections. It is hoped that the model can minimize assumptions and reflect the real-life welding process as closely as possible.

ACKNOWLEDGEMENTS

The lead author acknowledges financial support, in the form of a studentship, by the School of Engineering and the Built Environment of the University of Wolverhampton. The authors would also like to thank Steve Boyle for his technical assistance.

REFERENCES

1 **Leggatt, R. H., Smith, D. J., Smith, S. D.,** and **Faure, F.** Development and experimental validation of the deep hole method for residual stress measurement. *J. Strain Analysis*, 1996, **31**(3), 177–186.

2 **Murugan, S., Rai, S. K., Kumar, P. V., Jayakumar, T., Raj, B.,** and **Bose, M. S. C.** Temperature distribution and residual stresses due to multipass welding in type 304 stainless steel and low carbon steel weld pads. *Int. J. Pressure Vessels and Piping*, 2001, **78**(4), 307–317.
3 **Smith, D. J., Bouchard, P. J.,** and **George, D.** Measurement and prediction of residual stresses in thick-section steel welds. *J. Strain Analysis*, 2000, **35**(4), 287–305.
4 **Bouchard, J.** and **Bradford, C.** Validated axial residual stress profiles for fracture assessment of austenitic stainless steel pipe girth welds. Proceedings of the ASME Pressure Vessels and Piping Conference, 22–26 July 2001, Atlanta, Georgia, *Fracture and Fitness* (Ed. D. Lidbury), 2001, PVP Vol. 423, pp. 93–99 (American Society of Mechanical Engineers, New York).
5 **Dong, P.** On the mechanics of residual stresses in girth welds. Proceedings of the ASME Pressure Vessels and Piping Conference, 25–29 July 2004, San Diego, California, *Residual Stress, Fracture and Stress Corrosion Cracking* (Ed. Y. Y. Wang), 2004, PVP Vol. 479, pp. 119–124 (American Society of Mechanical Engineers, New York).
6 **Free, A.** and **Porter Goff, R. F. D.** Predicting residual stresses in multi-pass weldments with the finite element method. *Computers Structs*, 1989, **32**(2), 365–378.
7 **Leung, C. K.** and **Pick, R. J.** Finite element analysis of a multipass weld. *Welding Res. Council Bull.*, 1990, **356**, 11–33.
8 **Shim, Y., Feng, Z., Lee, S., Kim, D., Jaeger, J., Papritan, J. C.,** and **Tsai, C. L.** Determination of residual stresses in thick-section weldments. *Welding J.*, 1992, **71**(9), 305–312.
9 **Lindgren, L.-E., Runnemalm, H.,** and **Nîsstrîm, M. O.** Numerical and experimental investigation of multipass welding of a thick plate. *Int. J. Numer. Methods Engng*, 1999, **44**(9), 1301–1316.
10 **Rybicki, E. F., Schmueser, D. W., Stonesifer, R. B., Groom, J. J.,** and **Mishler, II. W.** A finite element model for residual stresses and deflections in girth-butt welded pipes. *ASME J. Pressure Vessel Technol.*, 1978, **100**(10), 256–262.
11 **Rosenthal, D.** Mathematical theory of heat distribution during welding and cutting. *Welding J. Res. Suppl.*, 1941, **20**(5), 220–234.
12 **Michaleris, P.** Residual stress distributions for multi-pass welds in pressure vessel and piping components. Proceedings of the ASME Pressure Vessels and Piping Conference, 21–26 July 1996, Montreal, Canada, *Residual Stresses in Design, Fabrication, Assessment and Repair* (Eds R. W. Warke, P. Dong, and A. Dermenjian), 1996, PVP Vol. 327, pp. 17–27 (American Society of Mechanical Engineers, New York).
13 **Tekriwal, P.** and **Mazumder, J.** Transient and residual thermal strain–stress analysis of GMAW. *ASME J. Engng Mater. Technol.*, 1991, **113**(3), 336–349.
14 **Karlsson, R. I.** and **Josefson, B. L.** Three-dimensional FE analysis of temperatures and stresses in a single-pass butt welded pipe. *ASME J. Pressure Vessel Technol.*, 1990, **112**(1), 77–84.
15 *ABAQUS User's Manual*, Version 6.3, 2002 (Hibbitt, Karlsson and Sorensen, Inc.).
16 **Dong, P.** Residual stress analysis of a multipass girth weld: 3D special shell versus axisymmetric models. *ASME J. Pressure Vessel Technol.*, 2001, **123**(2), 207–213.
17 ASM International Handbook Committee, *Metals Handbook*, 10th edition, 1990 (ASM International, Materials Park, Ohio).
18 **Jiang, W., Yahiaoui, K., Wang, C. J., Hall, F. R.,** and **Laoui, T.** FE predictions of temperature distributions in a multipass welded piping branch junction. Proceedings of the ASME Pressure Vessels and Piping Conference, 25–29 July 2004, San Diego, California, *High Pressure Technology – 2004: Innovations and Advances in High Pressure Equipment* (Ed. J. Pfeifer), 2004, PVP Vol. 473, pp. 93–100 (American Society of Mechanical Engineers, New York).

Proceedings of ASME PVP2004:
2004 ASME/JSME Pressure Vessels and Piping Conference
San Diego, California, July 25-29, 2004

SPC-15

FE PREDICTIONS OF TEMPERATURE DISTRIBUTIONS IN A MULTIPASS WELDED PIPING BRANCH JUNCTION

Wei Jiang, Kadda Yahiaoui, Chang J. Wang, Frank R. Hall, Tahar Laoui

School of Engineering and the Built Environment
University of Wolverhampton
Telford, TF2 9NT, UK

ABSTRACT

This contribution deals with the complex temperature profiles that are generated by the welding process in the intersection region of thick walled, cylinder-cylinder junctions. These affect material microstructure, mechanical properties and residual stresses. Knowledge of the thermal history and temperature distributions are thus critical in developing control schemes for acceptable residual stress distributions to improve in-service component behavior.

A comprehensive study of 3D temperature distributions in a stainless steel tee branch junction during a multipass welding process is presented. A newly developed partitioning technique has been used to mesh the complex intersection areas of the welded junction. Various phenomena associated with welding, such as temperature dependent material properties, heat loss by convection and latent heat have been taken into consideration. The temperature distribution at various times after deposition of certain passes and the thermal cycles at various locations are reported.

The results obtained in this study will be used for on-going and future analysis of residual stress distributions. The meshing technique and modeling method can also be applied to other curved, multipass welds in complex structures.

KEYWORDS multipass welding, temperature distribution, finite element analysis, tee branch junction

1. INTRODUCTION

Welded, thick walled, cylinder-cylinder intersections are piping components commonly used in the power industry and in oil or gas transport systems, amongst others. Owing to the relatively large wall thickness in such piping systems, the weldments are often constructed in several passes. The heat supplied by each welding pass produces complex thermal cycles, which greatly affect the material microstructure, mechanical properties and residual stress distributions. It is therefore important to predict the temperature history to develop control schemes for acceptable residual stress distributions to improve in-service behavior of components.

Thus far, the thermal cycle and temperature distributions of the welding process have been studied analytically, experimentally and numerically. The most significant analytical solution was proposed by Rosenthal [1]. It is a heat conduction analysis of a moving point heat source in an infinite solid. Rybicki et al. [2,3] developed a computational model, based on the analytical solution presented by Rosenthal, as a thermal load for the prediction of residual stresses during multipass girth-butt welding of 304 stainless steel pipes. However, the models ignored temperature dependent material properties and the effect of latent heat of fusion.

Very limited experimental data regarding the temperature distribution during multipass welding is available in the literature. Murugan et al. [4,5] reported experimentally obtained temperature distributions during multipass welding of low carbon steel and AISI type 304 stainless steel plates with thicknesses of 6, 8 and 12mm. These experimental results will be used for comparison with data obtained from the numerical model developed in the current study.

Compared with analytical and experimental studies, numerical simulation has attracted a lot of attention because of its capability to deal with complex geometries, nonlinear behavior and various boundary conditions [6]. To predict residual stresses in thick walled pipe, Scaramangas [7] simplified the analysis by assuming the heat flow to be axisymmetric, that is, heat was assumed to flow radially and axially but not circumferentially. The finite difference method was used, with a specified temperature distribution at the start of welding, corresponding to the melting temperature over the molten pool area and the preheat temperature over the pipe. The thermal properties were assumed to be temperature independent and heat loss from all exposed surfaces was taken into account. Brickstad and Josefson [8] used two-dimensional axisymmetric models to numerically simulate a series of

multipass circumferential butt-welds of stainless steel pipes up to 40 mm thick in a non-linear thermo-mechanical FE analysis. The rotational symmetry assumption was invoked in their analysis. Wen et al. [9] also used a 2D axisymmetric FE model to simulate three-pass pipe girth welding, with wall thickness of 19mm. In the thermal analysis, the heat input and filler metal deposition were simulated by the definition of a moving heat source with a uniform body heat flux. The element reactivation technique was used to simulate weld deposition.

Although many studies have been conducted for circumferential butt weld simulation, most of the results were based on axisymmetric assumptions. In addition, research has been limited to relatively thin pipes. There is a paucity of reliable information about thermal cycles and temperature distributions in thick steel weldments. No attempt has been made yet to simulate 3D temperature distribution of multipass welding of thick cylinder-cylinder intersections.

This paper presents a comprehensive study of 3D temperature distributions in a thick, stainless steel tee branch junction during a multipass welding process. The complexity of this weld geometry, together with the multipass process involved, is a particularly challenging FE weld simulation.

A newly developed meshing technique has been used for mesh generation of the complex intersection areas of the welded junction. An element remove/reactivate technique has been employed to simulate the deposition of filler material. In addition, material nonlinearities, i.e. latent heat and temperature dependent thermal properties, have been taken into account.

2. ANALYSIS PROCEDURE

2.1 Geometry and FE model

The component chosen for this simulation is an AISI 316L stainless steel tee branch junction. The outside diameter of the run pipe is 891 mm with a thickness of 77 mm. The outside diameter of the branch pipe is 356 mm with a thickness of 36mm. This configuration gives branch-to-run outside diameter and thickness ratios of 0.40 and 0.468, respectively. The direct branch on pipe requires welding along the "saddle-like" intersection between run and branch-pipe fittings and modeling a full circumferential fillet weld. This complex geometry, coupled with multipass welding, presents a challenging and tedious mesh generation task.

In order to produce a well-graded finite element mesh, the geometrical model was partitioned into different regions. Each region consists of meshes of different element density. In the critical fusion regions near the intersection area of the joint, where temperature gradients are expected to be the most severe, fine meshes are generated. On the other hand, in the regions remote from the joint, the meshes are rather coarse. Between the refined and the far field regions, transition regions with tetrahedral elements were used. Figure 1 shows the finite element model. It consists of 26682 eight-noded, 3D heat transfer brick elements (type DC3D8), 21599 four-noded, 3D heat transfer tetrahedron elements (type DC3D4) and 34954 nodes[10]. Figures 2a-b show details of the mesh at the flank and crotch corner locations, respectively. Figure 2c gives an indication of the elements representing the individual passes required to fill the groove.

The ABAQUS element removal/reactivation technique was applied in the thermal analysis. In this technique, the element sets representing each weld pass in the weld metal area were generated along with the FE meshes for the parent material. During analysis, elements associated with higher numbered passes were first removed and then reactivated at a time corresponding to the time at which the molten weld metal was deposited. When a group of weld pass elements were activated, a specified initial temperature was imposed for all nodes associated with the weld pass elements.

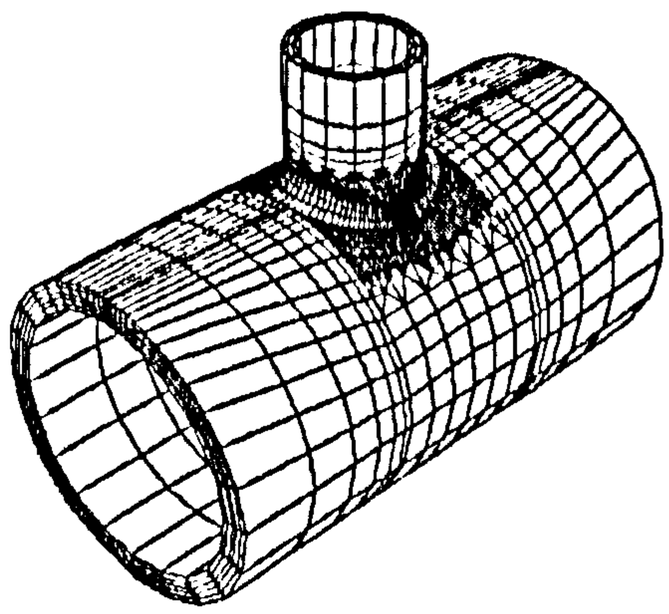

Fig. 1 FE mesh of a tee branch junction component

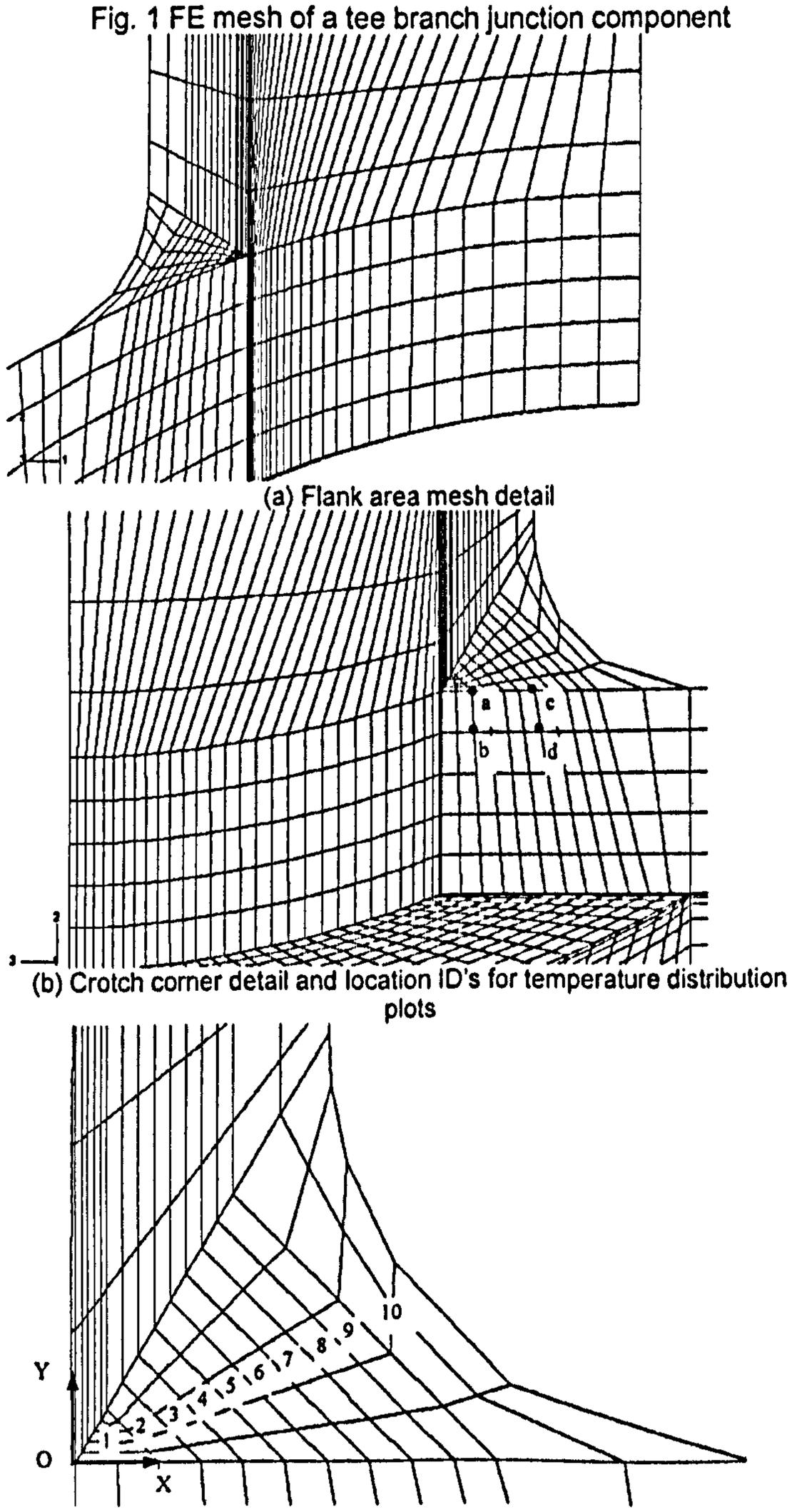

(a) Flank area mesh detail

(b) Crotch corner detail and location ID's for temperature distribution plots

(c) Weld pass numbers and local coordinate system

Fig.2 Detailed FE mesh near weld metal region

In order to reduce the computational requirement, a pragmatic approach to model the multipass weld deposits was adopted. The entire weld was represented by 10 layers of filler metal, sequentially added to the model, one layer at a time. However, each layer can generally represent more than one weld pass.

2.2 Material properties

The finite element heat transfer analysis requires accurate values of the thermal conductivity, specific heat, material density and latent heat of fusion up to the melting point. Temperature dependent thermal physical properties, which were assumed to be the same for both parent and weld materials up to the melting point of 1420°C [8,12], were used in the transient thermal analysis. These are shown in Fig.3. Above the melting temperature, the properties were held constant, except for the thermal conductivity. The latter was doubled to compensate for the effect of heat transfer due to convection stirring in the molten weld pool material [8,12]. Latent heat effects were assigned a value of 300 KJ/Kg between the solidus temperature of 1420°C and the liquidus temperature of 1460 °C.

Both temperature-dependent material properties and latent heat effects introduce nonlinearities in the heat transfer analysis, although the former has a lesser effect than the latter.

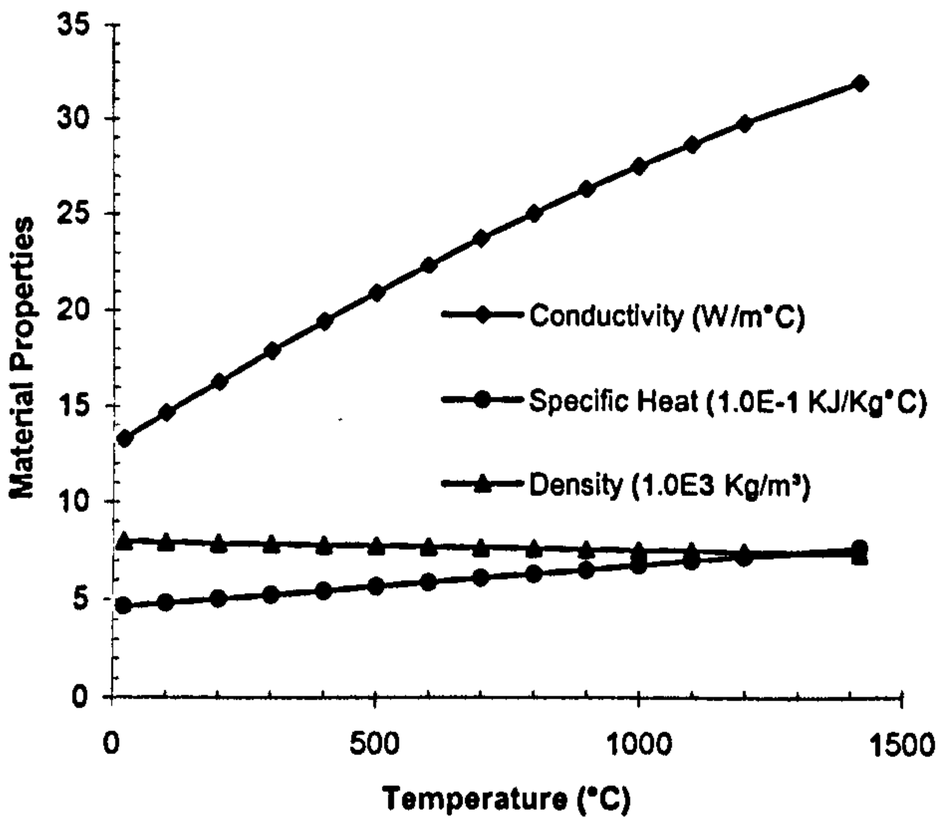

Fig.3 Material properties of 316L stainless steel [12]

2.3 Heat transfer analysis

The most significant heat transfer mechanisms in welding are the heat input from the heat source and the heat losses due to conduction, convection and radiation from the weld surfaces. In the present investigation, the radiation mode of heat transfer was ignored.

There are two types of heat input in metal welding: one is the heat flux and the other is the heat content of filler metal droplets. In the current thermal FE analysis, the first part of heat input was arranged as a column of elements with specified body heat flux instead of an infinitely thin line as used in analytical models. This heat input was imposed onto the specified newly activated elements representing a deposited pass at a given time. Body heat flux was uniformly distributed over the length of each weld layer. The simulation technique consists of: (a) a kind of ramp with linearly increasing heat input from the approaching heat source, (b) constant heat input when the elements are melted and (c) linearly decreasing heat input when the heat source is leaving the element. Heat input was modeled by a distributed heat flux working on individual elements. In ABAQUS [10], distributed heat fluxes are coded with the option called DFLUX. The second part of heat input, i.e. the heat content of filler metal droplets, was assumed to be deposited at melting temperature and additional solution steps in the thermal analysis were needed to account for this.

The heat loss by free convection was modeled by Newton's cooling law. Boundary conditions were applied to all free surfaces of the component except for the successive boundaries created after each new weld pass. The surfaces exposed to the environment were subjected to the same convective boundary conditions, using a heat transfer convection coefficient of $h=30W/m^2°C$ to ambient air. The ambient temperature for both parent and weld metal was set at 20°C. The regions near the weld bead were assumed to be preheated before weld execution.

The heat input was applied by assigning each element in the weld pass an initial temperature and body flux. Subsequent cooling, as the heat conducted into the parent material and was lost through surface convection, was analysed up to 1180s, 800s and 600s time periods for the first, second and third pass onward after welding deposition. The cooling time is dependent on pipe circumference and welding speed and includes a gradual start and finish. After these times, the model was reset to an assumed interpass temperature using a steady state heat transfer step, before applying the next pass.

After the final pass has been analyzed, the model was allowed to cool down for 6000s to ambient temperature. Automatic time stepping was used for the solution of this nonlinear transient heat transfer problem.

Table1. Weld parameters used in the simulation [8,11]

Pass number	Welding method	Weld voltage (V)	Weld current (A)	Weld speed (mm/min)	Heat input (KJ/mm)
1	TIG	9 6	75-120	60	0.48
2	MMA	17.3	85-140	80	1.09
3-10	MMA	17.6	150-190	110	1.14

The tee branch junction component was assumed to be welded by tungsten inert gas arc welding (TIG) for the first pass and manual metal arc welding (MMA) for the subsequent passes. The simulation parameters, as is common industry practice as reported by Brickstad and Josefson [8] and Rybicki [11], are listed in Table 1. For the stainless steel welds considered in this study, arc efficiencies equal to 50% and 70% have been assumed for the TIG and MMA, respectively.

3 VERIFICATION

In order to check the predictions of the present analysis method, a pilot simulation to reproduce the experimental results reported by Murugan et al. [4] was performed. In the latter experiment, a low carbon steel specimen butt weld was produced using a multipass manual metal arc welding technique. The length, width and thickness of the plate used are 150mm, 282.5mm and 8mm, respectively (see Fig.4). The location of the measurement points are also indicated in Fig. 4.

Table2. Weld parameters during welding of low carbon steel 8mm thick plates [4]

Pass number	Electrode diameter (mm)	Weld voltage (V)	Weld current (A)	Weld speed (mm/s)	Heat input (KJ/mm)
1	2.5	21	65-75	1.68	0.656
2	4	24	170-180	2.88	1.094
3	4	22	175-185	2.08	1.427

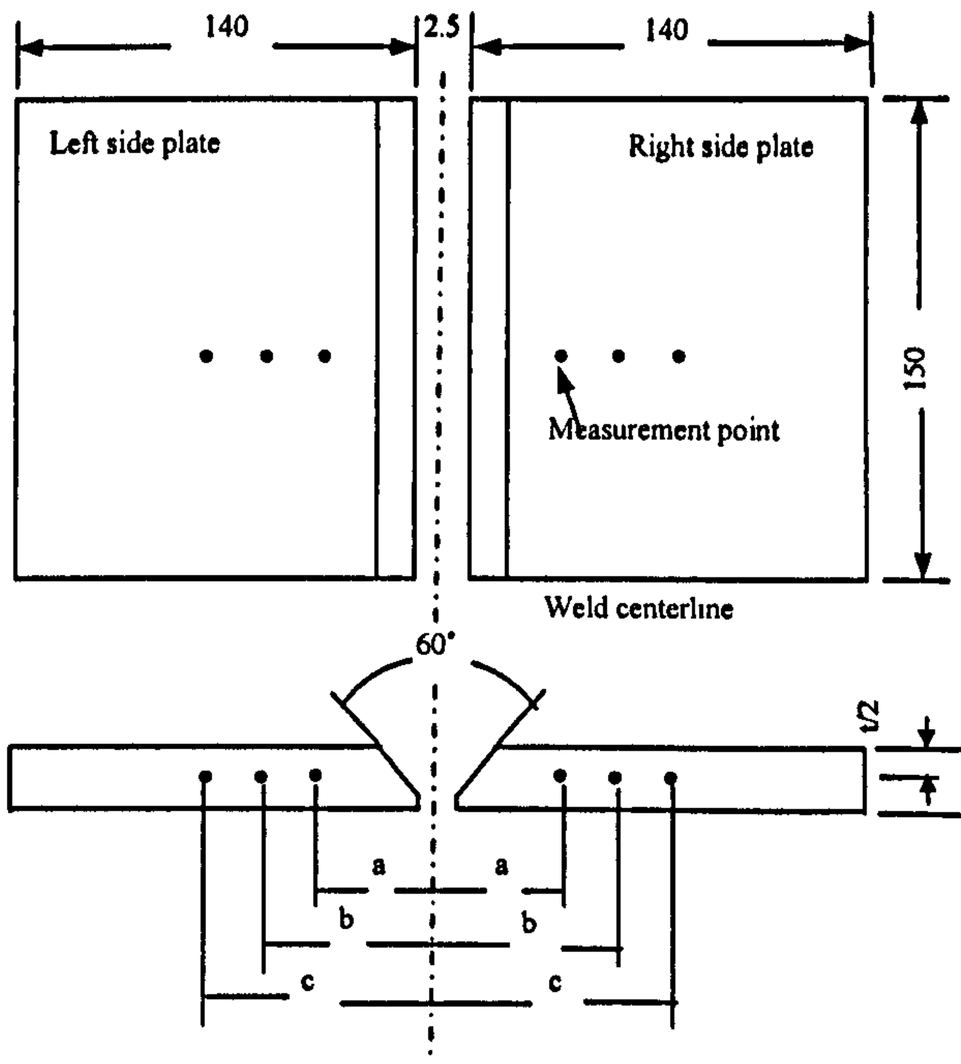

Fig.4 Dimensional details of experimental specimen [4,5]

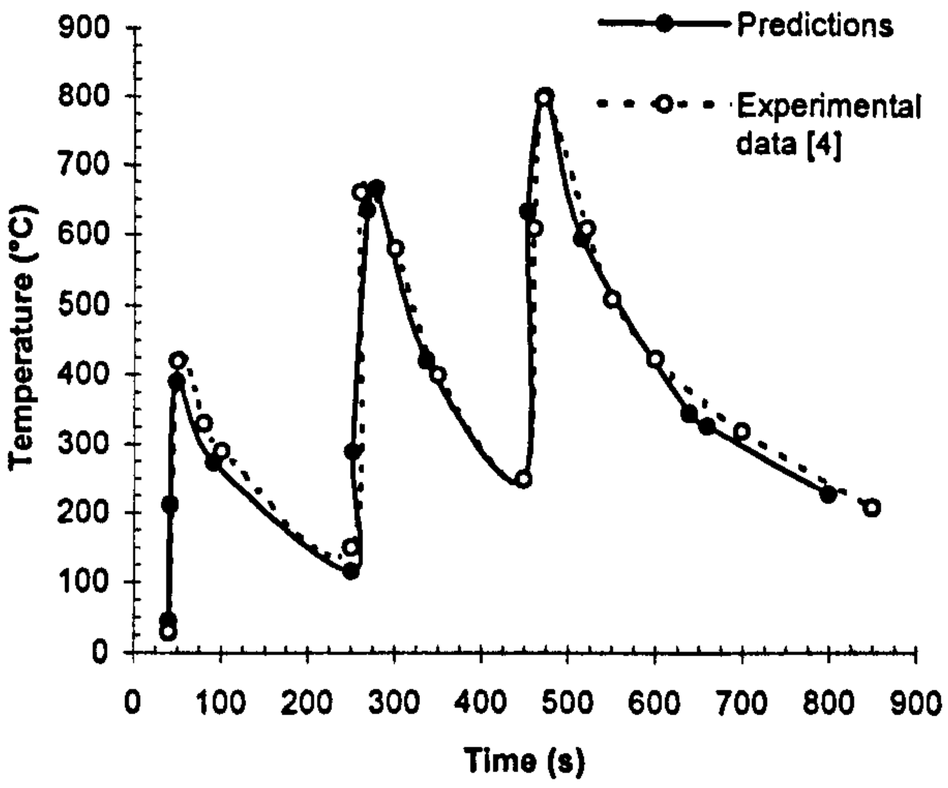

(a) Predicted v measured temperature distributions at location a (11.5mm from weld centerline)

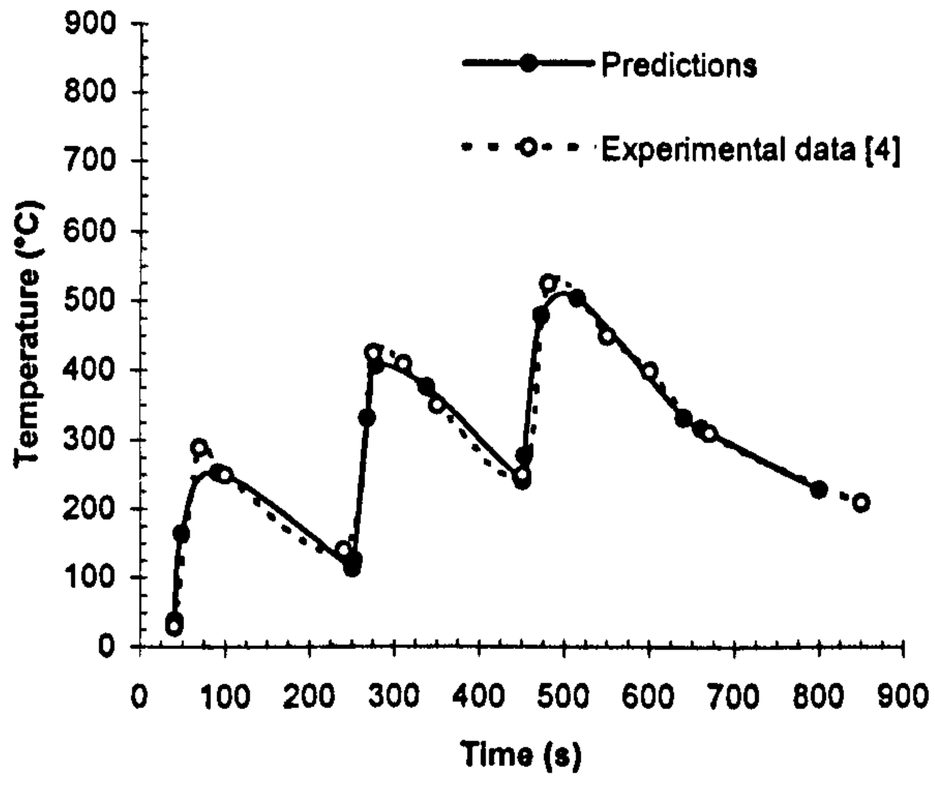

(b) Predicted v measured temperature distributions at location c (21.5mm from weld centerline)

Fig. 5 Comparison of experimental and calculated temperature distributions

For proper comparison, pass sequences and welding parameters, used in the simulation, were identical to those for the 8mm thick plate experiment, as shown in Table 2.

The calculated and measured temperature history at distance of a=11.5mm and c=21.5mm on the right side of the weld centerline are shown in Figs. 5 a-b, respectively. As the figures indicate, the temperature distribution results obtained by the present simulation method closely match those obtained experimentally. Similar comparisons are also evident for location b=16.5mm shown in Fig.4. A full description of the simulation technique and a detailed comparison with experimental data will be presented elsewhere. For the present purpose, it will suffice to conclude that in reproducing experimental results to this level of accuracy, the simulation method can be considered to be acceptable. Therefore, the procedure adopted here is considered suitable for the analysis of temperature distributions during multipass welding of tee branch junctions.

4 RESULTS AND DISCUSSION

A thorough understanding of the temperature patterns that are generated during execution of complex welds and subsequent cooling rates can give a clear insight into how welding residual stresses build up during the operation. Such understanding will help in formulating recommendations, regarding the weld execution itself, towards reducing the severity of 'as-welded' residual stress distributions.

Figure 6a shows the temperature patterns at times t=1.018s, 20.8s, 280.2s and 1180s respectively on a quarter of the model after deposition of the first pass. It can be seen from the graph that, as expected, the peak temperature and high gradient first appear in the area close to the deposited pass (t=1.018s) after which heat gradually conducts to the nearby area of both run and branch pipe (t=20.8s). At time 280.2s, which is about a quarter of the first pass welding time, a nonuniform temperature distribution can clearly be noticed in the intersection area.

The crotch area is shown to experience relatively higher temperature than that of the flank. This is explained by the fact that, while the welding parameters do not change during the process, the crotch area needs more metal deposition. Therefore more heat has been brought in at the crotch area than at flank area. At the end of the first pass, i.e. at time 1180s, the temperature distribution near the first pass area tends towards being uniform.

Figure 6b shows the temperature distribution at times t=1.042s, 20.52s, 122.4s and 600s after deposition of the fifth pass, respectively. At time 1.042s, which corresponds to the time shortly after deposition, the temperature appears to be highly localized. As time elapses, heat conducts almost uniformly to both run and branch pipe. The crotch area again shows higher temperatures than those experienced by the flank area (t=20.52s, 122.4s and 600s). Also noticeable is the heat conduction to the previously deposited passes. This confirms the intuitive expectation that both deposited weld material and heat affected zone undergo a process of thermal cycling by successive weld passes. This kind of thermal cycling will affect microstructure, mechanical properties and residual stress build up.

Figure 6c shows the temperature distribution at times t=1.052s, 20.14s, 169s and 600s after depositing of the last pass, respectively. At this stage the groove is fully filled and temperature patterns are similar to those observed at pass 5.

In summary, because of the locally concentrated heat source, high temperature and large gradients appear at the area

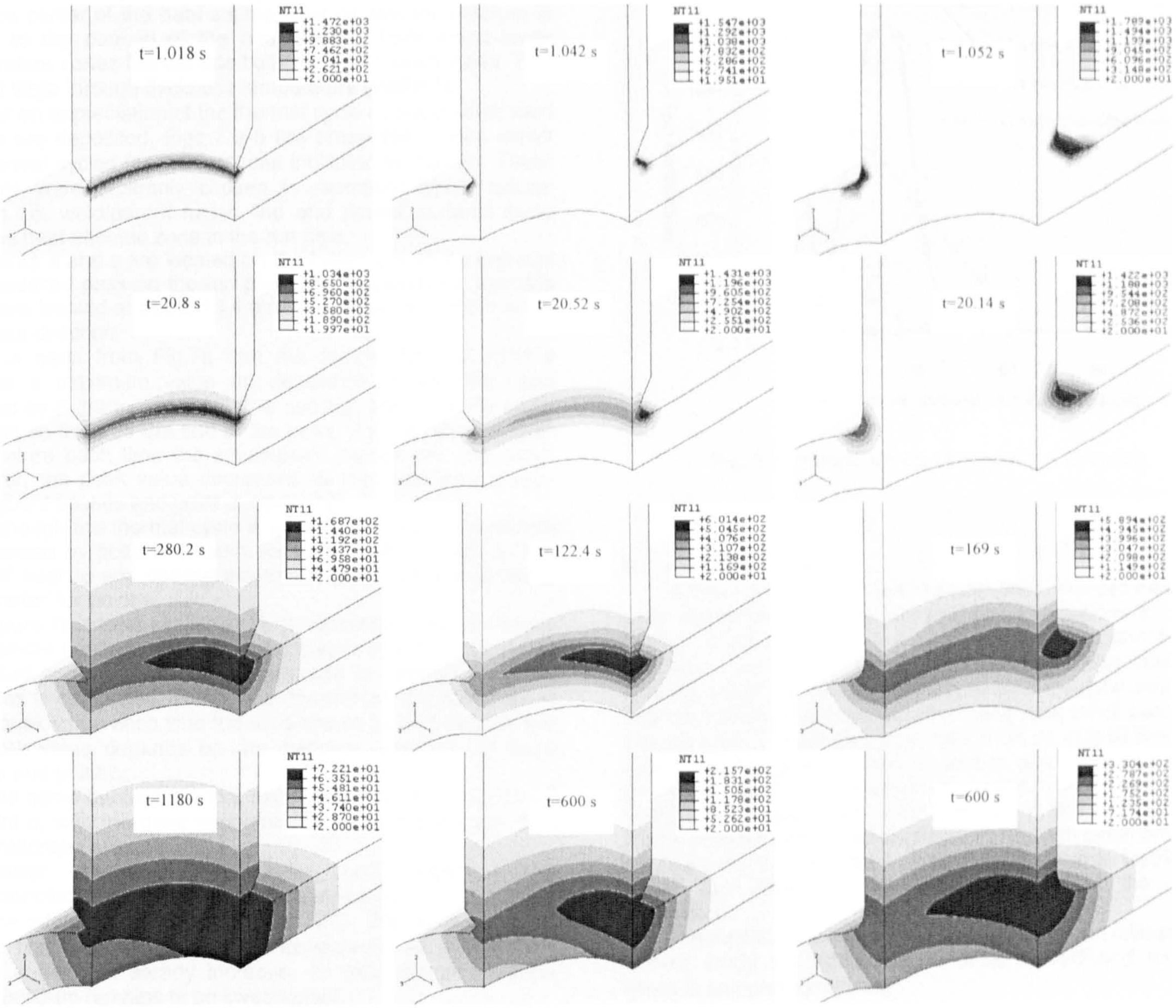

(a) (b) (c)

Fig. 6 Temperature distributions at various times after deposition of (a) pass 1,(b) pass 5 and (c) pass 10

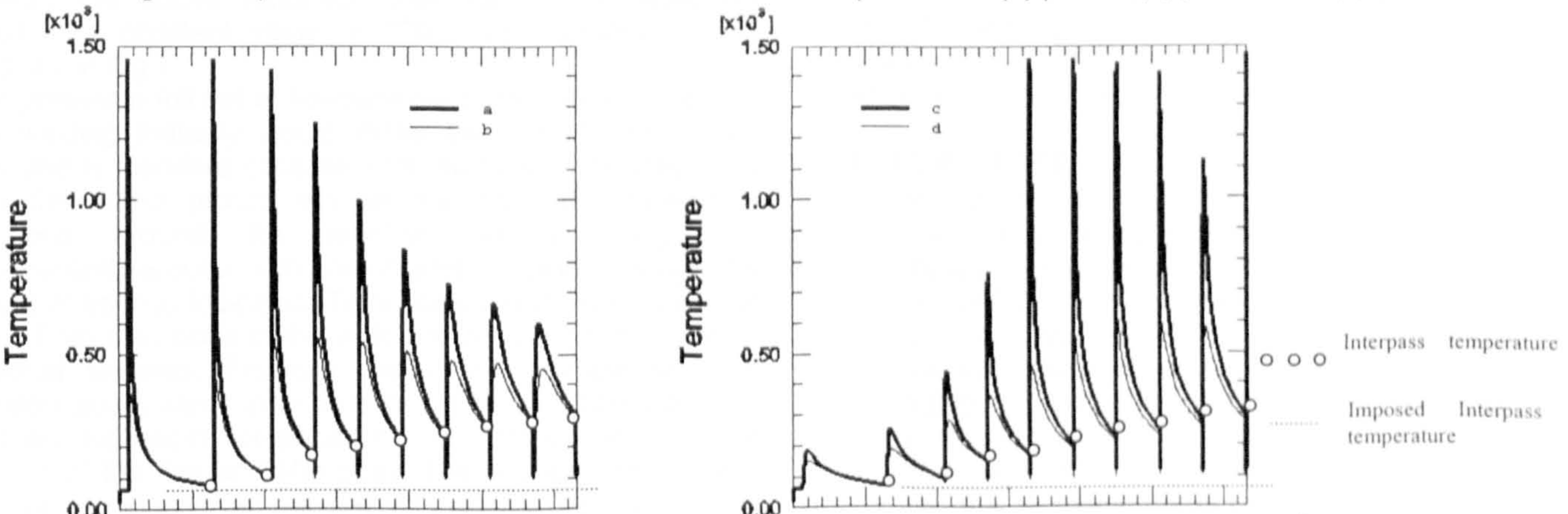

(a) Temperature cycle at point a and b

(b) Temperature cycle at point c and d

Fig. 7 Temperature cycles at various times and positions

close to individual passes and rapidly change with the distance from the center of the heat source. The highest temperature is limited to the domain of the heat source, from which lower temperature zones fan out into both run and branch pipes. This causes large through thickness temperature gradients.

For an appreciation of the thermal cycle as successive weld passes are deposited, Figs 7 a-b are presented. These depict the thermal cycles for the locations indicated in Fig. 2b. These locations were arbitrarily chosen to represent typical critical regions i.e. weld/parent fusion line and parent material away from the heat affected zone in the run pipe.

Points *a* and *c* are located on the fusion line of the first and fifth deposited pass on the run pipe side, respectively. Points *b* and *d* are located at about 15.4 mm below points *a* and *c* in the thickness direction.

It is seen from Fig.7a that the temperature at point *a* reaches a maximum value on deposition of the first pass followed by a gradual cooling. The cooling rate is initially steep and less so towards the end of the pass. Point *a* reaches peak temperature each time the subsequent passes are deposited. However, the peak value decreases as the distance between subsequent passes and point *a* increases.

Although the thermal cycle is similar, the peak temperature experienced by point *b* is much less than that at point *a*. The rates of heating and cooling are also not as high compared to those noted for point *a*.

Figure 7b shows similar plots for locations *c* and *d*. Point *c* experiences heating each time the lower numbered passes are deposited and the maximum temperature is reached when the fifth pass is completed. The temperature at point *c* continues to reach peak value each time the subsequent passes deposit and the peak value depends on the distance between individual passes and point *c*.

The same behavior as that experienced by point *b* is noted for point *d*, with the peak temperatures being much lower than those recorded at location *c*.

Similar thermal cycles have been obtained for corresponding locations on the branch pipe side.

The interpass temperatures are 72°C, 216 °C and 330 °C for the first, fifth and last pass, respectively. As expected, it shows a trend of steady increase. Its influence on residual stress build-up remains to be investigated.

In practice interpass temperatures are controlled to a certain level to provide adequate mechanical properties. In this simulation, the above reported value had to be artificially reduced to a constant value of 120°C as indicated by the dashed line in Fig.7.

To present a full set of temperature distributions of interest to the welding industry would make this contribution rather lengthy and is therefore considered to be beyond its scope. To convey the whole picture will require plots of temperature distributions around the weldline, axially along and circumferentially around both branch and run pipes through the thickness at various locations. Temperature distributions versus distance from the center of the weld are critical to the formation of residual stresses. Figure 8 shows an example of such distribution axially along the fusion line in the run pipe side. The solid lines represent temperature vs. distance at 1s after deposition of the first and fifth pass. The dashed lines display the above relationship at 25s and 41s after completion of the first and fifth pass, respectively. The locations of the origin and coordinate system are shown in Fig.2c. It is observed that peak temperature and HAZ move along the X direction as welding progresses. Each point on the fusion line experiences complex heating and cooling cycles which determine the build-up of residual stresses.

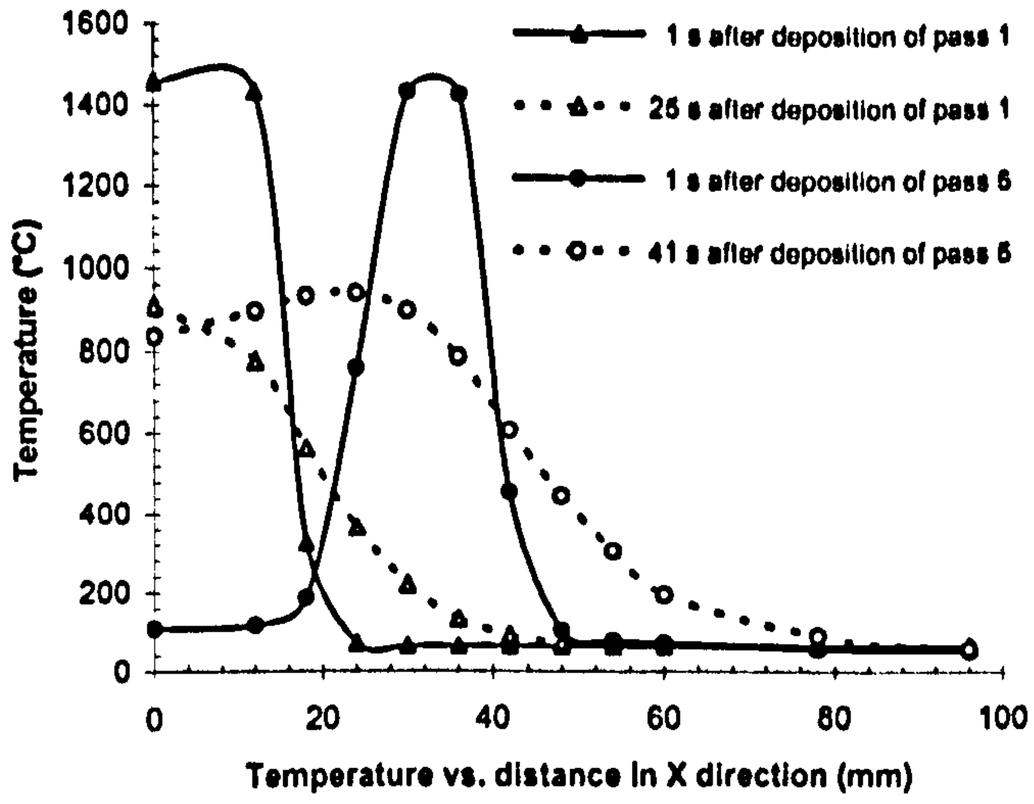

Fig. 8 Temperature vs. distance in X direction

5 CONCLUSIONS

A three-dimensional heat transfer finite element model has been developed to study temperature distributions in a thick walled, stainless steel tee branch junction component during multipass welding process. Nonlinearities associated with welding, such as temperature dependent material properties, heat loss through convection and latent heat have been taken into account. The temperature distribution at various times after deposition of a given number of passes and the thermal cycles at various locations are reported. These results are not only useful for estimating the likely changes in the microstructure, phase transformation and degradation in mechanical properties but also for the assessment of residual stress distributions which can affect the in-service behavior of the welded connection.

The meshing technique and modeling method utilized in the current study are applicable to other curved and multipass welds in complex structures.

ACKNOWLEDGEMENTS

The lead author acknowledges financial support, in the form of a studentship, by the School of Engineering and the Built Environment of the University of Wolverhampton. The authors would also like to thank Steve Boyle for his technical assistance.

REFERENCES

1. Rosenthal, D., 1941, Mathematical theory of heat distribution during welding and cutting, Welding Journal Research Supplement, 20(5), pp.220-234.
2. Rybicki, E. F., Schmueser, D. W., Stonesifer, R. B., Groom, J. J. and Mishler, H.W., 1978, A finite element model for residual stresses and deflections in girth-butt welded pipes, ASME Journal of Pressure Vessel Technology, 100(10), pp. 256-262.
3. Rybicki, E. F. and Stonesifer, R. B., 1979, Computation of residual stresses due to multipass welds in piping systems, ASME Journal of Pressure Vessel Technology, 101(5), pp.149-154.
4. Murugan, S., Kumar, P.V., Raj, B. and Bose, M.S.C., 1998, Temperature distribution during multipass welding of plates, International Journal of Pressure Vessels and Piping, 75, pp.891-905.
5. Murugan, S., Rai, S.K., Kumar, P.V., Jayakumar, T., RAJ, B.

and Bose, M.S.C., 2001, Temperature distribution and residual stresses due to multipass welding in type 304 stainless steel and low carbon steel weld pads, International Journal of Pressure Vessels and Piping, 78, pp.307-317.
6. Mackerle,J., 1996, Finite element analysis and simulation of welding: a bibliography (1976-1996), Modelling and Simulation in Materials Science and Engineering, 4, pp.501-533.
7. Scaramangas, A., 1984, Residual stresses in girth butt-welded pipes, Technical report no. CUED/D-struct/TR107, Department of Engineering, Cambridge University.
8. Brickstad, B. and Josefson, B. L., 1998, A parametric study of residual stresses in multi-pass butt-welded stainless steel pipes, International Journal of Pressure Vessels and Piping, 75, pp. 11-25.
9. Wen, S.W., Hilton, P. and Farrugia, D.C.J., 2001, Finite element modeling of residual stress in pipe welds, Strain, Journal of the BSSM, 37(1), pp.15-18.
10. ABAQUS. User's Manual 6.3 ,2002, Hibbitt, Karlsson and Sorensen, Inc.
11. Rybicki, E.F., McGuire, P.A., Merrick, E. and Wert, J., 1982, The effect of pipe thickness on residual stresses due to girth welds, ASME Journal of Pressure Vessel Technology, 104, pp. 204-209.
12. Dong, P., 2001, Residual stress analysis of a multipass girth weld: 3D special shell versus axisymmetric models, Journal of Pressure Vessel Technology, 123(2), pp.207-213.

COMPARISON OF SEQUENTIALLY AND FULLY COUPLED GENERALIZED PLANE STRAIN FE MODELLING OF MULTIPASS WELDING

Wei Jiang, Kadda Yahiaoui, Frank R. Hall, Tahar Laoui

RIATec, School of Engineering and the Built Environment

University of Wolverhampton, Telford Campus

Telford, TF2 9NT, UK

SUMMARY

Multipass welding is a reliable and effective method for permanently joining thick metal components. However, this process inevitably induces complex residual stresses, which can have adverse effects on the in-service performance of weldments. It is thus desirable to predict residual stress distributions well before welding execution.

Welding simulation is a multi-physics problem that is often assumed to involve the coupling between the thermal and mechanical fields. In this work, two kinds of finite element models, sequentially and fully coupled thermo-mechanical generalized plane strain models, have been developed to investigate the residual stress distribution in a thick multipass welded plate. Element removal/reactivation technique had been used to simulate the filler metal deposition. Material, geometry and boundary nonlinearities associated with welding were taken into account.

The predicted residual stress results from the two models did not differ much and both compared well with existing experimental data. However, in terms of computer resources, it was found that the sequentially coupled thermo-mechanical model required less computational time and disk storage than the fully coupled model.

These results indicate that the coupling between the thermal and mechanical fields in welding is rather weak and consequently the cheaper method, which involves sequential coupling, is recommended when simulating welding processes of the type reported here. Recently completed work indicate that the latter conclusion also applies for the case of 3D models.

COMPARISON OF SEQUENTIALLY AND FULLY COUPLED GENERALIZED PLANE STRAIN FE MODELLING OF MULTIPASS WELDING

1: Introduction

Multipass welding is a reliable and effective method for permanently joining thick metal components. However, due to the characteristic of intense heat concentration, the weld region undergoes severe thermal cycles during the process, which cause non-uniform plastic deformations and residual stresses in the weldment. These stresses can have adverse effects on the in-service performance of weldments. It is thus very desirable to be able to predict the residual stress distributions before welding execution.

Welding residual stress prediction is a multi-physics problem that involves coupling between the thermal and mechanical fields. This coupling is realised firstly by temperature dependent material properties, latent heat and thermal expansion related to the temperature difference at a given time interval and secondly by heat generated by plastic deformation. The thermal expansion, along with the sharp decrease in the mechanical properties during heating induces plasticity, yields non-homogeneous permanent strains and residual stresses after welding.

In order to ultimately determine the residual stresses in the weldment, this thermo-mechanical problem requires solutions to the thermal problem as well as to the mechanical problem. Two kinds of finite element models can be used to predict welding residual stress distribution: sequentially or fully coupled thermo-mechanical models.

The sequentially coupled thermo-mechanical analysis is conducted when the stress solution is dependent on a temperature field but there is no inverse dependency. It is performed by first solving the pure heat transfer problem, then reading the temperature solution into a stress analysis as a predefined field. Most of the early studies on multipass welding simulation were based on two-dimensional sequentially coupled models. Free and Porter [1] used a 2D sequentially coupled thermo-mechanical plane strain model. However, as the plane strain elements could not accommodate any thermal expansion in the welding direction, other researchers [2-3] favoured instead the use of generalized plane strain elements, which dramatically improved the predicted results.

COMPARISON OF SEQUENTIALLY AND FULLY COUPLED GENERALIZED PLANE STRAIN FE MODELLING OF MULTIPASS WELDING

The fully coupled thermo-mechanical procedure is used to solve simultaneously for the stress, displacement and the temperature fields. It is usually used when the thermal and mechanical solutions strongly affect each other. During the welding process, the temperature field is thermodynamically coupled with the mechanical field because of the heat generated by plastic energy dissipation. Although the heat due to elasto-visco-plastic straining can be considered to be small compared to the energy input during the welding process and is often ignored by many researchers, it is still necessary to investigate how much this coupling phenomenon will affect the residual stresses in order to gain more accurate knowledge of this multidisciplinary problem.

Therefore, the purpose of the present study is to develop and assess sequentially and fully coupled thermo-mechanical FE models in predicting residual stress built-up during multipass welding. Element removal/reactivation technique was used to simulate the filler metal deposition. Nonlinearities, including nonlinear material properties, large deformations and nonlinear boundary conditions were taken into account simultaneously. The accuracy and efficiency of these two models were evaluated both on the basis of comparison of residual stress prediction with experimental measurement and on comparison of computational time and disk storage requirement with each other. It was found that both models gave results that agreed well with the experimental data. On the other hand, and as suspected, the sequentially coupled thermo-mechanical model required less computational time and disk space than the fully coupled model.

2: Modelling

2.1 Geometry and mesh

For proper comparison with existing experimental data, the geometry, dimensions and welding parameters used in the simulation were identical to those reported by Shim [4]. ASTM A36, 25.4 mm thick, butt-welded plate was chosen for the validation and assessment of the sequentially and fully coupled thermo-mechanical models developed in this study. In both models, the same lumping scheme was used to reduce the computational cost. A total of 11 passes were lumped into 6 passes in a double V-groove thick plate. Heat flux for each pass in the same layer were added and distributed over the whole area of that layer.

Since the butt-welded plate is symmetrical about the plane passing through the weld centreline, only half of the plate was considered. Small size elements were chosen for the region with high temperature and stress gradients. Away from the

weld centreline, the element sizes were increased to reduce the total number of elements in the model. Exactly the same meshes were used for both the sequentially and fully coupled models. The meshes for the heat transfer analysis and the stress analysis in the sequentially coupled generalized plane strain model were also the same, as shown in Fig. 1.

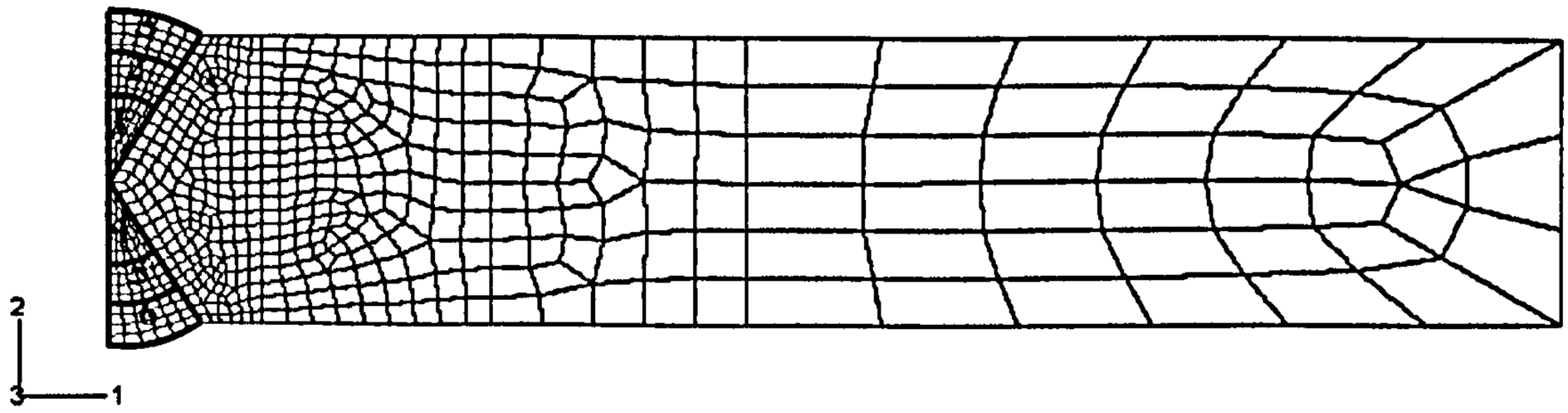

Figure 1: Finite element mesh

In the thermal model of the sequentially coupled model, 591 four-noded linear quadrilateral diffusive heat transfer elements (DC2D4) and a three-noded linear triangle heat transfer element (DC2D3) from the ABAQUS library were used [5]. In the mechanical model, the plane perpendicular to the direction of the weld was analysed as a generalized plane strain condition. The model consisted of 591 four-noded bilinear quadrilateral generalized plane strain elements (CPEG4) and a three-noded linear triangle generalized plane strain element (CPEG3).

In the fully coupled model, the plane perpendicular to the direction of the weld was also analysed as a generalized plane strain condition. It consisted again 641 nodes and 591 four-noded coupled temperature-displacement generalized plane strain bilinear quadrilateral elements (CPEG4T) and a three-noded coupled temperature-displacement generalized plane strain linear triangle element (CPEG3T) with full integration.

2.2 Material Properties

Temperature dependent thermal and mechanical properties were defined in the thermal and structural models respectively in the 2D sequentially coupled model. Latent heat effects were assigned a value of 247 kJ/kg between the solidus temperature of 1465°C and the liquidus temperature of 1544 °C in the thermal model [6].

Both the thermal and mechanical properties were defined in the fully coupled thermo-mechanical model. Exactly the same material properties were used in both models, as shown in Fig.2.

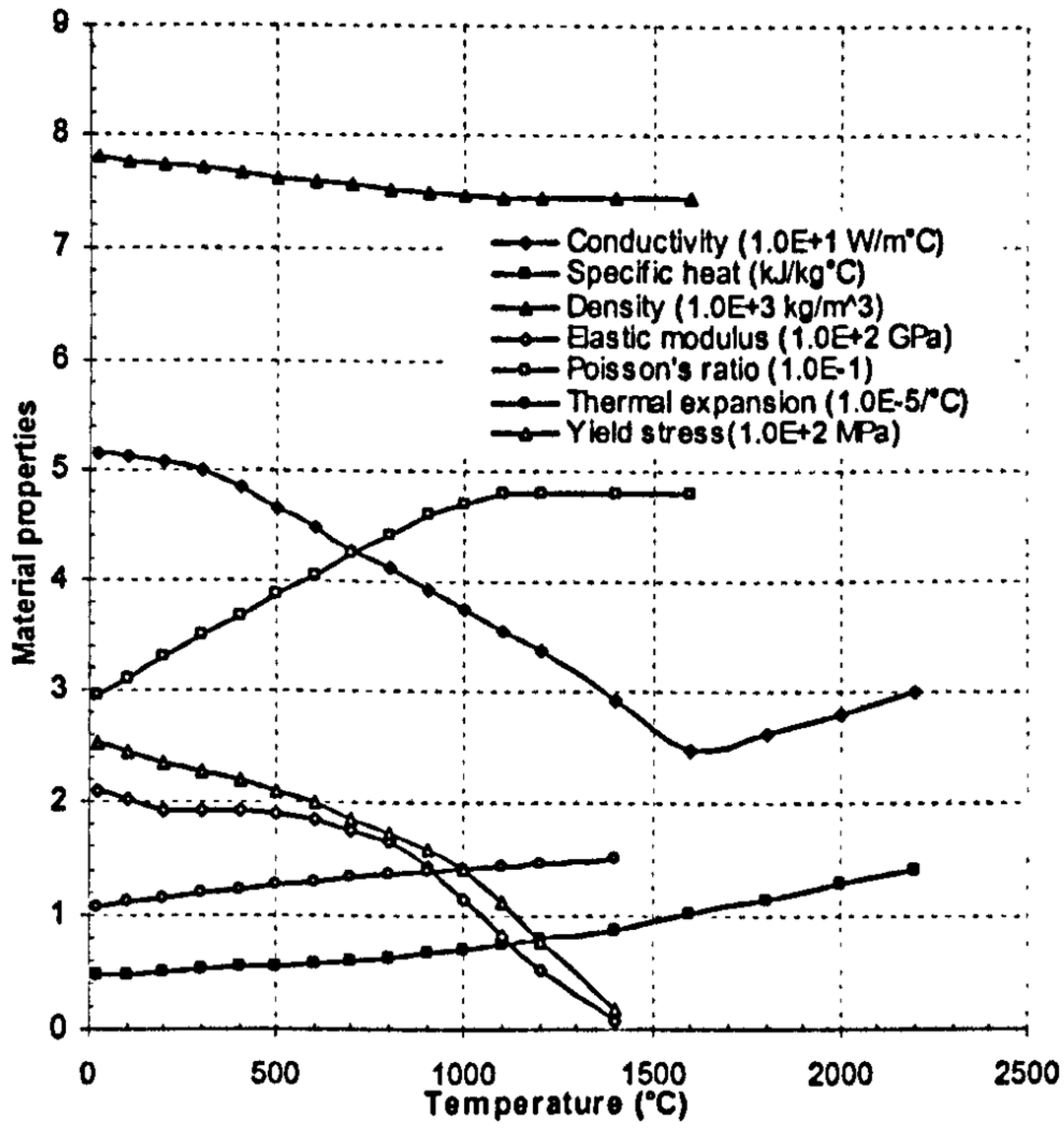

Figure 2: Material properties of ASTM A36 [4,7]

2.3 Boundary conditions

The heat loss by free convection was modelled by Newton's cooling law. The convection was applied to all element edges representing the free surfaces boundary using the *SFILM option to define the sink temperature and the film coefficient. A heat transfer coefficient of 30W/m^2°C was assumed for all surfaces, based on the surface heat transfer predictions by Simonson [8]. The ambient temperature for both parent and weld metal was set at 25°C. It was also assumed that the symmetry plane was impermeable to heat. The plate cross section used in the analysis was insulated on both sides in the Z direction.

Symmetry boundary conditions were imposed along the weld centreline since only half of the component was analysed. To simulate the free boundary condition in the experiment, only one node under the root of the first pass was constrained in the Y direction to prevent rigid body motion.

In ABAQUS, there are two additional degrees of freedom associated with generalized plane strain elements. The first defines the rotation of an imaginary

XY plane that is offset in the Z direction. This was restrained at a reference node. The second refers to the displacement of this plane in the Z direction. For generalized plane strain, this freedom remained in effect.

2.4 Analysis procedures

In the thermal model of the sequentially coupled thermo-mechanical analysis, two types of heat input were considered. One was the heat flux and the other was the heat content of filler metal droplets. The first part of heat input was arranged as an area of elements with specified heat flux. This heat input was imposed onto the specified newly activated elements representing a deposited pass at any given time. The heat flux was uniformly distributed over the area of each weld droplet. The second part of heat input, i.e. the heat content of filler metal droplets, was assumed to be deposited at melting temperature and additional solution steps were needed in the thermal analysis to account for this. After the final pass was analysed, the model was allowed to cool down for 1800 seconds.

The same mesh and step time period were used for both the heat transfer and the stress analysis. During the welding process, the temperature field changes with time as the heat source moves and the material properties change with temperature. When the temperature rises towards melting point, the yield strength decreases significantly, i.e. the elastic range is drastically reduced and plasticity initiates sooner. This requires a nonlinear transient thermo-elasto-plastic analysis. In the stress model, thermo-elasto-plastic constitutive formulation, together with the Von Mises yield criterion and the associated flow rule were used. Linear isotropic hardening was assumed. Creep strains were not included in the stress analysis because the time spent at high temperature was deemed to be very short.

The ABAQUS element removal/reactivation technique has been employed. The fusion zone elements were incrementally activated in strain-free states to model the continuous deposition of filler material. Geometric nonlinearity caused by large deformations was considered. The essential factors when calculating residual stresses introduced by thermal strains in welds are the effects of temperature and the thermal history on the mechanical properties. These temperature histories were obtained from the thermal analysis and were used as thermal loading for the structural model to calculate thermal strains and stresses for each time increment. The thermal strains and stresses were accumulated to produce the final state of residual stresses.

In the fully coupled thermo-mechanical analysis, the thermal and stress solutions were obtained simultaneously rather than sequentially. Simultaneous temperature/displacement solutions required the use of elements that have both displacements and temperatures as nodal variables. In using element removal/reactivation in the fully coupled thermo-mechanical analysis, continuum elements appear to reach their full mechanical stiffness immediately after strain-free reactivation; however, to ensure smoothness of the solution, the thermal conductivity was ramped up from zero over the step.

Combined nonlinearities due to large displacement effects, temperature dependent material properties, and boundary nonlinearities were considered in both models. ABAQUS uses Newton's method to solve the nonlinear equilibrium equations. Since the problem involves history-dependent response, the solution is obtained as a series of increments, with iterations to obtain equilibrium within each increment. The initial time increments were suggested as 0.0001s in each step. Time incrementations in both analyses were controlled automatically by keeping the largest temperature change at every integration point less than 100 °C. Default convergence criteria were used in both models.

3: Welding parameters and configurations

The butt-welded plates from Shim's paper [4] were chosen for the validation of the current 2D FE plate model. Two ASTM A36 mild steel plates of thickness 25.4 mm with a double-V-groove were welded by gas metal arc welding process (GMAW) during the experiments. The component was fabricated by 11 passes. The welding parameters are shown in Table 1. An arc efficiency of 0.85 was chosen as was reported in [4]. Free boundary conditions were applied to all free surfaces. The blind hole-drilling method was used to experimentally determine the surface residual stresses in the weldment.

Table 1: Parameters for welding 25.4mm thick ASTM A36 carbon steel plates [4]

Pass number	Weld voltage (V)	Weld current (A)	Weld speed (mm/s)	Heat input (kJ/mm)
1	25	190	3.34	1.21
2-5	26	215	4.7	1.01
6	25	190	3.34	1.21
7-9	26	220	4.7	1.03
10-11	27	250	4.7	1.22

4: Results and discussion

4.1 Thermal results

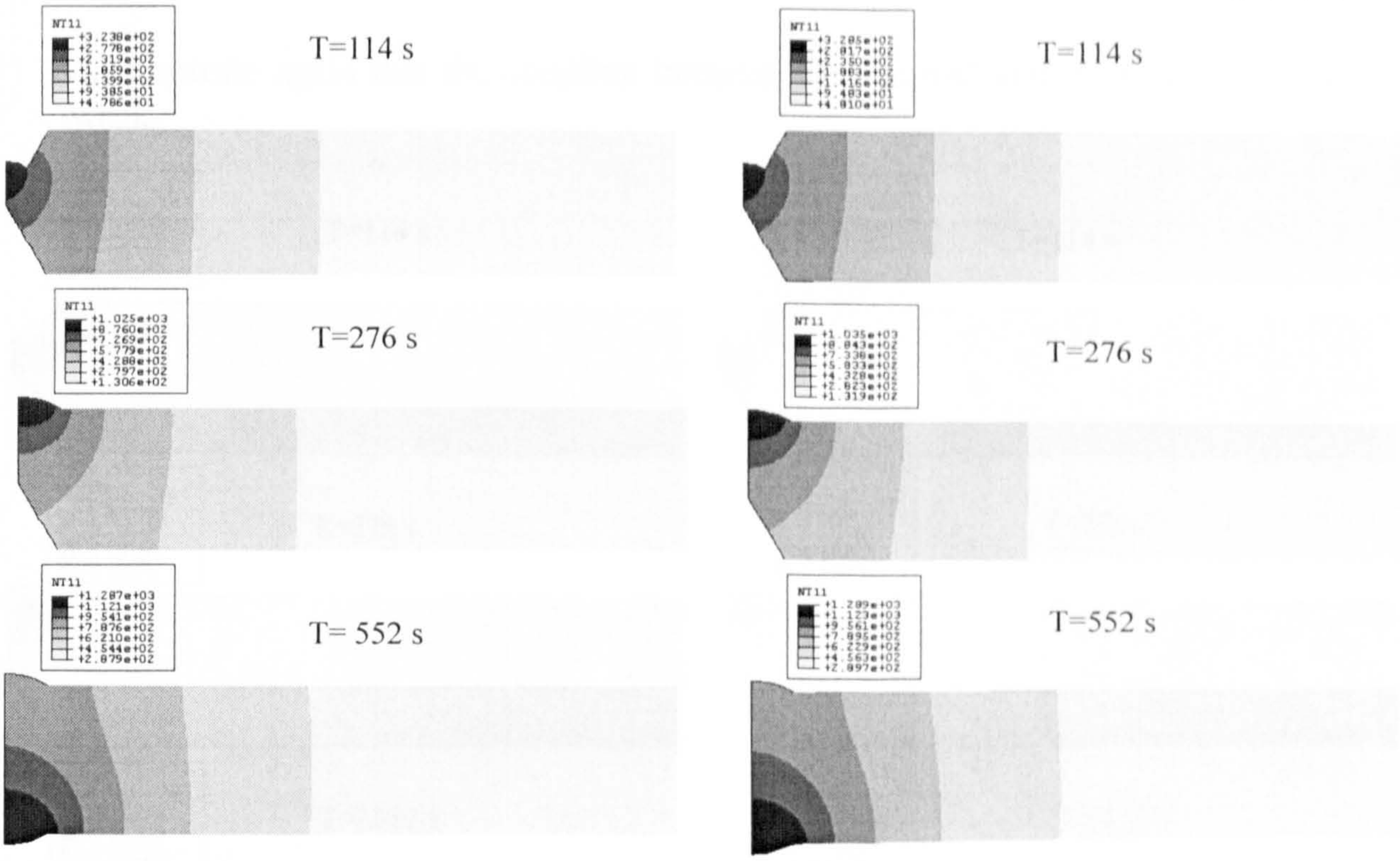

(a) Sequentially coupled model (b) Fully coupled model

Figure 3: Temperature distributions at times after deposition of pass1, pass3 and pass6

Figure 3 shows temperature distributions predicted by the two models at times after deposition of pass1, pass3 and pass6. Both models exhibit similar temperature distribution patterns, with the fully coupled model predictions being about 1-2% higher than those of the sequentially coupled model. These slight differences indicate that the fully coupled model has taken into account the heat generated by straining and at the same time show that the coupling is quite weak.

4.2 Stress results

Figure 4 shows the longitudinal thermal stress distribution predicted by the two models at times after deposition of pass1, pass3 and the final residual stress distribution. It is noticed that both models predicted similar thermal stress and residual stress distribution patterns and almost the same stress values at various welding stages.

Figure 5 shows the longitudinal residual stresses predicted by the sequentially and fully coupled models at the top surface of the midsection of the plate. The experimental measurements by Shim [4] are also included for comparison. The agreement with experimental data is rather good for both models. These results

demonstrate again that the coupling between the thermal and stress field is very weak.

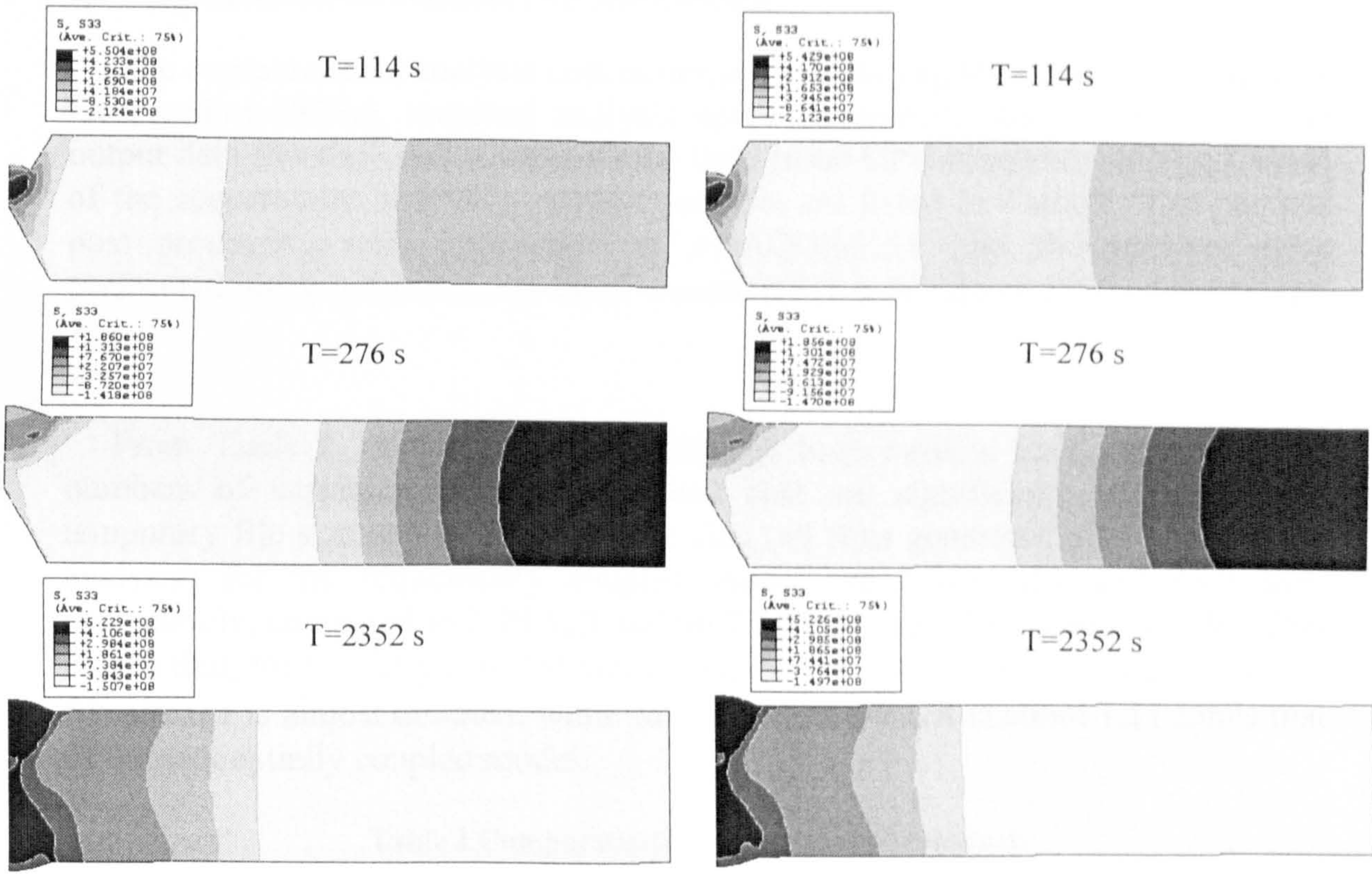

(a) Sequentially coupled model (b) Fully coupled model

Figure 4: Longitudinal thermal stress distributions at times after deposition of pass1, pass3 and the final residual stress distribution

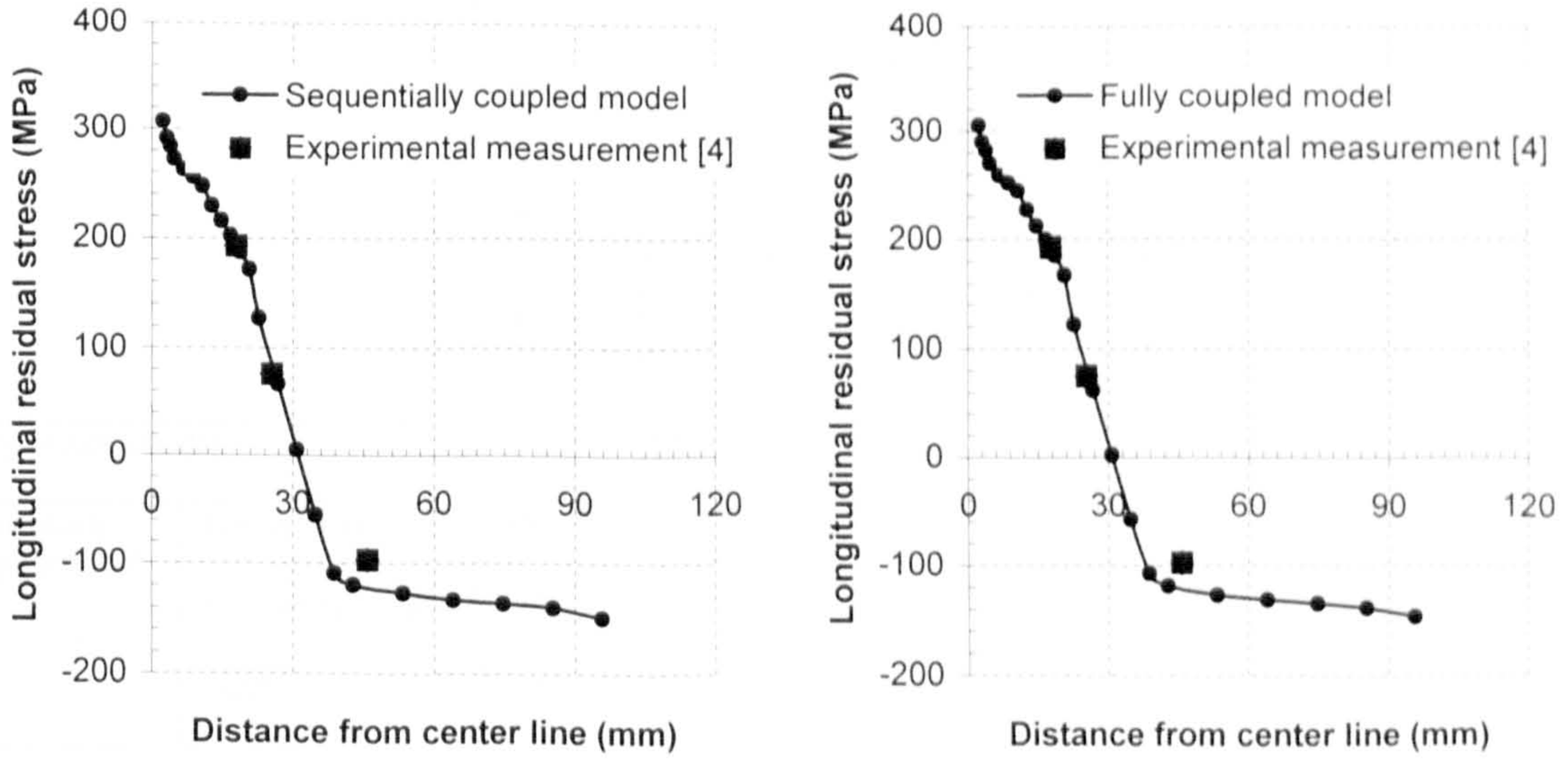

(a) Sequentially coupled model (b) Fully coupled model

Figure 5: Comparison of predicted residual stress with experimental measurement

4.3 Computational analysis cost comparison

The computational analysis cost parameters, including the model size (Degrees Of Freedom-DOFs), required analysis space (temporary analysis file size and output data file size) and computational time (total CPU time and wallclock time) of the sequentially and fully coupled models, are listed in Table.2. The pre and post processing were performed on ABAQUS/CAE and the analyses were performed using ABAQUS/Standard version 6.3 in a Windows 2000 environment.

From Table 2, it is noticed that although both models have the same total numbers of variables, the computational cost are significantly different. The temporary file size and total output file size (all files generated after running the analysis) for the sequentially coupled model are 1.375 MB and 86.9 MB, respectively, compared to 2.79 MB and 96.7 MB for the fully coupled model. This means that, for the fully coupled model, the disk space required for the temporary file storage is almost doubled, while for the output data, it is about 1.11 times that of the sequentially coupled model.

Table 2 Computational analysis cost parameters

		Number of model DOFs	Input file size (Kb)	Temporary analysis file size (Mb)	Output file size (Total) (Mb)	Analysis increments	Analysis iterations	User input processing wallclock time (s)	Total CPU time (s)	Wallclock time (s)
Fully coupled model		1923	50	2.79	96.7	369	1038	5	378.6	1029
Sequentially coupled model	Thermal model	640	45	0.175	22.8	385	1161	4	66.4	285
	Mechanical model	1283	47	1.2	64.1	304	726	13	147.1	469
	Total	1923	92	1.375	86.9	–	–	17	213.5	754

Although the times listed in Table 2 may differ from computer to computer, depending on the speed of the processor and the memory available, they did give relative values for comparison. It is noticed that the wallclock time for the user input processing was 17 seconds for the sequentially coupled model, significantly

higher than the time of 5 seconds for the fully coupled model. This time was mainly spent in reading the thermal history from the .fil file. When dealing with 3D sequentially coupled models that involve many more steps, the total numbers of increments can be very high, which means that considerable amount of time will be spent in reading data from the thermal analysis results file.

The total CPU time and wallclock time for the sequentially coupled analysis was 214 seconds and 754 seconds, respectively compared to 379 seconds and 1029 seconds for the fully coupled analysis. This shows that reductions of 44% and 27% in total CPU time and wallclock time, respectively, for the sequentially coupled model.

5: Conclusions

Two FE models to investigate the sequentially and fully coupled modelling techniques in thick-plate, multipass welding simulation have been developed. The element removal/reactivation technique has been used to simulate the filler metal deposition. Combined nonlinearities, including temperature dependent material properties, latent heat, large deformation and nonlinear boundary conditions, were also taken into account.

In comparing results, it was observed that the thermal and stress history and the longitudinal residual stress distributions predicted by both techniques did not differ much and the residual stresses obtained by both models compared well with independent experimental data.

However, in terms of computer resources, although the time spent on the user input processing for the sequentially coupled model is more than that for the fully coupled model, this time is only a small percentage of the total computational time. Overall, the sequentially coupled thermo-mechanical generalized plane strain model required less computational time and disk space than the fully coupled model.

These results indicate that the coupling between the thermal and mechanical fields in welding is rather weak and consequently the simpler and cheaper method, which involves sequential coupling, is recommended when simulating multipass

welding processes of the type reported here. Recently completed work indicate that the conclusion also applies for the case of 3D models.

ACKNOWLEDGEMENTS

The lead author acknowledges financial support, in the form of a studentship, by the School of Engineering and the Built Environment of the University of Wolverhampton. The authors would also like to thank Steve Boyle for his technical assistance.

REFERENCES

1. FREE, A. and PORTER GOFF, R.F.D.- Predicting residual stresses in multi-pass weldments with the finite element method, Computers & Structures, 32(2), pp. 365-378, 1989.

2. LEUNG, C.K. and PICK, R.J. - Finite element analysis of a multipass weld, Welding Research Council Bulletin, 356, pp.11–33, 1990.

3. LINDGREN, L-E., RUNNEMALM, H. and NÌSSTRÎM, M.O. - Numerical and experimental investigation of multipass welding of a thick plate, International Journal for Numerical Methods in Engineering, 44(9), pp.1301-1316, 1999.

4. SHIM, Y., FENG, Z., LEE, S., KIM, D., JAEGER, J., PAPRITAN, J.C. and TSAI, C.L. - Determination of residual stresses in thick-section weldments, Welding Journal, 71 (9), pp. 305-312, 1992.

5. ABAQUS User's Manual, Version 6.3, Hibbitt, Karlsson and Sorensen, Inc., 2002.

6. RAYMOND, L.O. and CHIPMAN, J. - Thermodynamic functions of iron, Transactions of the metallurgical society of ĂIME, 239, pp. 630-633, 1967.

7. ASM International Handbook Committee - Metals Handbook, 10th edition, Materials Park, Ohio, 1990.

8. J.R. SIMONSON - Engineering heat transfer, Macmillan, New York, 1972.